CHANNEL MODULATION IN NEURODEGENERATION AND NEUROPROTECTION

EDITED BY: Jacques Joubert, Sarel Francois Malan and
Werner J. Geldenhuys
PUBLISHED IN: Frontiers in Pharmacology

frontiers Research Topics

Frontiers eBook Copyright Statement

The copyright in the text of individual articles in this eBook is the property of their respective authors or their respective institutions or funders. The copyright in graphics and images within each article may be subject to copyright of other parties. In both cases this is subject to a license granted to Frontiers.

The compilation of articles constituting this eBook is the property of Frontiers.

Each article within this eBook, and the eBook itself, are published under the most recent version of the Creative Commons CC-BY licence. The version current at the date of publication of this eBook is CC-BY 4.0. If the CC-BY licence is updated, the licence granted by Frontiers is automatically updated to the new version.

When exercising any right under the CC-BY licence, Frontiers must be attributed as the original publisher of the article or eBook, as applicable.

Authors have the responsibility of ensuring that any graphics or other materials which are the property of others may be included in the CC-BY licence, but this should be checked before relying on the CC-BY licence to reproduce those materials. Any copyright notices relating to those materials must be complied with.

Copyright and source acknowledgement notices may not be removed and must be displayed in any copy, derivative work or partial copy which includes the elements in question.

All copyright, and all rights therein, are protected by national and international copyright laws. The above represents a summary only. For further information please read Frontiers' Conditions for Website Use and Copyright Statement, and the applicable CC-BY licence.

ISSN 1664-8714
ISBN 978-2-88974-915-7
DOI 10.3389/978-2-88974-915-7

About Frontiers

Frontiers is more than just an open-access publisher of scholarly articles: it is a pioneering approach to the world of academia, radically improving the way scholarly research is managed. The grand vision of Frontiers is a world where all people have an equal opportunity to seek, share and generate knowledge. Frontiers provides immediate and permanent online open access to all its publications, but this alone is not enough to realize our grand goals.

Frontiers Journal Series

The Frontiers Journal Series is a multi-tier and interdisciplinary set of open-access, online journals, promising a paradigm shift from the current review, selection and dissemination processes in academic publishing. All Frontiers journals are driven by researchers for researchers; therefore, they constitute a service to the scholarly community. At the same time, the Frontiers Journal Series operates on a revolutionary invention, the tiered publishing system, initially addressing specific communities of scholars, and gradually climbing up to broader public understanding, thus serving the interests of the lay society, too.

Dedication to Quality

Each Frontiers article is a landmark of the highest quality, thanks to genuinely collaborative interactions between authors and review editors, who include some of the world's best academicians. Research must be certified by peers before entering a stream of knowledge that may eventually reach the public - and shape society; therefore, Frontiers only applies the most rigorous and unbiased reviews.
Frontiers revolutionizes research publishing by freely delivering the most outstanding research, evaluated with no bias from both the academic and social point of view. By applying the most advanced information technologies, Frontiers is catapulting scholarly publishing into a new generation.

What are Frontiers Research Topics?

Frontiers Research Topics are very popular trademarks of the Frontiers Journals Series: they are collections of at least ten articles, all centered on a particular subject. With their unique mix of varied contributions from Original Research to Review Articles, Frontiers Research Topics unify the most influential researchers, the latest key findings and historical advances in a hot research area! Find out more on how to host your own Frontiers Research Topic or contribute to one as an author by contacting the Frontiers Editorial Office: frontiersin.org/about/contact

CHANNEL MODULATION IN NEURODEGENERATION AND NEUROPROTECTION

Topic Editors:
Jacques Joubert, University of the Western Cape, South Africa
Sarel Francois Malan, University of the Western Cape, South Africa
Werner J. Geldenhuys, West Virginia University, United States

Citation: Joubert, J., Malan, S. F., Geldenhuys, W. J., eds. (2022). Channel Modulation in Neurodegeneration and Neuroprotection.
Lausanne: Frontiers Media SA. doi: 10.3389/978-2-88974-915-7

Table of Contents

frontiers
in Pharmacology

EDITORIAL
published: 23 March 2022
doi: 10.3389/fphar.2022.872103

Editorial: Channel Modulation in Neurodegeneration and Neuroprotection

Jacques Joubert[1]*, *Sarel F. Malan*[1] *and Werner J. Geldenhuys*[2]

[1]Pharmaceutical Sciences, School of Pharmacy, University of the Western Cape, Bellville, South Africa, [2]Department of Pharmaceutical Science, School of Pharmacy, West Virginia University, Morgantown, WV, United States

Keywords: ion channels, neurological disorders, channelopathies, electrophysiology, neuropharmacology

Editorial on the Research Topic

Channel Modulation in Neurodegeneration and Neuroprotection

Ion channels are critically important for the normal function of the brain and excitable tissues. The Research Topic "*Channel Modulation in Neurodegeneration and Neuroprotection*" focused on the role of ion channel function or dysfunction in neurological and neurodegenerative conditions. Convergent efforts to establish a link between clinical neurology, genetics, loss of function of important proteins and channelopathies in neurological disorders have become an intense area of research interest. Several ion channels have been implicated as important players in these diseases. This research topic therefore includes ten key research articles and two up-to-date review papers in the field of ion channels, their structural features and their proposed modes of action, through the analyses of their structural characteristics, structure-function relationship, therapeutic modulation and neuropharmacology.

In this collection, several authors focused on exploring and further elaborating on glutamate receptor channels and their role in the development and treatment of neurological disorders. Gale et al. investigated whether glutaminergic N-methyl-D-aspartate (NMDA) receptor channel antagonists, other than memantine, are able to treat patients with GRIN mutations on the GluN2A subunit of the NMDA receptor by attenuating neurotoxicity associated with GluN2A-P552R expression. The authors found that treatment with ketamine does not effectively block GluN2A-P552R-mediated dendrotoxicity, despite the fact that both memantine and ketamine act as open NMDA receptor channel blockers binding at the phencyclidine binding site. These findings suggest that GluN2A-P552R induced dendrotoxicity is mediated through two distinct mechanisms that are yet to be elucidated. The group of Sebih et al. synthesised the glutathione (GSH) metabolite gamma-L-glutamyl-L-glutamate (γ-Glu-Glu) and explored its effects on activation of NMDA receptors. They observed that γ-Glu-Glu partially activated NMDA receptors and exhibited better efficacy for NMDA receptors containing the GluN2B subunit. γ-Glu-Glu was also found to potentiate glutamate responses on NMDA receptors. Further experiments revealed that extracellular γ-Glu-Glu concentration was directly linked to GSH metabolism, suggesting that γ-Glu-Glu could exert excitatory effects when GSH production is enhanced, leading to the overactivation of neuronal NMDA receptors. The research article by Dron et al. described the effect of different anticonvulsants on native glutaminergic calcium-permeable α-amino-3-hydroxy-5-methyl-4-isoxazolepropionic acid receptor (AMPA) receptors (CP-AMPARs) and calcium-impermeable AMPA receptors (CI-AMPARs) using a whole cell patch-clamp method. Amongst the ten anticonvulsants evaluated, phenytoin was the only one with significant ability to reversibly inhibit CP-AMPARs and Cl-AMPARs. The authors have

OPEN ACCESS

Edited by:
Giulia Maria Camerino,
University of Bari Aldo Moro, Italy

Reviewed by:
Stefania Schiavone,
University of Foggia, Italy

****Correspondence:***
Jacques Joubert
jjoubert@uwc.ac.za

Specialty section:
This article was submitted to Pharmacology of Ion Channels and Channelopathies, a section of the journal Frontiers in Pharmacology

Received: *09 February 2022*
Accepted: *07 March 2022*
Published: *23 March 2022*

Citation:
Joubert J, Malan SF and Geldenhuys WJ (2022) Editorial: Channel Modulation in Neurodegeneration and Neuroprotection. Front. Pharmacol. 13:872103. doi: 10.3389/fphar.2022.872103

shown, for the first time, that AMPA receptor inhibition by phenytoin may contribute to its anticonvulsant ability, as well as to its side effect profile.

Dysregulation of Ca^{2+} and Na^{+} homeostasis has been described as being central in the etiology of neurodegenerative and neurological diseases. Much however remains unknown in the pathogenesis of these disorders and the role of ion exchangers, ion channels and ion release in the mechanism. In an paper by Piccialli et al. the authors demonstrate enhanced reverse-mode Na^{+}-Ca^{2+} exchanger (NCX3) activity, dependent on interaction with the voltage gated sodium channel, Nav1.6, in primary hippocampal neurons of the Tg2576 mouse model for Alzheimer's disease. Even though it is not entirely clear whether this is the result of a mutation associated with the Tg2576 mouse or a compensatory mechanism, the authors propose that the upregulation of NCX3 exerts a neuroprotective effect in amyloid beta (Aβ) induced calcium dyshomeostasis by enhancing the endoplasmic reticulum (ER) Ca^{2+} content and thus preventing ER-stress. Katnik and Cuevas, investigated whether inhibition of the sodium-potassium-chloride cotransporter-1 (NKCC1) by its antagonists, bumetanide and ethacrynic acid, would affect Na^{+} and Ca^{2+} overload following *in vitro* ischemia-acidosis. They concluded that it is the inhibition of voltage-gated Ca^{2+} and Na^{+} channels by these loop diuretics, and not the inhibition of NKCC1, that results in the reduction of $[Ca^{2+}]$i overload in neurons during ischemia-acidosis. A review paper by Li et al. describes the post-translational modification of the Cav1.2 channel and its functions in neurodegenerative diseases. The authors expand on the potential of dihydropyridine Cav1.2 inhibitors that have recently been repurposed for the treatment of Parkinson's- and Alzheimer's disease.

Sodium and potassium channels are of significant interest in conditions such as neuropathic pain, neuroinflammation, migraine and epilepsy. Wang et al. report that the flavonoid Gastrodin, the bioactive ingredient of Gastrodia, a Chinese Herbal medicine used as an analgesic, effectively treats vincristine induced thermal and mechanical hyperalgesia in rats. These effects seem to be mediated by inhibition and/or suppression of expression of Nav1.7- and Nav1.8 channels in dorsal root ganglion neurons. Further *in silico* modeling showed possible direct binding of Gastrodin to the Nav1.7- and Nav1.8 channel in active sites previously associated with its inhibition. In the manuscript by Yao et al., the authors performed a genetic screen of 26 patients who suffer from febrile seizures through *de novo* sequencing and identified a novel missense mutation of the high-conductance calcium- and voltage-dependent K^{+} (BK) potassium channel gene KCNMA1 (E155Q). Electrophysiological characterization of different KCNMA1 mutants in HEK293T cells, the previously-reported R458T and E884K variants, and the newly-found E155Q variant, revealed characteristics of loss-of-function. Transcriptomic analysis on the hippocampus and cortex of BK knock-out and wild-type mice showed differentially expressed genes distributed in neuroinflammation, astrocyte activation, and epilepsy-related signal pathways. Eren-Koçak and Dalkara wrote a review on the possible contribution of ion channels to excitation-inhibition imbalance and neuroinflammation as a common mechanism for ion channel dysfunctions in migraine and depression. Finally, in an interesting opinion piece by Gascoigne et al. the authors are of the opinion that If chloride channels and/or GABAA receptors become dysfunctional, a lack of inhibitory control over neuronal activation is accompanied by a weakened hemodynamic response. Furthermore, they imply that such dysfunction is an important molecular hallmark of neurodegenerative and neurological disorders.

Two papers, published by Pesti et al. and Lukacs et al. describe unique approaches to identify the biophysical properties and detailed mechanism of action of voltage-gated sodium channel (VGSC) blockers using automated high-throughput screening compatible microfluidics-based patch clamp methods. The group showed that with their methods, they are able to distinguish state-dependent association, dissociation kinetics and identify concentration independent effects of VGSC blockers on time scales ranging from milliseconds to seconds. These two examples of automated patch clamp analysis may assist in the assessment of potential therapeutic agents for sodium channel induced hyperexcitability-related neurological disorders.

In summary, this Research Topic contributes to an "*in-depth*" knowledge of ion channels, their dysregulation and their effects in neurological conditions, opening the way to new attractive research in neuropharmacology, in parallel with the identification of new candidate drugs. We believe that this collection of articles will inspire many researchers and clinicians worldwide to continue working in or enter the field of ion channel research associated with neurological disorders.

AUTHOR CONTRIBUTIONS

JJ was invited by Frontiers in Pharmacology, suggested the title of this research topic and invited SM and WG as co-editors. The first draft of the Editorial was written by JJ with additions, corrections and comments received from SM and WG. All authors approved the final manuscript.

Conflict of Interest: The authors declare that the research was conducted in the absence of any commercial or financial relationships that could be construed as a potential conflict of interest.

Publisher's Note: All claims expressed in this article are solely those of the authors and do not necessarily represent those of their affiliated organizations, or those of the publisher, the editors and the reviewers. Any product that may be evaluated in this article, or claim that may be made by its manufacturer, is not guaranteed or endorsed by the publisher.

Copyright © 2022 Joubert, Malan and Geldenhuys. This is an open-access article distributed under the terms of the Creative Commons Attribution License (CC BY). The use, distribution or reproduction in other forums is permitted, provided the original author(s) and the copyright owner(s) are credited and that the original publication in this journal is cited, in accordance with accepted academic practice. No use, distribution or reproduction is permitted which does not comply with these terms.

frontiers in Pharmacology

ORIGINAL RESEARCH
published: 23 August 2021
doi: 10.3389/fphar.2021.738460

Characterization of Compound-Specific, Concentration-Independent Biophysical Properties of Sodium Channel Inhibitor Mechanism of Action Using Automated Patch-Clamp Electrophysiology

Krisztina Pesti[1,2†], *Mátyás C. Földi*[3,1†], *Katalin Zboray*[3], *Adam V. Toth*[3,1], *Peter Lukacs*[3,1‡] and *Arpad Mike*[3,1*‡]

[1]Department of Biochemistry, ELTE Eötvös Loránd University, Budapest, Hungary, [2]School of Ph.D. Studies, Semmelweis University, Budapest, Hungary, [3]Plant Protection Institute, Centre for Agricultural Research, Martonvásár, Hungary

OPEN ACCESS

Edited by:
Sarel Francois Malan,
University of the Western Cape,
South Africa

Reviewed by:
Vaibhavkumar S. Gawali,
University of Cincinnati, United States
Yanling Pan,
Indiana University, Purdue University
Indianapolis, United States

***Correspondence:**
Arpad Mike
arpadmike1@gmail.com

†These authors have contributed equally to this work and share first authorship

‡These authors have contributed equally to this work and share senior authorship

Specialty section:
This article was submitted to Pharmacology of Ion Channels and Channelopathies, a section of the journal Frontiers in Pharmacology

Received: *08 July 2021*
Accepted: *10 August 2021*
Published: *23 August 2021*

Citation:
Pesti K, Földi MC, Zboray K, Toth AV, Lukacs P and Mike A (2021) Characterization of Compound-Specific, Concentration-Independent Biophysical Properties of Sodium Channel Inhibitor Mechanism of Action Using Automated Patch-Clamp Electrophysiology. Front. Pharmacol. 12:738460. doi: 10.3389/fphar.2021.738460

We have developed an automated patch-clamp protocol that allows high information content screening of sodium channel inhibitor compounds. We have observed that individual compounds had their specific signature patterns of inhibition, which were manifested irrespective of the concentration. Our aim in this study was to quantify these properties. Primary biophysical data, such as onset rate, the shift of the half inactivation voltage, or the delay of recovery from inactivation, are concentration-dependent. We wanted to derive compound-specific properties, therefore, we had to neutralize the effect of concentration. This study describes how this is done, and shows how compound-specific properties reflect the mechanism of action, including binding dynamics, cooperativity, and interaction with the membrane phase. We illustrate the method using four well-known sodium channel inhibitor compounds, riluzole, lidocaine, benzocaine, and bupivacaine. Compound-specific biophysical properties may also serve as a basis for deriving parameters for kinetic modeling of drug action. We discuss how knowledge about the mechanism of action may help to predict the frequency-dependence of individual compounds, as well as their potential persistent current component selectivity. The analysis method described in this study, together with the experimental protocol described in the accompanying paper, allows screening for inhibitor compounds with specific kinetic properties, or with specific mechanisms of inhibition.

Keywords: automated patch-clamp, sodium channel inhibitor, binding kinetics, riluzole, lidocaine, benzocaine, bupivacaine

---

Abbreviations: EIP, effective inhibitor potency; RFI, “recovery from inactivation” protocol; SDO, “state-dependent onset” protocol; SSI, “steady-state inactivation” protocol; TTX, tetrodotoxin.

INTRODUCTION

In silico prediction of drug effects can save a tremendous amount of time and resources, and can accelerate drug discovery. To predict the therapeutic action of sodium channel inhibitors, an elementary knowledge about the mechanism of action is essential. These drugs show state-dependent accessibility and affinity to binding sites and can have radically different binding/unbinding kinetics. These properties determine their effect, as they dynamically bind and unbind depending on the activity pattern of individual cells.

In silico prediction is especially useful for multi-target drugs, where targets are not independent of each other but interact in a complex way. Voltage-gated ion channels both affect and are affected by the membrane potential. Similarly, they both affect and are affected by intracellular ion concentrations. This creates an intricate network of interactions, the outcome of which is difficult to predict without modeling. Ion channels also happen to be the most promiscuous drug targets, therefore multi-target effects among therapeutic drugs are much rather the rule, than the exception (Martin et al., 2004; Kramer et al., 2013; Crumb et al., 2016; Kramer et al., 2020). Predicting the effect of a specific drug – either to achieve therapeutic effects or to avoid adverse effects – in most cases requires considering its interaction with several ion channel and other targets, together with the complex network of interactions between the targets themselves. The best-studied example for this is the torsadogenic effect of certain compounds in the human heart, where *in silico* modeling of multi-target effects is now a generally accepted directive (Sager et al., 2014). This initially has been done by determining the IC_{50} value of a specific drug to all relevant ion channel targets, from which the inhibited fraction of specific ion channels can be determined at specific drug concentrations. These conductances then were reduced according to the inhibited fraction in the simulations. However, as it has been first shown by Di Veroli et al. (2013), Di Veroli et al. (2014), the predicted effect can be seriously underestimated if one does not consider the mechanism of action; most importantly the dynamics of perpetual state-dependent binding/unbinding. Indeed, simulated compounds at their IC_{50} concentration could have widely different effects on the action potential duration depending on their state preference and binding kinetics (Lee et al., 2017). Some of the more recent, improved models, therefore, include Markov models of hERG channels, where state-dependence and binding/unbinding dynamics is also simulated (Dutta et al., 2017; Lee et al., 2017; Li et al., 2017). The same approach should be applied for modeling drug effects on sodium channels, not only in the context of cardiac safety pharmacology, but in predicting therapeutic efficacy for all hyperexcitability-related conditions including neuromuscular disorders, pain syndromes, epilepsies, and cardiac arrhythmias. A dependable model should include several processes, such as aqueous phase – membrane phase partitioning, state-dependent access [as described by the guarded receptor hypothesis (Starmer et al., 1984)], and state-dependent affinity, which is inevitably linked with allosteric modulation of channel gating [as described by the modulated receptor hypothesis (Hille, 1977)]. The mechanism of inhibition for most sodium channel inhibitor drugs is not known in sufficient detail to allow the construction of adequate models, and a comprehensive analysis of mechanisms for a reasonable number of sodium channel inhibitors is still lacking. In the accompanying study, we aimed to develop a protocol by which an initial assessment of these processes can be completed with reasonably high throughput. In this study, our aim was to characterize the mechanism of action of individual drugs, not a specific concentration of a specific drug. For example, one may observe that the onset of effect for compound "A" is faster than for compound "B," or that compound "B" delays recovery more effectively than compound "A." Does this tell anything about their specific mechanisms of action? Not necessarily. It is possible that if we increase the concentration of compound "B", the onset will be just as fast as that of compound "A." It is also possible that if we increase the concentration of compound "A," it will delay recovery just as effectively as compound "B." We aimed to find compound-specific (and concentration-independent) properties of inhibition, and it turned out that each compound did have such properties, not only resting and inactivated state affinities (K_R and K_I), but more importantly the kinetics of approaching K_R upon hyperpolarization, and approaching K_I upon depolarization were also such compound-specific properties.

MATERIALS AND METHODS

Cell Culture and Automated Patch-Clamp Electrophysiology

Cell culture and electrophysiology were done as described in the accompanying paper (Lukacs et al., 2021). The recombinant rNaV1.4 channel-expressing cell line was generated as described before (Lukacs et al., 2018). Transfected HEK 293 cells were maintained in Dulbecco's Modified Eagle Medium, high glucose supplemented with 10% v/v fetal bovine serum, 100 U/ml of penicillin/streptomycin, and 0.4 mg/ml Geneticin (Life Technologies, Carlsbad, CA). For experiments, cells were dissociated from culture dishes with Accutase (Corning), shaken in serum-free medium for 60 min at room temperature, then centrifuged, and resuspended into the extracellular solution to a concentration of 5×10^6 cells/mL. Voltage-clamp recordings were performed on an IonFlux Mercury instrument (Fluxion Biosciences). The composition of solutions (in mM) was: Intracellular solution: 50 CsCl, 10 NaCl, 60 CsF, 20 EGTA, and 10 HEPES; pH 7.2 (adjusted with 1 M CsOH). Extracellular solution: 140 NaCl, 4 KCl, 1 $MgCl_2$, 2 $CaCl_2$, 5 D-Glucose, and 10 HEPES; pH 7.4 (adjusted with 1 M NaOH). The osmolality of intra-and extracellular solutions was set to ~320 and ~330 mOsm, respectively. Data were sampled at 20 kHz, and filtered at 10 kHz. Experiments were carried out at room temperature.

The 384-well IonFlux microfluidic plates are divided into four "zones", typically each zone was used for a separate experiment (one particular set of compounds on one particular cell line). Each zone consists of 8 separate sections, which are distinct

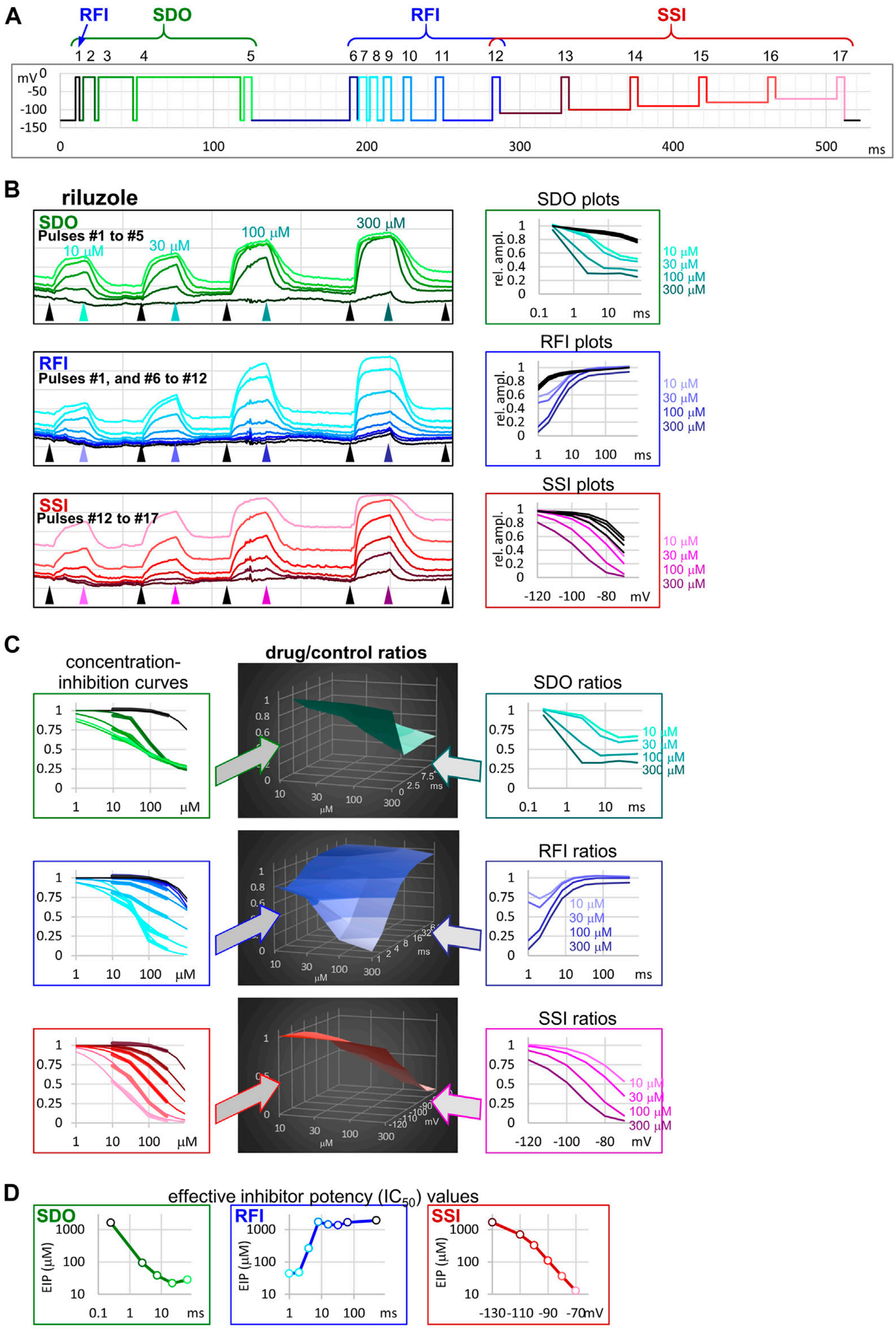

FIGURE 1 | The sequence of analysis to obtain effective inhibitor potency plots. The process is illustrated in an example of an experiment, where four concentrations of riluzole were applied to a cell ensemble (10, 30, 100, and 300 μM). **(A)** Schematic picture of the voltage protocol, which was repeated at 1 Hz frequency. The color of pulses match the color of amplitude plots in panel **(B)**, the color of concentration-inhibition curves in panel **(C)**, left column, and the color of open circles in EIP plots in panel **(D)**. The number of pulses, and the three main sections of the protocol: SDO, RFI, and SSI, are indicated. **(B)** Left column: Amplitude plots throughout the four riluzole applications, for the three main sections. Grid size: 1 nA (vertical), 100 s (horizontal). Arrowheads show the time points, from where data were collected to construct plots in the right column. Right column: SDO, RFI, and SSI plots for four different concentrations of riluzole, and four sets of control data

(*Continued*)

FIGURE 1 | before drug application. The color of curves match the color of arrowheads in the left column. **(C)** Middle column: 3D plots of drug/control ratios for each of the four concentrations (front axis), and for each of the 17 pulses (three different right-side axes at the three main sections). Left column: Concentration-inhibition plots for each of the 17 pulses (Projection of middle column 3D plots to the front plane). Thick lines show experimental data, thin lines show fits of the Hill equation to the data. Right column: Drug/control ratios shown on the same abscissae as SDO, RFI, and SSI plots in panel **(B)**, left column (Projection of middle column 3D plots to the right side plane). **(D)** Effective inhibitor potency plots show how EIP of riluzole was found to change depending on conditioning pulse duration (SDO), interpulse interval (RFI), and holding potential (SSI).

functional units, containing 12 wells: one well for the cell suspension, one well for the waste, two cell "traps" (intracellular solution-filled wells under negative pressure to establish high resistance seals and then whole-cell configuration), and eight compound wells. We kept one compound well for cell-free extracellular solution and typically used the remaining seven compound plates for two different compounds one of them in three, the other in four different concentrations. Two kinds of microfluidic plates are manufactured: In single-cell plates, each cell trap contains a single hole and therefore catches a single cell. In "ensemble plates" there are 20 holes in each cell trap, and 20 cells are recorded simultaneously. We used ensemble plates for experiments because success rate was higher. From the 16 cell ensembles of each zone, we chose $n = 6$ ensembles for analysis. At this sample size, an effect greater or equal to 2 standard deviations can be detected with a power of 0.8 at $p < 0.05$ significance level. Cell ensembles were excluded if: 1) the control sodium current amplitude was less than 2 nA, 2) the average seal resistance of the cells was less than 80 mOhm, 3) a larger than 20% gradual loss of seal resistance was observed during the experiment, 4) a sudden drop of amplitude with a concurrent drop of seal resistance was observed (indicating loss of one of the cells from the ensemble). From the remaining cell ensembles, the six with the highest and most stable seal resistances were included in the analysis.

We used a complex 17-pulse voltage protocol (**Figure 1A**), described in detail in the accompanying paper (Lukacs et al., 2021), which allowed the assessment of gating kinetics and gating equilibrium in the absence and the presence of inhibitor/modulator compounds. The protocol investigated the effect of different durations of depolarizations: 2.5, 7.5, 22.5, and 67.5 ms with 2.5 ms hyperpolarizing gaps between them; this section (pulses #1 to #5) is shown by different shades of green in **Figure 1**, and was named "state-dependent onset" (SDO). Next, pulses #6 to #12, as well as #1 investigated the effect of different durations of hyperpolarizations (1, 2, 4, 8, 16, 32, 64, and 498 ms, separated by 5 ms depolarizations) in the section shown by different shades of blue, and named "recovery from inactivation" (RFI). Finally, pulses #12 to #17 assessed the resting-inactivated equilibrium at different membrane potentials in the section named "steady-state inactivation" (SSI). The three sections were similar to protocols we used in previous studies (Lukacs et al., 2018; Földi et al., 2021).

Data Analysis

In addition to automatic fitting, described in the accompanying paper (Lukacs et al., 2021), in this study we used a different approach to process SDO, RFI, and SSI data. This analysis focused on deriving compound-specific but concentration-independent descriptors of the mechanism of action, which can lead to a more thorough understanding of the sub-processes involved in drug action, and which can later serve as a basis for constructing kinetic models for the simulation of drug-specific effects. All data analysis was done in Microsoft Excel (RRID:SCR_016137) environment, using VBA routines to accelerate repetitive data management tasks. For each of the 17 pulses peak amplitudes were measured after removing capacitive artifacts and subtracting the leak.

Inhibition of 1st and 17th pulse-evoked current amplitudes were used to obtain estimates of resting-state-, and inactivated-state-affinities (K_R and K_I). We constructed concentration-inhibition curves for both the 1st and 17th pulse-evoked currents, and fitted them with the Hill equation:

$$Inh = \frac{cc^{n_H}}{cc^{n_H} + {IC_{50}}^{n_H}}, \tag{1}$$

where Inh is the inhibited fraction of the current, cc is the drug concentration, and n_H is the Hill coefficient. K_R was approximated with the IC_{50} value for first pulse-evoked currents. For the calculation of K_I, we used the equation from Bean et al. (1983):

$$\frac{1}{K_{app}} = \frac{h}{K_R} + \frac{1-h}{K_I}, \tag{2}$$

where K_{app} was the IC_{50} for the 17th pulse, and $(1\text{-}h)$ was the ratio of 17th/first pulse evoked current amplitudes (from the average of the last 5 s before drug application; see pink traces (pulse #17) and black traces (pulse #1) in **Figure 1B**). K_R and K_I were the extreme values between which the potency of inhibition continuously fluctuated, depending on the voltage protocol. A detailed description of the analysis of dynamic changes in potency is found below in Results.

RESULTS

In the accompanying paper (Lukacs et al., 2021) we describe how different degrees of inhibition observed in the 17-pulse protocol can be interpreted as revealing the state-dependent onset (SDO; how the inhibition depended on the length of depolarizations), the recovery from inactivation (RFI; how the inhibition depended on the length of hyperpolarizations), and steady-state inactivation (SSI; how the inhibition depended on the membrane potential). We have distinguished "macro-dynamics," which was the onset/offset upon drug perfusion and removal, and occurred on the second-timescale; and "micro-dynamics," which was the onset/offset upon

TABLE 1 | Main parameters of inhibition by four compounds. Hill coefficients are shown in parentheses. K_I was calculated as described in Methods. Micro-association and micro-dissociation could not be fit with a single exponential, therefore we give the range within which the effective inhibitor potency was observed to change.

	Riluzole	Lidocaine	Benzocaine	Bupivacaine	Tetrodotoxin
IC$_{50}$ #1 (estimated K_R) (μM)	**1,362** ± 205 (1.38 ± 0.06)	**1,283** ± 461 (0.79 ± 0.07)	**2,245** ± 299 (1.58 ± 0.11)	**94.6** ± 10.7 (0.94 ± 0.05)	**0.028** ± 0.002 (1.27 ± 0.03)
IC$_{50}$ #5 (after 65.7 ms depol.) (μM)	**27.4** ± 6.44 (0.63 ± 0.06)	**31.9** ± 2.28 (1.05 ± 0.04)	**1,302** ± 142 (1.09 ± 0.06)	**27.3** ± 1.45 (1.38 ± 0.06)	**0.015** ± 0.002 (1.27 ± 0.10)
IC$_{50}$ #7 (after 1 ms hyperpol.) (μM)	**42.1** ± 3.62 (1.47 ± 0.12)	**71.7** ± 5.83 (0.85 ± 0.05)	**290** ± 22.3 (0.89 ± 0.05)	**33.5** ± 2.32 (1.21 ± 0.04)	**0.018** ± 0.002 (1.58 ± 0.22)
IC$_{50}$ #17 (−70 mV) (μM)	**6.86** ± 4.36 (0.73 ± 0.13)	**22.8** ± 2.04 (1.47 ± 0.10)	**170** ± 10.3 (1.42 ± 0.06)	**16.3** ± 1.70 (1.28 ± 0.05)	**0.018** ± 0.002 (1.39 ± 0.07)
K_I (calculated) (μM)	**5.63** ± 3.35	**18.4** ± 1.52	**79.4** ± 3.9	**12.7** ± 1.22	**0.017** ± 0.002
K_R/K_I ratio	**242** ± 147	**69.7** ± 20.9	**28.3** ± 3.8	**7.48** ± 0.68	**1.7** ± 0.11
macro-offset time constant (s)	**13.6** ± 0.71	**1.72** ± 0.05	**1.42** ± 0.59	**3.56** ± 0.43	**22.9** ± 1.50
micro-onset range (ms)	**1–10**	**1–100**	**0.1–2**	**100–1,000**	**1–100**
micro-offset range (ms)	**2–10**	**10–500**	**0.1–4**	**100–1,000**	**1–10**

Bold values serve to highlight the most important data.

conformational transitions of the channel population, and occurred on the millisecond timescale. In this study we focus on micro-dynamics. We first explain the sequence of analysis on the example of riluzole (in four different concentrations) using data from a single cell ensemble. Then we show the same analysis on examples for three additional compounds in order to demonstrate how similar compounds may radically differ in their micro-dynamics. Finally, we show how these compound-specific biophysical properties may affect their action at actively firing excitable cells.

Sequence of Analysis, and the Concept of "Effective Inhibitor Potency"

The 17-pulse protocol is shown in **Figure 1A**; it was repeated at each second (1 Hz). For the sake of clarity, we show the sequence of analysis on a single measurement (the ensemble of 20 simultaneously recorded cells) for different concentrations of riluzole. Peak amplitude plots for all 17 pulse-evoked currents are shown in **Figure 1B**, left panel; peak amplitudes were arranged into three separate groups as shown in **Figure 1A**, this allowed us to construct SDO, RFI, and SSI plots. In this procedure of analysis, we did not use every sweep of the experiment, only constructed one set of plots right before the start of each drug perfusion period (controls), as well as one set of plots at the end of each drug perfusion period (in this case 10, 30, 100, and 300 μM riluzole), as shown by the arrowheads in **Figure 1B**. The constructed plots are shown in **Figure 1B**, right panel.

It is obvious that the same concentration of riluzole differently affected currents evoked by different depolarizations. For example, the effect of 100 μM riluzole fluctuated between almost full inhibition (pulses #7 and #17) and no inhibition (pulses #1, #6, and #12). We termed this process "micro-dynamics," to distinguish from the onset and offset of drug effects upon perfusion and washout of riluzole ("macro-dynamics"), which occurred on a ~1000-fold slower time scale (**Figure 1B**, left panel; **Table 1**). For a more detailed discussion of micro- and macro-dynamics see the accompanying paper (Lukacs et al., 2021).

The term "apparent affinity" has been used to reflect different degrees of inhibition at different membrane potentials (Kuo and Bean, 1994; Lenkey et al., 2011). We have previously extended the use of this term to non-equilibrium conditions (such as during the course of recovery from inactivation) (Földi et al., 2021), however, for discussing non-equilibrium conditions we consider it better to introduce the term "effective inhibitor potency" (EIP). The term "affinity" in itself conveys that the effect is the consequence of a binding/unbinding equilibrium. During the onset of inhibition, or recovery from inhibition, however, there is no equilibrium, and there is a complex combination of different processes beyond simple binding/unbinding, such as modulation of gating, access into/egress from the central cavity, aqueous phase-membrane partitioning, deprotonation/protonation, etc. The term "potency," on the other hand, makes no reference to the mechanism, it simply expresses what fraction of the channel population can a certain concentration of a certain compound inhibit at a certain point in time. EIP, just like affinity, can be quantified by constructing concentration-response curves and determining the IC$_{50}$ values. We found that the EIP kept changing dynamically, it increased (*i.e.,* IC$_{50}$ values decreased) with longer conditioning pulses (SDO), and decreased with longer interpulse intervals (RFI). To calculate EIP for different conditions, we calculated drug-treatment/control ratios for all 17 pulses, and for all drug concentrations: we divided the amplitude of each 17 evoked currents in the presence of all four concentrations of riluzole by the corresponding control amplitude. The results are shown in **Figure 1C**. All three columns show the exact same set of amplitude ratios. The middle column of 3D plots shows drug-treatment/control ratios both as a function of riluzole concentration, and as a function of conditioning pulse duration (SDO, upper row),

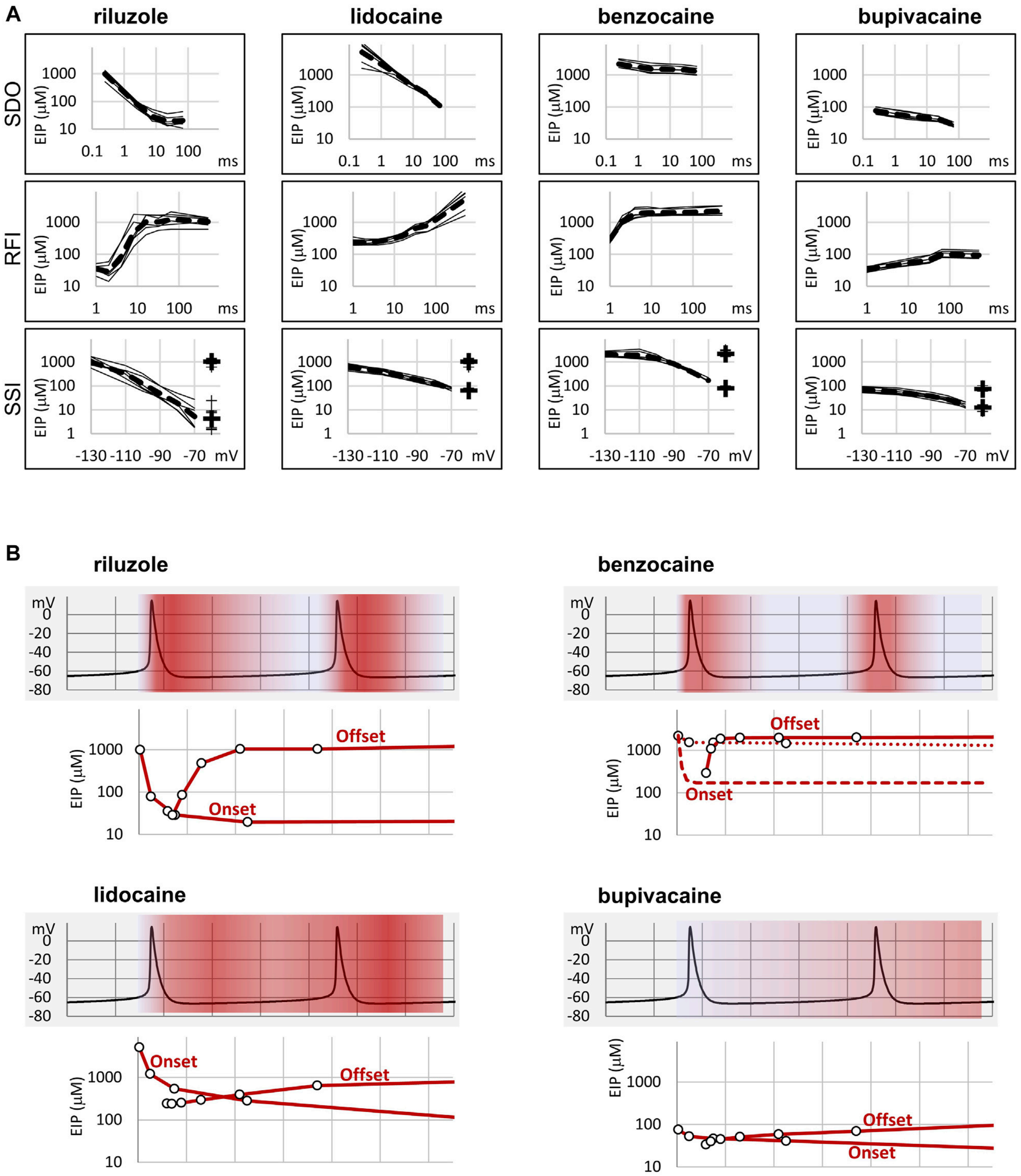

FIGURE 2 | Summary of EIP plots for the four compounds, and the significance of micro-dynamics. **(A)** The micro-dynamics (EIP plots for SDO and RFI), and voltage-dependence of EIP are compared for *n* = 6 measurements for each of the four compounds. Thin lines show data from individual measurements, thick dashed lines show the geometric mean. For SSI data the calculated K_R and K_I values are also shown on the right side of the figures (thin crosses for individual measurements, and thick crosses for the geometric mean). **(B)** One example of how micro-dynamics is translated into frequency-dependent inhibition. The activity pattern of a simulated neuron is shown in the background, SDO-EIP and RFI-EIP plots are shown under the activity pattern, these are identical to the ones shown in dashed lines in panel **(A)**, upper and middle row, but on a linear time scale. Horizontal grid: 10 ms. SDO-EIP plots were aligned with the upstroke of the first action potential because state-dependent onset is triggered by depolarization. RFI-EIP plots were aligned with the repolarization because hyperpolarization triggers recovery from inhibition. The intensity of red coloring illustrates how EIP is expected to change throughout the repetitive firing, and therefore what dynamics of inhibition is expected to be caused by the presence of the four compounds.

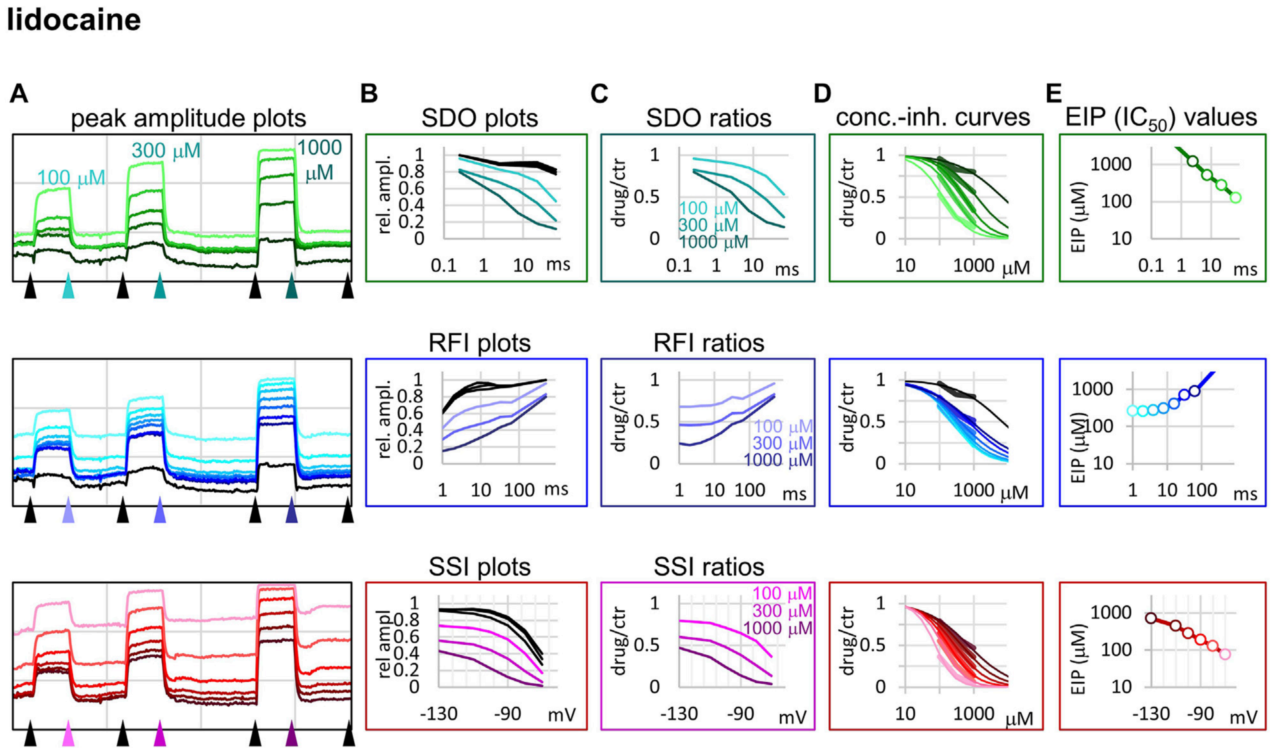

FIGURE 3 | Construction of EIP plots for lidocaine. The figure illustrates how EIP plots are constructed on the example of a single measurement of the effect of three concentrations of lidocaine (100, 300, and 1,000 μM). **(A)** Peak amplitudes of currents evoked by the 17-pulse protocol were grouped into three sections: SDO (upper row), RFI (middle row), and SSI (lower row). Grid size: 5 nA (vertical), 100 s (horizontal). **(B)** Amplitudes in control sections and during lidocaine perfusion were plotted against conditioning pulse duration (SDO), interpulse interval duration (RFI), and membrane potential (SSI). **(C)** Drug/control ratios were calculated for all three sections. **(D)** The same drug/control ratios were used to construct concentration-inhibition plots, as it was explained in **Figure 1** (thick lines), which were then fitted by the Hill equation (thin lines). **(E)** The resulting IC_{50} (EIP) values are plotted against the same abscissae as in the **(B)** and **(C)** columns: conditioning pulse duration (SDO), interpulse interval duration (RFI), and membrane potential (SSI).

interpulse interval (RFI, middle row), and membrane potential (SSI, lower row). The right column illustrates the projection of the 3D plot to the right side plane (as seen from the right side, shown by the teal, indigo, and purple arrows). These plots are rather similar to the ones shown in the right column of **Figure 1B**, but current amplitudes evoked by each pulse have been normalized, each to its own control. The left column (thick lines) illustrates the projection of the 3D plot to the front plane (as seen from the front; shown by the green, blue, and red arrows), thus forming 17 concentration-response plots. Note that all 17 concentration-response curves were different. From the fitted Hill equations (thin lines) the IC_{50} values were determined and plotted against conditioning pulse duration (SDO), interpulse interval (RFI), or membrane potential (SSI) (**Figure 1D**). Hill coefficients (n_H) ranged between 0.5 and 2.0; some of the reasons why Hill coefficients may have diverged from unity will be discussed below. EIP plots for the SDO and RFI sections of the protocol show the major parameters of micro-dynamics for individual compounds: how fast its effect develops, and how fast it is terminated, depending on the conformational dynamics of the channel protein. We can observe that riluzole showed fast micro-dynamics: essentially both the onset and the offset of its effect were complete within ~10 ms. Micro-dynamics data from $n = 6$ cell ensembles will be shown below in **Figure 2A**.

Comparison of Compound-Specific Properties of Five Different Compounds

We chose three additional compounds in order to illustrate differences in micro-dynamics, even among closely related compounds, which showed similarly fast macro-dynamics. Lidocaine, benzocaine, and bupivacaine are all well-known local anesthetics. In addition, we also included tetrodotoxin (TTX) as a reference compound. TTX is a well known channel blocker toxin, that binds to a distinct binding site at the outer vestibule of the channel (Fozzard and Lipkind, 2010; Tikhonov and Zhorov, 2018). Examples of peak amplitude plots for all 17 pulses, SDO, RFI, and SSI plots, amplitude ratios, concentration-inhibition curves for all 17 pulses, and EIP plots are shown for these additional four compounds in **Figures 3–6**. For each of the five compounds, we also calculated K_R and K_I estimates as described in Methods. **Table 1** shows major parameters of inhibition, including K_R and K_I estimates, as well as K_R/K_I ratios.

Lidocaine (**Figure 3**) showed a slower micro-onset than riluzole. SDO ratio plots indicate that at 100 and 300 μM the

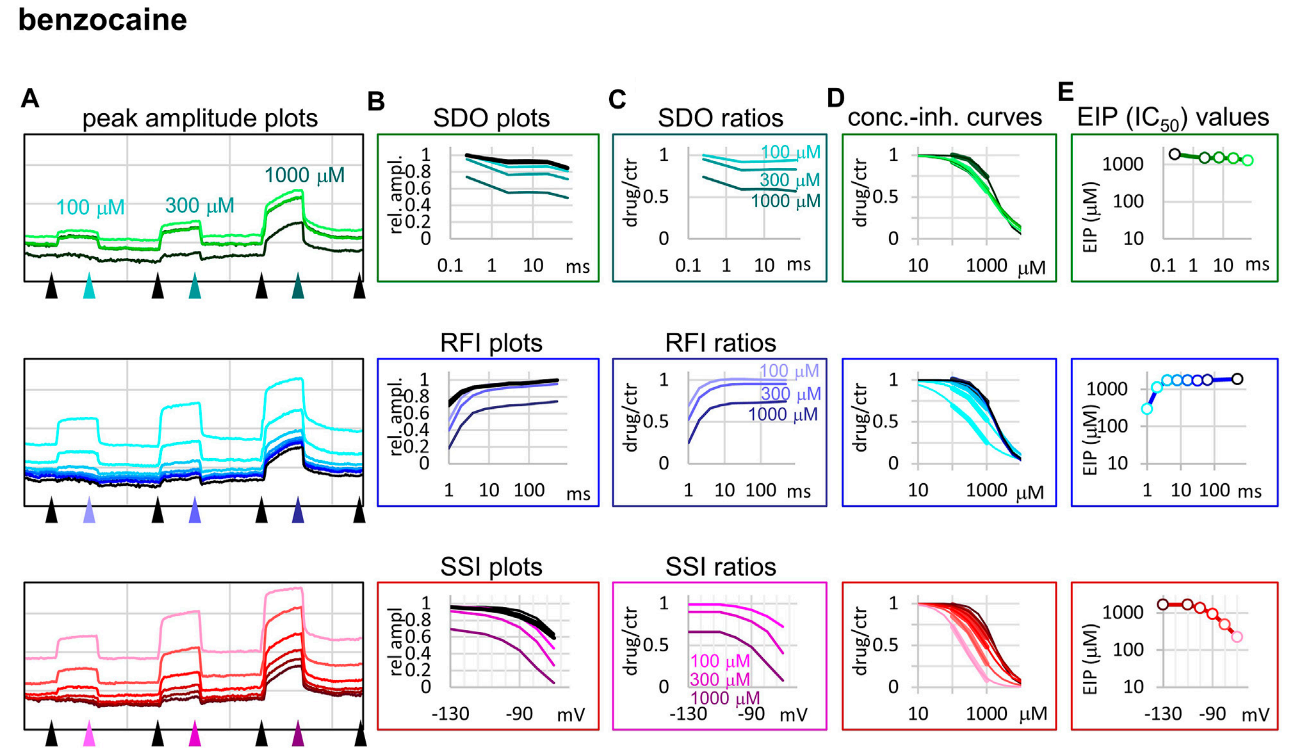

FIGURE 4 | Construction of EIP plots for benzocaine. The figure illustrates how EIP plots are constructed on the example of a single measurement of the effect of three concentrations of benzocaine (100, 300, and 1,000 μM). **(A)** Peak amplitudes of currents evoked by the 17-pulse protocol were grouped into three sections: SDO (upper row), RFI (middle row), and SSI (lower row). Grid size: 5 nA (vertical), 100 s (horizontal). **(B)** Amplitudes in control sections and during benzocaine perfusion were plotted against conditioning pulse duration (SDO), interpulse duration (RFI), and membrane potential (SSI). **(C)** Drug/control ratios were calculated for all three sections. **(D)** The same drug/control ratios were used to construct concentration-inhibition plots (thick lines), which were then fitted by the Hill equation (thin lines). **(E)** The resulting IC_{50} (EIP) values are plotted against the same abscissae as in the **(B)** and **(C)** columns.

onset did not reach its maximum even at the longest depolarization (67.5 ms) of the 17-pulse protocol. The recovery was also slower, substantial recovery only started after ~10 ms of hyperpolarization, and continued up to ~500 ms.

The fastest micro-dynamics we have encountered thus far was shown by benzocaine (**Figure 4**). Recovery in fact was so fast that it compromised the measurement of SDO. At 2 ms gap duration, ~70–90% of the channels have already recovered, therefore the 2.5 ms gap used in the SDO protocol was unable to reveal most of the inhibition caused by benzocaine binding. Although the plots of SDO ratios show the onset only on the remaining ~10–30% of channels, it is still discernible that the full onset has been completed within the shortest (2.5 ms) pulse. Calculation of K_I from SSI data (see **Table 1**) indicates that in fact more than half of the channels are inhibited by 100 μM of benzocaine, but this inhibition is difficult to detect whenever we use a hyperpolarizing gap before the test pulse.

When we tried to determine the kinetic behavior of bupivacaine (**Figure 5**) we encountered the exact opposite of the problem with benzocaine: Even though the macro-dynamics was fairly fast (the time constant of macro-offset was 3.56 ± 0.43 ms), the micro-onset did not reach its maximum during the longest depolarization, and the micro-offset also could not reach equilibrium during the longest hyperpolarization. For this reason estimates of K_R and K_I are probably both incorrect, K_R was underestimated (*i.e.,* resting affinity would be less, if sufficient time was allowed for recovery) and K_I was overestimated (*i.e.,* inactivated affinity would be higher, if there was sufficient time for association).

Tetrodotoxin is probably the most widely used inhibitor toxin of sodium channels, which shows selectivity towards certain isoforms, including the $Na_V1.4$. It is known to bind to a completely different site, in the outer vestibule of the channel (Fozzard and Lipkind, 2010; Tikhonov and Zhorov, 2018), therefore it can serve as a reference compound that should show no noticeable micro-dynamics upon conformational changes. However, inhibition by TTX has been found to display some use-dependence, frequency-dependence, and voltage-dependence (Cervenka et al., 2010), indicating that the outer vestibule also must reflect the overall conformational transitions of the channel. Our results with TTX are shown in **Figure 6**. We found that EIP of TTX did change during the SDO, RFI, and SSI sections of the protocols ($p < 0.01$ for all three sections), although the extent of change was small, less than 2-fold (**Table 1**).

In summary, we could detect radical differences between the micro-dynamics of four well-known sodium channel inhibitors. Summary of EIP values for the four compounds ($n = 6$ and their geometric mean for each one) are shown in **Figure 2A**. On the EIP – SSI plots we also show K_R and K_I estimates for individual

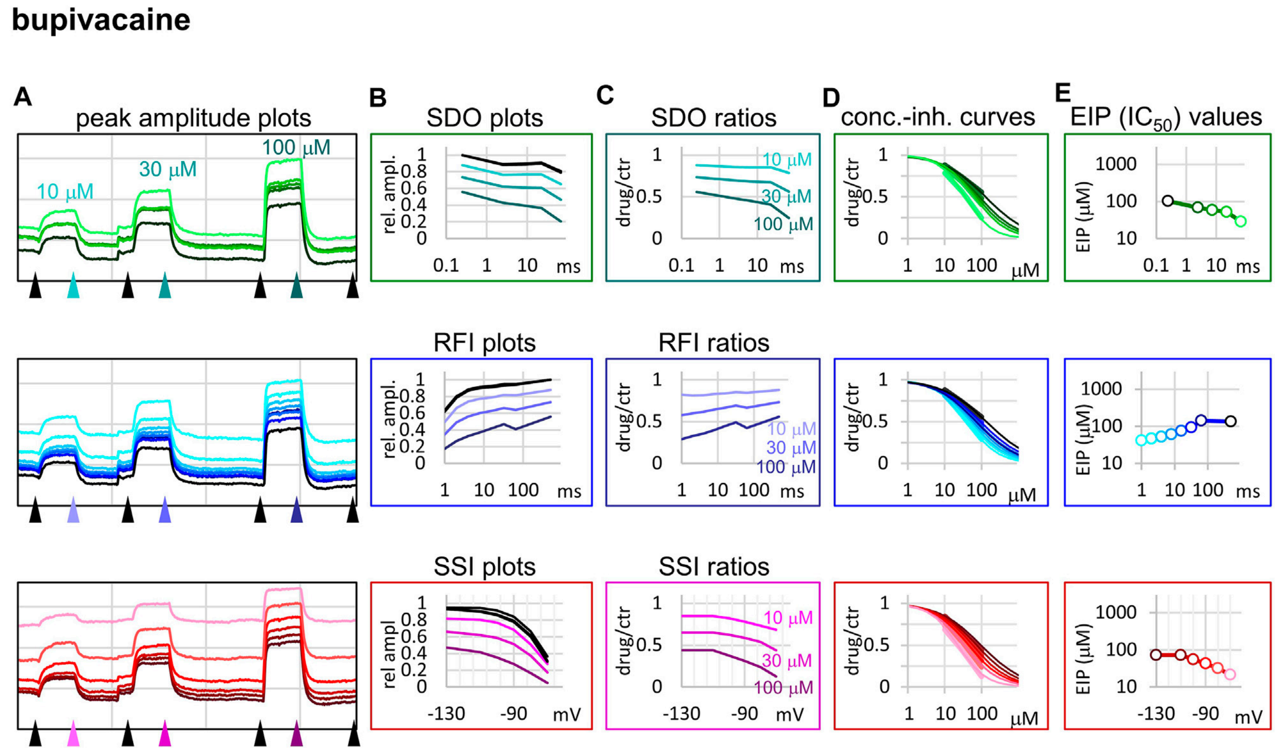

FIGURE 5 | Construction of EIP plots for bupivacaine. The figure illustrates how EIP plots are constructed on the example of a single measurement of the effect of three concentrations of bupivacaine (10, 30, and 100 μM). **(A)** Peak amplitudes of currents evoked by the 17-pulse protocol were grouped into three sections: SDO (upper row), RFI (middle row), and SSI (lower row). Grid size: 5 nA (vertical), 100 s (horizontal). **(B)** Amplitudes in control sections and during bupivacaine perfusion were plotted against conditioning pulse duration (SDO), interpulse duration (RFI), and membrane potential (SSI). **(C)** Drug/control ratios were calculated for all three sections. **(D)** The same drug/control ratios were used to construct concentration-inhibition plots (thick lines), which were then fitted by the Hill equation (thin lines). **(E)** The resulting IC_{50} (EIP) values are plotted against the same abscissae as in the **(B)** and **(C)** columns.

measurements (thin crosses), and their geometric mean (thick crosses). We propose that EIP values are the best means of characterizing micro-dynamics for individual compounds. In the Discussion, we examine why micro-dynamics is significant in predicting the effect of a compound on an active excitable cell. **Table 1** shows all major concentration-independent, compound-specific parameters of inhibition, including K_R and K_I estimates, K_R/K_I ratios, time constants of macro-offset ($\tau_{M\text{-}off}$), and time ranges of micro-onset and micro-offset. (Micro-onset and micro-offset could not be adequately described by exponentials; therefore instead we give the time range when the most substantial changes occur.)

DISCUSSION

Micro-Dynamics and Frequency-Selectivity

Riluzole has been originally described as an anti-epileptic compound (Mizoule et al., 1985), and has been found to be an especially efficient inhibitor at high firing frequencies (Urbani and Belluzzi, 2000; Wu et al., 2005; Desaphy et al., 2014). In addition, it has been shown to selectively inhibit the persistent component (I_{NaP}) of the sodium current (Urbani and Belluzzi, 2000). We believe that both I_{NaP} selectivity and selective inhibition at high firing frequencies can be explained by its special micro-dynamics. We propose that preclinical assessment of sodium channel inhibitors should include evaluating their kinetic properties since these are important determining factors of their therapeutic potential.

To elucidate this, and to illustrate the significance of micro-dynamics, we chose four well-known compounds, with different micro-dynamics, and show their dynamically changing potency over a simulated firing of a simple, single-compartment neuron model (**Figure 2B**). Our sole aim here is to illustrate how micro-dynamics of any compound can be interpreted, therefore we chose to visualize the EIP of the four compounds on the same firing pattern. We supposed that micro-onset is started upon depolarization, therefore the EIP plot from the SDO experiments was aligned with the upstroke of the action potential, and that micro-offset is started upon repolarization, therefore the EIP plot from the RFI experiments was aligned with the repolarization phase. The EIP plots are identical to the geometric mean curves shown in **Figure 2A**, but here we use a linear time axis. The rates derived from non-physiological voltage patterns (square pulses between −130 and −10 mV) of course do not exactly match the rates under physiological membrane potential patterns, but they provide a rough estimate of the overall behavior of individual drugs. These estimates must be later verified by constructing

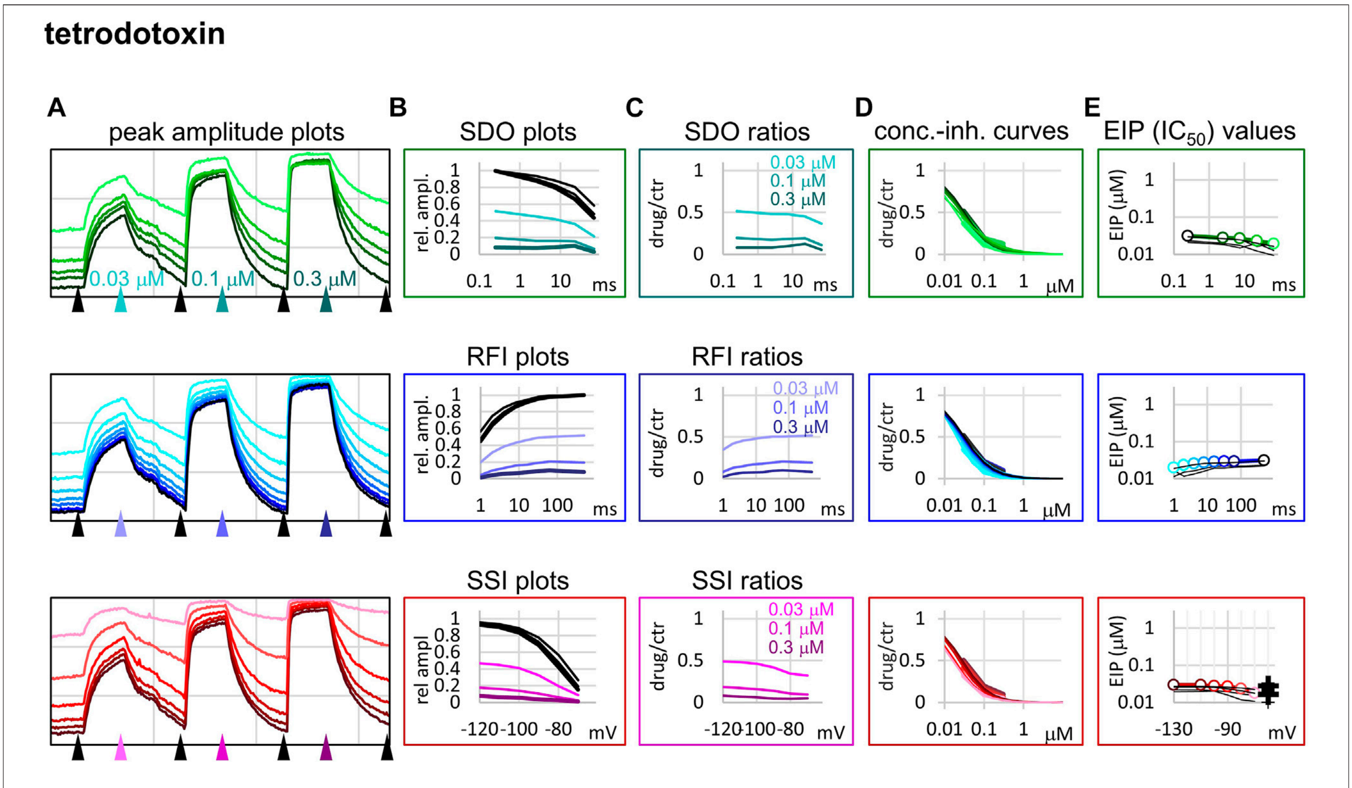

FIGURE 6 | Construction of EIP plots for TTX. The figure illustrates how EIP plots are constructed on the example of a single measurement of the effect of three concentrations of TTX (30, 100, and 300 nM). **(A)** Peak amplitudes of currents evoked by the 17-pulse protocol were grouped into three sections: SDO (upper row), RFI (middle row), and SSI (lower row). Grid size: 4 nA (vertical), 100 s (horizontal). **(B)** Amplitudes in control sections and during TTX perfusion were plotted against conditioning pulse duration (SDO), interpulse duration (RFI), and membrane potential (SSI). **(C)** Drug/control ratios were calculated for all three sections. **(D)** The same drug/control ratios were used to construct concentration-inhibition plots (thick lines), which were then fitted by the Hill equation (thin lines). **(E)** The resulting IC_{50} (EIP) values are plotted against the same abscissae as in the **(B)** and **(C)** columns. Data from the other five cell ensembles are shown in thin black lines. For the SSI plots the calculated K_R and K_I values are also shown on the right side of the figure (thin crosses for individual measurements, and thick crosses for the geometric mean).

models for their individual mechanisms of action, incorporating drug effects into the neuron model, and studying the interaction between different activity patterns and drug micro-dynamics.

In **Figure 2B** we show two subsequent action potentials of a cell that was induced to fire at ~25 Hz by a constant current injection. Changes in the intensity of red color illustrate dynamic changes in EIP during repeated action potentials. Dark red indicates high EIP (*i.e.*, IC_{50} approaches K_I), white indicates low EIP (*i.e.*, IC_{50} approaches K_R).

In the case of riluzole, we observed a massive state-dependence: with K_R = 1,362 ± 205 µM and K_I = 5.63 ± 3.35 µM, the K_R/K_I ratio was 242. The rate of micro-onset was somewhat slower than the action potential itself. This means that even if riluzole was present at a high concentration during an action potential, it would be ineffective: by the time riluzole could reach its maximal potency, the action potential would already be over. After the action potential riluzole stays very potent for ~10 ms, then it rapidly loses its potency again [for an explanation of this particularly fast micro-offset see Földi et al. (2021)]. This means that compounds with such micro-dynamics would be very potent inhibitors of high-frequency firing while being mostly ineffective at low frequencies. This is exactly what has been observed experimentally. For example, Desaphy et al. (2014) compared the frequency-dependent inhibition of seven compounds. Six of the compounds showed higher *in vitro* potency when the frequency of depolarizations was increased from 0.1 to 10 Hz but did not change much between 10 and 50 Hz. Riluzole, on the other hand, only started to “realize its potential” above 10 Hz, the apparent affinity increased 48-fold, from IC50 = 43 µM (10 Hz) to IC50 = 0.9 µM (50 Hz). Inhibition of I_{NaP} may also contribute to inhibition of high-frequency burst firing (Wu et al., 2005). As for I_{NaP} selectivity, we assume that it requires both a moderate micro-onset rate (not too fast so that it would miss the action potential, but not too slow so that it can inhibit I_{NaP} afterward) and a relatively fast offset rate (so that by the time of the next action potential it would lose its potency).

While the potency of riluzole could both fully develop and fully fade away within 10 ms, changes in the EIP of lidocaine required more than 100 ms (for both the micro-onset and the micro-offset). This micro-dynamics, when plotted over the firing pattern (**Figure 2B**), suggests that compounds with properties similar to lidocaine would follow firing frequencies with their micro-dynamics only up to ~5 Hz. Because micro-offset would require 100–200 ms, we would expect that for such compounds selective inhibition of the persistent component would best manifest itself in the 5–10 Hz range of firing frequencies. At higher frequencies, the extent of inhibition would simply depend on the average membrane potential in the course of firing activity.

Benzocaine is known as one of the fastest-acting sodium channel inhibitors, due to its small size and neutrality. Indeed, it is one of the few compounds, for which the whole process of partitioning, entry through the fenestration, and binding to the local anesthetic site has been observed in molecular dynamics simulations (Boiteux et al., 2014; Martin and Corry, 2014). In our experiments we found extremely fast micro-offset kinetics, the offset was complete within 4 ms, and even the shortest interpulse interval (1 ms) already showed decreased potency (291 ± 22 μM, while the calculated K_I was 79.4 ± 3.9 μM). This was the reason, why the SDO protocol only detected a small fraction of the onset of drug action. Even though depolarization must have caused a definite increase in EIP, as we can see from the membrane potential dependence of EIP (**Figure 4**), the 2.5 ms hyperpolarizing gap between pulses was enough to allow almost full recovery. Experimental results (which failed to detect the onset) are shown by open circles connected by a dotted line (**Figure 2B**), while we suppose that the actual dynamics of micro-onset must have been complete within a few milliseconds (dashed line in **Figure 2B**). It follows that significant frequency-dependence cannot be expected in the case of benzocaine, only at extremely high (>100 Hz) firing frequencies.

While benzocaine is a smaller, neutral compound that acts much faster than lidocaine, bupivacaine is larger, and has a higher pKa than lidocaine (therefore a somewhat larger fraction is charged at neutral pH). In an earlier comparative study, we found it to have higher potency, and slower onset/offset kinetics (only macro-dynamics was studied) (Lenkey et al., 2010). In this study, we found that although its macro-dynamics was still relatively fast (macro-offset time constants were 1.72 ± 0.05 s for lidocaine, and 3.56 ± 0.43 s for bupivacaine, see **Table 1**), its micro-dynamics was slow, and therefore its EIP varied within a strikingly shallow range (between 27.3 ± 1.45 and 94.6 ± 10.7 μM). The K_R/K_I ratio was only 7.48 (while for riluzole, lidocaine, and benzocaine, it was 242, 69.7, and 28.3, respectively). This can also be seen on the concentration-inhibition curves (**Figure 5**), where the 17 different curves are very close to each other. The reason for a shallow micro-dynamics may be either that complete micro-onset of inhibition would require a depolarization even longer than 64 ms, or that the complete micro-offset would require a hyperpolarization even longer than 498 ms. Considering estimations of K_R and K_I from the literature [$K_R \approx 317.4$ μM, and $K_I \approx 18.6$ μM (Vladimirov et al., 2000); $K_R \approx 618.9$ μM, and $K_I \approx 5.85$ μM (Lenkey et al., 2010)], both could be the case for bupivacaine, therefore a more accurate assessment of its range of EIS values would require a protocol containing both longer depolarizations and longer hyperpolarizations. We presume that micro-onset and micro-offset both must be complete within 2–3 s since these processes cannot be slower than macro-offset, for which we observed a time constant of 3.56 s (**Table 1**). In the case of the simulated neuron firing at ~25 Hz, we suppose that development of inhibition would require several tens of action potentials, and cells would not substantially recover from inhibition between two action potentials unless the firing rate was less than 1 Hz.

Micro-Dynamics and Persistent Current Selectivity

Micro-dynamics is a major determinant of the therapeutic profile. This is well known for the case of Class 1 antiarrhythmics, but the same principle can be applied to neuronal and skeletal muscle sodium channels, which can fire at a much higher rate. Micro-dynamics will determine which firing frequencies will be selectively inhibited, and it will also determine persistent current selectivity, as we have discussed above. Several compounds have been shown to selectively inhibit the persistent component of the sodium current (I_{NaP}) over the transient component (I_{NaT}) (Spadoni et al., 2002; Kahlig et al., 2010; Belardinelli et al., 2013; Terragni et al., 2016; El-Bizri et al., 2018), riluzole being one of them (Urbani and Belluzzi, 2000). The mechanism by which this selectivity is achieved, however, is not clear. It is not due to selectivity between sodium channel isoforms, but selectivity between conformations of the same channel isoforms may be part of the explanation. If an inhibitor compound has a higher affinity to the inactivated state, then I_{NaT} will be less affected because at the peak of the transient current there are few inactivated channels, but by the time I_{NaT} is over, and I_{NaP} is the only remaining sodium current, almost all channels have reached inactivated state. This is how I_{NaP} preference of riluzole was explained by (Ptak et al., 2005). However, almost all small molecule sodium channel inhibitors show higher affinity to inactivated state, and only a few of them are selective inhibitors of I_{NaP}. We propose that – at least in the case of riluzole – micro-dynamics may be the key. Both micro-onset and micro-offset rates are crucial. Delayed micro-onset ensures that the transient component I_{NaT} is "missed" by the drug. Fast micro-offset, on the other hand, ensures, that upon hyperpolarization the inhibition is rapidly relieved, therefore I_{NaT} will be minimally affected at the next action potential. Obviously, there must be other possible mechanisms of I_{NaP} selectivity because this property is shared by compounds with much slower micro-dynamics, like e.g., ranolazine or phenytoin (Kahlig et al., 2010; Terragni et al., 2016). Details of these mechanisms still remain to be explored.

Hill Coefficients

We found that the best way to express dynamic changes in potency is by constructing concentration-inhibition curves for all depolarizing pulses and determining IC_{50} values. In principle, potency could be calculated from even a single concentration, if we supposed: 1) one-to-one binding (i.e., the $n_H = 1$), and 2) that binding is equivalent with inhibition (channel block). In practice, however, for three out of the four compounds described here (riluzole, lidocaine, and benzocaine) we found Hill coefficients to vary widely, between ~0.5 and ~2 (**Table 1**, **Figures 1C**, **3–5**). Steady-state availability data at different inhibitor concentrations can be converted to concentration-inhibition curves at different holding potentials [Lenkey et al. (2011) - see Figures 1A,B of the cited paper]. In a study by Balser et al. (1996) this conversion was done on data with five different concentrations of lidocaine [Balser et al. (1996) - see Figure 6 and Figure 7 of the cited paper], and the results gave n_H values ranging from 0.64 to 1.83 (not given in the original paper, but could be reconstructed by fitting the data). Similarly to our results, $n_H < 1$ values were observed at more negative holding potentials (−110 to −90 mV), where the potency was low (IC_{50} between 1,900 and 2,500 μM); while $n_H > 1$ values were observed at less negative holding potentials (−70 to −50 mV). We assume, that $n_H < 1$ values might reflect binding to multiple low-affinity binding sites which do not all cause full inhibition of conductance. Values greater than one, on the other hand, indicate positive cooperativity, which may come from multiple possible mechanisms, as has been discussed by Leuwer et al. (2004). They fitted $V_{1/2}$ shift vs. concentration plots using a Hill-type exponent, which was found to range from 1.6 to 2.1. These and our own data show that although n_H may vary depending on the experimental protocol, it is quite common to find $n_H > 1$ for sodium channel inhibitors, indicating that more than one inhibitor molecule is needed for effective inhibition, at least under certain experimental conditions. The binding of one molecule may induce or stabilize a conformation that is more favorable for binding of the second molecule. Alternatively, it is also possible that two or more bound molecules are required to effectively inhibit channels either by channel block or modulation. Even if we disregard modulation, channel block may in itself be more effective with two bound lidocaine molecules, as shown in a recent molecular dynamics simulation (Nguyen et al., 2019).

CONCLUSION

Therapeutic usefulness of sodium channel inhibitor drugs depends on their ability to selectively inhibit pathological activity of cells, which often manifests in hyperexcitability. Pathological hyperexcitability is involved in a number of disorders, including pain syndromes, epilepsies, muscle spasms, or arrhythmias. Each of the different types of hyperexcitability-related diseases has its characteristic dynamics of firing. To counteract them it is best to choose an inhibitor that has the precise dynamics that can selectively inhibit that certain pathological pattern of activity. We have demonstrated how much dynamic properties can differ even in the case of closely related compounds. Prediction of drug effects in an excitable tissue requires a thorough understanding of their mechanism of action, which includes the kinetic aspects of their state-dependent effects. In this study we aimed to derive compound-specific but concentration-independent descriptors of the mechanism of action, which can serve as a basis for building credible kinetic models for the simulation of drug-specific effects.

Thus far there has been no method available for a comparative study of drug onset/offset dynamics at a satisfactory throughput. Studies on the mechanism of action for individual drugs usually took several months to complete. Automated patch clamp instruments are capable of flawlessly performing complex experimental protocols, however, obtaining a large mass of complex information does not necessarily mean obtaining meaningful information. “Asking” the right question (by designing the right protocol) is not trivial, and neither is deciphering a relevant “answer” from a huge amount of data. Furthermore, one needs to find the right degree of automation, which allows fast analysis, but also allows manual handling and monitoring of data. We assume that the method described in this study and its prequel will inspire other groups to use automated patch clamp instruments more creatively, in order to better exploit their potential.

DATA AVAILABILITY STATEMENT

The raw data supporting the conclusions of this article will be made available by the authors, without undue reservation.

AUTHOR CONTRIBUTIONS

PL and AM designed research; KP, MF, and AT performed experiments; KP, MF, AT, PL, and AM performed data analysis; KZ and PL contributed to the methodology and provided resources; PL and AM wrote the manuscript; all authors have read and approved the manuscript.

FUNDING

This work was supported by the Hungarian Brain Research Program (KTIA-NAP-13–2–2014–002), and by Hungary’s Economic Development, and Innovation Operative Programme (GINOP-2.3.2-15-2016-00051).

ACKNOWLEDGMENTS

The content of this paper has previously appeared online in bioRxiv: https://doi.org/10.1101/2021.07.05.451191.

REFERENCES

Balser, J. R., Nuss, H. B., Romashko, D. N., Marban, E., and Tomaselli, G. F. (1996). Functional Consequences of Lidocaine Binding to Slow-Inactivated Sodium Channels. *J. Gen. Physiol.* 107, 643–658. doi:10.1085/jgp.107.5.643

Bean, B. P., Cohen, C. J., and Tsien, R. W. (1983). Lidocaine Block of Cardiac Sodium Channels. *J. Gen. Physiol.* 81, 613–642. doi:10.1085/jgp.81.5.613

Belardinelli, L., Liu, G., Smith-Maxwell, C., Wang, W. Q., El-Bizri, N., Hirakawa, R., et al. (2013). A Novel, Potent, and Selective Inhibitor of Cardiac Late Sodium Current Suppresses Experimental Arrhythmias. *J. Pharmacol. Exp. Ther.* 344, 23–32. doi:10.1124/jpet.112.198887

Boiteux, C., Vorobyov, I., French, R. J., French, C., Yarov-Yarovoy, V., and Allen, T. W. (2014). Local Anesthetic and Antiepileptic Drug Access and Binding to a Bacterial Voltage-Gated Sodium Channel. *Proc. Natl. Acad. Sci. U S A.* 111, 13057–13062. doi:10.1073/pnas.1408710111

Cervenka, R., Zarrabi, T., Lukacs, P., and Todt, H. (2010). The Outer Vestibule of the Na+ Channel-Toxin Receptor and Modulator of Permeation as Well as Gating. *Mar. Drugs* 8, 1373–1393. doi:10.3390/md8041373

Crumb, W. J., Vicente, J., Johannesen, L., and Strauss, D. G. (2016). An Evaluation of 30 Clinical Drugs against the Comprehensive *In Vitro* Proarrhythmia Assay (CiPA) Proposed Ion Channel Panel. *J. Pharmacol. Toxicol. Methods* 81, 251–262. doi:10.1016/j.vascn.2016.03.009

Desaphy, J. F., Carbonara, R., Costanza, T., and Conte Camerino, D. (2014). Preclinical Evaluation of Marketed Sodium Channel Blockers in a Rat Model of Myotonia Discloses Promising Antimyotonic Drugs. *Exp. Neurol.* 255, 96–102. doi:10.1016/j.expneurol.2014.02.023

Di Veroli, G. Y., Davies, M. R., Zhang, H., Abi-Gerges, N., and Boyett, M. R. (2014). hERG Inhibitors with Similar Potency but Different Binding Kinetics Do Not Pose the Same Proarrhythmic Risk: Implications for Drug Safety Assessment. *J. Cardiovasc. Electrophysiol.* 25, 197–207. doi:10.1111/jce.12289

Di Veroli, G. Y., Davies, M. R., Zhang, H., Abi-Gerges, N., and Boyett, M. R. (2013). High-throughput Screening of Drug-Binding Dynamics to HERG Improves Early Drug Safety Assessment. *Am. J. Physiol. Heart Circ. Physiol.* 304, H104–H117. doi:10.1152/ajpheart.00511.2012

Dutta, S., Chang, K. C., Beattie, K. A., Sheng, J., Tran, P. N., Wu, W. W., et al. (2017). Optimization of an In Silico Cardiac Cell Model for Proarrhythmia Risk Assessment. *Front. Physiol.* 8, 616. doi:10.3389/fphys.2017.00616

El-Bizri, N., Xie, C., Liu, L., Limberis, J., Krause, M., Hirakawa, R., et al. (2018). Eleclazine Exhibits Enhanced Selectivity for Long QT Syndrome Type 3-associated Late Na+ Current. *Heart Rhythm* 15, 277–286. doi:10.1016/j.hrthm.2017.09.028

Földi, M. C., Pesti, K., Zboray, K., Toth, A. V., Hegedűs, T., Málnási-Csizmadia, A., et al. (2021). The Mechanism of Non-blocking Inhibition of Sodium Channels Revealed by Conformation-selective Photolabeling. *Br. J. Pharmacol.* 178, 1200–1217. doi:10.1111/bph.15365

Fozzard, H. A., and Lipkind, G. M. (2010). The Tetrodotoxin Binding Site Is within the Outer Vestibule of the Sodium Channel. *Mar. Drugs* 8, 219–234. doi:10.3390/md8020219

Hille, B. (1977). Local Anesthetics: Hydrophilic and Hydrophobic Pathways for the Drug-Receptor Reaction. *J. Gen. Physiol.* 69, 497–515. doi:10.1085/jgp.69.4.497

Kahlig, K. M., Lepist, I., Leung, K., Rajamani, S., and George, A. L. (2010). Ranolazine Selectively Blocks Persistent Current Evoked by Epilepsy-Associated Nav1.1 Mutations. *Br. J. Pharmacol.* 161, 1414–1426. doi:10.1111/j.1476-5381.2010.00976.x

Kramer, J., Himmel, H. M., Lindqvist, A., Stoelzle-Feix, S., Chaudhary, K. W., Li, D., et al. (2020). Cross-site and Cross-Platform Variability of Automated Patch Clamp Assessments of Drug Effects on Human Cardiac Currents in Recombinant Cells. *Sci. Rep.* 10, 5627. doi:10.1038/s41598-020-62344-w

Kramer, J., Obejero-Paz, C. A., Myatt, G., Kuryshev, Y. A., Bruening-Wright, A., Verducci, J. S., et al. (2013). MICE Models: Superior to the HERG Model in Predicting Torsade de Pointes. *Sci. Rep.* 3, 2100. doi:10.1038/srep02100

Kuo, C. C., and Bean, B. P. (1994). Slow Binding of Phenytoin to Inactivated Sodium Channels in Rat Hippocampal Neurons. *Mol. Pharmacol.* 46, 716–725. doi:10.1016/j.neuron.2018.05.025

Lee, W., Windley, M. J., Vandenberg, J. I., and Hill, A. P. (2017). *In Vitro* and In Silico Risk Assessment in Acquired Long QT Syndrome: The Devil Is in the Details. *Front. Physiol.* 8, 934. doi:10.3389/fphys.2017.00934

Lenkey, N., Karoly, R., Epresi, N., Vizi, E., and Mike, A. (2011). Binding of Sodium Channel Inhibitors to Hyperpolarized and Depolarized Conformations of the Channel. *Neuropharmacol.* 60, 191–200. doi:10.1016/j.neuropharm.2010.08.005

Lenkey, N., Karoly, R., Lukacs, P., Vizi, E. S., Sunesen, M., Fodor, L., et al. (2010). Classification of Drugs Based on Properties of Sodium Channel Inhibition: a Comparative Automated Patch-Clamp Study. *PLoS ONE* 5, e15568. doi:10.1371/journal.pone.0015568

Leuwer, M., Haeseler, G., Hecker, H., Bufler, J., Dengler, R., and Aronson, J. K. (2004). An Improved Model for the Binding of Lidocaine and Structurally Related Local Anaesthetics to Fast-Inactivated Voltage-Operated Sodium Channels, Showing Evidence of Cooperativity. *Br. J. Pharmacol.* 141, 47–54. doi:10.1038/sj.bjp.0705594

Li, Z., Dutta, S., Sheng, J., Tran, P. N., Wu, W., Chang, K., et al. (2017). Improving the In Silico Assessment of Proarrhythmia Risk by Combining hERG (Human Ether-À-Go-Go-Related Gene) Channel-Drug Binding Kinetics and Multichannel Pharmacology. *Circ. Arrhythm Electrophysiol.* 10, e004628. doi:10.1161/CIRCEP.116.004628

Lukacs, P., Földi, M. C., Valánszki, L., Casanova, E., Biri-Kovács, B., Nyitray, L., et al. (2018). Non-blocking Modulation Contributes to Sodium Channel Inhibition by a Covalently Attached Photoreactive Riluzole Analog. *Sci. Rep.* 8, 8110. doi:10.1038/s41598-018-26444-y

Lukacs, P., Pesti, K., Földi, M. C., Zboray, K., Toth, A. V., Papp, G., et al. (2021). An Advanced Automated Patch Clamp Protocol Design to Investigate Drug - Ion Channel Binding Dynamics. *bioRxiv*. doi:10.1101/2021.07.05.451189

Martin, L. J., and Corry, B. (2014). Locating the Route of Entry and Binding Sites of Benzocaine and Phenytoin in a Bacterial Voltage Gated Sodium Channel. *Plos Comput. Biol.* 10, e1003688. doi:10.1371/journal.pcbi.1003688

Martin, R. L., McDermott, J. S., Salmen, H. J., Palmatier, J., Cox, B. F., and Gintant, G. A. (2004). The Utility of hERG and Repolarization Assays in Evaluating Delayed Cardiac Repolarization: Influence of Multi-Channel Block. *J. Cardiovasc. Pharmacol.* 43, 369–379. doi:10.1097/00005344-200403000-00007

Mizoule, J., Meldrum, B., Mazadier, M., Croucher, M., Ollat, C., Uzan, A., et al. (1985). 2-Amino-6-trifluoromethoxy Benzothiazole, a Possible Antagonist of Excitatory Amino Acid Neurotransmission--I. Anticonvulsant Properties. *Neuropharmacol.* 24, 767–773. doi:10.1016/0028-3908(85)90011-5

Nguyen, P. T., DeMarco, K. R., Vorobyov, I., Clancy, C. E., and Yarov-Yarovoy, V. (2019). Structural Basis for Antiarrhythmic Drug Interactions with the Human Cardiac Sodium Channel. *Proc. Natl. Acad. Sci. U S A.* 116, 2945–2954. doi:10.1073/pnas.1817446116

Ptak, K., Zummo, G. G., Alheid, G. F., Tkatch, T., Surmeier, D. J., and McCrimmon, D. R. (2005). Sodium Currents in Medullary Neurons Isolated from the Pre-bötzinger Complex Region. *J. Neurosci.* 25, 5159–5170. doi:10.1523/JNEUROSCI.4238-04.2005

Sager, P. T., Gintant, G., Turner, J. R., Pettit, S., and Stockbridge, N. (2014). Rechanneling the Cardiac Proarrhythmia Safety Paradigm: A Meeting Report from the Cardiac Safety Research Consortium. *Am. Heart J.* 167, 292–300. doi:10.1016/j.ahj.2013.11.004

Spadoni, F., Hainsworth, A. H., Mercuri, N. B., Caputi, L., Martella, G., Lavaroni, F., et al. (2002). Lamotrigine Derivatives and Riluzole Inhibit INa,P in Cortical Neurons. *Neuroreport* 13, 1167–1170. doi:10.1097/00001756-200207020-00019

Starmer, C. F., Grant, A. O., and Strauss, H. C. (1984). Mechanisms of Use-dependent Block of Sodium Channels in Excitable Membranes by Local Anesthetics. *Biophys. J.* 46, 15–27. doi:10.1016/S0006-3495(84)83994-6

Terragni, B., Scalmani, P., Colombo, E., Franceschetti, S., and Mantegazza, M. (2016). Ranolazine vs Phenytoin: Greater Effect of Ranolazine on the Transient Na(+) Current Than on the Persistent Na(+) Current in central Neurons. *Neuropharmacol.* 110, 223–236. doi:10.1016/j.neuropharm.2016.06.029

Tikhonov, D. B., and Zhorov, B. S. (2018). Predicting Structural Details of the Sodium Channel Pore Basing on Animal Toxin Studies. *Front. Pharmacol.* 9, 880. doi:10.3389/fphar.2018.00880

Urbani, A., and Belluzzi, O. (2000). Riluzole Inhibits the Persistent Sodium Current in Mammalian CNS Neurons. *Eur. J. Neurosci.* 12, 3567–3574. doi:10.1046/j.1460-9568.2000.00242.x

Vladimirov, M., Nau, C., Mok, W. M., and Strichartz, G. (2000). Potency of Bupivacaine Stereoisomers Tested *In Vitro* and *In Vivo*: Biochemical, Electrophysiological, and Neurobehavioral Studies. *Anesthesiol.* 93, 744–755. doi:10.1097/00000542-200009000-00024

Wu, N., Enomoto, A., Tanaka, S., Hsiao, C. F., Nykamp, D. Q., Izhikevich, E., et al. (2005). Persistent Sodium Currents in Mesencephalic V Neurons Participate in Burst Generation and Control of Membrane Excitability. *J. Neurophysiol.* 93, 2710–2722. doi:10.1152/jn.00636.2004

Conflict of Interest: The authors declare that the research was conducted in the absence of any commercial or financial relationships that could be construed as a potential conflict of interest.

Publisher's Note: All claims expressed in this article are solely those of the authors and do not necessarily represent those of their affiliated organizations, or those of the publisher, the editors and the reviewers. Any product that may be evaluated in this article, or claim that may be made by its manufacturer, is not guaranteed or endorsed by the publisher.

Copyright © 2021 Pesti, Földi, Zboray, Toth, Lukacs and Mike. This is an open-access article distributed under the terms of the Creative Commons Attribution License (CC BY). The use, distribution or reproduction in other forums is permitted, provided the original author(s) and the copyright owner(s) are credited and that the original publication in this journal is cited, in accordance with accepted academic practice. No use, distribution or reproduction is permitted which does not comply with these terms.

frontiers
in Pharmacology

ORIGINAL RESEARCH
published: 15 September 2021
doi: 10.3389/fphar.2021.732922

Loop Diuretics Inhibit Ischemia-Induced Intracellular Ca^{2+} Overload in Neurons *via* the Inhibition of Voltage-Gated Ca^{2+} and Na^{+} Channels

Christopher Katnik and Javier Cuevas*

Department of Molecular Pharmacology and Physiology, Morsani College of Medicine, University of South Florida, Tampa, FL, United States.

One consequence of ischemic stroke is disruption of intracellular ionic homeostasis. Intracellular overload of both Na^{+} and Ca^{2+} has been linked to neuronal death in this pathophysiological state. The etiology of ionic imbalances resulting from stroke-induced ischemia and acidosis includes the dysregulation of multiple plasma membrane transport proteins, such as increased activity of sodium-potassium-chloride cotransporter-1 (NKCC-1). Experiments using NKCC1 antagonists, bumetanide (BMN) and ethacrynic acid (EA), were carried out to determine if inhibition of this cotransporter affects Na^{+} and Ca^{2+} overload observed following *in vitro* ischemia-acidosis. Fluorometric Ca^{2+} and Na^{+} measurements were performed using cultured cortical neurons, and measurements of whole-cell membrane currents were used to determine target(s) of BMN and EA, other than the electroneutral NKCC-1. Both BMN and EA depressed ischemia-acidosis induced $[Ca^{2+}]_i$ overload without appreciably reducing $[Na^{+}]_i$ increases. Voltage-gated Ca^{2+} channels were inhibited by both BMN and EA with half-maximal inhibitory concentration (IC_{50}) values of 4 and 36 μM, respectively. Similarly, voltage-gated Na^{+} channels were blocked by BMN and EA with IC_{50} values of 13 and 30 μM, respectively. However, neither BMN nor EA affected currents mediated by acid-sensing ion channels or ionotropic glutamatergic receptors, both of which are known to produce $[Ca^{2+}]_i$ overload following ischemia. Data suggest that loop diuretics effectively inhibit voltage-gated Ca^{2+} and Na^{+} channels at clinically relevant concentrations, and block of these channels by these compounds likely contributes to their clinical effects. Importantly, inhibition of these channels, and not NKCC1, by loop diuretics reduces $[Ca^{2+}]_i$ overload in neurons during ischemia-acidosis, and thus BMN and EA could potentially be used therapeutically to lessen injury following ischemic stroke.

Keywords: bumetanide, ethacrynic acid, voltage-gated channels, sodium, calcium, neurons, ischemia, acidosis

OPEN ACCESS

Edited by:
Sarel Francois Malan,
University of the Western Cape, South Africa

Reviewed by:
Xiangping Chu,
University of Missouri–Kansas City, United States
Jinwei Zhang,
University of Exeter, United Kingdom

Correspondence:
Javier Cuevas
jcuevas@usf.edu

Specialty section:
This article was submitted to Pharmacology of Ion Channels and Channelopathies,
a section of the journal Frontiers in Pharmacology

Received: *29 June 2021*
Accepted: *10 August 2021*
Published: *15 September 2021*

Citation:
Katnik C and Cuevas J (2021) Loop Diuretics Inhibit Ischemia-Induced Intracellular Ca^{2+} Overload in Neurons via the Inhibition of Voltage-Gated Ca^{2+} and Na^{+} Channels.
Front. Pharmacol. 12:732922.
doi: 10.3389/fphar.2021.732922

INTRODUCTION

Preservation of neuronal $[Ca^{2+}]_i$ and $[Na^{+}]_i$ homeostasis is dependent on ATPases, ion exchangers and cotransporters, and disruption of these during ischemia has a major impact on cell survival. For example, the Na^{+}-K^{+}-Cl^{-} cotransporter 1 (NKCC1) (X. Chen et al., 2008; Luo et al., 2008) promotes neuronal $[Na^{+}]_i$ overload upon reoxygenation, triggering reverse-mode operation of the Na^{+}/Ca^{2+}

exchanger, NCX1, Ca^{2+} influx, and cell death (Pignataro et al., 2004; Shono et al., 2010). In contrast, upregulation of the endoplasmic reticulum Ca(2+)-ATPases (SERCA2b subtype) in hippocampal neurons decreases Ca^{2+} store dysfunction and is neuroprotective during oxygen-glucose deprivation (Kopach et al., 2016).

Ionic imbalances are also a contributing factor to the acidotoxicity observed following cerebral ischemia (Siesjo, 1988). Our laboratory has shown that acidosis synergistically potentiates the intracellular Ca^{2+} dysregulation evoked by ischemia in cortical neurons, enhancing neuronal death (Mari et al., 2010). The acid-sensing ion channel, ASIC1a, contributes to this potentiation, but these channels alone cannot account for the long-lived synergy (Mari et al., 2010), since ASIC1a rapidly inactivates and release of Ca^{2+} from intracellular stores was also observed following ASIC1a activation (Herrera et al., 2008; Mari, Katnik, and Cuevas, 2010). It is of significant interest to identify other contributors to this synergistic potentiation of $[Ca^{2+}]_i$ dysregulation during ischemia and acidosis since these may, in part, account for the expansion of the ischemic lesion following stroke.

One possible molecular mechanism for this long-lived ionic imbalance during ischemia-acidosis is the prolonged activation of NKCC1. The role of NKCC1 during stroke and ischemia has been previously studied using the NKCC1-selective inhibitor, bumetanide. Bumetanide was shown to reduce reperfusion injury following focal cerebral ischemia in rats, presumably due to the inhibition of NKCC1 (Wang, Huang, He, Ruan, and Huang, 2014). Chronic bumetanide treatment following stroke has been shown to enhance neurogenesis and behavioral recovery in rats, although this effect was not unequivocally linked to NKCC1 (Xu et al., 2016). *In vitro* experiments have shown bumetanide can inhibit ischemia-induced $[Na^+]_i$ and $[Ca^{2+}]_i$ dysregulation in both neurons and astrocytes (X. Chen et al., 2008; Kintner et al., 2007; Lenart, Kintner, Shull, and Sun, 2004). These effects of bumetanide were suggested to be due to block of NKCC1.

Experiments were carried out to determine if inhibition of NKCC1 with bumetanide or ethacrynic acid alters ischemia-acidosis evoked $[Na^+]_i$ and $[Ca^{2+}]_i$ overload in neurons. Fluorometric Na^+ and Ca^{2+} measurements showed that bumetanide and ethacrynic acid inhibited ischemia-acidosis induced $[Ca^{2+}]_i$, but not $[Na^+]_i$, overload. The effects of bumetanide and ethacrynic acid were sufficiently different to suggest that these compounds were acting on distinct off-target sites. Whole-cell membrane current measurements indicated that both bumetanide and ethacrynic acid inhibit voltage-gated calcium and voltage-gated sodium channels, but that neither affects glutamatergic ionotropic receptors or acid-sensing ion channels. Ethacrynic acid was found to be a more efficacious inhibitor of VGCC than bumetanide, which may explain why it has a greater effect on ischemia-acidosis evoked $[Ca^{2+}]_i$ overload. The effects of bumetanide on ischemia-acidosis evoked $[Ca^{2+}]_i$ overload may in part explain the benefits of this compound following stroke. However, results presented here suggest that ethacrynic acid may be a superior compound for reducing stroke injury.

METHODS

Primary Rat Cortical Neuron Preparation

Cortical neurons from embryonic (E18) rats were isolated and cultured as previously described (Katnik, Guerrero, Pennypacker, Herrera, and Cuevas, 2006). Briefly, excised brains were digested with 0.25% trypsin. Isolated cells were suspended in DMEM supplemented with fetal bovine serum (FBS, 10%, heat inactivated), penicillin (100 IU/ml), streptomycin (100 μg/ml) and amphotericin B1 (0.25 μg/ml) (Antibiotic/Antimycotic) and plated on poly-L-lysine coated coverslips. Following 24-h incubation, the DMEM solution was replaced with Neurobasal media supplemented with B-27 (2%) and 0.5 mM L-glutamine. Cells were used after 10–21 days *in vitro*. All procedures were done in accordance with the regulations of the University of South Florida Institutional Animal Care and Use Committee.

Calcium Imaging Measurements

Changes in intracellular Ca^{2+} concentrations, $[Ca^{2+}]_i$, were measured in isolated cortical neurons using fluorescent imaging techniques and the Ca^{2+} sensitive dye, fura-2. Cells were loaded using the membrane permeable ester form of fura-2, fura-2 acetoxymethyl ester (fura-2 AM), as previously described (DeHaven and Cuevas, 2004). Cells plated on coverslips were incubated for 1 h at room temperature in Neurobasal media with 4 μM fura-2 AM and 0.4% dimethyl sulfoxide (DMSO). The coverslips were then washed in fura-2 AM free physiological saline solution (PSS) prior to experiments being performed. Cells (20–60 per field of view), visualized using a 40x Achroplan objective (Zeiss Microscopy, White Plains, N.Y.), were alternately illuminated with 340 and 380 nm light at 0.8 Hz (Lambda DG-4, Sutter Instruments, Novato CA) and fluorescent emissions at 510 nm were collected using a Sensicam digital CCD camera (Cooke Corp., Auburn Hills, MI).

Sodium Imaging Measurements

Changes in intracellular Na^+ concentrations were measured in isolated cortical neurons using fluorescent imaging techniques and the Na^+ sensitive dye, SBFI. Cells were loaded using the membrane permeable ester form of SBFI, SBFI acetoxymethyl ester (SBFI-2 AM). Cells plated on coverslips were incubated for 2 h at room temperature in Neurobasal media with 10 μM SBFI AM, 0.4% DMSO, 0.5% bovine serum albumin (BSA) and 0.1% pluronic. The coverslips were then washed in SBFI AM free physiological saline solution (PSS) prior to experiments being performed. The same microscope, objective, filter set, light source and camera as used for Ca^{2+} imaging were used. Images were acquired at 0.3 Hz.

Electrophysiological Measurements

Membrane currents were recorded using the conventional and perforated, whole-cell patch clamp configurations as previously described (Cuevas, Harper, Trequattrini, and Adams, 1997). The conventional (dialyzing configuration) was only used to record voltage-gated sodium channel currents to prevent space-clamp. Briefly, glass coverslips plated with neurons were transferred to a recording chamber and continuously perfused with external solution at a rate of 350 μL/min. Patch electrodes were pulled from thin-walled borosilicate glass (World Precision Instruments Inc., Sarasota, FL) using a Sutter Instruments P-87 pipette puller (Novato, CA) and had resistances of 2.0–3.0 MΩ for conventional whole-cell patches and 1.0–1.5 MΩ for perforated patches. Access resistances (R_s) were monitored throughout experiments for stable values ≤30 MΩ and were compensated at 40% (lag, 10 μs). When using the perforated-patch whole-cell configuration, electrical access was achieved with a pipette solution containing amphotericin B (Rae, Cooper, Gates, and Watsky, 1991). An amphotericin B stock solution (60 mg/ml in DMSO) was made fresh daily and diluted to 240 μg/ml (0.4% DMSO) in pipette solution immediately prior to use. To prevent current rundown when using the conventional whole-cell configuration, 3 mM ATP (disodium) was added to the internal solution. To isolate calcium currents, intracellular potassium was replaced with cesium, 70 mM external sodium was replaced with tetraethylammonium (TEA) and 2 μM tetrodotoxin (TTX) was added to the bathing solution. Perforated-patches were used to prevent clamping the intracellular calcium concentration by the pipet solution. To activate voltage-gated calcium currents, cells were held at −70 mV and stepped from −60 to +40 mV for 500 msec in 10 mV increments. To isolate sodium currents, intracellular potassium was replaced with cesium and 70 mM external sodium was replaced with TEA. 5 mM $BaCl_2$ and 400 μM $CdCl_2$ were added to a Ca^{2+}-free bathing solution. The internal solution contained 10 mM NaCl (replacing 10 mM KCl), 5 mM TEA, 5 mM $MgCl_2$ and 1 mM ethylene glycol tetraacetic acid (EGTA), requiring the use of conventional whole-cell patches to allow diffusion into the clamped cells. To activate voltage-gated sodium currents, cells were held at −70 mV and stepped from −50 to +5 mV for 50 msec in 5 mV increments. All membrane currents were amplified and filtered at 5 kHz with an Axon 200 amplifier, digitized at 10 kHz with a Digidata 1322A, and acquired using Clampex 10 (Axon) software. Currents were leak subtracted using the Clampex P/4 protocol.

Solutions and Reagents

The control bath solution for all experiments was PSS, which contained (in mM): 140 NaCl, 5.4 KCl, 1.3 $CaCl_2$, 1.0 $MgCl_2$, 20 glucose, and 25 4-(2-hydroxyethyl)-1-piperazineethanesulfonic acid (HEPES) (pH to 7.4 with NaOH). Acidosis was produced using this solution adjusted to pH 6.0. Ischemia-acidosis was produced using glucose-free PSS with 4 mM sodium azide added and adjusting the solution to pH 6.0. The control pipette solution consisted of (in mM): 75 K_2SO_4, 55 KCl, 5 $MgSO_4$, and 10 HEPES (titrated to pH 7.2 with N-methyl-d-glucamine). External solutions were applied using a rapid application system as previously described (Cuevas and Berg, 1998). To account for any rundown of responses, a paired protocol was used wherein cells were washed for 20 min between an initial control 2 min ischemia-acidosis application and the second 2 min ischemia-acidosis application in the absence or presence of bumetanide or ethacrynic acid, with second responses being normalized to the first responses (Katnik et al., 2006; Herrera et al., 2008). Bumetanide and ethacrynic acid were applied for 10 min prior to second ischemia-acidosis activations.

Materials

All chemicals used in this investigation were of analytical grade. The following reagents were used: TEA (Acros Organics, Waltham, MA); TTX (Alomone Labs, Jerusalem, Israel); Antibiotic/Antimycotic, BSA, DMEM, DMSO, FBS (Fisher Scientific, Fair Lawn, NJ); B-27, Fura-2 AM, Neurobasal (Life Technologies, Carlsbad, CA); Ethacrynic Acid (MP Biomedicals, LLC, Solon, OH); and Bumetanide, EGTA, HEPES, L-Glutamine, Poly-L-Lysine (Sigma-Aldrich, St. Louis, MO).

Data Analysis

Imaging data files were collected with SlideBook 4.02 (Intelligent Imaging Innovations, Inc.). Fluorescence emission intensities of individual fluorescent cells, measured using circular regions of interest (ROIs) placed over cell bodies, were collected as functions of time. For calcium imaging experiments, emission intensities were exported to SigmaPlot11, ratioed (R_{340}/R_{380}) and converted to $[Ca^{2+}]_i$ using the Grynkewicz equation with constant parameters R_{min}, R_{max} and β determined using calibration solutions containing fura-2 salt. Differences in the values of these parameters from those obtained using an *in situ* protocol are controlled for by normalizing responses in the same cell. However, since $[Ca^{2+}]_i$ is not a linear function of R_{340}/R_{380}, this calculation is necessary to preserve the dynamic changes produced in the cell. For sodium imaging experiments, because the emission intensity of SBFI excited by 340 nm light is highly pH sensitive (Diarra, Sheldon, and Church, 2001), changes in $[Na^+]_i$ were depicted as changes in R_{SBFI}, the emission intensity produced by 340 nm excitation of the cell at time 0 when pH = 7.4, $I_{340}(0)$, divided by the emission intensity of the cell excited by 380 nm light as a function of time, $I_{380}(t)$ ($R_{SBFI} = I_{340}(0)/I_{380}(t)$). Analyses of $[Ca^{2+}]_i$, R_{SBFI} and electrophysiological recordings were performed using Clampfit 10.5 (Axon Instruments). Statistical analysis was conducted using SigmaPlot 11 and SigmaStat 3 software (Systat Software, Inc.). Statistical differences were determined using paired and unpaired t-tests for within group and between group experiments, respectively, and were considered significant if $p < 0.05$. For multiple group comparisons 1- and 2-way ANOVAs, with or without repeat measures, were used, as appropriate. When significant differences were determined with an ANOVA, post-hoc analyses were conducted using a Dunn Test to determine differences between individual groups.

RESULTS

Our laboratory has shown that the concurrence of ischemia and acidosis, which occurs during stroke, results in a synergistic $[Ca^{2+}]_i$ overload in neurons and concomitant cell death (Mari et al., 2010). Given that NKCC1 has been implicated in $[Ca^{2+}]_i$ overload during reperfusion following oxygen-glucose

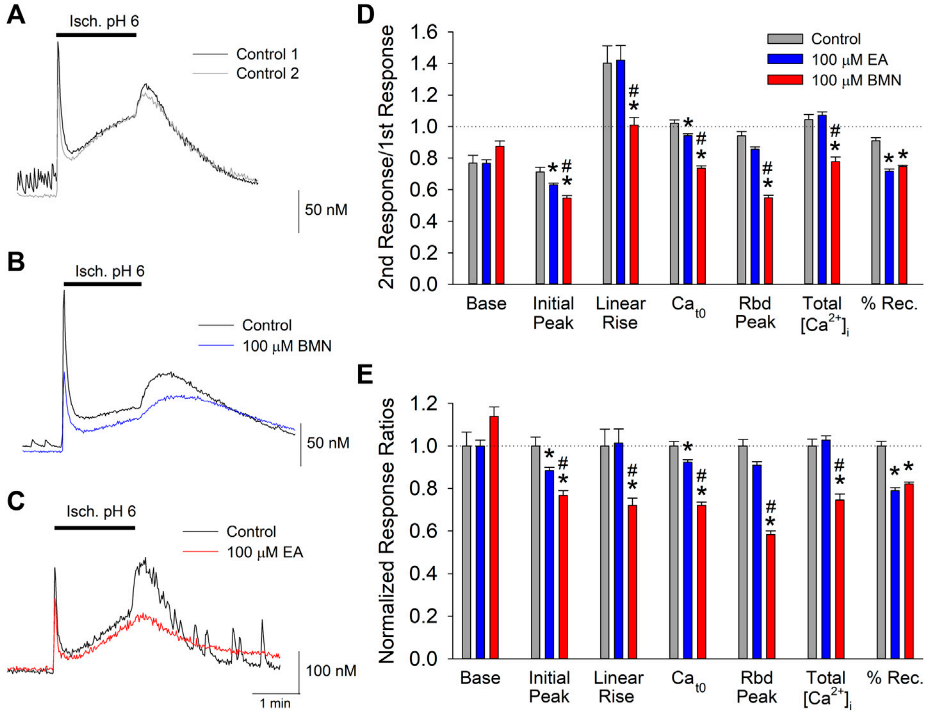

FIGURE 1 | Ischemia-acidosis evoked $[Ca^{2+}]_i$ increases in cultured rat cortical neurons are inhibited by bumetanide and ethacrynic acid. A, Representative traces of $[Ca^{2+}]_i$ as a function of time recorded from a single neuron in response to an initial 2-min ischemia-acidosis insult (Isc. pH 6; Control 1, black trace) and a second application of the Isc. pH 6 solution following a 20-min recovery period (Control 2, gray trace). Representative traces of $[Ca^{2+}]_i$ recorded from two neurons using the same protocol as in **(A)**, in the absence and presence of 100 µM bumetanide [**(B)**; Control, black trace; 100 µM BMN, blue trace] or 100 µM ethacrynic acid [**(C)**; Control, black trace, 100 µM EA, red trace]. **(D)**, Relative mean $[Ca^{2+}]_i$ (±SEM) responses obtained using the paired protocol with the second response, in the absence (Control, $n = 59$) and presence of 100 µM bumetanide (BMN, $n = 156$) or 100 µM Ethacrynic Acid (EA, $n = 140$), normalized to the first control response. Peak $[Ca^{2+}]_i$ increase was measured immediately after application of the ischemia-acidosis solution. Sustained $[Ca^{2+}]_i$ was measured just prior to washout of the Isc. pH 6 solution. Rebound $[Ca^{2+}]_i$ was the maximum $[Ca^{2+}]_i$ measured following washout of Isc. pH 6 solution. The percent recovery (%Rec) was calculated as the final $[Ca^{2+}]_i$ normalized to the maximum $[Ca^{2+}]_i$ after the initial transient peak ([final-baseline]/[rebound peak-baseline]). Total $[Ca^{2+}]_i$ increases were calculated by integrating beneath the traces of $[Ca^{2+}]_i$ vs. time. **(E)**, Same data in **(D)** with ratios normalized to Control/Control ratios. Asterisks denote significant difference from Control ($p < 0.05$) and pound symbols indicate significant difference between BMN and EA ($p < 0.05$). Bars above **(A)**, **(B)** and **(C)** indicate duration of ischemia-acidosis (Isc. pH 6.0).

deprivation (X. Chen et al., 2008), we examined the effects of the NKCC1 inhibitors, bumetanide and ethacrynic acid, on the $[Ca^{2+}]_i$ burden produced by simultaneous ischemia and acidosis in neurons. Consistent with previous studies, *in vitro* ischemia-acidosis (Isc. pH 6) induced a rapid, transient increase in $[Ca^{2+}]_i$ in cortical neurons followed by a slow steady rise in the continued presence of the Isc. pH 6 solution. Upon washout of the solution, the $[Ca^{2+}]_i$ rebounded to a second, slower decaying peak, before returning to near baseline levels (**Figure 1A**). Application of 100 µM bumetanide (**Figure 1B**, blue trace) or 100 µM ethacrynic acid (**Figure 1C**, red trace) resulted in a reduction in $[Ca^{2+}]_i$ elevations produced by ischemia-acidosis. Additionally, $[Ca^{2+}]_i$ recovered more slowly in the presence of these inhibitors. Combined data from identical experiments showed both bumetanide and ethacrynic acid reduced the initial peak increases and the sustained levels of $[Ca^{2+}]_i$ triggered by ischemia-acidosis. However, ethacrynic acid produced a statistically greater reduction in both of these $[Ca^{2+}]_i$ increases relative to bumetanide. Furthermore, ethacrynic acid, but not bumetanide, reduced the peak rebound increase in $[Ca^{2+}]_i$ observed upon washout of ischemia-acidosis (**Figures 1D,E**). While the loop diuretics inhibited the transient increases, they also decreased the rate of recovery from the elevated $[Ca^{2+}]_i$, resulting in an elevated $[Ca^{2+}]_i$ at the end of the recording period (9 min) relative to Control (**Figures 1D,E**). The total increase in $[Ca^{2+}]_i$ induced by ischemia-acidosis, as measured by integrating under the traces (Total $[Ca^{2+}]_i$), is dependent on the transient increases and as well as the degree of recovery during the recording period. For cells incubated in bumetanide, the decreased elevations in $[Ca^{2+}]_i$ occurring during ischemia-acidosis were offset by the reduced recovery during washout. Thus, bumetanide failed to reduce net $[Ca^{2+}]_i$ increases relative to Control. In contrast, ethacrynic acid, which produced a similar degree of inhibition of recovery as bumetanide, but a greater block of initial peak, sustained and rebound peak $[Ca^{2+}]_i$ than bumetanide, reduced the net $[Ca^{2+}]_i$ increase produced by ischemia-acidosis (**Figures 1D,E**).

In addition to affecting $[Ca^{2+}]_i$, NKCC1 has been implicated in elevations in $[Na^+]_i$ during post-ischemia reperfusion (X. Chen et al., 2008). This $[Na^+]_i$ overload causes cellular edema and promotes cell death. Thus, it was of interest to determine if NKCC1 plays a significant role in intracellular Na^+ homeostasis

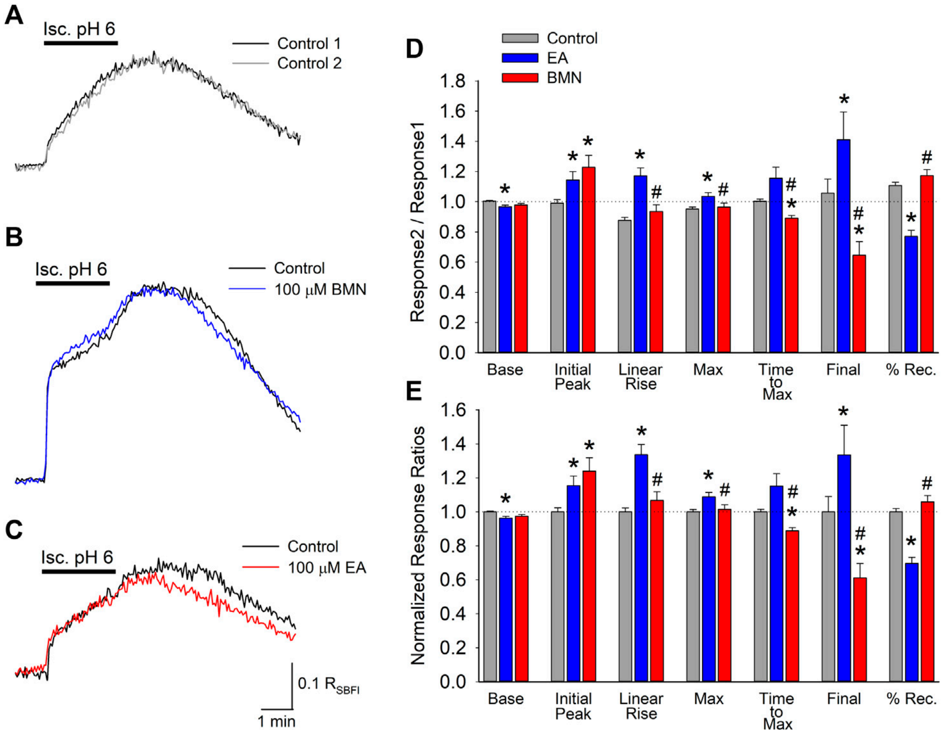

FIGURE 2 | Increases in $[Na^+]_i$, depicted by R_{SBFI}, evoked by concurrent ischemia and acidosis are not inhibited by NKCC1 inhibitors. **(A)**, Representative traces of R_{SBFI} as a function of time recorded from a single neuron during two, 2-min ischemia-acidosis insults with a 20 min recovery period in between. **(B)**, Representative traces of R_{SBFI} as a function of time recorded from a single neuron in response to two, 2-min ischemia-acidosis applications, first in the absence (Control, black trace) and 20 min later in the presence of 100 µM bumetanide (100 µM BMN, blue trace). **(C)**, Representative traces of R_{SBFI} as a function of time recorded from a single neuron in response to two, 2-min ischemia-acidosis applications, first in the absence (Control, black trace) and 20 min later in the presence of 100 µM ethacrynic acid (100 µM EA, red trace). **(D)**, Relative mean R_{SBFI} (±SEM) measured in the absence (Control) and presence of 100 µM bumetanide (100 µM BMN, *n* = 108) or 100 µM ethacrynic acid (100 µM EA, *n* = 49). Responses were normalized to control responses in the same cells. Baseline and Initial Peak represent R_{SBFI} values measured immediately prior to and 15 s after initiation of ischemia-acidosis. Max Peak represents highest R_{SBFI} measured during ischemia + acidosis. Recovery was calculated as (final-baseline)/(maximum-baseline). **(E)**, Same data presented in **(D)** but normalized to the Response2/Response1 ratio for Control. Asterisks denote significant difference from Control ($p < 0.05$) and pound symbol indicates significant difference between BMN and EA ($p < 0.05$). Bars above **(A)** and **(B)** indicate duration of ischemia + acidosis (Isc. pH 6.0).

during ischemia-acidosis and during reperfusion. SBFI loaded cultured cortical neurons were imaged to determine the effects of ischemia-acidosis on intracellular Na^+ by monitoring R_{SBFI}. Ischemia-acidosis was found to produce an immediate rapid rise in $[Na^+]_i$ followed by a slow steady increase that persisted for approximately 1 min following washout of the ischemia-acidosis solution before $[Na^+]_i$ returned towards baseline (**Figure 2A**). Application of either 100 µM bumetanide or 100 µM ethacrynic acid failed to significantly alter increases in $[Na^+]_i$ produced by ischemia-acidosis, but both effected recovery from these $[Na^+]_i$ elevations (**Figures 2B,C**). Compiled data showed that basal $[Na^+]_i$ was not affected by either bumetanide or ethacrynic acid (**Figures 2D,E**). Similarly, neither the initial peak $[Na^+]_i$ nor the maximum peak $[Na^+]_i$ were significantly affected by the NKCC1 inhibitors (**Figures 2D,E**). However, opposite effects on the recovery from these induced $[Na^+]_i$ increases were noted for the two NKCC1 inhibitors, with bumetanide slowing down recovery and ethacrynic acid accelerating return to baseline $[Na^+]_i$ (**Figure 2D**).

The fact the two NKCC1 antagonists, bumetanide and ethacrynic acid, failed to block elevations in $[Na^+]_i$ observed following ischemia-acidosis suggests that NKCC1 is not the site of action responsible for the mitigation of $[Ca^{2+}]_i$ overload by these drugs under these conditions. Our laboratory has previously shown the initial, transient rise in $[Ca^{2+}]_i$ following ischemia-acidosis is dependent on activation of acid-sensing ion channels (ASIC) (Mari et al., 2010). Since this rise was BMN- and EA-sensitive, we examined the effects of these loop diuretics on ASIC-mediated whole-cell currents in isolated cortical neurons. Application of acidic PSS (pH 6.0) evoked transient inward currents in neurons voltage-clamped at −70 mV, consistent with ASIC activation (**Figure 3A**). Bumetanide (100 µM) was found to increase peak current amplitudes by 13% and decay times by 25% which resulted in no significant difference in the net inward current induced by 10 s acidosis compared to control (**Figures 3B,D,E**). In contrast, while ethacrynic acid (100 µM) did not statistically alter the peak inward current amplitude or the time constant of its decay, the small apparent decrease in both resulted in a 10% block of the net inward current produced by 10 s acidosis (**Figure 3C,D,E**). These

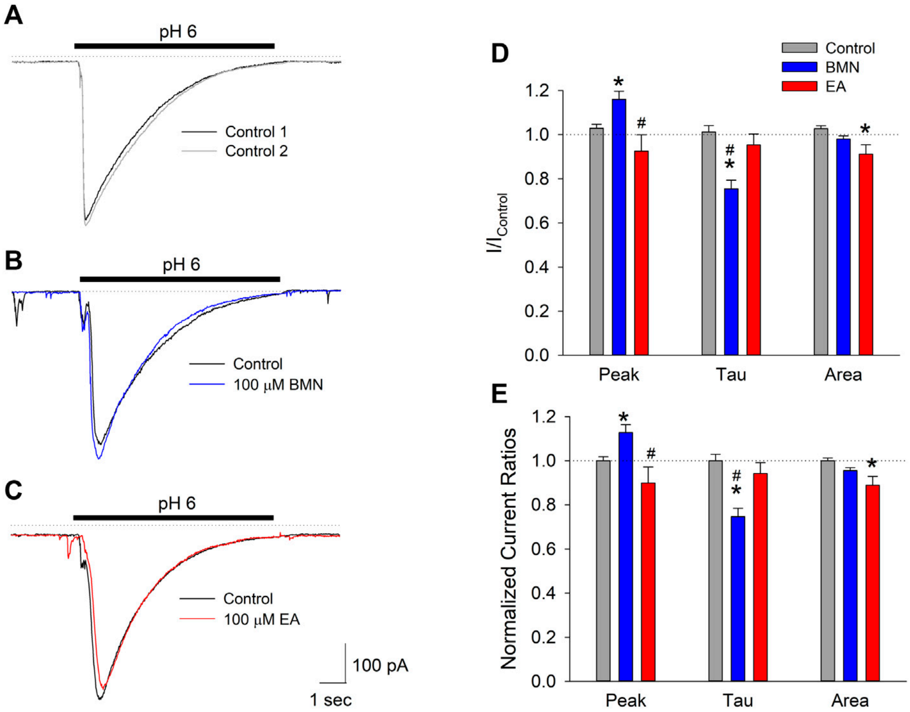

FIGURE 3 | Peak inward ASIC-mediated currents are not inhibited by bumetanide or ethacrynic acid. **(A)**, Representative traces of inward currents activated by two 10 s applications of acidic solution (pH 6.0) onto a single cell voltage clamped at –70 mV. **(B)**, Representative traces of inward currents activated by 10 s applications of PSS at pH 6.0 onto a single cell voltage-clamped at –70 mV in the absence (Control, black trace) and presence of 100 μM bumetanide (100 μM BMN, blue trace). **(C)**, Representative traces of inward currents activated by 10 s applications of PSS at pH 6.0 onto a single cell voltage-clamped at –70 mV in the absence (Control, black trace) and presence of 100 μM ethacrynic acid (100 μM EA, red trace). **(D)**, Mean peak inward currents, rates of current decay (τ) and net current (area under current trace) (±SEM) measured in the absence (Control, $n = 16$) and presence of 100 μM bumetanide (BMN, $n = 6$) and 100 μM ethacrynic acid (EA, $n = 10$) normalized to initial control responses (absence of drugs). **(E)**, Data in **(D)** normalized to Response2/Response1 ratio for Control. Asterisks denote significant difference from Control ($p < 0.05$) and pound symbols indicate significant difference between BMN and EA ($p < 0.05$). Bars above **(A)**, **(B)**, and **(C)** indicate duration of low pH application (pH 6.0). In all experiments, second low pH solution application was carried out after a 5 min washout of the initial acid stimulation.

results, however, are not consistent with the 10 and 20% blocks of initial $[Ca^{2+}]_i$ increases by BMN and EA, respectively (see **Figure 1**), which suggests that these drugs are modulating Ca^{2+} influx pathways distinct from ASIC.

Activation of NMDA receptors has also been shown to occur during ischemia-acidosis and produces increases in neuronal $[Ca^{2+}]_i$ (Mari et al., 2010). To determine if bumetanide and/or ethacrynic acid inhibit ionotropic glutamatergic currents, whole cell currents were recorded in neurons voltage clamped at -70 mV and perfused with 20 μM glutamate in the absence and presence of the two drugs (**Figures 4A–C**). The NCCK1 inhibitors did not produce appreciable changes in ionotropic glutamatergic responses (**Figures 4B,C**). **Figure 4D** shows bar graph of mean peak, steady-state and net inward currents (Charge Influx) recorded from multiple neurons during 10 s glutamate applications. Neither 100 μM bumetanide nor 100 μM ethacrynic acid significantly inhibited any of the components of the glutamate-evoked currents (**Figures 4D**).

The inability of bumetanide to inhibit acidosis- and glutamate-evoked inward currents in cultured cortical neurons raises the possibility that the reduction of ischemia-acidosis induced $[Ca^{2+}]_i$ increases produced by this NCCK1 inhibitor might be due to block of Ca^{2+} influx through voltage-gated Ca^{2+} channels (VGCC). Previous studies in our laboratory have shown VGCC are activated downstream of ASIC following ischemia-acidosis (Mari et al., 2010). Neurons were voltage-clamped at -70 mV and depolarizing membrane pulses applied to -10 mV, in the presence of TTX and TEA, to isolate currents through VGCC. **Figure 5A** shows representative membrane currents recorded from a single neuron in response to membrane depolarizations in the absence (Control) and presence of 10 μM bumetanide (BMN). At this concentration, bumetanide decreased the peak current amplitude by approximately 40%. **Figure 5B** shows representative membrane currents recorded from a single neuron in response to membrane depolarizations in the absence (Control) and presence of 56 μM ethacrynic acid (EA). In this cell, 56 μM ethacrynic acid produced an approximately 60% reduction in the VGCC-mediated current. Using identical methods, concentration-response relationships were constructed for bumetanide and ethacrynic acid inhibition of VGCC-mediated currents (**Figure 5C**). Data points were best fit with a single-site Langmuir-Hill equation (Cuevas and Adams, 1997) with half-maximal inhibitions (IC_{50}), Hill coefficients and non-reducible current (asymptotic minimum) values of 8 μM, 0.41 and 0.37, respectively for BMN (blue circles and line) and 36 μM, 0.75 and

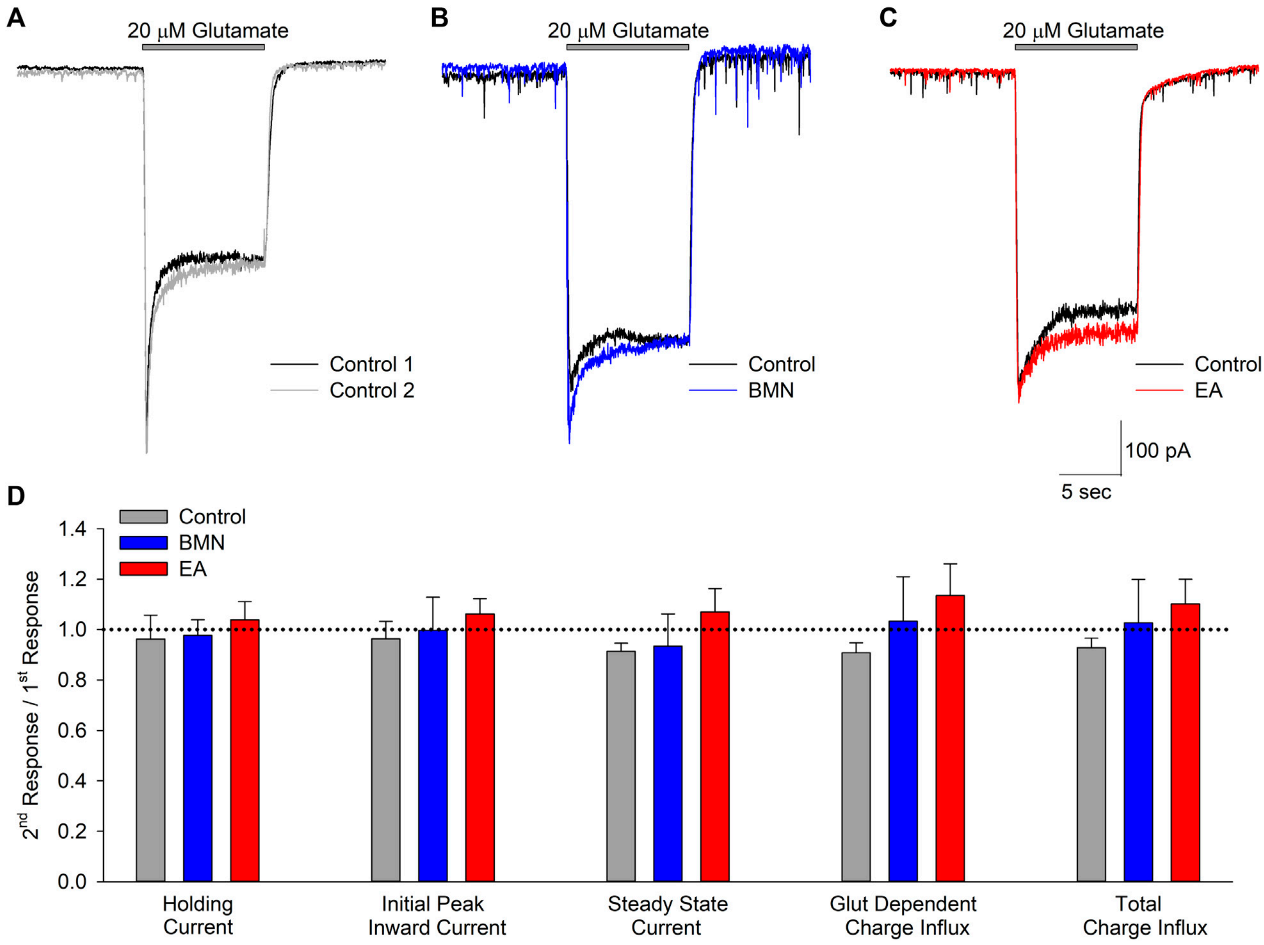

FIGURE 4 | Glutamate activated inward currents are not inhibited by bumetanide or ethacrynic acid. **(A)**, Representative traces of whole-cell currents recorded from a single neuron voltage clamped at −70 mV in response to two 10 s applications of 20 µM glutamate. **(B)**, Representative traces of whole-cell currents recorded from a single neuron voltage clamped at −70 mV in response to a 10 s application of 20 µM glutamate in the absence (Control, black trace) and presence of 100 µM bumetanide (100 µM BMN, blue trace). **(C)**, Representative traces of whole cell currents recorded from a single neuron voltage clamped at −70 mV in response to a 10 s application of 20 µM glutamate in the absence (Control, black trace) and presence of 100 µM ethacrynic acid (100 µM EA, red trace). **(D)**, Bar graph of compiled data from experiments identical to those in A ($n = 5$), B ($n = 4$) and C ($n = 4$). Data are shown as the ratio of second responses to first responses in the absence (Control) and presence of drug (BMN or EA). Data shown are mean response ratios (±SEM) of holding current, initial peak and steady state (measured at the end of the 10 s application) inward currents, and charge influx during glutamate application (Glut Dependent) and throughout the recording (Total). No significant differences were noted for any of the parameters measured ($p > 0.12$ for all). Bars above traces in A-C denote times of glutamate application.

0.0 for EA (red circles and line) (**Figure 5C**). Thus, ethacrynic acid has lower affinity for the channel, but greater efficacy than bumetanide for blocking VGCCs in cortical neurons.

Our laboratory has shown that elevations of $[Ca^{2+}]_i$ triggered by acidosis can also be reduced via the inhibition of voltage-gate Na^+ channels (VGSC). Furthermore, blocking of VGSC has been shown to lessen neuronal $[Ca^{2+}]_i$ increases observed after oxygen-glucose deprivation (LoPachin, Gaughan, Lehning, Weber, and Taylor, 2001; Herrera et al., 2008). Thus, we examined if the loop diuretics, bumetanide and ethacrynic acid, also effected VGSC in cortical neurons. Inward VGSC currents were activated by stepping voltage clamped neurons from −70 mV to −30 mV in the presence of TEA, Ba^{2+} and Cd^{2+}. Representative VGSC currents recorded from a single neuron are shown in **Figure 6A** and demonstrate BMN inhibit VGSC. Similarly, VGSC currents were reduced by micromolar concentrations of EA (**Figure 6B**). Concentration-response relationships were constructed using measurements from 86 neurons and concentrations of bumetanide ranging from 0.3 to 1,000 µM and on 46 neurons using concentrations of ethacrynic acid ranging from 3 to 1,000 µM. **Figure 6C** shows the data points were best fit with a single-site Langmuir-Hill equation with IC_{50}, Hill coefficient and non-reducible current (asymptotic minimum) values of 19 µM, 0.46 and 0.21, respectively for BMN (blue circles and line) and 36 µM, 0.72 and 0.22, respectively for EA (red circles and line). These results indicate nearly 20% of the VGSC current is BMN and EA-insensitive.

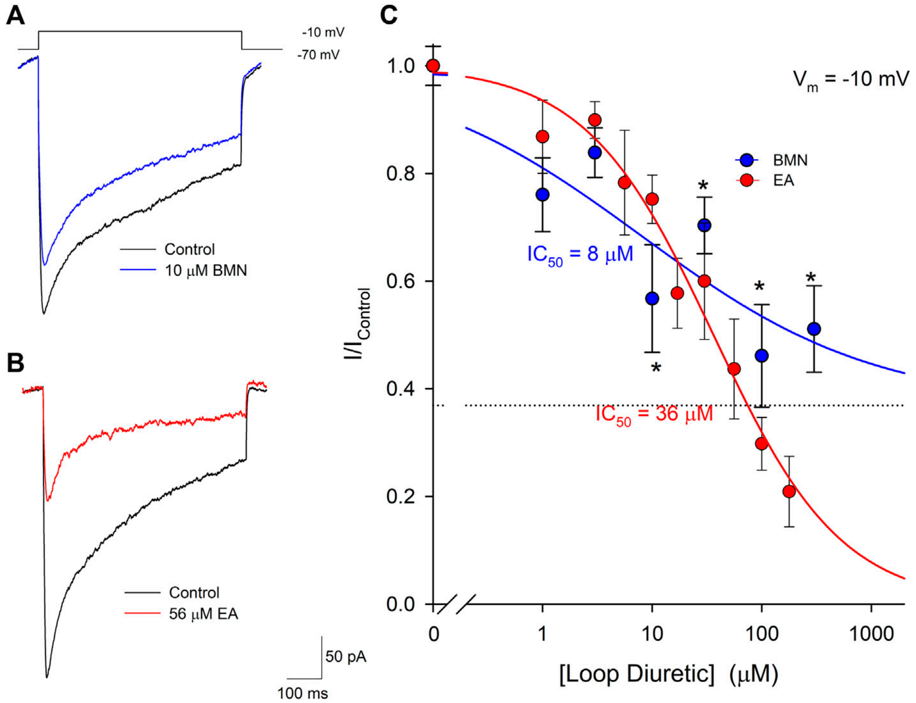

FIGURE 5 | Bumetanide and ethacrynic acid inhibit voltage-gated calcium channels in a dose-dependent manner. **(A)**, Representative traces of whole-cell VGCC currents recorded from a single neuron in response to a 500 msec step from a holding potential of –70 mV to –10 mV in the absence (Control, black trace) and presence of 10 μM bumetanide (10 μM BMN, blue trace). **(B)**, Representative traces of whole-cell VGCC currents recorded from a single neuron in response to a 500 msec step from a holding potential of -70 mV to –10 mV in the absence (Control, black trace) and presence of 56 μM ethacrynic acid (56 μM EA, red trace). **(C)**, Concentration-response relationships of relative peak inward VGCC currents (mean ± SEM) activated by voltage steps from –70 mV to –10 mV. Currents were normalized to control peak currents measured in the absence of bumetanide or ethacrynic acid. Data points (bumetanide blue circles; ethacrynic acid red circles) were best fit (bumetanide blue line, ethacrynic acid red line) using a single-site Langmuir-Hill equation with an asymptotic minimum (dashed line for BMN). *n* > 7 for each data point. Asterisks denote significant difference from Control ($p < 0.05$).

It should also be noted that the blocks of these voltage-gated currents by the loop diuretics were not voltage dependent. There were no observable shifts in the voltages for maximal current amplitude (**Supplementary Figure S1**) in the presence of half-maximal concentrations of BMN or EA compared to control.

The 70% block of VGSC currents by maximal concentrations of bumetanide only occurred in a fraction of the neurons tested. Of the 103 cells used to measure bumetanide inhibition of VGSC currents, 31 were found to be inhibited by ~20% by millimolar concentrations of bumetanide. A concentration-response relationship for VGSC currents in bumetanide-resistant neurons failed to exhibit any concentration-dependence of block (solid line), in contrast to the dose-response relationship observed in the bumetanide-sensitive neurons (dashed line) (**Figure 7A**). **Figure 7B** shows current traces from two different voltage clamped neurons stepped from a holding potential of −70 to −30 mV in the absence and presence of 1 mM bumetanide, 100 nM TTX and 1 mM BMN + 100 nM TTX. The current traces on the left are from a representative neuron resistant to bumetanide block, whereas the traces on the right are from a neuron sensitive to bumetanide block. The data from 10 cells exposed to this protocol were grouped according to bumetanide sensitivity and each group analyzed with a two-way ANOVA to determine if there were interactions between TTX and bumetanide (**Figure 7C**). For the bumetanide resistant currents, there was no interaction between the two compounds ($p = 0.336$) (**Figure 7C**), while, in bumetanide sensitive neurons there was a statistically significant interaction between the drugs, such that the response to bumetanide was dependent on the presence of TTX ($p < 0.02$) (**Figure 7C**). While both BMN and TTX reduced the VGSC current amplitude relative to control alone ($p < 0.001$ and $p = 0.002$, respectively), the combination BMN + TTX was not significantly different from either BMN ($p = 0.981$) or TTX ($p = 0.49$) alone (**Figure 7C**). To further facilitate comparison, we determined the percent block observed for each condition, BMN, TTX and BMN + TTX. **Figure 7D** shows the percent inhibition (mean ± SEM) observed for both bumetanide-resistant (left panel) and bumetanide-sensitive (right panel) neurons. In bumetanide-resistant neurons, 1 mM BMN inhibited VGSC currents by only ~26%, while TTX and BMN + TTX inhibited the responses by over 70% (**Figure 7D**). In these neurons, there were statistically significant blocks produced by TTX and BMN + TTX. The block by BMN alone was significantly different from inhibition with TTX present ($p < 0.001$). In contrast, VGSC currents from the bumetanide-sensitive cells were all blocked by >70% by BMN, TTX and BMN + TTX (**Figure 7C**) and these inhibitions were not significantly different from each other.

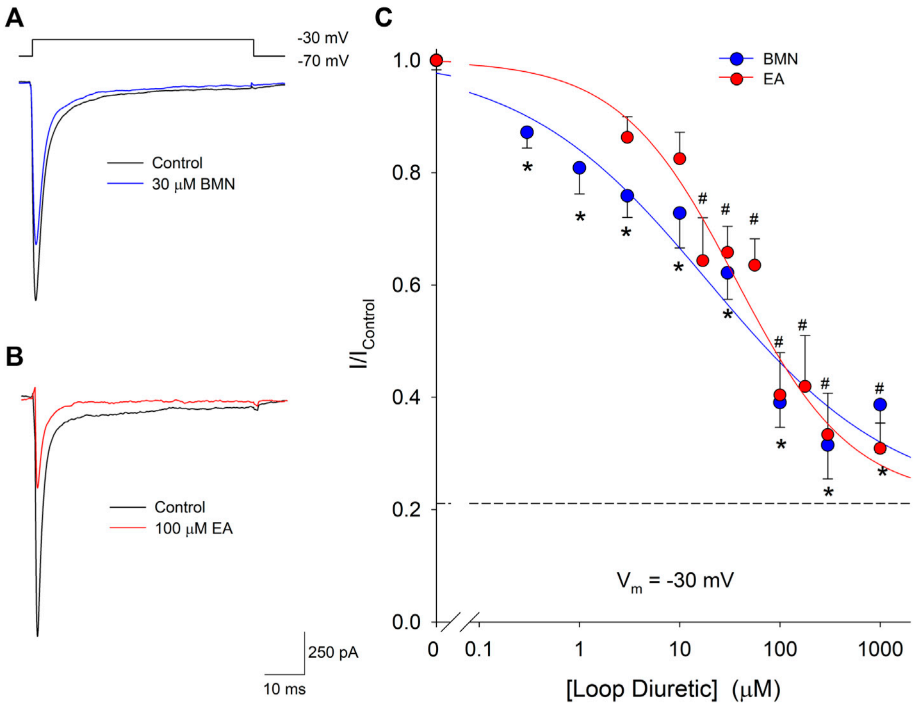

FIGURE 6 | Bumetanide and ethacrynic acid inhibit voltage-gated sodium channels in a dose-dependent manner. **(A)**, Representative traces of whole-cell VGSC currents recorded from a single neuron in response to 50 msec steps from a holding potential of –70 mV to –30 mV in the absence (Control, black trace) and presence of 30 µM Bumetanide (30 µM BMN, blue trace). **(B)**, Representative traces of whole-cell VGSC currents recorded from a single neuron in response to 50 msec steps from a holding potential of –70 mV to –30 mV in the absence (Control, black trace) and presence of 100 µM ethacrynic acid (100 µM EA, red trace). **(C)**, Concentration-response relationship of relative peak inward VGSC currents (mean ± SEM) elicited by voltage steps from –70 to –30 mV. Currents were normalized to control peak currents measured in the absence of bumetanide or ethacrynic acid. Data points (bumetanide blue circles; ethacrynic acid red circles) were best fit (bumetanide blue line, ethacrynic acid red line) to a single-site Langmuir-Hill equation with an asymptotic minimum (dashed line). $n > 15$ for all bumetanide data points and $n > 6$ for all ethacrynic acid data points. Asterisks and pound symbols denote significant difference from Control for BMN and EA, respectively ($p < 0.05$). Neurons for these experiments were electrically accessed using the conventional (dialyzing) whole-cell patch clamp recording configuration.

DISCUSSION

The primary finding of this study is the loop diuretics bumetanide and ethacrynic acid inhibit voltage-gated Ca^{2+} and Na^+ ion channels that contribute to intracellular Ca^{2+} dysregulation evoked by ischemia-acidosis in neurons. The IC_{50} values of BMN and EA for these channels are consistent with the concentrations of the loop diuretics required to inhibit the ischemia-acidosis evoked $[Ca^{2+}]_i$ overload. Neither loop diuretic significantly blocked acidosis- or glutamate-activated whole cell inward currents, suggesting that the inhibition of ischemia-acidosis induced $[Ca^{2+}]_i$ overload was not due to block of ASIC or glutamatergic ion channels. In addition, neither BMN nor EA significantly altered ischemia-acidosis induced increases in $[Na^+]_i$. Thus, the increase in $[Na^+]_i$ induced by ischemia-acidosis is not mediated by Na^+ influx through either VGSCs or NKCC. These observations further suggest that loop diuretic suppression of $[Ca^{2+}]_i$ overload during ischemia-acidosis is not a downstream effect of mechanisms activated to preserve $[Na^+]_i$ homeostasis.

Our laboratory first showed ischemia and acidosis interact to produce a synergistic increase in neuronal $[Ca^{2+}]_i$ overload (Mari et al., 2010). While several ion channels, including acid-sensing ion channels, VGCC and NMDA receptors were all found to contribute to the increases in $[Ca^{2+}]_i$, use of specific blockers of these channels suggested additional molecular mechanisms were likely involved in the ischemia-acidosis evoked $[Ca^{2+}]_i$ dysregulation. Both bumetanide and ethacrynic acid inhibited multiple components of the ischemia-acidosis evoked $[Ca^{2+}]_i$ overload, including the initial transient increase, sustained levels and rebound peak increase in $[Ca^{2+}]_i$. This suggested bumetanide and ethacrynic acid are either inhibiting multiple proteins that cause this $[Ca^{2+}]_i$ overload or are affecting mechanisms that directly or indirectly influence $[Ca^{2+}]_i$ handling throughout the ischemia-acidosis event. Activation of ASIC, NMDA and VGCC all produce rapid increases in neuronal $[Ca^{2+}]_i$ and impact the initial rapid transient increase in $[Ca^{2+}]_i$ (Mari et al., 2010; Mari, Katnik, and Cuevas, 2015). However, neither bumetanide nor ethacrynic acid were found to appreciably block ASIC- or NMDA-mediated currents at concentrations as high as 100 µM. Thus, it is unlikely inhibition of these channels by the loop diuretics produces the reduction in ischemia-acidosis evoked synergistic increases in neuronal $[Ca^{2+}]_i$ overload. In contrast, both bumetanide and ethacrynic acid were found to inhibit VGCC.

These loop diuretics are inhibitors of the renal Na-K-Cl cotransporters, NKCC1 and NKCC2. Bumetanide has been shown to inhibit rat NKCC1 and NKCC2 with IC_{50} values of ~6 µM (Hannaert, Alvarez-Guerra, Pirot, Nazaret, and Garay,

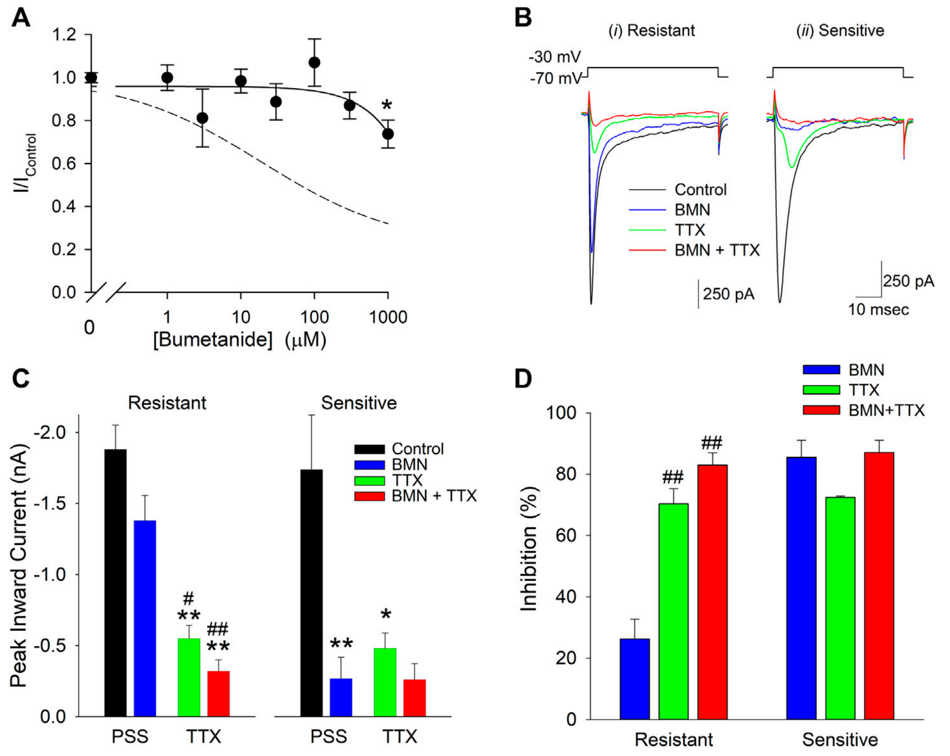

FIGURE 7 | Sensitivity to inhibition by bumetanide distinguishes two populations of voltage-gated sodium channels in cultured neurons. **(A)**, Normalized peak inward VGSC currents (mean ± SEM) as a function of bumetanide concentration recorded from neurons with VGSC resistant to bumetanide blockade ($n > 7$). Currents were activated by voltage steps from a holding potential of –70 mV to –30 mV and normalized to control peak currents measured in the absence of bumetanide at the indicated concentrations. Data points were best fit (solid line) to a linear equation with a slope of $-0.2\ nM^{-1}$. Dotted line is the single-site Langmuir-Hill equation fit to the data from the bumetanide-sensitive neurons shown in **Figure 6**. **(B)**, Representative traces of whole-cell currents evoked by 50 msec voltage steps from a holding potential of –70 mV to –30 mV recorded from two different neurons, one with primarily VGSC currents resistant to bumetanide (*i*, Resistant) and one with VGSC sensitive to inhibition by bumetanide (*ii*, Sensitive). Currents were elicited from the neurons in the absence of drug (Control, black traces), and in the presence of 1 mM Bumetanide (BMN, blue traces), 100 nM TTX (TTX, green traces) and 1 mM Bumetanide +100 nM TTX (BMN + TTX, red traces). **(C)**, Peak inward VGSC currents (mean ± SEM) measured from 4 bumetanide-resistant (Resistant, left panel) and 6 bumetanide-sensitive (Sensitive, right panel) neurons using the same protocol as **(B)**. A two-way ANOVA followed by a post-hoc Tukey Test indicates no significant interaction between BMN and TTX in the Resistant group ($p = 0.336$), but a significant interaction between TTX and BMN in the Sensitive group ($p < 0.02$). A one-way ANOVA followed by a post-hoc Tukey Test on the Resistant group indicates TTX and BMN + TTX are both significantly different from Control ($p < 0.001$) and BMN ($p < 0.05$ and 0.001, respectively) but not each other and BMN was not significantly different from Control ($p = 0.079$). **(D)**, Percent block of normalized peak VGSC currents (Percent block = $(1-I/I_{Control})*100$) calculated from the currents measured in **(B)** for cells Resistant (left panel) or Sensitive (right panel) to BMN. A one-way ANOVA indicates BMN produces a statistically significant lower block than TTX or TTX + BMN in resistant cells ($p < 0.001$). No significant differences were noted for block in the BMN-sensitive cells ($p = 0.10$). Asterisks indicate significant difference from Control, pound sign indicates significant difference from BMN determined by Two-Way ANOVA ($^{*,\#}p < 0.05$: $^{**,\#\#}p < 0.001$).

2002). The IC_{50} observed in the current study for bumetanide inhibition of voltage-gated Ca^{2+} channels, 8 μM, is nearly identical to that for NKCC1/NKCC2. However, while bumetanide at the highest concentrations (>50 μM) blocked nearly all of the activity of both NKCC1 and NKCC2 (Hannaert et al., 2002), over 40% of the VGCC current was resistant to 300 μM bumetanide. It remains to be determined if this bumetanide-resistant component represents a specific VGCC subtype or if the compound has low efficacy for VGCC in general. While the effects of loop diuretics on neuronal VGCC were previously unknown, bumetanide can inhibit VGCC in cardiac myocytes at low μM concentrations (Shimoni, 1991). Inhibition of VGCC in cardiomyocytes by bumetanide was found to be as high as 80% of the peak VGCC current and varied significantly from cell to cell (Shimoni, 1991).

Ethacrynic acid is structurally dissimilar to bumetanide and higher concentrations are required to inhibit both transporter subtypes. EA inhibits NKCC1 in avian erythrocytes and NKCC2 in canine renal epithelial cells with IC_{50} values of 180 and 20 μM, respectively, (Rugg, Simmons, and Tivey, 1986; Palfrey and Leung, 1993). Given the IC_{50} value for EA inhibition of VGCC is 36 μM, EA is a more potent inhibitor of VGCC than NKCC. While EA was less potent than bumetanide at inhibiting VGCC, EA exhibited greater efficacy for these channels, with 178 μM EA blocking ~80% of the VGCC currents in the neurons. Unlike bumetanide, ethacrynic acid, which is structurally dissimilar and does not contain a sulfonamide substituent, has not been previously shown to modulate VGCC in any cell type.

Bumetanide blocked voltage-gated Na^+ channels with an IC_{50} (19 μM) similar to its IC_{50} for NKCC1 and NKCC2. In contrast to observations of VGCC block by bumetanide in the current study, a population of cortical neurons expressed VGSC that were resistant to bumetanide block, even at the highest concentrations (1 mM). In both bumetanide-sensitive and bumetanide-insensitive cells, VGSC currents were blocked by >70% by TTX (100 nM). Bumetanide application did not have an additive effect with TTX, suggesting bumetanide specifically inhibits one of the TTX-sensitive channel subtypes expressed in cortical neurons. Cortical neurons express a variety of TTX-sensitive VGSC, including NaV1.1, NaV1.2, NaV1.3, NaV1.6 and NaV1.7 and the TTX-insensitive NaV1.9 (Jeong et al., 2000; de Lera Ruiz and Kraus, 2015; Rubinstein et al., 2016). Thus, bumetanide does not appear to affect NaV1.9. The specific TTX-sensitive NaV subtype affected by bumetanide remains to be determined.

The ethacrynic acid block of VGSC (IC_{50} = 36 μM) was more potent than its block of NKCC1 but comparable to its block of NKCC2. Like bumetanide, EA failed to completely block VGSC currents, with approximately 20% of the current remaining at 1 mM EA.

Inhibition of voltage-gated sodium channels by BMN and EA did not alter $[Na^+]_i$ accumulation caused by ischemia-acidosis. Neither the initial rapid rise in $[Na^+]_i$ due to ischemia-acidosis, nor the slow rise in $[Na^+]_i$ during the ischemic event were reduced by either compound at concentrations that significantly inhibit VGSC (100 μM). Both ischemia and acidosis are known to evoke increases in $[Na^+]_i$ resulting in reverse-mode activity of the Na^+/Ca^{2+} exchanger (Lenart et al., 2004; Kintner et al., 2007; Luo et al., 2008). Extrusion of Na^+ by NCX produces Ca^{2+} influx and $[Ca^{2+}]_i$ elevations. Given $[Na^+]_i$ is not affected by the loop diuretics, it does not appear a reduction in $[Na^+]_i$ produced by inhibition of VGSC and concomitant lessening of Ca^{2+} influx via NCX can explain the ability of these loop diuretics to mitigate ischemia-acidosis evoked $[Ca^{2+}]_i$ overload. NKCC activity has been implicated in the $[Na^+]_i$ accumulation that precedes NCX activity and $[Ca^{2+}]_i$ overload in astrocytes (Lenart et al., 2004; Kintner et al., 2007; Luo et al., 2008). Neither bumetanide nor ethacrynic acid reduced the $[Na^+]_i$ elevation in neurons suggesting NKCC is not a major conduit for ischemia-acidosis induced Na^+ influx which leads to $[Ca^{2+}]_i$ overload. The lack of NKCC contribution to $[Na^+]_i$ increases may be due to reduced activity of the cotransporter during ischemia-acidosis. It was previously reported the activity of NKCC1 is reduced by ~80% when extracellular pH approaches 6.0 (Hegde and Palfrey, 1992).

Stroke-induced gray and white matter injury in mice was shown to be reduced in NKCC knockout animals (H. Chen, Luo, Kintner, Shull, and Sun, 2005). Similarly, bumetanide was shown to reduce infarct volume in a rat middle cerebral artery occlusion stroke model (O'Donnell, Tran, Lam, Liu, and Anderson, 2004). NKCC1 effects on $[Na^+]_i$ in neurons and astrocytes appeared during re-oxygenation rather than during the ischemic event (H. Chen et al., 2005), consistent with our observation that bumetanide does not reduce $[Na^+]_i$ accumulation during ischemia-acidosis. While reduced edema associated with NKCC1 inhibition by bumetanide may lessen stroke injury (O'Donnell et al., 2004), the blunting of $[Ca^{2+}]_i$ overload in response to ischemia-acidosis by BMN would also improve outcomes in stroke. Similarly, inhibition of voltage-gated channels may explain how bumetanide reduces glutamate-mediated excitotoxicity (Beck, Lenart, Kintner, and Sun, 2003).

Bumetanide has been shown to decrease seizure activity in humans (Kahle and Staley, 2008). Results from the current study suggest this effect may be due to the inhibition of voltage-gated channels. The inhibition of voltage-gated Ca^{2+} channels is known to contribute to the actions of antiepileptic drugs, such as levetiracetam (Niespodziany, Klitgaard, and Margineanu, 2001; Yan et al., 2013). Similarly, inhibiting TTX-sensitive sodium channels, such as NaV1.6 has been shown to blunt seizure activity in rat epilepsy models (Hargus, Nigam, Bertram, and Patel, 2013; Shao et al., 2017). Finally, loop diuretics, including bumetanide, have been shown to promote direct vasorelaxation in the concentration range shown here to be effective for VGCC and VGSC block (Pickkers, Russel, Thien, Hughes, and Smits, 2003). Therefore, direct inhibition of these channels which contribute to vascular tone may explain these effects.

Clinically, bumetanide and ethacrynic acid, are used in edematous states, such as heart failure, to promote diuresis and natriuresis (Somberg and Molnar, 2009). This effect is due to the ability of these compounds to block the NKCC2 cotransporter, primarily in the Loop of Henle, and prevent the reuptake of Na^+, K^+, and Cl^- from the tubular fluid. Loop diuretics have additional effects, such as the lowering of blood pressure, which is often observed even prior to diuresis (Gabriel, 1983). The effective concentrations of bumetanide and ethacrynic acid reported here are consistent with clinically relevant doses (Ward and Heel, 1984; Lacreta et al., 1994; van der Heijden et al., 1998), and thus may contribute to the systemic effects of these compounds. It will be important to determine if other off-target effects of these loop diuretics contribute to the decrease in $[Ca^{2+}]_i$ overload reported here.

In conclusion, the loop diuretics, bumetanide and ethacrynic acid effectively suppress ischemia-acidosis induced $[Ca^{2+}]_i$ overload in neurons at concentrations near their respective IC_{50} values for NKCC inhibition. These effects appear to be in part mediated via the inhibition of voltage-gated Ca^{2+} and Na^+ channels and are not due to any direct effects on ionotropic glutamatergic receptors or acid-sensing ion channels. Furthermore, the inability of the loop diuretics to reduce ischemia-acidosis evoked $[Na^+]_i$ elevations suggest NKCC cotransporters are not involved in neuronal ionic imbalances during ischemia-acidosis; and inhibition of these transporters does not account for the beneficial effects of bumetanide and ethacrynic acid under these conditions. However, the ability of these loop diuretics to lessen ischemia-acidosis induced $[Ca^{2+}]_i$ overload suggests that they may be useful for reducing stroke injury and that their effect on Ca^{2+} and Na^+ channels may in part explain observations made in previous studies.

DATA AVAILABILITY STATEMENT

The raw data supporting the conclusions of this article will be made available by the authors, without undue reservation.

ETHICS STATEMENT

The animal study was reviewed and approved by University of South Florida Institutional Animal Care and Use Committee.

AUTHOR CONTRIBUTIONS

CK and JC contributed to conception and design of the study. CK performed all experiments. CK and JC performed statistical analysis. CK wrote the first draft of the manuscript. All authors contributed to manuscript revision, read, and approved the submitted version.

SUPPLEMENTARY MATERIAL

The Supplementary Material for this article can be found online at: https://www.frontiersin.org/articles/10.3389/fphar.2021.732922/full#supplementary-material

SUPPLEMENTARY FIGURE S1 | Bumetanide and Ethacrynic acid inhibition of voltage-gated sodium and calcium channels does not shift the voltages of maximal current activation. **(A)**, Current-voltage relationships of mean peak whole-cell VGSC currents (mean ± SEM, *n* = 27) recorded from neurons in response to 50 msec steps from a holding potential of −70 mV to test potentials from −70 to + 60 mV in both the absence (Control, black) and presence of 56 μM ethacrynic acid (56 μM EA, red). **(B)**, Current-voltage relationships of mean peak whole-cell VGSC currents (mean ± SEM, *n* = 12) recorded from neurons in response to 50 msec steps from a holding potential of −70 mV to test potentials from −50 to +5 mV in both the absence (Control, black) and presence of 30 μM bumetanide acid (30 μM BMN, blue). **(C)**, Current-voltage relationships of mean peak whole-cell VGCC currents (mean ± SEM, *n* = 11) recorded from neurons in response to 500 msec steps from a holding potential of −70 mV to test potentials from −60 to + 40 mV in both the absence (Control, black) and presence of 10 μM ethacrynic acid (10 μM EA, red). **(D)**, Current-voltage relationships of mean peak whole-cell VGCC currents (mean ± SEM, *n* = 6) recorded from neurons in response to 500 msec steps from a holding potential of −70 mV to test potentials from −40 to +10 mV in both the absence (Control, black) and presence of 10 μM bumetanide (10 μM BMN, blue).

REFERENCES

Beck, J., Lenart, B., Kintner, D. B., and Sun, D. (2003). Na-K-Cl Cotransporter Contributes to Glutamate-Mediated Excitotoxicity. *J. Neurosci.* 23 (12), 5061–5068. doi:10.1523/jneurosci.23-12-05061.2003

Chen, H., Luo, J., Kintner, D. B., Shull, G. E., and Sun, D. (2005). Na(+)-dependent Chloride Transporter (NKCC1)-Null Mice Exhibit Less gray and white Matter Damage after Focal Cerebral Ischemia. *J. Cereb. Blood Flow Metab.* 25 (1), 54–66. doi:10.1038/sj.jcbfm.9600006

Chen, X., Kintner, D. B., Luo, J., Baba, A., Matsuda, T., and Sun, D. (2008). Endoplasmic Reticulum Ca2+ Dysregulation and Endoplasmic Reticulum Stress Following *In Vitro* Neuronal Ischemia: Role of Na+-K+-Cl-Cotransporter. *J. Neurochem.* 106 (4), 1563–1576. doi:10.1111/j.1471-4159.2008.05501.x

Cuevas, J., and Adams, D. J. (1997). M4 Muscarinic Receptor Activation Modulates Calcium Channel Currents in Rat Intracardiac Neurons. *J. Neurophysiol.* 78 (4), 1903–1912. doi:10.1152/jn.1997.78.4.1903

Cuevas, J., and Berg, D. K. (1998). Mammalian Nicotinic Receptors with Alpha7 Subunits that Slowly Desensitize and Rapidly Recover from Alpha-Bungarotoxin Blockade. *J. Neurosci.* 18 (24), 10335–10344. doi:10.1523/jneurosci.18-24-10335.1998

Cuevas, J., Harper, A. A., Trequattrini, C., and Adams, D. J. (1997). Passive and Active Membrane Properties of Isolated Rat Intracardiac Neurons: Regulation by H- and M-Currents. *J. Neurophysiol.* 78 (4), 1890–1902. doi:10.1152/jn.1997.78.4.1890

de Lera Ruiz, M., and Kraus, R. L. (2015). Voltage-Gated Sodium Channels: Structure, Function, Pharmacology, and Clinical Indications. *J. Med. Chem.* 58 (18), 7093–7118. doi:10.1021/jm501981g

DeHaven, W. I., and Cuevas, J. (2004). VPAC Receptor Modulation of Neuroexcitability in Intracardiac Neurons: Dependence on Intracellular Calcium Mobilization and Synergistic Enhancement by PAC1 Receptor Activation. *J. Biol. Chem.* 279 (39), 40609–40621. doi:10.1074/jbc.M404743200

Diarra, A., Sheldon, C., and Church, J. (2001). *In Situ* calibration and [H+] Sensitivity of the Fluorescent Na+ Indicator SBFI. *Am. J. Physiol. Cel Physiol* 280 (6), C1623–C1633. doi:10.1152/ajpcell.2001.280.6.C1623

Gabriel, R. (1983). Comparison of the Hypotensive Effects of Bendrofluazide, Bumetanide and Xipamide. *Curr. Med. Res. Opin.* 8 (9), 645–648. doi:10.1185/03007998309109813

Hannaert, P., Alvarez-Guerra, M., Pirot, D., Nazaret, C., and Garay, R. P. (2002). Rat NKCC2/NKCC1 Cotransporter Selectivity for Loop Diuretic Drugs. *Naunyn Schmiedebergs Arch. Pharmacol.* 365 (3), 193–199. doi:10.1007/s00210-001-0521-y

Hargus, N. J., Nigam, A., Bertram, E. H., 3rd, and Patel, M. K. (2013). Evidence for a Role of Nav1.6 in Facilitating Increases in Neuronal Hyperexcitability during Epileptogenesis. *J. Neurophysiol.* 110 (5), 1144–1157. doi:10.1152/jn.00383.2013

Hegde, R. S., and Palfrey, H. C. (1992). Ionic Effects on Bumetanide Binding to the Activated Na/K/2Cl Cotransporter: Selectivity and Kinetic Properties of Ion Binding Sites. *J. Membr. Biol.* 126 (1), 27–37. doi:10.1007/BF00233458

Herrera, Y., Katnik, C., Rodriguez, J. D., Hall, A. A., Willing, A., Pennypacker, K. R., et al. (2008). sigma-1 Receptor Modulation of Acid-Sensing Ion Channel a (ASIC1a) and ASIC1a-Induced Ca2+ Influx in Rat Cortical Neurons. *J. Pharmacol. Exp. Ther.* 327 (2), 491–502. doi:10.1124/jpet.108.143974

Jeong, S. Y., Goto, J., Hashida, H., Suzuki, T., Ogata, K., Masuda, N., et al. (2000). Identification of a Novel Human Voltage-Gated Sodium Channel Alpha Subunit Gene, SCN12A. *Biochem. Biophys. Res. Commun.* 267 (1), 262–270. doi:10.1006/bbrc.1999.1916

Kahle, K. T., and Staley, K. J. (2008). The Bumetanide-Sensitive Na-K-2Cl Cotransporter NKCC1 as a Potential Target of a Novel Mechanism-Based Treatment Strategy for Neonatal Seizures. *Neurosurg. Focus* 25 (3), E22. doi:10.3171/FOC/2008/25/9/E22

Katnik, C., Guerrero, W. R., Pennypacker, K. R., Herrera, Y., and Cuevas, J. (2006). Sigma-1 Receptor Activation Prevents Intracellular Calcium Dysregulation in Cortical Neurons during *In Vitro* Ischemia. *J. Pharmacol. Exp. Ther.* 319 (3), 1355–1365. doi:10.1124/jpet.106.107557

Kintner, D. B., Luo, J., Gerdts, J., Ballard, A. J., Shull, G. E., and Sun, D. (2007). Role of Na+-K+-Cl- Cotransport and Na+/Ca2+ Exchange in Mitochondrial Dysfunction in Astrocytes Following *In Vitro* Ischemia. *Am. J. Physiol. Cel Physiol*, 292(3), C1113–C1122. doi:10.1152/ajpcell.00412.2006

Kopach, O., Maistrenko, A., Lushnikova, I., Belan, P., Skibo, G., and Voitenko, N. (2016). HIF-1α-mediated Upregulation of SERCA2b: The Endogenous Mechanism for Alleviating the Ischemia-Induced Intracellular Ca(2+) Store Dysfunction in CA1 and CA3 Hippocampal Neurons. *Cell Calcium* 59 (5), 251–261. doi:10.1016/j.ceca.2016.02.014

Lacreta, F. P., Brennan, J. M., Nash, S. L., Comis, R. L., Tew, K. D., and O'Dwyer, P. J. (1994). Pharmakokinetics and Bioavailability Study of Ethacrynic Acid as a Modulator of Drug Resistance in Patients with Cancer. *J. Pharmacol. Exp. Ther.* 270 (3), 1186–1191. Retrieved from https://www.ncbi.nlm.nih.gov/pubmed/7932170.

Lenart, B., Kintner, D. B., Shull, G. E., and Sun, D. (2004). Na-K-Cl Cotransporter-Mediated Intracellular Na+ Accumulation Affects Ca2+ Signaling in Astrocytes in an *In Vitro* Ischemic Model. *J. Neurosci.* 24 (43), 9585–9597. doi:10.1523/JNEUROSCI.2569-04.2004

LoPachin, R. M., Gaughan, C. L., Lehning, E. J., Weber, M. L., and Taylor, C. P. (2001). Effects of Ion Channel Blockade on the Distribution of Na, K, Ca and Other Elements in Oxygen-Glucose Deprived CA1 Hippocampal Neurons. *Neuroscience* 103 (4), 971–983. doi:10.1016/s0306-4522(01)00035-5

Luo, J., Wang, Y., Chen, H., Kintner, D. B., Cramer, S. W., Gerdts, J. K., et al. (2008). A Concerted Role of Na+ -K+ -Cl- Cotransporter and Na+/Ca2+ Exchanger in Ischemic Damage. *J. Cereb. Blood Flow Metab.* 28 (4), 737–746. doi:10.1038/sj.jcbfm.9600561

Mari, Y., Katnik, C., and Cuevas, J. (2015). σ-1 Receptor Inhibition of ASIC1a Channels Is Dependent on a Pertussis Toxin-Sensitive G-Protein and an AKAP150/Calcineurin Complex. *Neurochem. Res.* 40 (10), 2055–2067. doi:10.1007/s11064-014-1324-0

Mari, Y., Katnik, C., and Cuevas, J. (2010). ASIC1a Channels Are Activated by Endogenous Protons during Ischemia and Contribute to Synergistic

Potentiation of Intracellular Ca(2+) Overload during Ischemia and Acidosis. *Cell Calcium* 48 (1), 70–82. doi:10.1016/j.ceca.2010.07.002

Niespodziany, I., Klitgaard, H., and Margineanu, D. G. (2001). Levetiracetam Inhibits the High-Voltage-Activated Ca(2+) Current in Pyramidal Neurones of Rat Hippocampal Slices. *Neurosci. Lett.* 306 (1-2), 5–8. doi:10.1016/s0304-3940(01)01884-5

O'Donnell, M. E., Tran, L., Lam, T. I., Liu, X. B., and Anderson, S. E. (2004). Bumetanide Inhibition of the Blood-Brain Barrier Na-K-Cl Cotransporter Reduces Edema Formation in the Rat Middle Cerebral Artery Occlusion Model of Stroke. *J. Cereb. Blood Flow Metab.* 24 (9), 1046–1056. doi:10.1097/01.WCB.0000130867.32663.90

Palfrey, H. C., and Leung, S. (1993). Inhibition of Na-K-2Cl Cotransport and Bumetanide Binding by Ethacrynic Acid, its Analogues, and Adducts. *Am. J. Physiol.* 264 (5 Pt 1), C1270–C1277. doi:10.1152/ajpcell.1993.264.5.C1270

Pickkers, P., Russel, F. G., Thien, T., Hughes, A. D., and Smits, P. (2003). Only Weak Vasorelaxant Properties of Loop Diuretics in Isolated Resistance Arteries from Man, Rat and guinea Pig. *Eur. J. Pharmacol.* 466 (3), 281–287. doi:10.1016/s0014-2999(03)01536-x

Pignataro, G., Tortiglione, A., Scorziello, A., Giaccio, L., Secondo, A., Severino, B., et al. (2004). Evidence for a Protective Role Played by the Na+/Ca2+ Exchanger in Cerebral Ischemia Induced by Middle Cerebral Artery Occlusion in Male Rats. *Neuropharmacology* 46 (3), 439–448. doi:10.1016/j.neuropharm.2003.09.015

Rae, J., Cooper, K., Gates, P., and Watsky, M. (1991). Low Access Resistance Perforated Patch Recordings Using Amphotericin B. *J. Neurosci. Methods* 37 (1), 15–26. doi:10.1016/0165-0270(91)90017-t

Rubinstein, M., Patowary, A., Stanaway, I. B., McCord, E., Nesbitt, R. R., Archer, M., et al. (2016). Association of Rare Missense Variants in the Second Intracellular Loop of NaV1.7 Sodium Channels with Familial Autism. *Mol. Psychiatry* 23, 231–239. doi:10.1038/mp.2016.222

Rugg, E. L., Simmons, N. L., and Tivey, D. R. (1986). An Investigation of [3H] bumetanide Uptake in a Cultured Renal Cell Line (MDCK). *Q. J. Exp. Physiol.* 71 (2), 165–182. doi:10.1113/expphysiol.1986.sp002976

Shao, H., Yang, Y., Qi, A. P., Hong, P., Zhu, G. X., Cao, X. Y., et al. (2017). Gastrodin Reduces the Severity of Status Epilepticus in the Rat Pilocarpine Model of Temporal Lobe Epilepsy by Inhibiting Nav1.6 Sodium Currents. *Neurochem. Res.* 42 (2), 360–374. doi:10.1007/s11064-016-2079-6

Shimoni, Y. (1991). Loop Diuretics Block Calcium Currents in Cardiac Cells. *J. Mol. Cel Cardiol* 23 (11), 1209–1213. doi:10.1016/0022-2828(91)90078-z

Shono, Y., Kamouchi, M., Kitazono, T., Kuroda, J., Nakamura, K., Hagiwara, N., et al. (2010). Change in Intracellular pH Causes the Toxic Ca2+ Entry via NCX1 in Neuron- and Glia-Derived Cells. *Cell Mol Neurobiol* 30 (3), 453–460. doi:10.1007/s10571-009-9470-7

Siesjö, B. K. (1988). Acidosis and Ischemic Brain Damage. *Neurochem. Pathol.* 9, 31–88. doi:10.1007/BF03160355

Somberg, J. C., and Molnar, J. (2009). The Management of Acute Heart Failure and Diuretic Therapy. *Am. J. Ther.* 16 (1), 93–97. doi:10.1097/MJT.0b013e3181966c06

van der Heijden, M., Donders, S. H., Cleophas, T. J., Niemeyer, M. G., van der Meulen, J., Bernink, P. J., et al. (1998). A Randomized, Placebo-Controlled Study of Loop Diuretics in Patients with Essential Hypertension: the Bumetanide and Furosemide on Lipid Profile (BUFUL) Clinical Study Report. *J. Clin. Pharmacol.* 38 (7), 630–635. doi:10.1002/j.1552-4604.1998.tb04470.x

Wang, G., Huang, H., He, Y., Ruan, L., and Huang, J. (2014). Bumetanide Protects Focal Cerebral Ischemia-Reperfusion Injury in Rat. *Int. J. Clin. Exp. Pathol.* 7 (4), 1487–1494. Retrieved from http://www.ncbi.nlm.nih.gov/pubmed/24817944.

Ward, A., and Heel, R. C. (1984). Bumetanide. A Review of its Pharmacodynamic and Pharmacokinetic Properties and Therapeutic Use. *Drugs* 28 (5), 426–464. doi:10.2165/00003495-198428050-00003

Xu, W., Mu, X., Wang, H., Song, C., Ma, W., Jolkkonen, J., et al. (2016). Chloride Co-transporter NKCC1 Inhibitor Bumetanide Enhances Neurogenesis and Behavioral Recovery in Rats after Experimental Stroke. *Mol. Neurobiol.* 54, 2406–2414. doi:10.1007/s12035-016-9819-0

Yan, H. D., Ishihara, K., Seki, T., Hanaya, R., Kurisu, K., Arita, K., et al. (2013). Inhibitory Effects of Levetiracetam on the High-Voltage-Activated L-type Ca^{2+} Channels in Hippocampal CA3 Neurons of Spontaneously Epileptic Rat (SER). *Brain Res. Bull.* 90, 142–148. doi:10.1016/j.brainresbull.2012.10.006

Conflict of Interest: The authors declare that the research was conducted in the absence of any commercial or financial relationships that could be construed as a potential conflict of interest.

Publisher's Note: All claims expressed in this article are solely those of the authors and do not necessarily represent those of their affiliated organizations, or those of the publisher, the editors and the reviewers. Any product that may be evaluated in this article, or claim that may be made by its manufacturer, is not guaranteed or endorsed by the publisher.

Copyright © 2021 Katnik and Cuevas. This is an open-access article distributed under the terms of the Creative Commons Attribution License (CC BY). The use, distribution or reproduction in other forums is permitted, provided the original author(s) and the copyright owner(s) are credited and that the original publication in this journal is cited, in accordance with accepted academic practice. No use, distribution or reproduction is permitted which does not comply with these terms.

frontiers
in Pharmacology

ORIGINAL RESEARCH
published: 28 September 2021
doi: 10.3389/fphar.2021.738260

An Advanced Automated Patch Clamp Protocol Design to Investigate Drug—Ion Channel Binding Dynamics

Peter Lukacs[1], Krisztina Pesti[2,3], Mátyás C. Földi[1,2], Katalin Zboray[1], Adam V. Toth[1,2], Gábor Papp[4] and Arpad Mike[1,2]*

[1]Plant Protection Institute, Centre for Agricultural Research, Martonvásár, Hungary, [2]Department of Biochemistry, ELTE Eötvös Loránd University, Budapest, Hungary, [3]School of Ph.D. Studies, Semmelweis University, Budapest, Hungary, [4]Institute for Physics, ELTE Eötvös Loránd University, Budapest, Hungary

Standard high throughput screening projects using automated patch-clamp instruments often fail to grasp essential details of the mechanism of action, such as binding/unbinding dynamics and modulation of gating. In this study, we aim to demonstrate that depth of analysis can be combined with acceptable throughput on such instruments. Using the microfluidics-based automated patch clamp, IonFlux Mercury, we developed a method for a rapid assessment of the mechanism of action of sodium channel inhibitors, including their state-dependent association and dissociation kinetics. The method is based on a complex voltage protocol, which is repeated at 1 Hz. Using this time resolution we could monitor the onset and offset of both channel block and modulation of gating upon drug perfusion and washout. Our results show that the onset and the offset of drug effects are complex processes, involving several steps, which may occur on different time scales. We could identify distinct sub-processes on the millisecond time scale, as well as on the second time scale. Automated analysis of the results allows collection of detailed information regarding the mechanism of action of individual compounds, which may help the assessment of therapeutic potential for hyperexcitability-related disorders, such as epilepsies, pain syndromes, neuromuscular disorders, or neurodegenerative diseases.

Keywords: automated patch-clamp, sodium channel inhibitor, binding kinetics, epilepsy, pain, neuromuscular disorders, lidocaine, riluzole

OPEN ACCESS

Edited by:
Sarel Francois Malan,
University of the Western Cape,
South Africa

Reviewed by:
Clemens Möller,
Hochschule Albstadt-Sigmaringen,
Germany
Timm Danker,
University of Tübingen, Germany

Correspondence:
Arpad Mike
arpadmike1@gmail.com

Specialty section:
This article was submitted to
Pharmacology of Ion Channels and
Channelopathies,
a section of the journal
Frontiers in Pharmacology

Received: *08 July 2021*
Accepted: *13 September 2021*
Published: *28 September 2021*

Citation:
Lukacs P, Pesti K, Földi MC, Zboray K, Toth AV, Papp G and Mike A (2021) An Advanced Automated Patch Clamp Protocol Design to Investigate Drug—Ion Channel Binding Dynamics. Front. Pharmacol. 12:738260. doi: 10.3389/fphar.2021.738260

INTRODUCTION

Most small-molecule sodium channel inhibitors bind to the local anesthetic binding site, and they are strongly state-dependent, showing ~10-fold–1,000-fold higher affinity to inactivated channels (Lenkey et al., 2011). For this reason, as it has long been recognized, determining an IC_{50} value with a single voltage protocol means practically nothing. Radically different IC_{50} values can be measured at different holding potentials (as an example, a roughly hundredfold difference was found in the case of fluoxetine (Lenkey et al., 2006)), and a shift of the steady-state availability curve caused by drug binding is a common phenomenon. These two phenomena are not only related, but they both are manifestations of state-dependent affinity. Determining concentration-response curves at

---

Abbreviations: E_{rel}, relative error; *%RMSE*, percentage root mean square error; **RFI**, "recovery from inactivation" protocol; **SDO**, "state-dependent onset" protocol; **SSI**, "steady-state inactivation" protocol.

different holding potentials, and determining the shift of steady-state availability curves at different drug concentrations are essentially equivalent experiments, as it has been discussed before—see Figure 1 of Lenkey et al. (2011). It is a general practice, therefore, that instead of a single IC_{50} value, the resting-state-, and inactivated-state-affinities (K_R and K_I) are given for individual compounds. Once K_R and K_I are known, the potency at any membrane potential can be estimated. Excitable cells, however, do not keep a constant membrane potential, but fire action potentials regularly. Whenever an action potential is fired, sodium channels undergo a series of conformational transitions, and sodium channel inhibitors dynamically associate and dissociate depending on the actual conformational distribution of the channel population. The final effect of the inhibitor will depend on how the firing rate (the temporal pattern of the membrane potential) and binding/unbinding kinetics relate to each other. This is the basis of the well-known difference between subclasses of class I antiarrhythmics, but binding/unbinding kinetics is equally important in the therapy of hyperexcitability-related skeletal muscle disorders (Simkin, 2011; Cannon, 2018), as well as diseases of the peripheral and central nervous system, such as certain pain syndromes and epilepsies. When assessing the onset/offset kinetics of a sodium channel inhibitor, one must consider the special position of the local anesthetic binding site: it is located within the central cavity of the channel, accessible only through the lipid membrane. The onset/offset process, therefore, cannot be simplified into a single-step binding/unbinding reaction (Vauquelin, 2016). The onset is often not diffusion-limited, but hindered by other possible rate-limiting steps: deprotonation of charged nitrogens (evidenced by the pH-dependence of onset rates (Lazar et al., 2015)), partitioning into the membrane (evidenced by the correlation between lipophilicity and potency (Lenkey et al., 2010; Lenkey et al., 2011)), access to the central cavity through the fenestrations and the activation gate (these open up only at depolarized conformations (Yan et al., 2017)), and formation of the high-affinity binding site (the whole binding pocket is thought to be rearranged at depolarized conformations). Rate limiting steps during offset may include delayed conformational rearrangement of the protein, unbinding, egress from the central cavity, and partitioning of the drug molecule into the extracellular aqueous phase. The last process may be further delayed if the compound has accumulated within intracellular lipid compartments, the depletion of which might require a longer time.

The development of the automated patch-clamp technique has made it possible to directly test the effect of multiple compounds on ion channels. However, in the case of sodium channel inhibitors, determination of an IC_{50} value, or even K_R and K_I values will not predict the therapeutic potential of specific compounds. One should achieve a comprehensive characterization of the mechanism of action for each compound. This, however, usually requires several months of experiments and analysis in a conventional manual patch clamp lab. Our aim was to design a method that could give us a detailed picture of the processes involved in the mechanism of action for individual compounds, without increasing the required time or the cost of measurements. We attempted to reconcile high throughput screening with detailed analysis of the mechanism of action, by maximizing useful information obtained during a rapid test of the compounds.

MATERIALS AND METHODS

Cell Culture and Expression of Recombinant Sodium Channels

The recombinant rNaV1.4 channel-expressing cell line was generated as described before (Lukacs et al., 2018) by transfection of rNaV1.4 BAC DNA constructs into HEK 293 cells (ATCC CRL-1573, RRID:CVCL_0045) by Fugene HD (Promega, Fitchburg, WI, United States) transfection reagent according to the manufacturer's recommendations. Cell clones with stable vector DNA integration were selected by the addition of Geneticin (Life Technologies, Carlsbad, CA, United States) antibiotic to the culture media (400 mg/ml) for 14 days. HEK293 cells were maintained in Dulbecco's Modified Eagle Medium, high glucose supplemented with 10% v/v fetal bovine serum, 100 U/ml of penicillin/streptomycin, and 0.4 mg/ml Geneticin (Life Technologies, Carlsbad, CA, United States). T175 – T25 For experiments cells were plated onto T25 (for Port-a-Patch experiments) or T175 (for IonFlux experiments) flasks, and cultured for 24–36 h. Before experiments cells were dissociated from the dish with Accutase (Corning), shaken in serum-free medium for 60 min at room temperature, then centrifuged, and resuspended into the extracellular solution to a concentration of 5×10^6 cells/ml.

Automated Patch Clamp Electrophysiology

Ensemble voltage-clamp recordings were performed on an IonFlux Mercury instrument (Fluxion Biosciences, Alameda CA, United States). Cell suspension, intracellular solution, and drug-containing extracellular solution were pipetted into the 384-well IonFlux microfluidic ensemble plates. Ensemble plates, in contrast to single-cell plates, contain not one but 20 holes in each cell trap, and current recording is done from 20 cells simultaneously. While this arrangement provides a higher success rate, seal resistances or series resistances cannot be measured for individual cells (for example if the seal resistance for the ensemble is 10 MOhm, it may mean that all 20 cells have an equal seal resistance of 200 MOhm, but may also mean that 19 of the cells have seals in the GOhm range, while one hole missed its cell, and thus its resistance remained ~10 MOhm). Because of this uncertainty, we performed quality control experiments, repeating some of the experiments under single-cell, gigaohm seal conditions, and compared the results (see below). Plates are divided into four "zones," typically each zone was used for a separate experiment (one particular set of compounds on one particular cell line). Each zone consists of eight separate sections, which are distinct functional units, containing one well for the cell suspension, one well for the waste, two cell "traps" (intracellular solution-filled wells under negative pressure to establish high resistance seals and then whole-cell configuration), and eight compound wells. The composition of solutions (in mM) was:

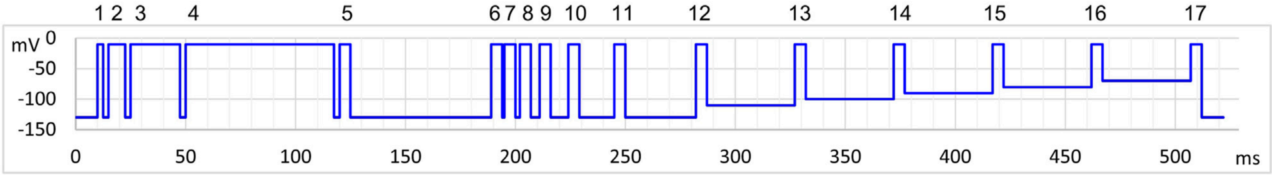

FIGURE 1 | Schematic picture of the voltage protocol. Pulses are numbered for reference.

Intracellular solution: 50 CsCl, 10 NaCl, 60 CsF, 20 EGTA, 10 HEPES; pH 7.2 (adjusted with 1 M CsOH). Extracellular solution: 140 NaCl, 4 KCl, 1 $MgCl_2$, 2 $CaCl_2$, 5 D-Glucose and 10 HEPES; pH 7.4 (adjusted with 1 M NaOH). The osmolality of intra- and extracellular solutions was set to ~320 and ~330 mOsm, respectively. All solutions were filtered with a 0.22 µm syringe filter right before the experiment. In the design of voltage protocols, the calculated 8.1 mV junction potential was taken into account. Data were sampled at 20 kHz, and filtered at 10 kHz. Experiments were carried out at room temperature. Cell ensembles were excluded if 1) the control sodium current amplitude was less than 2 nA, 2) the overall seal resistance of the cell ensemble was less than 5 MOhm, 3) a larger than 20% gradual loss of seal resistance was observed during the experiment, 4) a sudden drop of amplitude with a concurrent drop of seal resistance was observed (indicating loss of one of the cells from the ensemble). From the remaining cell ensembles of each zone, six cell ensembles were chosen for quantitative analysis, based on the stability of seal resistances. Mean seal resistances were 8.75 ± 0.30 MOhm, peak current amplitudes were 9.54 ± 0.51 nA (calculated for six-six chosen cell ensembles from 10 randomly chosen experiments).

Single-Cell Electrophysiology

Port-a-Patch (Nanion, Munich, Germany) experiments were used to validate the automated patch-clamp protocol and experimental data. Whole-cell currents were recorded using an EPC10 plus amplifier and the PatchMaster software (HEKA Electronic, Lambrecht, Germany, RRID:SCR_000034). During cell catching, sealing and whole-cell formation, the PatchControl software (Nanion) commanded the amplifier and the pressure control unit. The resistance of borosilicate chips was between 2.0 and 3.5 MΩ. The composition of solutions was identical to the ones used in IonFlux Mercury experiments.

Rationale for the Automated Patch Clamp Voltage- and Drug Perfusion-Protocol

In excitable cells sodium channels continuously change their conformations depending on the membrane potential. On the one hand, binding and unbinding of drugs are conformation-dependent, on the other hand, drug binding alters conformational transitions (gating) of channels. These interactions produce a special dynamics of continuously changing drug potency: it does not only depend on the actual value of membrane potential, but also on its recent history. To assess both membrane potential dependence and time dependence, we used the protocol illustrated in **Figure 1**. We choose to study three aspects of membrane potential-dependent dynamics of drug potency: First, the effect of inhibitors often needs some time to develop. In the first section of the protocol (pulse #1–#5), therefore, we intended to assess how fast the effect of the drug develops upon depolarization. We used progressively lengthened depolarizations and monitored the inhibition. Second, inhibitors most often dissociate from hyperpolarized (resting) channel conformation, therefore, drug potency gradually decreases upon prolonged hyperpolarization. In the second section of the protocol (pulses #6–#12) we assessed the dynamics of this recovery using progressively lengthened hyperpolarizations. Third, we assessed quasi-equilibrium conditions: we investigated in this section (pulses #13–#17) how the extent of inhibition depended on the membrane potential. The three sections of the protocol correspond with the protocols "state-dependent onset" (**SDO**), "recovery from inactivation" (**RFI**), and "steady-state inactivation" (**SSI**) we used in previous studies (Lukacs et al., 2018; Földi et al., 2021), although with some significant differences. Our priority with this current protocol was high time resolution.

For this reason, the duration of the whole 17-pulse protocol was only 522 ms, and it was repeated every second throughout the experiment. A standard experiment included seven different drug applications, 40 s long each, with 60 or 80 s wash periods between them, then the whole sequence was repeated. This means that the experiment lasted for 28–30 min, during which ~1,700–1,800 sweeps were recorded.

The microfluidic plate used in experiments contains eight compound wells, thus it would allow perfusion of eight different compounds. However, we found that solution exchange was faster and more reliable if we used compound well #1 to perfuse control extracellular solution throughout the experiment.

In the **SDO** section of the protocol (pulses #1–#5), we tested the effect of four depolarization durations (besides the control): 2.5, 7.5, 22.5, and 67.5 ms. We used a cumulative arrangement, not allowing full recovery between depolarizations (only 2.5 ms at hyperpolarized potential between depolarizations). We used Port-a-Patch experiments (i.e., in gigaseal, single-cell recordings) to verify the effects observed in IonFlux experiments (i.e., in multi-cell recordings with varying seal resistance); and also to compare the effect of this cumulative arrangement of the protocol with the conventional multi-sweep protocol, where all sweeps are started with the whole channel population in resting state. Protocols similar to this one are often used to study slow inactivation. It is important to note that in our experiments the **SDO** protocol was not intended for the study of

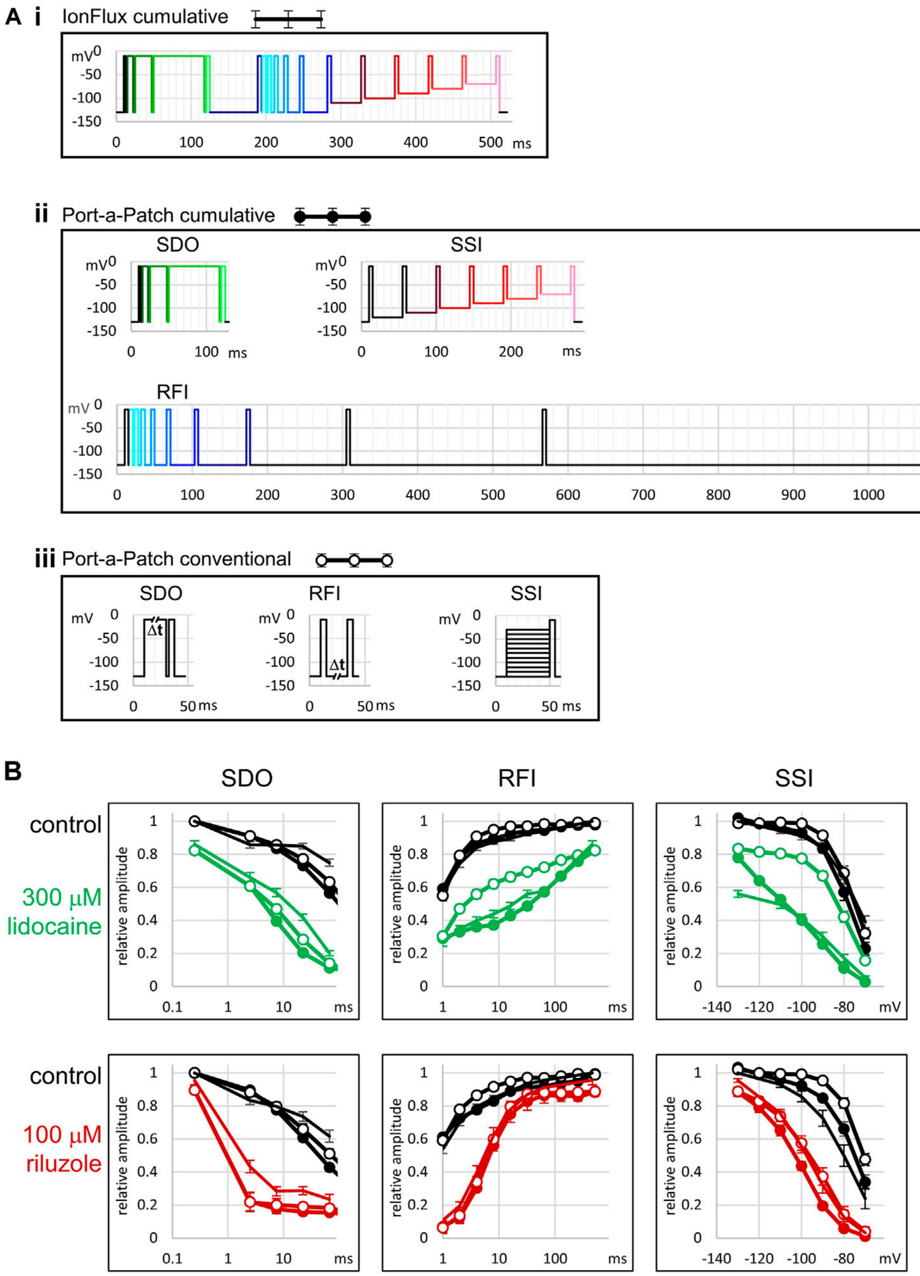

FIGURE 2 | Comparison with single-cell electrophysiology, and with conventional protocols. **(A)** Illustration of the voltage protocols under three different experimental conditions. **(i)** The 17-pulse cumulative protocol used in IonFlux experiments, as described in **Figures 1**, **3**. **(ii)** The three cumulative protocols used in Port-a-Patch experiments. Colors of pulses indicate corresponding pulses in the IonFlux protocol. The SDO protocol was exactly the same as in the IonFlux protocol The SSI section contained an extra 40 ms interpulse interval at −120 mV. The interpulse intervals of the RFI section were: 1, 2, 4, 8, 16, 32, 64, 128, 256, and 512 ms. In contrast, the interpulse intervals in the IonFlux protocol were: 1, 2, 4, 8, 16, 32, 64 ms (preceding the shorter intervals), and 498 ms (time between sweeps). **(iii)** The three conventional protocols used in Port-a-Patch experiments. **(B)** Results obtained by the protocols. This series of experiments was designed to address two questions: Are there differences between results obtained using ensemble recordings (IonFlux—lines with no circles) and single-cell recordings (Port-a-Patch—lines with closed circles)? Are there differences between results obtained using cumulative (Port-a-Patch—lines with closed circles) and conventional (Port-a-Patch—lines with open circles) protocols? Black color indicates control in all figures; Green—300 µM lidocaine; Red—100 µM riluzole.

slow inactivation, but the study of drug effect onset, upon depolarization-induced conformational change. Depolarized conformations (open and inactivated) provide increased affinity, and/or increased accessibility to the binding site, thereby allowing the development of a new binding/unbinding equilibrium. The protocol investigates how fast this new equilibrium is reached. Slow inactivation may only play a minor role in the development of the effect, since even the longest duration (64 ms) is insufficient to induce substantial slow inactivation. The interpulse interval (2.5 ms) was chosen so that it would not allow full recovery even from fast inactivation. This way we maximized sensitivity to drug effects: if any drug stayed bound for at least 2.5 ms then it produced either channel block or delayed recovery by modulation; in both cases, the effect was sure to be detected. Thus far we have encountered only one single compound that could fully dissociate within 2.5 ms, and thus its effect was undetected in the **SDO** protocol (see the accompanying paper (Pesti et al., 2021)). In order to assess the reliability and quality of measurements in the IonFlux Mercury instrument, we performed similar experiments using the Port-a-Patch instrument. The first question was, whether the results obtained by ensemble recording reliably reproduce data measured in single-cell, gigaseal recording. The second question was, whether cumulative protocols are as informative and as sensitive as conventional protocols. The protocols used in the Port-a-Patch experiments are shown in **Figure 2A**. The comparison in the case of **SDO** protocols (**Figure 2B**, **SDO**) showed that the overall patterns were reproduced, although the effect of prolonged depolarizations was somewhat compromised in IonFlux experiments, resulting in slightly less inhibition both in control and in the presence of inhibitor drugs. This may be due to the imperfect voltage control, when some of the cells in an ensemble are imperfectly sealed. The difference between the conventional multi-sweep protocol, and the cumulative protocol (both measured under single-cell conditions), however, was negligible.

In the case of the **RFI** protocol, we used 8 hyperpolarization durations: 1, 2, 4, 8, 16, 32, 64, and 498 ms. The 64 ms hyperpolarization also served to separate the **SDO** and **RFI** sections of the protocol (to allow time for recovery). In the case of slowly acting drugs, where state-dependent binding equilibrium was not reached within 64 ms, we occasionally observed non-monotonous recovery (see the legend of **Supplementary Figure S1** for discussion). The longest (498 ms) hyperpolarization was not recorded (except its first 10 ms after the last pulse and its last 10 ms before the first pulse of the next sweep). In **Figure 2B** (**RFI**), we can observe, that results obtained with the cumulative protocol were practically identical in ensemble recordings (IonFlux) and single-cell recordings (Port-a-Patch). The conventional protocol allowed a slightly faster recovery in control, while in the presence of inhibitor drugs there was either a definite difference (300 μM lidocaine) or no significant difference (100 μM riluzole), depending on the properties of the drug (see below). The higher sensitivity of the protocol to the effects of certain drugs does not make it irrelevant regarding *in vivo* effects, in fact, the prolonged inter-sweep hyperpolarizations of the conventional protocol are non-physiological, and the pattern of the cumulative protocol resembles high-frequency trains of action potentials more closely.

Instead of a conventional **SSI** protocol, where full recovery to resting state is allowed between sweeps of the protocol, we used an accelerated procedure to assess membrane potential dependence, which did not include hyperpolarizations. This means, that resting/inactivated equilibrium was approached from a fully inactivated channel population, not from a fully resting population. If there was a true steady-state, this would make no difference. We used 40 ms pre-pulse duration, which allowed ~90% recovery from fast inactivation at −130 mV membrane potential, and somewhat less at less negative potentials. Consequently, this "no-hyperpolarization" protocol gave similar results to the conventional protocol under control conditions (see **Figure 2C**, **SSI**), although the steady-state availability curve was slightly left-shifted (by less than 5 mV). Recording from cell ensembles could cause an additional <5 mV shift, probably because of the contribution of imperfectly sealed cells. (On the one hand, the leakage itself may weaken voltage control; on the other hand, imperfectly sealed cells may themselves show left-shifted availability curves, which is a sensitive marker of cell stress (Morris and Joos, 2016)). The effect of inhibitor compounds, nevertheless, was similar to the data recorded in single-cells. The cumulative protocol was more sensitive to drug effects: it detected a larger $V_{1/2}$ shift because the effect of shifted equilibrium was accompanied by the effect of delayed recovery from inactivation. The difference was small for riluzole but much larger for lidocaine, because the extent of difference depended on drug onset/offset dynamics (see below). Although this specific protocol is admittedly a result of compromise for the sake of high temporal resolution, we believe that a series of depolarizations occurring at 22.2 Hz from membrane potentials that are close to the resting membrane potential of excitable cells is more relevant with regard to physiological effect than a protocol with prolonged <−100 mV hyperpolarizations. There was an additional practical advantage of the "no-hyperpolarization" protocol: It eliminated the problem of sub-threshold activation during pre-pulses due to poor space clamp. This is important when seal resistance and series resistance values for individual cells are poorly controlled.

Data Analysis

Using the data acquisition software, all data traces were exported in csv file format. A custom software was developed in Octave (RRID:SCR_014398) to automatically process raw data. All traces were read in from the DataAcquisition*.ISD files containing the raw data. Separate csv files contained the description of the voltage protocol. First, 2 ms sections were selected after each of the 34 voltage steps. No online (P/n) leak subtraction was employed. Capacitive artifacts were removed by calculating the sum of the section recorded at the beginning and after the end of the pulse, and then subtracting the offset so that all currents started at zero current level. Although other voltage-gated channels were present in the cells, their contribution to the fast transient inward current was small (the peak amplitude of the TTX-resistant fraction of the fast transient inward current was 5.17 ± 3.44% of the full amplitude), thus allowing reasonably accurate assessment of the extent of sodium channel inhibition. For all ~1,700 sweeps, and for all 17 pulses, the minima (peak amplitudes) were extracted and saved in 64 csv files for the 64 cell ensembles. These data (all 17 peak amplitudes for each second of a ~1,700 s experiment plotted against time) are shown for one particular cell ensemble in **Figure 3**. From each of the four zones (separate experiments), we chose $n = 6$ ensembles for analysis,

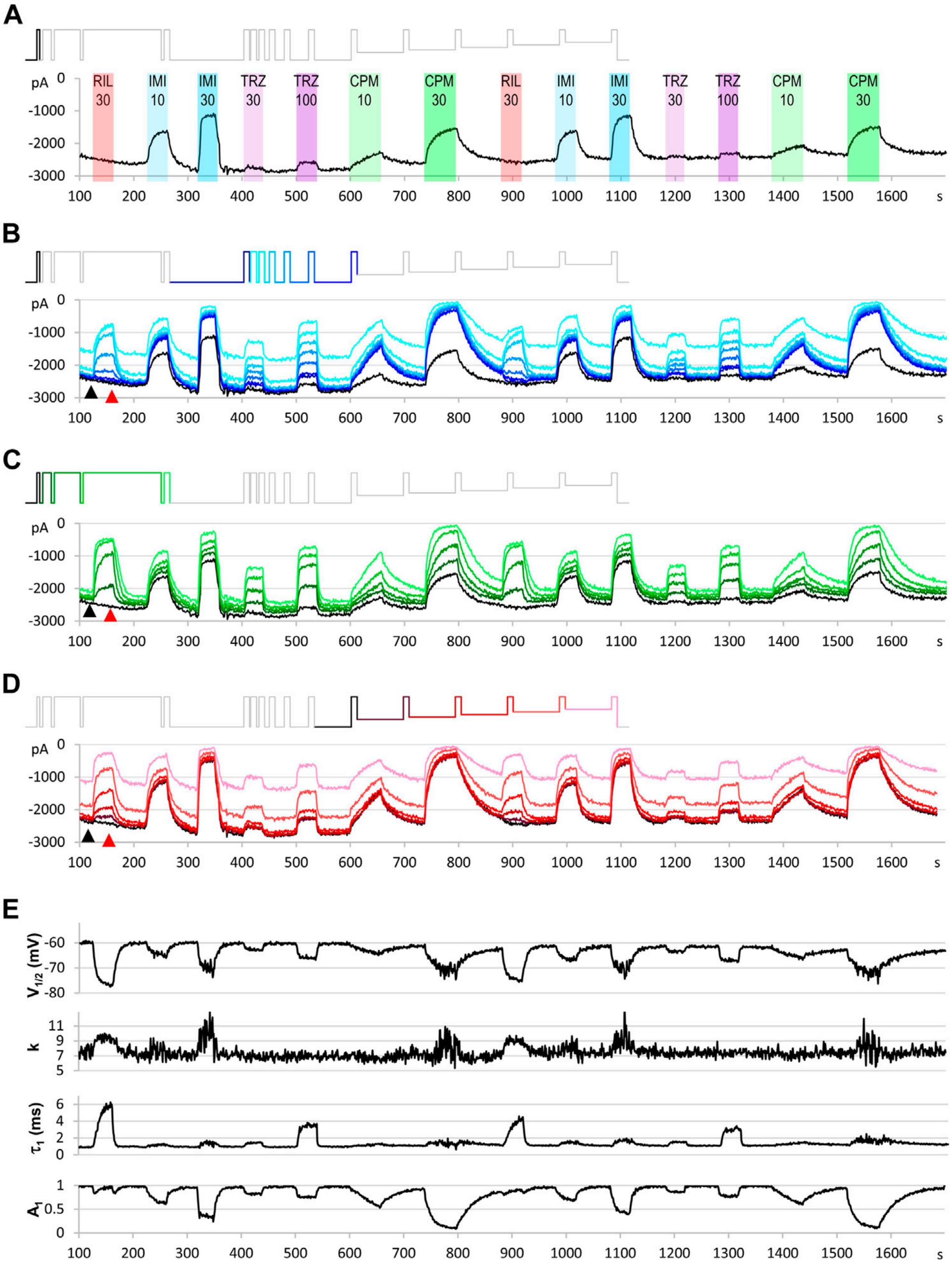

FIGURE 3 | An example for the plot of current amplitudes throughout the experiment. The experiment included two repetitions of seven different compound applications: 30 µM riluzole, 10 and 30 µM imipramine, 30 and 100 µM trazodone, 10 and 30 µM chlorpromazine. Currents evoked by all 17 depolarizations are shown, grouped into three functional assays, as described in the text. **(A)** Peak amplitude plot for pulse #1-evoked current throughout the experiment. **(B)** Currents evoked by pulses #1 and #6–#12; these allow second-to-second reconstruction of recovery from inactivation (RFI; see *Materials and Methods*) throughout the experiment. **(C)** Currents evoked by pulses #1–#5; these allow reconstruction of the **SDO** plots (see *Materials and Methods*). **(D)** Currents evoked by pulses #1 and #13–#17; these allow reconstruction of the **SSI** plots (see *Materials and Methods*). Insets show the schematic picture of the voltage protocol, where colors match the color of the corresponding amplitude plot. **(E)** Results of the automated analysis. Automated fitting of **SSI** and **RFI** data was done as described in *Materials and Methods*. The plot shows the changes in half inactivated voltage ($V_{1/2}$) and slope (k) values from **SSI** data, and the value (τ_1) and contribution (A_1) of the fast time constant from RFI data.

based on the stability of amplitude and seal resistance throughout the experiment.

SSI and **RFI** plots for each sweep were fitted by the Octave script. Fitting 64 × 1,700 plots could not be individually visually supervised, but parameters of the automated fitting were evaluated by comparing them to visually controlled fits of **SSI** and **RFI** plots, as shown in Results. At the end of all drug perfusion periods, as well as at the end of control periods before and after them, we fitted data using the Solver add-in of Microsoft Excel (RRID:SCR_016137). The precision of the automated fit and the adequacy of the equation used were evaluated; if we found the fitting inadequate, either the equation or the constraints were modified. To evaluate the precision of the fit we calculated the root mean square error (*RMSE*) values for each fit, as well as relative error (E_{rel}) values for each point, were recorded and saved in a separate csv file. The following formulas were used to calculate the extent of error:

$$RMSE = \sqrt{\frac{1}{n}\sum_{i=1}^{n}\left(I_{exp} - I_{fit}\right)^2} \tag{1}$$

$$E_{rel} = \frac{\left|I_{exp} - I_{fit}\right|}{I_{exp}} \tag{2}$$

where n is the number of points fitted, I_{exp} is the experimentally measured amplitude, and I_{fit} is the fitted amplitude. We expressed *RMSE* values as a percentage of the maximal amplitude (for each sweep, the amplitude of the current evoked by pulse #1 of that particular sweep). The advantage of automated fitting of all **SSI** and **RFI** plots throughout the experiment was, that second-to-second changes in $V_{1/2}$, k, A_1, and τ values reveal the dynamics of development/removal of modulatory drug effect more accurately; furthermore, even minimal effects were detectable, because the tests were repeated several times before, during, and after drug applications.

Peak amplitudes of currents evoked by pulses #12–#17 were used to construct **SSI** curves, which were fit using the Boltzmann function:

$$I = I_{max}*\left(1 - \frac{1}{1 + \exp\left(\frac{V_p - V_{1/2}}{-k}\right)}\right), \tag{3}$$

where V_p is the pre-pulse potential, $V_{1/2}$ is the voltage where the curve reached its midpoint and k is the slope factor. Currents evoked by pulses #1, and #6–#12 were used to construct **RFI** plots, which were fitted with a bi-exponential function:

$$I = I_{max}*\left(A_1*\left(1 - \exp\left(\frac{-t_{ip}}{\tau_1}\right)\right) + \left(A_2*\left(1 - \exp\left(\frac{-t_{ip}}{\tau_2}\right)\right)\right)\right), \tag{4}$$

where τ_1 and τ_2 are the fast and slow time constants, A_1 and A_2 are their respective contribution to the amplitude, and t_{ip} is the duration of the interpulse interval. We routinely used constrains $\tau_1 < \tau_2$, and $A_1 + A_2 = 1$; and for automated fitting we also constrained the slow time constant. We found that in the presence of riluzole **Eq. 4** could not adequately fit RFI plots, therefore we used an extended equation:

$$I = I_{max} * \left(A_1 * \left(1 - \exp\left(\frac{-t_{ip}}{\tau_1}\right)\right)^x + \left(A_2*\left(1 - \exp\left(\frac{-t_{ip}}{\tau_2}\right)\right)\right) + A_3\right), \tag{5}$$

where A_3 represents the unmodulated fraction of channels at low riluzole concentrations which recover as control channels, and the exponent "x" was needed because recovery in the presence of riluzole has been repeatedly found to be steeper than exponential. (This has been addressed either by including a time delay parameter in the equation (Benoit and Escande, 1991; Hebert et al., 1994), or by using an equation where the fast exponential component was on the x^{th} power (Lukacs et al., 2018; Földi et al., 2021). We prefer the latter, because introducing a delay parameter results in negative numbers at short time intervals.)

We did not perform an automated fit of **SDO** plots, because fitting often required different functions for different drugs. Analysis of **SDO** data is described in the accompanying paper (Pesti et al., 2021).

The microfluidics of the IonFlux instrument could provide complete solution exchange within the 498 ms hyperpolarization (478 ms of which was unrecorded), therefore solution exchange rate did not compromise kinetic analysis of data. Complete solution exchange between sweeps was verified using high Ca^{2+} ion concentration (35 mM) containing solution (which blocks sodium channels).

In a regular experiment, only the first set of compound applications were evaluated, repetition of the experiment served as an internal control: it helped to detect incomplete recovery (see e.g. after 30 μM chlorpromazine in **Figure 3**), and to verify onset and offset rates (see e.g. the offset after 30 μM imipramine, where some disturbance obscured the offset process). It also helped to assess the extent of the spontaneous leftward shift of the steady-state availability curve by observing the ratio of the 17th/12th pulse evoked current amplitudes (pink and darkest red traces in **Figure 3D**).

RESULTS

Initial Examination of Data

In order to better explain how to interpret our data, we will first show an example for a single experiment, and make a few important general observations. After explaining the interpretation of results, we will describe how quantitative analysis from multiple experiments with multiple concentrations is performed, on the example of lidocaine and riluzole.

Figure 2 illustrates the results of a single experiment. In this example, we perfused the following compounds: riluzole (30 μM), imipramine (10 and 30 μM), trazodone (30 and 100 μM), and chlorpromazine (10 and 30 μM). The full voltage protocol (**Figure 1**) is described in the Methods section, in the interest of clarity here we will discuss it as if it was built up step-by-step.

Let us first consider what would happen if we gave only single depolarizing pulses at every second (**Figure 3A**). The peak amplitude plot shows that the amplitude was fairly stable throughout the ~30-min experiment. Riluzole at 30 μM caused no inhibition whatsoever, trazodone inhibited peak amplitudes only minimally (~5% inhibition at 100 μM), the other two compounds caused concentration-dependent inhibition. Imipramine seemed to be the most potent compound, causing ~50–55% inhibition at 30 μM.

Let us now consider the section of the experiment in which we tested the rate of recovery from inactivation (**RFI**). Current amplitudes evoked by the highlighted part of the voltage protocol are plotted throughout the experiment in **Figure 3B**. Colors in the voltage protocol match colors in the current amplitude plot. We applied consecutive depolarizing pulses with increasing interpulse intervals between them within a

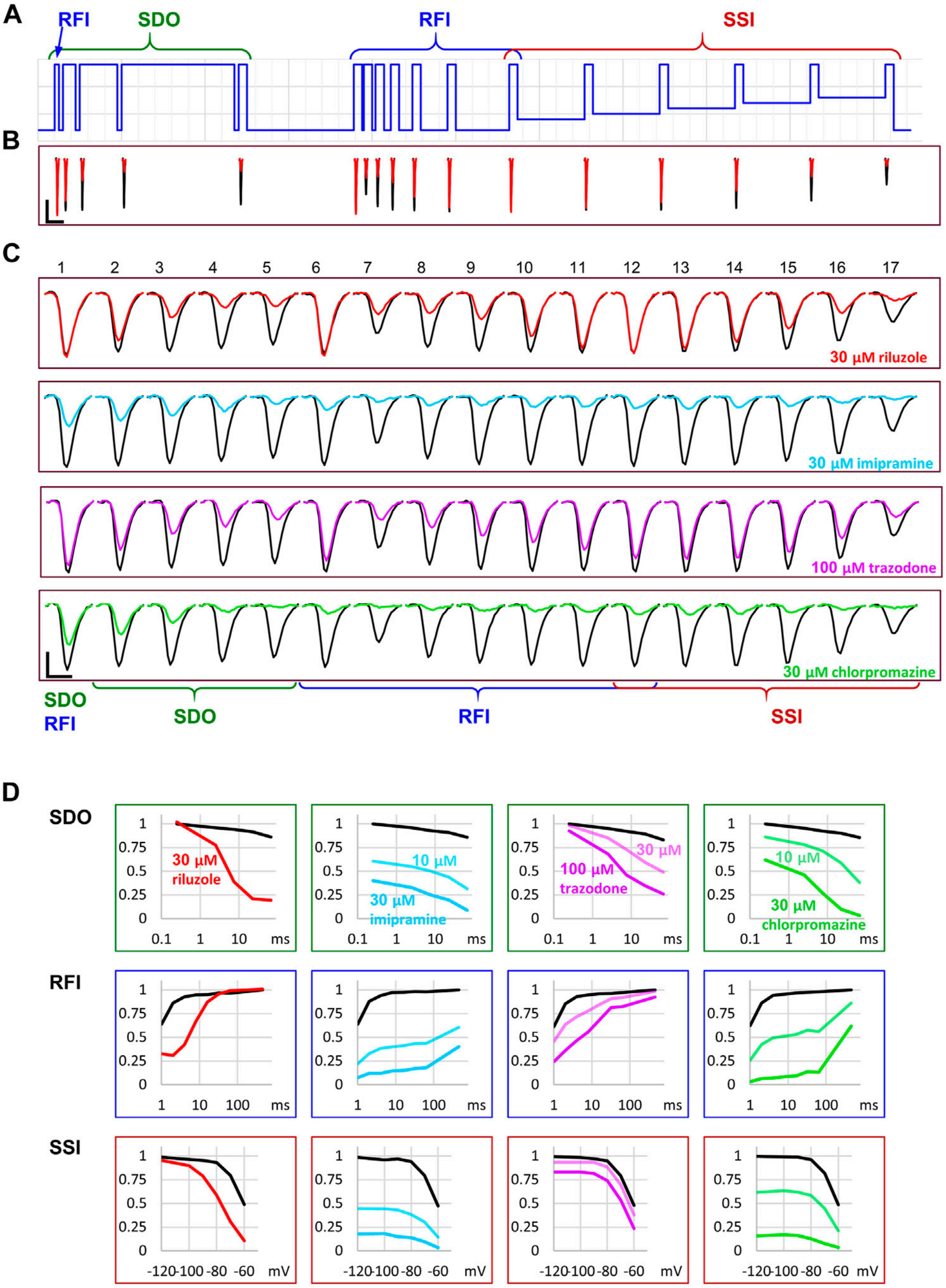

FIGURE 4 | Reconstruction of SDO, RFI, and SSI plots from the current amplitude plots. **(A)** The voltage protocol (for reference). **(B)** Evoked currents in control, and in the presence of 30 µM riluzole, shown on the same time scale as the scheme of the protocol. Note the difference in the potency of riluzole between subsequent depolarizations. Scale bars: 1 nA, 10 ms. **(C)** Evoked currents on an expanded time scale for visibility, before, and during the perfusion of riluzole, imipramine, trazodone, and chlorpromazine. Scale bars: 1 nA, 1 ms. **(D)** Reconstruction of **SDO**, **RFI**, and **SSI** plots before, and during the perfusion of the indicated compounds.

single sweep (i.e., within a single uninterrupted period of data acquisition). Interpulse intervals were 1, 2, 4, 8, 16, 32, 64, and 498 ms (not in this sequence, see colors in the protocol, as described in more details in Methods). Peak amplitudes evoked after 1 ms hyperpolarization are shown as a light blue line, currents evoked after progressively longer interpulse intervals are shown by increasingly darker shades of blue. The black line indicates the current evoked after 498 ms hyperpolarization, it is identical to the one shown in **Figure 3A**. We can observe that, in contrast to what we saw in **Figure 3A**, riluzole (30 µM) and trazodone (100 µM) did produce a massive inhibition, only the inhibition by these compounds was transient, re-appearing and disappearing within each 1 s cycle. We can observe in the case of riluzole

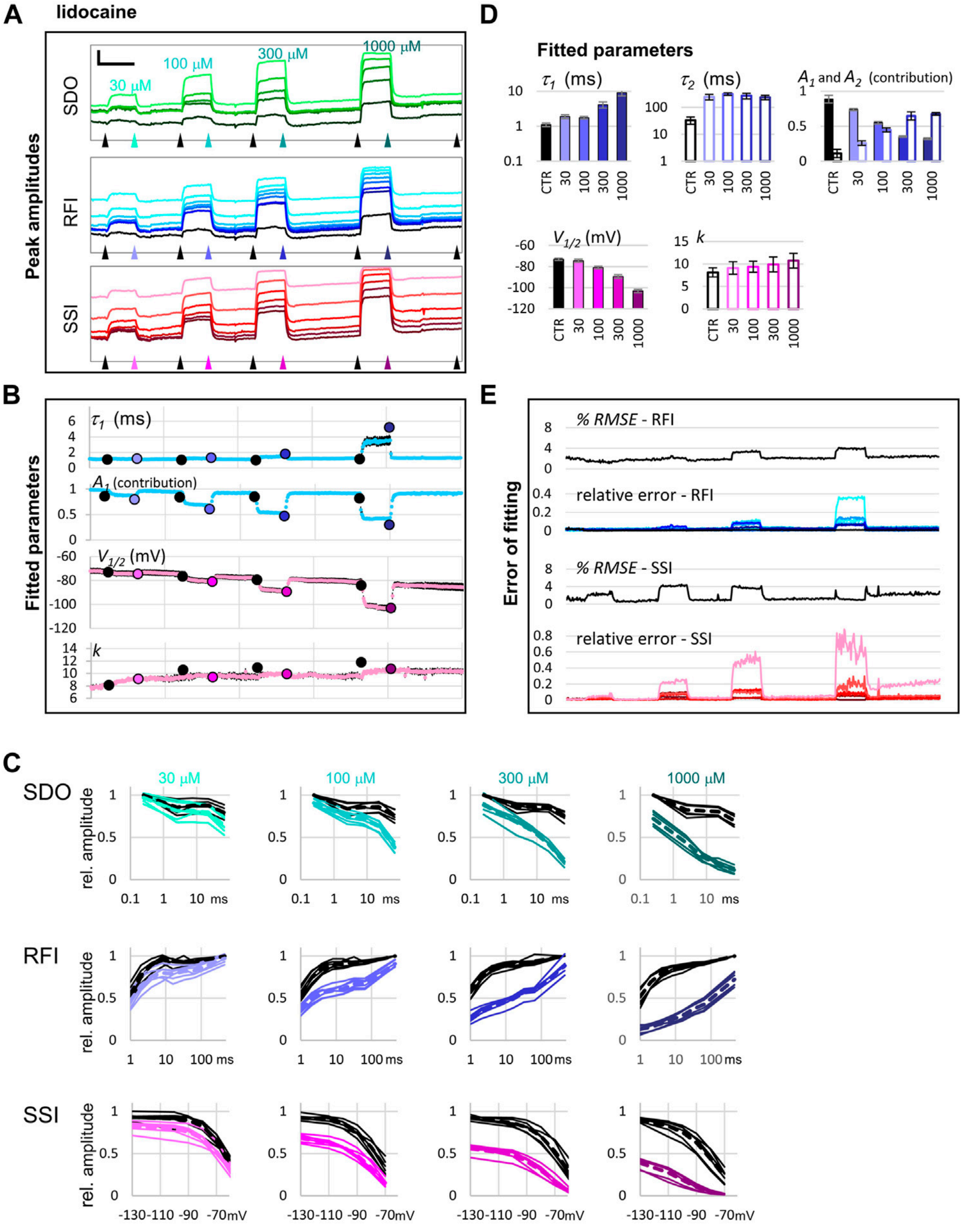

FIGURE 5 | The effect of four different concentrations of lidocaine on peak amplitudes. **(A)** An example of peak amplitude plots for all 17 pulse-evoked currents, grouped into the **SDO**, **RFI**, and **SSI** groups as shown in **Figure 2**. Scale bars: 2 nA, 50 s. Arrowheads indicate the time points immediately before, and at the end of drug perfusion periods. At each point, indicated by the arrowheads, the average of three consecutive data points was taken to construct the plots shown in panel **(C)**. **(B)** Parameters of Boltzmann, and bi-exponential automated fits throughout the four drug application periods. Colored circles indicate the values obtained by visually controlled fitting of $n = 6$ curves; the same data that is shown in panel **(C)**. **(C)** Reconstructed **SDO**, **RFI**, and **SSI** plots for $n = 6$ cell ensembles. Colors match the colors of arrowheads in panel **(A)**. Dotted lines show the average of the six cell ensembles. **(D)** Parameters obtained by visually controlled fitting of RFI and SSI plots. **(E)** The error of fitting throughout the four drug application periods. *RMSE* values are expressed as the percentage of the peak amplitude evoked by pulse #1 of the same sweep. Relative errors are shown for pulses #6–#12 and #1 (shades of blue and black, as shown in panel **(A)**), as well as for pulses #12–#17 (shades of red, as shown in panel **(A)**).

that inhibition already started to ease off at the 4 ms interpulse interval, and it almost completely disappeared by the end of the 16 ms interpulse. Inhibition by trazodone disappeared incrementally, some residual inhibition was present even at 498 ms. In contrast, inhibition by imipramine or chlorpromazine recovered minimally within 64 ms, substantial recovery only occurred during the longest (498 ms) interpulse interval. Note that two fundamentally different processes can be observed in **Figure 3B**: One can discern a dynamics of onset and recovery within individual sweeps, on a millisecond time scale (see **Figure 4**, below), in the continuous presence of the drug; we will call this "micro-dynamics." The dynamics of onset

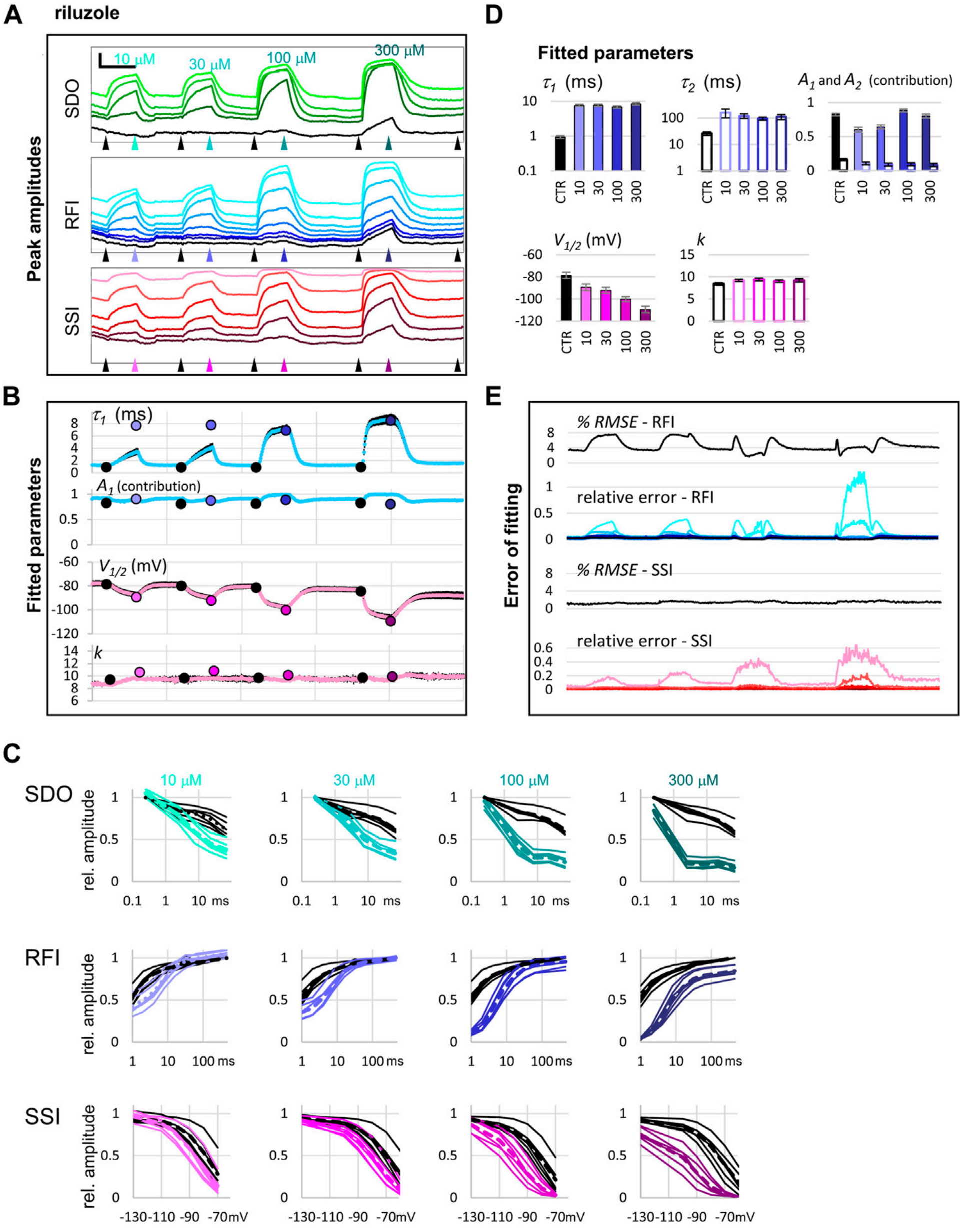

FIGURE 6 | The effect of four different concentrations of riluzole on peak amplitudes. **(A)** An example of peak amplitude plots for all 17 pulse-evoked currents, grouped into the **SDO**, **RFI**, and **SSI** groups as shown in **Figure 2**. Scale bars: 4 nA, 50 s. Arrowheads indicate the time points immediately before, and at the end of drug perfusion periods. At each point, indicated by the arrowheads, the average of three consecutive data points was taken to construct the plots shown in panel **(C)**. (B) Parameters of Boltzmann, and bi-exponential automated fits throughout the four drug application periods. Colored circles indicate the values obtained by visually controlled fitting of $n = 6$ curves; the same data that is shown in panel **(C)**. **(C)** Reconstructed **SDO**, **RFI**, and **SSI** plots for $n = 6$ cell ensembles. Colors match the colors of arrowheads in panel **(A)**. Dotted lines show the average of the six cell ensembles. **(D)** Parameters obtained by visually controlled fitting of RFI and SSI plots. For RFI plots **Eq. 5** was used, with the constraint of $x = 1$. **(E)** The error of fitting throughout the four drug application periods. *RMSE* values are expressed as the percentage of the peak amplitude evoked by pulse #1 of the same sweep. Relative errors are shown for pulses #6–#12 and #1 (shades of blue and black, as shown in panel **(A)**), as well as for pulses #12–#17 (shades of red, as shown in panel **(A)**).

and offset upon drug application and removal, on the other hand, occurred on the time scale of seconds, we will call that "macro-dynamics." Macro-dynamics provides valuable information regarding the physicochemical properties of individual compounds, which determine their *in vivo* pharmacokinetics, and the extent of their accumulation within the plasma membrane and intracellular compartments. Note, however, that it is micro-dynamics that determines firing frequency-dependent inhibition of excitable tissues. Macro-dynamics, as observed upon rapid wash-in and wash-out of drug-containing solution *in vitro*, does not occur during *in vivo* drug delivery.

Next, let us observe the section of the protocol which investigates "state-dependent onset" (**SDO**), i.e., the micro-dynamics of inhibition onset at depolarized membrane potential (**Figure 3C**). It shows currents evoked by depolarizations #1–#5, as shown by the colors of the highlighted section of the protocol. We can observe that the micro-dynamics of onset can be rather different from that of recovery, for example in the case of chlorpromazine, we see a gradual onset during the 2.5–67.5 ms depolarizations, while we can observe that most of the recovery occurred between 64 and 498 ms.

Finally, depolarizations #12–#17 assess steady-state availability at membrane potentials −130, −110, −100, −90, −80, and −70 mV (**Figure 3D**).

Parameters of the automatized fitting of **SSI** and **RFI** plots are shown in **Figure 3E**. We can observe again that different compounds behaved differently. Riluzole, which seemed to have no effect at all in **Figure 3A**, was the most potent of all drugs in terms of shifting the $V_{1/2}$ value. Trazodone was the only compound that did not affect the slope of the availability curve (k). Delayed recovery from inactivation in the case of riluzole and trazodone was predominantly due to an increase in the fast time constant, while in the case of imipramine and chlorpromazine, the fast time constant was unchanged, but its contribution was decreased. The accuracy of fits throughout the experiment can be monitored by automated calculation of *RMSE* and E_{rel} values (**Supplementary Figure S1**).

Let us call attention to a few important points: Note that some of the inhibitors cause widely different extents of inhibition, depending on which of the 17 traces we consider. **Figure 4** illustrates micro-dynamics that took place within a single 522 ms long sweep. The voltage protocol is shown again for reference in **Figure 4A**, evoked currents are illustrated on the same time scale in **Figure 4B**, right before the first application of 30 μM riluzole (black traces), and at the end of riluzole perfusion (red traces). Black and red triangles in **Figure 2** indicate the exact time of the sweep from which original currents were taken. **Figure 4C** shows currents on an expanded time scale, we illustrate micro-dynamics during the perfusion of 30 μM riluzole (red traces), 30 μM imipramine (blue traces), 100 μM trazodone (purple traces), and 30 μM chlorpromazine (green traces). Conventional plots of **RFI**, **SDO**, and **SSI** (see *e.g.* (Lukacs et al., 2018; Földi et al., 2021)) with the four compounds are shown in **Figure 4D**.

Note also in **Figure 3**, that the observed macro-dynamics (onset time constants upon drug application and offset time constants upon washout) can also be different depending on which of the 17 pulse-evoked currents we monitor. Let us consider for example the **SDO** section of the protocol (**Figure 3C**) during the onset and offset of inhibition by 30 μM chlorpromazine. Channels activated by pulses #1 (amplitudes plotted in black) to #5 (amplitudes shown in light green) encounter the same exact concentration of the same compound during drug perfusion and subsequent washout. We know from calibration experiments that solution exchange in the extracellular aqueous phase is complete between two sweeps, however, the buildup and depletion of drug concentration within the membrane phase can be much slower, and it is the intramembrane concentration that the channel can perceive (contribution of the hydrophilic pathway is probably negligible for these strongly lipophilic compounds). The difference in potency and dynamics between traces (e.g. the light green trace and the black trace in **Figure 3C**) reflects different sensitivities of the channel, depending on its recent gating history.

If we compare the pattern produced by 100 μM trazodone and 30 μM chlorpromazine, we can observe an obvious difference not only between their macro-dynamics (both onset and offset were clearly slower for chlorpromazine) but also between their micro-dynamics. In both cases we see a gradually deepening inhibition in the **SDO** section, indicating that the onset of inhibition occurred within the investigated time window (2.5–67.5 ms). Recovery, however, was different: the effect of trazodone recovered rapidly, mostly within 64 ms (see pulse #6 in **Figure 4C**); while inhibition by chlorpromazine was not much relieved throughout the whole 17-pulse sweep, and substantial recovery only occurred during the 498 ms inter-sweep intervals.

Riluzole and trazodone showed intensive micro-dynamics: during the inter-sweep intervals, much of the inhibition was relaxed, while it was repeatedly re-established upon depolarizations. Imipramine, in contrast, showed minimal micro-dynamics, once the inhibition was established (by the end of the **SDO** section), the hyperpolarizations within the sweep (up to 64 ms) were not long enough to allow significant recovery. Even the 498 ms inter-sweep hyperpolarization was enough only for partial recovery. For this reason, **SSI** data could not be correctly measured, much longer periods would be required for establishing equilibrium. This protocol was optimized for the study of compounds with fast micro-dynamics, therefore it was inaccurate for slower micro-dynamics compounds. Chlorpromazine was similar to imipramine, with somewhat faster micro-dynamics, but slower macro-dynamics. A larger fraction of channels recovered during inter-sweep intervals, but during each sweep, after the inhibition was re-established (by the end of pulse #5), all pulses were inhibited similarly, because of the insufficient time for equilibration.

From the initial examination of this single experiment, it is apparent that different drugs have their own characteristic "signature" pattern of inhibition. This is evident from the similarity of repeated drug application effects, as well as from the effect of different concentrations of the same drug. When different concentrations of the same compound were applied, we could observe different extents of inhibition, different onset rates, but the offset rates were similar, and there was a uniform overall pattern (i.e. which of the 17 pulse-evoked currents were affected to what extent). It is clear that the voltage protocol we used could only appropriately characterize drugs with fast micro-dynamics; this protocol was intended to characterize compounds that could selectively inhibit pathological high-frequency firing. Similar protocols, with longer hyperpolarization and depolarization durations (and, therefore, necessarily with less temporal resolution) can be used for compounds with slower micro-dynamics.

In summary, initial examination indicated that these four compounds acted in four different ways. In the next section, we will show an example for an initial analysis of the effect of two well-known drugs, lidocaine, and riluzole in different concentrations. The accompanying paper (Pesti et al., 2021) will discuss how to derive compound-specific biophysical properties from this initial analysis.

Quantitative Analysis

We illustrate quantitative analysis in the case of two well-known sodium channel inhibitors, lidocaine (30, 100, 300, and 1,000 μM; **Figure 5**), and riluzole (10, 30, 100, and 300 μM; **Figure 6**). **Figures 5A**, **6A** show an example of the effect of both drugs on all 17 pulse-evoked current amplitudes. From the 17 peak amplitudes of each sweep, **SDO**, **RFI,** and **SSI** plots were reconstructed, but only **RFI** and **SSI** plots were fitted. Two different methods were used for fitting: automated fitting was performed for each sweep of the ~1,700 sweep experiment, and to validate the (uncontrolled) automated fitting, we fitted **RFI** and **SSI** plots with visual control only for pairs of control and drug-treated cell ensembles, as marked by the arrowheads in **Figures 5A**, **6A**. For all visually controlled fits three consecutive sweeps were averaged; the last three before each drug perfusion period, and the last three at the end of each drug perfusion. The **SDO**, **RFI**, and **SSI** plots, constructed from these three-point averages for six cell ensembles as well as the average of the six measurements (dashed lines)are shown in **Figures 5C**, **6C**. Light to dark color of plots (teal for **SDO**, indigo for **RFI**, and purple for **SSI** plots) indicate increasing concentration, these colors match the colors of corresponding arrowheads in **Figures 5A**, **6A**, as well as the colors of columns in **Figures 5D**, **6D**, where parameters from the visually controlled fitting are summarized. Six parameters are shown, τ_1, τ_2, A_1, and A_2 values for **RFI** fits, $V_{1/2}$, and k for **SSI** plots. In the automated fitting procedure, the slow time constant (typically between 100 and 400 ms) was fixed, because there were few data points in this time range. We calculated the mean slow time constant from the visually controlled fitting and then used this fixed value throughout the automated fitting procedure. In addition, we used the constrain of $A_1 + A_2 = 1$. For this reason, only four parameters are shown, τ_1, and A_1 values for **RFI** fits (blue dots), $V_{1/2}$, and k for **SSI** plots (pink dots) (**Figures 5B**, **6B**). For the sake of comparison, parameters obtained from the visually controlled fitting are also shown in these figures, as large circles. We can observe that the automated fitting procedure quite reliably reproduced data from the visually controlled fitting, except in the case of 10 and 30 μM of riluzole (see below for an explanation). The overall quality of the fit could be monitored by observing the % *RMSE* values; from the E_{rel} values, we could see which particular point contributes most to the error. In the case of both riluzole and lidocaine E_{rel} values were quite low, except for pulses #7, #8, and #17; where peak amplitudes were the smallest. Small amplitudes necessarily result in a higher relative error, both because of the decreased signal-to-noise ratio and because the fitting procedure minimizes absolute, not relative, squared errors.

In the **RFI** plots, lidocaine caused a slowing of the fast time constant of recovery, which was moderate at lower concentrations (30 and 100 μM) but was substantial at 300 and 1000 μM concentrations (~4-fold and ~7-fold, respectively). More importantly, the contribution of the slow time constant gradually overcame the contribution of the fast one, increasing from 8.8 ± 2.1% at control, to 68.8 ± 1.4% at 1,000 μM, while the value of the slow time constant did not change with concentration (**Figure 5D**). In contrast, riluzole caused no change in either the contribution or the value of the slow time constant but caused a radical ~8-fold increase in the fast time constant. The extent of this increase did not change significantly with concentration (ranging from 7.4- to 8.9-fold), but at lower concentrations there seemed to be an unmodulated fraction of the channel population, as it can be seen on the contribution of A_1 at concentrations 10 and 30 μM (**Figure 6D**).

In the **SSI** plots, both compounds caused a concentration-dependent hyperpolarizing shift in the half inactivation voltage, while the slopes did not change significantly.

In summary, it was possible to perform automated fitting of ~1,700 **RFI** and **SSI** plots on 64 channels, with reasonable accuracy. *RMSE* values remained below 4%, except for **RFI** plots in the presence of riluzole, where the conventional bi-exponential equation was clearly inadequate for fitting the data. In this special case recovery data have been consistently found to be steeper than exponential, and therefore either have been fit with an equation that included a time delay parameter (Benoit and Escande, 1991; Hebert et al., 1994), or with an equation where the fast exponential component was on the n^{th} power (Lukacs et al., 2018; Földi et al., 2021). Visually controlled fits confirmed the parameters of automated fitting and gave somewhat better *RMSE* values (between 0.44 and 1.56% for all **SSI** fits, and between 1.12 and 2.27% for **RFI** fits in control, and in the presence of lidocaine). In the case of **RFI** plots in the presence of riluzole, visual control allowed us to identify the source of error, and to modify the equation accordingly. Fitting the **RFI** plot with the simple bi-exponential equation gave *RMSE* values 3.54, 2.97, 1.79, and 2.76%, for 10, 30, 100, and 300 μM riluzole, respectively. To improve these, we introduced the extended equation (**Eq. 5**) in two steps: in the first step, we allowed A_3 to be different from zero. Allowing a non-zero unmodulated fraction was important in the case of 10 and 30 μM concentrations, and improved their *RMSE* values to 0.64 and 0.67, respectively, but did not change the *RMSE* values for 100 and 300 μM riluzole. The parameters obtained with this modification are shown in **Figure 5D**. In the next step, we also allowed the exponent "x" to be different from 1. This improved *RMSE* values for all four concentrations: to 0.50, 0.64, 1.04 and 1.11% for 10, 30, 100, and 300 μM riluzole, respectively. By allowing the exponent to vary, however, we lost the comparability of fast time constants, because the time constant and the exponent are interdependent, as we have discussed before (Lukacs et al., 2018). This is the reason why in **Figure 5D** we show time constants from the fit when non-zero A_3 of **Eq. 5** was allowed, but the exponent was not allowed to differ from 1.

DISCUSSION

To understand the effect of drugs on ion channels, one must study the complex kinetics of ion channel gating, the complex dynamics of drug distribution (which includes partitioning between aqueous and membrane phases, entering/exiting the central cavity, and binding/unbinding), as well as the multiple interactions between the two (which come from state-dependent access, state-dependent binding, and drug-induced modulation of gating). Sodium channels undergo a fast but extensive conformational rearrangement during gating, which radically alters the accessibility and affinity of the binding site. Individual inhibitor compounds can react differently to these changes, which may confer them with unique abilities to selectively inhibit specific activity patterns. For example, riluzole is especially effective at high-frequency firing (Desaphy et al., 2014; Földi et al., 2021), phenytoin at prolonged depolarizations (Kuo and Bean, 1994; Liu et al., 2011; Terragni et al., 2016). The significance of functional selectivity, and the importance to test the effectiveness of sodium channel inhibitors under different conditions, has been recognized before, and adapting this approach to automated patch clamp instruments has been attempted. Three-pulse and four-pulse protocols have been used to study sodium channel inhibitors in order to address different aspects of functional selectivity (Liu et al., 2011; Liu, 2014). An initial attempt to study macro- and micro-dynamics in parallel, together with the effect on gating equilibrium has been made by our group earlier (Lenkey et al., 2010). In that case, however, we only used a simple 5 Hz train, which gives very limited information on micro-dynamics. In addition, the 0.05 Hz time resolution (the trains were repeated every 20 s) was inadequate for fast-acting drugs. Our method described here is novel in two aspects: First, it is able to give a simple, but complete assessment of state-dependent onset/offset dynamics of individual compounds, as well as the assessment of their effect on the conformational equilibrium of the channel, all within a single sweep of voltage steps. Second, it is able to provide this kinetic and equilibrium information at an unprecedented time resolution (1 Hz), which allowed us to monitor the development and decline of these effects upon drug application and removal.

The first important observation that this protocol allowed us to make was the obvious existence of two completely different processes, named micro- and macro-dynamics. This emphasizes the often unappreciated complexity of the processes which underlie the onset and offset of drug effect. Macro-dynamics is often studied using single pulses delivered at a certain fixed frequency, while the compound is washed in and then washed out. Macro-onset and macro-offset time constants are commonly interpreted as reflecting association and dissociation, and therefore are used to determine the affinity of binding. However, these processes never occur *in vivo*, and most likely do not reflect purely association and dissociation (only if partitioning into the membrane and access into the central cavity are relatively unobstructed, and therefore the rate-limiting step of onset is diffusion itself).

In contrast, micro-dynamics keeps going on incessantly all the time, in all excitable cells of the organism. Micro-offset is conventionally studied using the recovery from inactivation (RFI) protocol (using different interpulse intervals in separate sweeps). This recovery is also commonly interpreted as dissociation. Therefore, it is important to point out that for many inhibitor compounds micro- and macro-dynamics differ by several orders of magnitude, therefore it is not clear whether unbinding itself contributes to one, to the other, or both. For most compounds, we suppose that macro-onset may reflect deprotonation (as evidenced by the pH dependence of macro-dynamics (Lazar et al., 2015)), accumulation within the membrane phase, and state-dependent access to the central cavity. Macro-offset may reflect state-dependent egress from the central cavity and depletion of the membrane phase (and intracellular compartments). Micro-dynamics, for most inhibitors, probably reflects genuine binding/unbinding, but may also represent modulated gating (Földi et al., 2021) or the process of access/egress (diffusion between the central cavity and the membrane phase). Micro-dynamics is always dependent on conformational states, and in turn, it also affects the distribution of conformational states (by altering the rates of transitions between them).

Interestingly, although micro-dynamics obviously cannot be slower than macro-dynamics, the two are in fact not strongly correlated. We have found compounds with fast micro-dynamics but relatively slow macro-dynamics (e.g. riluzole, with more than 1,000-fold difference between micro- and macro-dynamics rates), and also some with relatively slow micro- but fast macro-dynamics (like bupivacaine, with less than 10-fold difference).

For slow micro-dynamics compounds, we will need to prolong the experimental protocol with both longer depolarizations and hyperpolarizations. Of course, this can only be done at the expense of time resolution, but for drugs, with slow dynamics, this seems acceptable. Allowing close-to-full equilibration of micro-onset and micro-offset should not compromise macro-dynamics.

In summary, automated analysis of data obtained using a complex voltage- and drug application protocol for an automated patch clamp instrument allowed us to assess the complex dynamics of drug-ion channel interaction, and to identify multiple sub-processes that constitute the onset and offset of drug effects during and after drug perfusion. Dynamics of drug binding/unbinding, access/egress, protonation/deprotonation, as well as the extent of modulation and channel block are crucial determinants of therapeutic effectiveness. We expect that a comprehensive assessment of the mechanism of action can provide a better prediction of therapeutic potential than the assessment of resting and inactivated affinity only.

DATA AVAILABILITY STATEMENT

The raw data supporting the conclusion of this article will be made available by the authors, without undue reservation.

AUTHOR CONTRIBUTIONS

PL and AM designed research; KP, MF, and AT performed automated patch-clamp experiments; AT performed single-cell patch-clamp experiments; PL, KZ, and GP contributed to the methodology and provided resources; PL and GP provided software tools; PL, MF, KP, AT, and AM analyzed data; PL and AM wrote the manuscript, all authors have read and approved the manuscript.

FUNDING

This work was supported by the Hungarian Brain Research Program (KTIA-NAP-13–2–2014–002), and by Hungary's Economic Development, and Innovation Operative Programme (GINOP-2.3.2-15-2016-00051).

ACKNOWLEDGMENTS

The content of this paper has previously appeared online in bioRxiv: https://doi.org/10.1101/2021.07.05.451189.

SUPPLEMENTARY MATERIAL

The Supplementary Material for this article can be found online at: https://www.frontiersin.org/articles/10.3389/fphar.2021.738260/full#supplementary-material

REFERENCES

Benoit, E., and Escande, D. (1991). Riluzole Specifically Blocks Inactivated Na Channels in Myelinated Nerve Fibre. *Pflugers Arch.* 419, 603–609. doi:10.1007/bf00370302

Cannon, S. C. (2018). Sodium Channelopathies of Skeletal Muscle. *Handb. Exp. Pharmacol.* 246, 309–330. doi:10.1007/164_2017_52

Desaphy, J. F., Carbonara, R., Costanza, T., and Conte Camerino, D. (2014). Preclinical Evaluation of Marketed Sodium Channel Blockers in a Rat Model of Myotonia Discloses Promising Antimyotonic Drugs. *Exp. Neurol.* 255, 96–102. doi:10.1016/j.expneurol.2014.02.023

Földi, M. C., Pesti, K., Zboray, K., Toth, A. V., Hegedűs, T., Málnási-Csizmadia, A., et al. (2021). The Mechanism of Non-blocking Inhibition of Sodium Channels Revealed by Conformation-Selective Photolabeling. *Br. J. Pharmacol.* 178, 1200–1217. doi:10.1111/bph.15365

Hebert, T., Drapeau, P., Pradier, L., and Dunn, R. J. (1994). Block of the Rat Brain IIA Sodium Channel Alpha Subunit by the Neuroprotective Drug Riluzole. *Mol. Pharmacol.* 45, 1055–1060.

Kuo, C. C., and Bean, B. P. (1994). Slow Binding of Phenytoin to Inactivated Sodium Channels in Rat Hippocampal Neurons. *Mol. Pharmacol.* 46, 716–725.

Lazar, A., Lenkey, N., Pesti, K., Fodor, L., and Mike, A. (2015). Different pH-Sensitivity Patterns of 30 Sodium Channel Inhibitors Suggest Chemically Different Pools along the Access Pathway. *Front. Pharmacol.* 6, 210. doi:10.3389/fphar.2015.00210

Lenkey, N., Karoly, R., Epresi, N., Vizi, E., and Mike, A. (2011). Binding of Sodium Channel Inhibitors to Hyperpolarized and Depolarized Conformations of the Channel. *Neuropharmacology* 60, 191–200. doi:10.1016/j.neuropharm.2010.08.005

Lenkey, N., Karoly, R., Kiss, J. P., Szasz, B. K., Vizi, E. S., and Mike, A. (2006). The Mechanism of Activity-Dependent Sodium Channel Inhibition by the Antidepressants Fluoxetine and Desipramine. *Mol. Pharmacol.* 70, 2052–2063. doi:10.1124/mol.106.026419

Lenkey, N., Karoly, R., Lukacs, P., Vizi, E. S., Sunesen, M., Fodor, L., et al. (2010). Classification of Drugs Based on Properties of Sodium Channel Inhibition: A Comparative Automated Patch-Clamp Study. *PLoS One* 5, e15568. doi:10.1371/journal.pone.0015568

Liu, Y., Beck, E. J., and Flores, C. M. (2011). Validation of a Patch Clamp Screening Protocol that Simultaneously Measures Compound Activity in Multiple States of the Voltage-Gated Sodium Channel Nav1.2. *Assay Drug Dev. Technol.* 9, 628–634. doi:10.1089/adt.2011.0375

Liu, Y. (2014). Electrophysiological Studies of Voltage-Gated Sodium Channels Using QPatch HT, an Automated Patch-Clamp System. *Curr. Protoc. Pharmacol.* 65, 11–45. doi:10.1002/0471141755.ph1114s65

Lukacs, P., Földi, M. C., Valánszki, L., Casanova, E., Biri-Kovács, B., Nyitray, L., et al. (2018). Non-Blocking Modulation Contributes to Sodium Channel Inhibition by a Covalently Attached Photoreactive Riluzole Analog. *Sci. Rep.* 8, 8110. doi:10.1038/s41598-018-26444-y

Morris, C. E., and Joos, B. (2016). Nav Channels in Damaged Membranes. *Curr. Top. Membr.* 78, 561–597. doi:10.1016/bs.ctm.2016.06.001

Pesti, K., Földi, M. C., Zboray, K., Toth, A. V., Lukacs, P., and Mike, A. (2021). Characterization of Compound-specific, Concentration-independent Biophysical Properties of Sodium Channel Inhibitor Mechanism of Action Using Automated Patch-Clamp Electrophysiology. *Front. Pharmacol.* 12, 738460. doi:10.3389/fphar.2021.738460

Simkin, D., and Bendahhou, S. (2011). Skeletal Muscle Na Channel Disorders. *Front. Pharmacol.* 2, 63. doi:10.3389/fphar.2011.00063

Terragni, B., Scalmani, P., Colombo, E., Franceschetti, S., and Mantegazza, M. (2016). Ranolazine vs Phenytoin: Greater Effect of Ranolazine on the Transient Na(+) Current Than on the Persistent Na(+) Current in central Neurons. *Neuropharmacology* 110, 223–236. doi:10.1016/j.neuropharm.2016.06.029

Vauquelin, G. (2016). Cell Membranes… and How Long Drugs May Exert Beneficial Pharmacological Activity *In Vivo* and How Long Drugs May Exert Beneficial Pharmacological Activity *In Vivo*. *Br. J. Clin. Pharmacol.* 82, 673–682. doi:10.1111/bcp.12996

Yan, Z., Zhou, Q., Wang, L., Wu, J., Zhao, Y., Huang, G., et al. (2017). Structure of the Nav1.4-β1 Complex from Electric Eel. *Cell* 170, 470–482.e11. doi:10.1016/j.cell.2017.06.039

Conflict of Interest: The authors declare that the research was conducted in the absence of any commercial or financial relationships that could be construed as a potential conflict of interest.

Publisher's Note: All claims expressed in this article are solely those of the authors and do not necessarily represent those of their affiliated organizations, or those of the publisher, the editors and the reviewers. Any product that may be evaluated in this article, or claim that may be made by its manufacturer, is not guaranteed or endorsed by the publisher.

Copyright © 2021 Lukacs, Pesti, Földi, Zboray, Toth, Papp and Mike. This is an open-access article distributed under the terms of the Creative Commons Attribution License (CC BY). The use, distribution or reproduction in other forums is permitted, provided the original author(s) and the copyright owner(s) are credited and that the original publication in this journal is cited, in accordance with accepted academic practice. No use, distribution or reproduction is permitted which does not comply with these terms.

frontiers
in Pharmacology

OPINION
published: 04 October 2021
doi: 10.3389/fphar.2021.754743

The Contribution of Dysfunctional Chloride Channels to Neurovascular Deficiency and Neurodegeneration

David A. Gascoigne[1], **Alexander Drobyshevsky**[2] and **Daniil P. Aksenov**[1,3]*

[1]Department of Radiology, NorthShore University HealthSystem, Evanston, IL, United States, [2]Department of Pediatrics, NorthShore University HealthSystem, Evanston, IL, United States, [3]Department of Anesthesiology, NorthShore University HealthSystem, Evanston, IL, United States

Keywords: GABA, hypoxia, development, anesthesia, interneurons

OPEN ACCESS

Edited by:
Jacques Joubert,
University of the Western Cape, South Africa

Reviewed by:
Ana Margarida Ledo,
University of Coimbra, Portugal

***Correspondence:**
Daniil P. Aksenov
daksenov@northshore.org

Specialty section:
This article was submitted to Pharmacology of Ion Channels and Channelopathies,
a section of the journal Frontiers in Pharmacology

Received: *06 August 2021*
Accepted: *21 September 2021*
Published: *04 October 2021*

Citation:
Gascoigne DA, Drobyshevsky A and Aksenov DP (2021) The Contribution of Dysfunctional Chloride Channels to Neurovascular Deficiency and Neurodegeneration. Front. Pharmacol. 12:754743. doi: 10.3389/fphar.2021.754743

INTRODUCTION

The brain is a metabolically demanding organ and its health directly depends on maintaining tissue oxygen that is sufficiently high to prevent hypoxia. Focal increases in oxygen demand, in response to sensory signals, motor output, etc., are supported by transient increases in cerebral blood flow via the hemodynamic response (Aksenov et al., 2016). Traditionally, specific products of glutamatergic and astrocytic pathways (i.e., nitric oxide (NO), arachidonic acid metabolites, calcium (Ca^{2+}) and potassium (K^+) ions) have been proposed as mechanistic contributors to the hemodynamic response (Archer et al., 1994; Attwell et al., 2010; Ross, 2012; Nippert et al., 2018). However, these mechanisms may not be sufficient drivers of the hemodynamic response. For example, a recent review (Nippert et al., 2018) concluded that, although NO must be present for vasodilation to occur in the cerebral cortex, it is not the active signaling molecule, arteriole vasodilation can occur in the absence of astrocyte Ca^{2+} increases, Ca^{2+} signals are characterized by long latencies occurring after the initiation of vasodilation and K^+ siphoning through astrocytes does not always play a major role in neurovascular coupling. Moreover, hemodynamic modulatory pathways can have differing levels of influence across various structures. For instance, studies have shown that NO can be an active signaling molecule in the cerebellum (Akgoren et al., 1996; Yang and Iadecola 1997) and hippocampus (Lourenco et al., 2014).

A possible addition to this conventional approach are chloride channel-dependent mechanisms of neurovascular coupling, which may participate in neurovascular deficiency and neurodegeneration. Prominent pathways which employ such chloride channels are gamma aminobutyric acid (GABA) ergic interneuron pathways, which operate via GABA-gated chloride channels ($GABA_A$ receptors) and provide a means of rapid signaling. The role of GABAergic interneurons and $GABA_A$ receptors in inhibition of neuronal activity is well-known. Interneurons suppress excessive neuronal activity and spatially limit neuronal responses by instigating the hyperpolarization of the cell membrane which has the added benefit of decreasing local oxygen consumption. Additionally, GABA-gated chloride channels can directly participate in regulating cerebral blood flow. $GABA_A$ receptors can be found along arterioles (Vaucher et al., 2000) where interneurons make direct morphological connections (Cauli et al., 2004; Tremblay et al., 2016). These chloride channels on brain vessels are functionally active and are able to facilitate substantial vasodilation in response to stimulation, attributable to the hyperpolarization of arteriolar smooth muscles with their subsequent relaxation. Multiple studies have shown that GABAergic interneurons are essential for the full expression of the hemodynamic response in the presence of chemical or electrical stimulation (Kocharyan et al., 2008), during epileptiform discharges (Saillet et al., 2016) as well as in response to both sensory (Aksenov et al., 2019) and optogenetic stimulation (Anenberg et al., 2015). Arteriolar GABA-gated chloride channels, can therefore play an important role in the hemodynamic response due to their fast and profound effect on vasodilation.

In essence, GABA-gated chloride channels can function to prevent hypoxia by both upregulating oxygen supply and downregulating oxygen consumption. Thus, it is our perspective that if the number of these channels or their main biochemical properties are affected, the combination of decreased inhibition and a weakened hemodynamic response can induce local hypoxia, which will alter the intracellular and extracellular environment with neurodegeneration evident thereafter. In support of this perspective, we will briefly review chloride channel dysfunction and neurodegeneration in different diseases, and then provide our interpretation regarding the role of neurovascular deficiency as a medium between chloride channel dysfunction and neurodegeneration.

NEURODEGENERATION AND CHLORIDE CHANNEL DEFICIENCY

Chloride channel deficiency accompanies many neurodegenerative diseases. For example, in Alzheimer's disease, which is characterized by progressive neurodegeneration starting in hippocampus and entorhinal cortex, the neurotransmission of GABA and GABAergic terminals have been shown to be significantly disrupted in areas neighboring beta-amyloid plaques (Li et al., 2016). Subsequent analysis has shown abnormal upregulation and downregulation of the α2, β1, γ1, and α1, γ2 subunits of GABA$_A$ receptors respectively (Limon et al., 2012). Another example is Parkinson's disease. This progressive neurodegenerative disorder is strongly associated with neuronal cell loss in the substantia nigra and striatum (Fahn and Sulzer, 2004). Although Parkinson's disease mostly corresponds with the loss of dopaminergic neurons, GABA and GABA$_A$ receptor deficiency has also been shown to play an important role in the early and non-motor symptoms of Parkinson's disease (Murueta-Goyena et al., 2019). These changes in GABAergic pathways are different from those observed in Huntington's disease. In Huntington's disease GABAergic interneurons undergo specific morphological alterations (i.e., reduced somatic areas and dendritic field complexity) which accompanies aggressive neurodegeneration in the striatum (Bano et al., 2011).

The etiologies of Alzheimer's, Parkinson's and particularly Huntington's diseases, are often attributed to genetics, however, some diseases (for example, epilepsy) can be independent of such substantial genetic factors. Distinctly, Drug-Resistant Epilepsy (DRE), which occurs in 40% of people with epilepsy (Engel, 2016), has been shown to cause neurodegeneration, often in the temporal lobe. Evidence has elucidated the association between the increased internalization of GABA$_A$ receptors and symptoms in DRE (Goodkin et al., 2005; Naylor et al., 2005; Goodkin et al., 2007).

Even complex psychiatric disorders can present with chloride channel affiliated neurodegeneration. For instance, patients with schizophrenia exhibit progressive bilateral neurodegeneration in the grey matter of the temporal and parietal lobes (Whitford et al., 2006), and can exhibit significant under-expression of the α5 subunit of GABA$_A$ receptors, the degree of which is correlated with the symptom severity (Marques et al., 2020). Furthermore, autism spectrum disorder (ASD) has demonstrated similar patterns of neurodegeneration to that of schizophrenia. Individuals with ASD have exhibited reduced grey matter volumes in the mirror neuron system (Hadjikhani et al., 2006; Marques et al., 2020). The severity of grey matter thinning in this area was further correlated with the severity of symptoms experienced by those with ASD. Moreover, genetic studies have identified copy number variations and entire locus duplications of the 15p11-q13 chromosomal region in patients with ASD, which lead to under and dysfunctional expression of the β3, α5, and γ3 subunits of GABA$_A$ receptors (Hadjikhani et al., 2006). This indicates the potential of chloride channel deficiency to both precede cases of ASD, and have further downstream consequences of neurodegeneration.

Chloride channel dysfunction and neurodegeneration can also occur as an acquired iatrogenic condition; the most notable example of which is neonatal exposure to anesthesia (Aksenov et al., 2020a). Anesthetics that are classified as GABA agonists and glutamate antagonists (Aksenov et al., 2019), have consistently been shown to produce significant neuroapoptosis that is directly correlated with dosage and duration of the anesthesia delivery (Hadjikhani et al., 2006; Zheng et al., 2015; Liu et al., 2018). Moreover, the severity of apoptosis can create a loss of cortical neurons, of which a significant proportion are GABAergic inhibitory interneurons (Istaphanous et al., 2013), and a further study has shown general anesthesia to directly disturb chloride channels (Cabrera et al., 2020) thereby broadening the known contributory effects of anesthesia on neurodegeneration (Aksenov, 2021). These neurodegenerative and apoptotic processes can alter the delicate excitatory/inhibitory balance of cortical networks (Aksenov et al., 2020a). This imbalance can account for, at least in part, the negative developmental changes (Johnston et al., 2002; Aksenov et al., 2020a; Aksenov et al., 2020b) and impeded GABAergic system development (Young et al., 2012; Nisimov et al., 2018) following neonatal anesthesia. This disproportionate cell death leading to a shift in the excitatory/inhibitory balance requires further research in terms of occurrence of the local chronic hypoxia in later years, and how this shift caused by anesthesia, adapts throughout development.

DISCUSSION

We suggest that, in the absence of normal GABA$_A$ receptor functioning, neurovascular deficiency could manifest where a weakened hemodynamic response, in combination with decreased inhibition, would be insufficient to support the present metabolic demand. Although this type of neurovascular deficiency does not result in actual ischemic stroke, it engenders chronic intermittent hypoxia which produces neurodegeneration. This clear sequence of events explains the importance of normal chloride channel functioning for preventing chronic hypoxia. Therefore, dysfunctional chloride channels could be a contributory factor to the neurodegeneration in the aforementioned diseases which are epiphenomenal with chloride channel dysfunction.

Indeed, the dangers of hypoxia on the intracellular and extracellular compositions of brain tissue have been well documented. It is known that insufficient oxygen for basic metabolic processes can lead to cell death (Mariotti et al., 2016). Although the neuronal damage is especially severe in sudden onset hypoxia–ischemia, such as in the case of an ischemic stroke, it can also occur as a result of chronic hypoxia (Dheer et al., 2018; Mahakizadeh et al., 2020). Depending on the severity, hypoxia has been shown to increase the production of reactive oxygen species which can accumulate beyond the protective abilities of anti-oxidative systems, causing oxidative stress (Chen et al., 2018). Oxidative stress has a high propensity to interact with macromolecules within cells (e.g., DNA/RNA oxidation, protein oxidation, nitration of tyrosine residues, and lipid peroxidation), leading to cell debilitation (Moreira et al., 2005). Other consequences of hypoxia include a reduction in intracellular and extracellular pH (Rolett et al., 2000; Yao and Haddad, 2004), phosphocreatine (Rolett et al., 2000), inorganic phosphate (Nioka et al., 1990; Rolett et al., 2000) and a buildup of NADH (Rolett et al., 2000; Shetty et al., 2014). These distinct alterations to the intracellular and extracellular environment significantly impair normal cellular functioning and have been shown to be biochemical indicators of neuroapoptosis. Such hypoxia-related events not only demonstrate the ability of insufficient cerebral blood flow to produce neurodegeneration in the immediate undersupplied tissues, but that it can also harmfully affect neighboring tissues as well.

Brain functioning and its metabolic support is a highly integrated process, and embedded within this complex system are GABAergic interneurons and the hemodynamic response. When neurodegeneration is present, determining if neurovascular deficiency precedes this process and exacerbates the neurodegeneration, or suffers as a direct consequence of an unbalanced excitatory/inhibitory system, remains a challenge. These two possibilities are accompanied by respective hypotheses and can therefore be examined by future studies in a controlled environment. A possibility of how one may address this issue includes *in vivo* studies providing longitudinal measurement of chloride channel and interneuron deficiencies in association with subsequent hemodynamic function and neurodegeneration.

Further interrogation into chloride channel subunit functioning may provide a bottom-up approach to more accurately describe their role in neurodegeneration. A family of genes have been identified (regions CLC2-7) to transcript chloride channels in the brain (Jentsch et al., 1999). These loci represent specific areas of potential genetic manipulation that could identify the discrete contribution of chloride channels and their subunits in degenerative diseases. In addition, the local modulation of chloride channel expression with a viral vector could be used. This type of methodology has proven effective in animal translational models (Miah et al., 2019). Unfortunately, little work has been done to use viral vectors to modulate chloride channel expression in the brain. However, in reference to GABA_A receptors, certain benzodiazepine derivatives have shown to allosterically bind to individual subunits. Namely, TPA023 (Atack et al., 2006), HZ166 (Di Lio et al., 2011) and SL651498 (Griebel et al., 2003) are reported to act as α2 and α3 agonists, while CGS 9865 binds to the β+α− interface (Maldifassi et al., 2016). Genetic and subunit-related research may provide further insights into chloride channel dysfunction and lead to etiologically-specific pharmacological solutions to both protect chloride channels, and prevent neurovascular deficiency, in the previously discussed diseases and conditions.

AUTHOR CONTRIBUTIONS

DA and DG wrote the manuscript, AD provided input on the manuscript. All authors contributed to manuscript revision, read, and approved the submitted version.

FUNDING

This work was supported by R01GM112715 (National Institute of General Medical Sciences), R01NS107383 (National Institute of Neurological Disorders and Stroke), R01NS119251 (National Institute of Neurological Disorders and Stroke).

REFERENCES

Akgören, N., Dalgaard, P., and Lauritzen, M. (1996). Cerebral Blood Flow Increases Evoked by Electrical Stimulation of Rat Cerebellar Cortex: Relation to Excitatory Synaptic Activity and Nitric Oxide Synthesis. *Brain Res.* 710 (1-2), 204–214. doi:10.1016/0006-8993(95)01354-7

Aksenov, D. P., Li, L., Miller, M. J., and Wyrwicz, A. M. (2016). Blood Oxygenation Level Dependent Signal and Neuronal Adaptation to Optogenetic and Sensory Stimulation in Somatosensory Cortex in Awake Animals. *Eur. J. Neurosci.* 44 (9), 2722–2729. doi:10.1111/ejn.13384

Aksenov, D. P., Li, L., Miller, M. J., and Wyrwicz, A. M. (2019). Role of the Inhibitory System in Shaping the BOLD fMRI Response. *Neuroimage* 201, 116034. doi:10.1016/j.neuroimage.2019.116034

Aksenov, D. P., Miller, M. J., Dixon, C. J., and Drobyshevsky, A. (2020a). Impact of Anesthesia Exposure in Early Development on Learning and Sensory Functions. *Dev. Psychobiol* 62 (5), 559–572. doi:10.1002/dev.21963

Aksenov, D. P., Miller, M. J., Dixon, C. J., and Wyrwicz, A. M. (2019). The Effect of Sevoflurane and Isoflurane Anesthesia on Single Unit and Local Field Potentials. *Exp. Brain Res.* 237 (6), 1521–1529. doi:10.1007/s00221-019-05528-9

Aksenov, D. P. (2021). Normal Development of Local Neurovascular Interactions and the Diagnostic Value of Resting State Functional MRI in Neurovascular Deficiency Based on the Example of Neonatal Anesthesia Exposure. *Front. Neurol.* 12, 664706. doi:10.3389/fneur.2021.664706

Aksenov, D. P., Venkatasubramanian, P. N., Miller, M. J., Dixon, C. J., Li, L., and Wyrwicz, A. M. (2020b). Effects of Neonatal Isoflurane Anesthesia Exposure on Learning-specific and Sensory Systems in Adults. *Sci. Rep.* 10 (1), 13832. doi:10.1038/s41598-020-70818-0

Anenberg, E., Chan, A. W., Xie, Y., LeDue, J. M., and Murphy, T. H. (2015). Optogenetic Stimulation of GABA Neurons Can Decrease Local Neuronal Activity while Increasing Cortical Blood Flow. *J. Cereb. Blood Flow Metab.* 35 (10), 1579–1586. doi:10.1038/jcbfm.2015.140

Archer, S. L., Huang, J. M., Hampl, V., Nelson, D. P., Shultz, P. J., and Weir, E. K. (1994). Nitric Oxide and cGMP Cause Vasorelaxation by Activation of a Charybdotoxin-Sensitive K Channel by cGMP-dependent Protein Kinase. *Proc. Natl. Acad. Sci. U S A.* 91 (16), 7583–7587. doi:10.1073/pnas.91.16.7583

Atack, J. R., Wafford, K. A., Tye, S. J., Cook, S. M., Sohal, B., Pike, A., et al. (2006). TPA023 [7-(1,1-Dimethylethyl)-6-(2-Ethyl-2h-1,2,4-Triazol-3-Ylmethoxy)-3-(2-Fluorophenyl)-1,2,4-Triazolo[4,3-B]pyridazine], an Agonist Selective for Alpha2- and Alpha3-Containing GABAA Receptors, Is a Nonsedating Anxiolytic in Rodents and Primates. *J. Pharmacol. Exp. Ther.* 316 (1), 410–422. doi:10.1124/jpet.105.089920

Attwell, D., Buchan, A. M., Charpak, S., Lauritzen, M., Macvicar, B. A., and Newman, E. A. (2010). Glial and Neuronal Control of Brain Blood Flow. *Nature* 468 (7321), 232–243. doi:10.1038/nature09613

Bano, D., Zanetti, F., Mende, Y., and Nicotera, P. (2011). Neurodegenerative Processes in Huntington's Disease. *Cell Death Dis* 2, e228. doi:10.1038/cddis.2011.112

Cabrera, O. H., Tesic, V., Tat, Q. L., Chastain, S., Quillinan, N., and Jevtovic-Todorovic, V. (2020). Sevoflurane-Induced Dysregulation of Cation-Chloride Cotransporters NKCC1 and KCC2 in Neonatal Mouse Brain. *Mol. Neurobiol.* 57 (1), 1–10. doi:10.1007/s12035-019-01751-1

Cauli, B., Tong, X. K., Rancillac, A., Serluca, N., Lambolez, B., Rossier, J., et al. (2004). Cortical GABA Interneurons in Neurovascular Coupling: Relays for Subcortical Vasoactive Pathways. *J. Neurosci.* 24 (41), 8940–8949. doi:10.1523/JNEUROSCI.3065-04.2004

Chen, R., Lai, U. H., Zhu, L., Singh, A., Ahmed, M., and Forsyth, N. R. (2018). Reactive Oxygen Species Formation in the Brain at Different Oxygen Levels: The Role of Hypoxia Inducible Factors. *Front Cel Dev Biol* 6, 132. doi:10.3389/fcell.2018.00132

Dheer, A., Jain, V., Kushwah, N., Kumar, R., Prasad, D., and Singh, S. B. (2018). Temporal and Spatial Changes in Glial Cells during Chronic Hypobaric Hypoxia: Role in Neurodegeneration. *Neuroscience* 383, 235–246. doi:10.1016/j.neuroscience.2018.04.026

Di Lio, A., Benke, D., Besson, M., Desmeules, J., Daali, Y., Wang, Z. J., et al. (2011). HZ166, a Novel GABAA Receptor Subtype-Selective Benzodiazepine Site Ligand, Is Antihyperalgesic in Mouse Models of Inflammatory and Neuropathic Pain. *Neuropharmacology* 60 (4), 626–632. doi:10.1016/j.neuropharm.2010.11.026

Engel, J., Jr. (2016). What Can We Do for People with Drug-Resistant Epilepsy? the 2016 Wartenberg Lecture. *Neurology* 87 (23), 2483–2489. doi:10.1212/WNL.0000000000003407

Fahn, S., and Sulzer, D. (2004). Neurodegeneration and Neuroprotection in Parkinson Disease. *NeuroRx* 1 (1), 139–154. doi:10.1602/neurorx.1.1.139

Goodkin, H. P., Sun, C., Yeh, J. L., Mangan, P. S., and Kapur, J. (2007). GABA(A) Receptor Internalization during Seizures. *Epilepsia* 48 (Suppl. 5), 109–113. doi:10.1111/j.1528-1167.2007.01297.x

Goodkin, H. P., Yeh, J. L., and Kapur, J. (2005). Status Epilepticus Increases the Intracellular Accumulation of GABAA Receptors. *J. Neurosci.* 25 (23), 5511–5520. doi:10.1523/JNEUROSCI.0900-05.2005

Griebel, G., Perrault, G., Simiand, J., Cohen, C., Granger, P., Depoortere, H., et al. (2003). SL651498, a GABAA Receptor Agonist with Subtype-Selective Efficacy, as a Potential Treatment for Generalized Anxiety Disorder and Muscle Spasms. *CNS Drug Rev.* 9 (1), 3–20. doi:10.1111/j.1527-3458.2003.tb00241.x

Hadjikhani, N., Joseph, R. M., Snyder, J., and Tager-Flusberg, H. (2006). Anatomical Differences in the Mirror Neuron System and Social Cognition Network in Autism. *Cereb. Cortex* 16 (9), 1276–1282. doi:10.1093/cercor/bhj069

Istaphanous, G. K., Ward, C. G., Nan, X., Hughes, E. A., McCann, J. C., McAuliffe, J. J., et al. (2013). Characterization and Quantification of Isoflurane-Induced Developmental Apoptotic Cell Death in Mouse Cerebral Cortex. *Anesth. Analg* 116 (4), 845–854. doi:10.1213/ANE.0b013e318281e988

Jentsch, T. J., Friedrich, T., Schriever, A., and Yamada, H. (1999). The CLC Chloride Channel Family. *Pflugers Arch.* 437 (6), 783–795. doi:10.1007/s004240050847

Johnston, M. V., Nakajima, W., and Hagberg, H. (2002). Mechanisms of Hypoxic Neurodegeneration in the Developing Brain. *Neuroscientist* 8 (3), 212–220. doi:10.1177/1073858402008003007

Kocharyan, A., Fernandes, P., Tong, X. K., Vaucher, E., and Hamel, E. (2008). Specific Subtypes of Cortical GABA Interneurons Contribute to the Neurovascular Coupling Response to Basal Forebrain Stimulation. *J. Cereb. Blood Flow Metab.* 28 (2), 221–231. doi:10.1038/sj.jcbfm.9600558

Li, Y., Sun, H., Chen, Z., Xu, H., Bu, G., and Zheng, H. (2016). Implications of GABAergic Neurotransmission in Alzheimer's Disease. *Front. Aging Neurosci.* 8, 31. doi:10.3389/fnagi.2016.00031

Limon, A., Reyes-Ruiz, J. M., and Miledi, R. (2012). Loss of Functional GABA(A) Receptors in the Alzheimer Diseased Brain. *Proc. Natl. Acad. Sci. U S A.* 109 (25), 10071–10076. doi:10.1073/pnas.1204606109

Liu, Y., Liu, C., Zeng, M., Han, X., Zhang, K., Fu, Y., et al. (2018). Influence of Sevoflurane Exposure on Mitogen-Activated Protein Kinases and Akt/GSK-3β/CRMP-2 Signaling Pathways in the Developing Rat Brain. *Exp. Ther. Med.* 15 (2), 2066–2073. doi:10.3892/etm.2017.5651

Lourenço, C. F., Santos, R. M., Barbosa, R. M., Cadenas, E., Radi, R., and Laranjinha, J. (2014). Neurovascular Coupling in hippocampus Is Mediated via Diffusion by Neuronal-Derived Nitric Oxide. *Free Radic. Biol. Med.* 73, 421–429. doi:10.1016/j.freeradbiomed.2014.05.021

Mahakizadeh, S., Mokhtari, T., Navaee, F., Poorhassan, M., Tajik, A., and Hassanzadeh, G. (2020). Effects of Chronic Hypoxia on the Expression of seladin-1/Tuj1 and the Number of Dark Neurons of hippocampus. *J. Chem. Neuroanat.* 104, 101744. doi:10.1016/j.jchemneu.2020.101744

Maldifassi, M. C., Baur, R., and Sigel, E. (2016). Molecular Mode of Action of CGS 9895 at α1β2γ2GABAAreceptors. *J. Neurochem.* 138 (5), 722–730. doi:10.1111/jnc.13711

Mariotti, L., Losi, G., Sessolo, M., Marcon, I., and Carmignoto, G. (2016). The Inhibitory Neurotransmitter GABA Evokes Long-Lasting Ca(2+) Oscillations in Cortical Astrocytes. *Glia* 64 (3), 363–373. doi:10.1002/glia.22933

Marques, T. R., Ashok, A. H., Angelescu, I., Borgan, F., Myers, J., Lingford-Hughes, A., et al. (2020). GABA-A Receptor Differences in Schizophrenia: a Positron Emission Tomography Study Using [(11)C]Ro154513. *Mol. Psychiatry.*

Miah, K. M., Hyde, S. C., and Gill, D. R. (2019). Emerging Gene Therapies for Cystic Fibrosis. *Expert Rev. Respir. Med.* 13 (8), 709–725. doi:10.1080/17476348.2019.1634547

Moreira, P. I., Smith, M. A., Zhu, X., Nunomura, A., Castellani, R. J., and Perry, G. (2005). Oxidative Stress and Neurodegeneration. *Ann. N. Y Acad. Sci.* 1043, 545–552. doi:10.1196/annals.1333.062

Murueta-Goyena, A., Andikoetxea, A., Gómez-Esteban, J. C., and Gabilondo, I. (2019). Contribution of the GABAergic System to Non-motor Manifestations in Premotor and Early Stages of Parkinson's Disease. *Front. Pharmacol.* 10, 1294. doi:10.3389/fphar.2019.01294

Naylor, D. E., Liu, H., and Wasterlain, C. G. (2005). Trafficking of GABA(A) Receptors, Loss of Inhibition, and a Mechanism for Pharmacoresistance in Status Epilepticus. *J. Neurosci.* 25 (34), 7724–7733. doi:10.1523/JNEUROSCI.4944-04.2005

Nioka, S., Chance, B., Smith, D. S., Mayevsky, A., Reilly, M. P., Alter, C., et al. (1990). Cerebral Energy Metabolism and Oxygen State during Hypoxia in Neonate and Adult Dogs. *Pediatr. Res.* 28 (1), 54–62. doi:10.1203/00006450-199007000-00013

Nippert, A. R., Biesecker, K. R., and Newman, E. A. (2018). Mechanisms Mediating Functional Hyperemia in the Brain. *Neuroscientist* 24 (1), 73–83. doi:10.1177/1073858417703033

Nisimov, H., Orenbuch, A., Pleasure, S. J., and Golan, H. M. (2018). Impaired Organization of GABAergic Neurons Following Prenatal Hypoxia. *Neuroscience* 384, 300–313. doi:10.1016/j.neuroscience.2018.05.021

Rolett, E. L., Azzawi, A., Liu, K. J., Yongbi, M. N., Swartz, H. M., and Dunn, J. F. (2000). Critical Oxygen Tension in Rat Brain: a Combined (31)P-NMR and EPR Oximetry Study. *Am. J. Physiol. Regul. Integr. Comp. Physiol.* 279 (1), R9–R16. doi:10.1152/ajpregu.2000.279.1.R9

Ross, W. N., and Manita, S. (2012). Imaging Calcium Waves and sparks in central Neurons. *Cold Spring Harb Protoc.* 2012 (3), 1087–1091. doi:10.1101/pdb.prot071480

Saillet, S., Quilichini, P. P., Ghestem, A., Giusiano, B., Ivanov, A. I., Hitziger, S., et al. (2016). Interneurons Contribute to the Hemodynamic/metabolic

Response to Epileptiform Discharges. *J. Neurophysiol.* 115 (3), 1157–1169. doi:10.1152/jn.00994.2014

Shetty, P. K., Galeffi, F., and Turner, D. A. (2014). Nicotinamide Pre-treatment Ameliorates NAD(H) Hyperoxidation and Improves Neuronal Function after Severe Hypoxia. *Neurobiol. Dis.* 62, 469–478. doi:10.1016/j.nbd.2013.10.025

Tremblay, R., Lee, S., and Rudy, B. (2016). GABAergic Interneurons in the Neocortex: From Cellular Properties to Circuits. *Neuron* 91 (2), 260–292. doi:10.1016/j.neuron.2016.06.033

Vaucher, E., Tong, X. K., Cholet, N., Lantin, S., and Hamel, E. (2000). GABA Neurons Provide a Rich Input to Microvessels but Not Nitric Oxide Neurons in the Rat Cerebral Cortex: a Means for Direct Regulation of Local Cerebral Blood Flow. *J. Comp. Neurol.* 421, 161–171. doi:10.1002/(sici)1096-9861(20000529)421:2<161::aid-cne3>3.0.co;2-f

Whitford, T. J., Grieve, S. M., Farrow, T. F., Gomes, L., Brennan, J., Harris, A. W., et al. (2006). Progressive Grey Matter Atrophy over the First 2-3 Years of Illness in First-Episode Schizophrenia: a Tensor-Based Morphometry Study. *Neuroimage* 32 (2), 511–519. doi:10.1016/j.neuroimage.2006.03.041

Yang, G., and Iadecola, C. (1997). Obligatory Role of NO in Glutamate-dependent Hyperemia Evoked from Cerebellar Parallel Fibers. *Am. J. Physiol.* 272 (4 Pt 2), R1155–R1161. doi:10.1152/ajpregu.1997.272.4.R1155

Yao, H., and Haddad, G. G. (2004). Calcium and pH Homeostasis in Neurons during Hypoxia and Ischemia. *Cell Calcium* 36 (3-4), 247–255. doi:10.1016/j.ceca.2004.02.013

Young, S. Z., Taylor, M. M., Wu, S., Ikeda-Matsuo, Y., Kubera, C., and Bordey, A. (2012). NKCC1 Knockdown Decreases Neuron Production through GABA(A)-regulated Neural Progenitor Proliferation and Delays Dendrite Development. *J. Neurosci.* 32 (39), 13630–13638. doi:10.1523/JNEUROSCI.2864-12.2012

Zheng, S. Q., Chen, X., Wang, Y. J., and An, L. X. (2015). [Effects of Sevoflurane on Brain Neuroapoptosis and Ability of Long-Term Learning and Memory in Newborn Rats]. *Beijing Da Xue Xue Bao Yi Xue Ban* 47 (4), 674–678.

Conflict of Interest: The authors declare that the research was conducted in the absence of any commercial or financial relationships that could be construed as a potential conflict of interest.

Publisher's Note: All claims expressed in this article are solely those of the authors and do not necessarily represent those of their affiliated organizations, or those of the publisher, the editors and the reviewers. Any product that may be evaluated in this article, or claim that may be made by its manufacturer, is not guaranteed or endorsed by the publisher.

Copyright © 2021 Gascoigne, Drobyshevsky and Aksenov. This is an open-access article distributed under the terms of the Creative Commons Attribution License (CC BY). The use, distribution or reproduction in other forums is permitted, provided the original author(s) and the copyright owner(s) are credited and that the original publication in this journal is cited, in accordance with accepted academic practice. No use, distribution or reproduction is permitted which does not comply with these terms.

frontiers in Pharmacology

BRIEF RESEARCH REPORT
published: 28 October 2021
doi: 10.3389/fphar.2021.773455

Imprecision in Precision Medicine: Differential Response of a Disease-Linked GluN2A Mutant to NMDA Channel Blockers

Jenna R. Gale, Gabrielle J. Kosobucki, Karen A. Hartnett-Scott and Elias Aizenman*

Department of Neurobiology and Pittsburgh Institute for Neurodegenerative Diseases, University of Pittsburgh School of Medicine, Pittsburgh, PA, United States

OPEN ACCESS

Edited by:
Werner J Geldenhuys,
West Virginia University, United States

Reviewed by:
Jacy Wagnon,
The Ohio State University,
United States
Vishwanath Jogini,
D. E. Shaw Research, United States

***Correspondence:**
Elias Aizenman
redox@pitt.edu

Specialty section:
This article was submitted to
Pharmacology of Ion Channels and
Channelopathies,
a section of the journal
Frontiers in Pharmacology

Received: *09 September 2021*
Accepted: *13 October 2021*
Published: *28 October 2021*

Citation:
Gale JR, Kosobucki GJ,
Hartnett-Scott KA and Aizenman E
(2021) Imprecision in Precision
Medicine: Differential Response of a
Disease-Linked GluN2A Mutant to
NMDA Channel Blockers.
Front. Pharmacol. 12:773455.
doi: 10.3389/fphar.2021.773455

Mutations in N-methyl-D-aspartate receptors (NMDAR) subunits have been implicated in a growing number of human neurodevelopmental disorders. Previously, a *de novo* mutation in *GRIN2A*, encoding the GluN2A subunit, was identified in a patient with severe epilepsy and developmental delay. This missense mutation, which leads to GluN2A-P552R, produces significant dendrotoxicity in transfected rodent cortical neurons, as evidenced by pronounced dendritic blebbing. This injurious process can be prevented by treatment with the NMDA antagonist memantine. Given the increasing use of FDA approved NMDA antagonists to treat patients with *GRIN* mutations, who may have seizures refractory to traditional anti-epileptic drugs, we investigated whether additional NMDA antagonists were effective in attenuating neurotoxicity associated with GluN2A-P552R expression. Intriguingly, we found that while treatment with memantine can effectively block GluN2A-P552R-mediated dendrotoxicity, treatment with ketamine does not, despite the fact that both drugs work as open NMDAR channel blockers. Interestingly, we found that neurons expressing GluN2A-P552R were more vulnerable to an excitotoxic insult—an effect that, in this case, could be equally rescued by both memantine and ketamine. These findings suggest that GluN2A-P552R induced dendrotoxicity and increased vulnerability to excitotoxic stress are mediated through two distinct mechanisms. The differences between memantine and ketamine in halting GluN2A-P552R dendrotoxicity could not be explained by NMDA antagonist induced changes in MAP or Src kinase activation, previously shown to participate in NMDA-induced excitotoxicity. Our findings strongly suggest that not all NMDA antagonists may be of equal clinical utility in treating *GRIN2A*-mediated neurological disorders, despite a shared mechanism of action.

Keywords: GRIN2A gene, GluN2A subunit, memantine, ketamine, precision medicine, N-methyl-D-aspartate receptor, channelopathy

INTRODUCTION

N-methyl-D-aspartate receptors (NMDARs) are ligand-gated, ionotropic glutamate receptors that are widely expressed in the brain, where they play key roles in neuronal developmental, synaptic plasticity, and survival. NMDARs are heterotetramers composed of three main subtypes: GluN1, which are obligatory, GluN2 of which there are four subunit types (A-D), and GluN3 subunits of which there are two subunit types (A-B) (Traynelis et al., 2010; Paoletti et al., 2013). The majority of NMDARs express two glycine-binding GluN1 subunits and two glutamate-binding GluN2 subunits (Köhr, 2006). The GluN2 subtype dictates many of the NMDAR's characteristics such as its biophysical, pharmacological, and signaling properties, as well as its spatiotemporal pattern of expression (Monyer et al., 1992; Watanabe et al., 1994; Paoletti et al., 2013; Vieira et al., 2020).

Mutations in NMDAR subunits have been increasingly implicated in neurological and neurodevelopmental diseases, including intellectual disability, autism spectrum disorders, developmental delay, and epilepsy (Myers et al., 2019). The identification of *GRIN* variants in pediatric patients is significant, as individuals *GRIN* mutations and epilepsy refractory to standard anti-convulsants have been successfully treated with the FDA-approved NMDAR antagonists memantine, ketamine, and dextromethorphan (Pierson et al., 2014; Li et al., 2016; Amador et al., 2020; Xu et al., 2021). Although mutations in four genes encoding NMDAR subunits (*GRIN1, GRIN2A, GRIN2B, and GRIN2D*) have been linked to human disease (Carvill et al., 2013; Li et al., 2016; Liu et al., 2017; Li et al., 2019; Bahry et al., 2021; Xu et al., 2021), mutations in *GRIN2A* account for the majority of disease-linked variants (46%) (Myers et al., 2019; Strehlow et al., 2019). Pathogenic variants cluster in the highly conserved agonist binding domains as well as transmembrane and linker domains, which are highly intolerant to genetic variation (Swanger et al., 2016; Ogden et al., 2017; Strehlow et al., 2019).

Recently, a *de novo* missense mutation in the pre-M1 helix region—the linker between the agonist binding domain and the first transmembrane domain—was identified in a patient with profound intellectual disability, developmental delay, and epilepsy (de Ligt et al., 2012). This mutation, which results in a substitution of arginine for proline at amino acid 552 (P552R), was further characterized as leading to neurotoxicity when expressed in cultured rat cortical neurons, as evidenced by pronounced dendritic swelling (Ogden et al., 2017). This neurotoxicity could be rescued by treatment with memantine. Given the superiority of ketamine as compared to memantine in treating some *GRIN* mutations (Li et al., 2016), and its widespread use in treating status epilepticus in adult and pediatric populations (Mewasingh et al., 2003; Ilvento et al., 2015; Zeiler, 2015), we sought to determine whether ketamine treatment was equally effective as memantine in abrogating GluN2A-P552R induced neurotoxicity *in vitro*. Surprisingly, our data indicate that the P552R mutation exerts neurotoxicity through two separate mechanisms, dendritic blebbing and increased susceptibility to excitotoxic injury—both responsive to treatment with memantine but only the latter responsive to treatment with ketamine, despite a shared mechanism of action between these two drugs.

METHODS

Materials

Primary antibodies used: rabbit anti-p38 MAPK (Cell Signaling, 9212S, 1:1,000), mouse anti-phospho-p38 MAPK (Cell Signaling, 9216S, 1:1,000), mouse anti-ERK (pan-ERK) (BD Transduction Lab, 610,123, 1:2000), rabbit anti-phospho-p44/42 MAPK (ERK 1/2) (Cell Signaling, 910, 1:1,000), mouse anti-JNK (Santa Cruz, sc-7345, 1:1,000), rabbit anti-pSAPK/JNK (Cell Signaling, 4668S, 1:1,000), rabbit anti-Src (Cell Signaling, 2108S, 1:1,000), rabbit anti-phospho-Src (Tyr416) (Cell Signaling, 2101S, 1:1,000), and mouse anti-β-actin (Sigma, A5441, 1:10,000). Mouse or rabbit secondary antibodies used: Li-cor IRDye 700 CW and Licor IRDye 800CW (LI-COR Biosciences). Chemicals were obtained from Sigma-Aldrich unless otherwise specified.

Neuronal Cultures

All procedures involving the use of animals were reviewed and approved by the University of Pittsburgh IACUC. Primary cortical cultures were prepared from embryonic day 16–17 Sprague-Dawley rats as previously described (Hartnett et al., 1997). Briefly, pregnant rats (Charles River Laboratories) were sacrificed via CO_2 inhalation. Embryonic cortices were dissociated with trypsin and cells were plated on 12-mm, poly-L-ornithine coated glass coverslips in six-well plates at a density of 670,000 cells per well. On day 14 *in vitro* (DIV 14) cytosine arabinoside (1–2 μM) was used to inhibit nonneuronal cell proliferation. Cultures were used at DIV 18–25.

Transfections

Transfections were performed using Lipofectamine 2000 (Thermo Fisher). Neurons were transfected with the following plasmid mixtures (total of 1.5 μg DNA/0.5 ml): for confocal imaging, cells were transfected with a GFP-expressing plasmid (pEGFP-N1; BD Biosciences), pCI-neo vector, human wild-type GluN2A, or human GluN2A-P552R (gifts from Drs. Hongjie Yuan and Stephen Traynelis). Plasmid mixtures (per well) contained either 0.9 μg pEGFP-N1 + 0.6 μg pCI-neo vector, 0.9 μg pEGFP-N1 + 0.3 μg pCI-neo empy vector + 0.3 μg GluN2A plasmid, or 0.9 μg pEGFP-N1 + 0.3 μg pCI-neo empy vector + 0.3 μg GluN2A-P552R plasmid (Ogden et al., 2017). For luciferase viability experiments, cells were transfected with a firefly luciferase-expressing plasmid (pUHC13-3 Luciferase, gift of Dr. H. Buchard) instead of one expressing GFP. Plasmid mixtures (per well) contained either 0.375 μg pUHC13-3 Luciferase + 1.125 μg pCI-neo vector plasmid, 0.375 μg pUHC13-3 Luciferase + 0.525 μg pCI-neo vector + 0.6 μg GluN2A plasmid, or 0.375 μg pUHC13-3 Luciferase + 0.525 μg pCI-neo vector plasmid + 0.6 μg GluN2A-P552R plasmid.

Confocal Imaging and Bleb Analysis

To analyze the effect of the GluN2A-P552R mutation on dendrite morphology, cells were imaged 24 h after transfection. All treatments were added to the cell media at the time of transfection. Images were obtained on a Nikon A1+ confocal microscope using a ×20 water immersion objective. Three separate culture dates were used per experiment, and three coverslips were transfected with each plasmid mixture per condition. Each coverslip was divided into four quadrants, and one field of view was randomly selected from each quadrant resulting in four images per coverslip. Bleb counts per field were added to determine a bleb count per coverslip (blebs/CS). For these experiments, *n* refers to the number of coverslips. Laser power was sometimes adjusted between coverslips due to differences in transfection efficiency of the GFP-expressing plasmid. Nikon Instruments Software Basic Research (NIS-Elements BR) was used for non-biased analysis of dendritic blebs. All images were subjected to intensity thresholding before analysis. The object count feature was used to quantify the number of blebs in each image field. Area was restricted to 0–5 μm^2 and circularity was set to 0.5–1.0. The smooth, clean, and separate features were used to reduce background noise and settings were consistent between control, ketamine, and MK-801 groups. Settings had to be adjusted once due to the installation of a new laser in our system.

Lactate Dehydrogenase Assays

Cortical neurons were treated with 10 μM glycine, 10 μM glycine + 30 μM NMDA, or 10 μM glycine + 30 μM NMDA with either 50 μM memantine or 10 μM ketamine for 30 min in HEPES-buffered minimal essential media with 0.01% BSA (MHB). After 30 min, cells were washed with fresh MHB and then incubated with MHB or MHB containing memantine or ketamine. Twenty-four hs following glycine + NMDA treatment, medium was collected for lactate dehydrogenase (LDH) assays. Toxicity is represented by increased OD490 values. Three experiments from separate culture dates were performed, each in quadruplicate.

Luciferase Viability Assays

Cortical cultures were transfected with plasmid mixtures containing a luciferase-expressing. Twenty-four hs following transfection, cells were either left untreated, treated with 45 μM DL-*threo*-β-Benzyloxyaspartate (TBOA) (Tocris Bioscience), or co-treated with 45 μM TBOA and either 50 μM memantine or 10 μM ketamine. TBOA is a glutamate uptake inhibitor that induces an excitotoxic injury *in vitro* (Bonde et al., 2003). Twenty-four hs after drug treatment, firefly luciferase expression was measured using the SteadyLite Plus Luminescence Gene Reporter Assay System (PerkinElmer) (Aras et al., 2008). Results for TBOA-treated groups were normalized to the luminescence values (counts per second) of their respective untreated groups. This assay was performed a minimum of four times with neurons from separate culture dates.

Immunoblotting

Cortical cultures were left untreated, treated with 50 μM memantine, or treated with 10 μM ketamine for 45 min. Control, memantine treated-, and ketamine treated neurons were collected from the same 6 well plate for each experiment. Following treatment, neurons were rinsed twice with ice-cold PBS, exposed to cell lysis buffer (Invitrogen) supplemented with protease inhibitor cocktail (Roche Diagnostics) and phenylmethlysulfonyl fluoride, and scraped off dishes. Debris was pelleted by centrifugation at 14,000 g for 10 min. The remaining lysates were stored at −80°C. Protein concentration of lysates was determined (Pierce BCA Protein Assay Kit; Thermo Fisher). Samples were prepared by incubating 30 μg of protein with a reducing sample buffer at 100°C for 5 minutes. Samples were loaded onto a 7.5% SDS-PAGE gel and proteins were separated using the Mini Protean 3 System (Biorad). Gels were transferred onto 0.2 μm nitrocellulose membranes and blocked at room temperature for 1 h with 1% BSA in PBS containing 0.05% Tween 20 (PBST). Membranes were incubated overnight at 4°C in primary antibody. After washing 3x in PBST, membranes were probed with Li-Cor IRDye-conjugated secondary antibodies labeled with IRDyes 700CW (685 nm) and 800CW (780 nm), at 1:10,000 for 1 h at room temperature. Fluorescent signals were

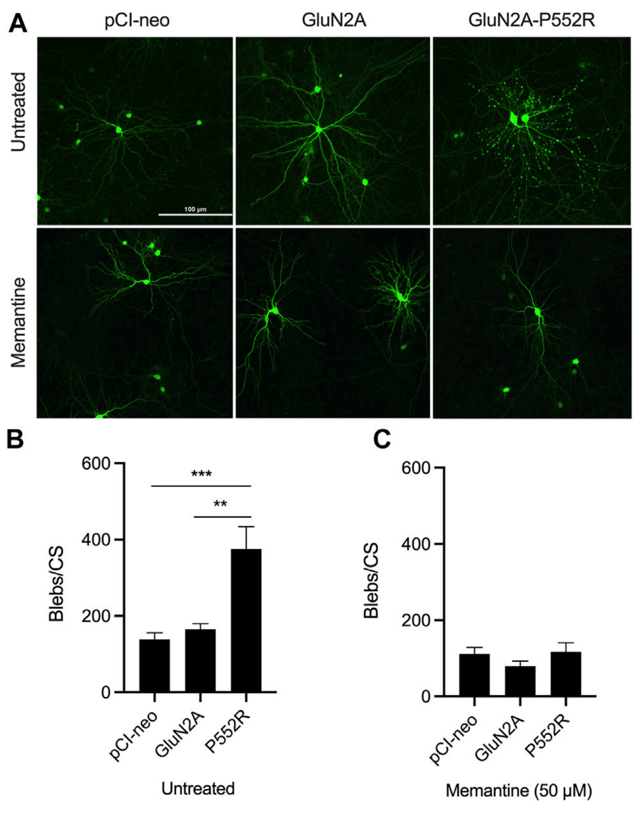

FIGURE 1 | GluN2A-P552R expression exerts dendrotoxicity in rat primary cortical cultures which can be rescued by treatment with memantine. Representative images of cortical neurons transfected with GFP and either pCI-neo (empty vector), GluN2A, or GluN2A-P552R. Top row shows untreated neurons and bottom row shows neurons co-treated with 50 μM memantine **(A)**. Quantification of dendritic blebs per coverslip (blebs/CS) revealed significantly more blebs in GluN2A-P552R transfected neurons as compared to those transfected with pCI-neo or GluN2A **(B)**. This difference is abolished by treatment with 50 μM memantine **(C)**. Data are expressed as mean ± SEM from three independent experiments with three coverslips per transfection condition in each experiment (***p* < 0.01, ****p* < 0.001, one-way ANOVA/Tukey post-hoc, n = 9).

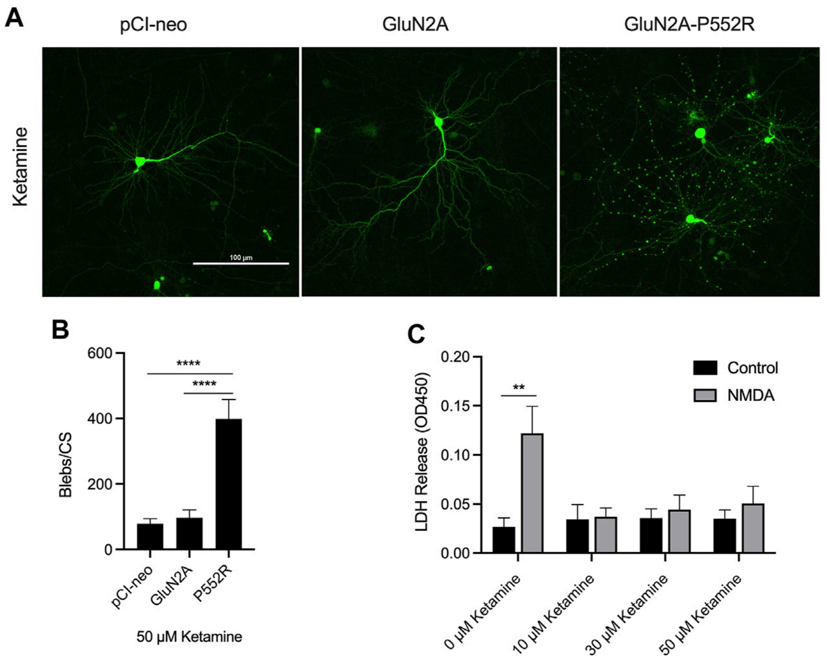

FIGURE 2 | Ketamine treatment does not rescue GluN2A-P552R-mediated dendritic blebbing. Representative images of cortical neurons transfected with GFP and either pCI-neo, GluN2A, or GluN2A-P552R and co-treated with 50 µM ketamine show that GluN2A-P552R transfected neurons exhibit pronounced blebbing that is not rescued by the open-channel blocker **(A)**. Quantification of dendritic blebbing confirmed significantly more blebs in the GluN2A-P552R group **(B)** (*****p* < 0.0001, one-way ANOVA/Tukey post-hoc, n = 9). LDH assays of untransfected primary cortical neurons treated with 10 µM glycine (control) or 10 µM glycine + 30 µM NMDA (NMDA) confirmed that ketamine is protective against excitotoxic injury **(C)** (***p* < 0.01, two-way ANOVA/Sidak post-hoc, n = 3). Therefore, the failure of ketamine to rescue GluN2A-P552R dendrotoxicity is not due to inefficacy of the drug in our culture system. Data are expressed as mean ± SEM from three independent experiments. Three transfections per condition were analyzed from each independent imaging experiment.

acquired (Odyssey Infrared Imaging System; LI-COR) and quantified using Fiji software.

Statistical Analysis

Data are presented as means ± SEM. All statistical analyses were performed using GraphPad Prism 9 (GraphPad). Prior to analyses, data were tested for normality using a Shapiro Wilk test. For comparison of two sample means, a two-tailed *t*-test was used. For comparison of more than two sample means, a one-way analysis of variance (ANOVA) with Tukey's test for multiple comparisons was used. For LDH assays, a two-way ANOVA with Sidak's multiple comparison test was used to compare the effect of drug treatments on viability between control and treatment groups.

RESULTS

A previous characterization of the GluN2A-P552R mutation found that the mutant NMDAR subunit exerted profound dendrotoxicity when expressed in primary neurons, as evidenced by dendritic swelling (blebbing) (Ogden et al., 2017). GluN2A-P552R mediated dendritic blebbing could be rescued by treating neurons with the FDA-approved NMDAR antagonist memantine (50 µM), consistent with clinical reports of NMDAR receptor antagonists being used to treat refractory epilepsy in patients with *GRIN* mutations (Pierson et al., 2014; Li et al., 2016; Amador et al., 2020). Given that ketamine, another FDA-approved NMDAR antagonist, is currently widely used to treat status epilepticus (Ilvento et al., 2015; Zeiler, 2015; Pribish et al., 2020), and has been used to treat refractory epilepsy in patient with a *GRIN2D* mutation (Li et al., 2016), we evaluated its neuroprotective profile in GluN2A-P552R mediated neurotoxicity.

We first confirmed our previous findings from the initial characterization of the GluN2A-P552R mutation (Ogden et al., 2017). As noted earlier, cortical neurons transfected with GluN2A-P552R displayed pronounced dendritic blebbing (Ogden et al., 2017) (**Figures 1A,B**). This effect was not observed in neurons transfected with the empty vector (pCI-neo) or, importantly, the wild-type subunit (GluN2A). GluN2A-P552R-mediated dendrotoxicity was attenuated by treatment with 50 µM memantine (One-way ANOVA, $p = 0.3025$, n = 9) (**Figures 1A,C**), as previously shown, confirming that FDA-approved NMDAR antagonists may be a viable treatment strategy for individual(s) with this mutation. Surprisingly, although ketamine and memantine share the same mechanism of action, similar pharmacodynamic profiles, and overlapping binding sites within NMDA receptors (Song et al., 2018; Zhang et al., 2021; Emnett et al., 2013), we found that ketamine treatment did not rescue GluN2A-P552R mediated dendritic blebbing (One-way ANOVA, $p < 0.0001$; Multiple comparisons, pCI-neo vs. GluN2A, $p = 0.9407$, pCI-neo vs. GluN2A-P552R, $p < 0.0001$, GluN2A vs. GluN2A-P552R, $p < 0.0001$, n = 9) (**Figures 2A,B**). Indeed, an unpaired *t*-test revealed that there was no difference in the number of dendritic blebs per coverslip between untreated neurons and those treated with 50 μM ketamine ($p = 0.7819$, n = 9). Although there are some reports of ketamine induced neurotoxicity in neurons exposed to the drug for prolonged periods (Liu et al., 2013; Wang et al., 2017), empty vector transfected neurons and GluN2A transfected neurons, which were also treated with ketamine in parallel with GluN2A-P552R transfected neurons, did not display any dendrotoxicity, suggesting that the dendritic blebbing observed in GluN2A-P552R group was not a result of the ketamine treatment itself. It is noteworthy that ketamine's ability to inhibit GluN1/GluN2A-P552R-mediated ionic currents does not significantly differ from its ability to block GluN1/GluN2A wild type channels. Ketamine's maximum blocking efficacy for GluN1/GluN2A-P552R channels is 96% as compared to 98% for wild-type channels. Furthermore, the GluN2A-P552R mutation enhances the potency of ketamine (IC_{50} =1.3 μM for GluN2A-P552R; IC_{50} = 4.7 μM for wild type GluN2A), without significantly affecting memantine's blocking actions at the receptor (IC_{50} = 3.7 μM for GluN2A-P552R; IC_{50} = 4.8 for wild type GluN2A) (Ogden et al., 2017). As such the lack of ketamine's ability to protect from the observed dendrotoxicity could not be accounted by an inability to antagonize the mutant channels.

Given these data, we sought to confirm that ketamine was indeed protective against canonical excitotoxic insults in our cell culture system. To this end, we exposed untransfected cortical cultures to either 10 μM glycine (control) or 10 μM glycine and 30 μM NMDA for 30 min and co-treated with either vehicle or ketamine (10 μM, 30 μM, or 50 μM). Cell viability was assessed using LDH assays 24 hs after the exposure. Cells not treated with ketamine displayed a significant loss of viability when exposed to glycine + NMDA as compared to the control, whereas no significant differences were found between the control and glycine + NMDA groups when cells were co-treated with ketamine (Two-way ANOVA, $p = 0.0158$ for interaction; Multiple comparisons, glycine vs glycine + NMDA: 0 μM ketamine, $p = 0.0021$, 10 μM ketamine, $p = 0.9997$, 30 μM ketamine, $p = 0.9820$, 50 μM ketamine, $p = 0.8645$, n = 3) (**Figure 2C**). Furthermore, comparison of control neurons in these assays confirmed that ketamine treatment is not neurotoxic in our system (One-way ANOVA, $p > 0.05$). These results indicate that ketamine is an effective excitotoxicity neuroprotectant in our preparation.

As the above data indicate that the inability of ketamine to rescue of GluN2A-P552R mediated dendrotoxicity is not due to a loss of potency or innate toxicity, we next aimed to determine whether memantine's ability to rescue this phenotype was through its classically defined role as an NMDA receptor channel antagonist or through an undefined, alternative mechanism. To this end, we exposed GluN2A-P55R expressing neurons to the open-channel blocker MK-801, which binds to the same pocket of the NMDAR as memantine and ketamine (Song et al., 2018; Zhang et al., 2021). Treatment with 10 μM MK-801 similarly abolished GluN2A-P552R mediated dendritic blebbing (One-way ANOVA, $p > 0.05$) (**Figures 3A,B**), strongly suggesting that memantine rescues GluN2A-P552R through its known mechanism of pharmacological action.

Having established the NMDAR blockade is sufficient to rescue GluN2A-P552R mediated dendrotoxicity, we next investigated downstream pathways that may be either activated or inhibited by ketamine, but not by memantine, which could account for the differential responses observed. Activation of MAP kinases (MAPKs) have previously been shown to be part of signaling cascades initiated downstream of NMDAR activation (Kawasaki et al., 1997; Chen et al., 2003), including those implicated in excitotoxicity (Kawasaki et al., 1997; Cao et al., 2004; Choo et al., 2012; Liu et al., 2014; Engin and Engin, 2021). Therefore, we assessed via western blot whether there were differences in kinase phosphorylation in primary cortical neurons treated with either ketamine or memantine. No significant differences were found between memantine and ketamine groups in levels of phosphorylated ERK1/2 or JNK (Paired *t*-test, $p > 0.05$, n = 5–6) (**Supplementary Figure S1F and S1G**). A small but significant reduction in phosphorylated p38 (p-p38) was found in ketamine treated neurons as compared to those treated with memantine (Paired *t*-test, $p = 0.\ 0.0036$, n = 5) (**Supplementary Figure S1E**). However, given that phosphorylation of p38 has been implicated in excitotoxic neuronal apoptosis (Kawasaki et al., 1997; Chen et al., 2003; Liu et al., 2014), it is unlikely that the reduction of p-p38 in the ketamine treated group is the mechanism underlying the persistent dendritic blebbing in ketamine treated GluN2A-P552R expressing neurons. As Src kinase has been shown to upregulate NMDAR activity (Manzerra et al., 2001; Zhao et al., 2015; Scanlon et al., 2017), we also assessed whether memantine and ketamine treatment differentially affected Src phosphorylation. However, no differences were found between groups (Paired *t*-test, $p > 0.05$, n = 5) (**Supplementary Figure S1H**). Thus, the mechanism underlying the inability of ketamine to rescue GluN2A-P552R-induced dendritic blebbing is yet to be identified. Nonetheless, the data presented thus far strongly suggests that human disease-linked *GRIN* mutations may be differentially responsive to NMDAR antagonists.

Because the GluN2A-P552R mutation results in increased agonist potency and mean channel open time (Ogden et al., 2017), we hypothesized that neurons that express this mutant subunit may show enhanced vulnerability to excitotoxic injury, perhaps due to exaggerated calcium influx upon activation. To test this, we transfected neurons with a plasmid expressing firefly luciferase along with the either the empty vector, GluN2A, or GluN2A-P552R. Co-transfection of the firefly luciferase construct allowed us to compare viability of cells expressing the mutant subunit as compared to wild-type GluN2A or the empty vector (Aras et al., 2008). Twenty-four hs after transfection, neurons were exposed to a mild excitotoxic insult (treatment with a sublethal concentration of the glutamate uptake inhibitor TBOA, 45 μM) for an additional 24 hs. Indeed, following TBOA exposure, we found a significant difference in viability

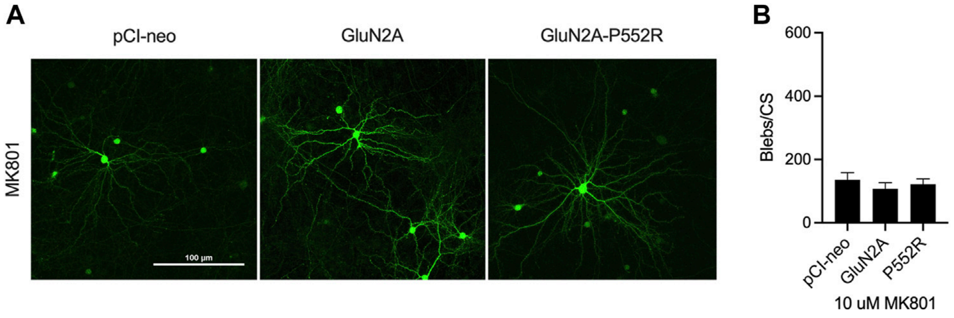

FIGURE 3 | Dendritic blebbing is attenuated by treatment with the channel blocker MK801. Representative images of rat cortical neurons transfected with pCI-neo empty vector, GluN2A-WT, and GluN2A-P552R and co-treated with 10 μM MK801 **(A)**. GluN2A-P552R expressing neurons treated with 10 μM MK801 show a significant reduction in blebbing **(B)** (one-way ANOVA, $p > 0.05$, n = 9). Data are ± SEM from three independent experiments with three coverslips analyzed per experiment.

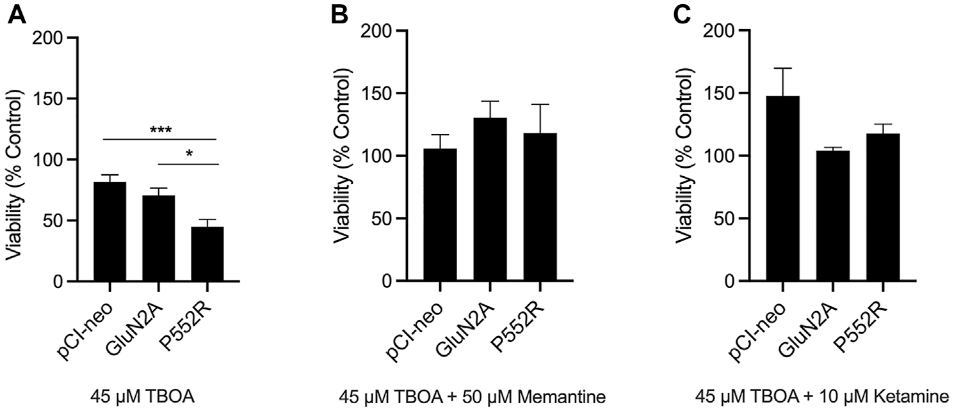

FIGURE 4 | GluN2A-P552R enhances vulnerability to excitotoxic stress which can be rescued by both memantine and ketamine. Luciferase assays were used as a measure of cell viability. Rat cortical neurons were co-transfected with a plasmid expressing firefly luciferase and pCI-neo vector, GluN2A-WT, or GluN2A-P552R. Treatments were applied 24 h after transfection and luciferase assays were performed 48 h following transfection. Neurons expressing GluN2A-P552R showed significantly reduced viability after exposure to 45 μM TBOA as compared to those expressing the empty vector or wild-type receptor **(A)** (*$p < 0.05$, ***$p < 0.001$, one-way ANOVA/Tukey post-hoc, n = 8). However, this reduction in viability was rescued by co-treatment with 50 μM memantine **(B)** (one-way ANOVA, $p > 0.05$) or 10 μM ketamine **(C)** (one-way ANOVA, $p > 0.05$). Luciferase values for TBOA treated neurons were normalized to their relevant vehicle-treated vector group. Data represent mean ± SEM from 4-8 independent experiments performed in triplicate or quadruplicate.

of GluN2A-P552R transfected neurons as compared to those transfected with the empty vector or the wild-type subunit (One-way ANOVA, $p = 0.001$; Multiple Comparisons, pCI-neo vs GluN2A, $p = 0.3983$, pCI-neo vs GluN2A-P552R, $p = 0.0008$, GluN2A vs GluN2A-P552R, $p = 0.0181$). (**Figure 4A**). Co-treatment with memantine rescued the loss of viability observed in GluN2A-P552R expressing neurons (One-way ANOVA, $p > 0.05$), consistent with its effect on GluN2A-P552R mediated dendrotoxicity (**Figure 4B**). In contrast to ketamine's failure to attenuate dendritic blebbing, co-treatment with this channel blocker also completely rescued TBOA-induced cell death in GluN2A-P552R expressing neurons (One-way ANOVA, $p > 0.05$) (**Figure 4C**). These data strongly suggest that the P552R mutation exerts dendrotoxicity and enhances vulnerability to excitotoxic stress through two separate cell injurious signaling pathways.

DISCUSSION

The rise of next-generation and whole exome sequencing (WES) has led to the increasing identification of clinically relevant gene variants and molecular diagnoses in patients with neurological diseases. Indeed, in one large observational study, WES was able to provide a molecular diagnosis for approximately 27% of patients with neurological and developmental disorders (Yang et al., 2014). In a smaller cohort of pediatric neurological patients, WES provided a presumptive diagnosis in 41% of patients. Importantly, the results of WES affected the management of all patients with a presumptive diagnosis in this cohort including, but not limited to, the cessation and initiation of medication (Srivastava et al., 2014). Thus, genetic testing has both a high diagnostic yield and significant implications for personalized clinical management for neurological patients.

The clinical utility of genetic sequencing is especially significant for patients with epileptic encephalopathies. It is estimated that the diagnosis yield for these disorders is 15–20% (EpiPM Consortium, 2015). Intriguingly, *GRIN* mutations make up a high proportion of these disease-linked mutations, and *GRIN2A* mutations, specifically, have been identified as key drivers of epilepsy aphasia spectrum disorders (Carvill et al., 2013; Li et al., 2020; Lemke et al., 2013; Lesca et al., 2013). The identification and *in vitro* characterization of human disease-linked *GRIN* mutations has led to the successful implementation of personalized medicine for several pediatric patients. More specifically, patients with *GRIN* mutations and intractable epilepsy have been treated with FDA-approved NMDAR blockers, including ketamine, memantine, and dextromethorphan (**Supplementary Table S1**), which led to a reduction in seizure burden in the majority of patients treated with these targeted therapies (Pierson et al., 2014; Li et al., 2016; Platzer et al., 2017; Amador et al., 2020; Xu et al., 2021). The results of these *n* of one clinical trials have important clinical implications for patients with *GRIN*-associated epileptic encephalopathies, as refractory epileptic activity in these disorders is thought to contribute to the co-morbid, and often progressive, cognitive impairments (Khan and Al Baradie, 2012; Auvin et al., 2016).

The increasing number of individuals with identified *GRIN* mutations along with the *in vitro* characterization of NMDAR subunit variants has led to an attempt by some to predict clinical phenotypes based upon molecular diagnoses. For example, it has been suggested that *GRIN2A* mutations predominantly lead to an epileptic phenotype while *GRIN2B* variants are more likely to lead to neurodevelopmental disorders (Myers et al., 2019). However, while this may be true in broad strokes, *GRIN2B* has been identified as a causative gene in encephalitic encephalopathies (Epi4K Consortium et al., 2013; Lemke et al., 2014). Moreover, the characterization of *GRIN2B* mutations in two patients with missense mutations at the same amino acid residue revealed a divergence in multiple aspects of both the patient phenotypes and the functional properties of the mutant channels (Kellner et al., 2021), underscoring the complexity of the NMDAR and the need for complete characterizations of *GRIN* variants for targeted therapies. Similarly, characterizing *GRIN* mutations as gain-of-function or loss-of-function based on their location in the protein domain may be overly simplistic and lead to improper pharmacological treatment strategies. While a large cohort analysis of individuals with *GRIN2A* variants identified two phenotypic groups based on whether mutations occurred within the N-terminal or agonist binding domains versus the transmembrane or linker domains, with the former corresponding to loss-of function (LOF) and the latter gain-of-function (GOF) (Strehlow et al., 2019), functional analysis of disease-linked mutations within the pre-M1 linker domain of GluN2A receptors identified both LOF and GOF variants (Ogden et al., 2017). Thus, a full functional characterization of *GRIN* mutations is warranted before the initiation of treatment with channel-blockers.

In this work, we uncover another layer of complexity in the application of precision medicine to *GRIN* mutations: the differential response of a mutant subunit to channel blockers that do not differ in their potency or maximal inhibition of the receptor. Specifically, we found that a missense *GRIN2A* variant resulting in a substitution of arginine for proline at amino acid 552 (P552R) exerts neurotoxicity through two distinct mechanisms—increased sensitivity to excitotoxic insults, which is sensitive to rescue by the channel blockers memantine and ketamine, and pronounced dendrotoxicity that is sensitive to rescue by memantine and MK801, but not ketamine.

Previous characterizations of *GRIN* mutations have found differential responses to channel blockers. For example, treatment with dextromethorphan results in increased inhibition of the NMDA channel as compared to memantine in the NMDA receptor GluN2AN-N615K variant (Marwick et al., 2019). However, memantine binds to the pore by interacting with the amino acids that cluster around the area of this mutation (N612, N613, and N614) (Song et al., 2018), while dextromethorphan is thought to interact with residues in a more extracellular portion of the vestibule (LePage et al., 2005). Thus, increased inhibition of GluN2A-N615K containing receptors by dextromethorphan is consistent with the understanding of its binding site, while differences in binding sites cannot explain the observed differential dendro-protective response of GluN2A-P552R-containing NMDA receptors to memantine and ketamine, as these channel blockers bind to an overlapping site in the pore (Emnett et al., 2013; Zhang et al., 2021). To account for the noted changes, we explored whether memantine and ketamine differentially activate or inhibit kinases downstream of neurotoxic NMDAR signaling. However, these experiments did not reveal significant differences between treatment groups. Given that memantine has been found to stabilize GluN1/GluN2A receptor desensitization in a calcium-dependent manner (Gao et al., 2017), one possible explanation for the discrepancy between memantine and ketamine's ability to rescue GluN2A-P552R mediated dendrotoxicity is that the mutation enhances calcium influx through NMDARs thereby enhancing memantine's potency. However, preliminary experiments showed that the IC50 of memantine in the presence of high and low intracellular calcium did not differ between wild-type and mutant receptors, suggesting this phenomenon does not account for our results (M. Phillips and J. Johnson, personal communication). Thus, the mechanism underlying the differential response of GluN2A-P552R containing NMDARs to memantine and ketamine remains to be elucidated. Nonetheless, our findings are significant in the context of personalized medicine for patients with neurological disorders attributable to *GRIN* mutations as they suggest that in addition to a functional characterization of the mutation, *in vitro* drug screening and investigation of rescue pharmacology may be necessary to identify the most appropriate therapeutic strategies to follow.

DATA AVAILABILITY STATEMENT

The original contributions presented in the study are included in the article/**Supplementary Material**, further inquiries can be directed to the corresponding author.

ETHICS STATEMENT

The animal study was reviewed and approved by University of Pittsburgh IACUC.

AUTHOR CONTRIBUTIONS

EA, JG, and GK conceived the project and designed the experiments. JG, GK, and KH-S performed the experiments and analyzed the data. JG and EA wrote the paper. All authors have read and agreed to the published version of the manuscript.

FUNDING

JG is supported by National Institute of Health Grant 5T32GM008208-32. This work was supported, in part, by National Institutes of Health grants NS117702 to EA.

ACKNOWLEDGMENTS

We thank Hongjie Yuan and Stephen Traynelis for the gift of plasmids and many useful discussions throughout this project, and Matthew Phillips and Jon Johnson for help and advice and preliminary studies performed for this study.

SUPPLEMENTARY MATERIAL

The Supplementary Material for this article can be found online at: https://www.frontiersin.org/articles/10.3389/fphar.2021.773455/full#supplementary-material

REFERENCES

Epi4K Consortium, Epilepsy Phenome/Genome ProjectAllen, A. S., Allen, A. S., Berkovic, S. F., Cossette, P., Delanty, N., Dlugos, D., et al. (2013). De novo mutations in epileptic encephalopathies. *Nature* 501, 217–221. doi:10.1038/nature12439

Amador, A., Bostick, C. D., Olson, H., Peters, J., Camp, C. R., Krizay, D., et al. (2020). Modelling and treating GRIN2A developmental and epileptic encephalopathy in mice. *Brain* 143, 2039–2057. doi:10.1093/brain/awaa147

Aras, M. A., Hartnett, K. A., and Aizenman, E. (2008). Assessment of cell viability in primary neuronal cultures. *Curr. Protoc. Neurosci.*, 44 Chapter 7, Unit 7.18. doi:10.1002/0471142301.ns0718s44

Auvin, S., Cilio, M. R., and Vezzani, A. (2016). Current understanding and neurobiology of epileptic encephalopathies. *Neurobiol. Dis.* 92, 72–89. doi:10.1016/j.nbd.2016.03.007

Bahry, J. A., Fedder-Semmes, K. N., Sceniak, M. P., and Sabo, S. L. (2021). An Autism-Associated de novo Mutation in GluN2B Destabilizes Growing Dendrites by Promoting Retraction and Pruning. *Front. Cel. Neurosci.* 15, 692232. doi:10.3389/fncel.2021.692232

Bonde, C., Sarup, A., Schousboe, A., Gegelashvili, G., Zimmer, J., and Noraberg, J. (2003). Neurotoxic and neuroprotective effects of the glutamate transporter inhibitor DL-threo-beta-benzyloxyaspartate (DL-TBOA) during physiological and ischemia-like conditions. *Neurochem. Int.* 43, 371–380. doi:10.1016/s0197-0186(03)00024-x

Cao, J., Semenova, M. M., Solovyan, V. T., Han, J., Coffey, E. T., and Courtney, M. J. (2004). Distinct requirements for p38alpha and c-Jun N-terminal kinase stress-activated protein kinases in different forms of apoptotic neuronal death. *J. Biol. Chem.* 279, 35903–35913. doi:10.1074/jbc.M402353200

Carvill, G. L., Regan, B. M., Yendle, S. C., O'Roak, B. J., Lozovaya, N., Bruneau, N., et al. (2013). GRIN2A mutations cause epilepsy-aphasia spectrum disorders. *Nat. Genet.* 45, 1073–1076. doi:10.1038/ng.2727

Chen, R. W., Qin, Z. H., Ren, M., Kanai, H., Chalecka-Franaszek, E., Leeds, P., et al. (2003). Regulation of c-Jun N-terminal kinase, p38 kinase and AP-1 DNA binding in cultured brain neurons: roles in glutamate excitotoxicity and lithium neuroprotection. *J. Neurochem.* 84, 566–575. doi:10.1046/j.1471-4159.2003.01548.x

Choo, A. M., Geddes-Klein, D. M., Hockenberry, A., Scarsella, D., Mesfin, M. N., Singh, P., et al. (2012). NR2A and NR2B subunits differentially mediate MAP kinase signaling and mitochondrial morphology following excitotoxic insult. *Neurochem. Int.* 60, 506–516. doi:10.1016/j.neuint.2012.02.007

de Ligt, J., Willemsen, M. H., van Bon, B. W., Kleefstra, T., Yntema, H. G., Kroes, T., et al. (2012). Diagnostic exome sequencing in persons with severe intellectual disability. *N. Engl. J. Med.* 367, 1921–1929. doi:10.1056/NEJMoa1206524

Emnett, C. M., Eisenman, L. N., Taylor, A. M., Izumi, Y., Zorumski, C. F., and Mennerick, S. (2013). Indistinguishable synaptic pharmacodynamics of the N-methyl-D-aspartate receptor channel blockers memantine and ketamine. *Mol. Pharmacol.* 84, 935–947. doi:10.1124/mol.113.089334

Engin, A., and Engin, A. B. (2021). N-Methyl-D-Aspartate Receptor Signaling-Protein Kinases Crosstalk in Cerebral Ischemia. *Adv. Exp. Med. Biol.* 1275, 259–283. doi:10.1007/978-3-030-49844-3_10

EpiPM Consortium (2015). A roadmap for precision medicine in the epilepsies. *Lancet Neurol.* 14, 1219–1228. doi:10.1016/S1474-4422(15)00199-4

Gao, K., Tankovic, A., Zhang, Y., Kusumoto, H., Zhang, J., Chen, W., et al. (2017). A de novo loss-of-function GRIN2A mutation associated with childhood focal epilepsy and acquired epileptic aphasia. *PLoS One* 12, e0170818. doi:10.1371/journal.pone.0170818

Hartnett, K. A., Stout, A. K., Rajdev, S., Rosenberg, P. A., Reynolds, I. J., and Aizenman, E. (1997). NMDA receptor-mediated neurotoxicity: a paradoxical requirement for extracellular Mg2+ in Na+/Ca2+-free solutions in rat cortical neurons *in vitro*. *J. Neurochem.* 68, 1836–1845. doi:10.1046/j.1471-4159.1997.68051836.x

Ilvento, L., Rosati, A., Marini, C., L'Erario, M., Mirabile, L., and Guerrini, R. (2015). Ketamine in refractory convulsive status epilepticus in children avoids endotracheal intubation. *Epilepsy Behav.* 49, 343–346. doi:10.1016/j.yebeh.2015.06.019

Kawasaki, H., Morooka, T., Shimohama, S., Kimura, J., Hirano, T., Gotoh, Y., et al. (1997). Activation and involvement of p38 mitogen-activated protein kinase in glutamate-induced apoptosis in rat cerebellar granule cells. *J. Biol. Chem.* 272, 18518–18521. doi:10.1074/jbc.272.30.18518

Kellner, S., Abbasi, A., Carmi, I., Heinrich, R., Garin-Shkolnik, T., Hershkovitz, T., et al. (2021). Two de novo GluN2B mutations affect multiple NMDAR-functions and instigate severe pediatric encephalopathy. *Elife* 10. doi:10.7554/eLife.67555

Khan, S., and Al Baradie, R. (2012). Epileptic encephalopathies: an overview. *Epilepsy Res. Treat.* 2012, 403592. doi:10.1155/2012/403592

Köhr, G. (2006). NMDA receptor function: subunit composition versus spatial distribution. *Cell Tissue Res* 326, 439–446. doi:10.1007/s00441-006-0273-6

Lemke, J. R., Hendrickx, R., Geider, K., Laube, B., Schwake, M., Harvey, R. J., et al. (2014). GRIN2B mutations in West syndrome and intellectual disability with focal epilepsy. *Ann. Neurol.* 75, 147–154. doi:10.1002/ana.24073

Lemke, J. R., Lal, D., Reinthaler, E. M., Steiner, I., Nothnagel, M., Alber, M., et al. (2013). Mutations in GRIN2A cause idiopathic focal epilepsy with rolandic spikes. *Nat. Genet.* 45, 1067–1072. doi:10.1038/ng.2728

LePage, K. T., Ishmael, J. E., Low, C. M., Traynelis, S. F., and Murray, T. F. (2005). Differential binding properties of [3H]dextrorphan and [3H]MK-801 in heterologously expressed NMDA receptors. *Neuropharmacology* 49, 1–16. doi:10.1016/j.neuropharm.2005.01.029

Lesca, G., Rudolf, G., Bruneau, N., Lozovaya, N., Labalme, A., Boutry-Kryza, N., et al. (2013). GRIN2A mutations in acquired epileptic aphasia and related childhood focal epilepsies and encephalopathies with speech and language dysfunction. *Nat. Genet.* 45, 1061–1066. doi:10.1038/ng.2726

Li, D., Yuan, H., Ortiz-Gonzalez, X. R., Marsh, E. D., Tian, L., McCormick, E. M., et al. (2016). GRIN2D Recurrent De Novo Dominant Mutation Causes a Severe Epileptic Encephalopathy Treatable with NMDA Receptor Channel Blockers. *Am. J. Hum. Genet.* 99, 802–816. doi:10.1016/j.ajhg.2016.07.013

Li, J., Zhang, J., Tang, W., Mizu, R. K., Kusumoto, H., XiangWei, W., et al. (2019). De novo GRIN variants in NMDA receptor M2 channel pore-forming loop are associated with neurological diseases. *Hum. Mutat.* 40, 2393–2413. doi:10.1002/humu.23895

Li, X., Xie, L. L., Han, W., Hong, S. Q., Ma, J. N., Wang, J., et al. (2020). Clinical Forms and GRIN2A Genotype of Severe End of Epileptic-Aphasia Spectrum Disorder. *Front. Pediatr.* 8, 574803. doi:10.3389/fped.2020.574803

Liu, F., Patterson, T. A., Sadovova, N., Zhang, X., Liu, S., Zou, X., et al. (2013). Ketamine-induced neuronal damage and altered N-methyl-D-aspartate receptor function in rat primary forebrain culture. *Toxicol. Sci.* 131, 548–557. doi:10.1093/toxsci/kfs296

Liu, S., Zhou, L., Yuan, H., Vieira, M., Sanz-Clemente, A., Badger, J. D., et al. (2017). A Rare Variant Identified within the GluN2B C-Terminus in a Patient with Autism Affects NMDA Receptor Surface Expression and Spine Density. *J. Neurosci.* 37, 4093–4102. doi:10.1523/JNEUROSCI.0827-16.2017

Liu, X. W., Ji, E. F., He, P., Xing, R. X., Tian, B. X., and Li, X. D. (2014). Protective effects of the p38 MAPK inhibitor SB203580 on NMDA induced injury in primary cerebral cortical neurons. *Mol. Med. Rep.* 10, 1942–1948. doi:10.3892/mmr.2014.2402

Manzerra, P., Behrens, M. M., Canzoniero, L. M., Wang, X. Q., Heidinger, V., Ichinose, T., et al. (2001). Zinc induces a Src family kinase-mediated up-regulation of NMDA receptor activity and excitotoxicity. *Proc. Natl. Acad. Sci. U S A.* 98, 11055–11061. doi:10.1073/pnas.191353598

Marwick, K. F. M., Skehel, P. A., Hardingham, G. E., and Wyllie, D. J. A. (2019). The human NMDA receptor GluN2AN615K variant influences channel blocker potency. *Pharmacol. Res. Perspect.* 7, e00495. doi:10.1002/prp2.495

Mewasingh, L. D., Sékhara, T., Aeby, A., Christiaens, F. J., and Dan, B. (2003). Oral ketamine in paediatric non-convulsive status epilepticus. *Seizure* 12, 483–489. doi:10.1016/s1059-1311(03)00028-1

Monyer, H., Sprengel, R., Schoepfer, R., Herb, A., Higuchi, M., Lomeli, H., et al. (1992). Heteromeric NMDA receptors: molecular and functional distinction of subtypes. *Science* 256, 1217–1221. doi:10.1126/science.256.5060.1217

Myers, S. J., Yuan, H., Kang, J.-Q., Tan, F. C. K., Traynelis, S. F., and Low, C.-M. (2019). Distinct roles of GRIN2A and GRIN2B variants in neurological conditions. *F1000Res* 8, 19408. doi:10.12688/f1000research.18949.1

Ogden, K. K., Chen, W., Swanger, S. A., McDaniel, M. J., Fan, L. Z., Hu, C., et al. (2017). Molecular Mechanism of Disease-Associated Mutations in the Pre-M1 Helix of NMDA Receptors and Potential Rescue Pharmacology. *Plos Genet.* 13, e1006536. doi:10.1371/journal.pgen.1006536

Paoletti, P., Bellone, C., and Zhou, Q. (2013). NMDA receptor subunit diversity: impact on receptor properties, synaptic plasticity and disease. *Nat. Rev. Neurosci.* 14, 383–400. doi:10.1038/nrn3504

Pierson, T. M., Yuan, H., Marsh, E. D., Fuentes-Fajardo, K., Adams, D. R., Markello, T., et al. (2014). GRIN2A mutation and early-onset epileptic encephalopathy: personalized therapy with memantine. *Ann. Clin. Transl Neurol.* 1, 190–198. doi:10.1002/acn3.39

Platzer, K., Yuan, H., Schütz, H., Winschel, A., Chen, W., Hu, C., et al. (2017). GRIN2B encephalopathy: novel findings on phenotype, variant clustering, functional consequences and treatment aspects. *J. Med. Genet.* 54, 460–470. doi:10.1136/jmedgenet-2016-104509

Pribish, A., Wood, N., and Kalava, A. (2020). A review of nonanesthetic uses of ketamine. *Anesthesiol Res. Pract.* 2020, 5798285. doi:10.1155/2020/5798285

Scanlon, D. P., Bah, A., Krzeminski, M., Zhang, W., Leduc-Pessah, H. L., Dong, Y. N., et al. (2017). An evolutionary switch in ND2 enables Src kinase regulation of NMDA receptors. *Nat. Commun.* 8, 15220. doi:10.1038/ncomms15220

Song, X., Jensen, M. Ø., Jogini, V., Stein, R. A., Lee, C. H., Mchaourab, H. S., et al. (2018). Mechanism of NMDA receptor channel block by MK-801 and memantine. *Nature* 556, 515–519. doi:10.1038/s41586-018-0039-9

Srivastava, S., Cohen, J. S., Vernon, H., Barañano, K., McClellan, R., Jamal, L., et al. (2014). Clinical whole exome sequencing in child neurology practice. *Ann. Neurol.* 76, 473–483. doi:10.1002/ana.24251

Strehlow, V., Heyne, H. O., Vlaskamp, D. R. M., Marwick, K. F. M., Rudolf, G., de Bellescize, J., et al. (2019). GRIN2A-related disorders: genotype and functional consequence predict phenotype. *Brain* 142, 80–92. doi:10.1093/brain/awy304

Swanger, S. A., Chen, W., Wells, G., Burger, P. B., Tankovic, A., Bhattacharya, S., et al. (2016). Mechanistic Insight into NMDA Receptor Dysregulation by Rare Variants in the GluN2A and GluN2B Agonist Binding Domains. *Am. J. Hum. Genet.* 99, 1261–1280. doi:10.1016/j.ajhg.2016.10.002

Traynelis, S. F., Wollmuth, L. P., McBain, C. J., Menniti, F. S., Vance, K. M., Ogden, K. K., et al. (2010). Glutamate receptor ion channels: structure, regulation, and function. *Pharmacol. Rev.* 62, 405–496. doi:10.1124/pr.109.002451

Vieira, M., Yong, X. L. H., Roche, K. W., and Anggono, V. (2020). Regulation of NMDA glutamate receptor functions by the GluN2 subunits. *J. Neurochem.* 154, 121–143. doi:10.1111/jnc.14970

Wang, C., Liu, F., Patterson, T. A., Paule, M. G., and Slikker, W. (2017). Relationship between ketamine-induced developmental neurotoxicity and NMDA receptor-mediated calcium influx in neural stem cell-derived neurons. *Neurotoxicology* 60, 254–259. doi:10.1016/j.neuro.2016.04.015

Watanabe, M., Mishina, M., and Inoue, Y. (1994). Distinct spatiotemporal expressions of five NMDA receptor channel subunit mRNAs in the cerebellum. *J. Comp. Neurol.* 343, 513–519. doi:10.1002/cne.903430402

Xu, Y., Song, R., Chen, W., Strong, K., Shrey, D., Gedela, S., et al. (2021). Recurrent seizure-related GRIN1 variant: Molecular mechanism and targeted therapy. *Ann. Clin. Transl Neurol.* 8, 1480–1494. doi:10.1002/acn3.51406

Yang, Y., Muzny, D. M., Xia, F., Niu, Z., Person, R., Ding, Y., et al. (2014). Molecular findings among patients referred for clinical whole-exome sequencing. *JAMA* 312, 1870–1879. doi:10.1001/jama.2014.14601

Zeiler, F. A. (20152015). Early use of the NMDA receptor antagonist ketamine in refractory and superrefractory status epilepticus. *Crit. Care Res. Pract.* 2015, 831260. doi:10.1155/2015/831260

Zhang, Y., Ye, F., Zhang, T., Lv, S., Zhou, L., Du, D., et al. (2021). Structural basis of ketamine action on human NMDA receptors. *Nature* 596, 301–305. doi:10.1038/s41586-021-03769-9

Zhao, C., Du, C. P., Peng, Y., Xu, Z., Sun, C. C., Liu, Y., et al. (2015). The upregulation of NR2A-containing N-methyl-D-aspartate receptor function by tyrosine phosphorylation of postsynaptic density 95 via facilitating Src/proline-rich tyrosine kinase 2 activation. *Mol. Neurobiol.* 51, 500–511. doi:10.1007/s12035-014-8796-4

Conflict of Interest: The authors declare that the research was conducted in the absence of any commercial or financial relationships that could be construed as a potential conflict of interest.

Publisher's Note: All claims expressed in this article are solely those of the authors and do not necessarily represent those of their affiliated organizations, or those of the publisher, the editors and the reviewers. Any product that may be evaluated in this article, or claim that may be made by its manufacturer, is not guaranteed or endorsed by the publisher.

Copyright © 2021 Gale, Kosobucki, Hartnett-Scott and Aizenman. This is an open-access article distributed under the terms of the Creative Commons Attribution License (CC BY). The use, distribution or reproduction in other forums is permitted, provided the original author(s) and the copyright owner(s) are credited and that the original publication in this journal is cited, in accordance with accepted academic practice. No use, distribution or reproduction is permitted which does not comply with these terms.

frontiers
in Pharmacology

REVIEW
published: 10 November 2021
doi: 10.3389/fphar.2021.777607

Ion Channel Dysfunction and Neuroinflammation in Migraine and Depression

Emine Eren-Koçak[1,2] *and Turgay Dalkara*[1]*

[1]*Institute of Neurological Sciences and Psychiatry, Hacettepe University, Ankara, Turkey,* [2]*Department of Psychiatry, Medical Faculty, Hacettepe University, Ankara, Turkey*

Migraine and major depression are debilitating disorders with high lifetime prevalence rates. Interestingly these disorders are highly comorbid and show significant heritability, suggesting shared pathophysiological mechanisms. Non-homeostatic function of ion channels and neuroinflammation may be common mechanisms underlying both disorders: The excitation-inhibition balance of microcircuits and their modulation by monoaminergic systems, which depend on the expression and function of membrane located K^+, Na^+, and Ca^{+2} channels, have been reported to be disturbed in both depression and migraine. Ion channels and energy supply to synapses not only change excitability of neurons but can also mediate the induction and maintenance of inflammatory signaling implicated in the pathophysiology of both disorders. In this respect, Pannexin-1 and P2X7 large-pore ion channel receptors can induce inflammasome formation that triggers release of pro-inflammatory mediators from the cell. Here, the role of ion channels involved in the regulation of excitation-inhibition balance, synaptic energy homeostasis as well as inflammatory signaling in migraine and depression will be reviewed.

Keywords: ATP1A2, HCN, KCNQ, CACNA, TREK, Pannnexin-1, P2X7R, neuroinflammation

OPEN ACCESS

Edited by:
Jacques Joubert,
University of the Western Cape, South Africa

Reviewed by:
Yong Li,
Shanghai Jiao Tong University, China
Massimo Mantegazza,
UMR7275 Institut de Pharmacologie Moléculaire et Cellulaire (IPMC), France

***Correspondence:**
Turgay Dalkara
tdalkara@hacettepe.edu.tr

Specialty section:
This article was submitted to Pharmacology of Ion Channels and Channelopathies,
a section of the journal Frontiers in Pharmacology

Received: *15 September 2021*
Accepted: *22 October 2021*
Published: *10 November 2021*

Citation:
Eren-Koçak E and Dalkara T (2021) Ion Channel Dysfunction and Neuroinflammation in Migraine and Depression.
Front. Pharmacol. 12:777607.
doi: 10.3389/fphar.2021.777607

INTRODUCTION

Migraine and depression are comorbid diseases (Amiri et al., 2019; Karsan and Goadsby, 2021). Migraine is a risk factor for depression, whereas migraine attack prevalence and intensity increase during depression. Despite this well-established epidemiological data, the biological basis of this comorbidity is unclear. Emerging data from animal models and human imaging studies suggest that neuroinflammation could be a common pathway in the pathophysiology of both disorders (Mueller and Schwarz, 2007; Richards et al., 2018; Albrecht et al., 2019; Hadjikhani et al., 2020; Afridi and Suk, 2021). However, how neuroinflammatory signaling is initiated without an injury to the brain tissue is unknown. A non-homeostatic synaptic transmission has been suggested as an initiator of neuroinflammatory signaling (Dalkara and Kilic, 2013; Kilic et al., 2018; Afridi and Suk, 2021; Petit et al., 2021). In this regard, some ion channels and activation of cellular stress sensors such as pannexin1 (Panx1) and P2X7 channels and the downstream inflammatory cascade may play a role. Here, we review the recent evidence suggesting that a non-homeostatic ion channel activity or a mismatch between synaptic energy supply and glutamatergic transmission can activate the inflammatory pathway in migraine and depression. Since we limit the scope of the review to these potentially common central mechanisms in both disorders, we will not be able to cover recent developments regarding

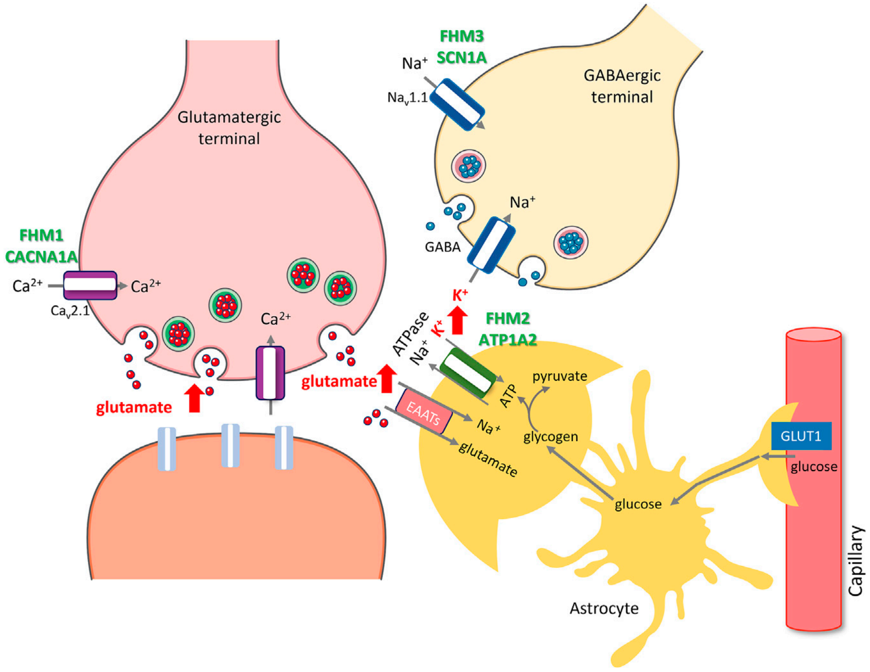

FIGURE 1 | Rises in extracellular glutamate and K+ caused by ion channel and transporter mutations or transcriptional changes induced by migraine triggers create susceptibility to migraine with aura. Facilitation of excitatory synaptic transmission by either promoting glutamate release (red arrows) due to gain of function mutations in P/Q type presynaptic calcium channels (purple) encoded by CACNA1A in FHM1 or decreasing its uptake along with K+ (red arrow) due to mutations in alpha2 subunit of Na+/K + ATPase (green) encoded by ATP1A2 in FHM2, increases susceptibility to CSD and migraine with aura. Glutamate released during synaptic activity is taken up to astrocyte processes (amber) by excitatory amino acid transporters (pink, EAATs), which is driven by the Na + gradient created by Na+/K + ATPase, hence, glutamate and K+ uptakes are coupled. Excess K+ released from overactive GABAergic terminals (red arrow) due to gain of function mutations in Na$_V$ 1.1 type sodium channels (blue) encoded by SCN1A in FHM3 also creates susceptibility to CSD and migraine with aura. Glycogen granules in peri-synaptic astrocyte processes instantly provide glycosyl units to meet the rapidly escalating energy demand during excitatory synaptic transmission (e.g., by Na+/K + ATPase), whereas glucose transported from circulation to astrocytes via GLUT1 is primarily used in replenishing glycogen. Insufficient glycogen breakdown due to transcriptional changes induced by migraine triggers such as sleep deprivation, which promote glycogen synthesis while reducing glycogen breakdown, hinders glutamate and K+ uptake as seen in FHM2, creating susceptibility to CSD and migraine in non-familial common migraine. The illustration is prepared by Dr. Zeynep Kaya. Cellular templates are copied from Servier Medical Art (smart.servier.com).

the success of CGRP antagonists as novel anti-migraine drugs and their implications for peripheral nociceptive mechanisms of migraine headache.

Lessons Learned From Familial Migraine Mutations

Most of our knowledge about the potential role of ion channels and glutamate in migraine comes from the discovery of mutant genes causing familial hemiplegic migraine (FHM) (Moskowitz et al., 2004; Russell and Ducros, 2011; Pietrobon and Moskowitz, 2014; Dalkara and Moskowitz, 2017; De Boer et al., 2019; Pietrobon and Brennan, 2019). FHM patients suffer from typical migraine with aura episodes along with transient hemiplegic or hemiparetic attacks (Russell and Ducros, 2011). Some patients may also experience confusion, memory loss, seizures and coma episodes and, rarely, persistent deficits like ataxia. However, these severe phenotypes are typical of FHM1 and 2 but not of FHM3 (Mantegazza, 2018) and, other than episodic attacks, majority of FHM 1 and 2 patients are healthy except being more sensitive to head trauma. Hemiplegic attacks and an autosomal dominant inheritance pattern distinguish them from non-familial, common forms of migraine (Sutherland H. G. et al., 2019). Although they are rare and the mutations have yet been detected in less than half of the cases (Sutherland et al., 2020), the three genes identified so far have provided insight into how a migraine attack can be initiated in an otherwise healthy brain (Moskowitz et al., 2004; Pietrobon and Brennan, 2019). Mutations in *CACNA1A, ATP1A2,* and *SCN1A* genes, which encode a P/Q-type voltage-gated calcium channel (Ca$_V$2.1), an astrocytic Na/K pump (α2 Na/K-ATPase) and the α1 subunit of voltage-gated Na$_V$1.1 sodium channel, account for FHM1, FHM2 and FHM3, respectively (**Figure 1**). Of these, *CACNA1A, ATP1A2* mutations have been comprehensively studied with regard to their effects on cortical excitability (for review, (Pietrobon and Brennan, 2019). *In vitro* and *in vivo* evidence suggests that *CACNA1A* mutations can lead to enhanced glutamate release during excitatory synaptic activity because gain-of-function mutations on the pore-forming α1-subunit of the presynaptic P/Q type calcium channels enable them to open at more hyperpolarized membrane potentials than normal, allowing more calcium influx to the terminal during action potential trains (Tottene et al., 2009). Interestingly, the P/Q type calcium channels on terminals of GABAergic neurons are not affected by these mutations (Vecchia et al., 2014). This causes a shift in cortical excitation/inhibition balance towards excitation (Vecchia and Pietrobon, 2012; Tottene et al., 2019), which is thought to account for the vulnerability to cortical spreading depolarization (CSD), the putative cause of migraine aura and, for the hyperexcitability seen in FHM1 brain (Takizawa et al., 2020a). Given the presence of glutamatergic synapses driving the feed-forward and feed-back inhibitory neurons, one may expect an increased inhibitory control as well. However, this is probably not the case owing to the fact that short-term depression develops faster in these glutamatergic synapses than does in glutamatergic synapses terminating on principal neurons (Tottene et al., 2019). Although the net effect of the excitation/inhibition balance might be different in various neuronal circuits depending on the organization of neuronal interconnections and release kinetics of synapses, including pain-transmitting/processing networks, it has been clearly shown that the CSD threshold is decreased in transgenic knock-in mice harboring human *CACNA1A* mutations (Van Den Maagdenberg et al., 2004). In fact, the threshold was found to be even lower in *S218L* compared to *R192Q* knock-in mouse in parallel with the clinical severity of FHM symptoms in patients carrying these mutations (Van Den Maagdenberg et al., 2010). However, some FHM1 and FHM2 patients also suffer from epileptic seizures suggesting that excitation/inhibition imbalance has also potential to generate epileptic discharges (Marconi et al., 2003; Lebas et al., 2008; Costa et al., 2014).

Cortical spreading depolarization is considered the electrophysiological correlate of migraine aura (Takizawa et al., 2020a). First discovered by Leao in 1944 on the rabbit brain, it is caused by intense depolarization of neurons and astrocytes, propagating along the cortical gray matter at a speed of 2–6 mm per minute (Leao, 1944). As it spreads, it depresses the ongoing electrical activity (e.g., the EEG as originally observed), hence, named spreading depression by Leao. However, cortical spreading depolarization is increasingly used instead of cortical spreading depression because of the confusion the term "depression" causes. Leao was the first to note the similarity between the propagation rate of visual aura in migraine and CSD (Leao, 1947). However, it only became possible to show the presence of CSD in migraineur brain in the past 4 decades with advances in imaging technologies that enabled detection of the CSD-induced cerebral blood flow changes (Olesen et al., 1982; Cao et al., 1999; Hadjikhani et al., 2001).

High extracellular levels of glutamate and K^+ are thought to be responsible for ignition and propagation of CSD (Pietrobon and Moskowitz, 2014). Rising extracellular glutamate levels along with K^+ concentration exceeding 15 mM appear to be necessary for synchronized depolarization of an aggregate of neurons involving, at least partly, the NR2 type NMDA receptors (Tang et al., 2014; Takizawa et al., 2020a; Bu et al., 2020). During CSD, K^+ levels further rise to 30–60 mM, which contribute to spread of the depolarizing wave to neighboring gray matter (Pietrobon and Moskowitz, 2014). Accordingly, application of glutamate, NMDA or high K^+ to the cortex all ignites CSD. Therefore, increased glutamate release in FHM1 knock-in mice is consistent with the enhanced susceptibility to CSD (Pietrobon and Brennan, 2019). Indeed, foci of glutamate "plumes" spontaneously bursting in the cortex of awake *ATP1A2* knock-in mice, a model of FHM2, have recently been demonstrated by expressing a fluorescent glutamate reporter in the cortex (Parker et al., 2021). The same study also showed that a surge of glutamate plumes preceded the onset of CSD as hypothesized before.

Astrocytic Na/K pump (α2 Na/K-ATPase) clears K^+ spilling out of the synaptic cleft during synaptic activity (Cholet et al., 2002). The transmembrane Na^+ gradient it creates as it takes up K^+ is essential for uptake of glutamate by astrocyte processes around excitatory synapses (Cholet et al., 2001; Petit et al., 2021). Accordingly, ATP1A2 hypofunction caused by FHM2 mutations leads to reduced K^+ and glutamate uptake as demonstrated both *in vitro* and in knock-in mice, *in vivo* (Capuani et al., 2016; Parker et al., 2021). As with *CACNA1A* mutations, GABA release is not affected in FHM2 because α2 Na/K-ATPase is not appreciably expressed on astrocyte processes around GABAergic terminals (Cholet et al., 2002; Capuani et al., 2016). Consistent with these findings, FHM2 knock-in mice have a low CSD induction threshold and spontaneously generate the glutamate plums mentioned above (Leo et al., 2011; Parker et al., 2021).

Although the pathophysiological phenotype for FHM1 and FHM2 converge on the glutamatergic synapse, this is not the case for *SCN1A* gene mutations underlying FHM3 (Desroches et al., 2019; Chever et al., 2021; Lemaire et al., 2021). *SCN1A* encodes the α1 subunit of the neuronal voltage-gated sodium channel Nav1.1, which contributes to the action potential firing on primarily GABAergic interneurons. Indeed, hundreds of loss-of-function *SCN1A* mutations have been reported in various epileptic syndromes caused by reduced GABAergic inhibition (Hedrich et al., 2014; Sutherland HG. et al., 2019; Mantegazza et al., 2021). In FHM3, however, mutations are gain-of-function, causing increased firing of GABAergic interneurons. Increased GABAergic activity may sound at odds with CSD generation but recent studies have shed light on the mechanism of CSD initiation by documenting that hyperactive GABAergic interneurons discharging at high frequencies can cause significant elevations in extracellular K^+ (over 12 mM), hence, increase CSD susceptibility as discussed above (Desroches et al., 2019; Chever et al., 2021; Lemaire et al., 2021). Supporting this view, knock-in mice bearing *L263V* or *L1649Q* human mutation exhibit a low CSD induction threshold (Jansen et al., 2020; Auffenberg et al., 2021) as well as spontaneous CSDs (Jansen et al., 2020) and hyperexcitable GABAergic neurons (Auffenberg et al., 2021).

Another gain of function change in glutamatergic transmission secondary to impairment of frequency-dependent presynaptic adaptation has been reported for mutations in casein kinase 1 delta, which cause a non-hemiplegic form of familial migraine along with disrupted sleep phases (Brennan et al., 2013). Knock-in mice harboring this mutation have also a reduced CSD induction threshold (Suryavanshi et al., 2019). Knock-in mouse models have been instrumental to study various aspects of migraine although they basically model familial migraines. In addition to enhanced susceptibility to CSD, these mice also exhibit heightened sensory perceptions such as hypersensitivity to light, consistent with sensory abnormalities reported by patients (Russell and Ducros, 2011; Chanda et al., 2013; Brennan and Pietrobon, 2018). They also seem to suffer from headaches and periorbital allodynia (Langford et al., 2010; Chanda et al., 2013). Mutations associated with severe clinical phenotypes additionally lead to spontaneous seizures or ataxia in FHM 1 and 2 knock-in mice (Van Den Maagdenberg et al., 2010; Kros et al., 2018).

Non-Familial Common Migraine

The mutations detected in familial migraine are usually not found in non-familial common migraine cases although migraine has been established to have a complex polygenic genetic heritability estimated to be as high as 60% (Sutherland H. G. et al., 2019). Meta analysis of several GWAS studies encompassing 59,674 patients and 316,078 controls reveled 44 susceptibility loci (Gormley et al., 2016). Most of them are associated with vascular and neuronal function, ion channels and circadian rhythm (Sutherland H. G. et al., 2019). Three of them are near ion channels (TRPM8 and KCNK5) or an ion transporter (sodium/potassium/calcium exchanger3 SLC24A3). TRPM8 is expressed on type C- and A-delta nociceptors and is activated by cold temperatures (Dussor and Cao, 2016). Although migraine is generally initiated by intrinsic brain mechanisms, it can also be triggered by some volatile irritants such as umbellulone emanating from the leaves of headache tree (*umbellularia californica*), which is thought to cause headache by stimulating TRPA1 channels on meningeal nociceptors (Edelmayer et al., 2012). KCNK5 belongs to the superfamily of potassium channel proteins containing two pore-forming P domains as does KCNK18 (Reyes et al., 1998). Although the neuronal function of KCNK5 is unclear, TRESK potassium channels encoded by *KCNK18* regulates neuronal excitability in the dorsal root and trigeminal ganglia (Enyedi and Czirjak, 2015). Supporting a role for two-pore-domain potassium channels in migraine, *KCNK18* mutations cause non-hemiplegic familial migraine with aura. F139Wfsx24 *KCNK18* frame-shift mutation has been shown to result in hyperexcitability of cultured trigeminal ganglion neurons as well as allodynia in rodent migraine models (isosorbide dinitrate injection) by a negative dominant effect on TREK1 and 2, two other two-pore-domain potassium channels with which TRESK channels form functional heterodimers (Liu et al., 2013; Royal et al., 2019). Suggesting a suppressive role of TRESK over trigeminal ganglia excitability, KCNK18 knockout mice reportedly exhibit mechanical and thermal hyperalgesia in response to systemic glyceryl trinitrate treatment (a migraine model) (Pettingill et al., 2019) and exaggerated nocifensive behaviors in response to dural application of inflammatory soup (Guo et al., 2019). Of note, these families with KCNK18 mutations exhibit migraine with aura, suggesting that reduced control over neuronal hyperexcitability due to hypofunction of TRESK channels in cortical neurons may also create susceptibility to CSD.

Initiation of Inflammatory Signaling That Causes Headache

CSD has been shown to activate neuronal pannexin1 channels and initiate the downstream inflammatory signaling following formation of the inflammasome complex (Karatas et al., 2013; Ghaemi et al., 2016; Takizawa et al., 2016; Chen et al., 2017; Eising et al., 2017; Ghaemi et al., 2018; Bu et al., 2020; Takizawa et al., 2020b). Inflammasome formation causes release of pro-inflammatory mediators such IL1-ß and HMGB1 from neurons, which triggers translocation of inflammatory transcription factor NF-kappaB to the nucleus in astrocytes (Karatas et al., 2013; Takizawa et al., 2016; Dehghani et al., 2021). NF-kappaB induces hundreds of transcripts including tens of inflammatory mediators such as iNOS, COX2, and cytokines (https://www.bu.edu/nf-kb/gene-resources/target-genes/). This is thought to cause release of prostanoids, NO, cytokines and other algesic mediators to CSF and, hence, to activate meningeal nociceptors and inflammatory cells, culminating in a sterile meningeal inflammation that can sustain migraine headache for hours to days (Karatas et al., 2013; Erdener and Dalkara, 2014; Dalkara and Moskowitz, 2017). With a single CSD, microglia do not switch to a pro-inflammatory state, which is only seen a few days after exposure to multiple CSDs (Takizawa et al., 2017), suggesting that aura (CSD)-triggered parenchymal inflammatory signaling is mainly mediated by astrocytes, whereas microglia may take part in inflammatory signaling in patients suffering from frequent migraine with aura attacks. Supporting this formulation, a recent PET/MRI study using a sensitive inflammatory tracer (^{11}C-PBR28) taken up by active glia, has documented the presence of parenchymal as well as meningeal inflammatory signaling in 13 patients suffering from repeated migraine with aura attacks in the past month (Albrecht et al., 2019; Hadjikhani et al., 2020).

Interestingly, in the absence CSD, it has been shown that parenchymal inflammatory signaling pathway can be initiated via activation of neuronal Panx1 channels, this time, by migraine triggers such as sleep deprivation (Kilic et al., 2018). Sleep deprivation induces transcriptional changes favoring glycogen synthesis over its breakdown (Petit and Magistretti, 2016; Petit et al., 2021). Insufficient glycogen breakdown within astrocyte processes around glutamatergic terminals can lead to Panx1 channel activation due to inadequate glutamate and K^+ clearance. This is because glycogen-derived ATP is preferentially used for glutamate and K^+ uptake even in the presence of sufficient glucose owing to more favorable kinetics of the enzymes involved in metabolizing the glycosyl units liberated from glycogen over glucose, whereas glucose is quickly metabolized to replenish glycogen (Petit et al., 2021). Thus, extracellular glutamate and K^+ accumulation during intense glutamatergic synaptic activity create a favorable extracellular milieu, first, for activation of Panx1 channels, and then, for CSD ignition upon further rise in extracellular glutamate

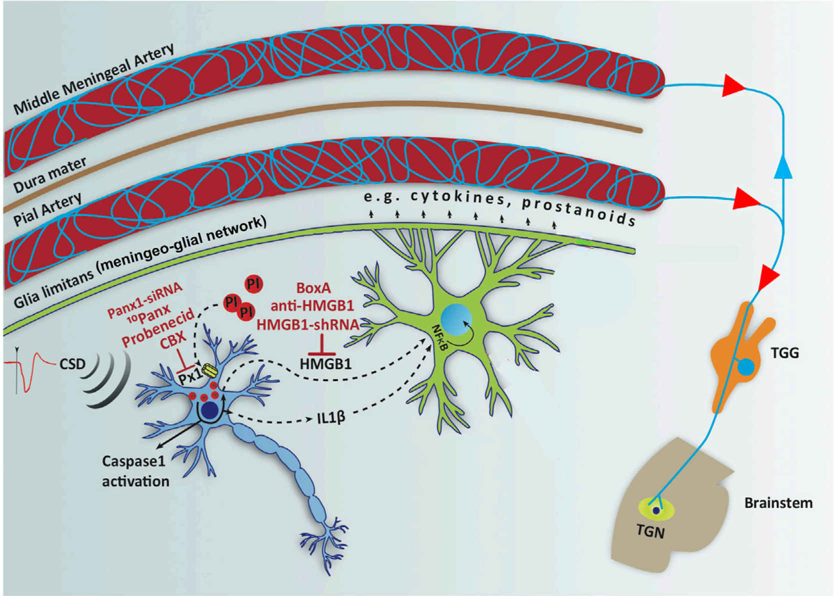

FIGURE 2 | Opening neuronal Panx1 channels after CSD initiates a neuroinflammatory signaling cascade, characterized by inflammasome formation and caspase-1 activation in neurons followed by release of HMGB1 and IL-1β, which trigger NF-κB nuclear translocation in astrocytes. Red labels show agents used to inhibit each step in the inflammatory cascade and red circles represent propidium iodide (PI) influx through open Panx1 (Px1) large-pore channels. NF-κB induces transcription of several pro-inflammatory genes including cytokines and prostanoids, which are thought to be released to CSF through glia limitans and meningeo-glial network and activate the nociceptive nerves around pial and dural vessels, causing headache. Modified from Karatas et al., 2013 with permission.

and K^+ (Kilic et al., 2018; Petit et al., 2021). This proposed mechanism could explain why migraine with and without aura attacks exist in the same person and how CSD can emerge in the absence of monogenic mutations but with transcriptional changes triggering the same mechanisms in non-familial migraine.

Master Switch of Inflammatory Signaling: Pannexin Channels

Pannexins are large-pore membrane channels similar to connexins but, unlike connexins, they do not form gap junctions (Macvicar and Thompson, 2010). Panx1 and Panx2 are widely expressed in the central nervous system on all main cell types (Yeung et al., 2020). *In vitro* studies have disclosed that Panx1 can open in three different states; a low conductance Cl-selective opening at positive membrane potentials (*in vivo* function unknown); large conductance, non-selective opening allowing calcium, ATP and molecules up to 900 Dalton to pass through; and a persistent opening due to caspase-mediated cleavage of the C-terminal domain, leading to cell death (Dahl, 2018). Panx1 channels can be physiologically activated in large-pore state by increases in extracellular K^+, glutamate and intracellular Ca^{2+} concentration, NMDA and P2X7 receptor stimulation, swelling (membrane stretch), c-Jun N-terminal kinases and Src family of tyrosine kinases (Whyte-Fagundes and Zoidl, 2018). Most of the Panx1 activating conditions are present during CSD as well as when glycogen breakdown, hence, K^+ and glutamate uptake is reduced as discussed above (Karatas et al., 2013; Kilic et al., 2018; Petit et al., 2021). Opening of neuronal Panx 1 channels can be monitored *in vivo* and *in vitro* by using membrane-impermeant fluorescent dyes like propidium iodide or YoPro-1 (Macvicar and Thompson, 2010), which flux into cells through Panx 1 channels opened in large conductance state (Karatas et al., 2013; Bu et al., 2020) (**Figure 2**). CSD-induced dye uptake to neurons was suppressed with several Panx1 inhibitors such as carbenoxolone, probenecid, ^{10}Panx peptide and inhibition of Panx1 expression by siRNA, supporting the view that the dye fluxed in neurons through Panx1 channels (Karatas et al., 2013; Bu et al., 2020). Large pore opening of P2X7 receptors can also mediate the dye influx (Bhaskaracharya et al., 2014). However, recent transcriptomics studies consistently show that P2X7 receptors are not expressed in adult neurons unlike macrophages where they are closely coupled with Panx1 channels (Illes et al., 2017; Kaczmarek-Hajek et al., 2018). Further supporting opening of Panx1 channels with CSD or insufficient glycogen breakdown, formation of the inflammasome complex and activation of caspase-1 along with HMGB1 release have also been demonstrated (Karatas et al., 2013; Takizawa et al., 2016; Kilic et al., 2018). These advances open the exciting possibility of developing Panx1 inhibitors as migraine prophylactic drugs; especially considering some Panx1 inhibitors such as carbenoxolone, probenecid and mefloquine are already clinically registered medicines (Yeung et al., 2020). Similarly, agents acting on downstream steps in the inflammatory cascade including inhibitors of inflammasome, caspase-1 or interleukins may be promising drug targets for migraine treatment. Successes of anakinra in relieving severe migraine headaches seen in cyropyrin-associated periodic syndromes characterized by IL1-ß over production due to inflammasome mutations (Parker et al., 2016) and, the relief obtained by NSAIDs in treating common migraine headaches support this view.

ION CHANNEL DYSFUNCTIONS IN STRESS AND DEPRESSION

As proposed for migraine, changes in the excitation/inhibition (E: I) balance resulting in increased excitability have also been implicated in major depression (Fee et al., 2017). Ion channels are important regulators of excitability, network activity as well as plasticity. Changes in ion channel attributes alter GABAergic and glutamatergic neuron excitability and firing, hence, modify the E: I balance in microcircuits. A recent transcriptomic analysis revealed that out of 1,153 differentially expressed genes (DEGs) in the hippocampi of chronically stressed rats, a rodent model of depression; 46 DEGs were related to potassium channels, calcium channels, sodium channels, and chloride channels on plasma membrane (Ren et al., 2021). This finding supports the hypothesis that changes in the expression or function of ion channels may disrupt the E: I balance throughout the brain regions relevant for depression, and contribute to the development of depression. Indeed, a recent paper reported that global inactivation of $\gamma 2$ subunit gene of GABA-A receptors on somatostatin interneurons (SST-IN) disinhibited effects of SST-IN on pyramidal cells, resulting in an anxiolytic and antidepressant phenotype (Fuchs et al., 2017). On the other hand, ionotropic P2X7 receptors can additionally trigger formation of the inflammasome complex, activating interleukin-1ß and downstream inflammatory signaling, as do Panx1 channels. Indeed, several lines of evidence implicate the involvement of P2X7 receptors and inflammatory signaling, including inflammasome formation in the pathophysiology of stress and depression (Dowlati et al., 2010; Iwata et al., 2016; Wohleb et al., 2016; Yue et al., 2017). Accordingly, in the second part of the article, we will review the potential roles of purinergic P2X7 receptors along with hyperpolarization-activated cyclic nucleotide-gated (HCN) channels, M-type K^+ (KCNQ) channels, TWIK-related K^+ channels (TREK) and Ca^{+2} channels in the pathophysiology of depression, dysfunction of which are also implicated in migraine.

P2X7 Receptor

The purinergic P2X7 receptor (P2X7R) is a ligand gated ion channel activated by binding of adenosine triphosphate (ATP) (Khakh and North, 2006). ATP is released from the presynaptic terminal as a co-transmitter as well as from astrocytes (Bezzi and Volterra, 2001; Burnstock, 2007). Its release is increased in response to physical stressors and cellular injury as part of an adaptive response. Psychological stressors like acute restraint stress, in which restriction of the movement of animals leads to stress, also have been shown to increase extracellular ATP concentrations in rat hippocampus and prefrontal cortex (PFC) (Iwata et al., 2016), which then can activate low affinity P2X7R (Donnelly-Roberts et al., 2009). Mice susceptible to chronic social defeat stress (CSDS), on the other hand, displayed lower ATP concentrations in hippocampus and PFC (Cao et al., 2013). In line with the latter finding, intracerebroventircular administration of ATP or its nonhydrolyzable analog, ATP-γ-S, for 7-days or 28-days reverses social avoidance caused by CSDS and anhedonia caused by chronic unpredictable mild stress (CUMS) (Cao et al., 2013) (**Table 1**). Inhibition of ATP release selectively from astrocytes by genetic knockout of inositol 1,4,5-trisphosphate (IP3) receptor type 2 (*IP3R2*$^{-/-}$) lead to increased behavioral despair and anhedonia (Cao et al., 2013) (**Table 1**). These findings suggest that increased ATP release from astrocytes in the hippocampus and PFC in response to stressors is an important mediator in developing adaptive responses to stress.

However, the story is more complex: Intra-PFC, but not intrahippocampal injections of ATP or ATP-γ-S reversed the depression-like behavior (Cao et al., 2013); whereas chronic (3weeks) intrahippocampal injections of ATP or BzATP, a P2XR agonist, induced depression-like behavior to a similar extent as chronic unpredictable stress (CUS) (**Table 1**). Long-term blockade of P2X7R for 3–4 weeks by systemic (intraperitoneal, i.p.) or intrahippocampal injections of selective P2XR7 antagonists Brilliant Blue G (BBG), A438079, A-804598, reversed depressogenic behavior, specifically behavioral despair, anhedonia and anxiety-like behavior caused by CUMS in rats (Iwata et al., 2016; Yue et al., 2017) (**Table 1**). Subacute (1 week) but not acute systemic treatment of mice with BBG also caused a reduction in behavioral despair (Csolle et al., 2013a) (**Table 1**). Further complicating understanding the role of P2X7R in depression, preinfusions of a non-selective P2XR antagonist, pyridoxal phosphate-6-azophenyl-2′-4′-disulphonic acid, and P2X2R shRNA into the mPFC blocked the antidepressant-like effect of ATP (Cao et al., 2013) (**Table 1**). These findings altogether suggest that; 1) ATP and P2XR signaling exhibit an inverted U-shaped relationship in mood regulation; i.e., both very low and very high doses of ATP and P2XR signaling are involved in the development of depression-like behavior whereas moderate doses are necessary to maintain euthymia (**Figure 3**); 2) effects of ATP and P2XR signaling are region-specific.

Genetic tools, in which control of the "dose effect" is far limited compared to pharmacological approaches, have confirmed the important role of P2XR signaling in the pathophysiology of depression but the net consequnce of their effect was also model-dependent. Studies using *P2RX7*$^{-/-}$ KO mice reported a decrease in behavioral despair, i.e. an antidepressant effect (Basso et al., 2009; Csolle et al., 2013a; Csolle et al., 2013b) (**Table 1**). In human genetic studies, polymorphisms of *P2RX7* the gene encoding P2X7R has been reported to be associated with increased risk/severity of mood disorders (Lucae et al., 2006; Mcquillin et al., 2009; Halmai et al., 2013; Vereczkei et al., 2019). As a more precise model of the human condition, a humanized transgenic mouse line was generated in which exon 2–13 of murine P2X7R was substituted by either human wild-type (WT) *hP2X7R* or *hP2X7R-Gln460Arg* variant. Intriguingly, the ion channel function of *hP2X7R-Gln460Arg* variant was not different than

TABLE 1 | Behavioral effects of interventions to P2X7R expression and functions.

Genetic interventions	Species	Results	References
P2RX7$^{-/-}$	C57BL/6 mice	Decreased immobility time in TST and FST.Reduced anhedonia in SPT after stimulation with a bacterial endotoxin, lipopolysaccharide	Basso et al., (2009), Csolle et al. (2013a), Csolle et al. (2013b)
hP2X7R/hP2RX7-Gln460Arg homozygotes and heterozygotes	C57BL/6 mice	Basal levels of depressive-like behavior were unaltered. CSDS induced increased social avoidance, decreased time spent in open arms in EPM in all genotypes studied.	Metzger et al. (2017)
hP2RX7-WT-hP2RX7-Gln460Arg heterozygotes	C57BL/6 mice	Decreased slow wave activity&NREM sleep duration and increased number of REM sleep bouts	Metzger et al. (2017)
IP3R2$^{-/-}$	C57BL/6 mice	Selective inhibition of astrocytic ATP release lead to increased behavioral despair and anhedonia	Cao et al. (2013)
P2X7R AGONISTS			
ATP/ATP-γ-S (icv)	C57BL/6J mice	Reversed social avoidance caused by CSDS and anhedonia caused by CUMS	Cao et al. (2013)
ATP/ATP-γ-S (intra mPFC)		Reversed the increase in immobility time in FST	
ATP/BzATP (intrahippocampal, 3 weeks)	SD rats	Increased immobility time in FST	Yue et al. (2017)
P2X7R ANTAGONISTS			
BBG/A438079 (3 weeks, intrahippocampal, with CUS)	SD rats	Reversed increased immobility caused by CUS	Yue et al. (2017)
A-804598 (4 weeks, ip with CUS)	SD rats	Reversed CUS-induced deficits in SPT, NSFT and EPM	Iwata et al. (2016)
Brilliant Blue G (1 week, ip)	C57BL/6 mice	Decreased immobility time in TST	Csölle et al. (2013a)
PPADS into mPFC	C57BL/6 mice	Blocked the antidepressant-like effect of ATP on immobility time in FST	Cao et al. (2013)

ATP, adenosine triphosphate; CSDS, chronic social defeat stress; CUMS, chronic unpredictable mild stress; CUS, chronic unpredictable stress; EPM, elevated plus maze; FST, forced swim test; icv, intracerebroventricular; IP3R2, *inositol 1,4,5- trisphosphate receptor type 2; ip, intraperitoneal; mPFC, medial prefrontal cortex; NSFT, novelty suppressed feeding test; SD, Sprague-Dawley; SPT, sucrose preference test; TST, tail suspension test.*

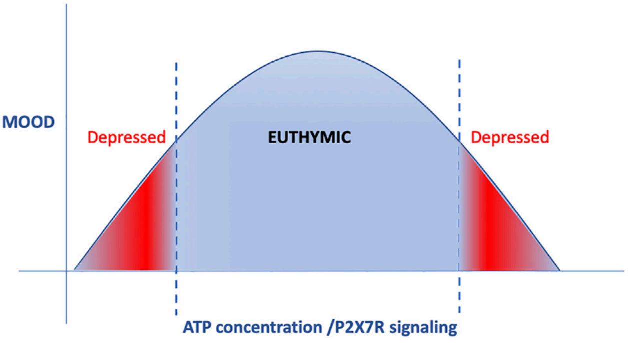

FIGURE 3 | ATP and P2XR signaling displays a reverse U-curve. Both very low and very high doses of ATP and P2XR signaling are involved in the development of depression-like behavior, whereas moderate doses are necessary to maintain euthymic mood.

that of the WT, but it was impaired when *hP2X7R-Gln460Arg* variant was co-expressed with WT P2X7R (Aprile-Garcia et al., 2016). Contrary to *P2x7R* KO mice, mice homozygous or heterozygous for *hP2X7R-Gln460Arg* allele displayed no change in depression-like behavior at basal conditions, but they showed increased depression- and anxiety-like behavior following social defeat stress (Metzger et al., 2017) (**Table 1**). These findings indicate that *P2X7R* polymorphism creates vulnerability to stress and depression and supports the involvement of gene X environment interactions in the development of mood disorders. Interestingly sleep quality was disturbed in heterozygous mice (*WT hP2X7R/hP2X7R-Gln460Arg*), but not in homozygous mice (*hP2X7R-Gln460Arg/hP2X7R-Gln460Arg*) (Metzger et al., 2017). Specifically, slow wave activity and NREM sleep duration were reduced and the number of REM sleep bouts was increased in heterozygous mice (Metzger et al., 2017) (**Table 1**), which is similar to sleep disturbances seen in depressive patients (Nutt et al., 2008). These findings have led to a randomized, placebo-controlled, double blinded clinical trial in order to evaluate the antidepressant efficacy of P2X7R antagonists in the treatment of major depression (ClinicalTrials.gov Identifier: NCT04116606).

Potential Mechanisms Underlying P2X7R's Effects on Mood Regulation

P2X7R mediates several physiological neural functions, disturbances of which may be involved in the pathophysiology of depression:

1. P2X7R increases the release of neurotransmitters noradrenaline (NA), serotonin (5-HT), glutamate and GABA (Sperlagh et al., 2002; Papp et al., 2004; Alloisio et al., 2008; Marcoli et al., 2008; Goloncser et al., 2017). These neurotransmitters long implicated in the pathophysiology of depression also modulate astrocytic ATP release by altering intracellular Ca^{+2} levels (Hirschfeld, 2000; Arcuino et al., 2002;

Luscher et al., 2011; Marpegan et al., 2011; Duman et al., 2019; Fogaca and Duman, 2019). Indeed, selective inhibition of ATP release from astrocytes by genetic knockout of IP3R2 mediating intra-astrocytic Ca^{+2} rise induces depression-like behavior (Cao et al., 2013), which may be related with the resulting dysregulation of the release of neurotransmitters.

2. P2X7R regulates synaptic plasticity. Chronic stress has been reported to decrease synaptic plasticity, which is thought to be involved in depression-like phenotype by limiting adaptive responses. In $P2RX7^{-/-}$ KO mice, whole genome microarray analysis disclosed changes in expression of genes involved in synaptic plasticity (Csolle et al., 2013a). P2X7R ligand ATP has been shown to alter synaptic plasticity by several mechanisms, including glutamate release and regulation of NMDA receptor expression and function (Pankratov et al., 2002; Sperlagh et al., 2002; Csolle et al., 2013b; Guo et al., 2015; Otrokocsi et al., 2017). ATP and BzATP application evoked glutamate efflux in hippocampal slices obtained from WT mice, which was abolished in hippocampal slices of $P2RX7^{-/-}$ mice (Sperlagh et al., 2002; Csolle et al., 2013b). There is an ongoing debate on the presence of P2X7R in adult neurons (Illes et al., 2017; Miras-Portugal et al., 2017). P2X7R was proposed to modulate presynaptic release of glutamate, however, recent transcriptomic studies report that neurons isolated from adult rodents do not express P2X7R unlike the *in vitro* preparations prepared from young or embryonic animals (Illes et al., 2017; Kaczmarek-Hajek et al., 2018). Therefore, the glutamate efflux induced by ATP and P2X7R agonists in adult animals can also be attributed to the astrocytic release (Parpura et al., 1994; Savtchouk and Volterra, 2018). The basal and stress-induced expression of the NR2B subunit of NMDA receptor was found to be upregulated in $P2RX7^{-/-}$ mice both *in vitro* and *in vivo* (Csolle et al., 2013b; Otrokocsi et al., 2017), possibly as a compensatory response to decreased glutamate release. As P2X7R ion channel has considerable Ca^{+2} permeability, when expressed at the synapse, P2X7R can modulate synaptic plasticity. Indeed, in hippocampal slices prepared from 3-week old rats, ATP blocked induction of long-term potentiation (LTP) with low frequency stimulation at the CA3-CA1 synapse by inhibiting NMDA-mediated currents through Ca^{+2}-dependent inactivation of NMDA receptors. At higher frequencies of stimulation, owing to desensitization of P2X receptors, ATP loses its inhibitory effect on LTP (Pankratov et al., 2002). In accordance with these observations inhibition or desensitization of P2XR with pyridoxal phosphate-6-azophenyl-2′-4′-disulphonic acid or nonhydrolyzable ATP analog α,β-methylene ATP facilitated LTP at the CA3-CA1 synapse (Pankratov et al., 2002).

3. P2X7R can induce neuroinflammation. Binding of ATP to P2X7R trigger NLRP3 inflammasome cascade resulting in the activation of caspase-1, which converts pro-IL-1ß and pro-IL-18 to their active forms: IL-1ß and IL18 (Guo et al., 2015). As mentioned above, psychological stressors increase extracellular ATP levels, which reportedly lead to activation of caspase-1 and IL-1ß release by binding to P2X7R on microglia (Iwata et al., 2016; Yue et al., 2017). This may be related to the increased peripheral levels of cytokines, acute phase proteins and chemokines detected in depressed patients (Levine et al., 1999; Lanquillon et al., 2000; Alesci et al., 2005; Pace et al., 2006; Dowlati et al., 2010; Milenkovic et al., 2019). Indeed, increased microglial activity in the prefrontal cortex, anterior cingulate cortex and insula of major depression patients was visualized by positron emission tomography (Setiawan et al., 2015).

The role of microglia in sculpturing synapses is well documented. Microglial processes in close contact with dendritic spines can function in both the elimination and formation of spines, suggesting that they play important roles in synaptic plasticity (Paolicelli et al., 2011; Zhan et al., 2014; Miyamoto et al., 2016; Weinhard et al., 2018; Cangalaya et al., 2020). Stress is known to cause a decrease in dendritic length and branching in apical dendrites of layer II/III and layer V pyramidal neurons of the medial prefrontal cortex as well as apical dendrites of CA3 pyramidal neurons (Mcewen, 1999; Mcewen, 2001; Cook and Wellman, 2004; Liston et al., 2006; Radley et al., 2006; Czeh et al., 2008; Goldwater et al., 2009). On the other hand, chronic stress increases the length of apical dendrites in the ventral orbital subregion of the orbitofrontal cortex as well as the dendritic arborization and spine density in the basolateral amygdala spiny neurons (Vyas et al., 2003; Dias-Ferreira et al., 2009). Recent work showed that microglia activated after chronic unpredictable stress were involved in pruning of spines both in the Layer-1 of mPFC and hippocampus (Milior et al., 2016; Wohleb et al., 2018). Interestingly, deletion of P2X7R gene inhibited the decrease in synapse numbers in dorsal dentate gyrus (DG) following inescapable footshock, a rodent model of depression (Otrokocsi et al., 2017), indicating a possible role of P2X7R in pruning of synapses, which needs to be addressed in future studies.

In conclusion, as with ATP release, ATP-P2X-mediated microglial activation may exert depressant or anti-depressant effect possibly depending on the intensity of the stimulus and brain region, which may yield contrasting results in *in vitro* and *in vivo* experiments. Further studies are needed to document the prevailing mechanisms involved under *in situ* conditions as well as in patients.

Hyperpolarization-Activated Cyclic Nucleotide-gated Channels and M-type K^+ (KCNQ) Channels

Hyperpolarization-activated cyclic nucleotide-gated (HCN) channels are nonselective cation channels located mainly at dendrites, but also present at axons and the neuronal soma. They open at membrane voltages more negative than −40 mV and when HCN channels open, membrane resistance decreases (Biel et al., 2009; Kase and Imoto, 2012). Thus, HCN channels can counteract both membrane hyperpolarization and depolarization allowing both neuronal excitation as well as inhibition (Kase and Imoto, 2012; Benarroch, 2013). Four subtypes of HCN's have been identified: HCN1 to HCN4. HCN1 and HCN2 were reported to be highly expressed in brain regions known to be involved in the pathophysiology of major depression, namely prefrontal cortex, hippocampus, ventral tegmental area (VTA) and nucleus accumbens (NAc) (Notomi and Shigemoto, 2004).

TABLE 2 | Effects of modulating HCN2 expression and function on depression-like behavior.

HCN channels			
Intervention	**Affected brain region**	**Results**	**References**
CUMS	VTA	Decreased DA neuronal firing and I(h) Increased depression-like behavior	Zhong et al. (2018)
CSDS	VTA	Increased DA neuronal firing and I(h) Increased depression-like behavior	Cao et al. (2010) Chaudhury et al. (2013)
CSDS *P11*$^{-/-}$	NAc	Decreased HCN 2 expression and I(h) in ChIN Increased depression-like behavior	Cheng et al. (2019)
HCN1$^{-/-}$ *HCN2*$^{-/-}$ *TRIP8b*$^{-/-}$	Global knockout	Decreased time spent immobile in TST and FST; increased social interaction	Lewis et al. (2011)
HCN2 antagonist			
ZD7288 (on NAc slices)	NAc	Decrease ChIN firing	Cheng et al. (2019)
ZD7288 (into VTA) DK-AH 269 (into VTA)	VTA	Reverse CSDS-induced social avoidance	Cao et al. (2010)
I(h) potentiator			
Lamotrigine (into VTA, for 5 days)	VTA	Reversed CSDS-induced social avoidance and decrease in sucrose preference	Friedman et al. (2014)
HCN2 overexpression	NAc ChIN	Reversed social avoidance in CSDS susceptible mice as well as depressogenic behavior in SPT, TST and FST in p11$^{-/-}$ mice	Cheng et al. (2019)
HSV-LS1L-HCN2-eYFP/AAV2-FLEX-HCN2			
AAV2-HCN2-eGFP/HSV-LS1L-HCN2	VTA DA	Reverse CSDS- and CUMS-induced depression- and anxiety-like behaviors in SPT, FST, NSFT and social interaction test	Zhong et al. (2018) Friedman et al. (2014)
HCN2 knockdown			
AAV2-HCN2shRNA-eGFP	VTA DA	Decreased sucrose preference in SPT, increased immobility time in FST, increased latency to feed in NSFT and decreased time spent in open arms of EPM	Zhong et al. (2018)
HCN1 knockdown			
LV-HCN1-shRNA	Dorsal hippocampus	Increased the time spent in the centre of OFT and in the open arms of EPM, decreased time spent immobile in FST	Kim et al. (2012)

ChIN, cholinergic interneurons; CUMS, chronic unpredictable mild stress; DA, dopamine; I(h), cationic current through HCN channels; FST, forced swim test; NAc, nucleus accumbens; NSFT, novelty suppressed feeding test; OFT, open field test; SPT, sucrose preference test; VTA, ventral tegmental area.

HCN's interact with cyclic adenosine monophosphate (cAMP), which modulates voltage dependence of their activation kinetics and facilitate their opening. Signaling through several neuromodulators like noradrenaline and dopamine, whose dysfunction may contribute to the pathophysiology of depression, alter cAMP levels in the dendrites and thus HCN channel functioning, especially of HCN 2, the subtype most strongly modulated by cAMP (Biel et al., 2009). HCN also interacts with tetratricopeptide repeat-containing Rab8b interacting protein (TRIP8b), which regulates trafficking of HCN to dendrites (Biel et al., 2009).

Global knockout of *HCN1*, *HCN2,* or *TRIP8b* genes (leading to a decrease in both HCN1 and HCN2 protein levels) in mice resulted in a reduction in behavioral despair, an antidepressant-like effect (Lewis et al., 2011) (**Table 2**). Studies showed that HCNs regulate neuronal excitability and plasticity in response to stress, depending on the brain region and cell type that they are expressed in, as well as the duration and type of the stressor. For example, VTA dopamine (DA) neurons in the brain reward circuit has important role in regulation of the stress response. Evidence indicates that there are disturbances in the brain reward circuitry in major depression, which is associated with anhedonia, one of the 2 cardinal symptoms of major depression (Nestler and Carlezon, 2006; Russo and Nestler, 2013; Nestler, 2015; Hoflich et al., 2019). Recent evidence showed that the social stress susceptible mice display increased VTA DA neuronal firing and increase in HCN mediated I(h) currents (Cao et al., 2010; Chaudhury et al., 2013), whereas mice exposed to chronic unpredictable mild stress show a reduction in I(h) and DA neuronal firing (Zhong et al., 2018) (**Table 2**). In NAc, one of the major targets of VTA DA neurons, both HCN 2 expression and function [I(h)] were reduced in cholinergic interneurons (ChIN) in two different mice depression models, namely chronic social defeat stress and *p11* knockout mice (Cheng et al., 2019) (**Figure 4**). Because decreased activity of ChIN in NAc was found to be related to depressive behavior, the possible involvement of HCN2 channels in regulating ChIN activity was studied by pharmacological and genetic interventions. Decreased tonic firing of ChIN by pharmacological blockade of HCN2 channels (ZD7288) suggest that dysfunction of HCN channels participates in the diminished ChIN firing rate observed in depressive mice (**Table 2**; **Figure 4**). Intriguingly, selective overexpression of HCN2 in both NAc ChIN and VTA DA neurons resulted in antidepressant-like effects (Friedman et al.,

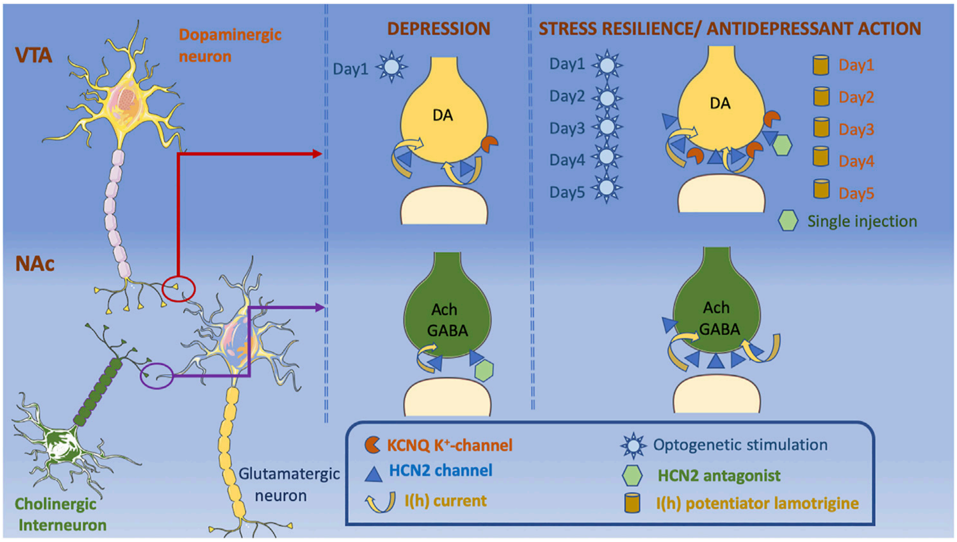

FIGURE 4 | The decrease in the expression of HCN2 channels in NAc on both dopaminergic terminals projecting from VTA and local ChIN terminals is depressogenic. Decrease in I(h) currents in ChIN terminals is associated with depression-like phenotype, whereas an increase in I(h) currents on the VTA dopaminergic terminals is observed in both stress susceptible and stress resilient mice. K^+ channels are increased only in the stress resilient mice counterbalancing the effects of increased I(h) currents. Application of an HCN2 antagonist into NAc causes a depressogenic phenotype, whereas it has antidepressant effects when applied into VTA. Lamotrigine administration for 5-days also reduce depressogenic behaviors. Acute optogenetic stimulation of VTA dopaminergic neurons increase depression-like behaviors, whereas chronic optogenetic stimulation of VTA dopaminergic neurons shows antidepressant effects. Cellular templates are copied from Servier Medical Art (smart.servier.com).

2014; Zhong et al., 2018; Cheng et al., 2019) (**Table 2**; **Figure 4**). Selective knockdown of HCN2 in VTA DA neurons by shRNA increased anxiety-like and depression-like behaviors (Zhong et al., 2018). Intriguingly, knockdown of HCN1 in CA1 region of dorsal hippocampus resulted in anxiolytic and antidepressant effects (Kim et al., 2012) (**Table 2**). Whether this effect was associated with the difference in HCN subtype or the brain region studied warrants further research investigating the role of HCN channels in other brain regions relevant to depression.

HCN2 channels' ability to modulate VTA DA neurons depend on the duration of neuronal excitation: Acute phasic optogenetic stimulation of VTA DA neurons projecting to NAc (20 Hz, 10 min) during a subthreshold social defeat stress increases spontaneous and evoked activity that lasts for 8–12 h after stimulation in parallel with increased depression-like behaviors in social interaction and sucrose preference tests (Chaudhury et al., 2013) (**Figure 4**). Repetitive optogenetic stimulation of VTA DA neurons for 5 days (20 Hz, 20 min), on the other hand, reduced DA neuron firing rate and displayed antidepressant-like effects in social interaction, forced swim and sucrose preference tests (Friedman et al., 2014) (**Figure 4**). In line with these observations, both acute injections of HCN channel blockers (ZD7288 or DK-AH 269) into VTA (Cao et al., 2010) and repeated infusions of the I(h) potentiator, lamotrigine into VTA for 5 days showed antidepressant-like effects (Friedman et al., 2014) (**Table 2**; **Figure 4**). The group treated with repeated lamotrigine displayed normalization of the hyperactivity of VTA DA neurons (Friedman et al., 2014). A more detailed look at the mechanisms underlying these opposite effects of acute vs repeated manipulations of HCN channels and DA neuron activity showed that I(h) currents were also amplified in social stress resilient mice whose DA neuronal firing rate was comparable to that of controls (Friedman et al., 2014) (**Figure 4**). Recordings in brain slices of VTA DA neuron demonstrated an increase in K^+ currents and reduction in firing rate in resilient mice (Friedman et al., 2014). Altogether, these findings suggest that increase in K^+ currents is a homeostatic plasticity mechanism that stabilizes VTA DA neuronal activity (**Figure 4**). In support of this proposition, I(h) was found to have a depolarizing effect on the peak voltage of weak EPSPs, whereas it exerted a hyperpolarizing effect on the peak voltage of stronger, but still subthreshold, EPSPs (George et al., 2009). George et al. (2009) showed that blockade of the delayed-rectifier M-type K(+) current resulted in shift of dual I(h) influence on EPSPs to only an excitatory effect, suggesting an interaction between M-type K(+) current and I(h) (George et al., 2009).

Intriguingly, M-type K^+ (KCNQ) channels have been linked to depression-like behavior and identified as a novel antidepressant drug target (Friedman et al., 2016; Li et al., 2017; Tan et al., 2020; Ren et al., 2021) (**Figure 4**). RNA sequencing analysis revealed that genes encoding K^+ channels are differentially expressed in chronically stressed rats (Ren et al., 2021). Transcript levels of KCNQ4 channels that are selectively expressed in VTA DA neurons were negatively correlated with firing rate of VTA DA neurons (Li et al., 2017). Supporting the involvement of KCNQ channels in the pathophysiology of depression, pharmacological activators of KCNQ channels normalized the hyperactivity of VTA DA neurons and alleviated stress-induced depression-like behaviors (Friedman et al., 2016; Li et al., 2017;

Ren et al., 2021). A recent open-label clinical study conducted in 18 major depression subjects reported that 10 weeks of treatment with KCNQ channel opener, retigabine, significantly reduced depressive symptoms and decreased functional connectivity between ventral caudate and mid-cingulate and posterior cingulate cortices (Tan et al., 2020).

In contrast to well documented mutations of HCN and KCNQ channel genes in a spectrum of epileptic diseases (Nappi et al., 2020; Rivolta et al., 2020), genetic studies in depressed patients have not conclusively acknowledged a convincing association between single nucleotide polymorphisms (SNPs) in HCN or KCNQ channel genes and depression. Polymorphisms in *HCN4* gene were reported to be associated with a broad spectrum of mood disorders including major depression, bipolar affective disorder and obsessive compulsive disorder (Kelmendi et al., 2011). A study with a larger sample failed to replicate these findings and reported no association between any HCN channel genes studied (HCN1-4) and depression (Mcintosh et al., 2012). Despite the lack of evidence from human genetic studies supporting the involvement of SNPs in HCN or KCNQ channel genes, the above summarized findings in animals suggest that both HCN channels and KCNQ channels are important players of the physiological adaptations to stress, perturbations of which can lead to depression.

Voltage-Gated Calcium Channels and Two-Pore Domain K+ Channels

Voltage-gated calcium channels and two-pore domain K^+ channels, the role of which are discussed in the context of migraine in the previous section are also involved in the pathophysiology of mood disorders: Genetic variations in *CACNA1C* gene, which encodes for the alpha subunit of L-type calcium channels (Cav1.2) as well as *CACNA1E*, which encodes for the alpha 1E subunit of R-type calcium channel ($Ca_V2.3$ channel) were reported in mood disorders (Ferreira et al., 2008; Psychiatric, 2011; Nurnberger et al., 2014; Howard et al., 2019). Animal studies have confirmed the involvement of *CACNA1C* in the pathophysiolgy of depression: Following CUMS, Cav1.2 levels were found to be increased in the PFC (Bavley et al., 2017). The depression-like behaviors were decreased in both $CACNA1C^{+/-}$ heterozygous and forebrain specific *CACNA1C* KO mice at baseline and after chronic stress (Dao et al., 2010; Bavley et al., 2017; Kabir et al., 2017; Dedic et al., 2018). In the NAc, on the other hand, CSDS decreased Cav1.2 channel expression in stress susceptible mice and selective KO of *CACNA1C* in the NAc resulted in an increase in susceptibility to subthreshold social defeat stress as well as a reduction in both the time spent sniffing female urine soaked cotton tips and the time spent in open arms of elevated plus maze (Terrillion et al., 2017). In line with these observations, alterations in calcium signaling has long been implicated in the pathophysiology of mood disorders and a recent metaanalysis of 21 studies reported that both basal and stimulated Ca^{+2} levels were found to be higher in platelets and lymphocytes of bipolar affective disorder patients (Harrison et al., 2019). The Ca^{+2} channel blocking properties of mood stabilizer drugs, lithium, valproic acid, carbamazepine and lamotrigine as well as efficacy of verapamil, a Ca^{+2} channel blocker as a mood stabilizing agent support the role of Ca^{+2} in the pathophysiology of mood disorders and point to the promising potential of BBB-permeable Ca^{+2} channel blockers in the treatment of mood disordes (for detailed reviews please see (Cipriani et al., 2016; Dubovsky, 2019; Harrison et al., 2020). Intriguingly, mood stabilizers valproic acid, lamotrigine and carbamazepine also block voltage-gated Na^+ channels, raising the possibility that their actions might, in part, be attributed to Na^+ channel blockade (Stahl, 2004). However voltage-gated Na^+ channels have not been implicated so far in the pathophysiology of depression (Mantegazza et al., 2021).

Among two-pore domain K^+ channels, the involvement of TWIK-related K^+ channel-1 (TREK-1) in depression pathophysiology is the most well documented (for detailed reviews see (Borsotto et al., 2015; Djillani et al., 2019)). They are involved in the regulation of plasma membrane potential and excitability similar to HCN channels (Lesage, 2003; Talley et al., 2003). SNPs in *kcnk2*, gene encoding TREK-1 channel, were reported in major depression patients, and some SNPs were found to be associated with antidepressant response and resistance to treatment (Perlis et al., 2008; Liou et al., 2009). TREK-1 inhibitors reversed behavioral despair and decreased sucrose preference induced by CUMS in rats when given intraperitoneously (Ye et al., 2015; Djillani et al., 2017). Deletion of TREK-1 channels resulted in depression-resistant phenotype (Heurteaux et al., 2006). Interestingly selective serotonin uptake inhibitors, fluoxetine, paroxetine and citalopram were reported to block both TREK-1 and TREK-2 mediated currents *in vitro* (Kennard et al., 2005; Kim et al., 2017). Mood stabilizers, lithium, valproic acid and carbamazepine, on the other hand, increased TREK-1 mediated currents without affecting TREK-2 mediated currents (Kim et al., 2017). The therapeutic use of SSRIs in the treatment of both depression and migraine patients may be in part related to their effects on TREK-mediated currents.

In conclusion, mutations detected in familial cases of migraine and polymorphisms creating susceptibility to depression as well as genetic manipulations in animal models of depression have provided novel insight to the pathophysiology of these disorders. Since subtle changes in, for instance, ATP release or K^+ channel activity may lead to variable consequences within a microcircuit, and hence, in network activity depending on the microcircuit structure and brain region, experimental studies (especially those using isolated preparations) have yielded to varying, sometimes contradictory, results. Therefore, identification of overlapping genetic variants in non-familial forms of migraine and depression can provide further insight to understand the phenotypic traits and role of ion channels, E:I balance, metabolic coupling of astrocytic glycogen to glutamatergic synaptic activity and neuroinflammation in migraine as well as depression, both of which display significant heritability and comorbidity. These findings can also help development of novel therapies for both conditions.

AUTHOR CONTRIBUTIONS

TD wrote the sections regarding ion channel dysfunctions in migraine (*Lessons Learned From Familial Migraine Mutations, Non-Familial Common Migraine, Initiation of Inflammatory Signaling That Causes Headache, and Master Switch of Inflammatory Signaling: Pannexin Channels*). EE-K wrote the sections regarding ion channel dysfunctions in depression (*P2X7 Receptor, Potential Mechanisms Underlying P2X7R's Effects on Mood Regulation?*) Hyperpolarization-activated cyclic nucleotide-gated (HCN) channels and M-type K+ (KCNQ) channels and Voltage-gated calcium channels and two-pore domain K+ channels. **Figures 3** and **4** were prepared by EE-K. **Figure 1** was prepared by Zeynep Kaya and **Figure 2** was adapted from Karatas et al. (2013)

FUNDING

TD's research is supported by Turkish Academy of Sciences and TUBITAK (120C122).

REFERENCES

Afridi, R., and Suk, K. (2021). Neuroinflammatory Basis of Depression: Learning from Experimental Models. *Front. Cell Neurosci.* 15, 691067. doi:10.3389/fncel.2021.691067

Albrecht, D. S., Mainero, C., Ichijo, E., Ward, N., Granziera, C., Zürcher, N. R., et al. (2019). Imaging of Neuroinflammation in Migraine With Aura: A [11C]PBR28 PET/MRI Study. *Neurology.* 92, e2038–e2050. doi:10.1212/WNL.0000000000007371

Alesci, S., Martinez, P. E., Kelkar, S., Ilias, I., Ronsaville, D. S., Listwak, S. J., et al. (2005). Major Depression Is Associated With Significant Diurnal Elevations in Plasma Interleukin-6 Levels, a Shift of its Circadian Rhythm, and Loss of Physiological Complexity in its Secretion: Clinical Implications. *J. Clin. Endocrinol. Metab.* 90, 2522–2530. doi:10.1210/jc.2004-1667

Alloisio, S., Cervetto, C., Passalacqua, M., Barbieri, R., Maura, G., Nobile, M., et al. (2008). Functional Evidence for Presynaptic P2X7 Receptors in Adult Rat Cerebrocortical Nerve Terminals. *FEBS Lett.* 582, 3948–3953. doi:10.1016/j.febslet.2008.10.041

Amiri, S., Behnezhad, S., and Azad, E. (2019). Migraine Headache and Depression in Adults: a Systematic Review and Meta-Analysis. *Neuropsychiatr.* 33, 131–140. doi:10.1007/s40211-018-0299-5

Aprile-Garcia, F., Metzger, M. W., Paez-Pereda, M., Stadler, H., Acuna, M., Liberman, A. C., et al. (2016). Co-Expression of Wild-Type P2X7R With Gln460Arg Variant Alters Receptor Function. *PLoS One.* 11, e0151862. doi:10.1371/journal.pone.0151862

Arcuino, G., Lin, J. H., Takano, T., Liu, C., Jiang, L., Gao, Q., et al. (2002). Intercellular Calcium Signaling Mediated by Point-Source Burst Release of ATP. *Proc. Natl. Acad. Sci. U S A.* 99, 9840–9845. doi:10.1073/pnas.152588599

Auffenberg, E., Hedrich, U. B., Barbieri, R., Miely, D., Groschup, B., Wuttke, T. V., et al. (2021). Hyperexcitable Interneurons Trigger Cortical Spreading Depression in an Scn1a Migraine Model. *J. Clin. Invest.* 21, e142202. doi:10.1172/jci142202

Basso, A. M., Bratcher, N. A., Harris, R. R., Jarvis, M. F., Decker, M. W., and Rueter, L. E. (2009). Behavioral Profile of P2X7 Receptor Knockout Mice in Animal Models of Depression and Anxiety: Relevance for Neuropsychiatric Disorders. *Behav. Brain Res.* 198, 83–90. doi:10.1016/j.bbr.2008.10.018

Bavley, C. C., Fischer, D. K., Rizzo, B. K., and Rajadhyaksha, A. M. (2017). Cav1.2 Channels Mediate Persistent Chronic Stress-Induced Behavioral Deficits That Are Associated With Prefrontal Cortex Activation of the p25/Cdk5-Glucocorticoid Receptor Pathway. *Neurobiol. Stress.* 7, 27–37. doi:10.1016/j.ynstr.2017.02.004

Benarroch, E. E. (2013). HCN Channels: Function and Clinical Implications. *Neurology.* 80, 304–310. doi:10.1212/WNL.0b013e31827dec42

Bezzi, P., and Volterra, A. (2001). A Neuron-Glia Signalling Network in the Active Brain. *Curr. Opin. Neurobiol.* 11, 387–394. doi:10.1016/s0959-4388(00)00223-3

Bhaskaracharya, A., Phuong, D. U., Jalilian, I., Spildrejorde, M., Skarratt, K. K., Fuller, S. J., et al. (2014). Probenecid Blocks Human P2X7 Receptor-Induced Dye Uptake via a Pannexin-1 Independent Mechanism. *Plos One.* 9, e93058. doi:10.1371/journal.pone.0093058

Biel, M., Wahl-Schott, C., Michalakis, S., and Zong, X. (2009). Hyperpolarization-Activated Cation Channels: From Genes to Function. *Physiol. Rev.* 89, 847–885. doi:10.1152/physrev.00029.2008

Borsotto, M., Veyssiere, J., Moha Ou Maati, H., Devader, C., Mazella, J., and Heurteaux, C. (2015). Targeting Two-Pore Domain K(+) Channels TREK-1 and TASK-3 for the Treatment of Depression: a New Therapeutic Concept. *Br. J. Pharmacol.* 172, 771–784. doi:10.1111/bph.12953

Brennan, K. C., Bates, E. A., Shapiro, R. E., Zyuzin, J., Hallows, W. C., Huang, Y., et al. (2013). Casein Kinase Iδ Mutations in Familial Migraine and Advanced Sleep Phase. *Sci. Transl Med.* 5 (183ra56), 1–11. doi:10.1126/scitranslmed.3005784

Brennan, K. C., and Pietrobon, D. (2018). A Systems Neuroscience Approach to Migraine. *Neuron.* 97, 1004–1021. doi:10.1016/j.neuron.2018.01.029

Bromet, E., Andrade, L. H., Hwang, I., Sampson, N. A., Alonso, J., De Girolamo, G., et al. (2011). Cross-National Epidemiology of DSM-IV Major Depressive Episode. *BMC Med.* 9, 90. doi:10.1186/1741-7015-9-90

Bu, F., Nie, L., Quinn, J. P., and Wang, M. (2020). Sarcoma Family Kinase-Dependent Pannexin-1 Activation After Cortical Spreading Depression Is Mediated by NR2A-Containing Receptors. *Int. J. Mol. Sci.* 21, 1269. doi:10.3390/ijms21041269

Burnstock, G. (2007). Physiology and Pathophysiology of Purinergic Neurotransmission. *Physiol. Rev.* 87, 659–797. doi:10.1152/physrev.00043.2006

Cangalaya, C., Stoyanov, S., Fischer, K. D., and Dityatev, A. (2020). Light-Induced Engagement of Microglia to Focally Remodel Synapses in the Adult Brain. *Elife.* 9, e58435. doi:10.7554/elife.58435

Cao, J. L., Covington, H. E., 3rd, Friedman, A. K., Wilkinson, M. B., Walsh, J. J., Cooper, D. C., et al. (2010). Mesolimbic Dopamine Neurons in the Brain Reward Circuit Mediate Susceptibility to Social Defeat and Antidepressant Action. *J. Neurosci.* 30, 16453–16458. doi:10.1523/JNEUROSCI.3177-10.2010

Cao, X., Li, L. P., Wang, Q., Wu, Q., Hu, H. H., Zhang, M., et al. (2013). Astrocyte-Derived ATP Modulates Depressive-Like Behaviors. *Nat. Med.* 19, 773–777. doi:10.1038/nm.3162

Cao, Y., Welch, K. M., Aurora, S., and Vikingstad, E. M. (1999). Functional MRI-BOLD of Visually Triggered Headache in Patients With Migraine. *Arch. Neurol.* 56, 548–554. doi:10.1001/archneur.56.5.548

Capuani, C., Melone, M., Tottene, A., Bragina, L., Crivellaro, G., Santello, M., et al. (2016). Defective Glutamate and K+ Clearance by Cortical Astrocytes in Familial Hemiplegic Migraine Type 2. *EMBO Mol. Med.* 8, 967–986. doi:10.15252/emmm.201505944

Chanda, M. L., Tuttle, A. H., Baran, I., Atlin, C., Guindi, D., Hathaway, G., et al. (2013). Behavioral Evidence for Photophobia and Stress-Related Ipsilateral Head Pain in Transgenic Cacna1a Mutant Mice. *Pain.* 154, 1254–1262. doi:10.1016/j.pain.2013.03.038

Chaudhury, D., Walsh, J. J., Friedman, A. K., Juarez, B., Ku, S. M., Koo, J. W., et al. (2013). Rapid Regulation of Depression-Related Behaviours by Control of Midbrain Dopamine Neurons. *Nature* 493, 532–536. doi:10.1038/nature11713

Chen, S. P., Qin, T., Seidel, J. L., Zheng, Y., Eikermann, M., Ferrari, M. D., et al. (2017). Inhibition of the P2X7-PANX1 Complex Suppresses Spreading Depolarization and Neuroinflammation. *Brain.* 140, 1643–1656. doi:10.1093/brain/awx085

Cheng, J., Umschweif, G., Leung, J., Sagi, Y., and Greengard, P. (2019). HCN2 Channels in Cholinergic Interneurons of Nucleus Accumbens Shell Regulate Depressive Behaviors. *Neuron.* 101, 662–e5. doi:10.1016/j.neuron.2018.12.018

Chever, O., Zerimech, S., Scalmani, P., Lemaire, L., Pizzamiglio, L., Loucif, A., et al. (2021). Initiation of Migraine-Related Cortical Spreading Depolarization by

Hyperactivity of GABAergic Neurons and NaV1.1 Channels. *J. Clin. Invest.* 7, 142203. doi:10.1172/jci142203

Cholet, N., Pellerin, L., Magistretti, P. J., and Hamel, E. (2002). Similar Perisynaptic Glial Localization for the Na+,K+-ATPase Alpha 2 Subunit and the Glutamate Transporters GLAST and GLT-1 in the Rat Somatosensory Cortex. *Cereb. Cortex.* 12, 515–525. doi:10.1093/cercor/12.5.515

Cholet, N., Pellerin, L., Welker, E., Lacombe, P., Seylaz, J., Magistretti, P., et al. (2001). Local Injection of Antisense Oligonucleotides Targeted to the Glial Glutamate Transporter GLAST Decreases the Metabolic Response to Somatosensory Activation. *J. Cereb. Blood Flow Metab.* 21, 404–412. doi:10.1097/00004647-200104000-00009

Cipriani, A., Saunders, K., Attenburrow, M. J., Stefaniak, J., Panchal, P., Stockton, S., et al. (2016). A Systematic Review of Calcium Channel Antagonists in Bipolar Disorder and Some Considerations for Their Future Development. *Mol. Psychiatry.* 21, 1324–1332. doi:10.1038/mp.2016.86

Cook, S. C., and Wellman, C. L. (2004). Chronic Stress Alters Dendritic Morphology in Rat Medial Prefrontal Cortex. *J. Neurobiol.* 60, 236–248. doi:10.1002/neu.20025

Costa, C., Prontera, P., Sarchielli, P., Tonelli, A., Bassi, M. T., Cupini, L. M., et al. (2014). A Novel ATP1A2 Gene Mutation in Familial Hemiplegic Migraine and Epilepsy. *Cephalalgia.* 34, 68–72. doi:10.1177/0333102413498941

Csölle, C., Andó, R. D., Kittel, Á., Gölöncsér, F., Baranyi, M., Soproni, K., et al. (2013a). The Absence of P2X7 Receptors (P2rx7) on Non-Haematopoietic Cells Leads to Selective Alteration in Mood-Related Behaviour With Dysregulated Gene Expression and Stress Reactivity in Mice. *Int. J. Neuropsychopharmacol.* 16, 213–233. doi:10.1017/S1461145711001933

Csölle, C., Baranyi, M., Zsilla, G., Kittel, A., Gölöncsér, F., Illes, P., et al. (2013b). Neurochemical Changes in the Mouse Hippocampus Underlying the Antidepressant Effect of Genetic Deletion of P2X7 Receptors. *PLoS One.* 8, e66547. doi:10.1371/journal.pone.0066547

Czéh, B., Perez-Cruz, C., Fuchs, E., and Flügge, G. (2008). Chronic Stress-Induced Cellular Changes in the Medial Prefrontal Cortex and Their Potential Clinical Implications: Does Hemisphere Location Matter? *Behav. Brain Res.* 190, 1–13. doi:10.1016/j.bbr.2008.02.031

Dahl, G. (2018). The Pannexin1 Membrane Channel: Distinct Conformations and Functions. *FEBS Lett.* 592, 3201–3209. doi:10.1002/1873-3468.13115

Dalkara, T., and Kiliç, K. (2013). How Does Fasting Trigger Migraine? A Hypothesis. *Curr. Pain Headache Rep.* 17, 368. doi:10.1007/s11916-013-0368-1

Dalkara, T., and Moskowitz, M. A. (2017). *From Cortical Spreading Depression to Trigeminovascular Activation in Migraine Neurobiological Basis of Migraine*. Hoboken, New Jersey: John Wiley & Sons, 267–284. doi:10.1002/9781118967225.ch16

Dao, D. T., Mahon, P. B., Cai, X., Kovacsics, C. E., Blackwell, R. A., Arad, M., et al. (2010). Mood Disorder Susceptibility Gene CACNA1C Modifies Mood-Related Behaviors in Mice and Interacts With Sex to Influence Behavior in Mice and Diagnosis in Humans. *Biol. Psychiatry.* 68, 801–810. doi:10.1016/j.biopsych.2010.06.019

De Boer, I., Van Den Maagdenberg, A. M. J. M., and Terwindt, G. M. (2019). Advance in Genetics of Migraine. *Curr. Opin. Neurol.* 32, 413–421. doi:10.1097/wco.0000000000000687

Dedic, N., Pöhlmann, M. L., Richter, J. S., Mehta, D., Czamara, D., Metzger, M. W., et al. (2018). Cross-Disorder Risk Gene CACNA1C Differentially Modulates Susceptibility to Psychiatric Disorders During Development and Adulthood. *Mol. Psychiatry.* 23, 533–543. doi:10.1038/mp.2017.133

Dehghani, A., Phisonkunkasem, T., Ozcan, S. Y., Dalkara, T., Van Den Maagdenberg, A. M. J. M., Tolner, E. A., et al. (2021). Widespread Brain Parenchymal HMGB1 and NF-KB Neuroinflammatory Responses Upon Cortical Spreading Depolarization in Familial Hemiplegic Migraine Type 1 Mice. *Neurobiol. Dis.* 156, 105424. doi:10.1016/j.nbd.2021.105424

Desroches, M., Faugeras, O., Krupa, M., and Mantegazza, M. (2019). Modeling Cortical Spreading Depression Induced by the Hyperactivity of Interneurons. *J. Comput. Neurosci.* 47, 125–140. doi:10.1007/s10827-019-00730-8

Dias-Ferreira, E., Sousa, J. C., Melo, I., Morgado, P., Mesquita, A. R., Cerqueira, J. J., et al. (2009). Chronic Stress Causes Frontostriatal Reorganization and Affects Decision-Making. *Science.* 325, 621–625. doi:10.1126/science.1171203

Djillani, A., Pietri, M., Mazella, J., Heurteaux, C., and Borsotto, M. (2019). Fighting Against Depression With TREK-1 Blockers: Past and Future. A Focus on Spadin. *Pharmacol. Ther.* 194, 185–198. doi:10.1016/j.pharmthera.2018.10.003

Djillani, A., Pietri, M., Moreno, S., Heurteaux, C., Mazella, J., and Borsotto, M. (2017). Shortened Spadin Analogs Display Better TREK-1 Inhibition, *In Vivo* Stability and Antidepressant Activity. *Front. Pharmacol.* 8, 643. doi:10.3389/fphar.2017.00643

Donnelly-Roberts, D. L., Namovic, M. T., Han, P., and Jarvis, M. F. (2009). Mammalian P2X7 Receptor Pharmacology: Comparison of Recombinant Mouse, Rat and Human P2X7 Receptors. *Br. J. Pharmacol.* 157, 1203–1214. doi:10.1111/j.1476-5381.2009.00233.x

Dowlati, Y., Herrmann, N., Swardfager, W., Liu, H., Sham, L., Reim, E. K., et al. (2010). A Meta-Analysis of Cytokines in Major Depression. *Biol. Psychiatry.* 67, 446–457. doi:10.1016/j.biopsych.2009.09.033

Dubovsky, S. L. (2019). Applications of Calcium Channel Blockers in Psychiatry: Pharmacokinetic and Pharmacodynamic Aspects of Treatment of Bipolar Disorder. *Expert Opin. Drug Metab. Toxicol.* 15, 35–47. doi:10.1080/17425255.2019.1558206

Duman, R. S., Sanacora, G., and Krystal, J. H. (2019). Altered Connectivity in Depression: GABA and Glutamate Neurotransmitter Deficits and Reversal by Novel Treatments. *Neuron.* 102, 75–90. doi:10.1016/j.neuron.2019.03.013

Dussor, G., and Cao, Y. Q. (2016). TRPM8 and Migraine. *Headache.* 56, 1406–1417. doi:10.1111/head.12948

Edelmayer, R. M., Le, L. N., Yan, J., Wei, X., Nassini, R., Materazzi, S., et al. (2012). Activation of TRPA1 on Dural Afferents: a Potential Mechanism of Headache Pain. *Pain.* 153, 1949–1958. doi:10.1016/j.pain.2012.06.012

Eising, E., Shyti, R., 't Hoen, P. A. C., Vijfhuizen, L. S., Huisman, S. M. H., Broos, L. A. M., et al. (2017). Cortical Spreading Depression Causes Unique Dysregulation of Inflammatory Pathways in a Transgenic Mouse Model of Migraine. *Mol. Neurobiol.* 54, 2986–2996. doi:10.1007/s12035-015-9681-5

Enyedi, P., and Czirják, G. (2015). Properties, Regulation, Pharmacology, and Functions of the K$_2$p Channel, TRESK. *Pflugers Arch.* 467, 945–958. doi:10.1007/s00424-014-1634-8

Erdener, S. E., and Dalkara, T. (2014). Modelling Headache and Migraine and its Pharmacological Manipulation. *Br. J. Pharmacol.* 171, 4575–4594. doi:10.1111/bph.12651

Fee, C., Banasr, M., and Sibille, E. (2017). Somatostatin-Positive Gamma-Aminobutyric Acid Interneuron Deficits in Depression: Cortical Microcircuit and Therapeutic Perspectives. *Biol. Psychiatry.* 82, 549–559. doi:10.1016/j.biopsych.2017.05.024

Ferreira, M. A., O'donovan, M. C., Meng, Y. A., Jones, I. R., Ruderfer, D. M., Jones, L., et al. (2008). Collaborative Genome-Wide Association Analysis Supports a Role for ANK3 and CACNA1C in Bipolar Disorder. *Nat. Genet.* 40, 1056–1058. doi:10.1038/ng.209

Fogaça, M. V., and Duman, R. S. (2019). Cortical GABAergic Dysfunction in Stress and Depression: New Insights for Therapeutic Interventions. *Front. Cel Neurosci.* 13, 87. doi:10.3389/fncel.2019.00087

Friedman, A. K., Juarez, B., Ku, S. M., Zhang, H., Calizo, R. C., Walsh, J. J., et al. (2016). KCNQ Channel Openers Reverse Depressive Symptoms via an Active Resilience Mechanism. *Nat. Commun.* 7, 11671. doi:10.1038/ncomms11671

Friedman, A. K., Walsh, J. J., Juarez, B., Ku, S. M., Chaudhury, D., Wang, J., et al. (2014). Enhancing Depression Mechanisms in Midbrain Dopamine Neurons Achieves Homeostatic Resilience. *Science.* 344, 313–319. doi:10.1126/science.1249240

Fuchs, T., Jefferson, S. J., Hooper, A., Yee, P. H., Maguire, J., and Luscher, B. (2017). Disinhibition of Somatostatin-Positive GABAergic Interneurons Results in an Anxiolytic and Antidepressant-Like Brain State. *Mol. Psychiatry.* 22, 920–930. doi:10.1038/mp.2016.188

George, M. S., Abbott, L. F., and Siegelbaum, S. A. (2009). HCN Hyperpolarization-Activated Cation Channels Inhibit EPSPs by Interactions With M-type K(+) Channels. *Nat. Neurosci.* 12, 577–584. doi:10.1038/nn.2307

Ghaemi, A., Alizadeh, L., Babaei, S., Jafarian, M., Khaleghi Ghadiri, M., Meuth, S. G., et al. (2018). Astrocyte-Mediated Inflammation in Cortical Spreading Depression. *Cephalalgia.* 38, 626–638. doi:10.1177/0333102417702132

Ghaemi, A., Sajadian, A., Khodaie, B., Lotfinia, A. A., Lotfinia, M., Aghabarari, A., et al. (2016). Immunomodulatory Effect of Toll-Like Receptor-3 Ligand Poly I:

C on Cortical Spreading Depression. *Mol. Neurobiol.* 53, 143–154. doi:10.1007/s12035-014-8995-z

Goldwater, D. S., Pavlides, C., Hunter, R. G., Bloss, E. B., Hof, P. R., Mcewen, B. S., et al. (2009). Structural and Functional Alterations to Rat Medial Prefrontal Cortex Following Chronic Restraint Stress and Recovery. *Neuroscience.* 164, 798–808. doi:10.1016/j.neuroscience.2009.08.053

Gölöncsér, F., Baranyi, M., Balázsfi, D., Demeter, K., Haller, J., Freund, T. F. F., et al. (2017). Regulation of Hippocampal 5-HT Release by P2X7 Receptors in Response to Optogenetic Stimulation of Median Raphe Terminals of Mice. *Front. Mol. Neurosci.* 10, 325. doi:10.3389/fnmol.2017.00325

Gormley, P., Anttila, V., Winsvold, B. S., Palta, P., Esko, T., Pers, T. H., et al. (2016). Meta-Analysis of 375,000 Individuals Identifies 38 Susceptibility Loci for Migraine. *Nat. Genet.* 48, 856–866. doi:10.1038/ng.3598

Guo, H., Callaway, J. B., and Ting, J. P. (2015). Inflammasomes: Mechanism of Action, Role in Disease, and Therapeutics. *Nat. Med.* 21, 677–687. doi:10.1038/nm.3893

Guo, Z., Qiu, C. S., Jiang, X., Zhang, J., Li, F., Liu, Q., et al. (2019). TRESK K+ Channel Activity Regulates Trigeminal Nociception and Headache. *eNeuro.* 6, ENEURO.0236-19.2019. doi:10.1523/ENEURO.0236-19.2019

Hadjikhani, N., Albrecht, D. S., Mainero, C., Ichijo, E., Ward, N., Granziera, C., et al. (2020). Extra-Axial Inflammatory Signal in Parameninges in Migraine With Visual Aura. *Ann. Neurol.* 87, 939–949. doi:10.1002/ana.25731

Hadjikhani, N., Sanchez Del Rio, M., Wu, O., Schwartz, D., Bakker, D., Fischl, B., et al. (2001). Mechanisms of Migraine Aura Revealed by Functional MRI in Human Visual Cortex. *Proc. Natl. Acad. Sci. U S A.* 98, 4687–4692. doi:10.1073/pnas.071582498

Halmai, Z., Dome, P., Vereczkei, A., Abdul-Rahman, O., Szekely, A., Gonda, X., et al. (2013). Associations between Depression Severity and Purinergic Receptor P2RX7 Gene Polymorphisms. *J. Affect Disord.* 150, 104–109. doi:10.1016/j.jad.2013.02.033

Harrison, P. J., Tunbridge, E. M., Dolphin, A. C., and Hall, J. (2020). Voltage-Gated Calcium Channel Blockers for Psychiatric Disorders: Genomic Reappraisal. *Br. J. Psychiatry.* 216, 250–253. doi:10.1192/bjp.2019.157

Harrison, P. J., Hall, N., Mould, A., Al-Juffali, N., and Tunbridge, E. M. (2019). Cellular Calcium in Bipolar Disorder: Systematic Review and Meta-Analysis. *Mol. Psychiatry.* doi:10.1038/s41380-019-0622-y

Hedrich, U. B., Liautard, C., Kirschenbaum, D., Pofahl, M., Lavigne, J., Liu, Y., et al. (2014). Impaired Action Potential Initiation in GABAergic Interneurons Causes Hyperexcitable Networks in an Epileptic Mouse Model Carrying a Human Na(V)1.1 Mutation. *J. Neurosci.* 34, 14874–14889. doi:10.1523/JNEUROSCI.0721-14.2014

Heurteaux, C., Lucas, G., Guy, N., El Yacoubi, M., Thümmler, S., Peng, X. D., et al. (2006). Deletion of the Background Potassium Channel TREK-1 Results in a Depression-Resistant Phenotype. *Nat. Neurosci.* 9, 1134–1141. doi:10.1038/nn1749

Hirschfeld, R. M. (2000). History and Evolution of the Monoamine Hypothesis of Depression. *J. Clin. Psychiatry.* 61 (Suppl. 6), 4–6.

Höflich, A., Michenthaler, P., Kasper, S., and Lanzenberger, R. (2019). Circuit Mechanisms of Reward, Anhedonia, and Depression. *Int. J. Neuropsychopharmacol.* 22, 105–118. doi:10.1093/ijnp/pyy081

Howard, D. M., Adams, M. J., Clarke, T. K., Hafferty, J. D., Gibson, J., Shirali, M., et al. (2019). Genome-wide Meta-Analysis of Depression Identifies 102 Independent Variants and Highlights the Importance of the Prefrontal Brain Regions. *Nat. Neurosci.* 22, 343–352. doi:10.1038/s41593-018-0326-7

Illes, P., Khan, T. M., and Rubini, P. (2017). Neuronal P2X7 Receptors Revisited: Do They Really Exist? *J. Neurosci.* 37, 7049–7062. doi:10.1523/JNEUROSCI.3103-16.2017

Iwata, M., Ota, K. T., Li, X. Y., Sakaue, F., Li, N., Dutheil, S., et al. (2016). Psychological Stress Activates the Inflammasome via Release of Adenosine Triphosphate and Stimulation of the Purinergic Type 2X7 Receptor. *Biol. Psychiatry.* 80, 12–22. doi:10.1016/j.biopsych.2015.11.026

Jansen, N. A., Dehghani, A., Linssen, M. M. L., Breukel, C., Tolner, E. A., and Van Den Maagdenberg, A. M. J. M. (2020). First FHM3 Mouse Model Shows Spontaneous Cortical Spreading Depolarizations. *Ann. Clin. Transl Neurol.* 7, 132–138. doi:10.1002/acn3.50971

Kabir, Z. D., Lee, A. S., Burgdorf, C. E., Fischer, D. K., Rajadhyaksha, A. M., Mok, E., et al. (2017). Cacna1c in the Prefrontal Cortex Regulates Depression-Related Behaviors via REDD1. *Neuropsychopharmacol.* 42, 2032–2042. doi:10.1038/npp.2016.271

Kaczmarek-Hajek, K., Zhang, J., Kopp, R., Grosche, A., Rissiek, B., Saul, A., et al. (2018). Re-Evaluation of Neuronal P2X7 Expression Using Novel Mouse Models and a P2X7-Specific Nanobody. *Elife.* 7, e36217. doi:10.7554/elife.36217

Karatas, H., Erdener, S. E., Gursoy-Ozdemir, Y., Lule, S., Eren-Koçak, E., Sen, Z. D., et al. (2013). Spreading Depression Triggers Headache by Activating Neuronal Panx1 Channels. *Science.* 339, 1092–1095. doi:10.1126/science.1231897

Karsan, N., and Goadsby, P. J. (2021). Migraine Is More Than Just Headache: Is the Link to Chronic Fatigue and Mood Disorders Simply Due to Shared Biological Systems? *Front. Hum. Neurosci.* 15, 646692. doi:10.3389/fnhum.2021.646692

Kase, D., and Imoto, K. (2012). The Role of HCN Channels on Membrane Excitability in the Nervous System. *J. Signal. Transduct.* 2012, 619747. doi:10.1155/2012/619747

Kelmendi, B., Holsbach-Beltrame, M., Mcintosh, A. M., Hilt, L., George, E. D., Kitchen, R. R., et al. (2011). Association of Polymorphisms in HCN4 with Mood Disorders and Obsessive Compulsive Disorder. *Neurosci. Lett.* 496, 195–199. doi:10.1016/j.neulet.2011.04.026

Kennard, L. E., Chumbley, J. R., Ranatunga, K. M., Armstrong, S. J., Veale, E. L., and Mathie, A. (2005). Inhibition of the Human Two-Pore Domain Potassium Channel, TREK-1, by Fluoxetine and its Metabolite Norfluoxetine. *Br. J. Pharmacol.* 144, 821–829. doi:10.1038/sj.bjp.0706068

Khakh, B. S., and North, R. A. (2006). P2X Receptors as Cell-Surface ATP Sensors in Health and Disease. *Nature.* 442, 527–532. doi:10.1038/nature04886

Kilic, K., Karatas, H., Dönmez-Demir, B., Eren-Kocak, E., Gursoy-Ozdemir, Y., Can, A., et al. (2018). Inadequate Brain Glycogen or Sleep Increases Spreading Depression Susceptibility. *Ann. Neurol.* 83, 61–73. doi:10.1002/ana.25122

Kim, C. S., Chang, P. Y., and Johnston, D. (2012). Enhancement of Dorsal Hippocampal Activity by Knockdown of HCN1 Channels Leads to Anxiolytic- and Antidepressant-like Behaviors. *Neuron.* 75, 503–516. doi:10.1016/j.neuron.2012.05.027

Kim, E. J., Lee, D. K., Hong, S. G., Han, J., and Kang, D. (2017). Activation of TREK-1, but Not TREK-2, Channel by Mood Stabilizers. *Int. J. Mol. Sci.* 18, 2460. doi:10.3390/ijms18112460

Kros, L., Lykke-Hartmann, K., and Khodakhah, K. (2018). Increased Susceptibility to Cortical Spreading Depression and Epileptiform Activity in a Mouse Model for FHM2. *Scientific Rep.* 8, 16959. doi:10.1038/s41598-018-35285-8

Langford, D. J., Bailey, A. L., Chanda, M. L., Clarke, S. E., Drummond, T. E., Echols, S., et al. (2010). Coding of Facial Expressions of Pain in the Laboratory Mouse. *Nat. Methods.* 7, 447–449. doi:10.1038/nmeth.1455

Lanquillon, S., Krieg, J. C., Bening-Abu-Shach, U., and Vedder, H. (2000). Cytokine Production and Treatment Response in Major Depressive Disorder. *Neuropsychopharmacology.* 22, 370–379. doi:10.1016/S0893-133X(99)00134-7

Leao, A. A. (1947). Further Observations on the Spreading Depression of Activity in the Cerebral Cortex. *J. Neurophysiol.* 10, 409–414. doi:10.1152/jn.1947.10.6.409

Leao, A. A. P. (1944). Spreading Depression of Activity in the Cerebral Cortex. *J. Neurophysiol.* 7, 359–390. doi:10.1152/jn.1944.7.6.359

Lebas, A., Guyant-Maréchal, L., Hannequin, D., Riant, F., Tournier-Lasserve, E., and Parain, D. (2008). Severe Attacks of Familial Hemiplegic Migraine, Childhood Epilepsy and ATP1A2 Mutation. *Cephalalgia.* 28, 774–777. doi:10.1111/j.1468-2982.2008.01603.x

Lemaire, L., Desroches, M., Krupa, M., Pizzamiglio, L., Scalmani, P., and Mantegazza, M. (2021). Modeling NaV1.1/SCN1A Sodium Channel Mutations in a Microcircuit With Realistic Ion Concentration Dynamics Suggests Differential GABAergic Mechanisms Leading to Hyperexcitability in Epilepsy and Hemiplegic Migraine. *Plos Comput. Biol.* 17, e1009239. doi:10.1371/journal.pcbi.1009239

Leo, L., Gherardini, L., Barone, V., De Fusco, M., Pietrobon, D., Pizzorusso, T., et al. (2011). Increased Susceptibility to Cortical Spreading Depression in the Mouse Model of Familial Hemiplegic Migraine Type 2. *Plos Genet.* 7, e1002129. doi:10.1371/journal.pgen.1002129

Lesage, F. (2003). Pharmacology of Neuronal Background Potassium Channels. *Neuropharmacology.* 44, 1–7. doi:10.1016/s0028-3908(02)00339-8

Levine, J., Barak, Y., Chengappa, K. N., Rapoport, A., Rebey, M., and Barak, V. (1999). Cerebrospinal Cytokine Levels in Patients With Acute Depression. *Neuropsychobiology.* 40, 171–176. doi:10.1159/000026615

Lewis, A. S., Vaidya, S. P., Blaiss, C. A., Liu, Z., Stoub, T. R., Brager, D. H., et al. (2011). Deletion of the Hyperpolarization-Activated Cyclic Nucleotide-Gated Channel Auxiliary Subunit TRIP8b Impairs Hippocampal Ih Localization and Function and Promotes Antidepressant Behavior in Mice. *J. Neurosci.* 31, 7424–7440. doi:10.1523/JNEUROSCI.0936-11.2011

Li, L., Sun, H., Ding, J., Niu, C., Su, M., Zhang, L., et al. (2017). Selective Targeting of M-type Potassium Kv 7.4 Channels Demonstrates Their Key Role in the Regulation of Dopaminergic Neuronal Excitability and Depression-Like Behaviour. *Br. J. Pharmacol.* 174, 4277–4294. doi:10.1111/bph.14026

Liou, Y. J., Chen, T. J., Tsai, S. J., Yu, Y. W., Cheng, C. Y., and Hong, C. J. (2009). Support for the Involvement of the KCNK2 Gene in Major Depressive Disorder and Response to Antidepressant Treatment. *Pharmacogenet Genomics.* 19, 735–741. doi:10.1097/FPC.0b013e32832cbe61

Liston, C., Miller, M. M., Goldwater, D. S., Radley, J. J., Rocher, A. B., Hof, P. R., et al. (2006). Stress-induced Alterations in Prefrontal Cortical Dendritic Morphology Predict Selective Impairments in Perceptual Attentional Set-Shifting. *J. Neurosci.* 26, 7870–7874. doi:10.1523/JNEUROSCI.1184-06.2006

Liu, P., Xiao, Z., Ren, F., Guo, Z., Chen, Z., Zhao, H., et al. (2013). Functional Analysis of a Migraine-Associated TRESK K+ Channel Mutation. *J. Neurosci.* 33, 12810–12824. doi:10.1523/JNEUROSCI.1237-13.2013

Lucae, S., Salyakina, D., Barden, N., Harvey, M., Gagné, B., Labbé, M., et al. (2006). P2RX7, a Gene Coding for a Purinergic Ligand-Gated Ion Channel, Is Associated with Major Depressive Disorder. *Hum. Mol. Genet.* 15, 2438–2445. doi:10.1093/hmg/ddl166

Luscher, B., Shen, Q., and Sahir, N. (2011). The GABAergic Deficit Hypothesis of Major Depressive Disorder. *Mol. Psychiatry.* 16, 383–406. doi:10.1038/mp.2010.120

Macvicar, B. A., and Thompson, R. J. (2010). Non-Junction Functions of Pannexin-1 Channels. *Trends Neurosci.* 33, 93–102. doi:10.1016/j.tins.2009.11.007

Mantegazza, M., Cestèle, S., and Catterall, W. A. (2021). Sodium Channelopathies of Skeletal Muscle and Brain. *Physiol. Rev.* 101, 1633–1689. doi:10.1152/physrev.00025.2020

Mantegazza, M. (2018). Epilepsy: Advances in Genetics and Pathophysiology. *Neurosci. Lett.* 667, 1–3. doi:10.1016/j.neulet.2017.10.026

Marcoli, M., Cervetto, C., Paluzzi, P., Guarnieri, S., Alloisio, S., Thellung, S., et al. (2008). P2X7 Pre-Synaptic Receptors in Adult Rat Cerebrocortical Nerve Terminals: a Role in ATP-Induced Glutamate Release. *J. Neurochem.* 105, 2330–2342. doi:10.1111/j.1471-4159.2008.05322.x

Marconi, R., De Fusco, M., Aridon, P., Plewnia, K., Rossi, M., Carapelli, S., et al. (2003). Familial Hemiplegic Migraine Type 2 Is Linked to 0.9Mb Region on Chromosome 1q23. *Ann. Neurol.* 53, 376–381. doi:10.1002/ana.10464

Marpegan, L., Swanstrom, A. E., Chung, K., Simon, T., Haydon, P. G., Khan, S. K., et al. (2011). Circadian Regulation of ATP Release in Astrocytes. *J. Neurosci.* 31, 8342–8350. doi:10.1523/JNEUROSCI.6537-10.2011

Mcewen, B. S. (1999). Stress and Hippocampal Plasticity. *Annu. Rev. Neurosci.* 22, 105–122. doi:10.1146/annurev.neuro.22.1.105

Mcewen, B. S. (2001). Plasticity of the hippocampus: Adaptation to Chronic Stress and Allostatic Load. *Ann. N. Y Acad. Sci.* 933, 265–277. doi:10.1111/j.1749-6632.2001.tb05830.x

Mcintosh, A. M., Simen, A. A., Evans, K. L., Hall, J., Macintyre, D. J., Blackwood, D., et al. (2012). Genetic Variation in Hyperpolarization-Activated Cyclic Nucleotide-Gated Channels and its Relationship With Neuroticism, Cognition and Risk of Depression. *Front. Genet.* 3, 116. doi:10.3389/fgene.2012.00116

Mclaughlin, K. A., Conron, K. J., Koenen, K. C., and Gilman, S. E. (2010). Childhood Adversity, Adult Stressful Life Events, and Risk of Past-Year Psychiatric Disorder: a Test of the Stress Sensitization Hypothesis in a Population-Based Sample of Adults. *Psychol. Med.* 40, 1647–1658. doi:10.1017/S0033291709992121

Mcquillin, A., Bass, N. J., Choudhury, K., Puri, V., Kosmin, M., Lawrence, J., et al. (2009). Case-Control Studies Show That a Non-Conservative Amino-Acid Change From a Glutamine to Arginine in the P2RX7 Purinergic Receptor Protein Is Associated with Both Bipolar- and Unipolar-Affective Disorders. *Mol. Psychiatry.* 14, 614–620. doi:10.1038/mp.2008.6

Metzger, M. W., Walser, S. M., Dedic, N., Aprile-Garcia, F., Jakubcakova, V., Adamczyk, M., et al. (2017). Heterozygosity for the Mood Disorder-Associated Variant Gln460Arg Alters P2X7 Receptor Function and Sleep Quality. *J. Neurosci.* 37, 11688–11700. doi:10.1523/JNEUROSCI.3487-16.2017

Milenkovic, V. M., Stanton, E. H., Nothdurfter, C., Rupprecht, R., and Wetzel, C. H. (2019). The Role of Chemokines in the Pathophysiology of Major Depressive Disorder. *Int. J. Mol. Sci.* 20, 2283. doi:10.3390/ijms20092283

Milior, G., Lecours, C., Samson, L., Bisht, K., Poggini, S., Pagani, F., et al. (2016). Fractalkine Receptor Deficiency Impairs Microglial and Neuronal Responsiveness to Chronic Stress. *Brain Behav. Immun.* 55, 114–125. doi:10.1016/j.bbi.2015.07.024

Miras-Portugal, M. T., Sebastián-Serrano, Á., de Diego García, L., and Díaz-Hernández, M. (2017). Neuronal P2X7 Receptor: Involvement in Neuronal Physiology and Pathology. *J. Neurosci.* 37, 7063–7072. doi:10.1523/JNEUROSCI.3104-16.2017

Miyamoto, A., Wake, H., Ishikawa, A. W., Eto, K., Shibata, K., Murakoshi, H., et al. (2016). Microglia Contact Induces Synapse Formation in Developing Somatosensory Cortex. *Nat. Commun.* 7, 12540. doi:10.1038/ncomms12540

Moskowitz, M. A., Bolay, H., and Dalkara, T. (2004). Deciphering Migraine Mechanisms: Clues From Familial Hemiplegic Migraine Genotypes. *Ann. Neurol.* 55, 276–280. doi:10.1002/ana.20035

Mueller, N., and Schwarz, M. J. (2007). The Immune-Mediated Alteration of Serotonin and Glutamate: towards an Integrated View of Depression. *Mol. Psychiatry.* 12, 988–1000. doi:10.1038/sj.mp.4002006

Nappi, P., Miceli, F., Soldovieri, M. V., Ambrosino, P., Barrese, V., and Taglialatela, M. (2020). Epileptic Channelopathies Caused by Neuronal Kv7 (KCNQ) Channel Dysfunction. *Pflugers Arch.* 472, 881–898. doi:10.1007/s00424-020-02404-2

Nestler, E. J., and Carlezon, W. A., Jr (2006). The Mesolimbic Dopamine Reward Circuit in Depression. *Biol. Psychiatry.* 59, 1151–1159. doi:10.1016/j.biopsych.2005.09.018

Nestler, E. J. (2015). Role of the Brain's Reward Circuitry in Depression: Transcriptional Mechanisms. *Int. Rev. Neurobiol.* 124, 151–170. doi:10.1016/bs.irn.2015.07.003

Notomi, T., and Shigemoto, R. (2004). Immunohistochemical Localization of Ih Channel Subunits, HCN1-4, in the Rat Brain. *J. Comp. Neurol.* 471, 241–276. doi:10.1002/cne.11039

Nurnberger, J. I., Jr., Koller, D. L., Jung, J., Edenberg, H. J., Foroud, T., Guella, I., et al. (2014). Identification of Pathways for Bipolar Disorder: a Meta-Analysis. *JAMA Psychiatry.* 71, 657–664. doi:10.1001/jamapsychiatry.2014.176

Nutt, D., Wilson, S., and Paterson, L. (2008). Sleep Disorders as Core Symptoms of Depression. *Dialogues Clin. Neurosci.* 10, 329–336. doi:10.31887/DCNS.2008.10.3/dnutt

Olesen, J., Lauritzen, M., Tfelt-Hansen, P., Henriksen, L., and Larsen, B. (1982). Spreading Cerebral Oligemia in Classical- and Normal Cerebral Blood Flow in Common Migraine. *Headache.* 22, 242–248. doi:10.1111/j.1526-4610.1982.hed2206242.x

Otrokocsi, L., Kittel, Á., and Sperlágh, B. (2017). P2X7 Receptors Drive Spine Synapse Plasticity in the Learned Helplessness Model of Depression. *Int. J. Neuropsychopharmacol.* 20, 813–822. doi:10.1093/ijnp/pyx046

Pace, T. W., Mletzko, T. C., Alagbe, O., Musselman, D. L., Nemeroff, C. B., Miller, A. H., et al. (2006). Increased Stress-Induced Inflammatory Responses in Male Patients with Major Depression and Increased Early Life Stress. *Am. J. Psychiatry.* 163, 1630–1633. doi:10.1176/ajp.2006.163.9.1630

Pankratov, Y. V., Lalo, U. V., and Krishtal, O. A. (2002). Role for P2X Receptors in Long-Term Potentiation. *J. Neurosci.* 22, 8363–8369. doi:10.1523/jneurosci.22-19-08363.2002

Paolicelli, R. C., Bolasco, G., Pagani, F., Maggi, L., Scianni, M., Panzanelli, P., et al. (2011). Synaptic Pruning by Microglia Is Necessary for normal Brain Development. *Science.* 333, 1456–1458. doi:10.1126/science.1202529

Papp, L., Vizi, E. S., and Sperlágh, B. (2004). Lack of ATP-Evoked GABA and Glutamate Release in the hippocampus of P2X7 Receptor-/- Mice. *Neuroreport.* 15, 2387–2391. doi:10.1097/00001756-200410250-00017

Parker, P. D., Suryavanshi, P., Melone, M., Sawant-Pokam, P. A., Reinhart, K. M., Kaufmann, D., et al. (2021). Non-canonical Glutamate Signaling in a Genetic Model of Migraine with Aura. *Neuron.* 109, 611–628. doi:10.1016/j.neuron.2020.11.018

Parker, T., Keddie, S., Kidd, D., Lane, T., Maviki, M., Hawkins, P. N., et al. (2016). Neurology of the Cryopyrin-Associated Periodic Fever Syndrome. *Eur. J. Neurol.* 23, 1145–1151. doi:10.1111/ene.12965

Parpura, V., Basarsky, T. A., Liu, F., Jeftinija, K., Jeftinija, S., and Haydon, P. G. (1994). Glutamate-mediated Astrocyte-Neuron Signalling. *Nature.* 369, 744–747. doi:10.1038/369744a0

Perlis, R. H., Moorjani, P., Fagerness, J., Purcell, S., Trivedi, M. H., Fava, M., et al. (2008). Pharmacogenetic Analysis of Genes Implicated in Rodent Models of Antidepressant Response: Association of TREK1 and Treatment Resistance in the STAR*D Study. *Neuropsychopharmacol.* 33, 2810–2819. doi:10.1038/npp.2008.6

Petit, J. M., Eren-Koçak, E., Karatas, H., Magistretti, P., and Dalkara, T. (2021). Brain Glycogen Metabolism: A Possible Link Between Sleep Disturbances, Headache and Depression. *Sleep Med. Rev.* 59, 101449. doi:10.1016/j.smrv.2021.101449

Petit, J. M., and Magistretti, P. J. (2016). Regulation of Neuron-Astrocyte Metabolic Coupling Across the Sleep-Wake Cycle. *Neuroscience.* 323, 135–156. doi:10.1016/j.neuroscience.2015.12.007

Pettingill, P., Weir, G. A., Wei, T., Wu, Y., Flower, G., Lalic, T., et al. (2019). A Causal Role for TRESK Loss of Function in Migraine Mechanisms. *Brain.* 142, 3852–3867. doi:10.1093/brain/awz342

Pietrobon, D., and Brennan, K. C. (2019). Genetic Mouse Models of Migraine. *J. Headache Pain.* 20, 79. doi:10.1186/s10194-019-1029-5

Pietrobon, D., and Moskowitz, M. A. (2014). Chaos and Commotion in the Wake of Cortical Spreading Depression and Spreading Depolarizations. *Nat. Rev. Neurosci.* 15, 379–393. doi:10.1038/nrn3770

Psychiatric, G. C. B. D. W. G. (2011). Large-scale Genome-wide Association Analysis of Bipolar Disorder Identifies a New Susceptibility Locus Near ODZ4. *Nat. Genet.* 43, 977–983. doi:10.1038/ng.943

Radley, J. J., Rocher, A. B., Miller, M., Janssen, W. G., Liston, C., Hof, P. R., et al. (2006). Repeated Stress Induces Dendritic Spine Loss in the Rat Medial Prefrontal Cortex. *Cereb. Cortex.* 16, 313–320. doi:10.1093/cercor/bhi104

Ren, J., Guo, J., Zhu, S., Wang, Q., Gao, R., Zhao, C., et al. (2021). The Role of Potassium Channels in Chronic Stress-Induced Brain Injury. *Biol. Pharm. Bull.* 44, 169–180. doi:10.1248/bpb.b20-00504

Reyes, R., Duprat, F., Lesage, F., Fink, M., Salinas, M., Farman, N., et al. (1998). Cloning and Expression of a Novel pH-Sensitive Two Pore Domain K+ Channel From Human Kidney. *J. Biol. Chem.* 273, 30863–30869. doi:10.1074/jbc.273.47.30863

Richards, E. M., Zanotti-Fregonara, P., Fujita, M., Newman, L., Farmer, C., Ballard, E. D., et al. (2018). PET Radioligand Binding to Translocator Protein (TSPO) Is Increased in Unmedicated Depressed Subjects. *Ejnmmi Res.* 8, 57. doi:10.1186/s13550-018-0401-9

Rivolta, I., Binda, A., Masi, A., and Difrancesco, J. C. (2020). Cardiac and Neuronal HCN Channelopathies. *Pflugers Arch.* 472, 931–951. doi:10.1007/s00424-020-02384-3

Royal, P., Andres-Bilbe, A., Ávalos Prado, P., Verkest, C., Wdziekonski, B., Schaub, S., et al. (2019). Migraine-Associated TRESK Mutations Increase Neuronal Excitability Through Alternative Translation Initiation and Inhibition of TREK.. *Neuron.* 101, 232–e6. doi:10.1016/j.neuron.2018.11.039

Russell, M. B., and Ducros, A. (2011). Sporadic and Familial Hemiplegic Migraine: Pathophysiological Mechanisms, Clinical Characteristics, Diagnosis, and Management. *Lancet Neurol.* 10, 457–470. doi:10.1016/S1474-4422(11)70048-5

Russo, S. J., and Nestler, E. J. (2013). The Brain Reward Circuitry in Mood Disorders. *Nat. Rev. Neurosci.* 14, 609–625. doi:10.1038/nrn3381

Savtchouk, I., and Volterra, A. (2018). Gliotransmission: Beyond Black-And-White. *J. Neurosci.* 38, 14–25. doi:10.1523/JNEUROSCI.0017-17.2017

Setiawan, E., Wilson, A. A., Mizrahi, R., Rusjan, P. M., Miler, L., Rajkowska, G., et al. (2015). Role of Translocator Protein Density, a Marker of Neuroinflammation, in the Brain During Major Depressive Episodes. *JAMA Psychiatry.* 72, 268–275. doi:10.1001/jamapsychiatry.2014.2427

Sperlágh, B., Köfalvi, A., Deuchars, J., Atkinson, L., Milligan, C. J., Buckley, N. J., et al. (2002). Involvement of P2X7 Receptors in the Regulation of Neurotransmitter Release in the Rat hippocampus. *J. Neurochem.* 81, 1196–1211. doi:10.1046/j.1471-4159.2002.00920.x

Stahl, S. M. (2004). Anticonvulsants as Mood Stabilizers and Adjuncts to Antipsychotics: Valproate, Lamotrigine, Carbamazepine, and Oxcarbazepine and Actions at Voltage-Gated Sodium Channels. *J. Clin. Psychiatry.* 65, 738–739. doi:10.4088/jcp.v65n0601

Suryavanshi, P., Pokam, P. S., and Brennan, K. C. (2019). *Altered Synaptic Adaptation and Gain in Sensory Circuits of the Casein Kinase 1 delta (CK1d$_{T44A}$) Mouse Model of Migraine.* bioRxiv

Sutherland, H. G., Albury, C. L., and Griffiths, L. R. (2019). Advances in Genetics of Migraine. *J. Headache Pain.* 20, 72. doi:10.1186/s10194-019-1017-9

Sutherland, H. G., Maksemous, N., Albury, C. L., Ibrahim, O., Smith, R. A., Lea, R. A., et al. (2020). Comprehensive Exonic Sequencing of Hemiplegic Migraine-Related Genes in a Cohort of Suspected Probands Identifies Known and Potential Pathogenic Variants. *Cells.* 9, 2368. doi:10.3390/cells9112368

Takizawa, T., Ayata, C., and Chen, S. P. (2020a). Therapeutic Implications of Cortical Spreading Depression Models in Migraine. *Prog. Brain Res.* 255, 29–67. doi:10.1016/bs.pbr.2020.05.009

Takizawa, T., Qin, T., Lopes De Morais, A., Sugimoto, K., Chung, J. Y., Morsett, L., et al. (2020b). Non-Invasively Triggered Spreading Depolarizations Induce a Rapid Pro-Inflammatory Response in Cerebral Cortex. *J. Cereb. Blood Flow Metab.* 40, 1117–1131. doi:10.1177/0271678X19859381

Takizawa, T., Shibata, M., Kayama, Y., Shimizu, T., Toriumi, H., Ebine, T., et al. (2017). High-Mobility Group Box 1 Is an Important Mediator of Microglial Activation Induced by Cortical Spreading Depression. *J. Cereb. Blood Flow Metab.* 37, 890–901. doi:10.1177/0271678X16647398

Takizawa, T., Shibata, M., Kayama, Y., Toriumi, H., Ebine, T., Koh, A., et al. (2016). Temporal Profiles of High-Mobility Group Box 1 Expression Levels after Cortical Spreading Depression in Mice. *Cephalalgia.* 36, 44–52. doi:10.1177/0333102415580100

Talley, E. M., Sirois, J. E., Lei, Q., and Bayliss, D. A. (2003). Two-Pore-Domain (KCNK) Potassium Channels: Dynamic Roles in Neuronal Function. *Neuroscientist.* 9, 46–56. doi:10.1177/1073858402239590

Tan, A., Costi, S., Morris, L. S., Van Dam, N. T., Kautz, M., Whitton, A. E., et al. (2020). Effects of the KCNQ Channel Opener Ezogabine on Functional Connectivity of the Ventral Striatum and Clinical Symptoms in Patients With Major Depressive Disorder. *Mol. Psychiatry.* 25, 1323–1333. doi:10.1038/s41380-018-0283-2

Tang, Y. T., Mendez, J. M., Theriot, J. J., Sawant, P. M., López-Valdés, H. E., Ju, Y. S., et al. (2014). Minimum Conditions for the Induction of Cortical Spreading Depression in Brain Slices. *J. Neurophysiol.* 112, 2572–2579. doi:10.1152/jn.00205.2014

Terrillion, C. E., Francis, T. C., Puche, A. C., Lobo, M. K., and Gould, T. D. (2017). Decreased Nucleus Accumbens Expression of Psychiatric Disorder Risk Gene Cacna1c Promotes Susceptibility to Social Stress. *Int. J. Neuropsychopharmacol.* 20, 428–433. doi:10.1093/ijnp/pyw112

Tottene, A., Conti, R., Fabbro, A., Vecchia, D., Shapovalova, M., Santello, M., et al. (2009). Enhanced Excitatory Transmission at Cortical Synapses as the Basis for Facilitated Spreading Depression in Ca(v)2.1 Knockin Migraine Mice. *Neuron.* 61, 762–773. doi:10.1016/j.neuron.2009.01.027

Tottene, A., Favero, M., and Pietrobon, D. (2019). Enhanced Thalamocortical Synaptic Transmission and Dysregulation of the Excitatory-Inhibitory Balance at the Thalamocortical Feedforward Inhibitory Microcircuit in a Genetic Mouse Model of Migraine. *J. Neurosci.* 39, 9841–9851. doi:10.1523/JNEUROSCI.1840-19.2019

Van Den Maagdenberg, A. M., Pietrobon, D., Pizzorusso, T., Kaja, S., Broos, L. A., Cesetti, T., et al. (2004). A Cacna1a Knockin Migraine Mouse Model With Increased Susceptibility to Cortical Spreading Depression. *Neuron.* 41, 701–710. doi:10.1016/s0896-6273(04)00085-6

Van Den Maagdenberg, A. M., Pizzorusso, T., Kaja, S., Terpolilli, N., Shapovalova, M., Hoebeek, F. E., et al. (2010). High Cortical Spreading Depression Susceptibility and Migraine-Associated Symptoms in Ca(V)2.1 S218L Mice. *Ann. Neurol.* 67, 85–98. doi:10.1002/ana.21815

Vecchia, D., and Pietrobon, D. (2012). Migraine: a Disorder of Brain Excitatory-Inhibitory Balance? *Trends Neurosci.* 35, 507–520. doi:10.1016/j.tins.2012.04.007

Vecchia, D., Tottene, A., Van Den Maagdenberg, A. M., and Pietrobon, D. (2014). Mechanism Underlying Unaltered Cortical Inhibitory Synaptic Transmission in Contrast With Enhanced Excitatory Transmission in CaV2.1 Knockin Migraine Mice. *Neurobiol. Dis.* 69, 225–234. doi:10.1016/j.nbd.2014.05.035

Vereczkei, A., Abdul-Rahman, O., Halmai, Z., Nagy, G., Szekely, A., Somogyi, A., et al. (2019). Association of Purinergic Receptor P2RX7 Gene Polymorphisms

With Depression Symptoms. *Prog. Neuropsychopharmacol. Biol. Psychiatry.* 92, 207–216. doi:10.1016/j.pnpbp.2019.01.006

Vyas, A., Bernal, S., and Chattarji, S. (2003). Effects of Chronic Stress on Dendritic Arborization in the Central and Extended Amygdala. *Brain Res.* 965, 290–294. doi:10.1016/s0006-8993(02)04162-8

Weinhard, L., Di Bartolomei, G., Bolasco, G., Machado, P., Schieber, N. L., Neniskyte, U., et al. (2018). Microglia Remodel Synapses by Presynaptic Trogocytosis and Spine Head Filopodia Induction. *Nat. Commun.* 9, 1228. doi:10.1038/s41467-018-03566-5

Whyte-Fagundes, P., and Zoidl, G. (2018). Mechanisms of Pannexin1 Channel Gating and Regulation. *Biochim. Biophys. Acta Biomembr.* 1860, 65–71. doi:10.1016/j.bbamem.2017.07.009

Wohleb, E. S., Franklin, T., Iwata, M., and Duman, R. S. (2016). Integrating Neuroimmune Systems in the Neurobiology of Depression. *Nat. Rev. Neurosci.* 17, 497–511. doi:10.1038/nrn.2016.69

Wohleb, E. S., Terwilliger, R., Duman, C. H., and Duman, R. S. (2018). Stress-Induced Neuronal Colony Stimulating Factor 1 Provokes Microglia-Mediated Neuronal Remodeling and Depressive-like Behavior. *Biol. Psychiatry.* 83, 38–49. doi:10.1016/j.biopsych.2017.05.026

Ye, D., Li, Y., Zhang, X., Guo, F., Geng, L., Zhang, Q., et al. (2015). TREK1 Channel Blockade Induces an Antidepressant-Like Response Synergizing With 5-HT1A Receptor Signaling. *Eur. Neuropsychopharmacol.* 25, 2426–2436. doi:10.1016/j.euroneuro.2015.09.007

Yeung, A. K., Patil, C. S., and Jackson, M. F. (2020). Pannexin-1 in the CNS: Emerging Concepts in Health and Disease. *J. Neurochem.* 154, 468–485. doi:10.1111/jnc.15004

Yue, N., Huang, H., Zhu, X., Han, Q., Wang, Y., Li, B., et al. (2017). Activation of P2X7 Receptor and NLRP3 Inflammasome Assembly in Hippocampal Glial Cells Mediates Chronic Stress-Induced Depressive-Like Behaviors. *J. Neuroinflammation.* 14, 102. doi:10.1186/s12974-017-0865-y

Zhan, Y., Paolicelli, R. C., Sforazzini, F., Weinhard, L., Bolasco, G., Pagani, F., et al. (2014). Deficient Neuron-Microglia Signaling Results in Impaired Functional Brain Connectivity and Social Behavior. *Nat. Neurosci.* 17, 400–406. doi:10.1038/nn.3641

Zhong, P., Vickstrom, C. R., Liu, X., Hu, Y., Yu, L., Yu, H. G., et al. (2018). HCN2 Channels in the Ventral Tegmental Area Regulate Behavioral Responses to Chronic Stress. *Elife.* 7, e32420. doi:10.7554/elife.32420

Conflict of Interest: The authors declare that the research was conducted in the absence of any commercial or financial relationships that could be construed as a potential conflict of interest.

Publisher's Note: All claims expressed in this article are solely those of the authors and do not necessarily represent those of their affiliated organizations, or those of the publisher, the editors and the reviewers. Any product that may be evaluated in this article, or claim that may be made by its manufacturer, is not guaranteed or endorsed by the publisher.

Copyright © 2021 Eren-Koçak and Dalkara. This is an open-access article distributed under the terms of the Creative Commons Attribution License (CC BY). The use, distribution or reproduction in other forums is permitted, provided the original author(s) and the copyright owner(s) are credited and that the original publication in this journal is cited, in accordance with accepted academic practice. No use, distribution or reproduction is permitted which does not comply with these terms.

frontiers
in Pharmacology

ORIGINAL RESEARCH
published: 07 December 2021
doi: 10.3389/fphar.2021.775040

Screening for Activity Against AMPA Receptors Among Anticonvulsants—Focus on Phenytoin

M. Y. Dron, A. S. Zhigulin, D. B. Tikhonov* and O. I. Barygin

I.M. Sechenov Institute of Evolutionary Physiology and Biochemistry RAS, Saint-Petersburg, Russia

The interest in AMPA receptors as a target for epilepsy treatment increased substantially after the approval of perampanel, a negative AMPA receptor allosteric antagonist, for the treatment of partial-onset seizures and generalized tonic-clonic seizures. Here we performed a screening for activity against native calcium-permeable AMPA receptors (CP-AMPARs) and calcium-impermeable AMPA receptors (CI-AMPARs) among different anticonvulsants using the whole-cell patch-clamp method on isolated Wistar rat brain neurons. Lamotrigine, topiramate, levetiracetam, felbamate, carbamazepine, tiagabin, vigabatrin, zonisamide, and gabapentin in 100-μM concentration were practically inactive against both major subtypes of AMPARs, while phenytoin reversibly inhibited them with IC50 of 30 ± 4 μM and 250 ± 60 μM for CI-AMPARs and CP-AMPARs, respectively. The action of phenytoin on CI-AMPARs was attenuated in experiments with high agonist concentrations, in the presence of cyclothiazide and at pH 9.0. Features of phenytoin action matched those of the CI-AMPARs pore blocker pentobarbital, being different from classical competitive inhibitors, negative allosteric inhibitors, and CP-AMPARs selective channel blockers. Close 3D similarity between phenytoin and pentobarbital also suggests a common binding site in the pore and mechanism of inhibition. The main target for phenytoin in the brain, which is believed to underlie its anticonvulsant properties, are voltage-gated sodium channels. Here we have shown for the first time that phenytoin inhibits CI-AMPARs with similar potency. Thus, AMPAR inhibition by phenytoin may contribute to its anticonvulsant properties as well as its side effects.

Keywords: AMPA receptor, pharmacological modulation, patch–clamp technique, screening, anticonvulsants, phenytoin

OPEN ACCESS

Edited by:
Jacques Joubert,
University of the Western Cape, South Africa

Reviewed by:
Scott Nawy,
University of California, Berkeley, United States
Alexander I. Sobolevsky,
Columbia University Irving Medical Center, United States

***Correspondence:**
D. B. Tikhonov
denistikhonov2002@yahoo.com

Specialty section:
This article was submitted to Pharmacology of Ion Channels and Channelopathies,
a section of the journal Frontiers in Pharmacology

Received: *13 September 2021*
Accepted: *20 October 2021*
Published: *07 December 2021*

Citation:
Dron MY, Zhigulin AS, Tikhonov DB and Barygin OI (2021) Screening for Activity Against AMPA Receptors Among Anticonvulsants—Focus on Phenytoin.
Front. Pharmacol. 12:775040.
doi: 10.3389/fphar.2021.775040

INTRODUCTION

Epilepsies are among the most common chronic brain disorders (Scharfman, 2007). They affect 0.5–1% of people around the world (Sirven, 2015). Despite the constant development of new antiseizure drugs during the last decades (Rho and White, 2018), 20–30% patients cannot control seizures even with modern medications. Thus, the search for new anticonvulsant drugs and detailed

---

Abbreviations: AMPA, α-amino-3-hydroxy-5-methyl-4-isoxazolepropionic acid; CP-AMPARs, calcium-permeable AMPA receptors; CI-AMPARs, calcium-impermeable AMPA receptors.

understanding of the mechanisms of action of older ones are extremely important for effective selection of therapy for each patient. Seizures may produce neurodegeneration within the brain, and different antiseizure drugs have different potential to prevent it (Miziak et al., 2020).

According to a recent review by Sills and Rogawski (2020), there are four major classes of antiseizure drug mechanisms: 1) modulation of voltage-gated ion channels; 2) enhancement of GABA-mediated inhibitory neurotransmission; 3) attenuation of glutamate-mediated excitatory neurotransmission; and 4) modulation of neurotransmitter release via a presynaptic action. Combining two or more of these mechanisms in one drug can be beneficial for seizure control.

Approval of perampanel—a negative allosteric AMPA receptor antagonist—enhanced the interest in testing whether older antiseizure drugs can affect AMPA receptors (Fukushima et al., 2020). Indeed, several other anticonvulsants were shown to affect AMPA receptors. Lamotrigine inhibited postsynaptic AMPA receptors and glutamate release in the dentate gyrus (Lee et al., 2008); however, 30 and 100 μM lamotrigine decreased the amplitude of the currents induced by exogenously applied AMPA by 10% only (Lee et al., 2008). Topiramate concentrations of 30 and 100 μM inhibited AMPA and kainate-evoked Ca^{2+} uptake in cultured cerebral cortical, hippocampal, and cerebellar neurons by up to 60% (Poulsen et al., 2004). But the effect of topiramate on AMPA receptors might be indirect (Gibbs et al., 2000; Angehagen et al., 2004). Levetiracetam (200 μM) decreased the amplitude of kainate-induced current in cultured cortical neurons by about 26% (Carunchio et al., 2007). Finally, phenytoin inhibited non-NMDA glutamate receptors expressed in *Xenopus* oocytes (Kawano et al., 1994) and in neocortical wedges (Phillips et al., 1997) with IC50 values ≥100 μM. These data attract attention to AMPA receptors as a potential target for different antiseizure drugs, but it is not clear whether AMPA receptor inhibition can contribute to their therapeutic and side effects. Thus, we decided to perform a broad screening for activity against AMPARs among these and some other antiepileptic agents.

Two major subtypes of AMPARs—calcium-permeable (CP-AMPARs) and calcium-impermeable (CI-AMPARs)—play different roles in maintaining the excitation–inhibition balance in the brain. CP-AMPARs are usually localized in GABA-ergic interneurons, whereas principal cells in many brain structures contain CI-AMPARs (Buldakova et al., 1999; Samoilova et al., 1999). Selective blocking of CP-AMPARs may cause disinhibition and further shift the excitation–inhibition balance toward excitation. On the other hand, CP-AMPARs are transiently upregulated in many epilepsy models (Rajasekaran et al., 2012; Joshi et al., 2017; Amakhin et al., 2018), and their block in this context may be beneficial. Different AMPA receptor antagonists differentially affect two main classes of AMPA receptors: calcium-permeable and calcium-impermeable. For instance, many polyamine toxins and dicationic adamantane and phenylcyclohexyl derivatives (Magazanik et al., 1997; Mellor and Usherwood, 2004; Bolshakov et al., 2005) are more active against calcium-permeable class, while pentobarbital is more selective against calcium-impermeable AMPA receptors (Taverna et al., 1994; Yamakura et al., 1995). In contrast, perampanel equipotently inhibits CP- and CI-AMPARs (Barygin, 2016; Fukushima et al., 2020). Thus, we decided to compare the action of antiseizure drugs on calcium-permeable and calcium-impermeable AMPA receptors.

In our experiments, lamotrigine, topiramate, levetiracetam, felbamate, carbamazepine, tiagabin, vigabatrin, zonisamide, and gabapentin did not demonstrate strong activity against CP- and CI-AMPARs indicating that these receptors do not play a significant role in their pharmacological profile. In contrast, phenytoin inhibited both major AMPA receptor subtypes, being much more active against CI-AMPARs (IC50 = 30 ± 4 μM) than against CP-AMPARs (250 ± 60 μM). The main target for phenytoin in the brain, which is believed to underlie its anticonvulsant properties, are voltage-gated sodium channels. Affinity of phenytoin to inactivated states of sodium channels is in the range of 7–21 μM (Kuo and Bean, 1994; Lenkowski et al., 2007). Thus, affinity of phenytoin to CI-AMPARs is only slightly lower than affinity to its primary target. Analysis of molecular mechanisms of action of phenytoin on AMPARs demonstrated close similarity with those of pentobarbital. The hypothesis about a common site is further supported by 3D similarity between these two compounds. Our data suggest that inhibition of CI-AMPARs is essential for phenytoin anticonvulsant effects.

MATERIALS AND METHODS

All experimental procedures were approved by the Animal Care and Use Committee of the I.M. Sechenov Institute of Evolutionary Physiology and Biochemistry of the Russian Academy of Sciences. Wistar rats (13–19 days old) were anesthetized with sevoflurane and then decapitated. Maximum effort was made to minimize the number of animals used. Brains were removed quickly and cooled to 2–4°C in an ice bath. Transverse hippocampal and striatal slices (250 μm thick) were prepared using a vibratome (Campden Instruments Ltd, Loughborough, United Kingdom) and stored in a solution containing (in mM) 124 NaCl, 5 KCl, 1.3 $CaCl_2$, 2.0 $MgCl_2$, 26 $NaHCO_3$, 1.24 NaH_2PO_4, and 10 D-glucose, aerated with carbogen (95% O_2, 5% CO_2). Single neurons were freed from slices by vibrodissociation (Vorobjev, 1991). The antagonism of CP-AMPARs was studied on striatal giant interneurons (Bernard et al., 1997; Gotz et al., 1997), which were identified by their shape and size. They have large (>25 μm) soma of polygonal shape, whereas principal cells are significantly smaller and nearly spherical. Previous works demonstrated that a nondesensitizing response to kainate in these neurons is mediated by GluA2-lacking AMPARs. The sensitivity to dicationic blockers like IEM-1460, IEM-1925, and polycationic toxins agrees with the data on recombinant receptors (Bolshakov et al., 2005; Barygin et al., 2011) The currents demonstrate inward rectification and significant Ca^{2+} permeability (Buldakova et al., 1999; Samoilova et al., 1999). The antagonism of CI-AMPARs was studied on pyramidal neurons from the CA1 area of the hippocampus. Kainate-induced currents in these neurons are

TABLE 1 | Action of anticonvulsants on CP- and CI-AMPARs

Anticonvulsant	CP-AMPARs% inhibition at 100 μM	CI-AMPARs% inhibition at 100 μM
Lamotrigine	13 ± 3	14 ± 5
Topiramate	14 ± 2	12 ± 2
Levetiracetam	9 ± 3	6 ± 2
Felbamate	10 ± 4	16 ± 4
Carbamazepine	15 ± 4	11 ± 3
Tiagabin	10 ± 2	14 ± 2
Vigabatrin	10 ± 3	8 ± 1
Zonisamide	11 ± 3	11 ± 2
Gabapentin	12 ± 5	20 ± 6

N = 5 for each compound both against CP-AMPARs and CI-AMPARs. The effect of all compounds on CP-AMPARs and CI-AMPARs was significant ($p < 0.05$*, paired t test).*

virtually insensitive to cationic blockers (Magazanik et al., 1997; Bolshakov et al., 2005).

The whole-cell patch-clamp technique was used for recording of membrane currents generated in response to applications of kainate. Series resistance of about 20 MΩ was compensated by 70–80% and monitored during experiments. Currents were recorded using an EPC-8 amplifier (HEKA Electronics, Lambrecht, Germany), filtered at 5 kHz, sampled, and stored on a personal computer. Drugs were applied using the RSC-200 perfusion system (BioLogic Science Instruments, Claix, France) under computer control. The solution exchange time in the whole-cell mode was 50–60 ms. The extracellular solution contained (in mM) NaCl 143, KCl 5, $MgCl_2$ 2.0, $CaCl_2$ 2.5, D-glucose 18, and HEPES 10 (pH was adjusted to 7.3 with HCl). The pipette solution contained (in mM) CsF 100, CsCl 40, NaCl 5, $CaCl_2$ 0.5, EGTA 5, and HEPES 10 (pH was adjusted to 7.2 with CsOH). Experiments were performed at room temperature (22–24°C). Phenytoin sodium (PHR1492) was purchased from Sigma (St Louis, MO, United States), as well as hydantoin, 5-benzylhydantoin, primidone, and ethosuximide. Lamotrigine, topiramate, levetiracetam, felbamate, carbamazepine, tiagabin, vigabatrin, zonisamide, and gabapentin were purchased from Tocris Bioscience (Bristol, United Kingdom). Perampanel was from MedChemExpress (Stockholm, Sweden). Kinetics of transient processes of more than 20-ms duration was approximated by exponential functions. Experiments were performed at −80 mV holding voltage. All experimental data are presented as mean ± SD estimated from at least four experiments. Significance of the effects was tested with paired *t* test. Differences were considered significant at $p < 0.05$. 3D structures of compounds were calculated by the ZMM software (zmmsoft.ca).

RESULTS

Screening for Activity Against AMPA Receptors Among Anticonvulsants

Application of 100 μM kainate on isolated hippocampal CA1 pyramidal neurons (CI-AMPARs) and giant striatal interneurons (CP-AMPARs) induced weakly or nondesensitizing inward currents. We initially checked if these kainate-induced currents will be inhibited by different anticonvulsants at 100-μM concentrations. In our experiments, lamotrigine, topiramate, levetiracetam, felbamate, carbamazepine, tiagabin, vigabatrin, zonisamide, and gabapentin were practically inactive (inhibition ≤20%, **Table 1**) against both CP-AMPARs and CI-AMPARs. These data agree well with the results of Fukushima et al. (2020), who also did not find significant activity of different anticonvulsants (topiramate, phenobarbital, lamotrigine, gabapentin, carbamazepine, valproate, levetiracetam, and lacosamide), except perampanel, against hGluA1-4 receptors. In contrast, phenytoin reversibly inhibited both CP-AMPARs and CI-AMPARs in our experiments, and we decided to study its molecular mechanisms of action in more detail. Fukushima et al. (2020) did not test phenytoin in their paper.

Concentration Dependence of Action of Phenytoin on Calcium-Impermeable and Calcium-Permeable AMPARs

Representative recordings demonstrating the action of different phenytoin concentrations on CI-AMPARs of hippocampal pyramidal neurons and CP-AMPARs of striatal giant interneurons are shown (**Figures 1A,B**). At the highest concentration tested—500 μM—phenytoin demonstrated almost complete inhibition of kainate-induced currents in hippocampal pyramidal neurons and only 58 ± 5% inhibition in striatal giant interneurons. Because of the poor solubility of phenytoin in the extracellular solution, we were not able to test higher concentrations. The IC50 value for CI-AMPARs obtained using the Hill equation was 30 ± 4 μM, and the Hill coefficient was 0.9 ± 0.2. For CP-AMPARs, approximation by the Hill equation gave IC50 value = 250 ± 60 μM and Hill coefficient = 0.7 ± 0.2 (**Figure 1C**). Thus, we have shown for the first time that phenytoin is more active against CI-AMPARs. Among known AMPAR antagonists, similar preference for CI-AMPARs demonstrated pentobarbital (Taverna et al., 1994; Yamakura et al., 1995; Jackson et al., 2003). So we decided to compare its activity in experiments on hippocampal CA1 pyramidal neurons and giant striatal interneurons (**Figure 1C**). Indeed, in our

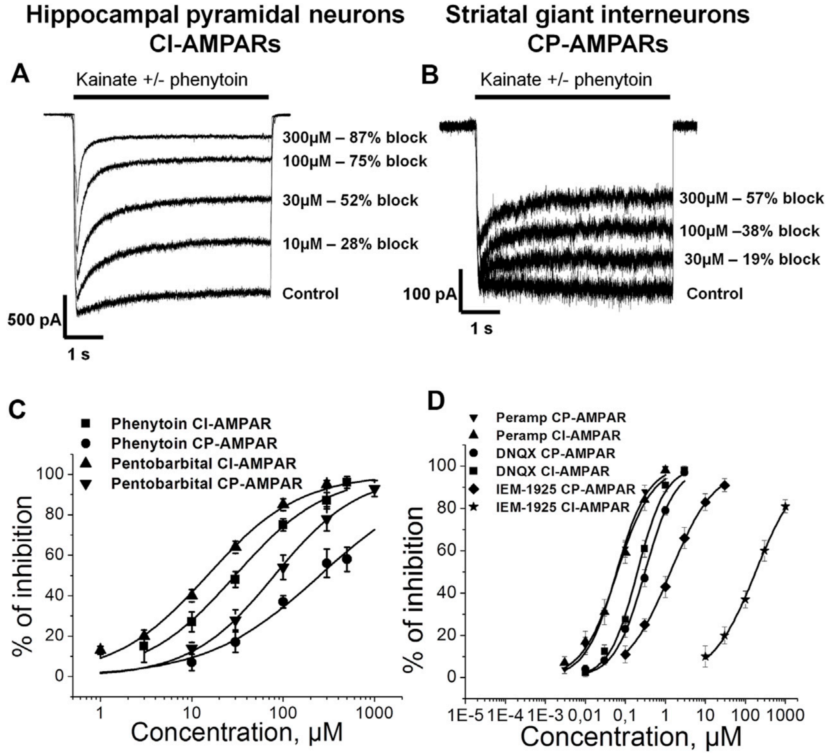

FIGURE 1 | Concentration dependence of action of phenytoin on calcium-impermeable and calcium-permeable AMPARs. **(A,B)** Representative examples of CI-AMPARs **(A)** and CP-AMPARs **(B)** inhibition by different concentrations of phenytoin. **(C,D)** Concentration-inhibition curves for phenytoin, pentobarbital **(C)**, and major AMPARs antagonists **(D)**.

TABLE 2 | Characteristic features of AMPAR inhibition by different antagonists

Compound/Feature	Phenytoin	DNQX	Perampanel	IEM-1925	Pentobarbital
More active against CI-AMPARs	Yes	Yes	No	No	Yes
IC50 CI-AMPARs	30 ± 4 M	0.20 ± 0.03 µM	63 ± 8 nM	180 ± 30 µM	14 ± 3 µM
IC50 CP-AMPARs	250 ± 60 µM	0.31 ± 0.06 µM	60 ± 6 nM	1.3 ± 0.4 µM	80 ± 13 µM
Activity drop at high (500 µM) kainate concentration	Yes	Yes	Yes	No	Yes
Activity drop in the presence of cyclothiazide	Yes	Yes	Yes	N.D.	Yes
Trap in kainate 100 µM	Yes	N.D.	No	Yes	Yes
Trap in kainate 500 µM	?	N.D.	No	Yes	N.D.
Competition with phenytoin for binding site	Not applicable	No	No	N.D.	N.D.
Difference in the % of inhibition in coapplication and preapplication protocols	Yes	N.D.	No	Yes	Yes
pH-dependence	Yes	Yes[a]	N.D.	N.D.	Yes

[a] *Dudic and Reiner, 2019.*

experiments, the IC50 values for pentobarbital were 14 ± 3 and 80 ± 13 µM for CI-AMPARs and CP-AMPARs, respectively. **Figure 1D** illustrates concentration dependencies of action of representatives of three major types of AMPARs antagonists—competitive antagonist DNQX (Honore et al., 1988), negative allosteric antagonist perampanel (Hanada et al., 2011; Chen et al., 2014), and use and voltage-dependent channel blocker IEM-1925—on CI- and CP-AMPARs. DNQX was slightly more active against hippocampal CI-AMPARs, perampanel equipotently inhibited both receptor subtypes (Barygin, 2016), and IEM-1925 was dramatically more active against CP-AMPARs. The IC50 values are provided in **Table 2**.

Action of Compounds Structurally Related to Phenytoin on CI-AMPARs

Phenytoin is a diphenyl derivative of hydantoin. So we decided to test whether hydantoin itself or 5-benzylhydantoin will be able to inhibit CI-AMPARs. Both compounds demonstrated only weak activity even at high 300-µM concentration (**Figures 2A,B**). Primidone and ethosuximide—two anticonvulsant compounds

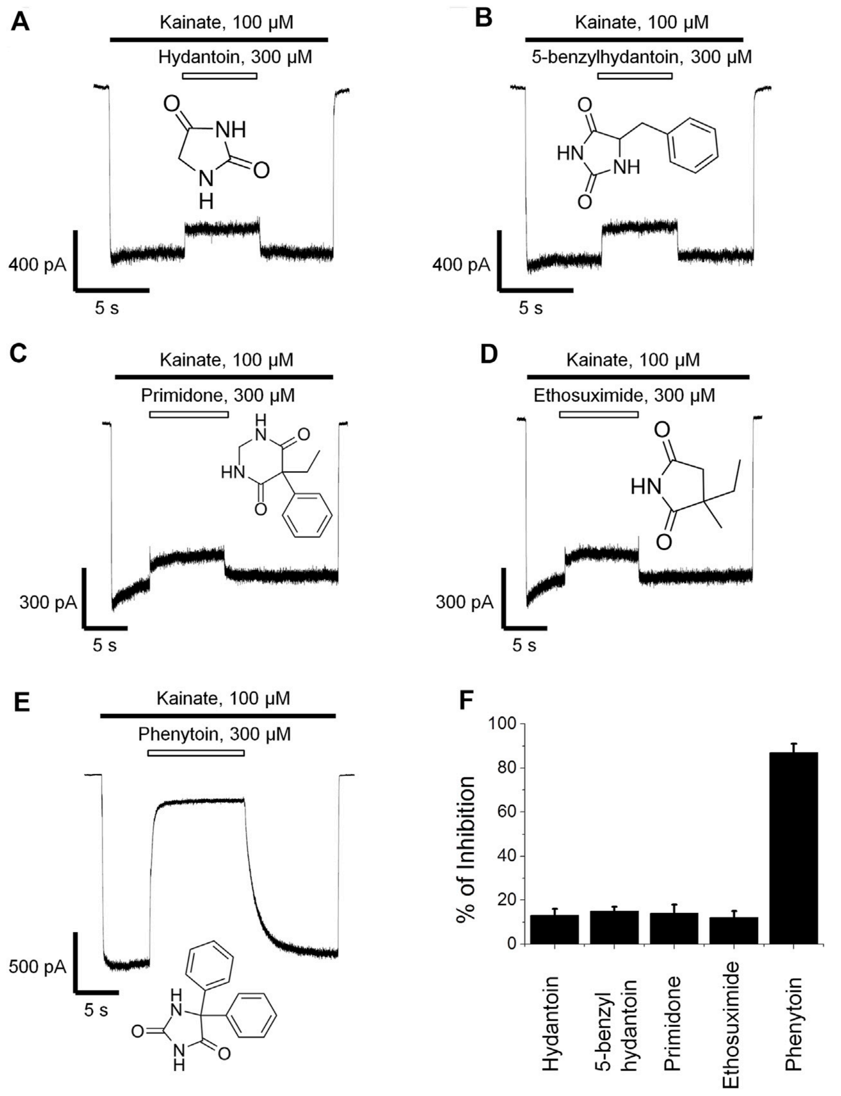

FIGURE 2 | Action of compounds structurally related to phenytoin on CI-AMPARs. Representative examples of weak inhibition by 300 μM hydantoin **(A)**, 5-benzylhydantoin **(B)**, primidone **(C)**, and ethosuximide **(D)** and strong inhibition by 300 μM phenytoin **(E)**. **(F)** Summarized results of AMPARs inhibition by these compounds at 300-μM concentrations.

structurally related to phenytoin—were only weakly active as well (**Figures 2C,D**). The percentage of inhibition by hydantoin, 5-benzylhydantoin, primidone, and ethosuximide at 300-μM concentration did not exceed 20%. A representative example of strong (≥80%) inhibition by 300 μM phenytoin is provided for comparison (**Figure 2E**). The inhibitory action of compounds is summarized in the bar graph in Figure 2F.

The Action of Phenytoin Is Attenuated in Experiments With High Kainate Concentrations but Is Not Competitive

Kawano et al. (1994) suggested that the action of phenytoin on AMPA receptors is competitive. So we initially compared the percentage of inhibition by phenytoin at two different kainate concentrations—50 and 500 μM (**Figure 3**). Indeed, in hippocampal pyramidal neurons, 30 μM phenytoin stronger inhibited currents induced by 50 μM kainate concentration, demonstrating 55 ± 3% inhibition, against 40 ± 7% at 500 μM kainate concentration ($n = 7$, $p < 0.001$). Likewise, 200 μM phenytoin stronger inhibited currents in striatal giant interneurons induced by 50 μM kainate concentration, demonstrating 59 ± 5% inhibition, against 48 ± 2% at 500 μM kainate concentration ($n = 5$, $p < 0.01$, data not shown). In this and further series of experiments, we used pentobarbital, DNQX, perampanel, and IEM-1925 as reference agents. The decrease in inhibitory activity with the increase in kainate concentration in the range from 50 to 3,000 μM was demonstrated for pentobarbital earlier (Jackson et al., 2003). In our experiments on hippocampal CI-AMPARs, 20 μM pentobarbital was also

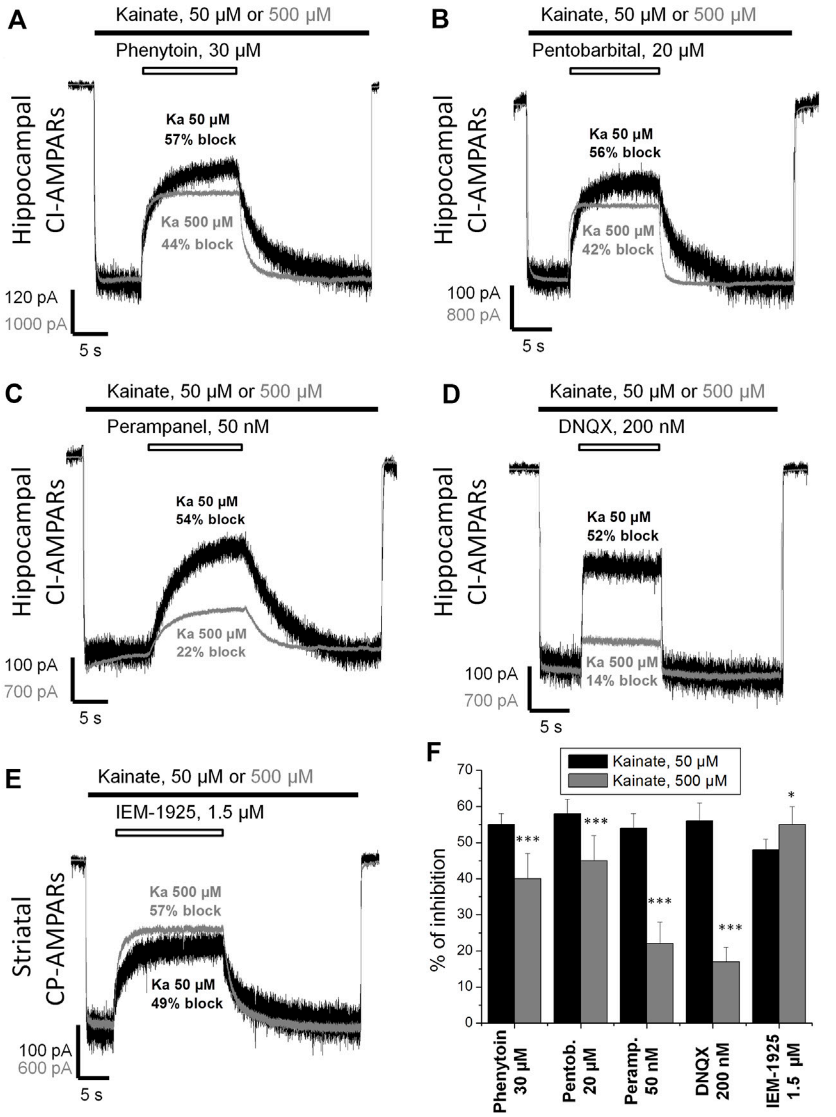

FIGURE 3 | Kainate concentration dependence of action of compounds on AMPA receptors. **(A–E)** Representative examples of CI-AMPARs inhibition by 30 μM phenytoin **(A)**, 20 μM pentobarbital **(B)**, 50 nM perampanel **(C)**, 200 nM DNQX **(D)**, and CP-AMPARs inhibition by 1.5 μM IEM-1925 **(E)** at 50 and 500 μM kainate concentrations. The amplitudes of responses at different kainate concentrations were normalized for visual clarity. **(F)** Summarized results of AMPARs inhibition by different compounds at 50 and 500 μM kainate concentrations. Phenytoin, pentobarbital, perampanel, and DNQX were more active in case of lower kainate concentration. In contrast, IEM-1925 was more active in case of higher kainate concentration. *–$p < 0.05$. ***–$p < 0.001$.

more active in the case of lower kainate concentration (**Figure 3B**), as well as 50 nM perampanel (**Figure 3C**) and 200 nM DNQX (**Figure 3D**). In contrast, IEM-1925 (**Figure 3E**) stronger inhibited currents induced by 500 μM kainate (55 ± 5%), then by 50 μM kainate (48 ± 3%) on striatal CP-AMPARs. The bar graph in Figure 3F summarizes the obtained results. Phenytoin and pentobarbital demonstrated moderate (10–15%) decrease in the % of inhibition with the increase in agonist concentration, while for perampanel and DNQX, the decrease was stronger (30–40%).

To further test whether inhibition by phenytoin is competitive or not, we studied the kainate concentration dependence in the absence and in the presence of phenytoin, 30 and 300 μM (**Figure 4A**). The EC50 for kainate was 150 ± 20 μM in control, and the Hill coefficient was 1.6 ± 0.2. The EC50 value was increased to 250 ± 30 μM and 360 ± 30 μM in the presence of 30 and 300 μM phenytoin, respectively. Maximal response to kainate was reduced to 84 ± 4% by 30 μM phenytoin and to 46 ± 3% by 300 μM phenytoin ($n = 5$ for both phenytoin concentrations, $p < 0.001$), clearly indicating that inhibition by phenytoin is not competitive. Pentobarbital of 14 μM decreased the maximal response to kainate as well (**Figure 4B**), while 0.2 μM DNQX did not change it (**Figure 4B**), which is typical for competitive inhibitors.

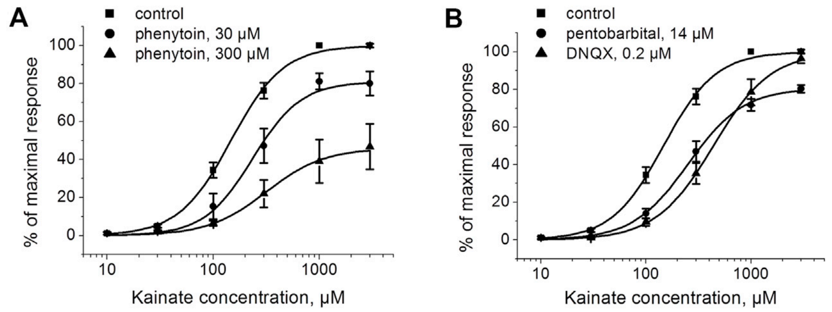

FIGURE 4 | The action of phenytoin is not competitive. **(A)** Activation curve for kainate in control and in the presence of 30 and 300 µM phenytoin. Phenytoin in both concentrations reduced the maximal response to kainate, which suggests that inhibition by phenytoin is not competitive. **(B)** Activation curve for kainate in the absence and presence of 14 µM pentobarbital and 0.2 µM DNQX. Pentobarbital demonstrated inhibition even at high kainate concentrations as well, while DNQX induced a parallel shift of the kainate activation curve, which is typical for competitive inhibitors.

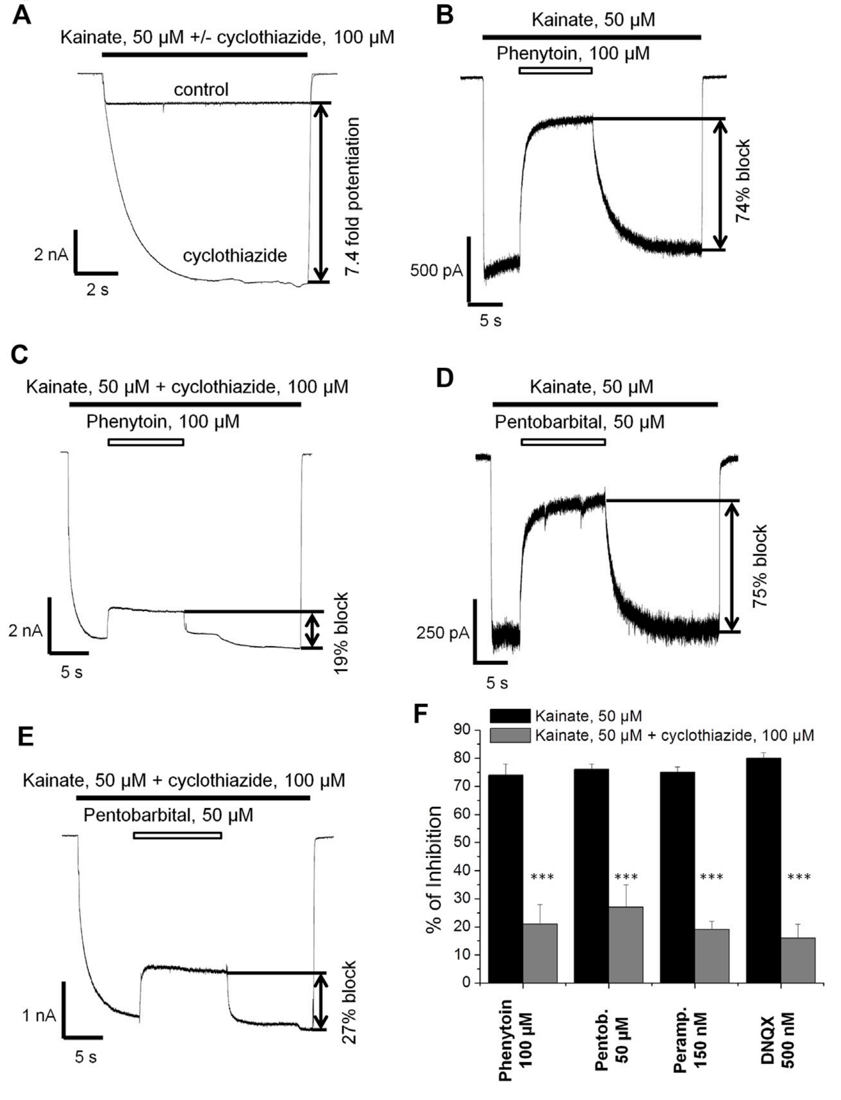

FIGURE 5 | The effect of phenytoin is attenuated in the presence of cyclothiazide. **(A)** Enhancement of kainate-induced currents in hippocampal CA1 pyramidal neurons by 100 µM cyclothiazide. **(B,C)** Representative examples of inhibition by 100 µM phenytoin in the absence **(B)** and presence **(C)** of 100 µM cyclothiazide. **(D,E)** Representative examples of inhibition by 50 µM pentobarbital in the absence **(D)** and presence **(E)** of 100 µM cyclothiazide. **(F)** Summarized results of CI-AMPARs inhibition by different compounds in the absence and presence of 100 µM cyclothiazide. The inhibitory effect of compounds was significantly attenuated in the presence of cyclothiazide. ***–$p < 0.001$.

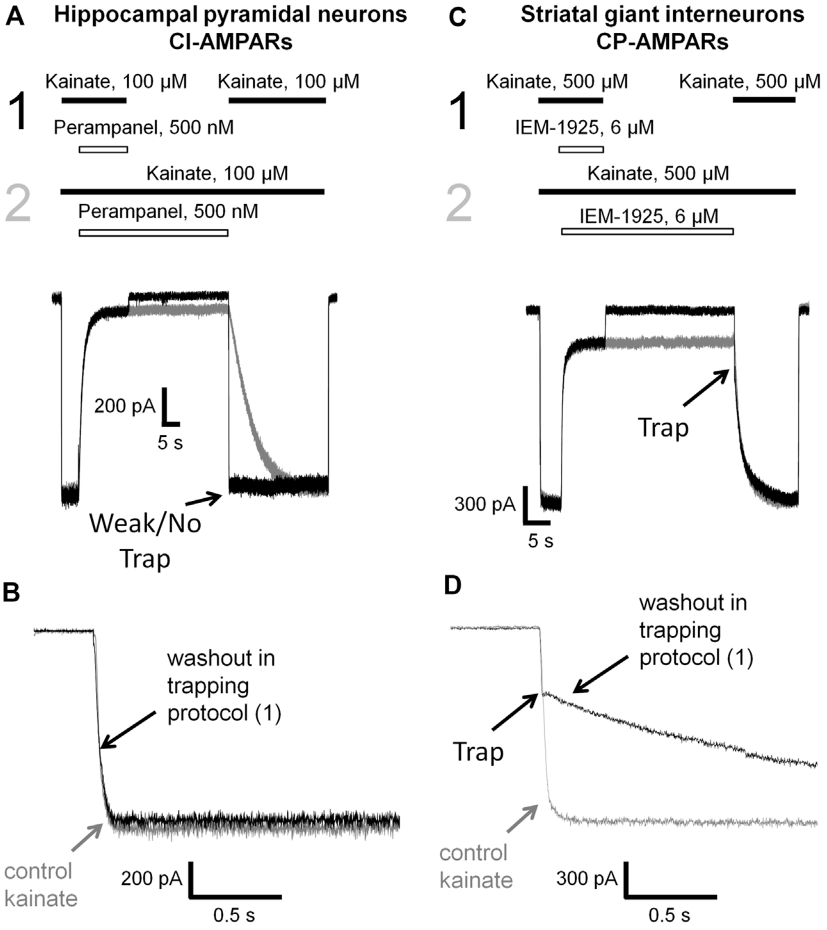

FIGURE 6 | Perampanel is not trapped in closed AMPAR channels in contrast to IEM-1925. **(A)** Representative example of the absence of trapping for 500 nM perampanel in the double-pulse protocol (black traces) and its recovery kinetics in the protocol without pause in extracellular solution (gray traces) on hippocampal pyramidal neuron. **(B)** Superimposition of rising fronts in control kainate application and testing kainate application in the double-pulse protocol for 500 nM perampanel. **(C)** Representative example of trapping for 6 μM IEM-1925 in the double-pulse protocol (black traces) and its recovery kinetics in the protocol without pause in extracellular solution (gray traces) on striatal giant interneuron. **(D)** Superimposition of rising fronts in control kainate application and testing kainate application in the double-pulse protocol for 6 μM IEM-1925.

The Effect of Phenytoin Is Attenuated in the Presence of Cyclothiazide

Next we decided to compare the action of phenytoin in the presence and absence of cyclothiazide, a positive AMPAR allosteric modulator. Cyclothiazide is mostly known as an agent that reduces AMPA receptor desensitization (Partin et al., 1993; Patneau et al., 1993). It also demonstrates slow onset increase in the steady-state current amplitudes and lengthens single-channel openings (Patneau et al., 1993; Fucile et al., 2006). Cyclothiazide strongly increases AMPAR currents in hippocampal CA1 pyramidal cells but only weakly affects those of giant striatal interneurons (Buldakova et al., 2000). Thus, we decided to study the effect of phenytoin (100 μM) at relatively low kainate concentration (50 μM) in the absence or presence of saturating concentration of cyclothiazide (100 μM) on hippocampal CA1 pyramidal neurons. Cyclothiazide of 100 μM increased the stationary current induced by 50 μM kainate by 8 ± 2 fold (**Figure 5A**). Representative examples of inhibition by 100 μM phenytoin in the absence and presence of 100 μM cyclothiazide are shown (**Figures 5B,C**). Phenytoin of 100 μM was drastically more active in the absence than in the presence of cyclothiazide (74 ± 4% vs. 21 ± 7% inhibition, respectively; $p < 0.001$). The inhibitory effect of 50 μM pentobarbital (**Figure 5D**) was also significantly attenuated in the presence of cyclothiazide (**Figure 5E**) in line with previous results (Jackson et al., 2003). DNQX was less active in the presence of cyclothiazide (data not shown), as well as perampanel (Barygin, 2016). Because cyclothiazide has only weak effect on CP-AMPARs of giant striatal interneurons, we decided not to test IEM-1925 in this protocol. The bar graph in Figure 5F summarizes the obtained results.

Trapping of Phenytoin in AMPAR Channels

Up to this point, the mechanisms of action of phenytoin closely resembled that of pentobarbital (preference for CI-AMPAR, the decrease in inhibitory activity in experiments with high kainate concentrations and in the presence of cyclothiazide). A distinctive

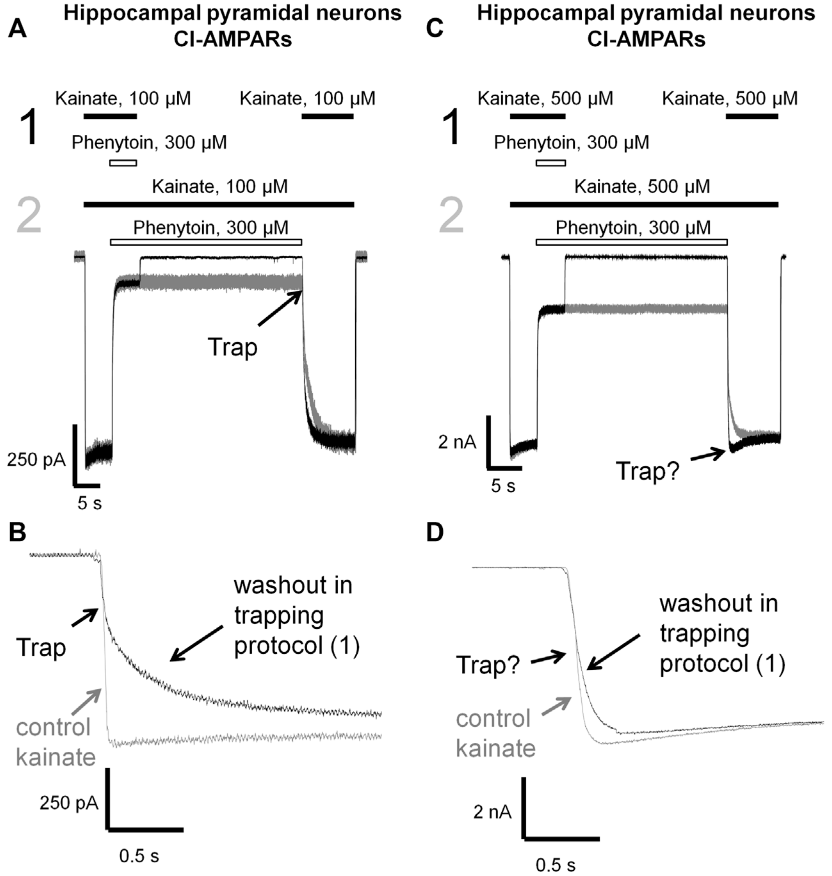

FIGURE 7 | Trapping of phenytoin in AMPAR channels. **(A,C)** Representative examples of phenytoin trapping in case of CI-AMPAR activation by 100 **(A)** and 500 μM **(C)** kainate in the double-pulse protocol (black traces) and recovery kinetics in the protocol without pause in extracellular solution (gray traces). Phenytoin of 300 μM demonstrated pronounced trapping at 100 μM kainate **(A)**, but trapping was questionable at 500 μM kainate **(C)**. **(B,D)** Superimpositions of rising fronts in control kainate application and testing kainate application in the double-pulse protocol in case of CI-AMPAR activation by 100 **(B)** and 500 μM **(D)** kainate.

feature of the open channel blockers of AMPARs, like IEM-1925, is the trapping effect. The blocked channels can close after agonist dissociation trapping the blocker molecules inside (Bahring and Mayer, 1998; Tikhonova et al., 2008). Pentobarbital demonstrated trapping in closed AMPA receptor channels that was stable over time but was much weaker in the presence of cyclothiazide (Jackson et al., 2003).

Here we decided to compare phenytoin trapping in case of CI-AMPAR activation by 100 and 500 μM kainate using the double-pulse protocol (Huettner and Bean, 1988; Blanpied et al., 1997). In this protocol, denoted as protocol 1 (black traces) in **Figures 6**, **7**, we initially apply kainate, then add an antagonist, then simultaneously remove both kainate and antagonist for a 30-s pause in the extracellular solution, and finally apply the testing kainate to study the recovery kinetics. If the response to testing kainate application resembles that of the first kainate application, then we can say that the antagonist was not trapped in the closed channels. If it includes a slower component, we can say that some molecules of the antagonist were trapped. Recovery kinetics for the protocol in which the 30-s pause in the extracellular solution is changed to 30 s in the presence of both kainate and antagonist (protocol 2, gray traces) is provided for comparison.

Kinetics of control kainate response is single-exponential (τ = 20–50 ms in different conditions). For perampanel (**Figures 6A,B**), the kinetics of the response to testing kainate application in the trapping protocol was also single-exponential, and the time constant (τ = 41 ± 12 ms, n = 4) was not significantly different from that of the control kainate response (τ = 43 ± 9, n = 4, $p \geq 0.05$), evidencing the absence of trapping effect. In contrast, IEM-1925 demonstrated at least double-exponential kinetics: the fast component was close to that of the kainate control, while the slow one (1,800 ± 400 ms, n = 4) did not differ significantly from recovery kinetics in protocol 2 (1,900 ± 500 ms, n = 4, $p \geq 0.05$), indicating trapping (**Figures 6C,D**).

Phenytoin in 100 μM kainate behaved similar to IEM-1925, demonstrating at least double-exponential washout kinetics in the trapping protocol with the fast component coinciding with the kinetics of the control response (**Figures 7A,B**). Thus, phenytoin demonstrated pronounced trapping in case of

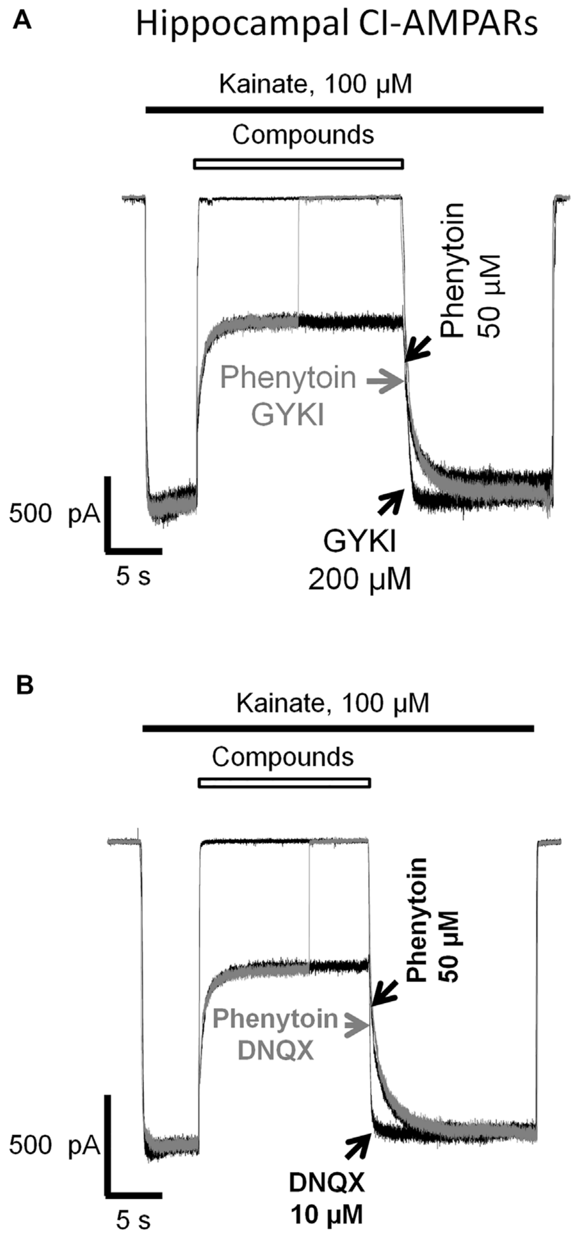

FIGURE 8 | Absence of competition of phenytoin with competitive and negative allosteric AMPA receptor antagonists. The slow phase of recovery from 50 µM phenytoin (black trace) remains unchanged in the presence of 200 µM negative allosteric antagonist GYKI-52466 **(A)** and 10 µM competitive antagonist DNQX **(B)** (gray trace) suggesting that the site of action of phenytoin is different from that of competitive and negative allosteric AMPAR antagonists.

AMPAR activation with 100 µM kainate. The situation in 500 µM kainate was markedly different (see **Figures 7C,D**). The kinetics of the testing response to kainate was well fitted by a single exponential function ($\tau = 81 \pm 17$ ms, $n = 4$), which was significantly slower than the kinetics of control kainate ($\tau = 39 \pm 13$ ms $n = 4$, $p < 0.05$). However, it was fivefold faster than recovery from phenytoin block in protocol 2 ($\tau = 390 \pm 60$ ms, $n = 4$, $p < 0.01$). Unambiguous conclusion is not possible in this situation, but the obvious difference between **Figures 7B,D** suggests that phenytoin trapping is dependent on kainate concentration.

Absence of Competition of Phenytoin With Competitive Antagonists and Negative Allosteric Antagonists

In our experiments (**Figures 1**, **3**, **4**, **5**, **6**, **7**), phenytoin demonstrated features that discriminated it from classical types of AMPAR antagonists (competitive antagonists, negative allosteric antagonists, CP-AMPARs selective channel blockers). However, it was somewhat similar to that of competitive and negative allosteric antagonists because all these compounds were less active in conditions, resulting in strong AMPAR activation (high agonist concentration or presence of cyclothiazide). To further ensure that this is the case, we performed direct experiments on competition for the same site of action with phenytoin and abovementioned types of ligands using the difference in recovery kinetics. Washout kinetics for 50 µM phenytoin is relatively slow, $\tau = 1,100 \pm 200$ ms for CI-AMPARs of hippocampal pyramidal neurons. To study the competition, we used excessive concentrations of “fast” negative allosteric antagonist GYKI-52466 or “fast” competitive antagonist DNQX. Experiments on the competition of phenytoin with GYKI-52466 (**Figure 8A**) and DNQX (**Figure 8B**) were performed on hippocampal pyramidal neurons. We initially studied the washout kinetics of each compound alone and then compared it with washout kinetics in the complex protocol, where we initially applied 50 µM phenytoin, and then added a mixture of phenytoin and excessive concentration of a “fast” antagonist. Indeed, if any fast antagonist would be able to displace phenytoin or somehow affect its binding, the washout kinetics in the complex protocol would be faster than that for phenytoin alone. Neither 200 µM GYKI-52466 nor 10 µM DNQX affected the kinetics of phenytoin washout in this complex protocol. On the other hand, fast negative allosteric antagonist GYKI-52466 was able to displace slow negative allosteric antagonist perampanel in our earlier experiments (Barygin, 2016). These data suggest that the binding site of phenytoin in CI-AMPARs is different from that of competitive antagonists and negative allosteric antagonists. Further studies using site-directed mutagenesis and cryo-electron microscopy/X-ray crystallography are needed to map it.

Phenytoin Preferentially Binds to the Open Channels and Is More Active at pH 7.4 Comparing to pH 9.0

Having shown that the mechanisms of action of phenytoin on AMPA receptors do not resemble those of competitive antagonists, negative allosteric antagonists, and CP-AMPARs selective channel blockers, we decided to further investigate them. So we compared the action of phenytoin on open (protocol 1, coapplication with agonist) and closed (protocol 2, preapplication without agonist) AMPAR channels (**Figure 9**).

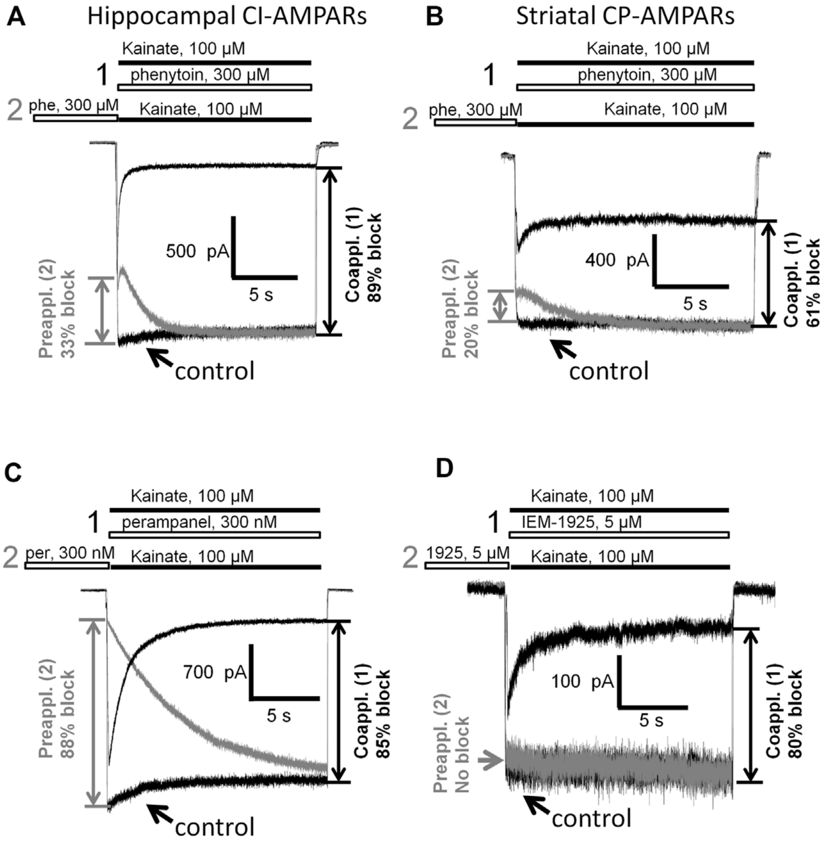

FIGURE 9 | Closed and open channel AMPAR inhibition by phenytoin, perampanel, and IEM-1925. **(A,B)** Comparison of the effects of 300 µM phenytoin on CI-AMPARs of hippocampal pyramidal neurons **(A)** and CP-AMPARs of striatal giant interneurons **(B)** in case of coapplication with kainate (black traces) and preapplication without kainate (gray traces). For both receptor types, phenytoin is more effective in the coapplication protocol. **(C)** Comparison of the effects of 300 nM perampanel on CI-AMPARs of hippocampal pyramidal neurons in case of coapplication with kainate (black trace) and preapplication without kainate (gray trace). Perampanel is equally effective in these two protocols. **(D)** Comparison of the effects of 5 µM IEM-1925 on CP-AMPARs of striatal giant interneurons in case of coapplication with kainate (black trace) and preapplication without kainate (gray trace). IEM-1925 is effective only in the coapplication protocol.

In experiments with hippocampal CI-AMPARs, 300 µM phenytoin was able to inhibit both closed (37 ± 7%) and open AMPA receptor channels (87 ± 5%), demonstrating preference for open channels (**Figure 9A**, $n = 5$, $p < 0.001$). Similar preference for open channels was found in experiments with CP-AMPARs of giant striatal interneurons. Phenytoin of 300 µM blocked 60 ± 6% in case of coapplication with agonist and 24 + 9% in case of preapplication without agonist (**Figure 9B**, $n = 8$, $p < 0.001$). Pentobarbital of 100 µM was also more active in the coapplication protocol in the experiment on hippocampal CI-AMPARs (data not shown). In contrast, 300 nM perampanel was equally effective in preapplication and coapplication protocols on hippocampal CI-AMPARs (**Figure 9C**). At a glance, this result contradicts with previous data, suggesting that perampanel binds to the resting receptors more efficiently than to activated ones (Yelshanskaya et al., 2016). However, this conclusion was made from experiments with recombinant GluA2 AMPA receptors that were done in the presence of cyclothiazide. We have shown earlier that cyclothiazide dramatically attenuates the effect of perampanel (ca. 20-fold reduction in activity) and fastens its washout kinetics in isolated CA1 pyramidal neurons (Barygin, 2016). An earlier work with perampanel on cultured hippocampal neurons, in which AMPA receptors were activated by kainate in the absence of cyclothiazide, also demonstrated similar efficiency in preapplication and coapplication protocols (Chen et al., 2014). IEM-1925 of 5 µM inhibited only open channels in a similar experiment on CP-AMPARs of giant striatal interneurons (**Figure 9D**). Because of the fast kinetics of washout, we were not able to test DNQX in this protocol.

In addition, we compared the action of 50 µM phenytoin at two different pHs: 7.4 and 9.0. The pKa value for phenytoin is 8.3 (Agarwal & Blake, 1968). Thus, at pH 7.4, it exists mostly in uncharged form, while at pH 9.0, it is mostly negatively charged. Phenytoin of 50 µM inhibited currents by 60 ± 3% at pH 7.4 and by 28 ± 8% at pH 9.0 ($n = 6$, $p < 0.001$, **Figures 10A,C**). Such a decrease in phenytoin activity in more basic conditions suggests that the uncharged form of phenytoin produces stronger AMPAR inhibition. Pentobarbital was also more active at neutral than at more basic pH (**Figures 10B,D**), in line with previous results (Jackson et al., 2003).

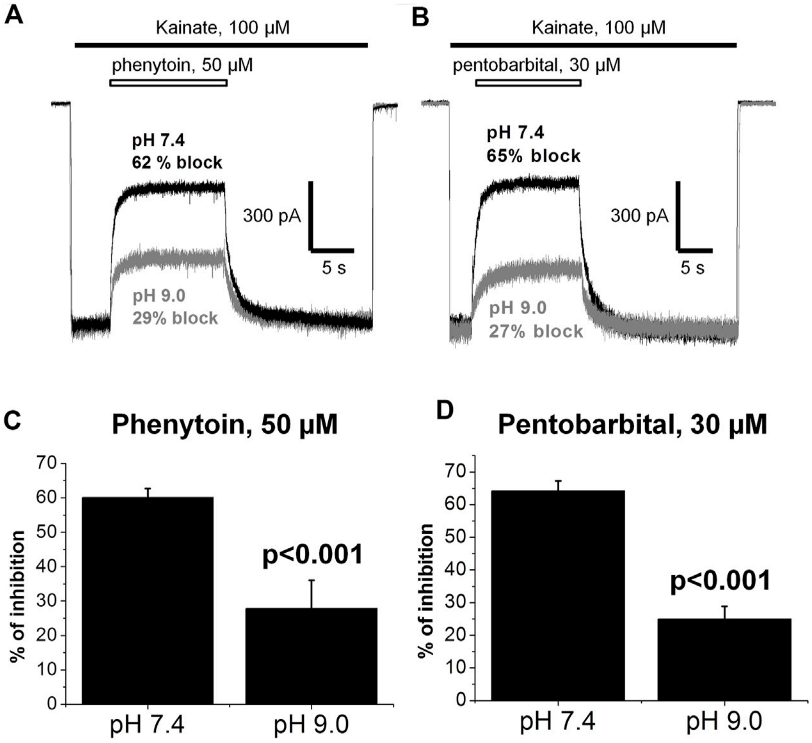

FIGURE 10 | The action of phenytoin and pentobarbital at pH 7.4 and 9.0. **(A,B)** Representative examples of CI-AMPARs inhibition by 50 μM phenytoin **(A)** and 30 μM pentobarbital **(B)** at pH 7.4 (black trace) and 9.0 (gray trace). **(C,D)** Summarized results of CI-AMPARs inhibition by 50 μM phenytoin **(C)** and 30 μM pentobarbital **(D)** at pH 7.4 and 9.0. Phenytoin and pentobarbital were more active at neutral than at more basic pH, which implies that their uncharged forms account for AMPAR inhibition.

DISCUSSION

In the present work, we have shown for the first time that phenytoin is significantly more active against CI-AMPAR compared to CP-AMPARs. Among known AMPAR antagonists similar selectivity demonstrated pentobarbital (Taverna et al., 1994; Yamakura et al., 1995; Jackson et al., 2003). The action of phenytoin on CI-AMPARs was attenuated in experiments with high agonist concentrations, in the presence of cyclothiazide and at pH 9.0. However, phenytoin was more active in the case of coapplication with agonist compared with preapplication without agonist. Phenytoin demonstrated pronounced trapping when receptors were activated by relatively low kainate concentrations (up to 100 μM), but the trapping was questionable in experiments with higher (500 μM) kainate concentration. This set of features (**Table 2**) is intriguing because it discriminates phenytoin from three main types of AMPA receptor antagonists: competitive antagonists (e.g., DNQX, CNQX), negative allosteric antagonists (e.g., GYKI-52466, perampanel), and CP-AMPARs selective voltage-dependent channel blockers (e.g., IEM-1925, IEM-1755, argiotoxins, phylantotoxins). Noteworthy, practically the same set of features was shown earlier for pentobarbital (Jackson et al., 2003) and was confirmed in our experiments.

The 3D structures of the compounds studied in the present work were calculated by the ZMM software (**Figure 11A**). They demonstrate huge structural diversity. However, lamotrigine, phenytoin, primidone, ethosuximide, and pentobarbital (compounds 1–5) possess some common motifs. They have a heterocycle (shown at the bottom) and aromatic/hydrophobic moieties (shown at the top). Only phenytoin and pentobarbital demonstrated activity against AMPA receptors, whereas lamotrigine, primidone, ethosuximide, and hydantoin were inactive. This structural comparison indicates that the binding site requirements are rather strong. Both hydrophobic/aromatic moieties and specific mutual disposition of CO and NH groups seen in hydantoin ring and in pyrimidine 2-4-6 trion ring are essential for this type of activity. **Figure 11B** shows a comparison of phenytoin and pentobarbital in different orientations. In fact, these 3D structures are very similar justifying the common mechanism of action revealed in our experiments.

We have shown that the molecular mechanism of action of phenytoin and pentobarbital on AMPARs is different from that of competitive antagonists, negative allosteric antagonists, and CP-AMPARs selective channel blockers (**Table 1**). The binding sites for these classical types of AMPAR antagonists are rather well characterized (Tikhonov et al., 2002; Balannik et al., 2005; Yelshanskaya et al., 2016; Twomey et al., 2018; Krintel et al., 2021). But where can the binding site for phenytoin and pentobarbital be situated? For pentobarbital, it has been demonstrated that the single mutation of the Q/R site residue in the GluA2 subunit (R586Q) dramatically decreases the sensitivity (Yamakura et al., 1995) suggesting binding in the central pore at the selectivity filter. Cationic blockers selectively inhibit CP-AMPAR, whereas neutral molecules of

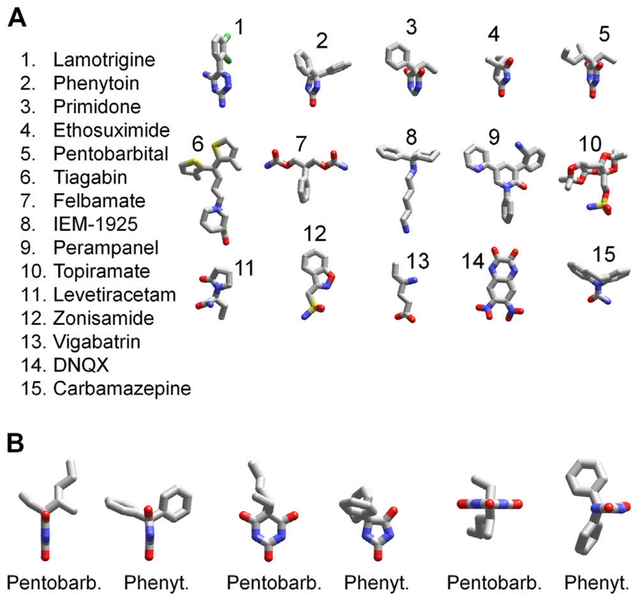

FIGURE 11 | 3D structures of compounds. **(A)** Comparison of 3D structures of the compounds. The structures demonstrate large diversity, although compounds 1–5 have certain similarity; they have a heterocycle shown in the bottom and aromatic/hydrophobic moieties shown in the top. **(B)** Comparison of 3D structures of phenytoin and pentobarbital in different orientations. The 3D structures demonstrate close similarity of orientation of functional groups.

pentobarbital and phenytoin can readily bind to the CI-AMPARs containing the Arg residue in the selectivity filter. Although present X-ray and cryo-EM structures seem not precise enough to characterize atomic-scale details of this site unambiguously, it obviously contains hydrophobic central cavity and polar groups serving as proton donors and acceptors (Tikhonov and Zhorov, 2020). Our structure–activity data demonstrate that such features are indeed required to provide inhibitory action of phenytoin and pentobarbital. At a glance, binding in the inner pore region near the selectivity filter is inconsistent with attenuation of inhibitory activity at high kainate concentrations and in the presence of cyclothiazide. However, there are data suggesting that gating rearrangements of AMPA receptor channels involve not only the C-part of the M2 segment but also the selectivity filter (Sobolevsky et al., 2005; Twomey et al., 2017). If it is so, specific drug binding to this site can affect activation properties of the channels and vice versa.

An apparent paradox of the mechanism of action is that phenytoin weakly block closed channels if applied without agonist. However, activation by saturating agonist concentration or enhancing the activation by cyclothiazide also reduces the inhibitory activity of pentobarbital and phenytoin. Although we have no convincing justification for these seemingly controversial data, double-gate mechanism of activation provides a possible explanation. Open conformation of the extracellular gate in the M3 segments is required to free access of external blockers to the binding site, whereas the open state of the gate at the selectivity filter can weaken the drug binding. Since the relationships between the extracellular and the selectivity filter gates are unknown, more detailed explanations seem impractical and premature.

The voltage-gated sodium channels are generally regarded as the main target to explain phenytoin's activity as an anticonvulsant (Tunnicliff, 1996; Hesselink and Kopsky, 2017a). Affinity of phenytoin to inactivated states of sodium channels is in the range of 7–21 μM (Kuo and Bean, 1994; Lenkowski et al., 2007). Here we have shown for the first time that phenytoin inhibits CI-AMPARs with similar potency. Thus, AMPAR inhibition by phenytoin may contribute to its anticonvulsant and neuroprotective properties, as well as its side effects. While the neuroprotective potential of phenytoin has been evaluated for decades (Stanton and Moskal, 1991; Boehm et al., 1994; Bartollino et al., 2018), the exact molecular mechanisms are not yet clear. It is not yet completely clear even if phenytoin is neuroprotective or neurotoxic (Hesselink and Kopsky, 2017b).

Voltage-gated sodium channels and AMPA receptors are important in keeping proper excitation–inhibition balance in the central nervous system, and the ability of phenytoin to inhibit both of them can underlie its efficiency in case of different types of seizures. Phenytoin is an old drug, and its usage is somewhat limited because of its side effects. Development of new multitarget compounds with the ability to inhibit voltage-gated sodium channels and AMPA receptors seems promising especially for the treatment of drug-resistant epilepsy. Our findings on the structural determinants of action provide a template for further design of selective antagonists of CI-AMPARs.

DATA AVAILABILITY STATEMENT

The original contributions presented in the study are included in the article/Supplementary Material. Further inquiries can be directed to the corresponding author.

ETHICS STATEMENT

The animal study was reviewed and approved by the Animal Care and Use Committee of the I.M. Sechenov Institute of Evolutionary Physiology and Biochemistry of the Russian Academy of Sciences.

AUTHOR CONTRIBUTIONS

MD: performed experiments and analyzed data. AZ: performed experiments and analyzed data. DT: designed the study and drafted the paper. OB: acquired funding, designed the study, performed experiments, analyzed data, and drafted the paper.

FUNDING

The reported study was funded by RFBR, project numbers 16-04-01080, 20-34-90039, and by Federal Statement for IEPhB RAS.

REFERENCES

Agarwal, S. P., and Blake, M. I. (1968). Determination of the pKa' Value for 5,5-diphenylhydantoin. *J. Pharm. Sci.* 57, 1434–1435. doi:10.1002/jps.2600570836

Amakhin, D. V., Soboleva, E. B., Ergina, J. L., Malkin, S. L., Chizhov, A. V., and Zaitsev, A. V. (2018). Seizure-Induced Potentiation of AMPA Receptor-Mediated Synaptic Transmission in the Entorhinal Cortex. *Front. Cel. Neurosci.* 12, 486. doi:10.3389/fncel.2018.00486

Angehagen, M., Ben-Menachem, E., Shank, R., Rönnbäck, L., and Hansson, E. (2004). Topiramate Modulation of Kainate-Induced Calcium Currents Is Inversely Related to Channel Phosphorylation Level. *J. Neurochem.* 88, 320–325. doi:10.1046/j.1471-4159.2003.02186.x

Bähring, R., and Mayer, M. L. (1998). An Analysis of Philanthotoxin Block for Recombinant Rat GluR6(Q) Glutamate Receptor Channels. *J. Physiol.* 509 (Pt 3), 635–650. doi:10.1111/j.1469-7793.1998.635bm.x

Balannik, V., Menniti, F. S., Paternain, A. V., Lerma, J., and Stern-Bach, Y. (2005). Molecular Mechanism of AMPA Receptor Noncompetitive Antagonism. *Neuron* 48, 279–288. doi:10.1016/j.neuron.2005.09.024

Bartollino, S., Chiosi, F., Di Staso, S., Uva, M., Pascotto, A., Rinaldi, M., et al. (2018). The Retinoprotective Role of Phenytoin. *Drug Des. Devel. Ther.* 12, 3485–3489. doi:10.2147/DDDT.S169621

Barygin, O. I., Grishin, E. V., and Tikhonov, D. B. (2011). Argiotoxin in the Closed AMPA Receptor Channel: Experimental and Modeling Study. *Biochemistry* 50, 8213–8220. doi:10.1021/bi200617v

Barygin, O. I. (2016). Inhibition of Calcium-Permeable and Calcium-Impermeable AMPA Receptors by Perampanel in Rat Brain Neurons. *Neurosci. Lett.* 633, 146–151. doi:10.1016/j.neulet.2016.09.028

Bernard, V., Somogyi, P., and Bolam, J. P. (1997). Cellular, Subcellular, and Subsynaptic Distribution of AMPA-type Glutamate Receptor Subunits in the Neostriatum of the Rat. *J. Neurosci.* 17, 819–833. doi:10.1523/jneurosci.17-02-00819.1997

Blanpied, T. A., Boeckman, F. A., Aizenman, E., and Johnson, J. W. (1997). Trapping Channel Block of NMDA-Activated Responses by Amantadine and Memantine. *J. Neurophysiol.* 77, 309–323. doi:10.1152/jn.1997.77.1.309

Boehm, F. H., Liem, L. K., Stanton, P. K., Potter, P. E., and Moskal, J. R. (1994). Phenytoin Protects against Hypoxia-Induced Death of Cultured Hippocampal Neurons. *Neurosci. Lett.* 175, 171–174. doi:10.1016/0304-3940(94)91106-1

Bolshakov, K. V., Kim, K. H., Potapjeva, N. N., Gmiro, V. E., Tikhonov, D. B., Usherwood, P. N., et al. (2005). Design of Antagonists for NMDA and AMPA Receptors. *Neuropharmacology* 49, 144–155. doi:10.1016/j.neuropharm.2005.02.007

Buldakova, S. L., Bolshakov, K. V., Tikhonov, D. B., and Magazanik, L. G. (2000). Ca2+-dependent Desensitization of AMPA Receptors. *Neuroreport* 11, 2937–2941. doi:10.1097/00001756-200009110-00021

Buldakova, S. L., Vorobjev, V. S., Sharonova, I. N., Samoilova, M. V., and Magazanik, L. G. (1999). Characterization of AMPA Receptor Populations in Rat Brain Cells by the Use of Subunit-specific Open Channel Blocking Drug, IEM-1460. *Brain Res.* 846, 52–58. doi:10.1016/s0006-8993(99)01970-8

Carunchio, I., Pieri, M., Ciotti, M. T., Albo, F., and Zona, C. (2007). Modulation of AMPA Receptors in Cultured Cortical Neurons Induced by the Antiepileptic Drug Levetiracetam. *Epilepsia* 48, 654–662. doi:10.1111/j.1528-1167.2006.00973.x

Chen, C. Y., Matt, L., Hell, J. W., and Rogawski, M. A. (2014). Perampanel Inhibition of AMPA Receptor Currents in Cultured Hippocampal Neurons. *Plos One* 9, e108021. doi:10.1371/journal.pone.0108021

Dudic, A., and Reiner, A. (2019). Quinoxalinedione Deprotonation Is Important for Glutamate Receptor Binding. *Biol. Chem.* 400, 927–938. doi:10.1515/hsz-2018-0464

Fucile, S., Miledi, R., and Eusebi, F. (2006). Effects of Cyclothiazide on GluR1/AMPA Receptors. *Proc. Natl. Acad. Sci. U S A.* 103, 2943–2947. doi:10.1073/pnas.0511063103

Fukushima, K., Hatanaka, K., Sagane, K., and Ido, K. (2020). Inhibitory Effect of Anti-seizure Medications on Ionotropic Glutamate Receptors: Special Focus on AMPA Receptor Subunits. *Epilepsy Res.* 167, 106452. doi:10.1016/j.eplepsyres.2020.106452

Gibbs, J. W., Sombati, S., Delorenzo, R. J., and Coulter, D. A. (2000). Cellular Actions of Topiramate: Blockade of Kainate-Evoked Inward Currents in Cultured Hippocampal Neurons. *Epilepsia* 41, 10–16. doi:10.1111/j.1528-1157.2000.tb02164.x

Götz, T., Kraushaar, U., Geiger, J., Lübke, J., Berger, T., and Jonas, P. (1997). Functional Properties of AMPA and NMDA Receptors Expressed in Identified Types of Basal Ganglia Neurons. *J. Neurosci.* 17, 204–215. doi:10.1523/jneurosci.17-01-00204.1997

Hanada, T., Hashizume, Y., Tokuhara, N., Takenaka, O., Kohmura, N., Ogasawara, A., et al. (2011). Perampanel: A Novel, Orally Active, Noncompetitive AMPA-Receptor Antagonist that Reduces Seizure Activity in Rodent Models of Epilepsy. *Epilepsia* 52, 1331–1340. doi:10.1111/j.1528-1167.2011.03109.x

Honoré, T., Davies, S. N., Drejer, J., Fletcher, E. J., Jacobsen, P., Lodge, D., et al. (1988). Quinoxalinediones: Potent Competitive Non-NMDA Glutamate Receptor Antagonists. *Science* 241, 701–703. doi:10.1126/science.2899909

Huettner, J. E., and Bean, B. P. (1988). Block of N-Methyl-D-Aspartate-Activated Current by the Anticonvulsant MK-801: Selective Binding to Open Channels. *Proc. Natl. Acad. Sci. U S A.* 85, 1307–1311. doi:10.1073/pnas.85.4.1307

Jackson, M. F., Joo, D. T., Al-Mahrouki, A. A., Orser, B. A., and Macdonald, J. F. (2003). Desensitization of Alpha-Amino-3-Hydroxy-5-Methyl-4-Isoxazolepropionic Acid (AMPA) Receptors Facilitates Use-dependent Inhibition by Pentobarbital. *Mol. Pharmacol.* 64, 395–406. doi:10.1124/mol.64.2.395

Joshi, S., Rajasekaran, K., Sun, H., Williamson, J., and Kapur, J. (2017). Enhanced AMPA Receptor-Mediated Neurotransmission on CA1 Pyramidal Neurons during Status Epilepticus. *Neurobiol. Dis.* 103, 45–53. doi:10.1016/j.nbd.2017.03.017

Kawano, H., Sashihara, S., Mita, T., Ohno, K., Kawamura, M., and Yoshii, K. (1994). Phenytoin, an Antiepileptic Drug, Competitively Blocked Non-NMDA Receptors Produced by Xenopus Oocytes. *Neurosci. Lett.* 166, 183–186. doi:10.1016/0304-3940(94)90481-2

Keppel Hesselink, J. M., and Kopsky, D. J. (2017a). Phenytoin: 80 Years Young, from Epilepsy to Breast Cancer, a Remarkable Molecule with Multiple Modes of Action. *J. Neurol.* 264, 1617–1621. doi:10.1007/s00415-017-8391-5

Keppel Hesselink, J. M., and Kopsky, D. J. (2017b). Phenytoin: Neuroprotection or Neurotoxicity? *Neurol. Sci.* 38, 1137–1141. doi:10.1007/s10072-017-2993-7

Krintel, C., Dorosz, J., Larsen, A. H., Thorsen, T. S., Venskutonytė, R., Mirza, O., et al. (2021). Binding of a Negative Allosteric Modulator and Competitive Antagonist Can Occur Simultaneously at the Ionotropic Glutamate Receptor GluA2. *FEBS J.* 288, 995–1007. doi:10.1111/febs.15455

Kuo, C. C., and Bean, B. P. (1994). Slow Binding of Phenytoin to Inactivated Sodium Channels in Rat Hippocampal Neurons. *Mol. Pharmacol.* 46, 716–725.

Lee, C. Y., Fu, W. M., Chen, C. C., Su, M. J., and Liou, H. H. (2008). Lamotrigine Inhibits Postsynaptic AMPA Receptor and Glutamate Release in the Dentate Gyrus. *Epilepsia* 49, 888–897. doi:10.1111/j.1528-1167.2007.01526.x

Lenkowski, P. W., Batts, T. W., Smith, M. D., Ko, S. H., Jones, P. J., Taylor, C. H., et al. (2007). A Pharmacophore Derived Phenytoin Analogue with Increased Affinity for Slow Inactivated Sodium Channels Exhibits a Desired Anticonvulsant Profile. *Neuropharmacology* 52, 1044–1054. doi:10.1016/j.neuropharm.2006.11.001

Magazanik, L. G., Buldakova, S. L., Samoilova, M. V., Gmiro, V. E., Mellor, I. R., and Usherwood, P. N. (1997). Block of Open Channels of Recombinant AMPA Receptors and Native AMPA/kainate Receptors by Adamantane Derivatives. *J. Physiol.* 505 (Pt 3), 655–663. doi:10.1111/j.1469-7793.1997.655ba.x

Mellor, I. R., and Usherwood, P. N. (2004). Targeting Ionotropic Receptors with Polyamine-Containing Toxins. *Toxicon* 43, 493–508. doi:10.1016/j.toxicon.2004.02.003

Miziak, B., Konarzewska, A., Ułamek-Kozioł, M., Dudra-Jastrzębska, M., Pluta, R., and Czuczwar, S. J. (2020). Anti-Epileptogenic Effects of Antiepileptic Drugs. *Int. J. Mol. Sci.* 21, 2340. doi:10.3390/ijms21072340

Partin, K. M., Patneau, D. K., Winters, C. A., Mayer, M. L., and Buonanno, A. (1993). Selective Modulation of Desensitization at AMPA versus Kainate Receptors by Cyclothiazide and Concanavalin A. *Neuron* 11, 1069–1082. doi:10.1016/0896-6273(93)90220-l

Patneau, D. K., Vyklicky, L., and Mayer, M. L. (1993). Hippocampal Neurons Exhibit Cyclothiazide-Sensitive Rapidly Desensitizing Responses to Kainate. *J. Neurosci.* 13, 3496–3509. doi:10.1523/jneurosci.13-08-03496.1993

Phillips, I., Martin, K. F., Thompson, K. S., and Heal, D. J. (1997). Weak Blockade of AMPA Receptor-Mediated Depolarisations in the Rat Cortical Wedge by

Phenytoin but Not Lamotrigine or Carbamazepine. *Eur. J. Pharmacol.* 337, 189–195. doi:10.1016/s0014-2999(97)01291-0

Poulsen, C. F., Simeone, T. A., Maar, T. E., Smith-Swintosky, V., White, H. S., and Schousboe, A. (2004). Modulation by Topiramate of AMPA and Kainate Mediated Calcium Influx in Cultured Cerebral Cortical, Hippocampal and Cerebellar Neurons. *Neurochem. Res.* 29, 275–282. doi:10.1023/b:nere.0000010456.92887.3b

Rajasekaran, K., Todorovic, M., and Kapur, J. (2012). Calcium-Permeable AMPA Receptors Are Expressed in a Rodent Model of Status Epilepticus. *Ann. Neurol.* 72, 91–102. doi:10.1002/ana.23570

Rho, J. M., and White, H. S. (2018). Brief History of Anti-seizure Drug Development. *Epilepsia Open* 3, 114–119. doi:10.1002/epi4.12268

Samoilova, M. V., Buldakova, S. L., Vorobjev, V. S., Sharonova, I. N., and Magazanik, L. G. (1999). The Open Channel Blocking Drug, IEM-1460, Reveals Functionally Distinct Alpha-Amino-3-Hydroxy-5-Methyl-4-Isoxazolepropionate Receptors in Rat Brain Neurons. *Neuroscience* 94, 261–268. doi:10.1016/s0306-4522(99)00326-7

Scharfman, H. E. (2007). The Neurobiology of Epilepsy. *Curr. Neurol. Neurosci. Rep.* 7, 348–354. doi:10.1007/s11910-007-0053-z

Sills, G. J., and Rogawski, M. A. (2020). Mechanisms of Action of Currently Used Antiseizure Drugs. *Neuropharmacology* 168, 107966. doi:10.1016/j.neuropharm.2020.107966

Sirven, J. I. (2015). Epilepsy: A Spectrum Disorder. *Cold Spring Harb. Perspect. Med.* 5, a022848. doi:10.1101/cshperspect.a022848

Sobolevsky, A. I., Yelshansky, M. V., and Wollmuth, L. P. (2005). State-dependent Changes in the Electrostatic Potential in the Pore of a GluR Channel. *Biophys. J.* 88, 235–242. doi:10.1529/biophysj.104.049411

Stanton, P. K., and Moskal, J. R. (1991). Diphenylhydantoin Protects against Hypoxia-Induced Impairment of Hippocampal Synaptic Transmission. *Brain Res.* 546, 351–354. doi:10.1016/0006-8993(91)91501-q

Taverna, F. A., Cameron, B. R., Hampson, D. L., Wang, L. Y., and Macdonald, J. F. (1994). Sensitivity of Ampa Receptors to Pentobarbital. *Eur. J. Pharmacol.* 267, R3–R5. doi:10.1016/0922-4106(94)90161-9

Tikhonov, D. B., Mellor, J. R., Usherwood, P. N., and Magazanik, L. G. (2002). Modeling of the Pore Domain of the GLUR1 Channel: Homology with K+ Channel and Binding of Channel Blockers. *Biophys. J.* 82, 1884–1893. doi:10.1016/S0006-3495(02)75538-0

Tikhonov, D. B., and Zhorov, B. S. (2020). The Pore Domain in Glutamate-Gated Ion Channels: Structure, Drug Binding and Similarity with Potassium Channels. *Biochim. Biophys. Acta-Biomembranes* 1862(10):183401. doi:10.1016/j.bbamem.2020.183401

Tikhonova, T. B., Barygin, O. I., Gmiro, V. E., Tikhonov, D. B., and Magazanik, L. G. (2008). Organic Blockers Escape From Trapping in the AMPA Receptor Channels by Leaking into the Cytoplasm. *Neuropharmacology* 54 (4), 653–664. doi:10.1016/j.neuropharm.2007.11.014

Tunnicliff, G. (1996). Basis of the Antiseizure Action of Phenytoin. *Gen. Pharmacol.* 27, 1091–1097. doi:10.1016/s0306-3623(96)00062-6

Twomey, E. C., Yelshanskaya, M. V., Grassucci, R. A., Frank, J., and Sobolevsky, A. I. (2017). Channel Opening and Gating Mechanism in AMPA-Subtype Glutamate Receptors. *Nature* 549, 60, 65. doi:10.1038/nature23479

Twomey, E. C., Yelshanskaya, M. V., Vassilevski, A. A., and Sobolevsky, A. I. (2018). Mechanisms of Channel Block in Calcium-Permeable AMPA Receptors. *Neuron* 99, 956. doi:10.1016/j.neuron.2018.07.027

Vorobjev, V. S. (1991). Vibrodissociation of Sliced Mammalian Nervous Tissue. *J. Neurosci. Methods* 38, 145–150. doi:10.1016/0165-0270(91)90164-u

Yamakura, T., Sakimura, K., Mishina, M., and Shimoji, K. (1995). The Sensitivity of AMPA-Selective Glutamate Receptor Channels to Pentobarbital Is Determined by a Single Amino Acid Residue of the Alpha 2 Subunit. *FEBS Lett.* 374, 412–414. doi:10.1016/0014-5793(95)01163-9

Yelshanskaya, M. V., Singh, A. K., Sampson, J. M., Narangoda, C., Kurnikova, M., and Sobolevsky, A. I. (2016). Structural Bases of Noncompetitive Inhibition of AMPA-Subtype Ionotropic Glutamate Receptors by Antiepileptic Drugs. *Neuron* 91, 1305–1315. doi:10.1016/j.neuron.2016.08.012

Conflict of Interest: The authors declare that the research was conducted in the absence of any commercial or financial relationships that could be construed as a potential conflict of interest.

Publisher's Note: All claims expressed in this article are solely those of the authors and do not necessarily represent those of their affiliated organizations, or those of the publisher, the editors and the reviewers. Any product that may be evaluated in this article, or claim that may be made by its manufacturer, is not guaranteed or endorsed by the publisher.

Copyright © 2021 Dron, Zhigulin, Tikhonov and Barygin. This is an open-access article distributed under the terms of the Creative Commons Attribution License (CC BY). The use, distribution or reproduction in other forums is permitted, provided the original author(s) and the copyright owner(s) are credited and that the original publication in this journal is cited, in accordance with accepted academic practice. No use, distribution or reproduction is permitted which does not comply with these terms.

frontiers
in Pharmacology

ORIGINAL RESEARCH
published: 08 December 2021
doi: 10.3389/fphar.2021.775271

The Na^+/Ca^{2+} Exchanger 3 Is Functionally Coupled With the $Na_V1.6$ Voltage-Gated Channel and Promotes an Endoplasmic Reticulum Ca^{2+} Refilling in a Transgenic Model of Alzheimer's Disease

Ilaria Piccialli*[1]*, *Roselia Ciccone*[1]*, *Agnese Secondo*[1]*, *Francesca Boscia*[1]*, *Valentina Tedeschi*[1]*, *Valeria de Rosa*[1]*, *Pasquale Cepparulo*[1]*, *Lucio Annunziato*[2]* and *Anna Pannaccione*[1]**

[1]Division of Pharmacology, Department of Neuroscience, Reproductive and Dentistry Sciences, School of Medicine, Federico II University of Naples, Naples, Italy, [2]IRCSS SDN, Naples, Italy

OPEN ACCESS

Edited by:
Jacques Joubert,
University of the Western Cape, South Africa

Reviewed by:
Cornelis Van Breemen,
University of British Columbia, Canada
Elena Popugaeva,
Peter the Great St.Petersburg Polytechnic University, Russia

***Correspondence:**
Anna Pannaccione
pannacio@unina.it

Specialty section:
This article was submitted to Pharmacology of Ion Channels and Channelopathies, a section of the journal Frontiers in Pharmacology

Received: *13 September 2021*
Accepted: *22 November 2021*
Published: *08 December 2021*

Citation:
Piccialli I, Ciccone R, Secondo A, Boscia F, Tedeschi V, de Rosa V, Cepparulo P, Annunziato L and Pannaccione A (2021) The Na^+/Ca^{2+} Exchanger 3 Is Functionally Coupled With the $Na_V1.6$ Voltage-Gated Channel and Promotes an Endoplasmic Reticulum Ca^{2+} Refilling in a Transgenic Model of Alzheimer's Disease.
Front. Pharmacol. 12:775271.
doi: 10.3389/fphar.2021.775271

The remodelling of neuronal ionic homeostasis by altered channels and transporters is a critical feature of the Alzheimer's disease (AD) pathogenesis. Different reports converge on the concept that the Na^+/Ca^{2+} exchanger (NCX), as one of the main regulators of Na^+ and Ca^{2+} concentrations and signalling, could exert a neuroprotective role in AD. The activity of NCX has been found to be increased in AD brains, where it seemed to correlate with an increased neuronal survival. Moreover, the enhancement of the NCX3 currents (I_{NCX}) in primary neurons treated with the neurotoxic amyloid β 1–42 ($A\beta_{1-42}$) oligomers prevented the endoplasmic reticulum (ER) stress and neuronal death. The present study has been designed to investigate any possible modulation of the I_{NCX}, the functional interaction between NCX and the $Na_V1.6$ channel, and their impact on the Ca^{2+} homeostasis in a transgenic *in vitro* model of AD, the primary hippocampal neurons from the Tg2576 mouse, which overproduce the $A\beta_{1-42}$ peptide. Electrophysiological studies, carried in the presence of siRNA and the isoform-selective NCX inhibitor KB-R7943, showed that the activity of a specific NCX isoform, NCX3, was upregulated in its reverse, Ca^{2+} influx mode of operation in the Tg2576 neurons. The enhanced NCX activity contributed, in turn, to increase the ER Ca^{2+} content, without affecting the cytosolic Ca^{2+} concentrations of the Tg2576 neurons. Interestingly, our experiments have also uncovered a functional coupling between NCX3 and the voltage-gated $Na_V1.6$ channels. In particular, the increased $Na_V1.6$ currents appeared to be responsible for the upregulation of the reverse mode of NCX3, since both TTX and the *Streptomyces griseolus* antibiotic anisomycin, by reducing the $Na_V1.6$ currents, counteracted the increase of the I_{NCX} in the Tg2576 neurons. In agreement, our immunofluorescence analyses revealed that the NCX3/$Na_V1.6$ co-expression was increased in the Tg2576 hippocampal neurons in comparison with the WT neurons. Collectively, these findings indicate that NCX3 might intervene in the Ca^{2+} remodelling occurring in the Tg2576 primary neurons thus emerging as a molecular target with a neuroprotective potential, and provide a new outcome of the $Na_V1.6$ upregulation related to the modulation of the intracellular Ca^{2+} concentrations in AD neurons.

Keywords: Na^+/Ca^{2+} exchanger, NCX3, $Na_V1.6$ channels, hippocampal neurons, Alzheimer's disease, Tg2576 mice

INTRODUCTION

Alzheimer's disease (AD) is one of the most common neurodegenerative disorders, with a clinical symptomatology ranging from cognitive disabilities to severe dementia (Querfurth and LaFerla, 2010). Dysfunctional ion channels and transporters have been implicated in neuronal loss and network disruption, thus emerging as a potential candidate responsible for neurodegeneration (Wada, 2006; Chakroborty and Stutzmann, 2014). Nonetheless, the remodelling of ionic homeostasis is historically considered a critical feature of the AD pathogenesis, being involved in neuronal and glial responses to amyloid β1-42 ($A\beta_{1-42}$)-mediated injury (Berridge, 2010). However, despite the variety of studies aimed at exploring the role of ionic dyshomeostasis in the AD etiopathogenesis, including Ca^{2+} and Na^+ dysregulation, many issues remain to be elucidated.

The involvement of the Na^+/Ca^{2+} exchanger (NCX) in AD has been proposed in different studies (Colvin et al., 1991 and, 1994; Sokolow et al., 2011; Pannaccione et al., 2012; Pannaccione et al., 2020). Indeed, as a crucial regulator of intracellular Na^+ and Ca^{2+} concentrations, NCX displays a neuroprotective role in many pathophysiological conditions affecting the central nervous system, thus emerging as a key target in neurodegeneration (Gomez-Villafuertes et al., 2007; Annunziato et al., 2020; Pannaccione et al., 2020). Although mainly considered as a Ca^{2+} extrusion mechanism, NCX works in fact in a bidirectional manner by mediating the Ca^{2+} influx along with the Na^+ efflux (reverse mode) or, *vice versa*, the Ca^{2+} efflux and Na^+ influx (forward mode) (Blaustein and Lederer, 1999). Of note, the proximity of NCX to different types of Na^+ channels, including the voltage-gated sodium (Na_V) channels, may render the exchanger an important source for Ca^{2+} influx (Poburko et al., 2007; Gershome et al., 2010).

Different reports have provided evidence about a neuroprotective role of NCX in the AD pathogenesis (Colvin et al., 1991 and, 1994; Pannaccione et al., 2012; Pannaccione et al., 2020). First, the increase of the NCX activity observed in surviving neurons in AD brain areas affected by neurodegeneration suggested that the exchanger could participate in the survival mechanisms occurring in AD neurons (Colvin et al., 1991). On the other hand, the modulation of the expression pattern of the three NCX isoforms, NCX1-3, was observed in AD brain tissues, with a marked loss of NCX3 in the parietal cortex of AD patients and in the synaptosomes from AD-affected brains (Sokolow et al., 2011). In agreement, we demonstrated that the upregulation of the NCX3 activity in primary hippocampal neurons exposed to $A\beta_{1-42}$ oligomers was involved in neuronal survival in the early phase of $A\beta_{1-42}$ injury (Pannaccione et al., 2012). In contrast, NCX3 dysfunction in the late phase of $A\beta_{1-42}$ exposure determined neuronal death *via* endoplasmic reticulum (ER) stress and caspase-12 activation (Pannaccione et al., 2012). Intriguingly, a genome wide association study for the age at onset of AD identified SLC8A3, the gene encoding for NCX3, as a candidate gene for AD since its rare variants were shown to affect the age at onset of the disease (Saad et al., 2015).

Notably, we have recently reported that the expression and activity of the $Na_V1.6$ channel subunit were upregulated in both primary hippocampal neurons exposed to exogenous $A\beta_{1-42}$ oligomers and those from Tg2576 mice, a well-known transgenic model of AD (Ciccone et al., 2019). $Na_V1.6$ channels, which are densely clustered at the axon initial segment (AIS) and at the nodes of Ranvier of myelinated axons, play a crucial role in the initiation and propagation of action potentials in excitable cells (Royeck et al., 2008; Akin et al., 2015; Solé and Tamkun, 2020). In line with several studies, our results showed that $Na_V1.6$ channels were largely expressed not only at the AIS but also as somatic nanoclusters and that their expression was significantly increased in the soma and neurites of Tg2576 hippocampal neurons, hence determining their hyperexcitability (Akin et al., 2016; Sikora et al., 2017; Ciccone et al., 2019). Several studies have suggested that Na_V channels might collaborate with NCX to constitute a linkage between the Na^+ and Ca^{2+} fluxes across the plasma membrane (Pappalardo et al., 2014; Radwański et al., 2016; Veeraraghavan et al., 2017; Torres, 2021). However, whether such cooperation may intervene in the neuronal Na^+ and Ca^{2+} regulation in AD has not been explored yet.

Based on these considerations, the purpose of the present study has been to investigate by means of electrophysiological studies any possible changes in the NCX activity in primary hippocampal neurons from the Tg2576 mouse, a transgenic model overproducing the $A\beta_{1-42}$ peptide. In addition, we have also assessed, through pharmacological and siRNA approaches, the possible involvement of a specific NCX isoform and explored the functional interaction between NCX and the $Na_V1.6$ channel.

MATERIALS AND METHODS

Animals

All the animals were handled according to the International Guidelines for Animal Research and the experimental protocols were approved by the Animal Care and Use Committee of the "Federico II" University of Naples. The heterozygous male Tg2576 mice and Wild Type (WT) females were purchased from a commercial source [B6; SJLTg(APPSWE) 2576Kha, model 1349, Taconic, Hudson, NY].

PCR Analysis

The genomic DNA from embryonic brain tissues was isolated by salt precipitation. Briefly, embryonic brain tissues were harvested during cerebral dissection and then thawed and homogenized with the TRI-reagent (SigmaAldrich, Milan, Italy). After adding one volume of chloroform to each sample, the DNA was precipitated with 100% ethanol and centrifuged at 4°C for 5 min at 16,000 × g. The DNA pellet was dried at room temperature and then re-suspended in Tris-EDTA buffer. The following primers were used to amplify the DNA region with the human APP Swedish mutation on both types of genomic DNA: 5′-CTGACCACTCGACCAGGTTCTGGGT-3′ and 5′GTGGAT AACCCCTCCCCC AGCCTAGACCA-3′ (Eurofins Genomics, Ebersberg, Germany). The DNA was amplified as previously described (Ciccone et al., 2019) to detect the transgenic genotype.

Primary Hippocampal Neurons

Primary neuronal cultures were prepared from the hippocampi of embryonic day 15 WT and Tg2576 mise as described by Ciccone et al. (2019). The cells were plated on 35 mm culture dishes coated with poly(D)-lysine hydrobromide Molecular Weight >300,000 (Sigma Aldrich, Milan, Italy), or onto 25 mm glass coverslips (Glaswarenfabrik Karl Hecht KG, Sondheim, Germany), coated with 100 μg/ml poly(D)-lysine hydrobromide Molecular Weight 30,000–70,000 (Sigma Aldrich, Milan, Italy), at a density of one embryo hippocampus/1 ml 10 μM of cytosine β-D-arabinofuranoside (Sigma Aldrich, Milan, Italy) were added 3 days after plating to inhibit non-neuronal cell growth. The neurons were cultured at 37°C in a humidified 5% CO_2 atmosphere. The experiments were performed not earlier than 8 days *in vitro* (DIV).

Electrophysiological Recordings: NCX and Na^+ Currents

The NCX and Na^+ currents (I_{NCX}; I_{Na}, respectively) were recorded in primary hippocampal neurons from the Tg2576 and WT mice by means of the patch-clamp technique in a whole-cell configuration using the commercially available amplifier Axopatch 200B and the Digidata 1322 A interface (Molecular Devices) as previously described (Molinaro et al., 2008; Pannccione et al., 2012; Secondo et al., 2015; Ciccone et al., 2019). The data were acquired and analyzed using the pClamp software (version 9.0, Molecular Devices). The I_{NCX} were recorded starting from a −60 mV holding potential up to a short-step depolarization at +60 mV as previously described (Molinaro et al., 2008; Pannccione et al., 2012). In particular, reverse mode of NCX is represented in rising portion of the ramp ranging from 0 mV to +60 mV and measured at the end of +60 mV whereas Forward mode is represented in the descending portion of the ramp (from −120 to −0 mV) and measured at the end of −120 mV.The I_{NCX}, sensitive to Ni^{2+}, were isolated by subtracting the Ni^{2+}-insensitive components from the total currents ($I_{NCX} = I_{TOT}\text{-}I_{Ni\text{-}Resistent}$). The tetrodotoxin (TTX)-sensitive I_{Na} were recorded using low resistance electrodes (1.4–2.3 MΩ), sampled at a rate of 100 kHz and filtered at 5 kHz. The neurons were held at −120 mV and stepped to a range of potentials (−100 to +30 mV in 10 mV increments) as reported previously (Secondo et al., 2015; Ciccone et al., 2019). The neurons were perfused with external Ringer's solution containing the following (in mM): 126 NaCl, 1.2 $NaHPO_4$, 2.4 KCl, 2.4 $CaCl_2$, 1.2 $MgCl_2$, 10 glucose, and 18 $NaHCO_3$, pH7.4. Tetraethylammonium (TEA) and nimodipine (20 mM and 10 μM, respectively) were added to the external solution in order to block the potassium and calcium currents. The pipettes were filled with 100 K-gluconate, 10 TEA, 20 NaCl, 1 Mg-ATP, 0.1 $CaCl_2$, 2 $MgCl_2$, 0.75 EGTA, and 10 HEPES, adjusted to pH 7.2 with $Cs(OH)_2$. Any possible changes in cell size were calculated by monitoring the capacitance of each cell membrane, which is directly related to the membrane surface area, and by expressing the current amplitude data as current densities (pA/pF). The capacitive currents were estimated from the decay of the capacitive transient induced by 5 mV depolarizing pulses from a holding potential of −80 mV and acquired at a sampling rate of 50 kHz. The capacitance of the membrane was calculated according to the following equation: $Cm = \tau c \bullet Io/\Delta Em(1\text{-}I\infty/Io)$, where Cm is the membrane capacitance, τc is the time constant of the membrane capacitance, Io is the maximum capacitance current value, ΔEm is the amplitude of the voltage step, and I∞ is the amplitude of the steady-state current (Pannaccione et al., 2012).

$[Ca^{2+}]_i$ Measurement

Hippocampal neurons were incubated with 10 μM Fura-2 AM for 30 min at 37°C in normal Krebs solution containing 5.5 mM KCl, 160 mM NaCl, 1.2 mM $MgCl_2$, 1.5 mM $CaCl_2$, 10 mM glucose, and 10 mM HEPES-NaOH (pH 7.4). At the end of the loading period, coverslips were placed into a perfusion chamber (Medical System Co., Greenvale, NY, United States), mounted onto the stage of an inverted Zeiss Axiovert 200 microscope (Carl Zeiss, Milan, Italy), equipped with a FLUAR 40X oil objective lens. The experiments were carried out with a digital imaging system composed of a MicroMax 512BFT cooled CCD camera (Princeton Instruments), LAMBDA10-2 filter wheeler (Sutter Instruments), and Meta-Morph/MetaFluor Imaging System software (Universal Imaging). Primary neurons were alternatively illuminated at wavelengths of 340 and 380 nm by a Xenon lamp. The emitted light was passed through a 512 nm barrier filter. Fura-2 fluorescence intensity was measured every 3 s. Fura-2 ratiometric values were automatically converted by MetaMorph/MetaFluor Imaging System software (Universal Imaging) to cytosolic Ca^{2+} levels, by using a preloaded calibration curve obtained in preliminary experiments, as previously described (Grynkiewicz et al., 1985).

To elicit ER Ca^{2+} release in neurons, ATP (100 μM) and the irreversible inhibitor of sarco-endoplasmic reticulum Ca^{2+} ATPase (SERCA) pump thapsigargin (1 μM) were added in a Ca^{2+}-free solution (containing 5.5 mM KCl, 160 mM NaCl, 1.2 mM $MgCl_2$, 10 mM glucose, and 10 mM HEPES-NaOH, pH 7.4), as indicated by the bar of **Figure 3**. Specifically, ATP was able to trigger a rapid ER Ca^{2+} release by activating its plasmalemmal purinergic receptors coupled to Gq, while thapsigargin, by blocking SERCA, inhibits tonic refilling into ER and determines a progressive and slow ER Ca^{2+} release. The use of both tools allows to recruit all components of ER Ca^{2+} store (Caputo et al., 2012; Criscuolo et al., 2019; Secondo et al., 2019; Tedeschi et al., 2019; Tedeschi et al., 2021).

Western Blotting

Total lysates for the immunoblotting analyses were obtained as follows: the primary hippocampal neurons were washed in phosphate buffered saline (PBS) and collected by gentle scraping in ice-cold RIPA buffer containing (in mM) 50 Tris pH 7.4, 100 NaCl, 1 EGTA, 1 PMSF, 1 sodium orthovanadate, 1 NaF, 0.5% NP-40, and 0.2% SDS supplemented with protease inhibitor cocktail II (Roche Diagnostic, Monza, Italy). The nitrocellulose membranes were incubated with the following antibodies: rabbit-polyclonal anti-NCX3, anti-NCX1, anti-NCX2 (1:1,000, Alomone Labs, Israel) and anti-β-actin peroxidase (1:10,000, Sigma-Aldrich, Milan, Italy). The immunoreactive bands were detected with thechemiluminescence system (Amersham-Pharmacia-Biosciences, UK). The films were developed with a standard photographic procedure and the quantitative analysis of the bands detected was carried out by densitometric scanning.

Confocal Immunofluorescence Analysis

The confocal immunofluorescence procedures in neuronal cultures were performed as previously described (Boscia et al., 2017; de Rosa et al., 2019). The cell cultures were fixed in 4% wt/vol paraformaldehyde in phosphate buffer for 30 min. After blocking with 3% BSA, the cells were incubated with monoclonal anti-NCX3 (1:1,000, Trans Genic Inc., Japan) and rabbit policlonal anti-$Na_V1.6$ (1:1,000, Alomone Labs, Israel). Next, the cells were incubated with Alexa594-conjugated anti-mouse IgGs and biotinylated anti-rabbit antibodies. NCX3 was detected by using the tyramide signal amplification (TSA) fluorescein system (Perkin-Elmer, Life Sciences). Hoechst 33258 was used to stain the nuclei. The images were observed using a Zeiss LSM 700 laser (Carl Zeiss) scanning confocal microscope. The single images were taken with an optical thickness of 0.7 μm and a resolution of 1024 × 1024. The NCX3 and $Na_V1.6$ fluorescence intensities were quantified in terms of pixel intensity by using the NIH image software, as previously described (Boscia et al., 2012). Briefly, digital images were taken with 63× objective and identical laser power settings and exposure times were applied to all the photographs from each experimental set. The co-localization between NCX3 and $Na_V1.6$ was analysed by line profiling the Cy3 (red) and FITC (green) fluorescence intensities using the ZEN lite software (Carl Zeiss) (Cammarota et al.,2021).

Statistical Analysis

GraphPad Prism 6.02 was used for the statistical analyses (GraphPad Software, La Jolla, CA). Thedata are expressed as the mean ± S.E.M. of the values obtained from individual experiments. The statistical comparisons between the groups were performed by means of the Student's t-test or one-way analysis of variance (ANOVA) followed by the Bonferroni post hoc test or Newman–Keuls' test. $p < 0.05$ was considered significant.

RESULTS

The Activity of NCX Is Significantly Upregulated in the Reverse Mode of Operation in the Tg2576 Hippocampal Neurons

First, we examined any possible changes of the NCX activity in the Tg2576 hippocampal neurons. We assessed the I_{NCX} in the forward and reverse modes of operation by patch-clamp experiments in a whole-cell configuration in both the WT and Tg2576 cultured hippocampal neurons after 8, 12, and 15 DIV. Electrophysiological recordings showed that the NCX activity was significantly modulated in a time-dependent manner only in the reverse mode of operation in the Tg2576 hippocampal neurons, while the forward mode was not affected (**Figures 1A,B**). In particular, the I_{NCX} in theTg2576 neurons were increased at 8, 12, and 15 DIV in comparison with those recorded in the WT neurons at the same DIV, with a marked peak at 12 DIV (**Figure 1A,B**).

NCX3 Silencing or Pharmacological Inhibition Prevents the Upregulation of the I_{NCX} in the Tg2576 Hippocampal Neurons

Patch-clamp experiments revealed that the silencing of NCX3 (siNCX3) prevented the upregulation of the I_{NCX} in the reverse mode in the Tg2576 hippocampal neurons (**Figures 2A,B**). Of note, the siRNA directed against NCX3 did not modify the expression of the other two NCX isoforms, NCX1 and NCX2 (**Figure 2C**). Moreover, the specific contribution of NCX3 to the I_{NCX} upregulation in the reverse mode was further confirmed by blocking the exchanger with the 2-{2-[4-(4-nitrobenzyloxy) phenyl]ethyl}isothiourea mesylate (KB-R7943). Of note, KB-R7943 was demonstrated to be three-fold more inhibitory to NCX3 than to NCX1 and NCX2, with IC_{50} values of 4.9 ± 0.4 μM and 4.1 ± 0.3 μM for NCX1 and NCX2, respectively, and of 1.5 ± 0.1 μM for NCX3 (Iwamoto and Shigekawa, 1998). Additionally, KB-R7943 at low concentrations inhibits the NCX3 activity preferentially in the reverse mode (IC_{50} = 1.1 ± 3.4 μM for the reverse mode and IC_{50} > 30 μM for the forward mode) (Iwamoto and Shigekawa, 1998; Watano et al., 1996; Annunziato et al., 2004). In particular, preliminary concentration/response experiments revealed that 0.5 μM kB-R7943 was the minimum concentration able to significantly inhibit NCX3 without interfering with NCX1 and NCX2 isoforms. Importantly, electrophysiological recordings showed that in the presence of KB-R7943 at the concentration of 0.5 μM, the upregulation of the I_{NCX} in the reverse mode in the Tg2576 hippocampal neurons was completely prevented, with the

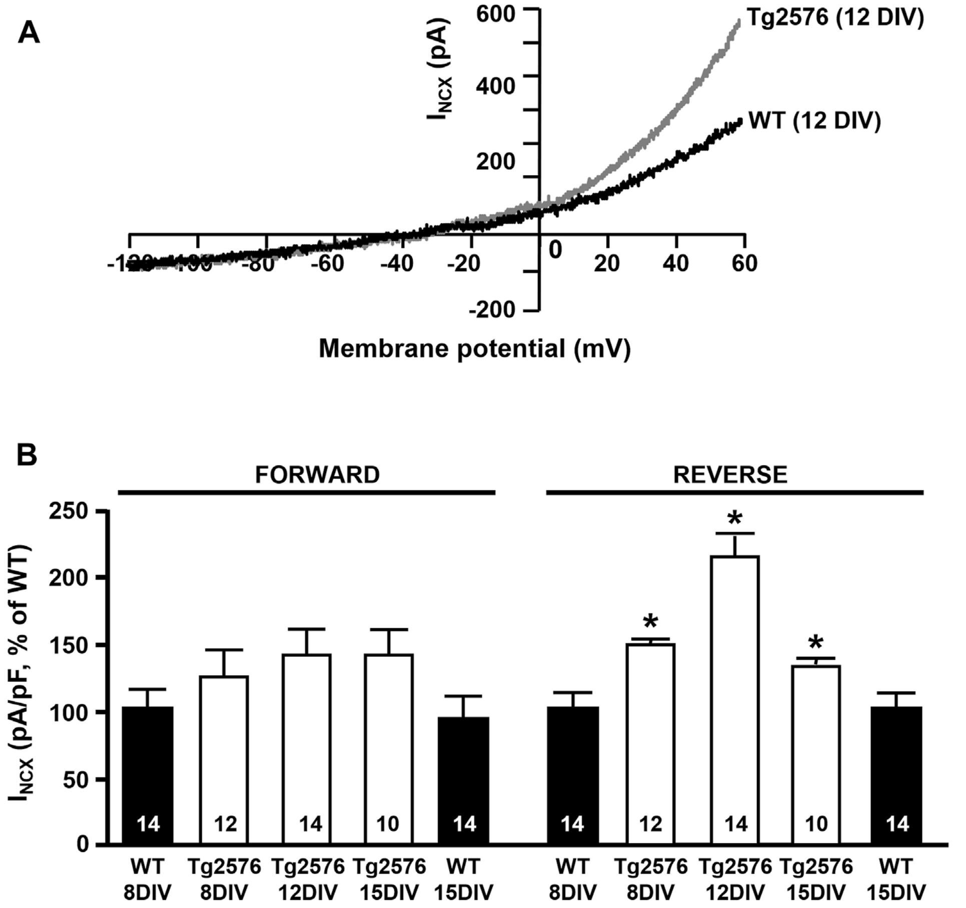

FIGURE 1 | I_{NCX} in WT and Tg2576 primary hippocampal neurons. **(A)** Representative superimposed traces of I_{NCX} in the reverse and forward modes of operation recorded in WT (black trace) and Tg2576 (gray trace) primary hippocampal neurons at 12 DIV. **(B)** Quantification of I_{NCX} in the reverse and forward modes of operation recorded in WT and Tg2576 primary hippocampal neurons at 8, 12, and 15 DIV, expressed as percentage of increase in comparison to WT. Values are expressed as mean ± SEM of 3 independent experimental sessions. Statistical comparisons between groups were performed by one-way ANOVA followed by Newman-Keuls' test. ($^*p < 0.05$ vs. WT). The number of cells used for each experimental condition is noted on the bars.

return of the I_{NCX} to levels similar to those of the WT neurons (**Figures 2D,E**). Interestingly, as previously observed in hippocampal neurons exposed to $A\beta_{1-42}$ oligomers (Pannaccione et al., 2012), Western blot analyses revealed that the Tg2576 neurons displayed an upregulation of the NCX3 truncated band migrating at around 65 kDa in comparison with the WT neurons (**Figures 2F,G**).

The Enhancement of the NCX3 Activity in the Reverse Mode Participates to the Filling State of ER but Not to the Maintenance of Cytosolic Ca^{2+} Levels in the Tg2576 Hippocampal Neurons

To study the intracellular Ca^{2+} homeostasis and the putative relationship between NCX3 and the ER Ca^{2+} content in the Tg2576 hippocampal neurons, we performed Ca^{2+} imaging analyses with the fluorescent Ca^{2+} indicator Fura-2AM. The $[Ca^{2+}]_i$ in the Tg2576 hippocampal neurons did not differ from that measured in the WT neurons (**Figures 3A,B**) unlike the ER Ca^{2+} levels (**Figures 3A,C**). Indeed, the exposure to ATP plus the SERCA inhibitor thapsigargin, both triggering an ER Ca^{2+} release, determined a significantly higher increase in $[Ca^{2+}]_i$ and in the area under the curve (AUC) value in the Tg2576 hippocampal neurons compared with those in the WT neurons (**Figures 3A,D**).

In particular, we measured a significant difference between WT and Tg2576 when ATP plus thapsigargin was added to 0 mM extracellular Ca^{2+}, showing that the simultaneous activation of NCX reverse mode is not necessary to measure changes in ER Ca^{2+} levels. This suggested that the addition of ATP and thapsigargin may unmask a tonic and stable ER Ca^{2+} dysfunction in Tg2576 neurons. Moreover, to study the putative contribution of NCX3 isoform to the filling state of ER Ca^{2+} stores, basal and ER Ca^{2+} levels were measured in the absence or presence of the well known NCX inhibitor KB-R7943. Specifically, KB-R7943 was preincubated for 20 min in a Ca^{2+}-containing solution at the final concentration of 0.5 μM, selectively inhibiting the NCX3 reverse activity. Under these conditions, it significantly reduced the amount of Ca^{2+} released from the ER both in the WT hippocampal neurons and

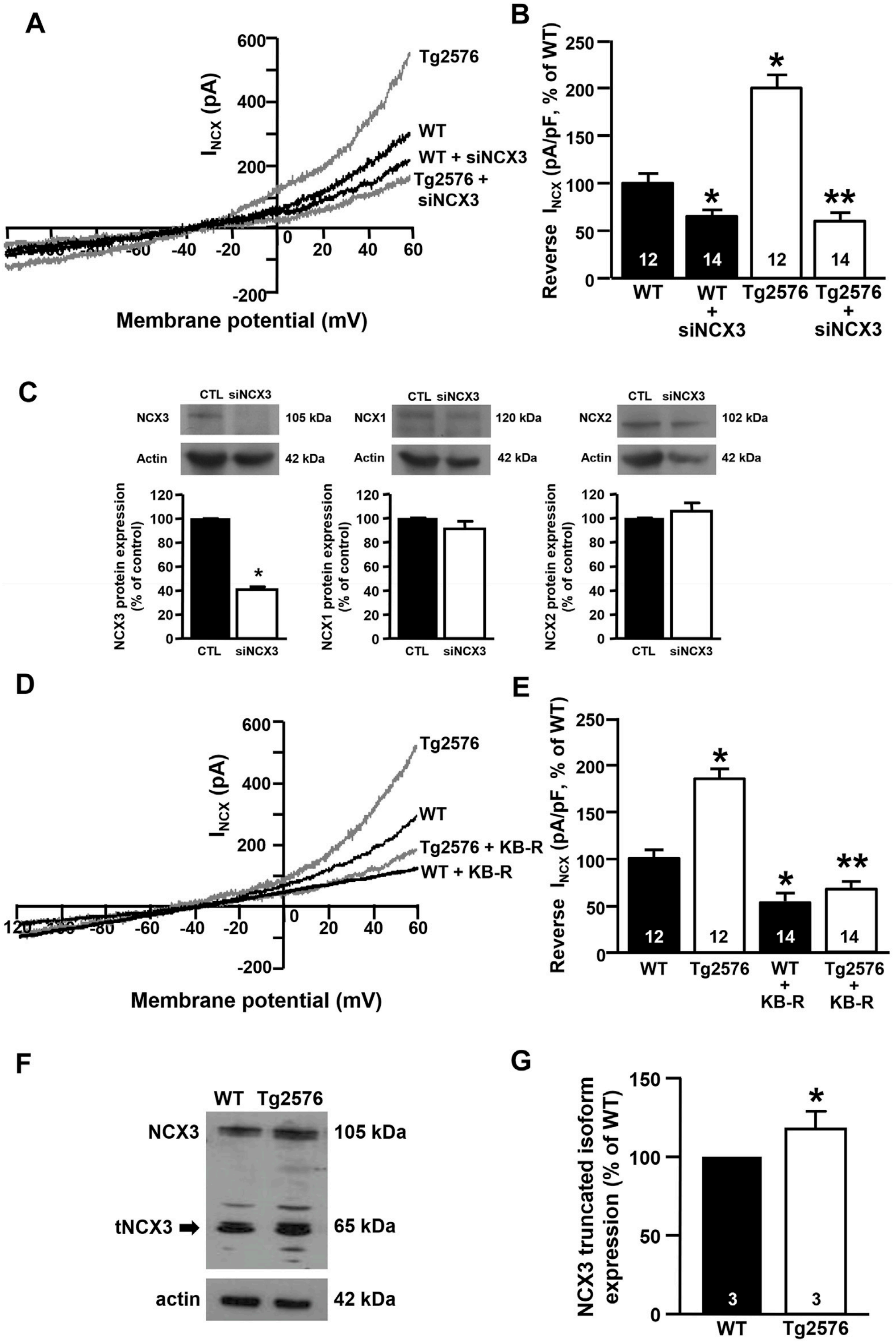

FIGURE 2 | Effect of NCX3 silencing or inhibition by KB-R7943 in WT and Tg2576 primary hippocampal neurons. **(A)** Representative superimposed traces of I_{NCX} in the reverse and forward modes of operation recorded in WT and WT plus siNCX3 (black traces), Tg2576 and Tg2576 plus siNCX3 (grey traces) primary hippocampal neurons at 12 DIV. **(B)** Quantification of I_{NCX} in the reverse mode of operation represented in A, expressed as percentage of variation in comparison to WT. Values are expressed as mean ± SEM of 3 independent experimental sessions. **(C)** Representative Western blotting experiments and relative quantifications showing the effect of NCX3 silencing (siNCX3) on NCX3, NCX1, and NCX2 protein expression in primary hippocampal neurons **(D)** Representative superimposed traces of I_{NCX} in the reverse and forward modes of operation recorded from WT and WT plus 0.5 μM kB-R7943 (black traces), Tg2576 and Tg2576 plus 0.5 μM kB-R7943 (grey traces)

(Continued)

FIGURE 2 | primary hippocampal neurons at 12 DIV. **(E)** Quantification of I_{NCX} in the reverse mode of operation represented in D, expressed as percentage of variation in comparison to WT. Values are expressed as mean ± SEM of 3 independent experimental sessions. The number of cells used for each experimental condition is noted on the bars. **(F, G)** Representative Western blot of NCX3 protein expression and densitometric quantification of NCX3 truncated band in WT and Tg2576 primary hippocampal neurons at 12 DIV, represented as percentage of WT. Values are expressed as mean ± SEM of 3 independent experimental sessions. Statistical comparisons between groups were performed by one-way ANOVA followed by Newman-Keuls' test. (*$p < 0.05$ vs. WT; **$p < 0.05$ vs. Tg2576 mice).

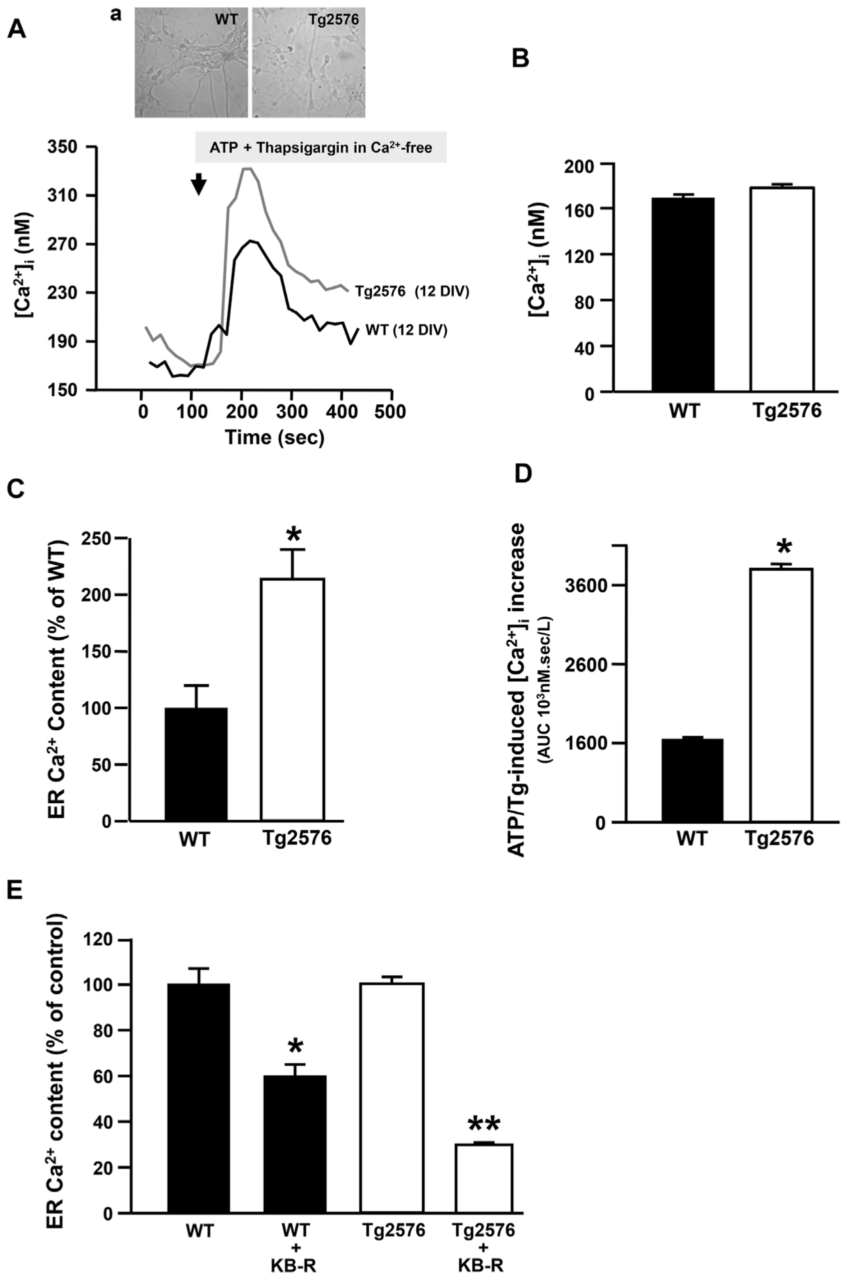

FIGURE 3 | Effect of NCX3 inhibition by KB-R7943 on ER Ca^{2+} content in WT and Tg2576 primary hippocampal neurons. **(A)** Representative superimposed traces of $[Ca^{2+}]_i$ measured in WT (black trace, $N = 36$) and Tg2576 (grey trace, $N = 34$) primary hippocampal neurons at 12 DIV, representative images in panel **(A)**. **(B)** Quantification of basal values of $[Ca^{2+}]_i$ in WT ($N = 36$) and Tg2576 primary hippocampal neurons at 12 DIV ($N = 34$). **(C)** ER Ca^{2+} content quantified as $[Ca^{2+}]_i$ increase induced by Thapsigargin (Tg; 1 μM) and ATP (100 μM) in 0 μM Ca^{2+}, and expressed as percentage of the effect observed in WT (considered as 100%). **(D)** AUCs of $[Ca^{2+}]_i$ calculated for **(A)**. **(E)** Quantification of ER Ca^{2+} content in WT and Tg2576 primary hippocampal neurons at 12 DIV treated with KB-R7943 at 0.5 μM. Values are represented as percentage of respective controls, expressed as mean ± SEM of 3 independent experimental sessions. Statistical comparisons between groups were performed by one-way ANOVA followed by Newman-Keuls' test. (*$p < 0.05$ vs. WT; **$p < 0.05$ vs. Tg2576 mice).

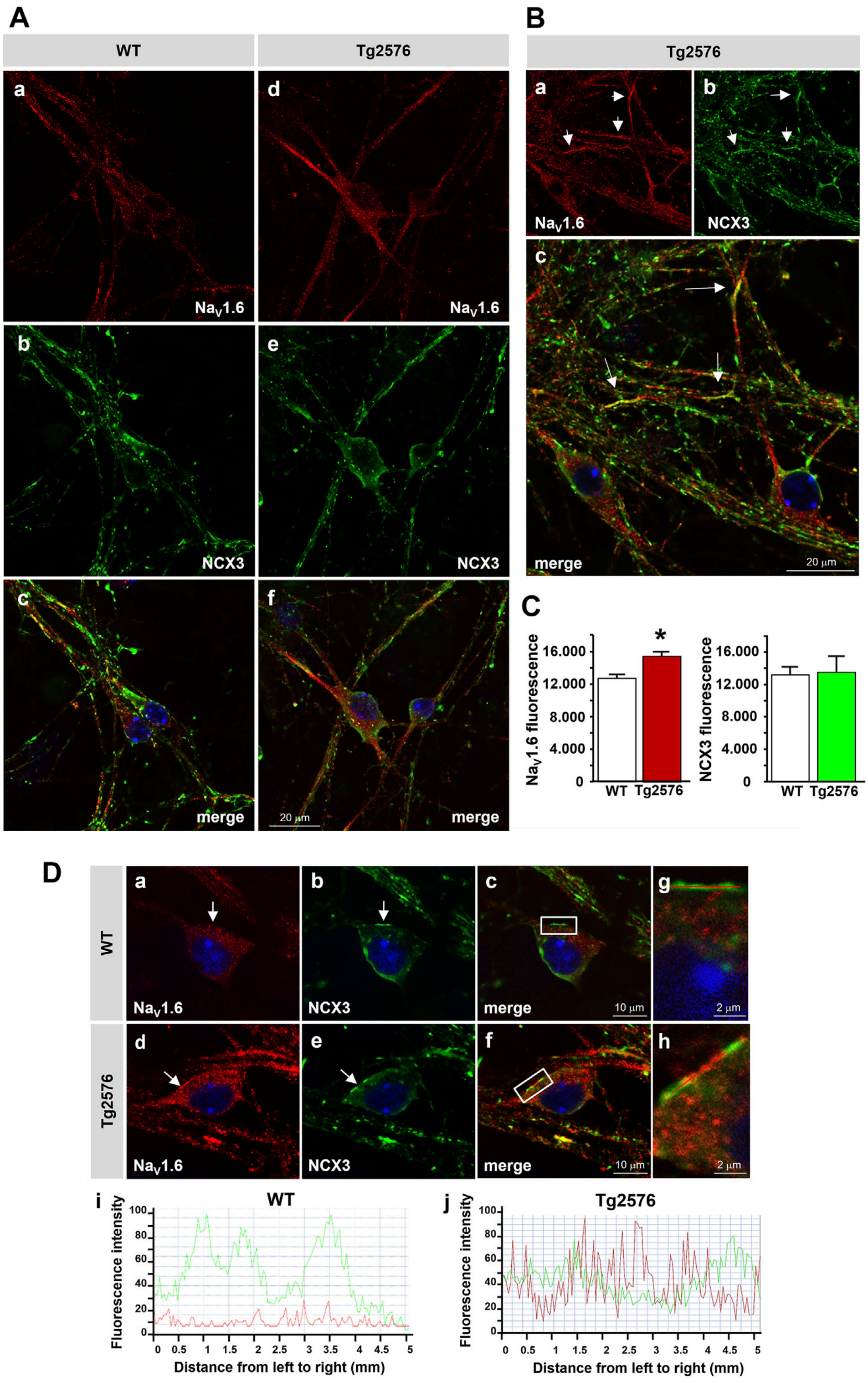

FIGURE 4 | Distribution of Na$_V$1.6 channels and NCX3 in Tg2576 primary hippocampal neurons. **(A)** Confocal microscopic images displaying the distribution of Na$_V$1.6 (red) and NCX3 (green) immunoreactivities in hippocampal neurons isolated from WT and Tg2576 mouse embryos and cultured for 12 DIV (scale bars: in a–f: 20 µm). **(B)** Confocal microscopic images displaying the distribution of Na$_V$1.6 (red) and NCX3 (green) immunoreactivities in Tg2576 primary hippocampal neurons at 12 DIV. Arrows in a-c point to the intense co-localization of Na$_V$1.6 and NCX3 immunostaining along neurites (scale bars: 20 µm). **(C)** Densitometric analysis of

(*Continued*)

FIGURE 4 | $Na_V1.6$ **(left)** and NCX3 **(right)** fluorescence intensities in WT and Tg2576 neurons at 12 DIV. The data are expressed in arbitrary units ($^*p < 0.05$ vs. WT). **(D)** Confocal microscopic images displaying the distribution of $Na_V1.6$ (red) and NCX3 (green) immunoreactivities in WT and Tg2576 primary hippocampal neurons at 12 DIV. Arrows in a–f point to $Na_V1.6$ and NCX3 immunoreactivities along the somatic plasma membrane of both WT and Tg2576 neurons. Panels g and h show higher magnification images of the frame depicted in c and f, respectively. Nuclei were counterstained with DAPI (blue) (scale bars: in a–f: 10 μm; in g and h: 2 μm). Panels i and j show the line profiling of $Na_V1.6$ (red) and NCX3 (green) fluorescence intensities along the line selected on the somatic plasma membrane of both WT (c) and Tg2576 (f) hippocampal neurons.

in the Tg2576 neurons (**Figure 3E**). However, this effect was significantly greater in the Tg2576 neurons than in the WT neurons (**Figure 3E**).

The Functional Coupling Between $Na_V1.6$ Channels and NCX3 Exchangers Underlies the Increased Reverse Activity of NCX3 in theTg2576 Hippocampal Neurons

We previously showed that the expression and activity of $Na_V1.6$ channels were time-dependently upregulated in the Tg2576 hippocampal neurons, with a maximum increase at 12 DIV (Ciccone et al., 2019). To explore whether the neuronal NCX3 and $Na_V1.6$ functions might be coupled, we first investigated the co-expression of NCX3 and $Na_V1.6$ in the 12 DIV Tg2576 hippocampal neurons. In line with our previous observations (Ciccone et al., 2019), quantitative immunofluorescence analyses showed that the $Na_V1.6$ immunofluorescence significantly increased intracellularly and along the plasma membrane of both the soma and neurites of the 12 DIV Tg2576 hippocampal neurons compared with the WT cultures (**Figures 4A–C**). Although the global immunofluorescence signal of NCX3 remained unaltered in the Tg2576 neurons compared to the WT, a clustered co-expression of the upregulated $Na_V1.6$ channels with NCX3 was clearly detected along several plasma membrane and cytosolic domains of both the soma and neurites of the Tg2576 neurons (**Figures 4A–C**).

Next, to test the hypothesis that the reversal of the NCX3 activity was driven by the increased Na^+ inward currents mediated by the $Na_V1.6$ channels, we measured both the I_{Na} and I_{NCX} in the presence of the sodium channel blocker TTX added to the extracellular recording solution, or after the treatment with anisomycin, a *Streptomyces griseolus* antibiotic that, by promoting p38 mitogen-activated protein (MAP) kinase activation, induces the selective endocytosis of $Na_V1.6$ and, subsequently, the reduction of the $Na_V1.6$-mediated currents (Wittmack et al., 2005; Gasser et al., 2010; Ciccone et al., 2019). We observed that the I_{Na} recorded in the presence of TTX or after the treatment with anisomycin were significantly reduced in both the WT and Tg2576 hippocampal neurons (**Figures 5A,B**). Moreover, both the pharmacological tools, TTX and anisomycin, were able to counteract the increase of the I_{NCX} in the reverse mode of operation not only in the Tg2576 hippocampal neurons but also in the WT neurons, despite the extent of the I_{NCX} reduction was greater in the Tg2576 neurons than in the WT neurons (**Figures 5C,D**).

DISCUSSION

The impact of the modulation of NCX on neuronal survival in AD has been investigated in several studies. Notably, a recent genome-wide association study by Saad and co-workers identified *SLC8A3*, the gene encoding for NCX3, among different genes in which multiple rare variations were associated with the age of onset of AD, thus proposing the exchanger as a possible molecular factor determining the timing of the onset of the disorder (Saad et al., 2015). However, although different reports have suggested a neuroprotective role of NCX in different experimental models of AD, further efforts should be made to characterize the involvement of the exchanger in the onset of AD. Many studies have demonstrated that the failure of the machinery regulating Ca^{2+} homeostasis is a crucial event in the AD etiopathogenesis (Berridge, 2010). Of note, disturbances in Ca^{2+} homeostasis were demonstrated to occur before the development of overt AD symptoms (Etcheberrigaray et al., 1998). This evidence suggested that the alteration of the systems regulating $[Ca^{2+}]_i$ may be an upstream event in the AD pathogenesis, inducing the early changes in learning and memory functions. In the present study, we have therefore moved to assess any possible modulation of the NCX activity and its impact on the $[Ca^{2+}]_i$ in primary hippocampal neurons from the Tg2576 mouse, an *in vitro* model of AD. Primary cultures from the Tg2576 mouse, which carries the APP_{SWE} double mutation of the amyloid precursor protein, accumulate $A\beta_{1-42}$ over time in culture, thus recapitulating some of the main features of the Aβ-induced neurodegeneration (Takahashi et al., 2004; Almeida et al., 2005; Takahashi et al., 2013).

Interestingly, we observed that the I_{NCX} were increased in the reverse, Ca^{2+} influx mode, while the forward mode was not affected. The enhancement of the I_{NCX} appeared to be mediated by a specific NCX isoform, NCX3, since both the silencing of NCX3 and the treatment with the isoform-selective inhibitor KB-R7943 significantly reduced the reverse I_{NCX} in the Tg2576 neurons. Interestingly, the upregulation of the NCX3 currents in the Tg2576 hippocampal neurons was time-dependent, with a maximum increase at 12 DIV. In agreement, a previous *in vitro* study by our group had demonstrated that NCX3 was modulated after the exposure of primary hippocampal neurons to synthetic $A\beta_{1-42}$ oligomers, thus strongly implicating NCX3 in the neuronal responses to $A\beta_{1-42}$ injury (Pannaccione et al., 2012). Of note, the upregulation of the activity of NCX3 was associated with an increased formation of its truncated isoform, which was demonstrated to be hyperfunctional (Pannaccione et al., 2012). In line with this finding, we observed that the maximum increase of the activity of NCX3 was concomitant with the over-expression of its truncated isoform also in the Tg2576 hippocampal neurons, as Western blot analyses revealed a marked increase of the NCX3 band migrating at around 65 kDa in the 12 DIV Tg2576 neuronal lysates in comparison with the WT lysates. Interestingly, different truncated isoforms of NCX3, as well as of NCX1, corresponding to any splicing variants or

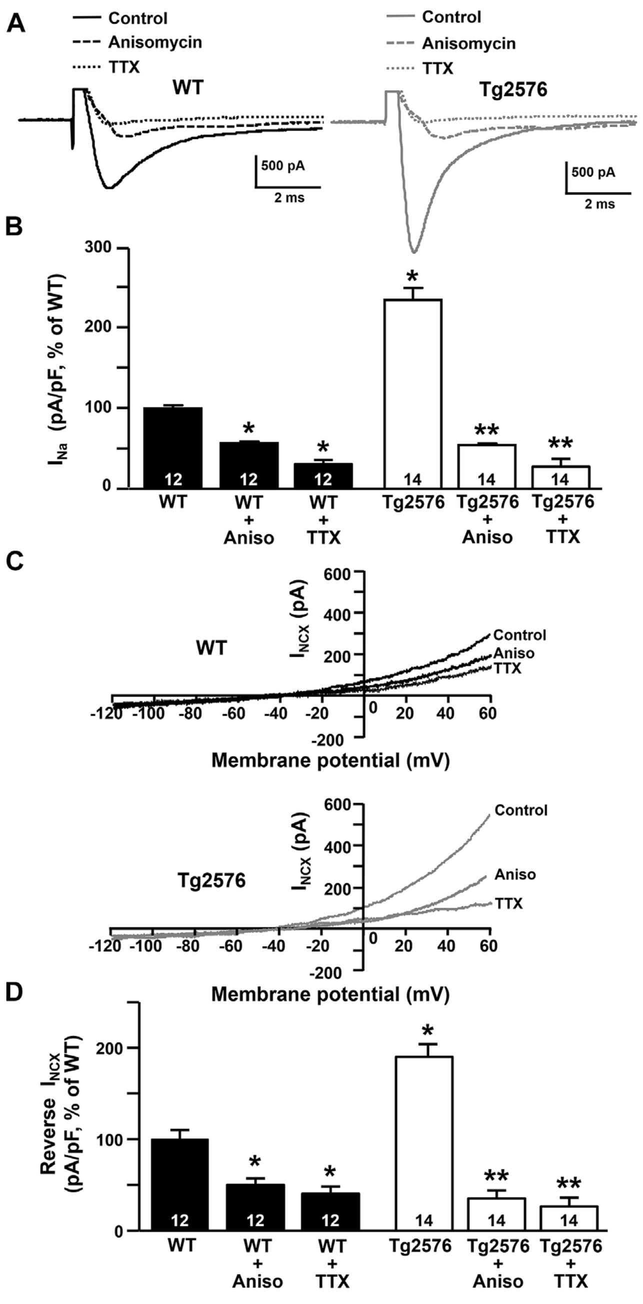

FIGURE 5 | Effect of TTX and anisomycin on I_{Na} and I_{NCX} in WT and Tg2576 primary hippocampal neurons. **(A)** Representative traces of I_{Na} recorded in control conditions and in the presence of TTX or anisomycin pre-treatment in WT (black traces) and Tg2576 (grey traces) primary hippocampal neurons at 12 DIV. **(B)** Quantification of I_{Na} represented in A, expressed as percentage of WT in control conditions. Values are expressed as mean ± SEM of 3 independent experimental sessions. **(C)** Representative superimposed traces of I_{NCX} in the reverse and forward modes of operation recorded in control conditions and in the presence of TTX or anisomycin pre-treatment in WT **(top)** and Tg2576 **(bottom)** primary hippocampal neurons at 12 DIV. **(D)** Quantification of I_{NCX} in the reverse mode of operation represented in C, expressed as percentage of WT in control conditions. Values are expressed as mean ± SEM of 3 independent experimental sessions. Statistical comparisons between groups were performed by one-way ANOVA followed by Newman-Keuls' test (*$p < 0.05$ vs. WT; **$p < 0.05$ vs. Tg2576 mice). The number of cells used for each experimental condition is noted on the bars.

cleavage products, have been found in the brain by different research groups and have been demonstrated to be functional or even hyper-functional, probably due to the loss of regulatory domains (Gabellini et al., 1996; Van Eylen et al., 2001; Lindgren et al., 2005; Michel et al., 2015; Michel et al., 2016). Of note, our group, and others, have shown that the cleavage of NCX3 by calpains could be a form of post-translational regulation providing a hyperactive NCX3 isoform by increasing, in particular, the reverse mode capacity of the exchanger (Pannaccione et al., 2012; Michel et al., 2016; Cammarota et al., 2021).

Ca^{2+} entry following NCX reversal has been implicated in a variety of pathophysiological conditions (Czyz and Kiedrowski, 2002; Floyd et al., 2005; Andrikopoulos et al., 2015; Gerkau et al., 2017; Brazhe et al., 2018; Secondo et al., 2020). In particular, the Ca^{2+} signalling mediated by reverse NCX has been shown to contribute to the astrocytic response to mechanical injury as well as to oligodendrocyte differentiation and myelin synthesis (Floyd et al., 2005; Boscia et al., 2012; Pappalardo et al., 2014; Hammann et al., 2018; Boscia et al., 2020). We also demonstrated in a previous study that the activation of the reverse mode of NCX1 induced by increased Na_V-mediated currents played a fundamental role in Akt signalling and neuronal differentiation (Secondo et al., 2015). In the present study we show that the Ca^{2+} influx mediated by NCX3 working in the reverse mode significantly increased the amount of Ca^{2+} ions in the ER, a mechanism that has been demonstrated to be crucial for neuroprotection (Sirabella et al., 2009; Pannaccione et al., 2012; Sisalli et al., 2014).

In order to refill the ER Ca^{2+} store, a privileged pathway may occur between NCX working in the reverse mode and SERCA (Fameli et al., 2007; van Breemen et al., 2013). Furthermore, the tonic Ca^{2+} signal elicited by the application of thapsigargin in a calcium-free medium may suggest that SERCA is the main pump clearing cytosolic Ca^{2+} in hippocampal neurons. On the other hand, in Tg2576 neurons a significant alteration of the Ca^{2+} clearing mechanisms has been already reported (Lee et al., 2012). Among these mechanisms, the impairment of mitochondrial Ca^{2+} uptake, associated with increased mitochondrial reactive oxygen species and depolarization of mitochondrial membrane potential, may play an important role. Of note, the dysfunctional ER Ca^{2+} content was associated to the abnormal NCX3 reverse mode activity in Tg2576 neurons. In particular, our $[Ca^{2+}]_i$ measurements through Fura-2 AM fluorescence did not reveal any significant change in the cytosolic Ca^{2+} levels in the Tg2576 neurons compared with the WT neurons. In contrast, we observed a marked enhancement of the ER Ca^{2+} content in the transgenic neurons compared with the WT neurons, thus identifying the organellar Ca^{2+} dyshomeostasis as a putative biomarker of the AD pathology. Importantly, the inhibition of NCX3 through KB-R7943 significantly reduced the ER Ca^{2+} levels in the Tg2576 hippocampal neurons, hence showing that the increased Ca^{2+} influx through reverse NCX3 contributed to enhance the Ca^{2+} refilling into the ER of these neurons. On the other hand, the reduction of the ER Ca^{2+} content induced by KB-R7943 in the WT neurons indicated that NCX3 plays a key role in the ER Ca^{2+} replenishment in hippocampal neurons also in physiological conditions. These results are in line with several studies showing that NCX is located at the plasma membrane next to the junctional ER in numerous cell types (Blaustein et al., 2002; Lencesova et al., 2004; Fameli et al., 2007; Di Giuro et al., 2017), where it participates in ER Ca^{2+} handling. In agreement, many experimental data reported thus far have supported the concept that the entire NCX family is involved in the regulation of Ca^{2+} levels in the ER and in the sarcoplasmic reticulum (SR) by working in its reverse modality (Hirota et al., 2007; Lemos et al., 2007; Sirabella et al., 2009; Di Giuro et al., 2017). In particular, NCX has been recognized as an important mediator of Ca^{2+} influx in vascular smooth muscle cells (Poburko et al., 2007; Lee et al., 2012; Fameli et al., 2007; van Breemen et al., 2013), where its spatial and functional linkage to the SERCA pump allows the SR Ca^{2+} refilling that sustains $[Ca^{2+}]_i$ oscillations underlying smooth muscle contraction (Fameli et al., 2007; van Breemen et al., 2013). Moreover, it has been demonstrated that NCX is functionally coupled with the transient receptor channel protein 6 (TRPC6) at specialized SR/ER-plasma membrane junctions, where it mediates Ca^{2+} influx and hence regulates SR Ca^{2+} content following the localized intracellular Na^{+} concentration elevations mediated by TRPC6 (Poburko et al., 2007).

While in muscle cells the SR-mediated Ca^{2+} signalling is essential for excitation-contraction coupling, in central neurons the ER represents a dynamic Ca^{2+} reservoir indispensable for neuronal signalling. Moreover, as it constitutes the location of protein synthesis and post-translational folding, the ER may be also considered a regulator of cell fate. Indeed, any alteration of ER Ca^{2+} homeostasis, including severe changes in luminal Ca^{2+} levels, may trigger the unfolded protein response and ER stress, thus turning the ER in a potential source of cell death signals (Morishima et al., 2002; Verkhratsky and Petersen, 2002; Verkhratsky, 2004; 2005). Such a mechanism has been reported in a variety of AD models and is currently considered a crucial aspect of the AD pathogenesis (Verkhratsky and Toescu, 2003; Alberdi et al., 2013; Pannaccione et al., 2020; Salminen et al., 2020; Uddin et al., 2020). Indeed, Aβ oligomers may affect ER Ca^{2+} homeostasis by inducing an exaggerated Ca^{2+} release or interacting with ER-residing Ca^{2+} regulators such as ryanodine and inositol triphosphate receptors (Ferreiro et al., 2004; Costa et al., 2012; Alberdi et al., 2013; Wang and Zheng, 2019; Pannaccione et al., 2020). ER Ca^{2+} dyshomeostasis, in turn, may exert detrimental effects on neuronal function and survival and, likewise damaging, may favour the APP amyloidogenic processing and subsequent Aβ accumulation hence triggering a vicious circle (Paschen, 2001).

In this context, the NCX-mediated Ca^{2+} refilling into the ER, counteracting the reduction of the ER Ca^{2+} levels and preventing the ER stress cascade, may be determinant for neuronal survival. Of note, previous works have demonstrated that the ER Ca^{2+} refilling mediated by NCX, in particular the isoform 1, represents a protective mechanism helping cortical neurons to survive anoxic conditions (Sirabella et al., 2009; Sisalli et al., 2014). More importantly, our previous study on primary hippocampal neurons exposed to exogenous $Aβ_{1–42}$ oligomers demonstrated that the increased reverse activity of NCX3 in the early phase contributed to a Ca^{2+} refilling into the ER, thus preventing an ER Ca^{2+} content reduction, ER stress activation and apoptotic cell death. Remarkably, the silencing or the knocking-out of the NCX3 gene prevented the enhancement of both the I_{NCX} and Ca^{2+} content in the ER stores and, in turn, activated caspase-12 (Pannaccione et al., 2012). Likewise, NCX3 loss in a late phase of Aβ exposure induced the activation of caspase-12 and the subsequent apoptotic cell death (Pannaccione et al., 2012). Interestingly, while NCX3 upregulation abruptly ceased in the late phase of a single exposure to exogenous $Aβ_{1–42}$ oligomers, we did not observe any reduction of the I_{NCX} in the Tg2576 neurons over time in culture. This result could be explained by the fact that Tg2576 primary neurons progressively accumulate intracellular and extracellular Aβ over time in culture, with the highest Aβ burden observed at 19–21 DIV (Takahashi et al., 2004; Almeida et al., 2005). Importantly, an increased NCX activity had been already observed by Colvin and colleagues (1991) as Na^{+}-dependent Ca^{2+} uptake in AD brains. In particular, an increased NCX activity was observed in the surviving neurons of AD brain areas suffering neurodegeneration. Although the exact mechanism involving the NCX upregulation was not clear, the authors concluded that NCX could have a role in the survival mechanisms implemented by the AD-affected neurons (Colvin et al., 1991). Based on our findings, we suggest that the neuroprotective effect of NCX observed in the AD neurons could be related to the ER Ca^{2+} remodelling.

We have previously shown that the I_{Na} carried by the $Na_V1.6$ channels were upregulated in the Tg2576 hippocampal neurons (Ciccone et al., 2019). Interestingly, our co-expression studies revealed that in Tg2576 hippocampal neurons at 12 DIV, a time point displaying the maximum NCX3 activity and the upregulation of $Na_V1.6$ currents (Ciccone et al., 2019), both the $Na_V1.6$ and NCX3 immunoreactivities clustered along several cellular domains of both the soma and neurites, thus suggesting their possible functional coupling. In support of this observation, we provided evidence that the upregulation of the reverse I_{NCX} in the 12 DIV Tg2576 neurons was significantly reduced by inhibiting the $Na_V1.6$ currents. In particular, we found that the widely used Na_V channel blocker TTX, by restricting the Na^{+} entry through the $Na_V1.6$ channels, was able to significantly reduce the reverse I_{NCX} in the Tg2576 hippocampal neurons. Similarly, but to a lesser extent, also anisomycin, which induces the selective endocytosis of $Na_V1.6$ and the subsequent reduction of $Na_V1.6$ currents on the plasma membrane (Wittmack et al., 2005; Gasser et al., 2010; Ciccone et al., 2019), was able to decrease the I_{NCX} in the Tg2576 hippocampal neurons. These results suggested that the $Na_V1.6$ over-expression and functional upregulation were responsible for the increased activation of the reverse mode of NCX in the Tg2576 hippocampal neurons. Of note, both TTX and anisomycin reduced the reverse I_{NCX} also in the WT neurons, a result suggesting that the Na^{+} influx through $Na_V1.6$ channels could be one of the major Na^{+} sources inducing NCX3 reversal in hippocampal neurons also in physiological conditions. However, we cannot exclude the possibility that the modulation of the NCX3 expression pattern, namely the increase of the expression of the NCX3 truncated isoform, might contribute to enhance the reverse I_{NCX} in the Tg2576 hippocampal neurons to further potentiate the Ca^{2+} uptake.

The concept that the Na_V channels may play a key role in the interplay between the Na^+ and Ca^{2+} cycling by modulating the NCX working modality has emerged from several studies. In particular, different experimental models of multiple sclerosis, astrogliosis and arrhythmogenesis have suggested that the Na_V/NCX co-localization supports NCX reversal following Na_V-mediated Na^+ influx (Craner et al., 2004a; Craner et al., 2004b; Floyd et al., 2005; Larbig et al., 2010; Pappalardo et al., 2014; Radwański et al., 2016; Struckman et al., 2020). Indeed, although the rapid inactivation of Na_V currents could theoretically prevent a Na^+ elevation sufficiently high to induce NCX reversal, the Na_V/NCX proximity in a restricted microdomain may in fact generate a localized Na^+ increase capable of activating the NCX reverse mode. The Ca^{2+} entry induced by NCX reversal following the Na_V-mediated Na^+ influx has been implicated in certain pathological conditions such as mechanical strain injury and *in vitro* astrogliosis (Floyd et al., 2005; Pappalardo et al., 2014). Pappalardo and colleagues (2014), in particular, showed that the $[Ca^{2+}]_i$ fluctuations through the reverse operation of NCX triggered by the $Na_V1.5$ subunit contributed to the astrocytic response to mechanical injury (Pappalardo et al., 2014). Evidence suggesting that the Na_V/NCX coupling might instead have a detrimental impact on cell functions has been provided by different studies focusing on axonal degeneration in multiple sclerosis. Craner and colleagues demonstrated that the $Na_V1.6$ channels were extensively expressed on demyelinated axons and strongly associated with NCX in injured axonal regions (Craner et al., 2004a; Craner et al., 2004b). Based on these results, the authors speculated that $Na_V1.6$ and NCX, inducing the accumulation of intra-axonal calcium, could participate in a cascade of deleterious events such as protease activation and mitochondrial failure leading to axonal injury. Nevertheless, due to the absence of functional analyses of the $Na_V1.6$ and NCX activity, these studies did not clarify the exact implication of the increased Na^+ influx nor whether the Ca^{2+} entering through reverse NCX underwent a further compartmentalization in order to trigger specific pathways. In this regard, it was shown that the inhibition of neuronal electrical activity with TTX reduced the number of myelinated fibers (Demerens et al., 1996) and decreased the proliferation of oligodendrocyte precursor cells (Barres and Raff, 1993), thus positively implicating TTX-sensitive Na^+ currents and axonal electrical activity in the myelinogenesis process.

In the present study, we have found that the I_{Na} mediated by the $Na_V1.6$ channel not only are crucial players in neuronal hyperexcitability (Patel et al., 2016; Wang et al., 2016; Ciccone et al., 2019; Zybura et al., 2021), but also modulate $[Ca^{2+}]_i$ by inducing the activation of the NCX reverse activity thus providing a Ca^{2+} source from the extracellular space to refill the ER Ca^{2+} stores. This evidence sheds new light on the $Na_V1.6$ upregulation in AD neurons and suggests that its downstream effects may also depend on channel sub-cellular localization as well as on $Na_V1.6$ interacting proteins.

CONCLUSION

The present study has shown that NCX3 activity was upregulated in the reverse, Ca^{2+} influx mode in Tg2576 hippocampal neurons. Moreover, the enhanced reverse activity of NCX3 was associated with an increased Ca^{2+} refilling into the ER. Notably, functional experiments have indicated that the $Na_V1.6$ channels, upregulated in the Tg2576 hippocampal neurons, were responsible for the increased activation of the NCX reverse mode, while confocal analyses have shown that their co-localization increased in the Tg2576 hippocampal neurons in comparison with the WT.

Collectively, these data reinforce the concept that the NCX3-mediated replenishment of the ER Ca^{2+} stores is a crucial mechanism intervening in neuronal homeostasis and promoting neuronal survival under pathological conditions such as those induced by $A\beta_{1-42}$ oligomers. In addition, the observation that the reverse activity of NCX3 is driven by the Na^+ influx mediated by $Na_V1.6$ channels implies a possible functional link between Na_V channels and Ca^{2+} homeostasis and provides a new outcome of the $Na_V1.6$ upregulation in AD hippocampal neurons.

DATA AVAILABILITY STATEMENT

The original contributions presented in the study are included in the article/supplementary material, further inquiries can be directed to the corresponding author.

ETHICS STATEMENT

The animal study was reviewed and approved by the Care and Use Committee of “Federico II” University of Naples.

AUTHOR CONTRIBUTIONS

AP and IP conceived the study. IP, RC, AS, FB, VT, VdR, and PC performed all the experiments. IP, AS, and AP wrote the manuscript. AP, AS, and LA reviewed and edited the final draft of the manuscript.

FUNDING

This study was supported by the following grants: Programma di finanziamento linea-1 54_2020_FRA to AP; Progetto Speciale di Ateneo CA.04_CDA_n_103 March 27, 2019 to AS, and Programma di finanziamento linea-1 54_2020_FRA to AS; Programma Operativo Nazionale (PON PERMEDNET ArSol-1226) from the Italian Ministry of Research, MIUR, to LA.

REFERENCES

Akin, E. J., Solé, L., Dib-Hajj, S. D., Waxman, S. G., and Tamkun, M. M. (2015). Preferential Targeting of Nav1.6 Voltage-Gated Na+ Channels to the Axon Initial Segment during Development. *PLoS One* 10, e0124397. doi:10.1371/journal.pone.0124397

Akin, E. J., Solé, L., Johnson, B., Beheiry, M. E., Masson, J. B., Krapf, D., et al. (2016). Single-Molecule Imaging of Nav1.6 on the Surface of Hippocampal Neurons Reveals Somatic Nanoclusters. *Biophys. J.* 111, 1235–1247. doi:10.1016/j.bpj.2016.08.016

Alberdi, E., Wyssenbach, A., Alberdi, M., Sánchez-Gómez, M. V., Cavaliere, F., Rodríguez, J. J., et al. (2013). Ca(2+) -dependent Endoplasmic Reticulum Stress Correlates with Astrogliosis in Oligomeric Amyloid β-treated Astrocytes and in a Model of Alzheimer's Disease. *Aging Cell* 12, 292–302. doi:10.1111/acel.12054

Almeida, C. G., Tampellini, D., Takahashi, R. H., Greengard, P., Lin, M. T., Snyder, E. M., et al. (2005). Beta-amyloid Accumulation in APP Mutant Neurons Reduces PSD-95 and GluR1 in Synapses. *Neurobiol. Dis.* 20, 187–198. doi:10.1016/j.nbd.2005.02.008

Andrikopoulos, P., Kieswich, J., Harwood, S. M., Baba, A., Matsuda, T., Barbeau, O., et al. (2015). Endothelial Angiogenesis and Barrier Function in Response to Thrombin Require Ca2+ Influx through the Na+/Ca2+ Exchanger. *J. Biol. Chem.* 290, 18412–18428. doi:10.1074/jbc.M114.628156

Annunziato, L., Pignataro, G., and Di Renzo, G. F. (2004). Pharmacology of Brain Na+/Ca2+ Exchanger: from Molecular Biology to Therapeutic Perspectives. *Pharmacol. Rev.* 56, 633–654. doi:10.1124/pr.56.4.5

Annunziato, L., Secondo, A., Pignataro, G., Scorziello, A., and Molinaro, P. (2020). New Perspectives for Selective NCX Activators in Neurodegenerative Diseases. *Cell Calcium* 87, 102170. doi:10.1016/j.ceca.2020.102170

Barres, B. A., and Raff, M. C. (1993). Proliferation of Oligodendrocyte Precursor Cells Depends on Electrical Activity in Axons. *Nature* 361, 258–260. doi:10.1038/361258a0

Berridge, M. J. (2010). Calcium Hypothesis of Alzheimer's Disease. *Pflugers Arch.* 459, 441–449. doi:10.1007/s00424-009-0736-1

Blaustein, M. P., Juhaszova, M., Golovina, V. A., Church, P. J., and Stanley, E. F. (2002). Na/Ca Exchanger and PMCA Localization in Neurons and Astrocytes: Functional Implications. *Ann. N. Y. Acad. Sci.* 976, 356–366. doi:10.1111/j.1749-6632.2002.tb04762.x

Blaustein, M. P., and Lederer, W. J. (1999). Sodium/calcium Exchange: its Physiological Implications. *Physiol. Rev.* 79, 763–854. doi:10.1152/physrev.1999.79.3.763

Boscia, F., D'Avanzo, C., Pannaccione, A., Secondo, A., Casamassa, A., Formisano, L., et al. (2012). Silencing or Knocking Out the Na(+)/Ca(2+) Exchanger-3 (NCX3) Impairs Oligodendrocyte Differentiation. *Cell Death Differ* 19, 562–572. doi:10.1038/cdd.2011.125

Boscia, F., de Rosa, V., Cammarota, M., Secondo, A., Pannaccione, A., and Annunziato, L. (2020). The Na+/Ca2+ Exchangers in Demyelinating Diseases. *Cell Calcium* 85, 102130. doi:10.1016/j.ceca.2019.102130

Boscia, F., Pannaccione, A., Ciccone, R., Casamassa, A., Franco, C., Piccialli, I., et al. (2017). The Expression and Activity of KV3.4 Channel Subunits Are Precociously Upregulated in Astrocytes Exposed to Aβ Oligomers and in Astrocytes of Alzheimer's Disease Tg2576 Mice. *Neurobiol. Aging* 54, 187–198. doi:10.1016/j.neurobiolaging.2017.03.008

Brazhe, A. R., Verisokin, A. Y., Verveyko, D. V., and Postnov, D. E. (2018). Sodium-Calcium Exchanger Can Account for Regenerative Ca2+ Entry in Thin Astrocyte Processes. *Front. Cel. Neurosci.* 12, 250. doi:10.3389/fncel.2018.00250

Cammarota, M., de Rosa, V., Pannaccione, A., Secondo, A., Tedeschi, V., Piccialli, I., et al. (2021). Rebound Effects of NCX3 Pharmacological Inhibition: A Novel Strategy to Accelerate Myelin Formation in Oligodendrocytes. *Biomed. Pharmacother.* 143, 112111. doi:10.1016/j.biopha.2021.112111

Caputo, I., Secondo, A., Lepretti, M., Paolella, G., Auricchio, S., Barone, M. V., et al. (2012). Gliadin Peptides Induce Tissue Transglutaminase Activation and ER-Stress through Ca2+ Mobilization in Caco-2 Cells. *PLoS One* 7, e45209. doi:10.1371/journal.pone.0045209

Chakroborty, S., and Stutzmann, G. E. (2014). Calcium Channelopathies and Alzheimer's Disease: Insight into Therapeutic success and Failures. *Eur. J. Pharmacol.* 739, 83–95. doi:10.1016/j.ejphar.2013.11.012

Ciccone, R., Franco, C., Piccialli, I., Boscia, F., Casamassa, A., de Rosa, V., et al. (2019). Amyloid β-Induced Upregulation of Nav1.6 Underlies Neuronal Hyperactivity in Tg2576 Alzheimer's Disease Mouse Model. *Sci. Rep.* 9, 13592. doi:10.1038/s41598-019-50018-1

Colvin, R. A., Bennett, J. W., Colvin, S. L., Allen, R. A., Martinez, J., and Miner, G. D. (1991). Na+/Ca2+ Exchange Activity Is Increased in Alzheimer's Disease Brain Tissues. *Brain Res.* 543, 139–147. doi:10.1016/0006-8993(91)91056-7

Colvin, R. A., Davis, N., Wu, A., Murphy, C. A., and Levengood, J. (1994). Studies of the Mechanism Underlying Increased Na+/Ca2+ Exchange Activity in Alzheimer's Disease Brain. *Brain Res.* 665, 192–200. doi:10.1016/0006-8993(94)91338-2

Costa, R. O., Ferreiro, E., Martins, I., Santana, I., Cardoso, S. M., Oliveira, C. R., et al. (2012). Amyloid β-induced ER Stress Is Enhanced under Mitochondrial Dysfunction Conditions. *Neurobiol. Aging* 33, 824, e5-16. e5. doi:10.1016/j.neurobiolaging.2011.04.011

Craner, M. J., Hains, B. C., Lo, A. C., Black, J. A., and Waxman, S. G. (2004a). Co-localization of Sodium Channel Nav1.6 and the Sodium-Calcium Exchanger at Sites of Axonal Injury in the Spinal Cord in EAE. *Brain* 127, 294–303. doi:10.1093/brain/awh032

Craner, M. J., Newcombe, J., Black, J. A., Hartle, C., Cuzner, M. L., and Waxman, S. G. (2004b). Molecular Changes in Neurons in Multiple Sclerosis: Altered Axonal Expression of Nav1.2 and Nav1.6 Sodium Channels and Na+/Ca2+ Exchanger. *Proc. Natl. Acad. Sci. U. S. A.* 101, 8168–8173. doi:10.1073/pnas.0402765101

Criscuolo, C., Cianflone, A., Lanzillo, R., Carrella, D., Carissimo, A., Napolitano, F., et al. (2019). Glatiramer Acetate Modulates Ion Channels Expression and Calcium Homeostasis in B Cell of Patients with Relapsing-Remitting Multiple Sclerosis. *Sci. Rep.* 9, 4208. doi:10.1038/s41598-018-38152-8

Czyz, A., and Kiedrowski, L. (2002). In Depolarized and Glucose-Deprived Neurons, Na+ Influx Reverses Plasmalemmal K+-dependent and K+-independent Na+/Ca2+ Exchangers and Contributes to NMDA Excitotoxicity. *J. Neurochem.* 83, 1321–1328. doi:10.1046/j.1471-4159.2002.01227.x

de Rosa, V., Secondo, A., Pannaccione, A., Ciccone, R., Formisano, L., Guida, N., et al. (2019). D-aspartate Treatment Attenuates Myelin Damage and Stimulates Myelin Repair. *EMBO Mol. Med.* 11, e9278. doi:10.15252/emmm.201809278

Demerens, C., Stankoff, B., Logak, M., Anglade, P., Allinquant, B., Couraud, F., et al. (1996). Induction of Myelination in the central Nervous System by Electrical Activity. *Proc. Natl. Acad. Sci. U. S. A.* 93, 9887–9892. doi:10.1073/pnas.93.18.9887

Di Giuro, C. M. L., Shrestha, N., Malli, R., Groschner, K., van Breemen, C., and Fameli, N. (2017). Na +/Ca2+ Exchangers and Orai Channels Jointly Refill Endoplasmic Reticulum (ER) Ca2+ via ER Nanojunctions in Vascular Endothelial Cells. *Pflugers Arch.* 469, 1287–1299. doi:10.1007/s00424-017-1989-8

Etcheberrigaray, R., Hirashima, N., Nee, L., Prince, J., Govoni, S., Racchi, M., et al. (1998). Calcium Responses in Fibroblasts from Asymptomatic Members of Alzheimer's Disease Families. *Neurobiol. Dis.* 5, 37–45. doi:10.1006/nbdi.1998.0176

Fameli, N., van Breemen, C., and Kuo, K. H. (2007). A quantitative model for linking Na^+/Ca^{2+} exchanger to SERCA during refilling of the sarcoplasmic reticulum to sustain $[Ca^{2+}]$ oscillations in vascular smooth muscle. *Cell Calcium* 42, 565-575. doi:10.1016/j.ceca.2007.02.001.10.1016/j.ceca.2007.02.001

Ferreiro, E., Oliveira, C. R., and Pereira, C. (2004). Involvement of Endoplasmic Reticulum Ca2+ Release through Ryanodine and Inositol 1,4,5-triphosphate Receptors in the Neurotoxic Effects Induced by the Amyloid-Beta Peptide. *J. Neurosci. Res.* 76, 872–880. doi:10.1002/jnr.20135

Floyd, C. L., Gorin, F. A., and Lyeth, B. G. (2005). Mechanical Strain Injury Increases Intracellular Sodium and Reverses Na+/Ca2+ Exchange in Cortical Astrocytes. *Glia* 51, 35–46. doi:10.1002/glia.20183

Gabellini, N., Zatti, A., Rispoli, G., Navangione, A., and Carafoli, E. (1996). Expression of an Active Na+/Ca2+ Exchanger Isoform Lacking the Six C-Terminal Transmembrane Segments. *Eur. J. Biochem.* 239, 897–904. doi:10.1111/j.1432-1033.1996.0897u.x

Gasser, A., Cheng, X., Gilmore, E. S., Tyrrell, L., Waxman, S. G., and Dib-Hajj, S. D. (2010). Two Nedd4-Binding Motifs Underlie Modulation of Sodium Channel Nav1.6 by P38 MAPK. *J. Biol. Chem.* 285, 26149–26161. doi:10.1074/jbc.M109.098681

Gerkau, N. J., Rakers, C., Petzold, G. C., and Rose, C. R. (2017). Differential Effects of Energy Deprivation on Intracellular Sodium Homeostasis in Neurons and Astrocytes. *J. Neurosci. Res.* 95, 2275–2285. doi:10.1002/jnr.23995

Gershome, C., Lin, E., Kashihara, H., Hove-Madsen, L., and Tibbits, G. F. (2010). Colocalization of Voltage-Gated Na+ Channels with the Na+/Ca2+ Exchanger in Rabbit Cardiomyocytes during Development. *Am. J. Physiol. Heart Circ. Physiol.* 300, H300–H311. doi:10.1152/ajpheart.00798.2010

Gomez-Villafuertes, R., Mellström, B., and Naranjo, J. R. (2007). Searching for a Role of NCX/NCKX Exchangers in Neurodegeneration. *Mol. Neurobiol.* 35, 195–202. doi:10.1007/s12035-007-0007-0

Grynkiewicz, G., Poenie, M., and Tsien, R. Y. (1985). A New Generation of Ca2+ Indicators with Greatly Improved Fluorescence Properties. *J. Biol. Chem.* 260, 3440–3450. doi:10.1016/s0021-9258(19)83641-4

Hammann, J., Bassetti, D., White, R., Luhmann, H. J., and Kirischuk, S. (2018). α2 Isoform of Na+,K+-ATPase via Na+,Ca2+ Exchanger Modulates Myelin Basic Protein Synthesis in Oligodendrocyte Lineage Cells *In Vitro*. *Cell Calcium* 73, 1–10. doi:10.1016/j.ceca.2018.03.003

Hirota, S., Pertens, E., and Janssen, L. J. (2007). The Reverse Mode of the Na(+)/Ca(2+) Exchanger Provides a Source of Ca(2+) for Store Refilling Following Agonist-Induced Ca(2+) Mobilization. *Am. J. Physiol. Lung Cel. Mol. Physiol.* 292, L438–L447. doi:10.1152/ajplung.00222.2006

Iwamoto, T., and Shigekawa, M. (1998). Differential Inhibition of Na+/Ca2+ Exchanger Isoforms by Divalent Cations and Isothiourea Derivative. *Am. J. Physiol.* 275, C423–C430. doi:10.1152/ajpcell.1998.275.2.C423

Larbig, R., Torres, N., Bridge, J. H., Goldhaber, J. I., and Philipson, K. D. (2010). Activation of Reverse Na+-Ca2+ Exchange by the Na+ Current Augments the Cardiac Ca2+ Transient: Evidence from NCX Knockout Mice. *J. Physiol.* 588, 3267–3276. doi:10.1113/jphysiol.2010.187708

Lee, S. H., Kim, K. R., Ryu, S. Y., Son, S., Hong, H. S., Mook-Jung, I., et al. (2012). Impaired Short-Term Plasticity in Mossy Fiber Synapses Caused by Mitochondrial Dysfunction of Dentate Granule Cells Is the Earliest Synaptic Deficit in a Mouse Model of Alzheimer's Disease. *J. Neurosci.* 32, 5953–5963. doi:10.1523/JNEUROSCI.0465-12.2012

Lemos, V. S., Poburko, D., Liao, C. H., Cole, W. C., and van Breemen, C. (2007). Na+ Entry via TRPC6 Causes Ca2+ Entry via NCX Reversal in ATP Stimulated Smooth Muscle Cells. *Biochem. Biophys. Res. Commun.* 352, 130–134. doi:10.1016/j.bbrc.2006.10.160

Lencesova, L., O'Neill, A., Resneck, W. G., Bloch, R. J., and Blaustein, M. P. (2004). Plasma Membrane-Cytoskeleton-Endoplasmic Reticulum Complexes in Neurons and Astrocytes. *J. Biol. Chem.* 279, 2885–2893. doi:10.1074/jbc.M310365200

Lindgren, R. M., Zhao, J., Heller, S., Berglind, H., and Nistér, M. (2005). Molecular Cloning and Characterization of Two Novel Truncated Isoforms of Human Na+/Ca2+ Exchanger 3, Expressed in Fetal Brain. *Gene* 348, 143–155. doi:10.1016/j.gene.2005.01.003

Michel, L. Y., Hoenderop, J. G., and Bindels, R. J. (2016). Calpain-3-mediated Regulation of the Na^{+}-Ca^{2+} Exchanger Isoform 3. *Pflugers Arch.* 468, 243–255. doi:10.1007/s00424-015-1747-8

Michel, L. Y., Hoenderop, J. G., and Bindels, R. J. (2015). Towards Understanding the Role of the Na^{2+}-Ca^{2+} Exchanger Isoform 3. *Rev. Physiol. Biochem. Pharmacol.* 168, 31–57. doi:10.1007/112_2015_23

Molinaro, P., Cuomo, O., Pignataro, G., Boscia, F., Sirabella, R., Pannaccione, A., et al. (2008). Targeted Disruption of Na+/Ca2+ Exchanger 3 (NCX3) Gene Leads to a Worsening of Ischemic Brain Damage. *J. Neurosci.* 28, 1179–1184. doi:10.1523/JNEUROSCI.4671-07.2008

Morishima, N., Nakanishi, K., Takenouchi, H., Shibata, T., and Yasuhiko, Y. (2002). An Endoplasmic Reticulum Stress-specific Caspase cascade in Apoptosis. Cytochrome C-independent Activation of Caspase-9 by Caspase-12. *J. Biol. Chem.* 277, 34287–34294. doi:10.1074/jbc.M204973200

Pannaccione, A., Piccialli, I., Secondo, A., Ciccone, R., Molinaro, P., Boscia, F., et al. (2020). The Na+/Ca2+exchanger in Alzheimer's Disease. *Cell Calcium* 87, 102190. doi:10.1016/j.ceca.2020.102190

Pannaccione, A., Secondo, A., Molinaro, P., D'Avanzo, C., Cantile, M., Esposito, A., et al. (2012). A New Concept: Aβ1-42 Generates a Hyperfunctional Proteolytic NCX3 Fragment that Delays Caspase-12 Activation and Neuronal Death. *J. Neurosci.* 32, 10609–10617. doi:10.1523/JNEUROSCI.6429-11.2012

Pappalardo, L. W., Samad, O. A., Black, J. A., and Waxman, S. G. (2014). Voltage-gated Sodium Channel Nav 1.5 Contributes to Astrogliosis in an *In Vitro* Model of Glial Injury via Reverse Na+ /Ca2+ Exchange. *Glia* 62, 1162–1175. doi:10.1002/glia.22671

Paschen, W. (2001). Dependence of Vital Cell Function on Endoplasmic Reticulum Calcium Levels: Implications for the Mechanisms Underlying Neuronal Cell Injury in Different Pathological States. *Cell Calcium* 29, 1–11. doi:10.1054/ceca.2000.0162

Patel, R. R., Barbosa, C., Brustovetsky, T., Brustovetsky, N., and Cummins, T. R. (2016). Aberrant Epilepsy-Associated Mutant Nav1.6 Sodium Channel Activity Can Be Targeted with Cannabidiol. *Brain* 139, 2164–2181. doi:10.1093/brain/aww129

Poburko, D., Liao, C. H., Lemos, V. S., Lin, E., Maruyama, Y., Cole, W. C., et al. (2007). Transient Receptor Potential Channel 6-mediated, Localized Cytosolic [Na+] Transients Drive Na+/Ca2+ Exchanger-Mediated Ca2+ Entry in Purinergically Stimulated Aorta Smooth Muscle Cells. *Circ. Res.* 101, 1030–1038. doi:10.1161/CIRCRESAHA.107.155531

Querfurth, H. W., and LaFerla, F. M. (2010). Alzheimer's Disease. *N. Engl. J. Med.* 362, 329–344. doi:10.1056/NEJMra0909142

Radwański, P. B., Ho, H. T., Veeraraghavan, R., Brunello, L., Liu, B., Belevych, A. E., et al. (2016). Neuronal Na+ Channels Are Integral Components of Pro-arrhythmic Na+/Ca2+ Signaling Nanodomain that Promotes Cardiac Arrhythmias during β-adrenergic Stimulation. *JACC Basic Transl. Sci.* 1, 251–266. doi:10.1016/j.jacbts.2016.04.004

Royeck, M., Horstmann, M. T., Remy, S., Reitze, M., Yaari, Y., and Beck, H. (2008). Role of Axonal NaV1.6 Sodium Channels in Action Potential Initiation of CA1 Pyramidal Neurons. *J. Neurophysiol.* 100, 2361–2380. doi:10.1152/jn.90332.2008

Saad, M., Brkanac, Z., and Wijsman, E. M. (2015). Family-based Genome Scan for Age at Onset of Late-Onset Alzheimer's Disease in Whole Exome Sequencing Data. *Genes Brain Behav.* 14, 607–617. doi:10.1111/gbb.12250

Salminen, A., Kaarniranta, K., and Kauppinen, A. (2020). ER Stress Activates Immunosuppressive Network: Implications for Aging and Alzheimer's Disease. *J. Mol. Med. (Berl)* 98, 633–650. doi:10.1007/s00109-020-01904-z

Secondo, A., Esposito, A., Sirabella, R., Boscia, F., Pannaccione, A., Molinaro, P., et al. (2015). Involvement of the Na+/Ca2+ Exchanger Isoform 1 (NCX1) in Neuronal Growth Factor (NGF)-induced Neuronal Differentiation through Ca2+-dependent Akt Phosphorylation. *J. Biol. Chem.* 290, 1319–1331. doi:10.1074/jbc.M114.555516

Secondo, A., Petrozziello, T., Tedeschi, V., Boscia, F., Pannaccione, A., Molinaro, P., et al. (2020). Nuclear Localization of NCX: Role in Ca2+ Handling and Pathophysiological Implications. *Cell Calcium* 86, 102143. doi:10.1016/j.ceca.2019.102143

Secondo, A., Petrozziello, T., Tedeschi, V., Boscia, F., Vinciguerra, A., Ciccone, R., et al. (2019). ORAI1/STIM1 Interaction Intervenes in Stroke and in Neuroprotection Induced by Ischemic Preconditioning through Store-Operated Calcium Entry. *Stroke* 50, 1240–1249. doi:10.1161/STROKEAHA.118.024115

Sikora, G., Wyłomańska, A., Gajda, J., Solé, L., Akin, E. J., Tamkun, M. M., et al. (2017). Elucidating Distinct Ion Channel Populations on the Surface of Hippocampal Neurons via Single-Particle Tracking Recurrence Analysis. *Phys. Rev. E.* 96, 062404. doi:10.1103/PhysRevE.96.062404

Sirabella, R., Secondo, A., Pannaccione, A., Scorziello, A., Valsecchi, V., Adornetto, A., et al. (2009). Anoxia-induced NF-kappaB-dependent Upregulation of NCX1 Contributes to Ca2+ Refilling into Endoplasmic Reticulum in Cortical Neurons. *Stroke* 40, 922–929. doi:10.1161/STROKEAHA.108.531962

Sisalli, M. J., Secondo, A., Esposito, A., Valsecchi, V., Savoia, C., Di Renzo, G. F., et al. (2014). Endoplasmic Reticulum Refilling and Mitochondrial Calcium Extrusion Promoted in Neurons by NCX1 and NCX3 in Ischemic Preconditioning Are Determinant for Neuroprotection. *Cel Death Differ* 21, 1142–1149. doi:10.1038/cdd.2014.32

Sokolow, S., Luu, S. H., Headley, A. J., Hanson, A. Y., Kim, T., Miller, C. A., et al. (2011). High Levels of Synaptosomal Na(+)-Ca(2+) Exchangers (NCX1, NCX2, NCX3) Co-localized with Amyloid-Beta in Human Cerebral Cortex Affected by Alzheimer's Disease. *Cell Calcium* 49, 208–216. doi:10.1016/j.ceca.2010.12.008

Solé, L., and Tamkun, M. M. (2020). Trafficking Mechanisms Underlying Nav Channel Subcellular Localization in Neurons. *Channels (Austin)* 14, 1–17. doi:10.1080/19336950.2019.1700082

Struckman, H. L., Baine, S., Thomas, J., Mezache, L., Mykytyn, K., Györke, S., et al. (2020). Super-Resolution Imaging Using a Novel High-Fidelity Antibody

Reveals Close Association of the Neuronal Sodium Channel NaV1.6 with Ryanodine Receptors in Cardiac Muscle. *Microsc. Microanal.* 26, 157–165. doi:10.1017/S1431927619015289

Takahashi, R. H., Almeida, C. G., Kearney, P. F., Yu, F., Lin, M. T., Milner, T. A., et al. (2004). Oligomerization of Alzheimer's Beta-Amyloid within Processes and Synapses of Cultured Neurons and Brain. *J. Neurosci.* 24, 3592–3599. doi:10.1523/JNEUROSCI.5167-03.2004

Takahashi, R. H., Capetillo-Zarate, E., Lin, M. T., Milner, T. A., and Gouras, G. K. (2013). Accumulation of Intraneuronal β-amyloid 42 Peptides Is Associated with Early Changes in Microtubule-Associated Protein 2 in Neurites and Synapses. *PLoS One* 8, e51965. doi:10.1371/journal.pone.0051965

Tedeschi, V., Petrozziello, T., Sisalli, M. J., Boscia, F., Canzoniero, L. M. T., and Secondo, A. (2019). The Activation of Mucolipin TRP Channel 1 (TRPML1) Protects Motor Neurons from L-BMAA Neurotoxicity by Promoting Autophagic Clearance. *Sci. Rep.* 9, 10743. doi:10.1038/s41598-019-46708-5

Tedeschi, V., Sisalli, M. J., Petrozziello, T., Canzoniero, L. M. T., and Secondo, A. (2021). Lysosomal Calcium Is Modulated by STIM1/TRPML1 Interaction Which Participates to Neuronal Survival during Ischemic Preconditioning. *FASEB J.* 35, e21277. doi:10.1096/fj.202001886R

Torres, N. S. (2021). Activation of Reverse Na+-Ca2+ Exchanger by Skeletal Na+ Channel Isoform Increases Excitation-Contraction Coupling Efficiency in Rabbit Cardiomyocytes. *Am. J. Physiology-Heart Circulatory Physiol.* 320, H593–H603. doi:10.1152/ajpheart.00545.2020

Uddin, M. S., Tewari, D., Sharma, G., Kabir, M. T., Barreto, G. E., Bin-Jumah, M. N., et al. (2020). Molecular Mechanisms of ER Stress and UPR in the Pathogenesis of Alzheimer's Disease. *Mol. Neurobiol.* 57, 2902–2919. doi:10.1007/s12035-020-01929-y

Van Breemen, C., Fameli, N., and Evans, A. M. (2013). Pan-junctional sarcoplasmic reticulum in vascular smooth muscle: nanospace Ca^{2+} transport for site- and function-specific Ca^{2+} signalling. *J. Physiol.* 591, 2043-2054. doi:10.1113/jphysiol.2012.246348

Van Eylen, F., Kamagate, A., and Herchuelz, A. (2001). A New Na/Ca Exchanger Splicing Pattern Identified *In Situ* Leads to a Functionally Active 70kDa NH(2)-terminal Protein. *Cell Calcium* 30, 191–198. doi:10.1054/ceca.2001.0223

Veeraraghavan, R., Györke, S., and Radwański, P. B. (2017). Neuronal Sodium Channels: Emerging Components of the Nano-Machinery of Cardiac Calcium Cycling. *J. Physiol.* 595, 3823–3834. doi:10.1113/JP273058

Verkhratsky, A. (2004). Endoplasmic Reticulum Calcium Signaling in Nerve Cells. *Biol. Res.* 37, 693–699. doi:10.4067/s0716-97602004000400027

Verkhratsky, A., and Petersen, O. H. (2002). The Endoplasmic Reticulum as an Integrating Signalling Organelle: from Neuronal Signalling to Neuronal Death. *Eur. J. Pharmacol.* 447, 141–154. doi:10.1016/s0014-2999(02)01838-1

Verkhratsky, A. (2005). Physiology and Pathophysiology of the Calcium Store in the Endoplasmic Reticulum of Neurons. *Physiol. Rev.* 85, 201–279. doi:10.1152/physrev.00004.2004

Verkhratsky, A., and Toescu, E. C. (2003). Endoplasmic Reticulum Ca(2+) Homeostasis and Neuronal Death. *J. Cel. Mol. Med.* 7, 351–361. doi:10.1111/j.1582-4934.2003.tb00238.x

Wada, A. (2006). Roles of Voltage-dependent Sodium Channels in Neuronal Development, Pain, and Neurodegeneration. *J. Pharmacol. Sci.* 102, 253–268. doi:10.1254/jphs.crj06012x

Wang, X., Zhang, X. G., Zhou, T. T., Li, N., Jang, C. Y., Xiao, Z. C., et al. (2016). Elevated Neuronal Excitability Due to Modulation of the Voltage-Gated Sodium Channel Nav1.6 by Aβ1-42. *Front. Neurosci.* 10, 94. doi:10.3389/fnins.2016.00094

Wang, X., and Zheng, W. (2019). Ca2+ Homeostasis Dysregulation in Alzheimer's Disease: a Focus on Plasma Membrane and Cell Organelles. *FASEB J.* 33, 6697–6712. doi:10.1096/fj.201801751R

Watano, T., Kimura, J., Morita, T., and Nakanishi, H. (1996). A Novel Antagonist, No. 7943, of the Na+/Ca2+ Exchange Current in guinea-pig Cardiac Ventricular Cells. *Br. J. Pharmacol.* 119, 555–563. doi:10.1111/j.1476-5381.1996.tb15708.x

Wittmack, E. K., Rush, A. M., Hudmon, A., Waxman, S. G., and Dib-Hajj, S. D. (2005). Voltage-gated Sodium Channel Nav1.6 Is Modulated by P38 Mitogen-Activated Protein Kinase. *J. Neurosci.* 25, 6621–6630. doi:10.1523/JNEUROSCI.0541-05.2005

Zybura, A., Hudmon, A., and Cummins, T. R. (2021). Distinctive Properties and Powerful Neuromodulation of Nav1.6 Sodium Channels Regulates Neuronal Excitability. *Cells* 10, 1595. doi:10.3390/cells10071595

Conflict of Interest: The authors declare that the research was conducted in the absence of any commercial or financial relationships that could be construed as a potential conflict of interest.

Publisher's Note: All claims expressed in this article are solely those of the authors and do not necessarily represent those of their affiliated organizations, or those of the publisher, the editors and the reviewers. Any product that may be evaluated in this article, or claim that may be made by its manufacturer, is not guaranteed or endorsed by the publisher.

Copyright © 2021 Piccialli, Ciccone, Secondo, Boscia, Tedeschi, de Rosa, Cepparulo, Annunziato and Pannaccione. This is an open-access article distributed under the terms of the Creative Commons Attribution License (CC BY). The use, distribution or reproduction in other forums is permitted, provided the original author(s) and the copyright owner(s) are credited and that the original publication in this journal is cited, in accordance with accepted academic practice. No use, distribution or reproduction is permitted which does not comply with these terms.

frontiers
in Pharmacology

ORIGINAL RESEARCH
published: 16 December 2021
doi: 10.3389/fphar.2021.744663

Mechanisms Underlying Gastrodin Alleviating Vincristine-Induced Peripheral Neuropathic Pain

Xiangyu Wang[1], Boxuan Zhang[1], Xuedong Li[2,4], Xingang Liu[1], Songsong Wang[1], Yuan Xie[1], Jialing Pi[1], Zhiyuan Yang[1], Jincan Li[1], Qingzhong Jia[1,2,3,4]* and Yang Zhang[2,4]*

[1]Departments of Pharmacology, Hebei Medical University, Shijiazhuang, China, [2]School of Pharmacy, Hebei Medical University, Shijiazhuang, China, [3]Key Laboratory of Innovative Drug Research and Evaluation of Hebei Province, Shijiazhuang, China, [4]Laboratory of Neural and Vascular Biology of Ministry of Education, Hebei Medical University, Shijiazhuang, China

Gastrodin (GAS) is the main bioactive ingredient of Gastrodia, a famous Chinese herbal medicine widely used as an analgesic, but the underlying analgesic mechanism is still unclear. In this study, we first observed the effects of GAS on the vincristine-induced peripheral neuropathic pain by alleviating the mechanical and thermal hyperalgesia. Further studies showed that GAS could inhibit the current density of $Na_V1.7$ and $Na_V1.8$ channels and accelerate the inactivation process of $Na_V1.7$ and $Na_V1.8$ channel, thereby inhibiting the hyperexcitability of neurons. Additionally, GAS could significantly reduce the over-expression of $Na_V1.7$ and $Na_V1.8$ on DRG neurons from vincristine-treated rats according to the analysis of Western blot and immunofluorescence results. Moreover, based on the molecular docking and molecular dynamic simulation, the binding free energies of the constructed systems were calculated, and the binding sites of GAS on the sodium channels ($Na_V1.7$ and $Na_V1.8$) were preliminarily determined. This study has shown that modulation of $Na_V1.7$ and $Na_V1.8$ sodium channels by GAS contributing to the alleviation of vincristine-induced peripheral neuropathic pain, thus expanding the understanding of complex action of GAS as a neuromodulator.

Keywords: $Na_V1.7$/$Na_V1.8$, vincristine, neuropathic pain, molecular docking, MD simulation, gastrodin

OPEN ACCESS

Edited by:
Jacques Joubert,
University of the Western Cape, South Africa

Reviewed by:
Eugen Khomula,
University of California, San Francisco, United States
Heike Wulff,
University of California, Davis, United States

***Correspondence:**
Qingzhong Jia
qizhjia@hebmu.edu.cn
Yang Zhang
20162901007@cqu.edu.cn

Specialty section:
This article was submitted to Pharmacology of Ion Channels and Channelopathies, a section of the journal Frontiers in Pharmacology

***Received:** 20 July 2021*
***Accepted:** 30 November 2021*
***Published:** 16 December 2021*

Citation:
Wang X, Zhang B, Li X, Liu X, Wang S, Xie Y, Pi J, Yang Z, Li J, Jia Q and Zhang Y (2021) Mechanisms Underlying Gastrodin Alleviating Vincristine-Induced Peripheral Neuropathic Pain. Front. Pharmacol. 12:744663. doi: 10.3389/fphar.2021.744663

INTRODUCTION

Cancer, characterized by uncontrolled cell proliferation and an absence of cell death, has become the second worldwide cause of death, only exceeded by cardiovascular diseases, seriously threatening the public health (Mattiuzzi and Lippi, 2019). In addition to surgery and radiotherapy, chemotherapy has become the main strategy of cancer treatment (Coffeen et al., 2019), especially the metastatic cancers, and chemotherapeutic drugs are evolving toward increasingly effective treatments. However, chemotherapy-induced neuropathic pain (CINP) is one of the most serious adverse events in the course of chemotherapy (van Schie et al., 2011; Old et al., 2014; Zajaczkowska et al., 2019; Finnerup et al., 2021), and long-term CINP is associated with depression, anxiety, and insomnia, severely impairing the quality of patients' life and leading to the dose reduction or even cessation of treatment (Rosenthal and Kaufman, 1974; Bär et al., 2005; Jackson et al., 2015; Jha et al., 2021). Currently, the investigation of pathological mechanisms of CINP mainly focuses on the injury of dorsal root ganglion (DRG) sensory neurons, including mitochondrial dysfunction (Argyriou et al., 2013), microfilament and microtubule damage (Sittl et al., 2012), immune-inflammatory response (Zhang and Dougherty, 2014), and ion channels dysfunction (Aromolaran and Goldstein, 2017), and such injury types will lead to ectopic discharges, further contributing to CINP (Doyle and Salvemini, 2021; Yang et al., 2021).

DRG, located between the dorsal horn of the spinal cord and the peripheral nerve terminals, is the cell body of primary afferent neurons, playing a vital role in the transmission and integration of sensory information (Ohshiro et al., 2007; Sapunar et al., 2012). DRG and peripheral axons lack the efficient neurovascular barrier and allow the compounds with larger molecular mass or skeleton to simply diffuse into the interstitium, which is susceptible to the influence of chemotherapeutic drugs and leads to the peripheral pain (Gu and MacDermott, 1997; Kawasaki et al., 2008). In addition, the abnormal expression of TTX-sensitive ($Na_V1.6$ and $Na_V1.7$) and TTX-resistant ($Na_V1.8$ and $Na_V1.9$) sodium channels, mainly expressed in DRG neurons, could induce the neuronal hyperexcitability and promoting the development of neuropathic pain (Zimmermann et al., 2007; Ding et al., 2019; Kingwell, 2019; Zhou et al., 2020). Among the above channel proteins, $Na_V1.7$ and $Na_V1.8$ can be up-regulated under the stimulus of some antitumor agents (such as oxaliplatin and paclitaxel), which is the main cause of CIPN and indicated the vital roles of $Na_V1.7$ and $Na_V1.8$ in the transmission of pain signals (Argyriou et al., 2013; Zhang and Dougherty, 2014; Vysokov et al., 2019).

Nowadays, the American Society of Clinical Oncology recommends the combination of chemotherapeutics and anti-epileptic (carbamazepine and lamotrigine) or antidepressant drugs (duloxetine and amitriptyline) during chemotherapy to alleviate the severe central side effects (ataxia, conscious confusion), promoting the research and development of higher effectiveness and lower toxicity of analgesic drugs (Hershman et al., 2014; Gül et al., 2020). It's worth mentioning that there is a famous Chinese herb named Rhizoma Gastrodiae, widely applied as an analgesic. Gastrodin (GAS) is the primary component of Rhizoma Gastrodiae, which is commonly used in the treatment of neurasthenia, vascular headache, pain symptoms caused by radiotherapy or chemotherapy, and neuropathic pain caused by diabetes. GAS has promising physical and chemical properties, especially the polarity and water solubility, and could accumulate in the peripheral nerves and quickly reach the effective drug concentration, showing great potential in the treatment of CINP (Sun et al., 2012; Sun et al., 2016; Xiao et al., 2016; Qin et al., 2021). In this study, a variety of biological and computational experimental methods have been applied to evaluate the efficacy of GAS in the treatment of CINP, and to explore the action mechanisms of GAS alleviating CINP from the molecular level.

MATERIALS AND METHODS

Animals Behavioral Testing

Animal feeding and model establishing methods used in this study complied with the International Association for the Study of Pain Guidelines and have been approved by the Laboratory Animal Ethical and Welfare Committee, the Center for New Drug Safety Evaluation and Research, Hebei Medical University (NO. IACUC-Hebyd AP-2020033). The behavioral measurements on male Sprague Dawley (SD) rats (6–8 weeks) were all done in the awake state. The SD rats weighing 180–220 g were used in this study and were housed individually in automatically controlled environmental conditions, namely 12 h light-dark cycle (lights on from 08:00 to 20:00) and free access to food and water. Prior to the experiment, the rats were placed in the above-mentioned environment for 7 days to fully adapt, and the researchers should observe the rats' health status every day. SD rats were randomly divided into 3 groups based on mechanical pain threshold (control group, model group, and GAS group) (Qiu et al., 2014; Xiao et al., 2016; Chen et al., 2017; Ye et al., 2018), the specific operations were as follows:

Control group: rats were intraperitoneally injected with the same volume of normal saline (vehicle) daily. Vincristine group: the rats were intraperitoneally injected with vincristine (Shenzhen Wanle Pharmaceutical Co., LTD.) at 9 a.m. every day (DAY 1–7) (0.125 mg/kg, diluted in saline before injection); then normal saline was injected into the abdominal cavity of rats at the same time period (DAY 8–10); finally, vincristine was injected intraperitoneally at the same time (9 a.m.) period on day 11–14. GAS group: DAY 1–7, rats received intraperitoneal injection of vincristine (Shenzhen Wanle Pharmaceutical Co., LTD.) at 9 am daily (0.125 mg/kg, diluted in saline before injection); then rats were injected with normal saline at 9 a.m. and GAS (4-hydroxybenzyl alcohol-4-O--D-glucopyranoside, Purity > 98%, purchased from Nanjing Daosifu Biotechnology Co., Ltd., product batch number: 20170811s) at 16:00 p.m. (60 mg/kg, diluted in saline before injection) from day 8 to 10 daily; finally, rats were intraperitoneally injected with vincristine at 9 a.m. and GAS at 4 p.m. according to the above-mentioned drug dosage (DAY 11–14) (Qiu et al., 2014; Xiao et al., 2016; Chen et al., 2017; Ye et al., 2018).

Mechanical and Thermal Hyperalgesia

The von Frey instrument was used to assess the threshold sensitivity of mechanical stimuli in rats. The calibrated nylon filaments (von Frey hair, Stoelting) with various bending forces were applied to stimulate the middle plantar surface of the right hind paw of rats. The rats were stimulated from the minimum gram of nylon yarn and the hardness gradually increased. When the hindlimb of the rats was quickly retracted, the rats were considered to have a positive reaction. Hargreaves strategy was applied to measure thermal hyperalgesia using thermal radiation meter (Mengtai Technology). The paw withdrawal latency of the right hind-paw in response to heat was measured using 30% radiant intensity, and the elapsed time was recorded.

Cell Culture and Electrophysiology

In the DRG neuron excitability recording experiment, the neurons were selected from 32 adult male SD rats (provided by the Experimental Animal Center of Hebei Province, People's Republic of China), and according to literature reports (Nie et al., 2017; Zhang et al., 2018), DRG neurons were selected from the L4-L6 segment of rats. DRG ganglia were digested with collagenase (3 mg/mL) and dispase (7.5 mg/mL) for 30 min at

37°C, and then mechanically triturated and washed twice with DMEM supplemented with 10% fetal calf serum, which were further plated on poly-D-lysine-coated glass coverslips. Next, the action potential, $Na_V1.8$ current density, and TTX-sensitive sodium current were recorded.

Action Potential Recording

In this part, the selected DRG neurons were derived from the constructed rat model of vincristine and treated with different concentrations of GAS to observe the effects of GAS on the excitability of model neurons. Based on previous literature reports, GAS bath solutions with concentrations of 30, 100, and 200 μM were configured in reference to the effective GAS concentration (about 90 μM) (Qiu et al., 2014; Nepal et al., 2019; Qi et al., 2019). The configured GAS bath solution directly perfused the DRG model neurons for 10 min to observe the effect of GAS on the excitability of the neurons.

Action potentials of dissociated rat small-diameter DRG neurons (17–25 μm) were recorded with a current clamp using the HEKA EPC10. Pipettes (1–6 MΩ) were filled with the solution containing the following components: KCl (140 mM), $CaCl_2$ (1 mM), $MgCl_2$ (2 mM), HEPES (10 mM), EGTA (11 mM), and the pH of the solution was adjusted to 7.4 with NaOH. Small DRG neurons were injected with various currents with different intensities (ranging from 0 to 500 pA with 10 pA as the gradient) to examine the action potential. This experiment mainly detects the action potential amplitude, threshold, rheobase, depolarization slope (V/s), etc.

$Na_V1.8$ Sodium Currents Recording

GAS was dissolved in bath solution containing specific components, and then used to treat DRG neurons from vincristine model rats for 10 min to observe the effects of GAS on $Na_V1.8$ channel current. The specific operations were as follows:

The $Na_V1.8$ current of small-diameter model DRG neurons was recorded in whole-cell configuration by voltage-clamp. The pipettes solution mainly consisted of CsCl (70 mM), NaCl (30 mM), TEA-cl (30 mM), EGTA (10 mM), $CaCl_2$ (1 mM), $MgCl_2$ (2 mM), HEPES (10 mM), D-glucose (5 mM), Na_2ATP (2 mM), GTP (0.05 mM), and the pH value was adjusted to 7.3 by CsOH. The bath solution (pH = 7.4) contained NaCl (80 mM), Choline-Cl (50 mM), TEA-Cl (30 mM), $CaCl_2$ (2 mM), $CdCl_2$ (0.2 mM), HEPES (10 mM), and D-glucose (5 mM). Since $Na_V1.8$ and $Na_V1.9$ were TTX-resistant channels in contrast to TTX-sensitive $Na_V1.7$, Tetrodotoxin (TTX, 500 nM) was added to block its sensitive sodium channel currents and retain TTX-resistant $Na_V1.8$ and $Na_V1.9$ sodium channels. Compared with $Na_V1.8$, $Na_V1.9$ was inactivated at a relatively high voltage. Therefore, when the prepulse voltage was set to −44 mV, 500 ms, the $Na_V1.9$ current was inactivated and the $Na_V1.8$ current was separated. The specific operations were as follows: the preset voltage of −44 mV, 500 ms was set to inactivate the $Na_V1.9$ current, and then the $Na_V1.8$ current was excited using a series of 50 ms steps depolarization (−80–0 mV in 5 mV increments) (Cummins et al., 1999; Tyrrell et al., 2001). The HEKA EPC10 has an acquisition rate of 20 kHz, and the signals were filtered at 5 kHz.

$Na_V1.7$ Sodium Currents Recording

The stable expression system of $Na_V1.7$ on HEK239B cell line was provided by Inovogen (Inovogen Tech. Co., Beijing, China), and the construction method was roughly divided into the following four steps: 1) The full-length $Na_V1.7$ gene (SCN9A) was obtained using gene synthesis method and constructed into the transposon vector (pTP6-puro) by KpnI-NotII. 2) The plasmid was extracted with bacterial solution containing pTP6-puro-1.7 and transfected into HEK239B cells, followed by polyclonal screening with 3 μg/ml puromycin. After 2 weeks of screening, the culture medium was changed or puromycin was added again after passages. 3) The selected polyclonal cells were frozen until no new dead cells appeared in the clone system. 4) Finally, Realtime PCR was used to detect the expression of target genes. Based on the above method, the vitro expression system of $Na_V1.7$ was constructed to directly record the current changes of $Na_V1.7$. In addition, the primary structure of the expression system was determined by Inovogen, which was aligned to the sequence template from *Rattus norvegicus* (NP_579823.1) using blastx (99% identity).

The Na_V 1.7 current of HEK293B was recorded in whole-cell configuration by voltage-clamp. The pipettes solution contained CsF (145 mM), NaF (5.6 mM), HEPES (5 mM), and the pH was adjusted to 7.3 using CsOH. The acquisition rate was 20 kHz, and signals were filtered at 5 kHz. The protocol was set to increase from −80 to 20 mV (increments of 10 mV each time) to evoke the $Na_V1.7$ current, and each stimulation last for 50 ms. The applied bath solution contained NaCl (140 mM), KCl (5.4 mM), $CaCl_2$ (1.8 mM), and $MgCl_2$ (0.5 mM), HEPES (5 mM), D-glucose (5.5 mM), NaH_2PO_4 (0.4 mM), and the pH was adjusted to 7.4 with NaOH.

TTX-Sensitive Sodium Current of DRG Neurons Recording

The TTX-sensitive sodium current of small-diameter model DRG neurons was recorded in whole-cell configuration by voltage-clamp. The pipettes solution mainly consisted of CsCl (70 mM), NaCl (30 mM), TEA-cl (30 mM), EGTA (10 mM), $CaCl_2$ (1 mM), $MgCl_2$ (2 mM), HEPES (10 mM), D-glucose (5 mM), Na_2ATP (2 mM), GTP (0.05 mM), and the pH value was adjusted to 7.3 by CsOH. The bath solution (pH = 7.4) containing NaCl (80 mM), Choline-Cl (50 mM), TEA-Cl (30 mM), $CaCl_2$ (2 mM), $CdCl_2$ (0.2 mM), HEPES (10 mM), and D-glucose (5 mM). Total sodium current was elicited by the stimulation of −10 mV, 50 ms, and the TTX-sensitive sodium current was obtained by subtracting the current after TTX processing from the total Na current.

Quantitative PCR

According to the instructions, 800 ng RNA was reversely transcribed using PrimeScriptTM RT reagent Kit with gDNA Eraser (perfect real time) kit (Takara, Japan) (Wang et al., 2017; Wang et al., 2021); then, gene-specific mRNA analyses were conducted with SYBR premix ex TaqTMII (TliRnaseH plus) kit (Takara, Japan) as standard protocol. In this study, Gapdh was applied as a reference to normalize the mRNA expression of SCN9A and SCN10A. After amplification, each qPCR product was electrophoresed to ensure specificity. After the components required for the PCR reaction were configured, the cycling systems were placed on the PCR machine and preheated at 95°C for 3 min to fully denature the template DNA, and then enter the amplification cycle stage.

In each cycle, the template was denatured at 95°C for 30 s, and then the temperature was lowered to the renaturation environment of 60°C for 30 s to fully anneal the primer and template. Finally, the prepared systems were kept in 72°C for 1 min (amplifying 1 kb fragment) to make the primer extend on the template and synthesize DNA. The above cycle was repeated 39 times to accumulate a large amount of amplified DNA fragments, and then kept at 72°C for 5 min to complete the extension of the products. Finally, the products were preserved at 4°C.

The genbank accession number of SCN9A and SCN10A were NM_133289.1 and NM_017247.1, respectively. The position of primer sequences of SCN9A located between 1174 and 1293 base pairs, and the primer sequences of SCN10A were located between 581 and 737 base pairs. In addition, SCN9A was the gene expressing the $Na_V1.7$ channel, and the primer was detailed in the following sequence: $Na_V1.7$ (SCN9A): forward TACCTG ATAAACTTGATCCTGGC; reverse TTTGAGTCGGTCTAA CATCTGCT; SCN10A was the gene expressing the $Na_V1.8$ channel, and the primer was detailed in the following sequence: $Na_V1.8$ (SCN10A): forward GTCTGTCCATTCCTG GTTCTCC; reverse ACAAAACCCTCTTGCCAGTATCT.

Western Blot

The DRG neuron lysates were prepared with RIPA lysis buffer, and the protein loading amount was 40 μg. Equal amounts of protein were separated by SDS-PAGE and electro-transferred to the polyvinylidene fluoride (PVDF) membrane. PVDF membrane was blocked with 5% nonfat dairy milk, and incubated with primary antibody of $Na_V1.7$, $Na_V1.8$, and β-actin overnight at 4°C, which was further incubated with IRDye800-conjugated secondary antibody (1: 50,000; EARTHOX) for 2 h at room temperature and subsequently scanned with the Odyssey Infrared Imaging System (LI-COR). The primary antibody of $Na_V1.7$ (item number ARG56140) was monoclonal antibody provided by Shanghai Bio-Platform Technology Company (Shanghai, China), and the host was mice. The production number of $Na_V1.8$ was ARG56141, and the rest of the information was consistent with $Na_V1.7$. Monoclonal antibody for mouse β-actin (product number 66009-1-Ig) was provided by proteintech (Rosemont, IL, United States). The integrated intensity of polyvinylidene fluoride membrane was detected by Odyssey Imager software (version 3.0).

Cell Immunofluorescence Pretreatment and Structured Illumination Microscopy Image Preparations

The model group neurons were incubated with vincristine for 24 h, and the GAS group was incubated with the mixture of GAS and vincristine for 24 h. DRG neurons were collected after washed by PBS for 3 times, and then washed with 4% paraformaldehyde for 30 min, which were transferred to 3% BSA and 0.3% Triton solution for 60 min. DRG neurons were blocked with 10% normal goat serum containing 0.3% Triton-X-100 (co-incubation for 1 h, 37°C). The sections were incubated with primary antibody for 12 h at 4°C (anti-Nav1.7 channel antibody: ARG56140; anti-Nav1.8 channel antibody: ARG56141), which were washed 5 times with PBS solution for minutes each time. The sections were incubated with secondary antibody for 2 h at room temperature, and then the secondary antibody was removed using PBS solution. Finally, the sections containing DRG were sealed with gelatin coating and placed in the dark for SIM imaging.

DRG Tissue Immunofluorescence Preparation

The ascending aorta of SD rats was perfused with saline solution, and then perfused with 4% paraformaldehyde (PFA, pH 7.4, 4°C). Subsequently, the DRG L5 ganglion was removed and fixed in 4% PFA for 24 h (4°C), and then soaked in 30% sucrose for 48 h (4°C) to dehydrate. After that, the dehydrated ganglion was sectioned into 14 μm thick slices in the cryostat using gelatinized slides, and then subjected to immunofluorescence treatment. Then, the sections were blocked with 0.2% Triton X-100 containing 2% BSA for 1 h at room temperature, and then incubated with primary antibody (anti-$Na_V1.7$ channel antibody: ARG56140; anti-$Na_V1.8$ channel antibody: ARG56141) overnight at 4°C. Finally, the sections were washed 3 times with PBS at room temperature (5 min for each time), and then co-incubated with secondary antibodies at room temperature for 1 h.

Molecular Docking

We constructed the three-dimensional structures of $Na_V1.7\&1.8$ using homology modeling method.

In this study, Discovery Studio 2020 Client (DS 2020) was used for the prediction of binding pockets, molecular docking, and the estimation of the binding interactions between the receptor and GAS. Molecular docking was performed by CDOCKER module with the CHARMm force field. First, the three-dimensional (3D) structures of $Na_V1.7$ and $Na_V1.8$ were constructed using homology modeling method (Waterhouse et al., 2018), and processed by "prepare proteins module," including Loop domain optimization, protonation, removing water, energy minimization using conjugate gradient algorithm with CHARMm force field. Second, GAS was sketched by ChemDraw 19.0, and prepared by the "Prepare Ligands module," consisting of pH-based ionization, tautomers generation, generating 3D coordinates, rearranging hydrogens, and minimization. Then, the binding sites of the receptor were defined by the "From Receptor Cavities" method within the "Define and Edit Binding Site module," and referring to the active sites reported in the literature (Ito et al., 1989; Swain et al., 2017; Moyer et al., 2018; Wu et al., 2018; Xu et al., 2019). Finally, the CDOCKER method was applied to evaluate the binding interactions of GAS at different sites with the docking score as an important criterion (Zhang et al., 2019a; Zhang et al., 2020a).

Molecular Dynamic Simulation

Molecular dynamic (MD) simulation was further used to evaluate the binding interactions between the GAS and the predicted pockets. MD simulations of the constructed systems were performed using GPU-accelerated PMEMD in Amber18 on 28 cores of an array of two 2.9 GHz Intel Gold 6226R processors and 6 pieces of Nvidia Tesla v100s 32 GB graphic card. Prior to MD simulation, all components (protein-ligand complex, protein, and ligand) were processed with program tleap embedded in AmberTools to generate the corresponding coordinate files and topology files. Amber ff14SB and general Amber force fields were applied for the receptor protein and the docked ligand, and the Li/Merz ion parameters for SPC/E water model were directly used based on the previous publications (Wang et al., 2018; Wang et al., 2019; Zhang et al., 2020b; Li et al., 2021; Liang et al., 2021). Antechamber was chosen to assign the charges of the docked ligands via the restrained electrostatic potential partial charges, and Gaussian 09 was used to optimize the ligand's geometry and calculate the electrostatic potential calculations at HF/6–31G* level. Then, the processed systems were subjected to 200 ns MD simulation, mainly consisting of 2 steps energy minimization optimization process, progressive heating process, 5 ns equilibrium process, and the final 200 ns MD process. Program cpptraj was used to analyze the RMSD and representative conformations of MD trajectories, and mm_pbsa.pl program was selected to explore the binding free energies between the ligand and receptor.

Statistical Analysis

The behavioral experiment results were processed and analyzed by OriginPro (version 9.1.0). Statistical difference among multiple groups was compared by one/two-way ANOVA, and Bonferroni Test was used for two group comparisons, which was presented as mean ± SD. HEKA FitMaster (version 2x90.3) and OriginPro (version 9.1.0) were used to analyze the electrophysiological data, and the above-mentioned method was applied to analyze and compare the statistical difference, presented by mean ± SEM. Threshold represents the voltage value at the inflection point during the rising phase of the action potential, recorded with the current clamp (Zhang et al., 2019b). Additionally, $G = I/(V_m - E_{Na})$ was applied to convert the peak inward currents obtained from activation protocols (G represented the conductance; I indicated the peak inward current; V_m represented the instantaneous membrane potential; E_{Na} indicated the equilibrium potential for sodium channel.) Maximum conductance value was used to normalize the conductance data, which was further fit with Boltzmann equation, namely $G = G_{max} + (G_{min} - G_{max})/(1 + \exp[(V_m - V_{1/2})/k])$ (G also represented the conductance; $V_{1/2}$ was the midpoint of activation; k indicated the slope factor.). The IC_{50} values were calculated using logistic equation fitting. Licor Odyssey software was applied to quantify the gray values of proteins in WB, and fluorescence intensity in immunofluorescence was measured by NIS-Elements Viewer (version 4.20, Nikon, Japan) software.

RESULTS AND DISCUSSION

Alleviation of GAS on Vincristine-Induced Mechanical and Thermal Hyperalgesia in Rat

Vincristine has been reported to induce various pains, such as postherpetic neuralgia, diabetic neuralgia (Feld et al., 1980), and type I complex regional pain syndrome (Benzon et al., 2003), which has been associated with damage to the peripheral nerve terminal (Rosenthal and Kaufman, 1974; Dupuis et al., 1985; Old et al., 2014). Additionally, more than half of the rats treated with vincristine have been found to respond abnormally to thermal and mechanical pain induced by C fiber stimulus (Tanner et al., 1998; Xiao and Bennett, 2008; Xu et al., 2017). Therefore, vincristine was used to construct the CINP rat model, and thresholds of mechanical and thermal pains were measured (**Figure 1A**).

There was no difference in the mean paw withdrawal threshold of the three groups as determined by von Frey and radiant heat stimulus. The selected experimental rats were randomly divided into three groups (control group, vincristine group, and GAS group), and the basic values of mechanical and thermal thresholds were preliminarily evaluated before drug administration. The specific values were as follows: mechanical thresholds: 7.11 ± 1.03 g (control group), 7.02 ± 0.62 g (vincristine group), 6.83 ± 1.25 g (GAS group); thermal thresholds: 19.65 ± 1.78 s (control group), 20.19 ± 2.65 s (vincristine group), 20.21 ± 1.73 s (GAS group). After 7 days of vincristine administration (ip, 0.125 mg/kg), the values of mechanical and thermal thresholds were calculated, and the mean paw withdrawal threshold was significantly reduced compared with the control group: mechanical thresholds: 7.05 ± 1.00 g (control group), 3.69 ± 1.11 g (vincristine group), 4.02 ± 1.21 g (GAS group); thermal thresholds: 19.76 ± 2.15 s (control group), 17.11 ± 1.68 s (vincristine group), 16.63 ± 1.16 s (GAS group).

Continuous administration of GAS (ig, 60 mg/kg) for 7 days significantly attenuated the development of mechanical ($n = 10$) and thermal hyperalgesia ($n = 23$), as shown in **Figure 1B**. Quantitative analysis showed that, compared with the vincristine model, GAS increased the mechanical pain threshold from 3.11 ± 1.34 g to 8.92 ± 1.14 g, and the thermal withdrawal latency from 14.77 ± 2.32 s to 20.97 ± 3.01 s on the 14th day of modeling (mean ± SD, $^{***}p < 0.001$ and $^{***}p < 0.001$) (**Figure 1C**). Apparently, the applied modeling method successfully induced mechanical pain and thermal hyperalgesia in rats. After treatment with GAS, the thresholds of mechanical and thermal hypersensitivity were greatly improved, and the mechanical tactile and thermal allergic of the model rats could be restored to normal levels. In addition, in order to better illustrate the mechanisms underlying GAS alleviating vincristine induced peripheral neuropathic pain, the influences of GAS on the mechanical and thermal thresholds in normal SD rats were also observed. The results showed that the mechanical and thermal thresholds didn't increase significantly after 3 days of

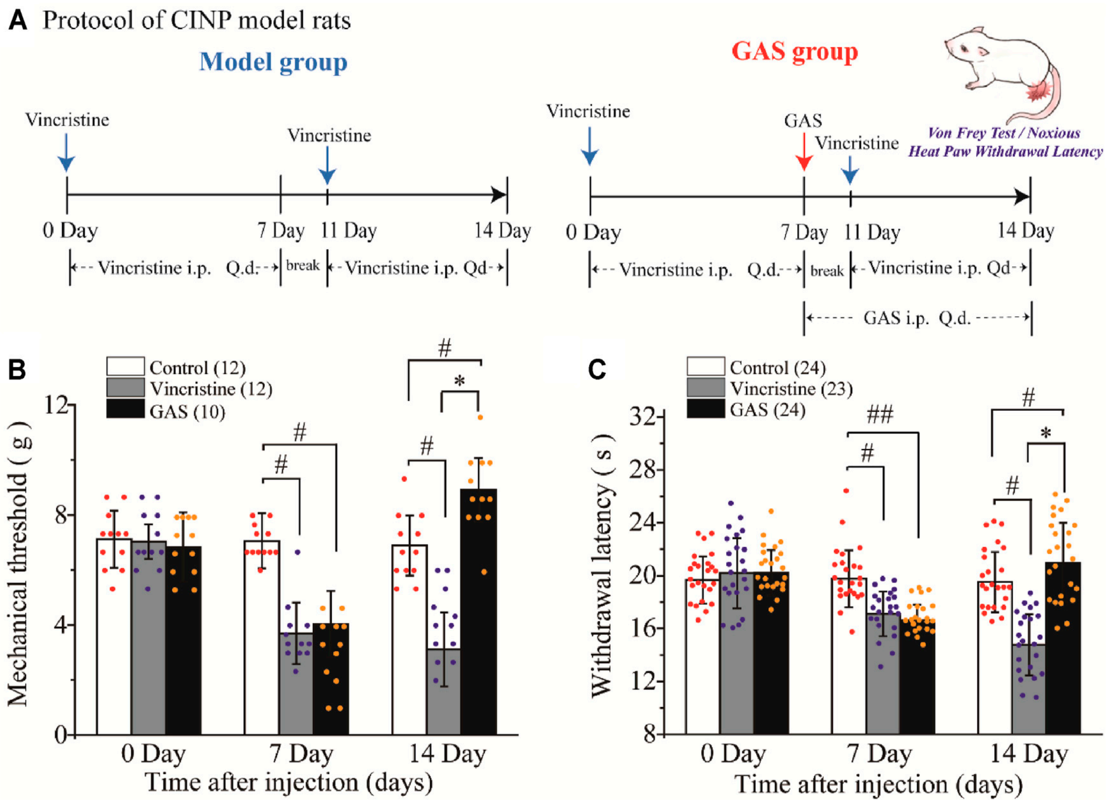

FIGURE 1 | The effects of GAS on alleviating the symptoms of vincristine-induced CINP rats: **(A)** Administration protocol of GAS in the treatment of neuropathic pain model rats caused by vincristine; **(B)** The effects of GAS against vincristine-induced hyperalgesia on mechanical paw withdrawal duration in a pinprick test, and the mechanical paw withdrawal threshold was measured at 0, 7, 14 Day; **(C)** Effects of GAS on plantar thermal pain in vincristine model rats, and the thresholds were measured at 0, 7, 14 Day (#$p < 0.05$, ##$p < 0.01$, compared to the control group; *$p < 0.05$, compared to the model group; *ANVOA- Bonferroni Test*).

GAS administration, indicating that the mechanism of GAS reversing vincristine-induced hyperalgesia was different from that of anesthetic effects (**Supplementary Figure S1**). The behavioral results suggested that GAS had a good curative effect on CINP model rats, which was expected to be a small active molecule for the treatment of peripheral neuropathic pain.

Inhibitory Effects of GAS on the Hyperexcitability of Small-Sized DRG Neurons Induced by Vincristine

As primary sensory afferent neurons, the ectopic afferent discharge of DRG neurons is widely considered to be the main cause of chronic pain after peripheral nerve injury (Seijffers et al., 2007; Norcini et al., 2016). Thus, DRG neurons were isolated to observe the changes of their firing patterns. The alleviation of vincristine-induced rat hyperalgesia by GAS indicated that GAS might directly decrease the excitability of neurons. In order to explore the mechanism of GAS, the firing spikes of action potentials were recorded on small-diameter (17–25 μm) DRG neurons, which were closely related to the afferent noxious signal. GAS (100 μM) significantly attenuated hyperexcitability of vincristine-induced DRG neurons, and reduced the number of action potentials triggered by 500 pA (**Figures 2A,C**). 200 μM GAS and 500 nM PF-05089771 (Cat. No.: HY-12883, MCE) notably increased the rheobase current (depolarization current threshold eliciting the 1st action potential), namely, from 86.8 ± 3.1 pA ($n = 22$) to 203.3 ± 10.7 pA ($n = 15$, $^{**}p < 0.01$) and 640.0 ± 66.2 pA ($n = 10$, $^{**}p < 0.01$) (**Figure 2D**); the action potential threshold voltage also remarkably increased from −36.6 ± 0.7 mV ($n = 17$) to −21.3 ± 1.8 mV ($n = 10$, $^{***}p < 0.001$) and −12.3 ± 1.8 mV ($n = 10$, $^{***}p < 0.001$) (**Figure 2F**); 200 μM GAS and 500 nM PF-05089771 significantly reduced the amplitude of action potentials in DRG neurons ($^{**}p < 0.01$) (**Figure 2E**). **Figure 2B** showed that GAS decreased the rate of action potential slope rise (dV/dt). Therefore, GAS could significantly reduce the number of action potential bursts of DRG neurons in model rats, decrease the amplitude of action potentials, and increase the rheobase and threshold of action potentials (**Table 1**), thereby inhibiting the excitability of DRG neurons in model rats, which was similar to that of the inhibitory effects of PF-05089771 on excitability of model DRG neurons.

The repetitive firing of DRG neurons depends on the inherent resonance characteristics of the cell membrane. Most small or medium-diameter DRG neurons cannot produce repeated firing during continuous depolarization, and step depolarization stimulus only causes a single spike or transient burst (Amir and Devor, 1996; Amir et al., 2005). According to **Figures**

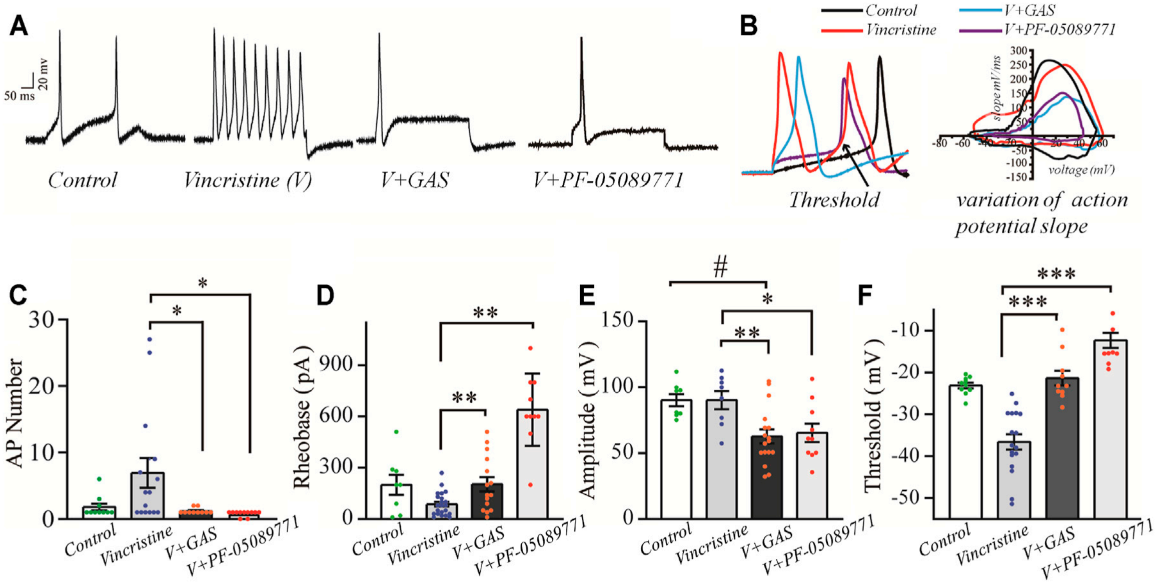

FIGURE 2 | The influences of GAS on the excitability of vincristine-induced hyperexcitability of small-sized DRG neurons: **(A)** typical action potential curve of spike firing of each experimental group; **(B)** phase plot of the action potential **(left),** and the raising slope of action potential **(right); (C)** the effect of GAS on the number of action potentials fired by DRG neurons in each group; **(D)** histogram of the effects of GAS on action potential rheobase of DRG neurons in each group; **(E)** the influence of GAS on the amplitude of the first peak of action potential fired by DRG neurons; **(F)** regulation of GAS on the firing threshold of action potentials of DRG neurons in each group (#*p* < 0.05, ###*p* < 0.001, compared to the control group; **p* < 0.05, ***p* < 0.01, ****p* < 0.001, compared to the model group; ANVOA- Bonferroni Test).

TABLE 1 | Summarized effects of GAS on vincristine-induced hyperexcitability of the action potential in DRG neuron.

Groups	RMP (mV)	Rheobase (pA)	Amplitude (mV)	AP duration (ms)	AP number
Control	−49.6 ± 0.9 (10)	200.0 ± 16.5 (8)	90.2 ± 1.6 (8)	13.9 ± 0.7 (10)	1.8 ± 0.2 (10)
Vincristine	−45.53 ± 0.8 (10)	86.8 ± 3.1 (22)[c]	90.1 ± 2.4 (8)	6.5 ± 0.3 (10)[d]	6.9 ± 0.6 (15)
V+GAS 30 μM	−47.1 ± 0.4 (12)	108.0 ± 6.8 (10)	80.4 ± 2.8 (8)	6.7 ± 0.7 (10)[d]	4.3 ± 0.6 (10)
V+GAS 100 μM	−48.5 ± 0.9 (11)	120.9 ± 7.2 (11)	71.7 ± 2.3 (8)[c]	7.8 ± 0.3 (10)[c]	3.6 ± 0.6 (10)
V+GAS 200 μM	−47.2 ± 0.5 (15)	203.3 ± 10.7 (15)[b]	62.6 ± 1.3 (17)[b, d]	9.0 ± 0.9 (10)	1.2 ± 0.04 (10)[a]

[a] *Compared with vincristine group,* p *< 0.05.*

[b] *Compared with vincristine group,* p *< 0.01.*

[c] *Compared with control group,* p *< 0.05.*

[d] *Compared with control group,* p *< 0.01. All data are given as the mean ± SEM.*

2A,C, it could be found that vincristine significantly increased the number of repetitive discharges of DRG neurons, and the increase of ectopic discharges was the internal cause of neuropathy-induced pain sensation. GAS effectively suppressed the number and amplitude of action potential, thereby reducing the occurrence of hyperalgesia. In addition, GAS also significantly increased the thresholds and rheobase of action potentials and reduced the probability of action potential bursts. Furthermore, GAS reduced the upstroke slope of action potential's rising phase, and slowed down the depolarization of the action potential, thus retarding the occurrence process of the action potential. Furthermore, based on the effects of GAS on the excitability of DRG neurons in normal SD rats, it could be found that GAS could increase the threshold and rheobase of action potentials to a certain extent, but had fewer effects on the number and amplitude of action potential, indicating that DRG neurons from normal SD rats were less sensitive to GAS compared to that of model DRG neurons (**Supplementary Figure S2**). In short, based on the biological functions of GAS discussed above, GAS reduced vincristine-induced hyperalgesia of primary sensory neurons associated with pain.

Inhibitory Activities of GAS Against Na$_V$1.7 and Na$_V$1.8 Sodium Channel Currents From the Cells Pre-Treatment With Vincristine

The Influence of GAS on the Kinetic Process of Na$_V$1.7 Channel

Na$_V$1.7 has been recognized as an important target in the nociceptive pathway, and the peripheral expression of the Na$_V$1.7 channel can stimulate pain signals in the DRG neurons by promoting minor stimulation, prompting the

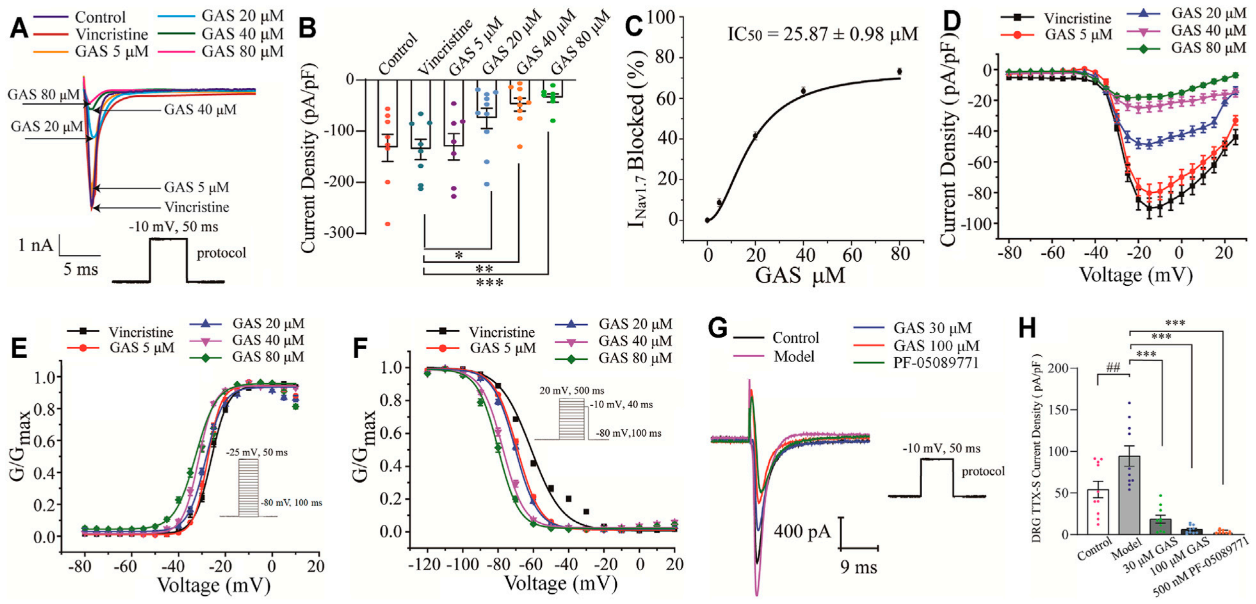

FIGURE 3 | Influences of GAS on $Na_V1.7$ channel current: **(A)** typical inhibition curve of GAS on $Na_V1.7$ channel current; **(B)** histogram of the influence of GAS on $Na_V1.7$ channel current density; **(C)** concentration-response curves of GAS on $Na_V1.7$ current (IC_{50} = 25.87 ± 0.98 μM); **(D)** the influence of different concentrations of GAS on the I-V curve of $Na_V1.7$ channel current density; **(E)** the influence of GAS on the activation curve of $Na_V1.7$ channel; **(F)** the voltage-dependent inactivation curves of $G_{Nav1.7}$; **(G)** the typical curve of GAS inhibiting the sodium current of DRG neurons; **(H)** the effects of GAS on the TTX-sensitive sodium current of DRG neurons (##$p < 0.001$, compared to the control group; *$p < 0.05$, **$p < 0.01$, ***$p < 0.001$, compared to the model group; ANVOA- Bonferroni Test).

release of neurotransmitters at the first synaptic site in the spinal cord and participating in pain signal transduction (Kingwell, 2019). $Na_V1.7$ is expressed on the sensory neurons or nociceptors, depolarizes the cell membrane of the injured site by mediating the inward flow of sodium ions, thereby triggering the firing of action potentials and mediating the transmission of pain signals (Waxman and Zamponi, 2014; Xia et al., 2016; Kingwell, 2019).

In this part, the whole-cell patch-clamp was applied to examine the effects of GAS on the over-expressed $Na_V1.7$ channel current on the HEK239B cell line. Firstly, the selected cell line was pre-incubated with vincristine (30 μg/L) for 24 h, and then the $Na_V1.7$ channel currents were recorded with different concentrations of GAS (5, 20, 40, 80 μM), making the current density decrease significantly from −135.7 ± 7.0 pA/pF ($n = 10$) to −30.7 ± 9.8 pA/pF ($n = 10$), −74.9 ± 6.2 pA/pF ($n = 8$), *$p < 0.05$), −47.8 ± 4.2 pA/pF ($n = 8$, **$p < 0.01$), −35.1 ± 3.1 pA/pF ($n = 6$, ***$p < 0.001$) (**Figures 3A,B**). Obviously, GAS presented a dose-dependent inhibition of the current density of $Na_V1.7$. In addition, Hill fitting was used to calculate the IC_{50} value of GAS's inhibitory activities against $Na_V1.7$ (IC_{50} = 25.87 ± 0.98 μM), as shown in **Figures 3C,D**.

Voltage-dependent activation and steady-state inactivation are vital characteristics of ion channels directly influencing the excitability of cells. The $Na_V1.7$ channel is characterized by rapid activation, rapid inactivation, and slow resurgent (Herzog et al., 2003). Compared with other sodium channels, the activation and inactivation curves of $Na_V1.7$ current present a hyperpolarization trend, generating a larger inward current and then activating the $Na_V1.8$ channel on the nociceptive receptors. Thus, the $Na_V1.7$ current activation experiment and the $Na_V1.7$ current inactivation experiment were performed using a patch clamp. The current density-voltage relationship was converted to the conductance ($G_{Nav1.7}$)-voltage, which was fitted into the Boltzmann equation. Compared with the vincristine group, the activation curve and steady-state inactivation curve of the $Na_V1.7$ channel in the GAS group shifted to the hyperpolarization direction, and the effects of GAS on the steady-state inactivation was more obvious. The slopes of the activation and inactivation curves of the $Na_V1.7$ channel remained basically unchanged (**Figures 3E,F**), and the half-maximum activation voltage ($V_{1/2}$) of $G_{Nav1.7}$ changed a little (**Figure 3E**; **Table 2**). However, the inactivated $V_{1/2}$ of $G_{Nav1.7}$ shifted to the hyperpolarized direction, and the movement effect was observed in a dose-dependent manner (**Figure 3F**; **Table 2**). In summary, GAS mainly suppressed the inward current of the $Na_V1.7$ channel and promoted the inactivation state of the $Na_V1.7$ channel.

According to the above results, GAS produced a large slope current by directly inhibiting the $Na_V1.7$ channel current, making the action potential produce small and slow depolarization in the process of discharge, and thus playing the regulatory role of reducing neuronal excitation. GAS mainly promoted the inactivation of the $Na_V1.7$ channel, making the channel more likely to be inactivated or more sodium channels be in an inactive state under a negative membrane potential (**Figures 3E,F**). Similar to other small sodium channel blockers, most of the blockers currently being developed around $Na_V1.7$ make the channels be in the fast or slow inactivation state, or prolonging the process of resurrection, reducing the number of sodium channels contributing to the action potential and inhibiting the abnormal firing of action potentials.

TABLE 2 | The effect of GAS on $V_{1/2}$ of $Na_V1.7$ channel and $Na_V1.8$ channel in cells.

	$Na_V1.7$ channel $V_{1/2}$			$Na_V1.8$ channel $V_{1/2}$	
	Activation	**Inactivation**		**Activation**	**Inactivation**
Vincristine	−26.1 ± 0.3	−61.3 ± 1.6	Control	−24.1 ± 1.2	−35.2 ± 1.4
GAS 5 μM	−27.6 ± 0.7	−69.1 ± 0.8	Model	−33.7 ± 0.7	−24.2 ± 1.2
GAS 20 μM	−28.4 ± 0.5	−70.2 ± 1.2	GAS 3 μM	−32.6 ± 1.3	−27.8 ± 1.3
GAS 40 μM	−32.3 ± 0.7	−77.3 ± 1.1	GAS 10 μM	−34.4 ± 0.8	−29.1 ± 1.2
GAS 80 μM	−32.7 ± 1.2	−79.9 ± 1.2	GAS 30 μM	−29.2 ± 1.1	−37.4 ± 1.9
			GAS 100 μM	−34.4 ± 0.6	−34.4 ± 1.0
			GAS 300 μM	−31.9 ± 1.1	−37.7 ± 1.9
			GAS 1,000 μM	−32.7 ± 1.4	−37.3 ± 0.3

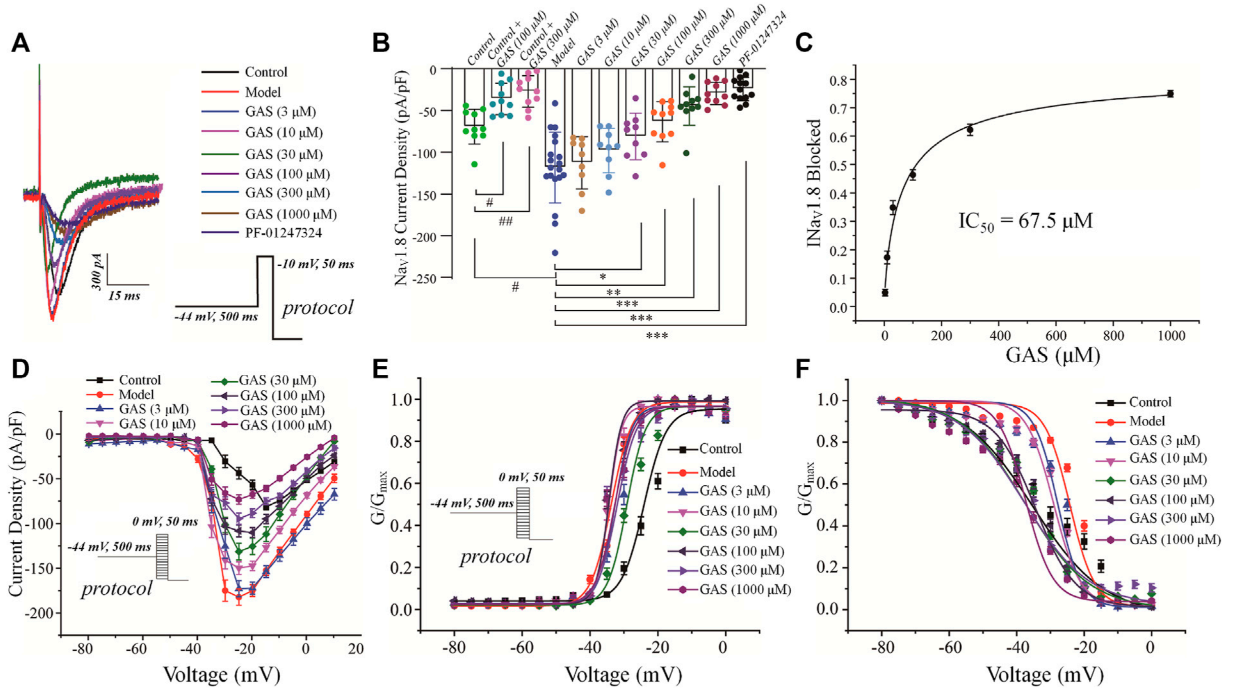

FIGURE 4 | Effects of GAS on $Na_V1.8$ channel current in DRG neurons from model rats: **(A)** typical curve of GAS inhibiting $Na_V1.8$ channel current of DRG neurons; **(B)** histogram of the inhibitory effects of GAS on the current density; **(C)** concentration-response curves of GAS on $Na_V1.8$ current (IC_{50} = 67.5 ± 20.7 μM); **(D)** influence of different doses of GAS on the current density-voltage relationship of DRG neurons. **(E)** effects of different concentrations of GAS on the activation curve of $Na_V1.8$ channel; **(F)** influence of different concentrations of GAS on the inactivation curve of $Na_V1.8$ channel of DRG neurons (#$p < 0.05$, compared to the control group; *$p < 0.05$, **$p < 0.01$, ***$p < 0.001$, compared to the model group; ANVOA- Bonferroni Test).

Besides, the effects of GAS on TTX-sensitive sodium current were recorded on DRG neurons. While $Na_V1.6$ was mainly distributed in medium and large diameter neurons (Chen et al., 2020), the small-diameter neurons that were concerned in this study expressed $Na_V1.7$ (TTX-sensitive), $Na_V1.8$ and $Na_V1.9$ (TTX-resistant) (Wang et al., 2020). In this section, since the current of $Na_V1.7$ couldn't be directly observed, the TTX-sensitive sodium current obtained by subtracting the current after TTX processing from the total Na current, indicating the large component of the TTX-sensitive sodium current was $Na_V1.7$. Furthermore, according to **Figures 3G,H**, it could be found that TTX-sensitive sodium current density of model DRG neurons decreased from −94.3 ± 12.4 pA (n = 10) to −18.4 ± 4.7 pA (n = 10), −18.4 ± 4.7 pA (n = 10) to −6.1 ± 1.6 pA (n = 9) after being treated with 30 μM, 100 μM GAS, respectively. Moreover, such TTX-sensitive sodium current density couldn't be further inhibited by selective $Na_V1.7$ inhibitor PF-05089771 [from −6.1 ± 1.6 pA (n = 9) to −3.3 ± 0.6 pA (n = 10)]. The experimental results showed that the above TTX-sensitive sodium channels were very sensitive to low concentration of GAS (30 μM), and most of the current could be inhibited by GAS, consisting with the results recorded in HEK293B cell line.

The Influence of GAS on the $Na_V1.8$ Channel

Since the $Na_V1.8$ channel plays a vital role in the rising phase of the action potential, it has a profound influence on the evoked discharge of the action potential (Waxman and Zamponi, 2014; Xia et al., 2016; Klein et al., 2017). The depolarization activation and the slow inactivation of $Na_V1.8$ are related to the repetitive firing of DRG neurons. It was observed in **Figures 2C,E** that GAS could significantly decrease the action potential amplitude and reduce repetitive discharges of CINP model rats. Therefore, it is necessary to further explore the influence of GAS on the current and inactivation of the $Na_V1.8$ channel.

In order to isolate TTX-resistant $Na_V1.8$ current, TTX (500 nM) was used to block TTX-sensitive component of sodium current and a conditioning prepulse of −44 mV (500 ms) was used to inactivate TTX-resistant $Na_V1.9$ channel (see *Materials and Methods* for details). GAS presented a concentration-dependent inhibition of the current density of $Na_V1.8$ in DRG neurons in model rats (**Figure 4A**). Before GAS perfusion, the current density of the control group and the vincristine group were recorded: −69.52 ± 6.5 pA/pF (control, n = 10), −118.5 ± 9.8 pA/pF (vincristine, n = 19) (**Figures 4A,B**). Then, the bath solution containing different concentrations of GAS processed the vincristine group, and the current density was recorded was follows: 3 μM GAS, −112.7 ± 9.4 pA/pF (n = 10);10 μM GAS, −98.1 ± 8.11 pA/pF (n = 10); 30 μM GAS, −77.2 ± 2.2 pA/pF (n = 10); 100 μM GAS, −63.5 ± 7.3 pA/pF (n = 10); 300 μM GAS, −44.8 ± 6.9 pA/pF (n = 10); 1,000 μM GAS, −29.7 ± 3.9 pA/pF (n = 10); PF-01247324 (Cat. No.: HY-101383, MCE) (1 μM) −24.5 ± 3.9 pA/pF (n = 13) (**Figures 4A,B**).

Based on the **Figure 4B**, the inhibitory effects of GAS on $Na_V1.8$ sodium channel current from normal DRG neurons depended on relative high concentrations, but GAS could exhibit significant inhibitory effects on $Na_V1.8$ sodium channel current from model DRG neurons at the low concentration (30 μM). In addition, when the DRG model neurons were treated with 300 or 1,000 μM GAS, the $Na_V1.8$ selective inhibitor PF-01247324 wouldn't have further significant inhibitory effects on the channel current, indicating that GAS inhibited most of $Na_V1.8$ channel current at such concentrations. Certainly, **Figure 4B** also showed that $Na_V1.8$ channel current could be isolated from DRG neuron using such specific biophysical protocol. Besides, the IC_{50} values of inhibitory activities of GAS on the $Na_V1.8$ channel current of the model neuron was calculated, i.e., IC_{50} = 67.5 ± 20.7 μM (**Figure 4C**). The relationship between conductance ($G_{Nav}1.8$) and voltage was presented by scatter plot, which was further fitted with Boltzmann equation to generate activation and inactivation curves.

Besides, GAS had no significant effects on the activation curve of $Na_V1.8$ channel, making the inactivation curve shift to the hyperpolarization direction, and the specific results were as follows: The inactivation voltage ($V_{1/2}$) value of the vincristine model group was −24.2 ± 1.2 mV, and the inactivation $V_{1/2}$ of GAS at different concentrations were summarized in **Table 1**. By further comparing the effects of GAS on the inactivation $V_{1/2}$ of the vincristine model (3 μM GAS group, $\Delta V_{1/2}$ = −3.6 mV; 10 μM GAS group, $\Delta V_{1/2}$ = −4.9 mV; 30 μM GAS group, $\Delta V_{1/2}$ = −13.2 mV; 100 μM GAS group, $\Delta V_{1/2}$ = −10.2 mV; 300 μM GAS group, $\Delta V_{1/2}$ = −13.5 mV; 1,000 μM GAS group, $\Delta V_{1/2}$ = −13.1 mV), it is found that GAS affected the inactivation $V_{1/2}$ of the model in a dose-dependent manner (**Figure 4F**).

Compared with the neuronal activation curve of the vincristine group, GAS did not affect the activation curve (**Figures 4E,E**), but all the groups treated with GAS could make the steady-state inactivation curve of conductance ($G_{Nav1.8}$)-voltage shift to hyperpolarization, indicating that GAS only affected the steady-state inactivation curve and hardly influenced the slope of the steady-state inactivation curve of the $Na_V1.8$ channel (**Figure 4F**). The $V_{1/2}$ value inactivating $G_{Nav1.8}$ shifted to the hyperpolarization direction by a dose-dependent manner (**Table 2**). In short, GAS significantly reduced the current amplitude of the $Na_V1.8$ current, mainly mediating the inactivation state of the $Na_V1.8$ channel. In summary, GAS significantly decreased the current density of the $Na_V1.8$ channel and promoted the inactivation state of the $Na_V1.8$ channel, further influencing the dynamics of the $Na_V1.8$ channel. Based on the above results (**Figures 2F**, **4B**), GAS significantly suppressed the current density of the $Na_V1.8$ channel, which is the main reason for the effective reduction of the peak action potential. In addition, GAS made $Na_V1.8$ channels prone to inactivation (namely, more sodium channels were in an inactive state at the relatively negative membrane potential), which in turn produced inhibitory activity.

Additionally, it was also reported that GAS could also inhibit the activities of $Na_V1.6$, indicating that GAS had certain broad-spectrum inhibition activity on sodium ion channels (Shao et al., 2017). Furthermore, GAS could decrease the transient sodium current (I_{NaT}) and increase slowly inactivating potassium currents (I_{AS}) of streptozotocin-induced painful diabetic neuropathy rat model, exerting analgesic effects. Meanwhile, previous studies also pointed out that GAS had certain inhibitory activities on other ion channels, such as acid-sensing ion channels, which had certain therapeutic significance for pain caused by extracellular acidification or spinal synaptic potentiation (Xiao et al., 2016).

The Down-Regulation of GAS on $Na_V1.7$ Channel and $Na_V1.8$ Channel Protein in DRG Neurons

The up-regulation of $Na_V1.7$ and 1.8 has been found in a variety of pain models, such as experimentally induced diabetes and inflammation models leading to mechanical allodynia and thermal pain (Renganathan et al., 2001; Kretschmer et al., 2002; Black et al., 2004; Shields et al., 2012). Additionally, the intrathecal injection of $Na_V1.8$ antisense oligonucleotides could partially reduce mechanical allodynia and thermal hyperalgesia by down-regulating the expression of SNS transcripts. Therefore, it was necessary to explore whether GAS had influences on the expression of $Na_V1.7$ and $Na_V1.8$ channels in DRG neurons of CINP rat model, which was helpful to reveal the inhibitory mechanism of GAS on neurons.

After the behavioral test on the 14th day, the rats were deeply anesthetized with 3% sodium pentobarbital (50 mg/kg, i.p.), and the DRG neurons were extracted for Q-PCR and WB. GAS had no significant effects on the expression of SCN9A's mRNA, but significantly inhibited the expression of SCN10A's mRNA.

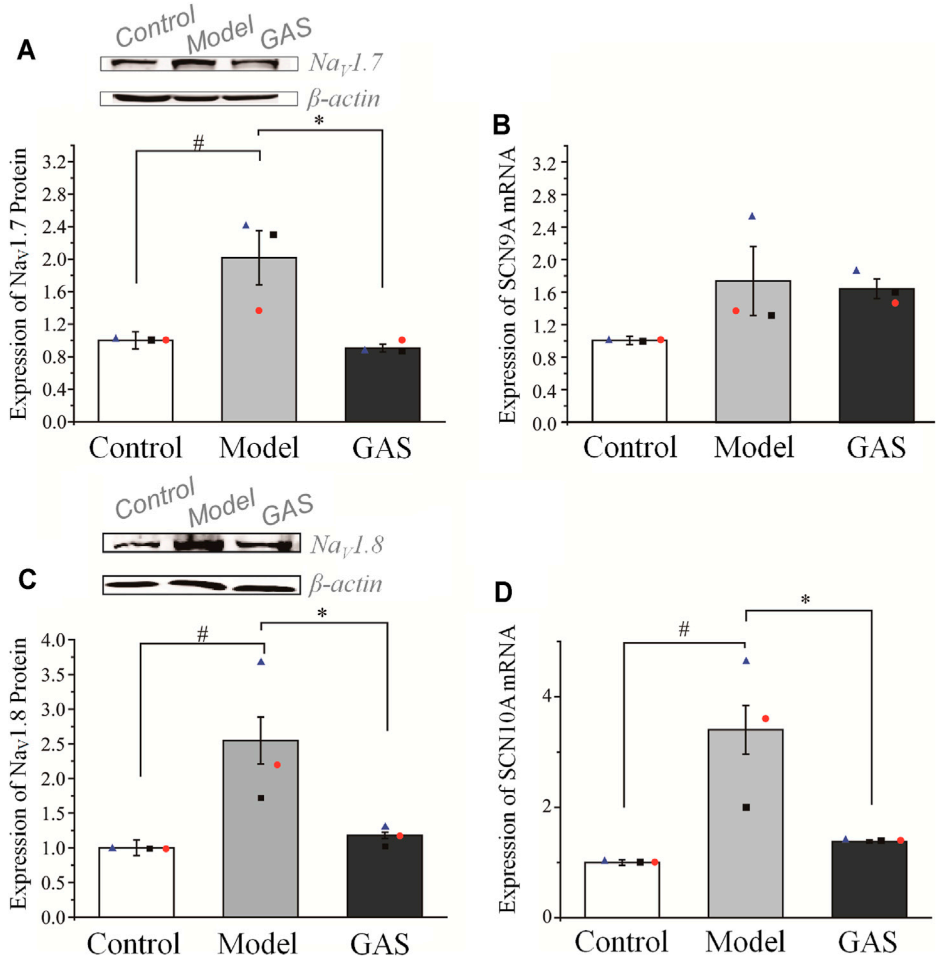

FIGURE 5 | Effects of GAS on the expression level of SCN9A and SCN10A genes and corresponding proteins: **(A)** down-regulation of $Na_V1.7$ channel proteins in DRG neurons of vincristine model by GAS ($n = 3$); **(B)** effects of GAS on the expression of SCN9A mRNA in DRG neurons in vincristine model; **(C)** the effects of GAS on the expression of $Na_V1.8$ channel protein in DRG neurons ($n = 3$); **(D)** influences of GAS on the expression of SCN10A mRNA in DRG neurons of vincristine model (#$p <$ 0.05, compared to the control group; $^*p < 0.05$, compared to the model group; ANVOA- Bonferroni Test).

(SCN9A: 1.74 ± 0.42 in the vincristine group, $n = 3$; 1.64 ± 0.12 in GAS group, $n = 3$, $p > 0.05$; SCN10A: 3.47 ± 0.38 in the vincristine group, $n = 3$; 1.38 ± 0.01 in GAS group, $n = 3$, $^*p < 0.05$), as shown in **Figures 5B,D**. Next, it was observed that GAS could reduce the upregulation of $Na_V1.7$ and $Na_V1.8$ channel proteins induced by vincristine ($^*p < 0.05$, $n = 3$), as shown in **Figures 5A,C**. The above results show that GAS plays an important inhibitory role in resisting the up-regulation of SCN10A mRNA, $Na_V1.7$, and $Na_V1.8$ channel proteins caused by vincristine. Next, it was observed that GAS could reduce the upregulation of $Na_V1.7$ and $Na_V1.8$ channel proteins induced by vincristine ($^*p <$ 0.05, $n = 3$) (**Figures 5A,C**). These results showed that GAS played an important role in inhibiting the up-regulation of mRNA of SCN10A, $Na_V1.7$ and $Na_V1.8$ channel proteins induced by vincristine.

This part verified that $Na_V1.7$ and $Na_V1.8$ were indeed accumulated in the DRG neurons of the CINP rat model, which was the main cause of pain. Regardless of the level of mRNA or protein expression, GAS has played a vital role in inhibiting the abnormally high expression of $Na_V1.7$ and $Na_V1.8$. Therefore, GAS not only affects the function of $Na_V1.7$ and $Na_V1.8$ channels, but also inhibits the protein expression of $Na_V1.7$ and $Na_V1.8$ channels, indicating that GAS has more abundant regulatory effects than the specific blockers of $Na_V1.7$ and $Na_V1.8$ channels.

GAS Counteracts the Up-Regulation of $Na_V1.7$&1.8 Protein Distribution Induced by Vincristine

In order to determine whether GAS affects protein expression, we first observed the effects of GAS on the fluorescence intensity of $Na_V1.7$ & 1.8 channels on DRG small-diameter neurons in the L5 segment of model rats from the slice level. And the average fluorescence intensity of each group was as follows: 1) $Na_V1.7$ system: control group, 1.5 ± 0.5 ($n = 82$, N = 4); vincristine group, 2.6 ± 0.9 ($n = 80$, N = 5); GAS, 1.4 ± 0.5 ($n = 115$, N = 5) (**Figures 6A,B**). 2) $Na_V1.8$ system: control group, 1.5 ± 0.4 ($n = 79$, N = 4);

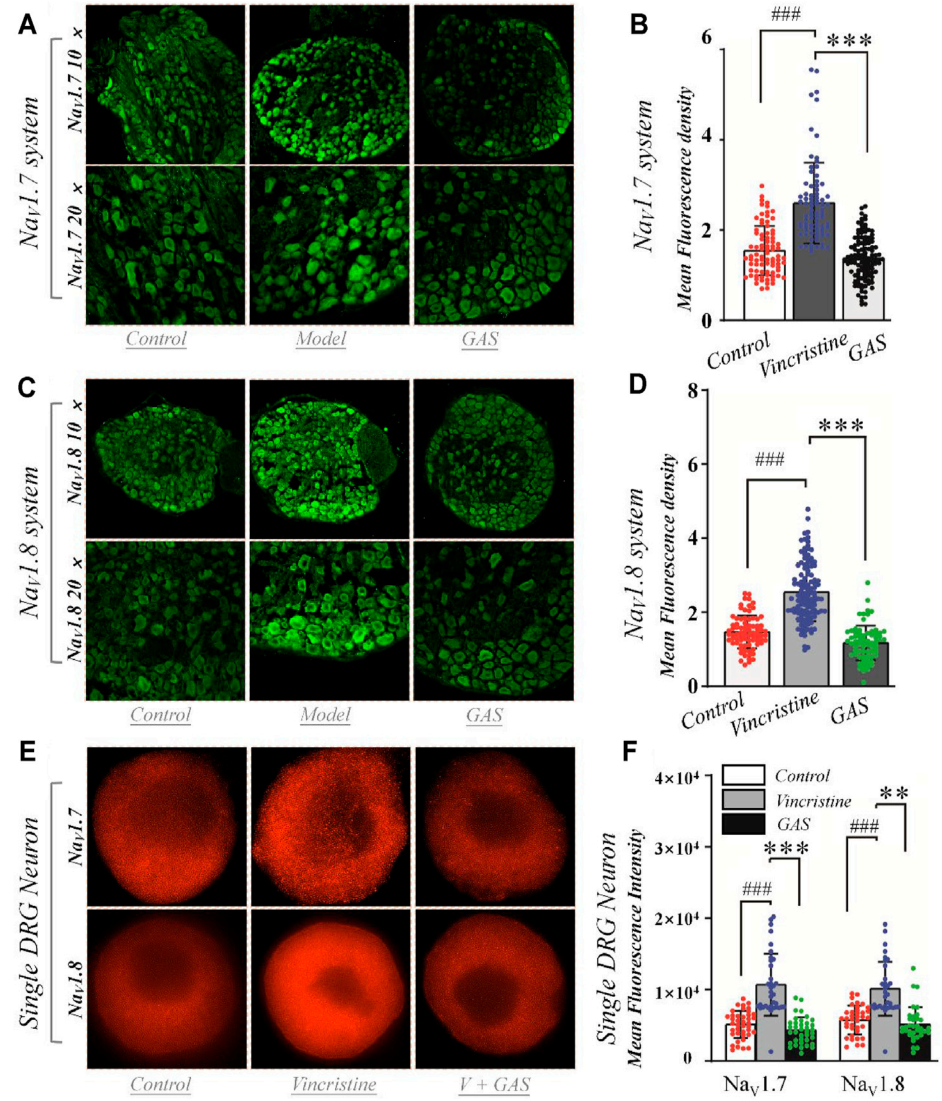

FIGURE 6 | Effects of GAS on the expression of $Na_V1.7$ and $Na_V1.8$ channel proteins in DRG neurons: **(A)** typical diagram of the effects of GAS on $Na_V1.7$ protein expression in DRG ganglion; **(B)** the effects of GAS on the average fluorescence density of $Na_V1.7$ protein in DRG tissue (control: *n* = 82, vincristine: *n* = 80, GAS: *n* = 115, N = 4, 5, 5); **(C)** typical diagram of the effects of GAS on $Na_V1.8$ protein expression in DRG ganglion; **(D)** the effects of GAS on the average fluorescence density of $Na_V1.8$ protein in DRG tissue (control: *n* = 79, vincristine: *n* = 120, GAS: *n* = 74, N = 4, 5, 4); **(E)** SIM image of the distribution of $Na_V1.7$ and $Na_V1.8$ protein and the depiction of intensity; **(F)** histogram of the influence of GAS on fluorescence intensity of $Na_V1.7$ protein (control: *n* = 40, vincristine: *n* = 33, GAS: *n* = 37) and $Na_V1.8$ (control: *n* = 37, vincristine: *n* = 32, GAS: *n* = 35) (###$p < 0.001$, compared to the control group; **$p < 0.01$, ***$p < 0.001$ compared to the model group; ANVOA- Bonferroni Test).

vincristine group: 2.5 ± 0.8 (*n* = 120, N = 5); GAS group, 1.2 ± 0.5 (*n* = 74, N = 4) (**Figures 6C,D**), where "n" representing the number of cells and "N" representing the number of ganglions. The above results indicated that GAS could significantly reduce the fluorescence intensity of $Na_V1.7$ & 1.8 protein in DRG neurons of model rats.

DRG cells were incubated with vincristine and GAS mixture for 24 h and imaged using structured illumination microscopy (SIM) and confocal fluorescence microscopy. Immunohistofluorescence utilized moiré fringes generated by high-frequency stripe illumination to separate the high-frequency and low-frequency signals of the sample, making the ultrafine structure of the cell be seen. Fluorescence staining results showed that vincristine could up-regulate the distribution of $Na_V1.7$ and $Na_V1.8$ channel proteins in the DRG neurons, as shown in **Figures 6E,F**. GAS mixture incubation significantly reduced the enhanced fluorescence intensity of $Na_V1.7$ and $Na_V1.8$ membrane proteins induced by vincristine (**$p < 0.01$, **Figures 6E,F**). Therefore, GAS significantly reduced the fluorescence intensity of $Na_V1.7$ and $Na_V1.8$ membrane

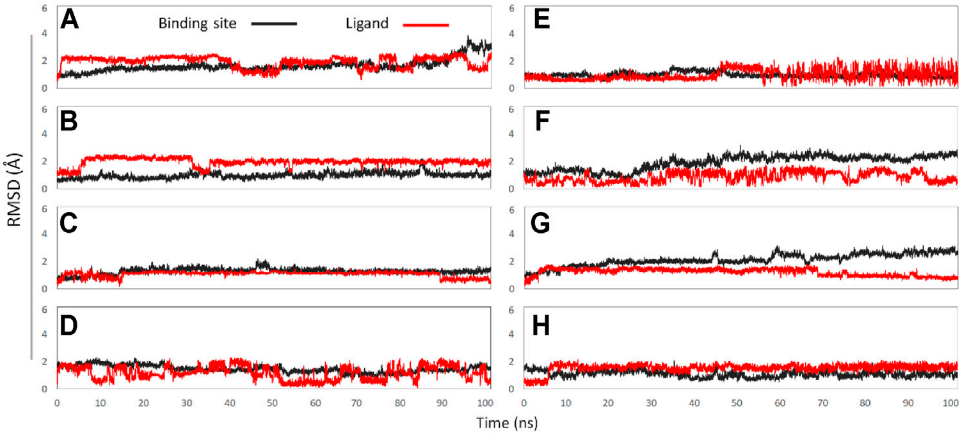

FIGURE 7 | The RMSD values of binding sites (black line) and ligand (red line): **(A)** GAS in Site 1; **(B)** GAS in Site 2; **(C)** GAS in Site 3; **(D)** GAS in Site 4; **(E)** GAS in Site 5; **(F)** GAS in Site 6; **(G)** GAS in Site 7; **(H)** GAS in Site 8.

TABLE 3 | Calculated $\Delta G_{MM/GBSA}$ values of GAS in $Na_V1.7$ and 1.8.

Constructed systems	**Calculated binding free energies (kcal mol^{-1})**	
	$Na_V1.7$	**$Na_V1.8$**
GAS-Site 1	−28.24 ± 0.24	−9.36 ± 0.17
GAS-Site 2	−8.16 ± 0.27	−16.59 ± 0.26
GAS-Site 3	−19.30 ± 0.21	−17.30 ± 0.30
GAS-Site 4	−7.64 ± 0.25	−4.36 ± 0.25
GAS-Site 5	−9.18 ± 0.08	−12.31 ± 0.45
GAS-Site 6	−14.31 ± 0.27	−11.63 ± 0.25
GAS-Site 7	−20.73 ± 0.29	
GAS-Site 8	−10.01 ± 0.10	

proteins enhanced by vincristine. The results further verified that GAS inhibits the expression of $Na_V1.7$ and $Na_V1.8$ channels. Nowadays, studies also pointed out that GAS could alleviate the peripheral neuropathy to some extend by inhibiting some signal pathways or receptors, such as the inhibitory activity of GAS on the P38/MAPK signal pathway (Sun et al., 2016; Qin et al., 2021), indicating the various action mechanisms of GAS, which was worthy of further study.

Prediction of the Possible Docking Sites of GAS on Sodium Ion Channels

In this part, we constructed the three-dimensional structures of $Na_V1.7$ & 1.8 using homology modeling method, and evaluated and optimized the construction results with Ramachandran plots and molecular dynamics (MD) simulations.

$Na_V1.7$ System

The amino acid sequence of $Na_V1.7$ used in homology modeling was consistent with that of the stable-state expression of $Na_V1.7$ in HEK293B cell line in this experiment. The SWISS-MODEL server (https://swissmodel.expasy.org/) was used to perform the homology modelling of the target sequence, and the structure of human voltage-gated sodium channel $Na_V1.7$ (PDB ID: 6j8g) (Shen et al., 2019) was used for the template based on the results of "Search For Templates." Then, the constructed 3D structure was subject to 5 ns molecular dynamic simulation to optimize the unreasonable interatomic contact or collision and minimize the conformational energies. Afterwards, the optimized conformation was used for active pockets prediction, and the corresponding molecular docking and MD simulations were performed.

In this experiment, a total of 8 active binding sites were predicted in $Na_V1.7$ (**Supplementary Figure S3**), and receptor-ligand ($Na_V1.7$-GAS) complexes systems were established based on CDOCKER docking method, which were further subjected to 100 ns MD simulation. In addition, RMSD calculation (**Figure 7**) and binding free energy analysis (MMPBSA.py) were carried out for the simulation trajectories (**Table 3**). According to **Figure 7**, it could be found that GAS had varying degrees of volatility at different binding sites, among which the binding on the Site 1 was relatively stable and the absolute binding free energy was relatively large, indicating that Site 1 may be the action site of GAS on $Na_V1.7$.

NaV1.8 System

Based on literature research and Protein Data Bank (PDB) (https://www.rcsb.org/) search, the crystal structure of $Na_V1.8$ has not yet been resolved. Considering that the DRG neurons used in the electrophysiology and Western blotting experiments in this study were derived from SD rats (belonging to Rattus Norvegicus species), NP_058943.2 (Scn10a, Gene ID = 29571, organism = *Rattus norvegicus*) (Yu et al., 2014) was used as the amino acid sequence of $Na_V1.8$ for homology modelling. Subsequently, in accordance with the operation of the $Na_V1.7$ system, the built 3D conformation was first optimized by MD simulation, and then used for active pocket prediction, molecular docking, and MD simulation (He et al., 2020; Li et al., 2021).

In this part, 6 active binding pockets were predicted in $Na_V1.8$ (**Supplementary Figure S4**), and the corresponding receptor-ligand ($Na_V1.8$-GAS) complexes systems were

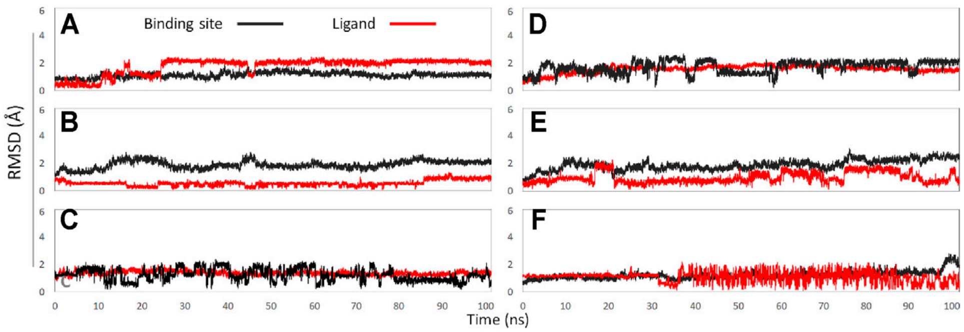

FIGURE 8 | The RMSD values of binding sites (black line) and ligand (red line): **(A)** GAS in Site 1; **(B)** GAS in Site 2; **(C)** GAS in Site 3; **(D)** GAS in Site 4; **(E)** GAS in Site 5; **(F)** GAS in Site 6.

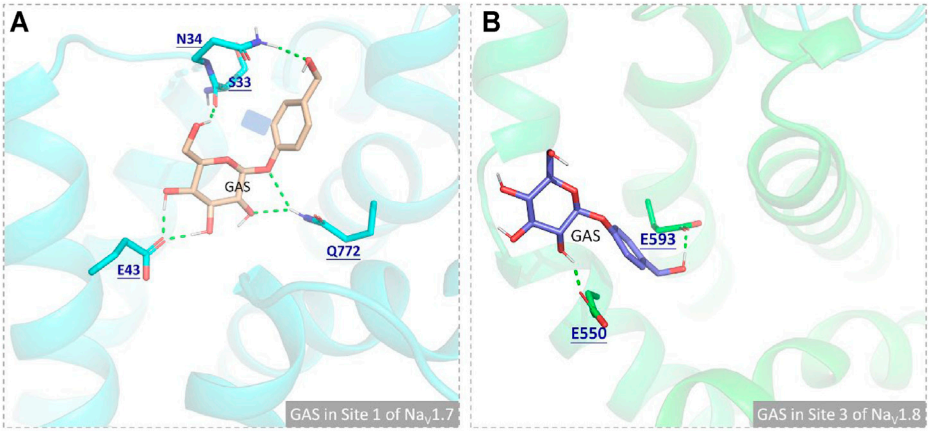

FIGURE 9 | Comparison of the binding interactions of GAS on the active pockets of $\mathrm{Na_V}$1.7 and $\mathrm{Na_V}$1.8, and the hydrogen bonds were shown in green dashed lines: **(A)** GAS in Site 1 of $\mathrm{Na_V}$1.7; **(B)** GAS in Site 3 of $\mathrm{Na_V}$1.8.

constructed, which were also subjected to 100 ns MD simulation to evaluate the binding interactions between $\mathrm{Na_V}$1.8 and GAS. According to **Figure 8** and **Table 3**, it could be found that there were varying degrees of difference in the binding interactions of GAS on $\mathrm{Na_V}$1.8 (from Site 1 to Site 6). By overall comparison of the effects of GAS on $\mathrm{Na_V}$1.7 and $\mathrm{Na_V}$1.8, the affinity of GAS on $\mathrm{Na_V}$1.7 was better than that of $\mathrm{Na_V}$1.8, indicating that GAS was more inclined to bind to $\mathrm{Na_V}$1.7, which was basically consistent with the inhibition of GAS on the current density of $\mathrm{Na_V}$1.7 & 1.8. In addition, we analyzed the most likely binding conformations of GAS on $\mathrm{Na_V}$1.7 & 1.8, and found that GAS could form 6 hydrogen bonds with residues (E43, N34, S33, and Q772) on the Site 1 of $\mathrm{Na_V}$1.7 (**Figure 9A**). However, only 2 residues in Site 3 of $\mathrm{Na_V}$1.8 could form hydrogen bonds with GAS (**Figure 9B**), indicating that GAS could bind more stably on $\mathrm{Na_V}$1.7.

CONCLUSION

GAS could modulate the $\mathrm{Na_V}$1.7 and $\mathrm{Na_V}$1.8 channels to promote their inactivation. As $\mathrm{Na_V}$1.7 and $\mathrm{Na_V}$1.8 channels act on the initial and rising stages of action potentials, GAS could inhibit the abnormal discharge of action potentials of DRG neurons, especially ectopic discharge induced by vincristine. In addition, GAS could significantly down-regulate the total protein expression of $\mathrm{Na_V}$1.7 & 1.8 proteins. By regulating the channel function of $\mathrm{Na_V}$1.7 and $\mathrm{Na_V}$1.8 and the regulation of protein levels, the pain behavior of CINP rats induced by vincristine can be alleviated. In conclusion, GAS not only modulated the biological functions of $\mathrm{Na_V}$1.7/$\mathrm{Na_V}$1.8 channels but also down-regulated the protein expression, which expanded the understanding of the action mechanism of GAS as neuromodulator, pointing out the direction for application of natural products in peripheral nerve pain caused by chemotherapy.

DATA AVAILABILITY STATEMENT

The original contributions presented in the study are included in the article/**Supplementary Material**, further inquiries can be directed to the corresponding authors.

ETHICS STATEMENT

The animal study was reviewed and approved by the Laboratory Animal Ethical and Welfare Committee, the Center for New Drug Safety Evaluation and Research, Hebei Medical University.

AUTHOR CONTRIBUTIONS

QJ and YZ conceived the work and directed the experiments. XW, BZ, and XDL constructed the CINP model. XW, XGL, and SW evaluated the electrophysiological activities of the compound and analyzed the experimental results. YX, JP, ZY, and JL collected the data. QJ, YZ, and XW drafted the first and second version of the manuscript. All authors read, edited, and approved the final version of manuscript.

FUNDING

This work was financially supported by Consultative Foundation from Hebei Province (2020TXZH01), the Key Project from Hebei Provincial Department of science and Technology (21372601D), Natural Science Foundation of Hebei Province (H2020206474, H2021206352, H2021206448), and Foundation of the Hebei Education Department Science Research Project (No. QN2021100 and BJ2021052).

SUPPLEMENTARY MATERIAL

The Supplementary Material for this article can be found online at: https://www.frontiersin.org/articles/10.3389/fphar.2021.744663/full#supplementary-material

REFERENCES

Amir, R., and Devor, M. (1996). Chemically Mediated Cross-Excitation in Rat Dorsal Root Ganglia. *J. Neurosci.* 16 (15), 4733–4741. doi:10.1523/jneurosci.16-15-04733.1996

Amir, R., Kocsis, J. D., and Devor, M. (2005). Multiple Interacting Sites of Ectopic Spike Electrogenesis in Primary Sensory Neurons. *J. Neurosci.* 25 (10), 2576–2585. doi:10.1523/JNEUROSCI.4118-04.2005

Argyriou, A. A., Cavaletti, G., Antonacopoulou, A., Genazzani, A. A., Briani, C., Bruna, J., et al. (2013). Voltage-gated Sodium Channel Polymorphisms Play a Pivotal Role in the Development of Oxaliplatin-Induced Peripheral Neurotoxicity: Results from a Prospective Multicenter Study. *Cancer* 119 (19), 3570–3577. doi:10.1002/cncr.28234

Aromolaran, K. A., and Goldstein, P. A. (2017). Ion Channels and Neuronal Hyperexcitability in Chemotherapy-Induced Peripheral Neuropathy; Cause and Effect? *Mol. Pain* 13, 1744806917714693. doi:10.1177/1744806917714693

Bär, K. J., Brehm, S., Boettger, M. K., Boettger, S., Wagner, G., and Sauer, H. (2005). Pain Perception in Major Depression Depends on Pain Modality. *Pain* 117 (1-2), 97–103. doi:10.1016/j.pain.2005.05.016

Benzon, H. T., Iqbal, M., Tallman, M. S., Boehlke, L., and Russell, E. J. (2003). Superior Sagittal Sinus Thrombosis in a Patient with Postdural Puncture Headache. *Reg. Anesth. Pain Med.* 28 (1), 64–67. doi:10.1053/rapm.2003.50007

Black, J. A., Liu, S., Tanaka, M., Cummins, T. R., and Waxman, S. G. (2004). Changes in the Expression of Tetrodotoxin-Sensitive Sodium Channels within Dorsal Root Ganglia Neurons in Inflammatory Pain. *Pain* 108 (3), 237–247. doi:10.1016/j.pain.2003.12.035

Chen, L., Huang, J., Benson, C., Lankford, K. L., Zhao, P., Carrara, J., et al. (2020). Sodium Channel Nav1.6 in Sensory Neurons Contributes to Vincristine-Induced Allodynia. *Brain* 143 (8), 2421–2436. doi:10.1093/brain/awaa208

Chen, S., Hao, X., Yu, L., Zhang, P., Cao, W., Chen, H., et al. (2017). Gastrodin Causes Vasodilation by Activating KATP Channels in Vascular Smooth Muscles via PKA-dependent Signaling Pathway. *J. Recept Signal. Transduct Res.* 37 (6), 543–549. doi:10.1080/10799893.2017.1369118

Coffeen, U., Sotomayor-Sobrino, M. A., Jiménez-González, A., Balcazar-Ochoa, L. G., Hernández-Delgado, P., Fresán, A., et al. (2019). Chemotherapy-induced Neuropathic Pain Characteristics in Mexico's National Cancer Center Pain Clinic. *J. Pain Res.* 12, 1331–1339. doi:10.2147/JPR.S186107

Cummins, T. R., Dib-Hajj, S. D., Black, J. A., Akopian, A. N., Wood, J. N., and Waxman, S. G. (1999). A Novel Persistent Tetrodotoxin-Resistant Sodium Current in SNS-Null and Wild-type Small Primary Sensory Neurons. *J. Neurosci.* 19 (24), RC43. doi:10.1523/jneurosci.19-24-j0001.1999

Ding, H. H., Zhang, S. B., Lv, Y. Y., Ma, C., Liu, M., Zhang, K. B., et al. (2019). TNF-α/STAT3 Pathway Epigenetically Upregulates Nav1.6 Expression in DRG and Contributes to Neuropathic Pain Induced by L5-VRT. *J. Neuroinflammation* 16 (1), 29. doi:10.1186/s12974-019-1421-8

Doyle, T. M., and Salvemini, D. (2021). Mini-Review: Mitochondrial Dysfunction and Chemotherapy-Induced Neuropathic Pain. *Neurosci. Lett.* 760, 136087. doi:10.1016/j.neulet.2021.136087

Dupuis, L. L., King, S. M., and Zipursky, A. (1985). Vincristine Toxicity. *Lancet* 2 (8447), 161–162. doi:10.1016/s0140-6736(85)90271-5

Feld, R., Evans, W. K., and DeBoer, G. (1980). Herpes Zoster in Patients with Small-Cell Carcinoma of the Lung Receiving Combined Modality Treatment. *Ann. Intern. Med.* 93 (2), 282–283. doi:10.7326/0003-4819-93-2-282

Finnerup, N. B., Kuner, R., and Jensen, T. S. (2021). Neuropathic Pain: From Mechanisms to Treatment. *Physiol. Rev.* 101 (1), 259–301. doi:10.1152/physrev.00045.2019

Gu, J. G., and MacDermott, A. B. (1997). Activation of ATP P2X Receptors Elicits Glutamate Release from Sensory Neuron Synapses. *Nature* 389 (6652), 749–753. doi:10.1038/39639

Gül, Ş. K., Tepetam, H., and Gül, H. L. (2020). Duloxetine and Pregabalin in Neuropathic Pain of Lung Cancer Patients. *Brain Behav.* 10 (3), e01527. doi:10.1002/brb3.1527

He, J., Wang, S., Liu, X., Lin, R., Deng, F., Jia, Z., et al. (2020). Synthesis and Biological Evaluation of HDAC Inhibitors with a Novel Zinc Binding Group. *Front. Chem.* 8, 256. doi:10.3389/fchem.2020.00256

Hershman, D. L., Lacchetti, C., Dworkin, R. H., Lavoie Smith, E. M., Bleeker, J., Cavaletti, G., et al. (2014). Prevention and Management of Chemotherapy-Induced Peripheral Neuropathy in Survivors of Adult Cancers: American Society of Clinical Oncology Clinical Practice Guideline. *J. Clin. Oncol.* 32 (18), 1941–1967. doi:10.1200/JCO.2013.54.0914

Herzog, R. I., Cummins, T. R., Ghassemi, F., Dib-Hajj, S. D., and Waxman, S. G. (2003). Distinct Repriming and Closed-State Inactivation Kinetics of Nav1.6 and Nav1.7 Sodium Channels in Mouse Spinal Sensory Neurons. *J. Physiol.* 551 (Pt 3), 741–750. doi:10.1113/jphysiol.2003.047357

Ito, C., Fukuda, A., Nabekura, J., and Oomura, Y. (1989). Acetylcholine Causes Nicotinic Depolarization in Rat Dorsal Motor Nucleus of the Vagus, *In Vitro*. *Brain Res.* 503 (1), 44–48. doi:10.1016/0006-8993(89)91701-0

Jackson, T., Thomas, S., Stabile, V., Han, X., Shotwell, M., and McQueen, K. (2015). Prevalence of Chronic Pain in Low-Income and Middle-Income Countries: a Systematic Review and Meta-Analysis. *Lancet* 385 (Suppl. 2), S10. doi:10.1016/S0140-6736(15)60805-4

Jha, M. K., Schatzberg, A., Minhajuddin, A., Fatt, C. C., Mayes, T. L., and Trivedi, M. H. (2021). Cross-Sectional Associations Among Symptoms of Pain, Irritability, and Depression and How These Symptoms Relate to Social Functioning and Quality of Life: Findings from the EMBARC and STRIDE Studies and the VitalSign6 Project. *J. Clin. Psychiatry* 82 (3), 20m13740. doi:10.4088/jcp.20m13740

Kawasaki, Y., Xu, Z. Z., Wang, X., Park, J. Y., Zhuang, Z. Y., Tan, P. H., et al. (2008). Distinct Roles of Matrix Metalloproteases in the Early- and Late-phase Development of Neuropathic Pain. *Nat. Med.* 14 (3), 331–336. doi:10.1038/nm1723

Kingwell, K. (2019). Nav1.7 Withholds its Pain Potential. *Nat. Rev. Drug Discov.* 18, 321–323. doi:10.1038/d41573-019-00065-0

Klein, A. H., Vyshnevska, A., Hartke, T. V., De Col, R., Mankowski, J. L., Turnquist, B., et al. (2017). Sodium Channel Nav1.8 Underlies TTX-Resistant Axonal Action Potential Conduction in Somatosensory C-Fibers of Distal Cutaneous Nerves. *J. Neurosci.* 37 (20), 5204–5214. doi:10.1523/JNEUROSCI.3799-16.2017

Kretschmer, T., Happel, L. T., England, J. D., Nguyen, D. H., Tiel, R. L., Beuerman, R. W., et al. (2002). Accumulation of PN1 and PN3 Sodium Channels in Painful Human Neuroma-Evidence from Immunocytochemistry. *Acta Neurochir (Wien)* 144 (8), 803–810. doi:10.1007/s00701-002-0970-1

Li, M., Xue, N., Liu, X., Wang, Q., Yan, H., Liu, Y., et al. (2021). Discovery of Potent EGFR Inhibitors with 6-Arylureido-4-Anilinoquinazoline Derivatives. *Front. Pharmacol.* 12, 647591. doi:10.3389/fphar.2021.647591

Liang, Y., Quan, H., Bu, T., Li, X., Liu, X., Wang, S., et al. (2021). Comparison of the Inhibitory Binding Modes between the Planar Fascaplysin and its Nonplanar Tetrahydro-β-Carboline Analogs in CDK4. *Front. Chem.* 9, 614154. doi:10.3389/fchem.2021.614154

Mattiuzzi, C., and Lippi, G. (2019). Current Cancer Epidemiology. *J. Epidemiol. Glob. Health* 9 (4), 217–222. doi:10.2991/jegh.k.191008.001

Moyer, B. D., Murray, J. K., Ligutti, J., Andrews, K., Favreau, P., Jordan, J. B., et al. (2018). Pharmacological Characterization of Potent and Selective NaV1.7 Inhibitors Engineered from Chilobrachys Jingzhao Tarantula Venom Peptide JzTx-V. *PLoS One* 13 (5), e0196791. doi:10.1371/journal.pone.0196791

Nepal, M. R., Jeong, K. S., Kim, G. H., Cha, D. H., Kang, M. J., Kim, J. S., et al. (2019). Role of Intestinal Microbiota in Metabolism of Gastrodin *In Vitro* and *In Vivo*. *Metabolites* 9 (4), 69. doi:10.3390/metabo9040069

Nie, B., Zhang, S., Huang, Z., Huang, J., Chen, X., Zheng, Y., et al. (2017). Synergistic Interaction between Dexmedetomidine and Ulinastatin against Vincristine-Induced Neuropathic Pain in Rats. *J. Pain* 18 (11), 1354–1364. doi:10.1016/j.jpain.2017.06.007

Norcini, M., Sideris, A., Adler, S. M., Hernandez, L. A., Zhang, J., Blanck, T. J., et al. (2016). NR2B Expression in Rat DRG Is Differentially Regulated Following Peripheral Nerve Injuries that Lead to Transient or Sustained Stimuli-Evoked Hypersensitivity. *Front. Mol. Neurosci.* 9, 100. doi:10.3389/fnmol.2016.00100

Ohshiro, H., Ogawa, S., and Shinjo, K. (2007). Visualizing Sensory Transmission between Dorsal Root Ganglion and Dorsal Horn Neurons in Co-culture with Calcium Imaging. *J. Neurosci. Methods* 165 (1), 49–54. doi:10.1016/j.jneumeth.2007.05.018

Old, E. A., Nadkarni, S., Grist, J., Gentry, C., Bevan, S., Kim, K. W., et al. (2014). Monocytes Expressing CX3CR1 Orchestrate the Development of Vincristine-Induced Pain. *J. Clin. Invest.* 124 (5), 2023–2036. doi:10.1172/JCI71389

Qi, Y. H., Zhu, R., Wang, Q., Li, Q., Liu, Y. D., Qian, Z. Y., et al. (2019). Early Intervention with Gastrodin Reduces Striatal Neurotoxicity in Adult Rats with Experimentally-induced D-iabetes M-ellitus. *Mol. Med. Rep.* 19 (4), 3114–3122. doi:10.3892/mmr.2019.9954

Qin, B., Luo, N., Li, Y., Gong, D., Zheng, J., Tan, X., et al. (2021). Protective Effect of Gastrodin on Peripheral Neuropathy Induced by Anti-tumor Treatment with Vincristine in Rat Models. *Drug Chem. Toxicol.* 44 (1), 84–91. doi:10.1080/01480545.2018.1547739

Qiu, F., Liu, T. T., Qu, Z. W., Qiu, C. Y., Yang, Z., and Hu, W. P. (2014). Gastrodin Inhibits the Activity of Acid-Sensing Ion Channels in Rat Primary Sensory Neurons. *Eur. J. Pharmacol.* 731, 50–57. doi:10.1016/j.ejphar.2014.02.044

Renganathan, M., Cummins, T. R., and Waxman, S. G. (2001). Contribution of Na(v)1.8 Sodium Channels to Action Potential Electrogenesis in DRG Neurons. *J. Neurophysiol.* 86 (2), 629–640. doi:10.1152/jn.2001.86.2.629

Rosenthal, S., and Kaufman, S. (1974). Vincristine Neurotoxicity. *Ann. Intern. Med.* 80 (6), 733–737. doi:10.7326/0003-4819-80-6-733

Sapunar, D., Kostic, S., Banozic, A., and Puljak, L. (2012). Dorsal Root Ganglion - a Potential New Therapeutic Target for Neuropathic Pain. *J. Pain Res.* 5, 31–38. doi:10.2147/JPR.S26603

Seijffers, R., Mills, C. D., and Woolf, C. J. (2007). ATF3 Increases the Intrinsic Growth State of DRG Neurons to Enhance Peripheral Nerve Regeneration. *J. Neurosci.* 27 (30), 7911–7920. doi:10.1523/JNEUROSCI.5313-06.2007

Shao, H., Yang, Y., Qi, A. P., Hong, P., Zhu, G. X., Cao, X. Y., et al. (2017). Gastrodin Reduces the Severity of Status Epilepticus in the Rat Pilocarpine Model of Temporal Lobe Epilepsy by Inhibiting Nav1.6 Sodium Currents. *Neurochem. Res.* 42 (2), 360–374. doi:10.1007/s11064-016-2079-6

Shen, H., Liu, D., Wu, K., Lei, J., and Yan, N. (2019). Structures of Human Nav1.7 Channel in Complex with Auxiliary Subunits and Animal Toxins. *Science* 363 (6433), 1303–1308. doi:10.1126/science.aaw2493

Shields, S. D., Cheng, X., Uçeyler, N., Sommer, C., Dib-Hajj, S. D., and Waxman, S. G. (2012). Sodium Channel Na(v)1.7 Is Essential for Lowering Heat Pain Threshold after Burn Injury. *J. Neurosci.* 32 (32), 10819–10832. doi:10.1523/JNEUROSCI.0304-12.2012

Sittl, R., Lampert, A., Huth, T., Schuy, E. T., Link, A. S., Fleckenstein, J., et al. (2012). Anticancer Drug Oxaliplatin Induces Acute Cooling-Aggravated Neuropathy via Sodium Channel Subtype Na(V)1.6-resurgent and Persistent Current. *Proc. Natl. Acad. Sci. U S A.* 109 (17), 6704–6709. doi:10.1073/pnas.1118058109

Sun, T., Wang, J., Li, X., Li, Y. J., Feng, D., Shi, W. L., et al. (2016). Gastrodin Relieved Complete Freund's Adjuvant-Induced Spontaneous Pain by Inhibiting Inflammatory Response. *Int. Immunopharmacol* 41, 66–73. doi:10.1016/j.intimp.2016.10.020

Sun, W., Miao, B., Wang, X. C., Duan, J. H., Ye, X., Han, W. J., et al. (2012). Gastrodin Inhibits Allodynia and Hyperalgesia in Painful Diabetic Neuropathy Rats by Decreasing Excitability of Nociceptive Primary Sensory Neurons. *PLoS One* 7 (6), e39647. doi:10.1371/journal.pone.0039647

Swain, N. A., Batchelor, D., Beaudoin, S., Bechle, B. M., Bradley, P. A., Brown, A. D., et al. (2017). Discovery of Clinical Candidate 4-[2-(5-Amino-1h-Pyrazol-4-Yl)-4-Chlorophenoxy]-5-Chloro-2-Fluoro-N-1,3-Thiazol-4-Ylbenzenesulfonamide (PF-05089771): Design and Optimization of Diaryl Ether Aryl Sulfonamides as Selective Inhibitors of NaV1.7. *J. Med. Chem.* 60 (16), 7029–7042. doi:10.1021/acs.jmedchem.7b00598

Tanner, K. D., Reichling, D. B., and Levine, J. D. (1998). Nociceptor Hyper-Responsiveness during Vincristine-Induced Painful Peripheral Neuropathy in the Rat. *J. Neurosci.* 18 (16), 6480–6491. doi:10.1523/jneurosci.18-16-06480.1998

Tyrrell, L., Renganathan, M., Dib-Hajj, S. D., and Waxman, S. G. (2001). Glycosylation Alters Steady-State Inactivation of Sodium Channel Nav1.9/NaN in Dorsal Root Ganglion Neurons and Is Developmentally Regulated. *J. Neurosci.* 21 (24), 9629–9637. doi:10.1523/jneurosci.21-24-09629.2001

van Schie, R. M., Brüggemann, R. J., Hoogerbrugge, P. M., and te Loo, D. M. (2011). Effect of Azole Antifungal Therapy on Vincristine Toxicity in Childhood Acute Lymphoblastic Leukaemia. *J. Antimicrob. Chemother.* 66 (8), 1853–1856. doi:10.1093/jac/dkr223

Vysokov, N., McMahon, S. B., and Raouf, R. (2019). The Role of NaV Channels in Synaptic Transmission after Axotomy in a Microfluidic Culture Platform. *Sci. Rep.* 9 (1), 12915. doi:10.1038/s41598-019-49214-w

Wang, J. T., Zheng, Y. M., Chen, Y. T., Gu, M., Gao, Z. B., and Nan, F. J. (2020). Discovery of Aryl Sulfonamide-Selective Nav1.7 Inhibitors with a Highly Hydrophobic Ethanoanthracene Core. *Acta Pharmacol. Sin* 41 (3), 293–302. doi:10.1038/s41401-019-0267-z

Wang, Q., An, X., Xu, J., Wang, Y., Liu, L., Leung, E. L., et al. (2018). Classical Molecular Dynamics and Metadynamics Simulations Decipher the Mechanism of CBP30 Selectively Inhibiting CBP/p300 Bromodomains. *Org. Biomol. Chem.* 16 (35), 6521–6530. doi:10.1039/c8ob01526k

Wang, Q., Li, Y., Xu, J., Wang, Y., Shi, D., Liu, L., et al. (2019). Computational Study on the Selective Inhibition Mechanism of MS402 to the First and Second Bromodomains of BRD4. *Proteins* 87 (1), 3–11. doi:10.1002/prot.25611

Wang, Q., Yang, J., Wang, H., Shan, B., Yin, C., Yu, H., et al. (2021). Fibroblast Growth Factor 13 Stabilizes Microtubules to Promote Na+ Channel Function in Nociceptive DRG Neurons and Modulates Inflammatory Pain. *J. Adv. Res.* 31, 97–111. doi:10.1016/j.jare.2020.12.009

Wang, X., Tang, H., Wei, E. Q., Wang, Z., Yang, J., Yang, R., et al. (2017). Conditional Knockout of Fgf13 in Murine Hearts Increases Arrhythmia Susceptibility and Reveals Novel Ion Channel Modulatory Roles. *J. Mol. Cel Cardiol* 104, 63–74. doi:10.1016/j.yjmcc.2017.01.009

Waterhouse, A., Bertoni, M., Bienert, S., Studer, G., Tauriello, G., Gumienny, R., et al. (2018). SWISS-MODEL: Homology Modelling of Protein Structures and Complexes. *Nucleic Acids Res.* 46 (W1), W296–W303. doi:10.1093/nar/gky427

Waxman, S. G., and Zamponi, G. W. (2014). Regulating Excitability of Peripheral Afferents: Emerging Ion Channel Targets. *Nat. Neurosci.* 17 (2), 153–163. doi:10.1038/nn.3602

Wu, B., Murray, J. K., Andrews, K. L., Sham, K., Long, J., Aral, J., et al. (2018). Discovery of Tarantula Venom-Derived NaV1.7-Inhibitory JzTx-V Peptide 5-Br-Trp24 Analogue AM-6120 with Systemic Block of Histamine-Induced Pruritis. *J. Med. Chem.* 61 (21), 9500–9512. doi:10.1021/acs.jmedchem.8b00736

Xia, Z., Xiao, Y., Wu, Y., and Zhao, B. (2016). Sodium Channel Nav1.7 Expression Is Upregulated in the Dorsal Root Ganglia in a Rat Model of Paclitaxel-Induced Peripheral Neuropathy. *Springerplus* 5 (1), 1738. doi:10.1186/s40064-016-3351-6

Xiao, M. M., Zhang, Y. Q., Wang, W. T., Han, W. J., Lin, Z., Xie, R. G., et al. (2016). Gastrodin Protects against Chronic Inflammatory Pain by Inhibiting Spinal Synaptic Potentiation. *Sci. Rep.* 6, 37251. doi:10.1038/srep37251

Xiao, W. H., and Bennett, G. J. (2008). Chemotherapy-evoked Neuropathic Pain: Abnormal Spontaneous Discharge in A-Fiber and C-Fiber Primary Afferent Neurons and its Suppression by Acetyl-L-Carnitine. *Pain* 135 (3), 262–270. doi:10.1016/j.pain.2007.06.001

Xu, H., Li, T., Rohou, A., Arthur, C. P., Tzakoniati, F., Wong, E., et al. (2019). Structural Basis of Nav1.7 Inhibition by a Gating-Modifier Spider Toxin. *Cell* 176 (4), 1238–1239. doi:10.1016/j.cell.2019.01.047

Xu, T., Li, D., Zhou, X., Ouyang, H. D., Zhou, L. J., Zhou, H., et al. (2017). Oral Application of Magnesium-L-Threonate Attenuates Vincristine-Induced Allodynia and Hyperalgesia by Normalization of Tumor Necrosis Factor-α/Nuclear Factor-Kb Signaling. *Anesthesiology* 126 (6), 1151–1168. doi:10.1097/ALN.0000000000001601

Yang, F., Zou, Y. Q., Li, M., Luo, W. J., Chen, G. Z., and Wu, X. Z. (2021). Intervertebral Foramen Injection of Plerixafor Attenuates Neuropathic Pain after Chronic Compression of the Dorsal Root Ganglion: Possible Involvement of the Down-Regulation of Nav1.8 and Nav1.9. *Eur. J. Pharmacol.* 908, 174322. doi:10.1016/j.ejphar.2021.174322

Ye, T., Meng, X., Wang, R., Zhang, C., He, S., Sun, G., et al. (2018). Gastrodin Alleviates Cognitive Dysfunction and Depressive-like Behaviors by Inhibiting ER Stress and NLRP3 Inflammasome Activation in Db/db Mice. *Int. J. Mol. Sci.* 19 (12), 3977. doi:10.3390/ijms19123977

Yu, Y., Fuscoe, J. C., Zhao, C., Guo, C., Jia, M., Qing, T., et al. (2014). A Rat RNA-Seq Transcriptomic BodyMap across 11 Organs and 4 Developmental Stages. *Nat. Commun.* 5, 3230. doi:10.1038/ncomms4230

Zajaczkowska, R., Kocot-Kępska, M., Leppert, W., Wrzosek, A., Mika, J., and Wordliczek, J. (2019). Mechanisms of Chemotherapy-Induced Peripheral Neuropathy. *Int. J. Mol. Sci.* 20 (6), 1451. doi:10.3390/ijms20061451

Zhang, F., Wang, Y., Liu, Y., Han, H., Zhang, D., Fan, X., et al. (2019). Transcriptional Regulation of Voltage-Gated Sodium Channels Contributes to GM-CSF-Induced Pain. *J. Neurosci.* 39 (26), 5222–5233. doi:10.1523/JNEUROSCI.2204-18.2019

Zhang, H., and Dougherty, P. M. (2014). Enhanced Excitability of Primary Sensory Neurons and Altered Gene Expression of Neuronal Ion Channels in Dorsal Root Ganglion in Paclitaxel-Induced Peripheral Neuropathy. *Anesthesiology* 120 (6), 1463–1475. doi:10.1097/ALN.0000000000000176

Zhang, Y., Fu, T., Ren, Y., Li, F., Zheng, G., Hong, J., et al. (2020). Selective Inhibition of HDAC1 by Macrocyclic Polypeptide for the Treatment of Glioblastoma: A Binding Mechanistic Analysis Based on Molecular Dynamics. *Front. Mol. Biosci.* 7, 41. doi:10.3389/fmolb.2020.00041

Zhang, Y., Ying, J. B., Hong, J. J., Li, F. C., Fu, T. T., Yang, F. Y., et al. (2019). How Does Chirality Determine the Selective Inhibition of Histone Deacetylase 6? A Lesson from Trichostatin A Enantiomers Based on Molecular Dynamics. *ACS Chem. Neurosci.* 10 (5), 2467–2480. doi:10.1021/acschemneuro.8b00729

Zhang, Y., Zheng, G., Fu, T., Hong, J., Li, F., Yao, X., et al. (2020). The Binding Mode of Vilazodone in the Human Serotonin Transporter Elucidated by Ligand Docking and Molecular Dynamics Simulations. *Phys. Chem. Chem. Phys.* 22 (9), 5132–5144. doi:10.1039/c9cp05764a

Zhang, Z. J., Guo, J. S., Li, S. S., Wu, X. B., Cao, D. L., Jiang, B. C., et al. (2018). TLR8 and its Endogenous Ligand miR-21 Contribute to Neuropathic Pain in Murine DRG. *J. Exp. Med.* 215 (12), 3019–3037. doi:10.1084/jem.20180800

Zhou, X., Ma, T., Yang, L., Peng, S., Li, L., Wang, Z., et al. (2020). Spider Venom-Derived Peptide Induces Hyperalgesia in Nav1.7 Knockout Mice by Activating Nav1.9 Channels. *Nat. Commun.* 11 (1), 2293. doi:10.1038/s41467-020-16210-y

Zimmermann, K., Leffler, A., Babes, A., Cendan, C. M., Carr, R. W., Kobayashi, J., et al. (2007). Sensory Neuron Sodium Channel Nav1.8 Is Essential for Pain at Low Temperatures. *Nature* 447 (7146), 855–858. doi:10.1038/nature05880

Conflict of Interest: The authors declare that the research was conducted in the absence of any commercial or financial relationships that could be construed as a potential conflict of interest.

Publisher's Note: All claims expressed in this article are solely those of the authors and do not necessarily represent those of their affiliated organizations, or those of the publisher, the editors and the reviewers. Any product that may be evaluated in this article, or claim that may be made by its manufacturer, is not guaranteed or endorsed by the publisher.

Copyright © 2021 Wang, Zhang, Li, Liu, Wang, Xie, Pi, Yang, Li, Jia and Zhang. This is an open-access article distributed under the terms of the Creative Commons Attribution License (CC BY). The use, distribution or reproduction in other forums is permitted, provided the original author(s) and the copyright owner(s) are credited and that the original publication in this journal is cited, in accordance with accepted academic practice. No use, distribution or reproduction is permitted which does not comply with these terms.

frontiers
in Pharmacology

ORIGINAL RESEARCH
published: 03 January 2022
doi: 10.3389/fphar.2021.794680

The Glutathione Metabolite γ-Glutamyl-Glutamate Partially Activates Glutamate NMDA Receptors in Central Neurons With Higher Efficacy for GluN2B-Containing Receptors

Fatiha Sebih†, Nawfel Mokrane†, Pierre Fontanel, Mete Kayatekin, Mahira Kaabeche, Janique Guiramand, Catherine Cohen-Solal, Thierry Cens, Matthieu Rousset, Pierre Charnet, Marie-Céleste De Jésus Ferreira, Jean-Baptiste Thibaud, Claudine Ménard, Sonia Cantel, Valérie Rolland*, Michel Vignes* and Julien Roussel*

UMR5247 IBMM University of Montpellier, Montpellier, France

OPEN ACCESS

Edited by:
*Jacques Joubert,
University of the Western Cape, South Africa*

Reviewed by:
*John J. Woodward,
Medical University of South Carolina, United States
Kenji Sakamoto,
Teikyo University, Japan*

****Correspondence:***
*Valérie Rolland
valerie.rolland@umontpellier.fr
Michel Vignes
michel.vignes@umontpellier.fr
Julien Roussel
julien.roussel@umontpellier.fr*

†These authors have contributed equally to this work

Specialty section:
*This article was submitted to Pharmacology of Ion Channels and Channelopathies,
a section of the journal Frontiers in Pharmacology*

Received: *13 October 2021*
Accepted: *18 November 2021*
Published: *03 January 2022*

Citation:
Sebih F, Mokrane N, Fontanel P, Kayatekin M, Kaabeche M, Guiramand J, Cohen-Solal C, Cens T, Rousset M, Charnet P, De Jésus Ferreira M-C, Thibaud J-B, Ménard C, Cantel S, Rolland V, Vignes M and Roussel J (2022) The Glutathione Metabolite γ-Glutamyl-Glutamate Partially Activates Glutamate NMDA Receptors in Central Neurons With Higher Efficacy for GluN2B-Containing Receptors. Front. Pharmacol. 12:794680. doi: 10.3389/fphar.2021.794680

Gamma-L-glutamyl-L-glutamate (γ-Glu-Glu) was synthetized and further characterized for its activity on cultured neurons. We observed that γ-Glu-Glu elicited excitatory effects on neurons likely by activating mainly the N-methyl-D-aspartate (NMDA) receptors. These effects were dependent on the integrity of synaptic transmission as they were blocked by tetrodotoxin (TTX). We next evaluated its activity on NMDA receptors by testing it on cells expressing these receptors. We observed that γ-Glu-Glu partially activated NMDA receptors and exhibited better efficacy for NMDA receptors containing the GluN2B subunit. Moreover, at low concentration, γ-Glu-Glu potentiated the responses of glutamate on NMDA receptors. Finally, the endogenous production of γ-Glu-Glu was measured by LC-MS on the extracellular medium of C6 rat astroglioma cells. We found that extracellular γ-Glu-Glu concentration was, to some extent, directly linked to GSH metabolism as γ-Glu-Glu can be a by-product of glutathione (GSH) breakdown after γ-glutamyl transferase action. Therefore, γ-Glu-Glu could exert excitatory effects by activating neuronal NMDA receptors when GSH production is enhanced.

Keywords: NMDA receptors, GluN2B, GSH metabolism, gamma-Glu-Glu, partial effect

INTRODUCTION

Gamma-glutamyl dipeptides (γ-Glu-AA) are naturally occurring compounds which result from the transfer of an amino acid moiety on the carboxyl group in the gamma position of glutamic acid. In cells, these compounds are possibly yielded by the action of two enzymes: either gamma-glutamyl transferase (γ-GT) or glutamate cysteine ligase (GCL) (Bachhawat and Yadav, 2018). γ-Glu-AA synthesis is therefore linked to glutathione (GSH) metabolism. Indeed, the first step of glutathione (γ-Glu–Cys–Gly) synthesis, that is, the condensation of cysteine and on the gamma carboxylic group of glutamate is catalyzed by GCL. In addition, γ-GT is involved in GSH/GSSG degradation (Lu, 2013). To some extent, γ-Glu-AA production may reflect the activity of the GSH cycle, and thus, indirectly, the cell antioxidant builds up defense against oxidative stress. In this line, changes in seric γ-Glu-AA concentration

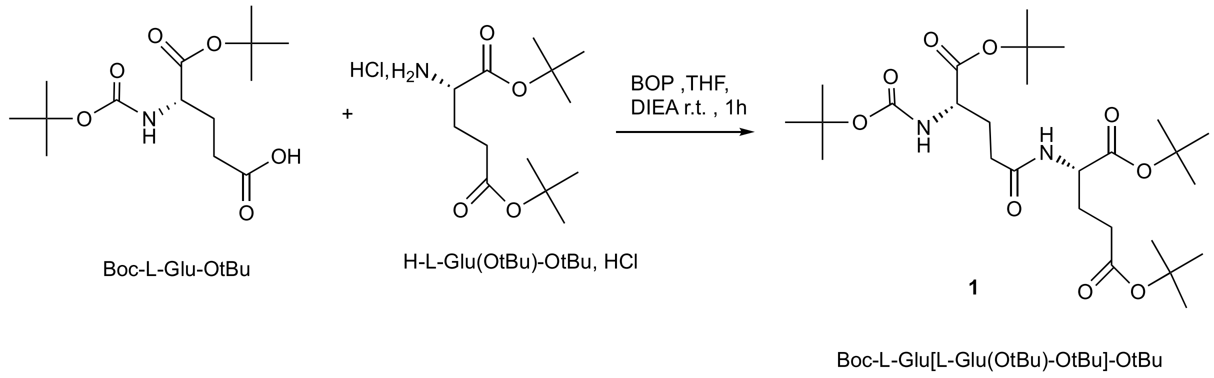

SCHEME 1 | Peptide coupling procedure.

are considered biomarkers of liver diseases (Kobayashi et al., 2020) and neurodegenerative diseases (Nemes et al., 2001). They could also play a critical role in the regulation of the central concentration of the neurotransmitters glutamate and GABA, as shown when a ketogenic diet is applied to treat epilepsy (Olson et al., 2018).

As these dipeptides contain glutamate in their structure, some of them exhibit high affinity for ionotropic glutamate receptors, including AMPA, kainate, and NMDA receptors (AMPAr, KAr, and ANMDAr), as evidenced recently by binding studies (Tamborini et al., 2016). In fact, the affinity for NMDA receptors appears to be a broad feature shared by many γ-glutamyl–substituted derivatives. Indeed, it is known for long that γ-D-Glu-Gly displays NMDA receptor antagonist activity (Francis et al., 1980). In this line, our laboratory has shown recently that the green tea amino acid L-theanine (or L-γ-N-ethyl-glutamine) potentiated NMDA responses on hippocampal neurons by exhibiting a partial agonist activity of the glycine site of NMDA receptors (Sebih et al., 2017a).

In the present study, we aimed first to develop a new, simple, and efficient synthesis of γ-glutamyl dipeptides and second to characterize their effect on glutamatergic neurotransmission. This step was performed, thanks to calcium imaging and electrophysiological recordings on cultured neuronal cells and on cells expressing glutamate receptors, including C6 astroglioma cells and *Xenopus* oocytes. Third, we aimed to examine the link between the GSH cycle and γ-Glu-AA production. With this aim, the γ-Glu-AA concentration was measured by LC-MS on C6 cell supernatants treated with GSH synthesis modulators.

For this study, we have focused on the characterization of γ-Glu-Glu as its occurrence has been evidenced in the brain (Reichelt, 1970), and as it can be released by depolarization from the hippocampal slices (Li et al., 1996). In addition, it has better affinity for ionotropic glutamate receptors among other γ-Glu-AAs (Tamborini et al., 2016).

RESULTS

Chemical Synthesis of γ-Glu-Glu

The gamma-glutamyl dipeptide γ-L-Glu-L-Glu has been prepared using conventional methods for peptide synthesis. The synthesis of gamma-glutamyl dipeptides was described using a flow chemistry reactor in combination with an immobilized coupling reagent (polymer-supported (PS-HOBt) and scavengers (Baxendale et al., 2006). The authors avoided purification and chromatography steps, but they had to perform the immobilization of HOBt and two elutions, respectively, on Amberlyst A21 (to remove HCl) and Amberlyst A-15 for the coupling reaction (Tamborini et al., 2016).

The synthesis of H-Glu (Glu-OH)-OH described in **Scheme 1** started with suitably commercial protected amino acid without purification. Boc-L-Glu-O*t*Bu was dissolved in THF in the presence of BOP, Castro's reagent as the coupling reagent, di-isopropylethylamine (DIEA) as the base, and finally the protected amino acid hydrochloride H-L-Glu (O*t*Bu)-O*t*Bu, HCl was added; the pH of the mixture was adjusted at 8.5 with DIEA for optimum coupling. The mixture was stirred for 1 h at room temperature. After acid–base treatments and purification, the dipeptide Boc-L-Glu [L-Glu (O*t*Bu)-O*t*Bu]-O*t*Bu***1*** was obtained in a 92% yield.

The final compounds γ-L-H-Glu(L-Glu-OH)OH***2*** ((*S*,*S*) 4-amino-4-carboxybutanoyl) glutamic acid) as chlorhydrate salt were obtained in 90% yield by removing *N*-BOC and *tert*butyl esters protecting groups in acidic conditions using HCl 4N aqueous solution in dioxane (**Scheme 2**). This step was monitored by analytical HPLC to follow the disappearance of all protecting groups and to check default of racemization. This acidic hydrolytic step can also be performed with 80% trifluoroacetic acid solution in CH_2Cl_2 in very high yield. However, trifluoroacetic salts are toxic for the cells.

Effect of γ-Glu-Glu on Glutamate Receptors in Cultured Hippocampal Cells

The binding studies led by Tamborini *et al* have shown that γ-Glu-Glu has the best binding affinity for all ionotropic glutamate receptors, including AMPA, kainate, and NMDA receptors (AMPAr, KAr, and ANMDAr), compared to other γ-Glu-AAs (Tamborini et al., 2016). But, the pharmacological activities of this dipeptide on these receptors are unknown.

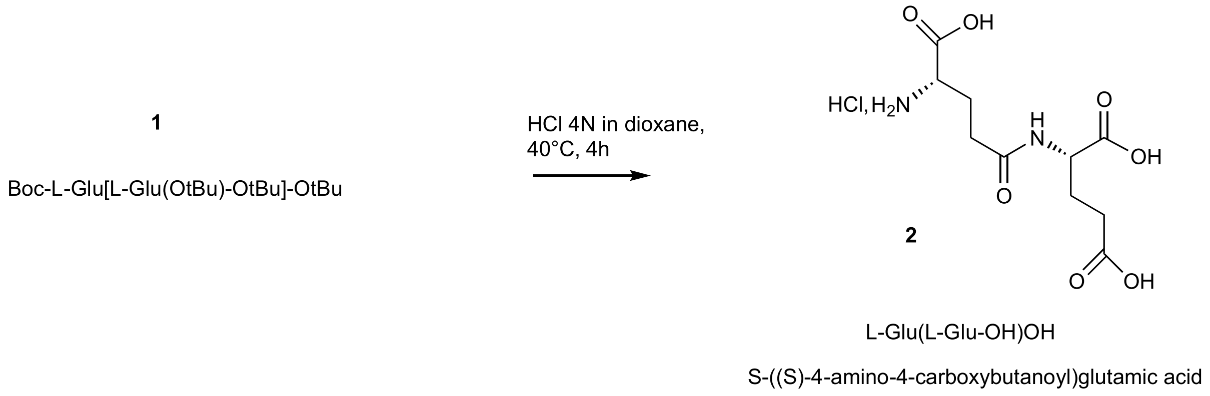

SCHEME 2 | Hydrolysis of protecting groups.

The first objective of this study was to determine if γ-Glu-Glu activated glutamatergic receptors. With this aim, intracellular Ca^{2+} ($[Ca^{2+}]_i$) changes were monitored in cultured hippocampal neurons in the presence of γ-Glu-AAs. When Mg^{2+} ions were omitted from the extracellular medium $[Ca^{2+}]_i$ increases were observed in the presence of γ-Glu-Glu (**Figure 1A**). Its activity was further compared to that elicited by other γ-L-Glu-AAs which exhibit good affinity for one or more ionotropic glutamate receptors, that is, γ-L-Glu–Lys, γ-L-Glu–Gly, γ-Glu–Cys, and γ-Glu–Ala. When tested at 10 μM, γ-Glu-Glu was the only one among the γ-L-Glu-AAs tested to elicit significant excitatory action evidenced by a Ca^{2+} increase (68.5 ± 11.10% after normalizing the response elicited by the dipeptides to the response induced by 10 μM glutamate; *n* = 75). This response was significantly different from the "background" response which was obtained by applying Glu in the presence of glutamate receptor blockers, namely, AP5 25 μM, a broad-spectrum NMDAr antagonist, DNQX 10 μM, a non-NMDA receptor antagonist, and MPEP 10 μM, a type 5 metabotropic glutamate receptor antagonist.

In order to further characterize the excitatory effect of γ-Glu-Glu, it was applied in the presence of NMDAr or AMPAr/KAr antagonists, that is, AP5 or DNQX, respectively. The application of ionotropic glutamatergic receptor inhibitors prevented γ-Glu-Glu–induced Ca^{2+} increase independently of each other. This result indicates that γ-Glu-Glu–induced Ca^{2+} increase involved NMDAr and/or AMPAr. The $[Ca^{2+}]_i$ increases observed in cultured neurons under these conditions may result from a direct excitatory action by binding ionotropic receptors and/or from an indirect effect involving the stimulation of endogenous glutamate synaptic release. In order to test this hypothesis, experiments were carried out in the presence of tetrodotoxin (TTX, 500 nM) in order to block synaptic transmission. In the presence of TTX, γ-Glu-Glu–elicited responses were completely blocked, indicating that global $[Ca^{2+}]_i$ increases resulted from the excitatory action of γ-Glu-Glu *via* NMDAr activation and subsequent AMPAr and NMDAr activation likely by endogenous glutamate release. As expected, the potentiating effect of glycine on NMDAr-mediated responses was still observed in the presence of TTX. In addition, this response was unchanged in the presence of γ-Glu-Glu, suggesting no direct additive action of glycine and γ-Glu-Glu on glutamate-mediated actions under these conditions. Such an excitatory effect of γ-Glu-Glu on synaptic transmission was further examined by recording spontaneous glutamate-mediated synaptic transmissions. γ-Glu-Glu increased spontaneous excitatory postsynaptic current (sEPSC) frequency. Spontaneous EPSCs were recorded in an Mg^{2+}-free state to uncover NMDA receptor–mediated synaptic events (**Figure 2A**). The application of γ-Glu-Glu significantly and reversibly enhanced the frequency of sEPSC (220 ± 12% of basal frequency; *n* = 3). This excitatory effect was not observed on mEPSCs isolated by applying TTX either in the presence (*n* = 3) or absence (*n* = 4) of Mg^{2+} ions in the extracellular medium (**Figures 2B,C**, respectively). Both the mean amplitude and frequency of appearance were unaffected by γ-Glu-Glu application. This result precludes that presynaptic NMDA receptors are involved in the excitatory effect of γ-Glu-Glu on synaptic transmission. Taken together, these data confirmed those obtained by measuring intracellular Ca^{2+} changes in the presence of TTX.

Characterization of γ-Glu-Glu Actions on Cells Expressing NMDAr

Taken together, our data raised on hippocampal neurons suggest that γ-Glu-Glu behaves as a partial agonist of NMDA receptors. In order to further characterize this effect, γ-Glu-Glu was then tested on cells expressing either of GluN1 and GluN2A or GluN1 and GluN2B NMDAr subunits, bearing in mind that they are the most abundant NMDA receptors found in the hippocampus (Shipton and Paulsen, 2014).

NMDA receptors were expressed first in astroglioma C6 cells. We have first checked that functional NMDArs were correctly expressed in this cell line. First, glutamate elicited a $[Ca^{2+}]_i$ rise only in transfected cells. Second, this response was potentiated by glycine (10 μM), inhibited NMDAr antagonist AP5, and in the presence of Mg^{2+} ions in the extracellular medium (**Figure 3A**).

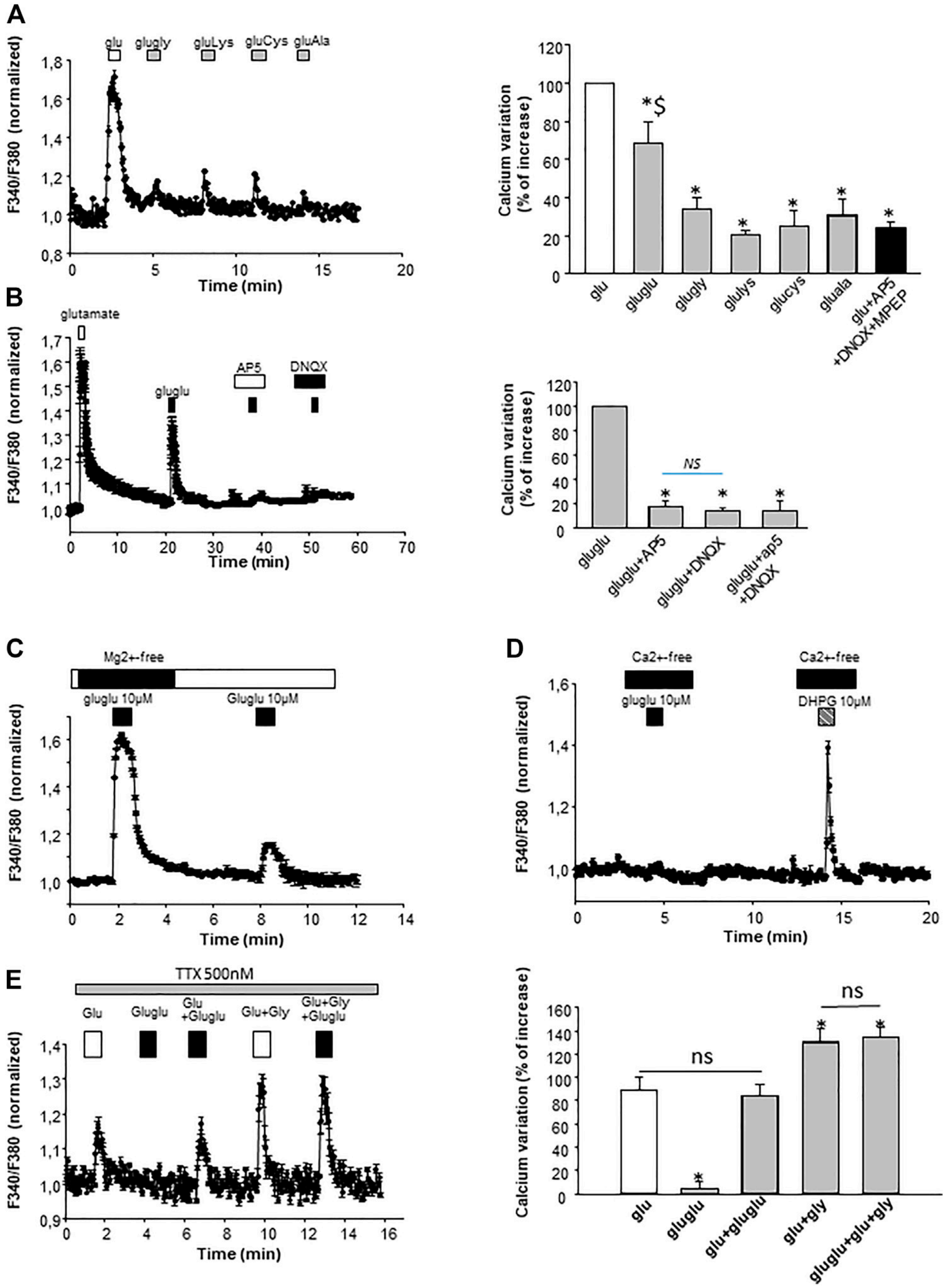

FIGURE 1 | Characterization on the γ-Glu-AA effect on [Ca^{2+}]$_i$ in cultured neurons. **(A)** γ-Glu–Gly, γ-Glu–Lys, γ-Glu–Cys, and γ-Glu–Ala were sequentially applied at 10 µM on cultured neurons. On the left, an illustrative sample trace obtained by averaging [Ca^{2+}]$_i$ changes recorded in the three cells is shown. On the right, the recapitulative graph plot peak [Ca^{2+}]$_i$ normalized to glutamate response (at 10 µM; 100%) for all the γ-Glu-AA tested (*n* = 75). *$p < 0.05$ when comparing γ-Glu-AA- *vs* the Glu-elicited response; \$$p < 0.05$ when comparing γ-Glu-Glu- *vs* other γ-Glu-AA–elicited responses. **(B)** Pharmacological characterization of γ-Glu-Glu targets with glutamate ionotropic receptor antagonists AP5 (25 µM; NMDAr antagonist) and DNQX (10 µM; AMPAr and KAr antagonist). On the left, a graph plotting averaged sample traces of the 27 cells recorded during one individual experiment is shown. On the right, the recapitulative graph plot peak [Ca^{2+}]$_i$ normalized to γ-Glu-Glu response (at 10 µM; 100%) for all the conditions tested (*n* = 193). **(C)** Illustrative experiment depicting the dependency of γ-Glu-Glu–elicited [Ca^{2+}]$_i$ increase on the presence of Mg^{2+} ions in the extracellular medium. The graph was obtained by averaging traces recorded in the 30 individual cells. **(D)** Representative experiment illustrating the dependency of γ-Glu-Glu effects on the extracellular Ca^{2+} ions. The metabotropic glutamate receptor (mGlu5) agonist DHPG (10 µM) was tested as a control for the stimulation Ca^{2+} release from intracellular stores. The graph has been generated by averaging the responses of 25 individual cells recorded. **(E)** Effect of TTX of γ-Glu-Glu–elicited responses. On the left, a graph plotting the responses of Glu and γ-Glu-Glu is shown. It has been obtained by averaging [Ca^{2+}]i changes from 12 individual cells recorded during a single experiment. On the right, the graph recapitulates the [Ca^{2+}]i increases elicited by Glu, γ-Glu-Glu, Glu+γ-Glu-Glu, γ-Glu-Glu + Gly, and Glu+γ-Glu-Glu + Gly. Data are presented as [Ca^{2+}]i increases normalized to the responses of Glu (*n* = 68).

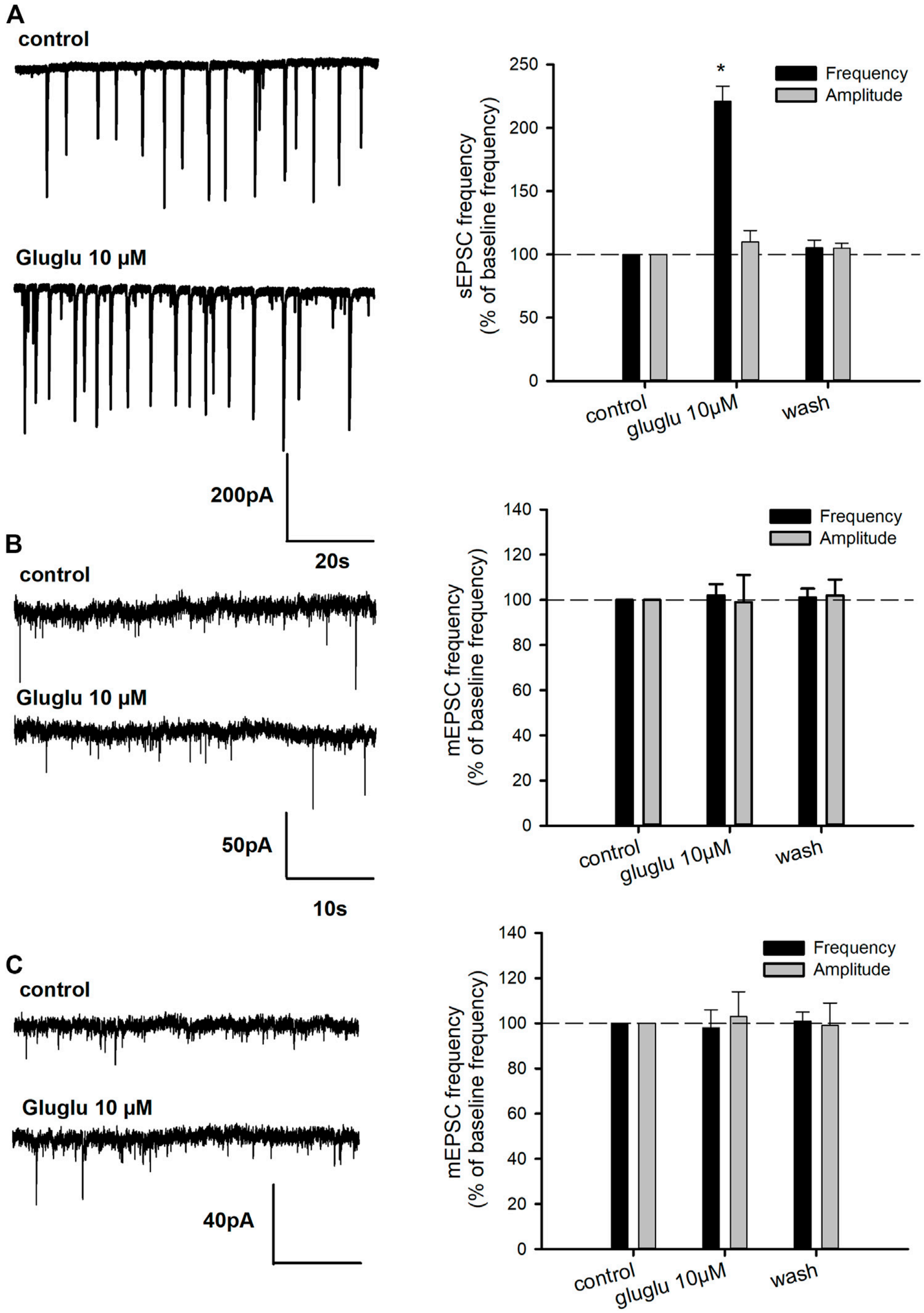

FIGURE 2 | Effect of γ-Glu-Glu on spontaneous excitatory synaptic transmission. **(A)** On the left, representative traces showing the exciting effect of γ-Glu-Glu on sEPSC recorded in the Mg^{2+}-free medium. A recapitulative graph plotting the changes in sEPSC frequency and amplitude is shown. Data are expressed as averages (±SEM) of sEPSC frequencies or amplitudes, normalized to respective basal sEPSC frequency or amplitude. $^*p < 0.05$ *vs.* baseline frequency (one-way ANOVA followed by the Holm–Sidak t-test) **(B)** Miniature spontaneous transmission (mEPSC) was recorded in the presence of TTX (500 nM) in a Mg^{2+} ion–containing extracellular medium. On the left, the extracts of mEPSC recordings obtained in the control and in the presence of γ-Glu-Glu are shown. On the right, a graph plot mEPSC frequency and amplitude. Data are expressed as averages (±SEM) of mEPSC frequencies or amplitudes normalized to the respective basal mEPSC frequency or amplitude. **(C)** Miniature EPSCs were recorded in the presence of TTX (500 nM) in a Mg^{2+} ion–free medium. On the right, a graph plot mEPSC frequency and amplitude is shown. Data are expressed as averages (±SEM) of mEPSC frequencies or amplitudes normalized to the respective basal sEPSC frequency or amplitude.

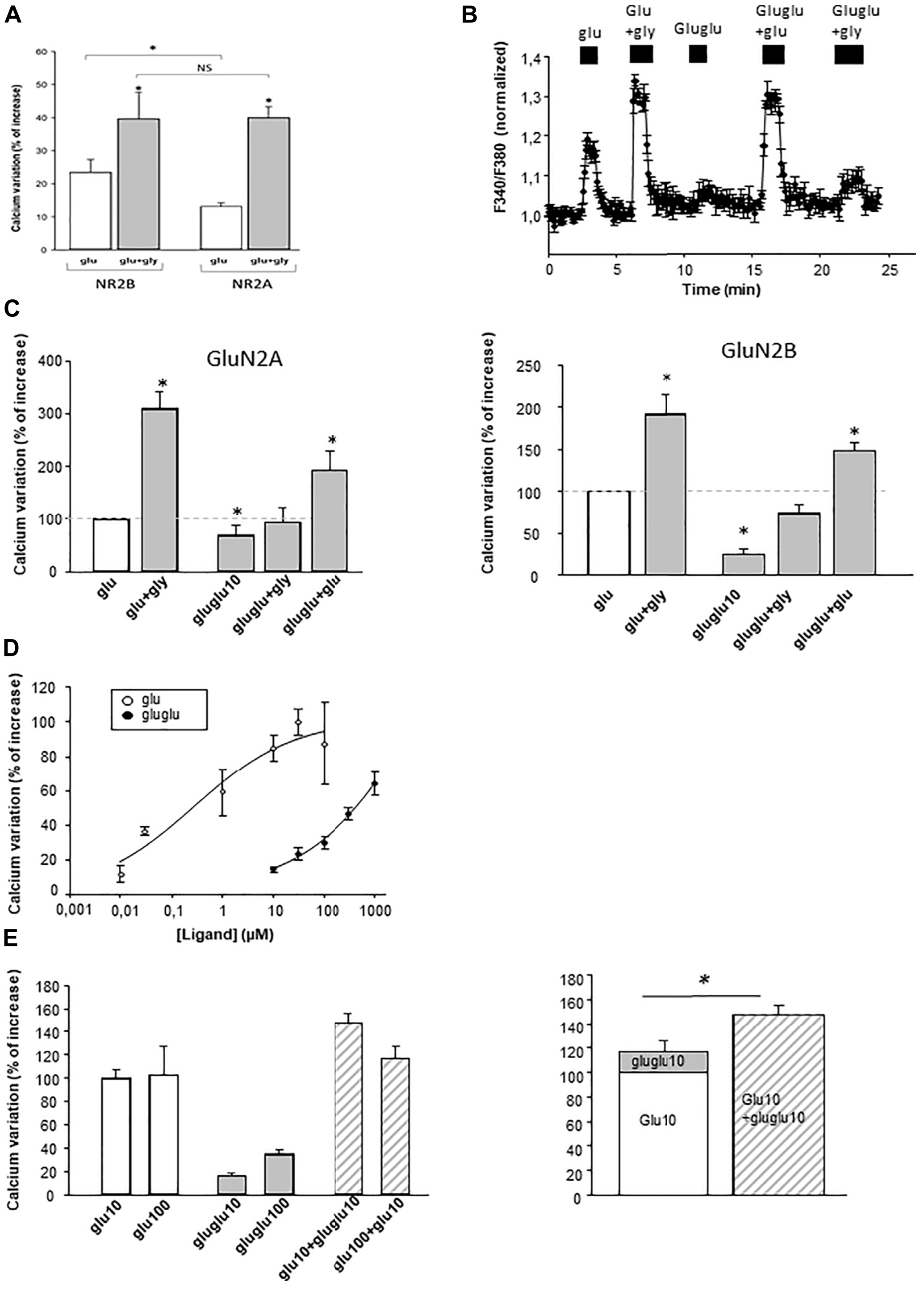

FIGURE 3 | Effect of γ-Glu-Glu on [Ca^{2+}]i on C6 cells transfected with the NMDAr. **(A)** Comparative effect of 10 μM glutamate and 10 μM glutamate + glycine application in the NMDAr comprising the GluN2A or Glu2B subunit ($n = 100$). **(B)** Illustrative experiment depicting the effect of γ-Glu-Glu and Glu, both applied at 10 μM in the presence or not of glycine (gly, 10 μM) on the GluN2B-expressing C6 cells ($n = 3$). **(C)** Recapitulative graphs plotting the effects of γ-Glu-Glu in the presence of Glu or Gly on GluN2A- (left; $n = 10$) and GluN2B-expressing cells (right; $n = 17$). **(D)** Concentration-dependent curve of the effect of Glu and γ-Glu-Glu on $[Ca^{2+}]_i$ measured in GluN2B-expressing cells ($n = 15$ each). **(E)** Quantitative analysis of the effect of the combination of Glu (10 μM or 100 μM) with γ-Glu-Glu (10 μM) (left, $n = 15$). On the right, the graph compares the theoretical response obtained by adding the individual responses elicited by Glu (10 μM) and of γ-Glu-Glu (10 μM) (right histogram) with the experimental response obtained by co-applying Glu (10 μM) with γ-Glu-Glu (10 μM). *$p < 0.05$ when comparing both conditions (one-way ANOVA followed by the Holm–Sidak t-test).

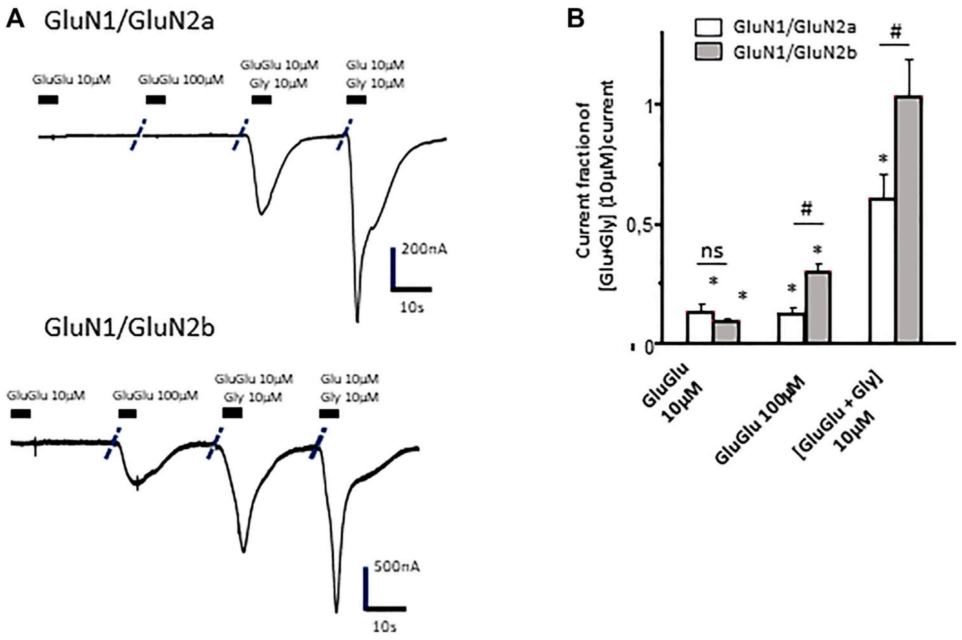

FIGURE 4 | Effect of γ-Glu-Glu on GluN1/GluN2A- and GluN1/GluN2B NMDAr-expressing *Xenopus* oocytes. **(A)** Current traces obtained from GluN1/GluN2A- **(top)** and GluN1/GluN2B- **(bottom)** expressing oocytes in the presence of γ-Glu-Glu and Glu alone or in combination with glycine. **(B)** Recapitulative graph plotting current amplitudes expressed as fractions of the current obtained by co-applying Glu and Gly (each at 10 µM) in both GluN1/GluN2A- and GluN1/GluN2B-expressing oocytes. Data are presented as averages (±SEM) of 12 independent experiments. * indicates a significant difference between a given condition and the glutamate + glycine effect. $^{\#}$ indicates a significant difference between the current amplitudes recorded on GluN2A-expressing oocytes and those recorded on GluN2B-expressing oocytes (two-way ANOVA).

The transfected NMDArs thus retained their functional properties when transfected in C6 cells. We also observed that GluN2B-expressing cells were more sensitive to glutamate than GluN2A-expressing cells. Gamma-Glu-Glu–elicited $[Ca^{2+}]_i$ increases were detected when it was applied at a concentration of 10 µM on both GluN2A- and GluN2B-expressing C6 cells (**Figures 3B,C**). It had no effect on untransfected cells (data not shown). In addition, glycine potentiated γ-Glu-Glu responses. Gamma-Glu-Glu dose-dependently increased $[Ca^{2+}]_i$ with an EC50 value circa 300 µM. It was less potent than glutamate which exhibited an EC50 value in the micromolar range (**Figure 3D**). Therefore, γ-Glu-Glu displayed partial agonist effect on NMDA receptors. In this line, γ-Glu-Glu was further tested in combination with Glu to evaluate whether it could antagonize Glu effects. In fact, we observed that γ-Glu-Glu when tested at 10 µM consistently potentiated the responses elicited by Glu at 10 µM. However, this potentiation was lost when Glu was tested at 100 µM (**Figure 3E**). Therefore, γ-Glu-Glu does not really behave as a "conventional" partial agonist as it does not elicit any blocking action on glutamate-evoked responses.

Concentration-dependent effects of γ-Glu-Glu were further evaluated on oocytes expressing GluN2A- or GluN2B-containing NMDA receptors. Interestingly, γ-Glu-Glu elicited different responses according to the concentration applied and to NMDAr subunit composition. GluN2A-containing NMDArs were more sensitive to low concentrations of γ-Glu-Glu than GluN2B-containing NMDArs. At higher concentrations (100 µM), the opposite was observed. Such a discrepancy was retained when γ-Glu-Glu was applied in the presence of glycine (**Figures 4A,B**). This was also observed on C6 cells expressing NMDAr.

γ-Glu-Glu Production by Astroglioma Cells Depends on Glutathione Metabolism

In the brain, γ-Glu-AAs can be obtained after GSH lysis by γ-GT. They are further released in the extracellular space. In addition, astrocytes appear to be the major source of γ-Glu-AAs (Dringen et al., 1999). We have thus evaluated whether γ-Glu-Glu was found in the extracellular medium of cultured C6 astroglioma cells and whether its concentration was linked to GSH metabolism (**Figure 5**). For this, the cells were treated either with acivicin (ACV), a blocker of γ-GT, or with L-buthionine-(S, R)-sulfoximine (BSO), a blocker of GCLC and sulforaphane (SFN), which boosts GSH formation by stimulating GCLC expression *via* Nrf2 pathway activation. First, intracellular GSH changes were evaluated in C6 cells in order to confirm the activity of these modulators. BSO (10 µM) significantly reduced GSH as measured *in cellulo* with monobromobimane (mBrB) fluorescence (63 ± 2% of basal; *n* = 3), while ACV (100 µM) and SFN (10 µM) elicited a significant increase in mBrB fluorescence (132 ± 2% and 165 ± 12% of basal, respectively; *n* = 3). The extracellular γ-Glu-Glu concentration ($[\gamma\text{-Glu-Glu}]_e$) was further measured, thanks to LC-MS. Basal $[\gamma\text{-Glu-Glu}]_e$ was 262 ± 56 nM (*n* = 3). In the presence of ACV, $[\gamma\text{-Glu-Glu}]_e$ was significantly increased to 170 ± 17% of the basal

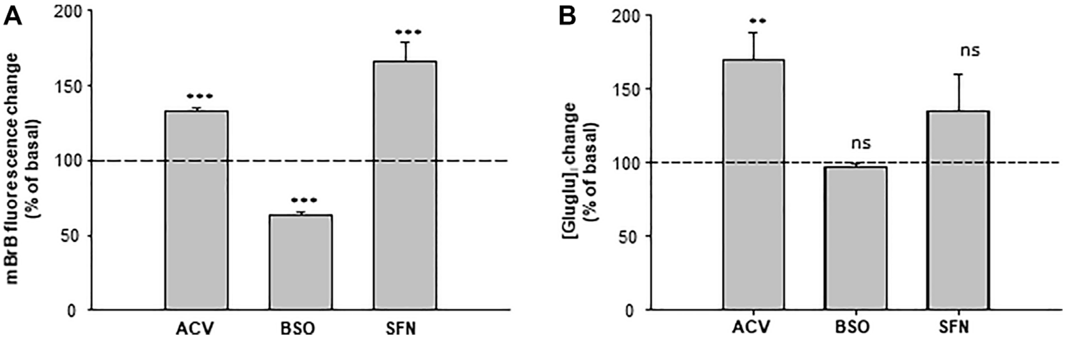

FIGURE 5 | Quantification of γ-Glu-Glu in the extracellular medium of astroglioma C6 cells. **(A)** [GSH]$_i$ content in the control, BSO-, ACV-, and SFN- pretreated C6 cells. GSH was measured *in cellulo* with monobromobimane (mBrB) 24 h following the treatments. On the graph, data are presented as percentages of mBrB fluorescence intensity normalized to basal mBrB fluorescence measured in the control-untreated cells. ***$p < 0.001$ when comparing mBrB fluorescence measured in the control cells with either treatment (one-way ANOVA followed by the Holm–Sidak t-test). **(B)** Measurement of [γ-Glu-Glu] in the extracellular medium of C6 cells. Analysis of the C6 extracellular medium was performed on 100 µl samples of the culture medium of cells treated with BSO, ACV, and SFN. On the graph, [γ-Glu-Glu]e has been normalized to [γ-Glu-Glu]e detected in the control-untreated cells. **$p < 0.01$ and "not significant" (ns) when comparing [γ-Glu-Glu]e measured in control cells with either treatment (one-way ANOVA followed by the Holm–Sidak t-test).

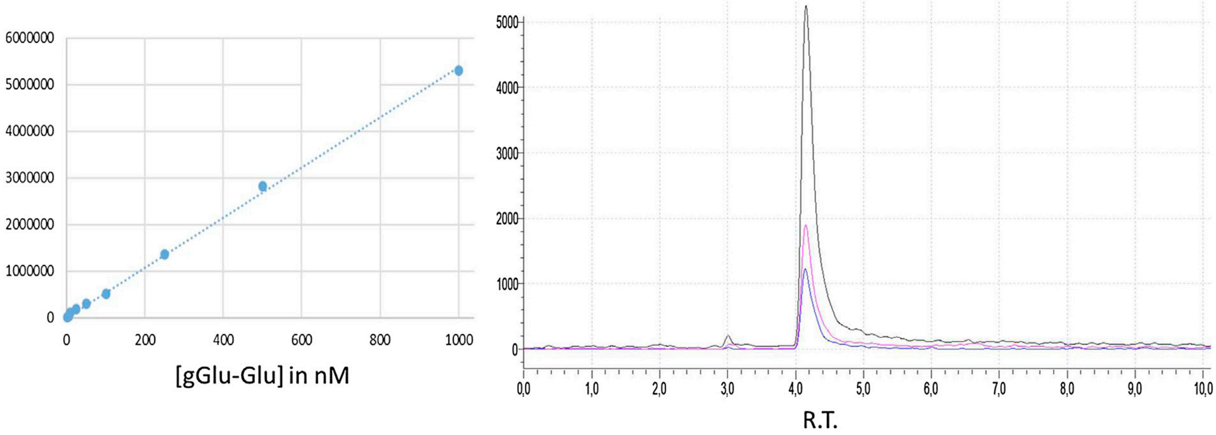

FIGURE 6 | Standard curve for γ-Glu-Glu. γ-Glu-Glu LC-MS/MS in the MRM mode showing the three transitions.

concentration ($n = 3$). BSO had merely no effect on [γ-Glu-Glu]$_e$, while SFN enhanced it, although not significantly (135 ± 25%, $n = 3$). Therefore, [γ-Glu-Glu]$_e$ tends to be linked to GSH metabolism in astroglioma cells. It is noteworthy that γ-Glu-Glu was not detected in the extracellular medium of cultured neurons (not shown).

DISCUSSION

We found here that γ-Glu-Glu produced excitatory actions on cultured hippocampal neurons by activating partially NMDA receptors, although γ-Glu-Glu has good affinity for all ionotropic glutamate receptors (Tamborini et al., 2016). This result is in good agreement with a previous study showing such an activity in olfactory bulb neurons (Li et al., 1993). In addition, we also observed that γ-Glu-Glu effects were consistently detected above 10 µM. Nevertheless, γ-Glu-Glu excitatory actions could also involve a positive modulation of glutamate effects. Indeed, at specific concentrations, γ-Glu-Glu potentiated glutamate-elicited responses, while an inhibitory action was more likely expected if it had behaved as a partial agonist of the glutamate binding site on the NMDAr. This suggests that the γ-Glu-Glu binding site could impinge on a positive allosteric and/or co-agonist binding site on NMDAr. Further structural analysis is required to define the potential binding site(s) of this dipeptide on NMDAr. Moreover, we found that γ-Glu-Glu elicited greater selectivity for the NMDAr containing the GluN2B subunit than for those containing the GluN2A subunit. The endogenous occurrence of γ-Glu-Glu could thus favor neurophysiological mechanisms involving GluN2B-containing NMDAr (Sun et al., 2018).

Nevertheless, γ-Glu-Glu elicited excitatory actions at low concentration (10 µM) which were dependent on the integrity of synaptic transmission as TTX (500 nM) blocked both γ-Glu-

Glu–elicited [Ca^{2+}]i increases and increase in spontaneous synaptic transmission. It is noticeable that γ-Glu-Glu excitatory action was prominently detected on sEPSC frequency than on their amplitude. This most likely arises from the fact that sEPSCs were recorded in Mg^{2+} ion–free medium. Under these conditions, sEPSCs occur as chronic bursts with a steady amplitude and frequency (so-called “network activity”). Moreover, excitations or inhibitions of this activity are detected mainly by changes in the bursting frequency. This is probably due to the fact that network activity results from the synchronized activation of all excitatory synapses at the same time, and as a consequence, modulations are detected mainly by changes in the frequency of burst occurrence. The fact that the excitatory effect of γ-Glu-Glu on synaptic transmission was blocked by TTX indicates that it most likely resulted from an indirect mechanism involving first the partial effect on NMDAr leading and second the endogenous synaptic release of glutamate and glycine, in turn activating both AMPAr and NMDAr (Vignes, 2001). We have previously reported a similar effect with theanine which exerted excitatory effects sensitive to TTX in cultured hippocampal neurons; the excitatory effect of theanine involves a positive modulation of NMDAr (Sebih et al., 2017). The endogenous presence of γ-Glu-Glu could thus be at the origin of the tonic activation of NMDAr which has been identified in the hippocampus (Le Meur et al., 2007). Indeed, Le Meur et al. have shown that NMDArs were chronically activated by ambient glutamate of non-synaptic origin. Thus, γ-Glu-Glu could be involved in this tonic activation of NMDAr since, in addition, it has mainly a glial origin (Dringen et al., 1999). Indeed, gamma-glutamyl dipeptides (γ-Glu-AA) are by-products of glutathione (GSH) metabolism as they result from the breakdown of GSH by the action of γ-GT. They are further released in the extracellular space. We have thus verified whether γ-Glu-Glu production was related to GSH metabolism in astroglial cells. In fact, while boosting GSH cell content with the Nrf2 activator, it resulted, as expected, in an increased occurrence of γ-Glu-Glu. By contrast, rather surprisingly, γ-Glu-Glu concentration was enhanced after treating cells with acivicin, an efficient blocker of γ-GT activity, while a decrease was expected. Nevertheless, as acivicin also enhanced GSH cellular content, one may speculate that there should be another enzymatic route leading to γ-Glu-Glu from GSH. In support of this, Bachhawat and Yadav (2018) indicate that there are alternative pathways to γ-GT activity, including the glutamate–cysteine ligase activity, which could lead to the production of γ-Glu-AA.

The changes in γ-Glu-Glu in the extracellular medium may thus reflect the production of GSH by astroglial cells. As GSH is the major antioxidant in the CNS, increased production of GSH is required in order to build up antioxidant defense during oxidative stress. Therefore, enhanced production of GSH may result in enhanced γ-Glu-Glu, which, in turn, could produce a stronger activation of NMDA receptors. Such an effect could aggravate indirectly the detrimental action of oxidative stress on neurons, which is particularly enhanced in the progression of neurodegenerative diseases.

MATERIALS AND METHODS

1-Chemical Syntheses

The melting points were obtained using a Büchi 510 capillary apparatus and were uncorrected. ^{1}H NMR and ^{13}C NMR spectra were recorded at 300 and 75 MHz using a Brüker AC300 instrument and at 600 MHz using a Brüker AC600 instrument. Chemical shifts are quoted in parts per million (ppm) and were referenced to the residual solvent peak. The following abbreviations are used: s, singlet; d, doublet; t, triplet; q, quartet; and m, multiplet. Coupling constants are reported in hertz (Hz). High-resolution mass spectra (HRMS) were recorded on a Micromass Q-TOF electrospray instrument with only molecular ion and other major peaks being reported. LC-MS identification was carried out by electrospray on HPLC Waters Alliance 2690. Flash chromatography was carried out using E-Merck silica gel (Kieselgel 60, 230–400 mesh) as the stationary phase. Thin-layer chromatography (TLC) was carried out on aluminum plates precoated with Merck silica gel 60F254 and visualized by quenching of ultraviolet fluorescence or by staining with a 10% methanol phosphomolybdic acid solution followed by heating. Column chromatography on silica gel was carried out with Merck Kieselgel 60 silica (230–400 mesh). Analytic HPLC was performed on a Waters apparatus 717 plus autosampler with Millenium^{32} program on SymmetryShield^{TM} RP$_{18}$ 3.5 µm 2.1 mm × 20 mm column using a linear gradient of ACN in H$_2$O with 0.1% TFA in 5 min with 3 ml/min flow. THF was distilled from sodium/benzophenone ketyl. The reagents were supplied by commercial sources (Merck, Fluka, Sigma-Aldrich, BACHEM, Acros, and Novabiochem).

General Procedure for Peptide Coupling

Synthesis of (S,S) Di-Tert-Butyl (5-(Tert-Butoxy)-4-((Tert-Butoxycarbonyl) Amino)-5-Oxopentanoyl)Glutamate 1

(*S*)Boc-Glu-O*t*Bu (1 mmol, 303.4 mg), (*S*)HCl,H-Glu(O*t*Bu)-O*t*Bu (1 mmol, 295.8 mg), BOP (1.2 mmol, 530.7 mg), and DIEA (3 mmol, 0.52 ml, pH = 8.5) were dissolved in THF (15 ml) and stirred at room temperature. After stirring 1 h, the solvent was removed under reduced pressure, the organic layer was extracted with ethyl acetate (15 ml), and then washed with 2 × 5 ml of 10% citric acid, 2 × 5 ml NaHCO3 (1M), and then with 2 × 5 ml brine. The organic phase was dried over anhydrous MgSO$_4$ and, after evaporation of the solvent under reduced pressure, the totally protected dipeptide *1* was purified on a silica gel column in AcOEt/cyclohexane, 7:3, as the eluent.

Yield: 95%; white solid; Rf = 0.58 (AcOEt/cyclohexane, 7:3); tR = 1.98 min. MS (ES+) m/z 544.1.1H NMR (300 MHz, MeOD): δH (ppm) 1.39 (s, 9H, BOC), 1.48–1.49 (m, 27H, 3xOtBu), 2.05 (t, 2H), 2.18 (m, 2H), 2.29 (m, 2H), 2.35 (t, 2H), 3.90 (dd, 1H,CHα, 3J = 9.4 Hz, 3J = 4.27 Hz), 4.27 (dd, 1H,CHα, 3J = 8.95 Hz, 3J = 5.29 Hz).13C NMR (75 MHz, MeOD):δC (ppm) 26.48, 26.6, 27.1, 28.7, 30.43, 32.8, 52.97, 54.22, 79.87, 82.11, 156.58, 171.75, 173.1, 174.13.

(S)-2-((S)-4-Amino-4-Carboxybutanoyl) Glutamic Acid 2: γ-L-H-Glu (L-Glu-OH)-OH

The final compound γ-L-Glu (L-Glu-OH)-OH ***2*** was obtained by removing N- and C- protecting groups (i.e., BOC and *tert*butyl esters) in acidic conditions. Boc-L-Glu[L-Glu(O*t*Bu)-O*t*Bu]-O*t*Bu***1*** (1 mmole, 544 mg) was stirred in HCl 4N aqueous solution in dioxan (10 ml) for 4 h at 40°C. The dioxan was evaporated under reduced pressure, and the N-chlorhydrate salts of gamma dipeptide were precipitated and dried in diethylether. γ-L-Glu (L-Glu-OH)-OH ***2*** was obtained in a 90% yield. It can also be lyophilized.

Yield 90%; hygroscopic white solid; Rf = 0.15 (AcOEt/cyclohexane, 7:3); tR = 0.4 min mp: 98–102°C; Mw C10H26O7N2. MS (ES+) m/z 277.2 (M + H)+. HRMS (ESI) m/z Calcd for [M + H]+ 277.1036, found 277.1041.1H NMR (300 MHz, D2O): δH (ppm) 1.99–2.08 (m, 4H), 2.30–2.41 (m, 2H), 2.39–2.47 (m, 2H), 3.67–3.73 (t, 2H, 2xCHα). 13C NMR (75 MHz, D2O):δC (ppm) 25.55, 26.08, 30.14, 30.74, 53.88, 53.98, 173.80, 173.86, 177.22, 177.56.

2-Cell Cultures

Functional characterization of gamma-Glu-Glu was performed on primary hippocampal neurons and cells expressing NMDAr, including transfected astroglioma C6 cells and *Xenopus* oocytes. All experiments were carried out in accordance with the European Community Council Directive of 24th November 1986 (86/609/ECC). Sprague–Dawley rats were obtained from Janvier Laboratories (France). Culture media (DMEM/Ham F12 with HEPES and 4.5 g/L glucose), Dulbecco's phosphate-buffered saline (Dulbecco's PBS), Versene, antibiotics, and fetal calf serum (FCS) were purchased from Invitrogen. Culture dishes were obtained from Nunc. All chemicals were obtained from Sigma.

Hippocampal Neuron-Enriched Cultures

Primary neuronal cultures were established from 18-day-old embryonic rat hippocampi, as previously described (De Jesus Ferreira et al., 2005), with minor modifications. After preincubation with Versene, hippocampal cells were mechanically dissociated and plated at a density of 2 × 106 cells/dish, on 8-well plates containing square (10 × 10 mm^2) glass coverslips, previously coated with poly(D-lysine) (50 µg/ml) and then with DMEM/HAM F12 containing 10% FCS. The cells were grown in a defined medium containing DMEM/HAM F12, supplemented with 33 mM glucose, 2 mM glutamine, 100 U/ml penicillin, 100 µg/ml streptomycin, 13 mM sodium bicarbonate, 5.5 µg/ml transferrin, 10 µg/ml insulin, 1 pM β-estradiol, 3 nM triiodothyronine, 20 nM progesterone, 5 ng/ml sodium selenite, and 100 µM putrescine. The experiments were performed on cell cultures grown from 6 to 16 DIV.

C6 Astroglioma Cells

Rat C6 glioma cells were gifted by Dr Nathalie Chevalier (INSERM U1198). They were maintained in DMEM supplemented by 10% fetal calf serum in the presence of 100 U/ml penicillin and 100 µg/ml streptomycin. C6 cells were transfected at 80% confluence with a combination of GluN1 and GluN2A or GluN2B (3.75 µg cDNA/wells) + 10 µl of Lipofectamine (Invitrogen) diluted in Opti-MEM^{TM} (Gibco^{TM}). The cells were used 24 h after transfection. All constructions of NMDA receptor subunits have been kindly provided by Pierre Paoletti (IBENS, ENS, Paris). C6 cells were used for less than 15 passages.

Xenopus Oocyte Injection and Oocyte Current Recording

Xenopus oocytes were prepared and injected with *in vitro*–transcribed RNA at 1 µg/µl (20–40 nl) of rat GluN1-1a (named GluN1 herein) and rat GluN2A or mouse ε2 (named GluN2B herein) with a stoichiometric ratio of 1:1 (Sebih et al., 2017a). Macroscopic currents were recorded under a two-electrode voltage clamp using a GeneClamp 500 amplifier (Axon Instruments) and analyzed in the ND96 HERG recording solution (in mM, 96 NaCl, 3 KCl, 0.5 CaCl2, 5 HEPES, pH = 7.2). Current and voltage electrodes (less than 1 MΩ) were filled with 3 M KCl. The currents were filtered (20 Hz) and digitized (66 Hz) using a Digidata-1200 interface (Axon Instruments). Data acquisition was performed using version 7 of pClamp software (Axon Instruments). On the graphs depicting pooled data, the currents recorded on oocytes were expressed as fractions of the maximal current obtained on NMDA receptors—expression obtained by applying a combination of glutamate and glycine, both at 10 µM (Yuan et al., 2009).

3-Measurement of GSH Content

Changes in the cellular content of GSH were measured after monobromobimane (mBrB) labeling as previously described (De Jesus Ferreira et al., 2005) (Baxter et al., 2015). For this, C6 rat glioma cells were seeded in 96-well culture plates. When reaching 80% confluence, the cells were treated with BSO (10 µM) or SFN (10 µM) or ACV (100 µM) for 24 h. The culture medium was then replaced by the extracellular medium containing 50 µM mBrB. The extracellular medium comprised 124 mM NaCl, 3.5 mM KCl, 25 mM $NaHCO_3$, 1.25 mM NaH_2PO_4, 1 mM $CaCl_2$, 2 mM $MgSO_4$, 10 mM D-glucose, and 10 mM HEPES (pH: 7.4). Incubation with mBrB lasted for 30 min, and then the cells were washed with the extracellular medium to remove unbound mBrB. Fluorescence was then measured *in cellulo* with a plate reader (Tecan "Spark" 20M) at 527 nm after excitation at 380 nm. Background fluorescence was obtained from mBrB unlabeled cells. For data processing, the background fluorescence was subtracted to all fluorimetric signals which were further normalized to mBrB fluorescence recorded in control cells. An experimental determination was performed eight times per experiment. The data are expressed as percentages of at least three distinct experiments performed on different cell cultures.

TABLE 1 | Mass spectrometric parameters: MRM parameters, chromatographic attributes, and quantitative response of γ-Glu-Glu compounds in standard samples.

Analyte	Formula	Mass (Da)	Precursor ion (m/z)	MRM transition m/z	
γ-Glu-Glu	$C_{10}H_{17}N_2O_7$	276.1	277.1	148.1, 130.0, 84.0 (quanti)	
LOD (mol/L)	LOQ (mol/L)	SD	R^2	Linearity	Retention time (min)
10-9	10-9	8%	0.999	1000	4.2

4-Measurement of Intracellular Ca^{2+} Concentration

Intracellular calcium concentration ($[Ca^{2+}]_i$) was measured using the fluorescent indicator fura-2. For this purpose, the cells grown on glass coverslips were loaded with fura-2 by a 30-min incubation at 37°C with 1 µM fura-2-AM and 0.02% Pluronic in the extracellular solution described above. $[Ca^{2+}]_i$ was monitored by video microscopy. After rinsing, the glass coverslip was transferred to the recording chamber mounted on an inverted microscope (Leica, DMIRB) and continuously superfused with the extracellular medium described above without adding MgSO4 (Mg^{2+} ions free medium). Fura-2 emission was obtained by exciting alternatively at 340 and 380 nm with a rotating filter wheel (Sutter Instruments) and by monitoring emissions (F340 and F380) at 510 nm. Fluorescent signals were collected with a CCD camera (Hamamatsu), digitized, and analyzed with image analysis software (Acquacosmos, Hamamatsu). The ratio of emissions at 510 nm (F340/F380) was recorded in the cells every second. Experiments were carried out at room temperature. Drugs were applied for 1 min with a gravity-fed system. The data are expressed as averages (±SEM) of the ratio between the fura-2 fluorescence values of 340/380 nm excitation wavelength ratios (F340/F380), normalized to the corresponding basal F340/F380 measured prior to any drug application.

Graphs presenting time courses of F340/F380 ratio changes have been obtained by averaging data from a population of cells recorded individually during one single representative experiment. In the graphs of pooled data, "n" values represent the entire population of cells recorded from at least three independent cultures.

5-Electrophysiology

Spontaneous excitatory and inhibitory postsynaptic currents (sESPC and sIPSC) were recorded using the whole-cell patch-clamp method. Neurons grown on glass coverslips were transferred to a recording chamber of an upright microscope and continuously superfused with the extracellular medium (in the presence or absence of MgSO4, according to the experimental condition). Experiments were performed at room temperature with glass pipettes (4-5MΩ resistance) filled with the intracellular solution comprising 140 mM $CsMeSO_3$, 4 mM NaCl, 1 mM $MgCl_2$, 1 mM EGTA, 5 mM HEPES, 2 mM MgATP, and 0.6 mM NaGTP, pH = 7.4 (CsOH). Tetrodotoxin (500 nM) was included to record miniature EPSCs (mEPSCs) (Vignes, 2001). Access resistance was monitored by applying a 10-mV voltage steps. The currents were collected and amplified with an Axoclamp 200B amplifier (Molecular Devices) and digitized (Digidata 1322, Molecular Devices). Spontaneous PSCs were analyzed with John Dempter's software packages WinEDR and WinWCP. Drugs were applied at the desired concentration *via* a gravity-fed application system.

6-LIQUID CHROMATOGRAPHIC AND MS/MS CONDITIONS FOR γ-GLU-GLU

The extracellular concentration of γ-Glu-Glu was measured with the extracellular medium of cultured rat C6 astroglioma cells. With this aim, C6 cells were grown in 24-well cell culture plates until 80% cell confluence was reached. The cells were further treated with ACV (100 µM) or BS0 (10 µM) or SFN (10 µM). After a 24-h treatment, the samples of 100 µL of the extracellular medium were taken from 500 µL of the total culture well volume. Sample analyses were further conducted using a LC-MS/MS-8050 (Shimadzu Scientific, Inc., Columbia, MD, USA) Triple Quad mass spectrometer (QqQ) equipped with a UHPLC NexeraX2 system.

Peak resolution and separation for all samples were optimized by using a Nucleoshell HILIC 50 × 2.1 mm; 2.7 µm (Macherey–Nagel) maintained at 30°C. Mobile phase A: ammonium acetate 100 mM and mobile phase B: ACN/ammonium acetate 100 mM (95/5, v/v) with a 1 ml/min flow and a gradient of 0–80% in 10 min (**Figure 6**).

System control, data acquisition, and quantitative analysis were performed using Labsolutions software (Shimadzu). Optimal detection conditions were determined from the injection of 594 standard samples over six different parameters. Mass spectrometric detection was operated in positive electrospray ionization and multiple reaction monitoring. The multiple reaction monitoring (MRM) transitions and compound dependent parameters are shown in **Table 1**. Optimized parameters were obtained by the product ion scan mode of the individual analyte at 10 uM. The parameters for multiple reaction monitoring (MRM) detection in the positive mode are as follows: nebulizing gas flow: 3.0 L/min; heating gas flow: 15 L/min; drying gas flow: 5 L/min; interface temperature: 350°C; desolvation line temperature: 250°C; and heat block temperature: 400°C.

Extracellular sample analysis was performed in triplicate per experiment. On the graphs, "n" applies to individual experiments.

7-Statistical Analyses

On the recapitulative graphs, "n" applies to the total number of cells recorded and is the sum of all individual cells from at least three independent cell cultures. Statistical analyses were performed using SigmaStat software (Systat software Inc.). One-way ANOVA was generally used for comparison followed by an adequate t-test.

DATA AVAILABILITY STATEMENT

The raw data supporting the conclusion of this article will be made available by the authors, without undue reservation.

ETHICS STATEMENT

The animal study was reviewed and approved by the local Committee on Ethics of the University of Montpellier (Comité local d'éthique de l'Université de Montpellier).

REFERENCES

Bachhawat, A. K., and Yadav, S. (2018). The Glutathione Cycle: Glutathione Metabolism beyond the γ-glutamyl Cycle. *IUBMB Life* 70, 585–592. doi:10.1002/iub.1756

Baxendale, I. R., Ley, S. V., Smith, C. D., and Tranmer, G. K. (2006). A Flow Reactor Process for the Synthesis of Peptides Utilizing Immobilized Reagents, Scavengers and Catch and Release Protocols. *Chem. Commun. (Camb)* 46, 4835–4837. doi:10.1039/b612197g

Baxter, P. S., Bell, K. F., Hasel, P., Kaindl, A. M., Fricker, M., Thomson, D., et al. (2015). Synaptic NMDA Receptor Activity Is Coupled to the Transcriptional Control of the Glutathione System. *Nat. Commun.* 6, 1–13. doi:10.1038/ncomms7761

De Jesus Ferreira, M. C., Crouzin, N., Barbanel, G., Cohen-Solal, C., Récasens, M., Vignes, M., et al. (2005). A Transient Treatment of Hippocampal Neurons with Alpha-Tocopherol Induces a Long-Lasting protection against Oxidative Damage via a Genomic Action. *Free Radic. Biol. Med.* 39, 1009–1020. doi:10.1016/j.freeradbiomed.2005.05.021

Dringen, R., Pfeiffer, B., and Hamprecht, B. (1999). Synthesis of the Antioxidant Glutathione in Neurons: Supply by Astrocytes of CysGly as Precursor for Neuronal Glutathione. *J. Neurosci.* 19, 562–569. doi:10.1523/jneurosci.19-02-00562.1999

Francis, A. A., Jones, A. W., and Watkins, J. C. (1980). Dipeptide Antagonists of Amino Acid-Induced and Synaptic Excitation in the Frog Spinal Cord. *J. Neurochem.* 35, 1458–1460. doi:10.1111/j.1471-4159.1980.tb09025.x

Kobayashi, S., Ikeda, Y., Shigeno, Y., Konno, H., and Fujii, J. (2020). γ-Glutamylcysteine Synthetase and γ-glutamyl Transferase as Differential Enzymatic Sources of γ-glutamylpeptides in Mice. *Amino Acids* 52, 555–566. doi:10.1007/s00726-020-02835-2

Li, X., Orwar, O., Persson, J., Sandberg, M., and Jacobson, I. (1993). Gamma-L-glutamyl-L-glutamate Is an Endogenous Dipeptide in the Rat Olfactory Bulb Which Activates N-Methyl-D-Aspartate Receptors. *Neurosci. Lett.* 155, 42–46. doi:10.1016/0304-3940(93)90669-C

Li, X., Orwar, O., Revesjö, C., and Sandberg, M. (1996). Gamma-glutamyl Peptides and Related Amino Acids in Rat hippocampus *In Vitro*: Effect of Depolarization and Gamma-Glutamyl Transpeptidase Inhibition. *Neurochem. Int.* 29, 121–128. doi:10.1016/0197-0186(95)00148-4

Lu, S. C. (2013). Glutathione Synthesis. *Biochim. Biophys. Acta* 1830, 3143–3153. doi:10.1016/j.bbagen.2012.09.008

Nemes, Z., Fésüs, L., Egerházi, A., Keszthelyi, A., and Degrell, I. M. (2001). N(epsilon)(gamma-glutamyl)lysine in Cerebrospinal Fluid marks Alzheimer Type and Vascular Dementia. *Neurobiol. Aging* 22, 403–406. doi:10.1016/S0197-4580(01)00224-X

Olson, C. A., Vuong, H. E., Yano, J. M., Liang, Q. Y., Nusbaum, D. J., and Hsiao, E. Y. (2018). The Gut Microbiota Mediates the Anti-seizure Effects of the Ketogenic Diet. *Cell* 173, 1728–e13. e13. doi:10.1016/j.cell.2018.04.027

AUTHOR CONTRIBUTIONS

FS, NM, PF, MaK, MeK, JG, CC-S, MR, SC, VR, MV, and JR designed and performed the experiments. NM, PF, MeK, MaK, JG, TC, MR, PC, M-CF, J-BT, CM, SC, VR, MV, and JR analyzed the data.

ACKNOWLEDGMENTS

The authors thank Guillaume Cazals from "Laboratoire de Mesures Physiques" (LMP) of the University of Montpellier for performing HPLC-MS/MS analyses.

Reichelt, K. L. (1970). The Isolation of Gamma-Glutamyl Peptides from Monkey Brain. *J. Neurochem.* 17, 19–25. doi:10.1111/j.1471-4159.1970.tb00497.x

Sebih, F., Rousset, M., Bellahouel, S., Rolland, M., De Jesus Ferreira, M. C., Guiramand, J., et al. (2017). Characterization of L-Theanine Excitatory Actions on Hippocampal Neurons: Toward the Generation of Novel N-Methyl-D-Aspartate Receptor Modulators Based on its Backbone. *ACS Chem. Neurosci.* 8, 1724–1734. doi:10.1021/acschemneuro.7b00036

Shipton, O. A., and Paulsen, O. (2014). GluN2A and GluN2B Subunit-Containing NMDA Receptors in Hippocampal Plasticity. *Philos. Trans. R. Soc. Lond. B Biol. Sci.* 369, 1–17. doi:10.1098/rstb.2013.0163

Sun, Y., Xu, Y., Cheng, X., Chen, X., Xie, Y., Zhang, L., et al. (2018). The Differences between GluN2A and GluN2B Signaling in the Brain. *J. Neurosci. Res.* 96, 1430–1443. doi:10.1002/jnr.24251

Tamborini, L., Nicosia, V., Conti, P., Dall'Oglio, F., De Micheli, C., Nielsen, B., et al. (2016). γ-Glutamyl-dipeptides: Easy Tools to Rapidly Probe the Stereoelectronic Properties of the Ionotropic Glutamate Receptor Binding Pocket. *Tetrahedron* 72, 8486–8492. doi:10.1016/j.tet.2016.11.025

Vignes, M. (2001). Regulation of Spontaneous Inhibitory Synaptic Transmission by Endogenous Glutamate via Non-NMDA Receptors in Cultured Rat Hippocampal Neurons. *Neuropharmacology* 40, 737–748. doi:10.1016/S0028-3908(00)00213-6

Yuan, H., Hansen, K. B., Vance, K. M., Ogden, K. K., and Traynelis, S. F. (2009). Control of NMDA Receptor Function by the NR2 Subunit Amino-Terminal Domain. *J. Neurosci.* 29, 12045–12058. doi:10.1523/JNEUROSCI.1365-09.2009

Conflict of Interest: The authors declare that the research was conducted in the absence of any commercial or financial relationships that could be construed as a potential conflict of interest.

Publisher's Note: All claims expressed in this article are solely those of the authors and do not necessarily represent those of their affiliated organizations, or those of the publisher, the editors, and the reviewers. Any product that may be evaluated in this article, or claim that may be made by its manufacturer, is not guaranteed or endorsed by the publisher.

Copyright © 2022 Sebih, Mokrane, Fontanel, Kayatekin, Kaabeche, Guiramand, Cohen-Solal, Cens, Rousset, Charnet, De Jésus Ferreira, Thibaud, Ménard, Cantel, Rolland, Vignes and Roussel. This is an open-access article distributed under the terms of the Creative Commons Attribution License (CC BY). The use, distribution or reproduction in other forums is permitted, provided the original author(s) and the copyright owner(s) are credited and that the original publication in this journal is cited, in accordance with accepted academic practice. No use, distribution or reproduction is permitted which does not comply with these terms.

frontiers in Pharmacology

ORIGINAL RESEARCH
published: 13 January 2022
doi: 10.3389/fphar.2021.775328

Molecular Mechanisms of Epileptic Encephalopathy Caused by KCNMA1 Loss-of-Function Mutations

Yu Yao[1†], Dongxiao Qu[2†], Xiaoping Jing[3†], Yuxiang Jia[1], Qi Zhong[1], Limin Zhuo[1], Xingxing Chen[2], Guoyi Li[2], Lele Tang[2], Yudan Zhu[2], Xuemei Zhang[4], Yonghua Ji[1]*, Zhiping Li[5]* and Jie Tao[2]**

[1]School of Medicine and School of Life Sciences, Shanghai University, Shanghai, China, [2]Department of Neurology and Central Laboratory, Putuo Hospital, Shanghai University of Traditional Chinese Medicine, Shanghai, China, [3]Department of Traditional Chinese Medicine, Shanghai Children's Hospital, Shanghai Jiao Tong University, Shanghai, China, [4]Department of Pharmacology, School of Pharmacy, Fudan University, Shanghai, China, [5]Department of Clinical Pharmacy, Children's Hospital of Fudan University, National Children's Medical Center, Shanghai, China

OPEN ACCESS

Edited by:
Werner J. Geldenhuys,
West Virginia University, United States

Reviewed by:
Yong Li,
Shanghai Jiao Tong University, China
Jacy Wagnon,
The Ohio State University,
United States

***Correspondence:**
Xuemei Zhang
xuemzhang@fudan.edu.cn
Yonghua Ji
yhji@staff.shu.edu.cn
Zhiping Li
zpli@fudan.edu.cn
Jie Tao
jietao_putuo@foxmail.com

†These authors have contributed equally to this work and share first authorship

Specialty section:
This article was submitted to Pharmacology of Ion Channels and Channelopathies, a section of the journal Frontiers in Pharmacology

Received: *13 September 2021*
Accepted: *12 November 2021*
Published: *13 January 2022*

Citation:
Yao Y, Qu D, Jing X, Jia Y, Zhong Q, Zhuo L, Chen X, Li G, Tang L, Zhu Y, Zhang X, Ji Y, Li Z and Tao J (2022) Molecular Mechanisms of Epileptic Encephalopathy Caused by KCNMA1 Loss-of-Function Mutations. Front. Pharmacol. 12:775328. doi: 10.3389/fphar.2021.775328

The gene *kcnma1* encodes the α-subunit of high-conductance calcium- and voltage-dependent K^+ (BK) potassium channel. With the development of generation gene sequencing technology, many KCNMA1 mutants have been identified and are more closely related to generalized epilepsy and paroxysmal dyskinesia. Here, we performed a genetic screen of 26 patients with febrile seizures and identified a novel mutation of KCNMA1 (E155Q). Electrophysiological characterization of different KCNMA1 mutants in HEK 293T cells, the previously-reported R458T and E884K variants (not yet determined), as well as the newly-found E155Q variant, revealed that the current density amplitude of all the above variants was significantly smaller than that of the wild-type (WT) channel. All the above variants caused a positive shift of the I-V curve and played a role through the loss-of-function (LOF) mechanism. Moreover, the β4 subunit slowed down the activation of the E155Q mutant. Then, we used *kcnma1* knockout (BK KO) mice as the overall animal model of LOF mutants. It was found that BK KO mice had spontaneous epilepsy, motor impairment, autophagic dysfunction, abnormal electroencephalogram (EEG) signals, as well as possible anxiety and cognitive impairment. In addition, we performed transcriptomic analysis on the hippocampus and cortex of BK KO and WT mice. We identified many differentially expressed genes (DEGs). Eight dysregulated genes [i.e., (Gfap and Grm3 associated with astrocyte activation) (Alpl and Nlrp10 associated with neuroinflammation) (Efna5 and Reln associated with epilepsy) (Cdkn1a and Nr4a1 associated with autophagy)] were validated by RT-PCR, which showed a high concordance with transcriptomic analysis. Calcium imaging results suggested that BK might regulate the autophagy pathway from TRPML1. In conclusion, our study indicated that newly-found point E155Q resulted in a novel loss-of-function variant and the dysregulation of gene expression, especially astrocyte activation, neuroinflammation and autophagy, might be the molecular mechanism of BK-LOF meditated epilepsy.

Keywords: BK channel, KCNMA1, loss-of-function variants, epilepsy, neuroinflammation, autophagy

INTRODUCTION

Ion channels are expressed throughout the body and perform important physiological functions, such as neuronal excitability and the tone of smooth muscle. Ion channel disease, also known as ion channelopathy, is unusually considered to be caused by the gene mutation and abnormal function of ion channel subunits (Zheng and Trudeau, 2015; Bailey et al., 2019). BK channel is widely expressed in neurons and muscles (Fagerberg et al., 2014), and is also related to functions such as membrane potential repolarization, neuronal excitability control, neurotransmitter release, innate immunity, and cochlear hair cell regulation (Petersen and Maruyama, 1984; Murrow and Fuchs, 1990; Brayden and Nelson, 1992; Robitaille and Charlton, 1992).

Human *kcnma1* encodes the α-subunit of high-conductance calcium- and voltage-dependent K^+ (BK) potassium channel. The α subunit of BK channel contains seven transmembrane fragments (S0-S6) and a large intracellular COOH terminal, consisting of two RCK domains (responsible for calcium sensing through the high-affinity Ca^{2+} binding sites), and S1-S4 acts as the voltage sensor, S5 and S6 fragments as well as P-loop form the pore region of the channel, and the (TVGYG) sequence of S6 is considered as a selective filter for potassium ions (Latorre et al., 2017). BK channel is allosterically activated by the changes of not only intracellular calcium concentration, but also membrane potential. The main sources of BK channel dysfunction are *de novo* and genetic nucleotide changes, which are roughly divided into gain-of-function (GOF) and loss-of-function (LOF) (Bailey et al., 2019). LOF mutation changes the channel activity by reducing the current amplitude or duration, while GOF mutation activates faster, increases Ca^{2+} sensitivity and current amplitude (Du et al., 2005; Moldenhauer et al., 2020).

In 2005, the abnormality of the BK channel was associated with human diseases for the first time. The substitution of aspartic acid at position 434 of the alpha subunit of BK channel by glycine would induce repolarization of action potentials, accelerate the firing rate, and increase the overall excitability of neurons, leading to systemic epilepsy (Du et al., 2005). Interestingly, the GOF phenotype of D434G mutant is due to increased BK channel Ca^{2+} sensitivity (Du et al., 2005), but in N995S (also called N999S and N1053S) mutants, the mechanism for BK GOF is the left shift of conductance-voltage (G-V) curve (Moldenhauer et al., 2020). However, different from the phenotype of the mutants above, BK channel C413Y, P805L, D984N (Bailey et al., 2019) and G354S-LOF (Du et al., 2020) mutations have been found to reduce the channel currents, with varying presence of seizures, dyskinesia, and dystonia (Bailey et al., 2019). In addition to the genetic mutation and abnormal expression of the channel itself, the physiological characteristics of the BK channel are also affected by the interaction of its α subunit and auxiliary subunits (e.g., β1-4 subunits or γ1-4 subunits). The β4 subunit is an auxiliary subunit specifically expressed by neurons, dominantly expressed in brain. The BK channel composed of it and the α subunit activates relatively slowly than the channel composed of only the α subunit. The mice lacking the β4 subunit show significant symptoms of temporal lobe epilepsy (Brenner et al., 2005). In addition, mutations in the β3 subunit also cause epilepsy (Lorenz et al., 2007).

The unique physiological behavior of the BK channel enables it to both enhance and reduce the excitability of neurons. Therefore, the role of BK channel in the pathogenesis of epilepsy is still controversial and is an increasingly intense research field (Zhu et al., 2018).

Here, we report a novel *de novo* KCNMA1 mutant (E155Q) in a patient. Electrophysiological results show that E155Q, R458T (not yet determined), and E884K (not yet determined) mutant all present a LOF phenotype. A series of behavioral experiments show that BK KO mice (as the overall animal model of LOF) have spontaneous epilepsy, motor impairment, abnormal electroencephalogram (EEG) signals, autophagic dysfunction, as well as possible anxiety and cognitive impairment. This study expands the mutation spectrum of KCNMA1-epilepsy, explores the possible mechanism of epilepsy by transcriptome, reveals the relationship between KCNMA1-LOF and epilepsy, and provides a possible molecular template for individualized treatment of epilepsy.

METHODS

Mutation Screening

Genomic DNA was extracted from peripheral blood with kit (DP348, Tiangen, Beijing, China). The samples were assessed by Shanghai Biotechnology Corp, China. KCNMA1 variants were examined in children with febrile seizures by whole-exome sequencing. This study was approved by the Institutional Review Board at Children's Hospital of Fudan University, Shanghai (National Children's Medical Center, Fudan University). And informed consent was given by the parent or guardian.

Site-Directed Mutagenesis of KCNMA1 (hBKα) Plasmids

The plasmids containing hSloα (U23767) and β4 (KCNMB4; AF 160967.1) were gifts from J.D. Lippiat (Leeds university) (Lippiat et al., 2003). Three individual point-mutations (E155Q, R458T, and E884K) were constructed. Each amino-acid substitution was introduced into the hSloα plasmid using a Hieff Mut™ Site-Directed Mutagenesis Kit (11004ES10, Yeasen, Shanghai, China) according to the manufacturer's protocol. Site-directed mutagenesis was performed with the following primers [P1: 5′-CCAGCCGACCTGGGCGGCCACTG-3′, P2: 5′-CAGTGGCCGCCCAGGTCGGCTGG-3′ (E155Q); P1: 5′-CCACCTGAGTAAAATGTGTTTTGAACAGAGCTTCAAGCTCCAG-3′, P2: 5′-CTGGAGCTTGAAGCTCTGTTCAAAACACATTTTACTCAGGTGG-3′ (R458T); P1: 5′-GACGCCAAGATGCATTTCTTGTCCTGCAGCGAA-3′, P2: 5′-TTCGCTGCAGGACAAGAAATGCATCTTGGCGTC-3′ (E884K)]. All mutant constructs were verified by sequencing (GENEWIZ, Jiangsu, China).

Cell Culture and Transfection

All experiments were performed on HEK 293T cell lines. HEK 293T cells were obtained from Shanghai cell bank of Chinese Academy of Science. The cells were both cultured in Dulbecco's modified Eagle medium (DMEM; Life Technologies, Grand Island, NY) supplemented with 10% heat-inactivated fetal bovine serum (FBS; Gibco, Grand Island, NY). Culture dishes were incubated at 37°C in a humidified atmosphere containing 5% CO_2, and subcultured approximately every 2–3 days. One day before transfection, HEK 293T cells were transferred to 24 well plates. At 90% confluence, cells were transiently transfected using Lipofectamine-3000 (Invitrogen, United States) at a ratio of 2 μl reagent with 1 μg total plasmid per well. Electrophysiological recordings from fluorescent cells were made 48 h after transfection.

Electrophysiological Recordings

Whole-cell voltage-clamp experiments were performed following the procedures described previously (Hamill et al., 1981), using an EPC-9 amplifier (HEKA Eletronik, Germany) at room temperature (21–25°C). Patch pipettes were fabricated from glass capillary tubes by PC-10 Puller (Narishige, Japan) with the resistance of 2–3 MΩ. Data acquisition and stimulation protocols were controlled by a Pentium III computer (Legend, Beijing, China) equipped with Pulse/PulseFit 8.3 software (HEKA Eletronik, Germany). Capacitance transients were cancelled. Cells with a seal resistance (Rseal) below 1 GΩ were omitted. Series resistance (Rs) was compensated (80–85%) to minimize voltage errors, and cells with an uncompensated Rs above 10 MΩ were omitted. Leak subtraction was performed using P/6 protocol. Data were low-passed at 10 kHz. Unless stated specially, for HEK 293T cells, the holding potential was −80 mV. BK channel currents were elicited by the step pulses ranging from −100 to +150 mV for 200 ms with the increments of 10 mV. The holding potentials were held at −80 mV for BK channel. Current density calculation formula (pA/pF), where pA represents the current of BK channel and pF represents the membrane area of measured cell.

Solutions

In the patch-clamp recordings, the standard bath solution for HEK 293T cells was consisted of the following components (in mM): NaCl 135, KCl 5, MgCl2·6H2O 1, CaCl2 1.8, HEPES 10, glucose 10 (pH 7.4 with NaOH). Pipette solutions for HEK 293T cells were composed of the following components (in mM): NaCl 10, KCl 117, MgSO4 4, HEPES 10, EGTA 1 (pH 7.2 with KOH). The total Ca^{2+} to be added to give the desired free concentration was calculated using the program WEBMAXC STANDARD (https://somapp.ucdmc.ucdavis.edu/pharmacology/bers/maxchelator/webmaxc/webmaxcS.htm).

Animals and Genotyping

The BK knockout (BK KO, *kcnma1* $^{-/-}$) mice were established by breeding $BK^{+/-}$ males and females. These breeding pairs provided wild-type (*kcnma1* $^{+/+}$), heterozygous (*kcnma1* $^{+/-}$) and BK KO (*kcnma1* $^{-/-}$) littermates (Wang et al., 2019), and three-month-old (10–12 weeks) male BK KO mice were subjected to subsequent experiments, such as gait analysis, morris water maze, field potential recordings, etc. The *kcnma1* knockout was generated by a frameshift mutation (− 16bp) in exon 4. Genotyping was performed with the following primers: P1: 5′-CTTCCTGCTTGTCCTTCCTC-3′, P2: 5′-CATTGCTTCAAACCCTTCCT-3′, and the PCR products were directly sequenced. In this study, all animals were randomly fed and watered in SPF standard animal facilities and were fed and watered in 21°C, 50% humidity, 12 h light: under the schedule of 12 h dark, five animals were raised in each cage, and all the animal work was carried out under the moral permission of the ethics review group of Shanghai University of traditional Chinese Medicine.

FP Recordings

Four BK KO and WT male mice were implanted with electrodes for the field potential (FP) recordings. At the age of 3 months (10–12 weeks), the animals were first anaesthetized by pentobarbital sodium [in a dose of 40 mg/kg through intraperitoneal injection (i.p.)]. Then, they were put in a stereotaxic frame (Narishige, Tokyo, Japan). Their heads were shaved and sterilized with povidone-iodine. In order to expose the sagittal, coronal, and lambdoid sutures, cut the scalp along the center. Subsequently, the recording electrode was also inserted into the lateral dorsal hippocampus (AP −2.0 mm posterior to bregma, V 1.5 mm ventral to the dura surface, and L 1.5 mm lateral to the skull midline). The reference wire is located in the electrode bundle, and the grounding electrode is placed at the front of the skull. The wound surface was sealed with dental cement. The electrode was fixed simultaneously. Data were collected only for animals with accurately positioned electrode. The FP recorded after the mice were awake. The FP signals together with synchronized video could be recorded with the OmniPlex (Plexon, United States). The mount of the head was linked to a preamplifier which is tied with the analog-digital converter box. According to Nesquet's sampling theory, take 1 Hz as the sampling frequency of local FP recording and set 50 Hz high-pass filter and 300 Hz low-pass filter to record for more than 30 min continuously. The results of local FP recording were exported as the *.pl2 file format, and offline sorter v4 software was used for visualization preview. Local FP analysis selected the same channel through MATLAB (MathWorks, United States) program to export data. The wavelet transform is used to decompose the signal of different frequencies of local FP and get the physiological rhythm of different frequencies (δ: from 0 to 4 Hz, θ: from 4 to 8 Hz, α: from 8 to 13 Hz: β: from 13 to 30 Hz, and γ: from 30 to 100 Hz). The Welch method, hamming window, and fast Fourier transform method were used to calculate the frequency domain information of the local FP in power spectrum analysis. The time domain of energy change is calculated by weighted operation. The PSD calculations follow the formula given below.

$$\int_{-\infty}^{+\infty} x^2(t)dt = \frac{1}{2\pi}\int_{-\infty}^{+\infty} \left|X(jw)\right|^2 d\omega$$

$$P = \lim_{T\to\infty} \frac{1}{2T} \int_{-T}^{T} x^2 (t)dt = \frac{1}{2\pi} \int_{-\infty}^{+\infty} \lim_{T\to\infty} \frac{1}{2T} |X_T (\omega)|^2 d\omega$$

Behavioral Observation of Epilepsy

In order to eliminate the possibility of the human error, behavioral observations are double-blind during experiments. The Racine's five-point scale (Racine, 1972), improved by Fathollahi et al. (1997), was employed to classify the seizure-like behavior at different stages. Stage 0 is termed no response; stage 1 is called facial and ear twitching; stage 2 is myoclonic jerks without an upright position; stage 3 represents myoclonic jerks and upright position with bilateral forelimb clonus; stage 4 stands for clonic-tonic seizure; stage 5 is named generalized clonic-tonic seizures and loss of postural control. The severity of seizures in BK KO mice was evaluated according to the grade and time of seizures. The least interval between two countable seizures was set as 5 s during the quantification of all seizure numbers.

Immunofluorescence Staining

Frozen sections were permeabilized with 0.5% Triton X-100, and blocked for 1 h at room temperature (RT) with 5% bovine serum albumin. Without washing, sections were incubated overnight at 4°C with primary antibodies. These include against LC3B (1:200 dilution; ab48394; Abcam), LAMP1(1: 500 dilution; ab25630; Abcam), and Iba-1 (1:500 dilution; ab178846; Abcam). washing four times in PBS (4 × 5 min), sections were incubated with goat anti-rabbit antibody conjugated with Alexa Fluor 594 (for LC3B; 1:200 dilution; ab150080; Abcam); goat polyclonal secondary antibody to mouse conjugated with Alexa Fluor 488 (for LAMP1; 1:200 dilution; ab150113; Abcam) and Alexa Fluor 350-labeled goat anti-rabbit IgG (H + L) (for Iba-1; 1:500 dilution; A0408; Beyotime) for 1 h at RT, washing four times in PBS (4 × 5 min). Slices were cover-slipped with 50% glycerin. Fluorescence images were captured using a Virtual/Digital Slice Microscope (Olympus, Tokyo, Japan). Quantification was performed using ImageJ software.

Calcium Imaging

HEK293T cells, co-transfected with pcDNA3-TRPML1-GCaMP3, gifted from Prof. Xu HX (University of Michigan, United States), were kept in HBSS (Hank's balanced salt solution) at RT for 30 min. Confocal imaging was performed by using a Zeiss confocal LSM 880, a laser scanning microscope system (Zeiss, Germany). GCaMP3 was evoked with a laser wavelength at 488 nm, and the fluorescence images were collected with the resolution of 512 × 512 pixels. The ROI (regions of interest; 3 × 3 pixels) were selected in individual HEK293T cells by Zeiss LSM Image Browser (Zeiss, Germany) to track the changes in the ratio of fluorescence intensity. The ratio (F/F0) of fluorescence intensity was calculated by dividing fluorescence intensity at time t (F) with the beginning fluorescence intensity (F0) of the experiment.

Y-Maze Test

Y-maze test was performed as previously described (Watanabe et al., 2011). Exploratory activity was measured using a Y-maze apparatus (arm length: 40 cm, arm bottom width: 10 cm, arm upper width: 10 cm, height of wall: 12 cm). The floor and the wall of the maze is made of black PVC plastic. Each subject was placed in the arm I of the Y-maze field. The alteration (%) and total distance (m) was recorded using a modified version of the image software. Data were collected for a period of 10 min.

Gait Analysis

We analyzed gait of the mice during walk/trot locomotion by ventral plane videography as described (Hampton et al., 2004; Koshimizu et al., 2014), using digigait imaging system (Mouse Specifics Inc.). This system enables mice to walk on a motorized transparent treadmill belt, and the software automatically identifies the stance and swing components of stride and calculates stride length, print area, mean intensity, and swing speed. Briefly, we placed the mice on a treadmill belt that moves at constant speed. We collected digital video images of mice.

Morris Water Maze Test

A dark blue pool (diameter: 120 cm, depth: 50 cm) was placed in a quiet room and filled with white-colored water. The water was equilibrated to room temperature (between 22 and 23°C) before the MWM test. Colored papers with a variety of different shapes were posted around the pool as visual cues. A platform of 10 cm in diameter was used. For hidden platform trials, the platform was positioned 1.5 cm below water surface. The MWM test was performed in the period of 11AM—3PM to minimize circadian effects. The BK KO and control mice were tested in same days, and testing sequences for individual mice were altered in each test day. A protocol with 5 days of visible platform trials and 1 day of hidden platform trials were employed. In the trials, individual mice underwent four trials per day, and the maximal time for each trial was 60 s. If mice did not find the platform within 60 s, they were guided to the platform by the experimenter's hand and allowed to stay on the platform for 60 s. For the probe tests in which the platform was removed from the pool, individual mice underwent a trial of 60 s in each quadrant. If mice exhibited convulsions shortly before or during a trial, they were allowed to recover for 20–30 min before next trial. Any trial interfered with convulsions were excluded from analysis. Frequency and the time in aim-quadrant during the probe trials were analyzed. Group data for the BK KO and WT mice were compared.

Open Filed Test

The open field behavior experiment device is a very effective device for measuring spontaneous and exploratory behaviors to measure the degree of anxiety in mice. Place the animal in an unknown environment with walls around it, and the rodents will spontaneously tend to move on the edges rather than the open center of the area. In this experiment,

TABLE 1 | Clinical data of 26 patients with one LOF variants in BK channels.

Patient ID genomic variant	2 p. E155Q	13 NA	4 p. E471G	20 c. 344A > G
Gene	KCNMA1	SCN1A	UPF3B	Panel ASXL3
De novo variant	Yes	NA	NA	NA
Gender	M	M	F	F
Age	6	6	17	3
Course (years)	5	5	8	2
Age of seizure onset (years)	1	1	9	1
Epilepsy details	Tonic-clonic limbs, unconsciousness, eyes rolled up and staring, no answer	Tonic-clonic limbs, unconsciousness, foaming at the mouth, lasting 2–10min	Often onset in sleep and early morning, accompanied by disturbances in consciousness and urinary incontinence	Series of spasmodic seizures
Anticonvulsant treatment	VPA	VPA, LEV, CLB, Ketogenic diet	OXC, VPA	VPA
EEG features	Sharp wave, sharp slow wave and spike slow wave. Rhythmic energy intensity of δ and θ increased	Sharp wave and sharp slow wave	A few sharp waves, sharp slow waves and spike slow waves	Peak rhythm disorder with intermittent phenomenon
MRI	NA	Normal	Normal	Brain dysplasia, left brain atrophy
Family history of epilepsy	No	No	No	Yes
Other details	Premature delivery 2/26 History of head trauma 2/26 History of severe pneumonia 1/26 History of suffocation and oxygen 2/26 Developmental delay 3/26 EEG abnormality 11/26 Abnormal MRI 5/26 Family history of epilepsy 2/26			

F, female; M, male; NA, data not available; VPA, valproate acid; LEV, levetiracetam; CLB, clobazam; OXC, oxcarbazepine.

the device is composed of a black polystyrene box (50 × 50 × 50 cm), which is divided into two areas: the outer square (periphery) and the inner square (center). Each mouse was placed in the center of the box and explored freely for 10 min. Observe their behavior through the animal video monitoring with the behavior software, and measure the stay time (s), the total distance of movement in the central area (m), the average speed (mm/s) through the computer tracking system, evaluate spontaneous and exploratory behavior.

Tissue Sample Collections

Three different BK KO and WT adult mice were randomly sampled, sacrificed, and their cortices and hippocampi extracted under 2-min, frozen, and stored at −80°C.

RNA Extraction

Total RNA was extracted from the mouse cortex/hippocampus using TRIzol Reagent (15596018, Invitrogen) according to the manufacturer’s protocol. Using the a nanodrop (Thermo Scientific NanoDrop 2000c Spectrophotometer), the RNA concentration of each sample was determined by measuring the absorbance at 260 nm (A260), and its purity was determined by the ratio of the absorbance measured at 260 nm (A260) and 280 nm (A280). The ratios of A260/A280 between 1.9 and 2.1 were considered acceptable.

Library Preparation for Transcriptome Sequencing

A total amount of 2 μg RNA per sample was used as input material for the RNA sample preparations. Sequence libraries were generated using NEBNext UltraTM RNA Library Prep Kit for Illumina (NEB, United States) following manufacturer’s recommendations and index codes were added to attribute sequences in each sample. Briefly, mRNA was purified from total RNA using poly-T oligo-attached magnetic beads. Fragmentation was carried out using divalent cations under elevated temperature in NEBNext First Strand Synthesis Reaction Buffer (5×). First strand cDNA was synthesized using random hexamer primer and M-MuLV Reverse transcriptase (RNase H). Second strand cDNA synthesis was subsequently performed using DNA Polymerase I and RNase H. Remaining overhangs was converted into blunt ends to exonuclease/polymerase activities. After adenylate of 3′ ends of DNA fragments, NEBNext Adaptor with hairpin loop structure was ligated to prepare for hybridization. In order to select cDNA fragments of preferentially 200–250 bp in length, the library fragments were purified with AMPure XP system (Beckman Coulter, Beverly, United States). Then 3 μl USER Enzyme (NEB, United States) was used with size-selected, adaptor-ligated cDNA at 37°C for 15 min followed by 5 min at 95°C before PCR. Then PCR was performed with Phusion High-

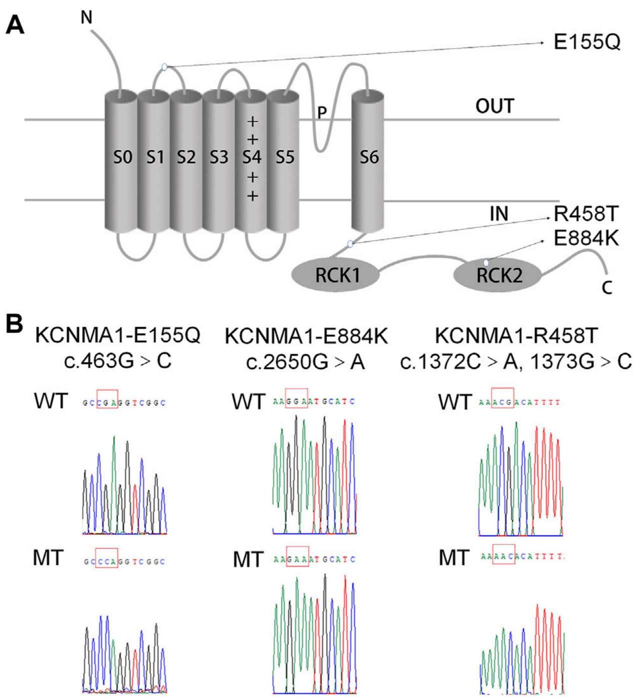

FIGURE 1 | Location and sequencing of the KCNMA1 variants. **(A)** Predicted transmembrane topology of KCNMA1 depicting the location of the variants. **(B)** DNA sequencing identified the mutations in the constructed hBKα plasmid. The mutation sites are marked by a red square.

Fidelity DNA polymerase, Universal PCR primers and Index (X) Primer. At last, PCR products were purified (AMPure XP system) and library quality was assessed in the Agilent Bioanalyzer 2,100 system.

Clustering and Sequencing

The clustering of the index-coded samples was performed on a cBot Cluster Generation System using TruSeq PE Cluster Kit v4-cBot-HS (Illumia) according to the manufacturer's instructions. After cluster generation, the library preparations were sequenced on an Illumina Hiseq 4,000 platform and paired-end 150 bp reads were generated.

Differential Expression Genes Analysis

Differential expression analysis of two conditions/groups was performed using the DESeq R package (1.10.1). DESeq2 provides statistical routines for determining differential expression of digital gene expression data using a model based on the negative binomial distribution. The resulting *p* values were adjusted using the Benjamini and Hochberg's approach to controlling the false discovery rate. Genes with pvalue <0.05 and |log2FC| > 0.58 found by DESeq were assigned as differentially expressed.

GO Enrichment Analysis

Gene Ontology (GO) enrichment analysis of the DEGs was implemented by the GOseq R packages based Wallenius non-central hyper-geometric distribution, which can adjust for gene length bias in DEGs.

KEGG Pathway Enrichment Analysis

KEGG is a database resource for understanding high-level functions and utilities of the biological system, such as the cell, the organism and the ecosystem, from molecular level information, especially large-scale molecular datasets generated by genome sequence and other high-throughput experimental technologies (http//:www.genome.Jp/kegg/) (Jiang et al., 2018). We used KOBAS (Mao et al., 2005) software to test the statistical enrichment of differential expression genes in KEGG pathways.

PCR Primer Design and Testing

We first looked through NCBI's Primer-Bank (https://pga.mgh.harvard.edu/primerbank/) to find PCR primers for selected genes. Primers were checked for specificity using NCBI's Primer-BLAST program (https://www.ncbi.nlm.nih.gov/tools/primer-blast/) against RefSeq RNA to ensure no non-specific matches. When designing primers that could match multiple transcript variants, their sequences were aligned in ClustalW (http://www.genome.jp/tools/clustalw/), and only the primers that amplified a consensus region were used. All PCR primers were purchased from GENEWIZ (Jiangsu, China) and listed in **Supplementary Table S3** with sizes of the resulting PCR products in base pairs (bp).

Real-Time RT-PCR Validation of Selected DEGs

To validate the transcriptome gene expression data, six DEGs identified by transcriptome were validated by real-time RT-PCR using QuantityNova SYBR Green PCR Kit (208052, Qiagen, Valencia, CA). RT- PCR was performed in a one-step RT-PCR process according to the protocol on Roche480II using 30 ng RNA. Housekeeping gene β-actin was used as endogenous control. RNA was first reverse transcribed into cDNA at 65°C for 5 min. After enzyme activation at 95°C for 2 min, PCR was carried out at 95°C for 5 s and 60°C for 10 s for 45 cycles. For RT-PCR analysis, each sample was run in triplicates. Comparative Ct method (delta Ct method) was used to calculate the fold differences between BK KO and WT groups.

Statistical Analysis

Data were analyzed with Origin 8.5 (OriginLab, United States), Excel 2016 (Microsoft, WA) and Prism 6 (GraphPad software, San Diego, CA). Data are presented as the mean ± standard error of the mean (SEM). Student's t-test or one-way ANOVA was used to assess the statistical significance of differences. When $p < 0.05$, differences were accepted as significant.

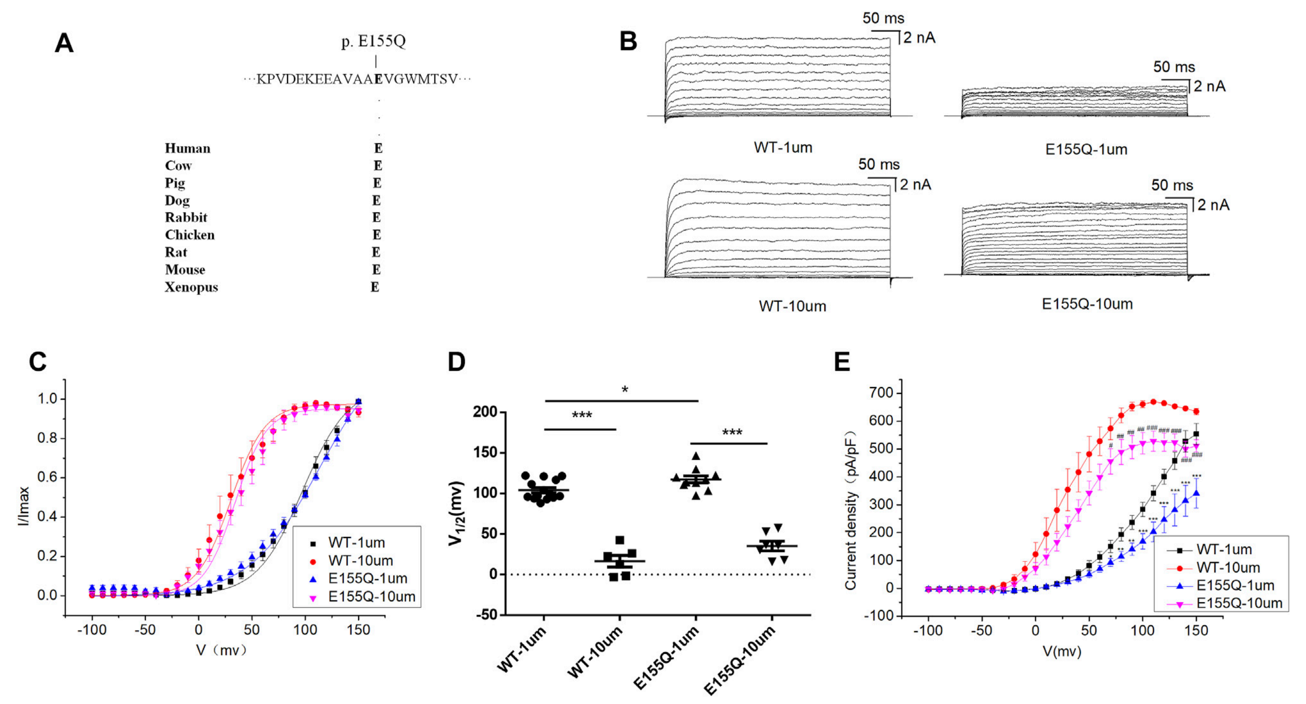

FIGURE 2 | Electrophysiological characterization of variant E155Q. **(A)** The E155Q variant occur at an evolutionarily conserved amino acid residues. **(B)** Representative macroscopic currents of WT and mutant BK channels with variant E155Q from whole-cell patch experiments in the presence of 1 and 10 μm Ca^{2+}. **(C)** The I-V curves of WT and E155Q mutant BK channels are shown at 1 and 10 μm Ca^{2+}. The I-V curves are fitted by Boltzmann function (solid lines) with V1/2 and slope factor at nominal at 1 μm Ca^{2+} [97.5 ± 4.1 mV, 21.4 ± 2.1 WT, and 113.4 ± 6.4 mV, 33.2 ± 3.3 p.(E155Q)] and at 10 μm Ca^{2+} [30.4 ± 2.4 mV, 15.9 ± 0.8 WT, and 34.2 ± 2.9 mV, 14.6 ± 1.6 p.(E155Q)]. **(D)** Scatter plots of voltage at half-maximal activation (V1/2) for WT and variants. **(E)** The current density of WT and E155Q mutant BK channels are shown at 1 and 10 μm Ca^{2+}. The data are presented as mean ± SEM. (Compared with WT-1um, *$p < 0.05$, **$p < 0.01$, ***$p < 0.001$. Compared with WT-10um, #$p < 0.05$, ##$p < 0.01$, ###$p < 0.001$. n = 6–14/group).

RESULTS

Identification of a *de novo* Variant in KCNMA1 (hbkα) From a Patient With Febrile Seizures

In this study, among the 26 clinical patients, two patients had a history of head trauma, two patients had a history of asphyxia and oxygen inhalation, two patients had premature delivery and one patient had severe pneumonia, which might be the inducement of epilepsy. In addition, eleven patients had abnormal EEG, five patients had abnormal MRI, and two patients had a family history of epilepsy (**Table 1**).

A novel variant c.463G > C [p.(E155Q)] in a patient with febrile seizures was identified. The patient, male, full-term born on August 26, 2015, bw3500 g, had a history of oligohydramnios and intrauterine distress, and no family history of epilepsy. He had several histories of febrile convulsions, which was characterized by tetanic clonus of limbs, unconsciousness, upturned eyes, unable to call, hyperactivity, repeated daze, poor language development and developmental delay. There was no abnormality in blood tandem mass spectrometry, and the energy of urine tandem mass spectrometry was disordered. EEG showed that there were some sharp waves, and spike waves on both sides of the brain. We predicted that the location of amino-acid E155 was in the domain S1/S2 linker of BK α (**Figure 1A**). A previous study already reported that R458T and E884K mutants were located in the domain S6/RCK1 cytoplasmic linker and the RCK2 domain of BKα (**Figure 1A**). Therefore, we constructed three plasmids: KCNMA1-E155Q, KCNMA1-R458T, and KCNMA1-E884K (**Figure 1B**).

Electrophysiological Characteristics of BK Channel LOF Variant E155Q

E155Q variant is highly conserved among different species during evolution (**Figure 2A**). To determine whether the c.463 G > C [p.(E155Q)] variant had an effect on BK channel function, we expressed mutant E155Q channel and control wild-type (WT) channel, recorded potassium currents, and analyzed the current voltage relationship. The results showed that in 1 and 10 μM free Ca^{2+} concentration, the macro currents amplitude of E155Q mutant was always smaller than that of WT (**Figure 2B**). Moreover, we found that the I-V curve of the mutant E155Q moved in the direction of positive potential (**Figures 2C,D**). Regardless of whether the free calcium concentration was 1 μM ($p < 0.05$ at 70 mv, $p < 0.01$ at 80–90 mv, $p < 0.001$ at 100–150 mv) or 10 μM ($p < 0.05$ at 70 mv, $p < 0.01$ at 80 mv −100 mv, $p < 0.001$ at 110 mv −150 mv), the E155Q mutant

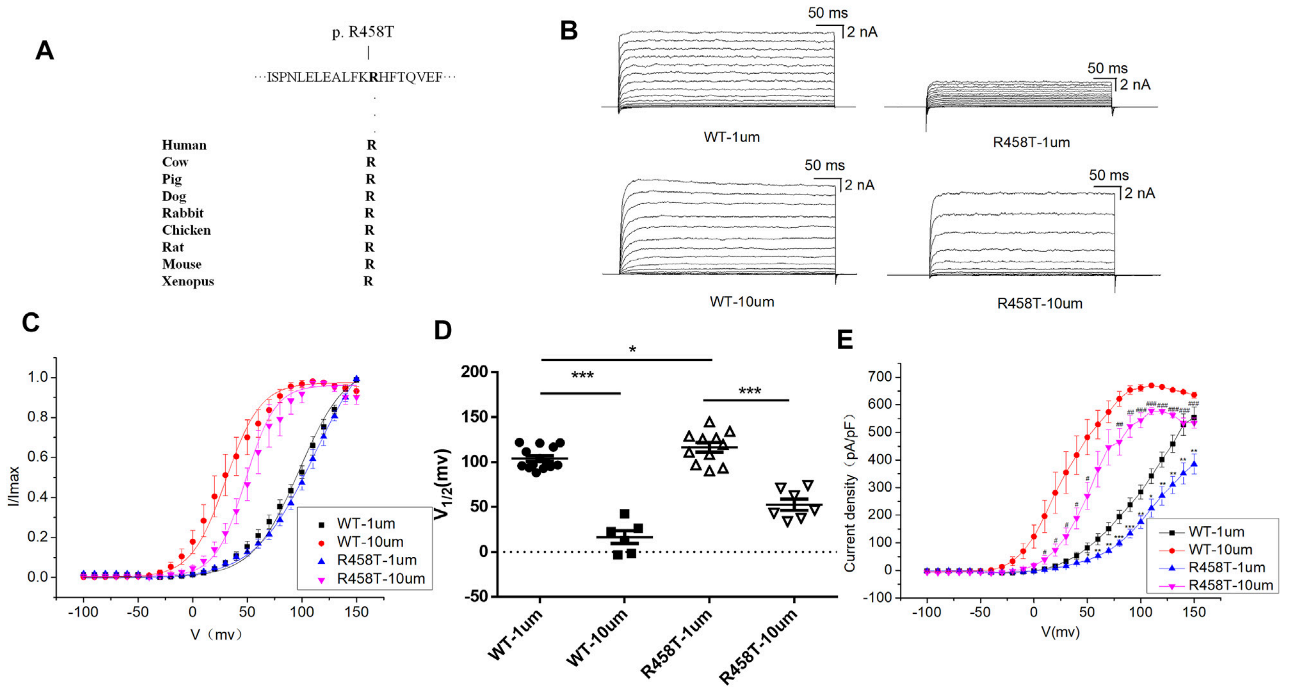

FIGURE 3 | Electrophysiological characterization of variant R458T. **(A)** The R458T variant occur at an evolutionarily conserved amino acid residues. **(B)** Representative macroscopic currents of WT and mutant BK channels with variant R458T from whole-cell patch experiments in the presence of 1 and 10 μm Ca^{2+}. **(C)** The I-V curves of WT and R458T mutant BK channels are shown at 1 and 10 μm Ca^{2+}. The I-V curves are fitted by Boltzmann function (solid lines) with V1/2 and slope factor at nominal at 1 μm Ca^{2+} [97.5 ± 4.1 mV, 21.4 ± 2.1 WT, and 111.9 ± 6.3 mV, 27.5 ± 2.4 p.(R458T)] and at 10 μm Ca^{2+} [30.4 ± 2.4 mV, 15.9 ± 0.8 WT, and 48.2 ± 2.6 mV, 13.7 ± 1.1 p.(R458T)]. **(D)** Scatter plots of voltage at half-maximal activation (V1/2) for WT and variants. **(E)** The current density of WT and R458T mutant BK channels are shown at 1 and 10 μm Ca^{2+}. The data are presented as mean ± SEM. (Compared with WT-1um, $^*p < 0.05$, $^{**}p < 0.01$, $^{***}p < 0.001$. Compared with WT-10um, $\#p < 0.05$, $\#\#p < 0.01$, $\#\#\#p < 0.001$. n = 6–14/group).

significantly reduced the current density of BK when the stimulation voltage reached 70–150 mv (**Figure 2E**, n = 6–14/group). Thus, the E155Q mutant is identified as a LOF variant.

Effect of the β4 Subunit on the BK Channel Variant E155Q

The β4 subunit is an auxiliary subunit specifically expressed by neurons, dominantly expressed in brain. To determine whether the β4 subunit and the E155Q mutation interact, we co-transformed the β4 subunit and the E155Q mutant in HEK 293T cells. Compared with E155Q mutant, the β4 subunit had no effect on the macro current density amplitude, I-V curve, or V1/2 (**Supplementary Figures S1A–D**). Further analysis of the activation time constant (τ) revealed that τ of the E155Q+ β4 mutant was significantly greater than that of the E155Q mutant (**Supplementary Figure S1E**, n = 6–9/group), and thus the β4 subunit slowed down the activation of the E155Q mutant.

Electrophysiological Characteristics of BK Channel LOF Variant R458T

R458T variant is highly conserved among different species during evolution (**Figure 3A**). We used the HEK 293T cell system to express and compare WT and mutant R458T channels. The results showed that R458T mutant significantly reduced the macro currents and current density amplitude of BK channel (**Figures 3B,E**). The I-V curve of R458T mutant shifted to the positive voltage direction (**Figures 3C,D**). Noticed, the smaller Ca^{2+}-induced leftward shift of the I–V in the mutant suggests that its apparent Ca^{2+} sensitivity is less than that of the WT, further exacerbating the LOF phenotype.

E884K Variant in the RCK2 Domain Markedly Reduced the Amplitude of the BK Currents

E884K variant is highly conserved among different species during evolution (**Figure 4A**). The E884K variant significantly reduced the amplitude of the BK currents (**Figure 4B**). Moreover, the I-V curve of E884K variant shifted to the positive voltage direction similar to E155Q and R458T (**Figures 4C,D**). Regardless of whether the free calcium concentration was 1 μM ($p < 0.01$ at 50 mv, $p < 0.001$ at 60–150 mv) or 10 μM ($p < 0.05$ at 50–60 mv, $p < 0.01$ at 70–130 mv, $p < 0.001$ at 140–150 mv) the E884K mutant markedly reduced the current density of BK when the stimulation voltage reached 50–150 mv (**Figure 4E**). Therefore, the E884K variant is also considered as a LOF variant.

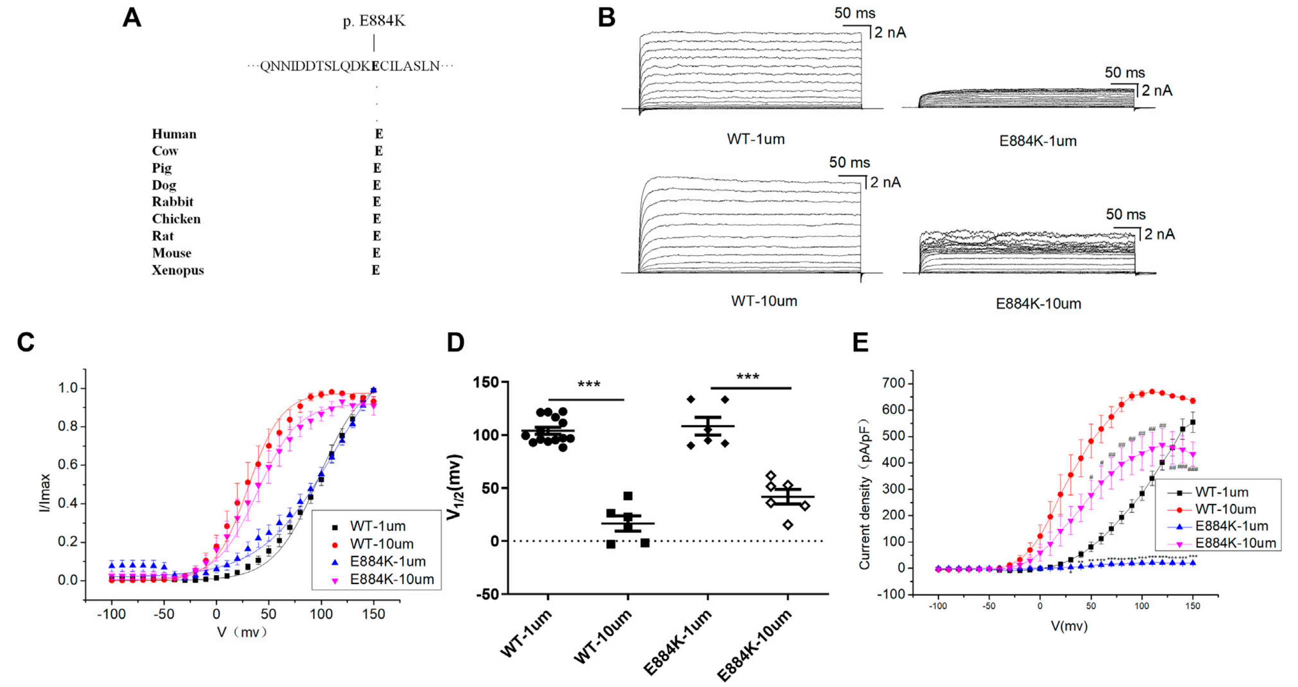

FIGURE 4 | Electrophysiological characterization of variant E884K. **(A)** The E884K variant occur at an evolutionarily conserved amino acid residues. **(B)** Representative macroscopic currents of WT and mutant BK channels with variant E884K from whole-cell patch experiments in the presence of 1 and 10 μm Ca^{2+}. **(C)** The I-V curves of WT and E884K mutant BK channels are shown at 1 and 10 μm Ca^{2+}. The I-V curves are fitted by Boltzmann function (solid lines) with V1/2 and slope factor at nominal at 1 μm Ca^{2+} [97.5 ± 4.1 mV, 21.4 ± 2.1 WT, and 112.0 ± 6.7 mV, 34.8 ± 4.2 p.(E884K)] and at 10 μm Ca^{2+} [30.4 ± 2.4 mV, 15.9 ± 0.8 WT, and 39.3 ± 2.2 mV, 19.3 ± 1.4 p.(E884K)]. **(D)** Scatter plots of voltage at half-maximal activation (V1/2) for WT and variants. **(E)** The current density of WT and E884K mutant BK channels are shown at 1 and 10 μm Ca^{2+}. The data are presented as mean ± SEM. (Compared with WT-1um, $^{*}p < 0.05$, $^{**}p < 0.01$, $^{***}p < 0.001$. Compared with WT-10um, $\#p < 0.05$, $\#\#p < 0.01$, $\#\#\#p < 0.001$. n = 6–14/group).

BK Channel Knockout Mediates Epilepsy

BK channel knockout (BK KO, *kcnma1* $^{-/-}$) mice were generated by the deletion of exon four of *kcnma1* (gene encoding the α subunit of BK, BKα) using the CRISPR/Cas9 strategy (**Figure 5A**) (Wang et al., 2019). The BK KO mice, which carried a 16 bp fragment deletion in exon 4, was identified by PCR (**Figure 5B**) and confirmed by sequencing (**Figure 5C**). By observing movie (**Supplementary Movies S1, S2**), it is more intuitive to show that BK KO mice have an epileptic phenotype. Through continuous recording for 2 h, it was found that BK KO mice showed nearly 25% of grade 4–5 convulsive seizures (**Figure 5D**, n = 3). In addition, the seizure time and grade of BK KO mice were significantly greater than those of WT mice (**Figure 5D**, $p < 0.001$, n = 3). Thus, we found that BK KO mice have spontaneous epileptic symptoms, mainly manifested as generalized tonic clonic seizures and absence seizures (**Figure 5D**), which corresponds to the epileptic phenotype of human BK channel functional inactivation gene mutation (BK channel frameshift mutation) (Tabarki et al., 2016).

FP Characteristics of BK KO Mice

Then, to determine differences of BK KO and control mice in EEG levels, the power spectral density (PSD) of BK KO and control mice on was directly measured. We compared the field potential (FP) signals of BK KO and control mice, and differences in FP activity were visualized via using heat maps of spectral density generated by OmniPlex software (Plexon, United States). Compared with the control mice, BK KO mice had no significant differences on the FP activity (**Figure 6A**). The results showed that the EEG of WT mice presented basic waves with low frequency and amplitude, and there were no abnormal epileptic waves. The EEG of BK KO mice showed the basic wave with lower frequency and amplitude, accompanied by a small number of spike-waves (**Figure 6B**). The energy intensity values of five common rhythms collected by EEG were counted, δ Wave (0.5–4 Hz) belongs to a slow wave, which is the main rhythm in the sleep state of mice. Compared with control group, the δ rhythmic energy intensity of BK KO mice decreased significantly (**Figure 6C**, $p < 0.001$, n = 4). θ wave (4–7 Hz) and δ wave is similar to the rhythm that appears during sleep. θ rhythmic energy intensity in BK KO mice was lower than that in control group (**Figure 6C**, $p < 0.001$, n = 4). α wave (8–13 Hz) is the normal brain wave of mice. Compared with control group, α rhythmic energy intensity of BK KO mice increased significantly (**Figure 6C**, $p < 0.001$, n = 4). β wave (15–30 Hz) is the main rhythm when the brain is excited. Compared with control group, β rhythmic energy intensity in BK KO mice increased significantly (**Figure 6C**, $p < 0.001$, n = 4). γ wave (>30 Hz) belongs to a fast wave that occurs during rapid eye movement sleep and γ rhythmic energy intensity in BK KO mice decreased

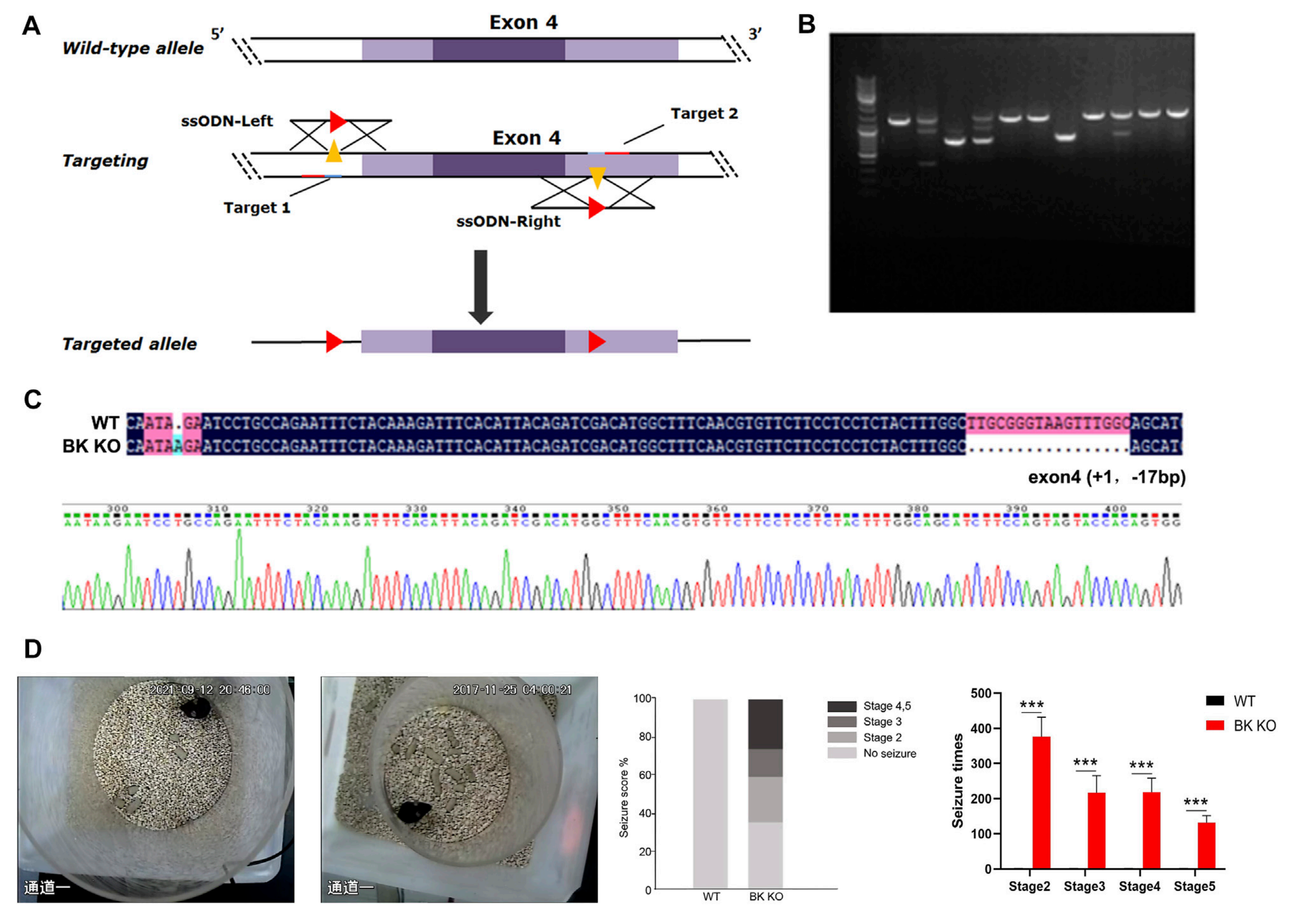

FIGURE 5 | Construction of BK KO mice with spontaneous epilepsy. **(A)** Schematic outlining the generation of BK knockout mice using the CRISPR/Cas9 system. The targeting sites of KCNMA1 (gene encoding the α subunit of BK, BKα) are shown. **(B,C)** BK KO mice were established by breeding $BK^{+/-}$ males and females. The targeted fragment of KCNMA1 was amplified by PCR using genomic DNA templates, and the BK channel deletion was confirmed by sequencing. Genome sequencing of BK KO mice showed a frameshift mutation (- 16 bp) in exon 4. **(D)** Spontaneous epileptic behavior of BK KO mice. The proportion of different seizure stages in BK KO/WT mice was observed for 2 h (***$p < 0.001$, $n = 3$).

significantly (**Figure 6C**, $p < 0.01$, $n = 4$). Moreover, the PSD of total frequency waves of BK KO mice was obviously smaller than that of the control group (**Figure 6D**). Thus, the slow-wave power was reduced, normal and excited wave power was enhanced in BK KO mice.

Motor Impairment in BK KO Mice

Using the catwalk gait analysis system, a number of gait abnormalities were identified. By observing movie (**Supplementary Movies S3, S4**), it can be intuitively found that BK KO mice have abnormal gait and shorter stride phenotype (**Figures 7A–C**). The print area (RF, RH, LF, LH) of BK KO mice was narrower than that of control mice (**Figure 7D**, $p < 0.001$, $n = 5$). Moreover, the mean intensity (RF, LF) of BK KO mice less than that of control mice (**Figure 7D**, $p < 0.01$, $n = 5$). Swing speed and stride length were smaller, with an unsteady gait pattern in the BK KO mice, compared to the gait of control mice (**Figure 7D**, $n = 5$). Results revealed BK KO mice presented motor impairment.

In addition, the total distance (**Supplementary Figure S2A**, $p < 0.001$, $n = 8$), average speed (**Supplementary Figure S2C**, $p < 0.001$, $n = 8$) of BK KO mice significantly reduced in the open field, and the total distance (**Supplementary Figure S2G**, $p < 0.001$, $n = 8$) of BK KO mice markedly decreased in the *Y*-maze test. Thus, BK KO mice also showed motor impairment in the Y-maze and open field test. What' more, BK KO mice showed smaller time in the central area (**Supplementary Figure S2B**, $p < 0.001$, $n = 8$), frequency and aim-quadrant stay time (**Supplementary Figures S2D,E**, $p < 0.001$, $p < 0.05$, $n = 6$), and the percentage of spontaneous alternation (**Supplementary Figure S2F**, $p < 0.001$, $n = 8$) as compared with the WT mice. Although motor impairment suggested that it might have an impact on anxiety and cognitive impairment of BK KO mice, there were also literatures supporting that BK KO have the cognitive impairment phenotype without the interference factor of locomotion (Sausbier et al., 2004). This strongly suggested that BK KO mice might be accompanied by anxiety and cognitive impairment in addition to the phenotype of motor impairment.

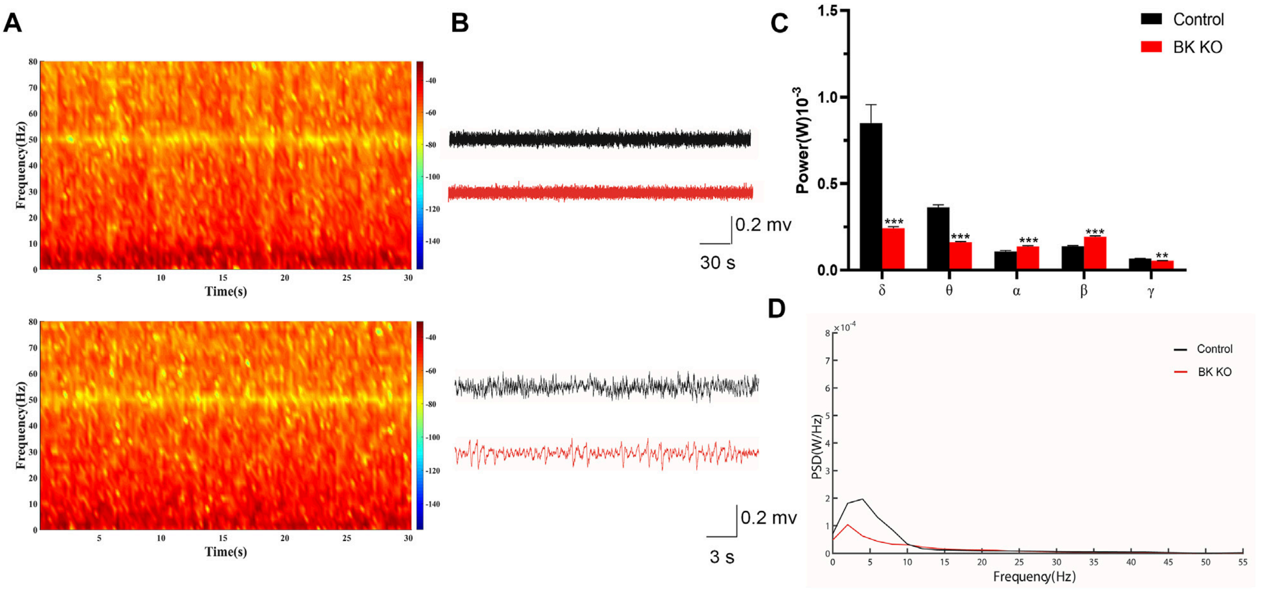

FIGURE 6 | *In vivo* multichannel EEG recording of mice. **(A,B)** FP signals and spectral heat maps from a representative WT (black) and BK KO (red) mice are shown, respectively. **(C)** Spectral analysis of PSD values on different frequency δ, θ, α, β, and γ waves in each group. **(D)** The PSD of mice in each group (Compared with control group, *$p < 0.05$, **$p < 0.01$, ***$p < 0.001$, $n = 4$).

Transcriptome Sequencing and Analysis of Hippocampus and Cortex of BK KO Mice

In this study, we used RNA-Seq to analyze the transcriptome of BK KO/WT mice hippocampus and cortex, and performed transcriptome profiling to characterize the differentially expressed genes. A total of 652 genes were screened with the threshold of significance at $p < 0.05$ and |log2foldchange| > 0.58, among which 382 genes were down-regulated and 270 genes were up-regulated in hippocampus tissues. In cortex tissues, we detected a total of 561 differentially expressed genes with the threshold of significance at $p < 0.05$ and |log2foldchange| > 0.58, including 162 up-regulated genes and 399 down-regulated genes (**Figure 8A**).

In order to better understand the potential functions of differentially expressed genes, Gene Ontology (GO) enrichment analysis was carried out to assess the involved pathways. Biological process pathway in GO analysis results showed that development process and biological adhesion were enriched (**Figure 8B**). The results of kyoto encyclopedia of genes and genomes (KEGG) showed that insulin secretion, axon guidance, p53 signaling pathway, HIF-1 signaling pathway and calcium signaling pathway were enriched in hippocampus (**Figure 8C**). On the other hand, cortical KEGG results showed that cell adhesion molecules (CAMs), ECM-receptor interaction, phagosome and calcium signaling pathway were enriched (**Figure 8C**).

Genes Were Verified

The transcriptomic results were compared with NCBI genebank (https://www.ncbi.nlm.nih.gov/gene/?term=), and it was found that DEGs in **Supplementary Tables S1, S2** were closely related to epilepsy, astrocyte activation, neuroinflammation and microglia autophagy. Through RT-PCR, we used three groups of the cortex and hippocampus between WT and BK KO mice to verify the bold eight genes in the **Supplementary Tables S1, S2**. (Foldchange was larger in the same group of genes). Gfap and Cdkn1a gene highly expressed in BK KO mice (**Figure 9**, $p < 0.01$, $n = 3$). There were three genes that were lowly expressed in BK KO mice, Grm3, Alpl and Nr4a1 (**Figure 9**, $p < 0.05$, $n = 3$). In all, the results of RT-PCR and transcriptomics were highly consistent. We continued to explore the possible mechanisms of epilepsy through transcriptome.

Abnormal Autophagy in BK KO Mice

Autophagy is a normal catabolic process in cells. Various types of biological macromolecules undergo degradation and circulation through lysosomal digestion to maintain cell homeostasis. Improving the neuroinflammation response in the pathogenesis of multiple sclerosis (MS) can be achieved by enhancing autophagy (Liang and Le, 2015; Feng et al., 2017). This suggests that neuroinflammation and autophagy can influence each other, which in turn affects the progression of CNS-related diseases.

Transcriptomics results showed that there were 11 differentially expressed genes (DEGs) related to microglia autophagy in hippocampus and 5 DEGs related to microglia autophagy in cortical tissues (**Supplementary Table S2**). In order to further explore the role of autophagy in epilepsy, immunofluorescence experiments were performed on the hippocampus of WT and BK KO mice. In the hippocampal CA3 region of Ctrl group mice, autophagosome marker

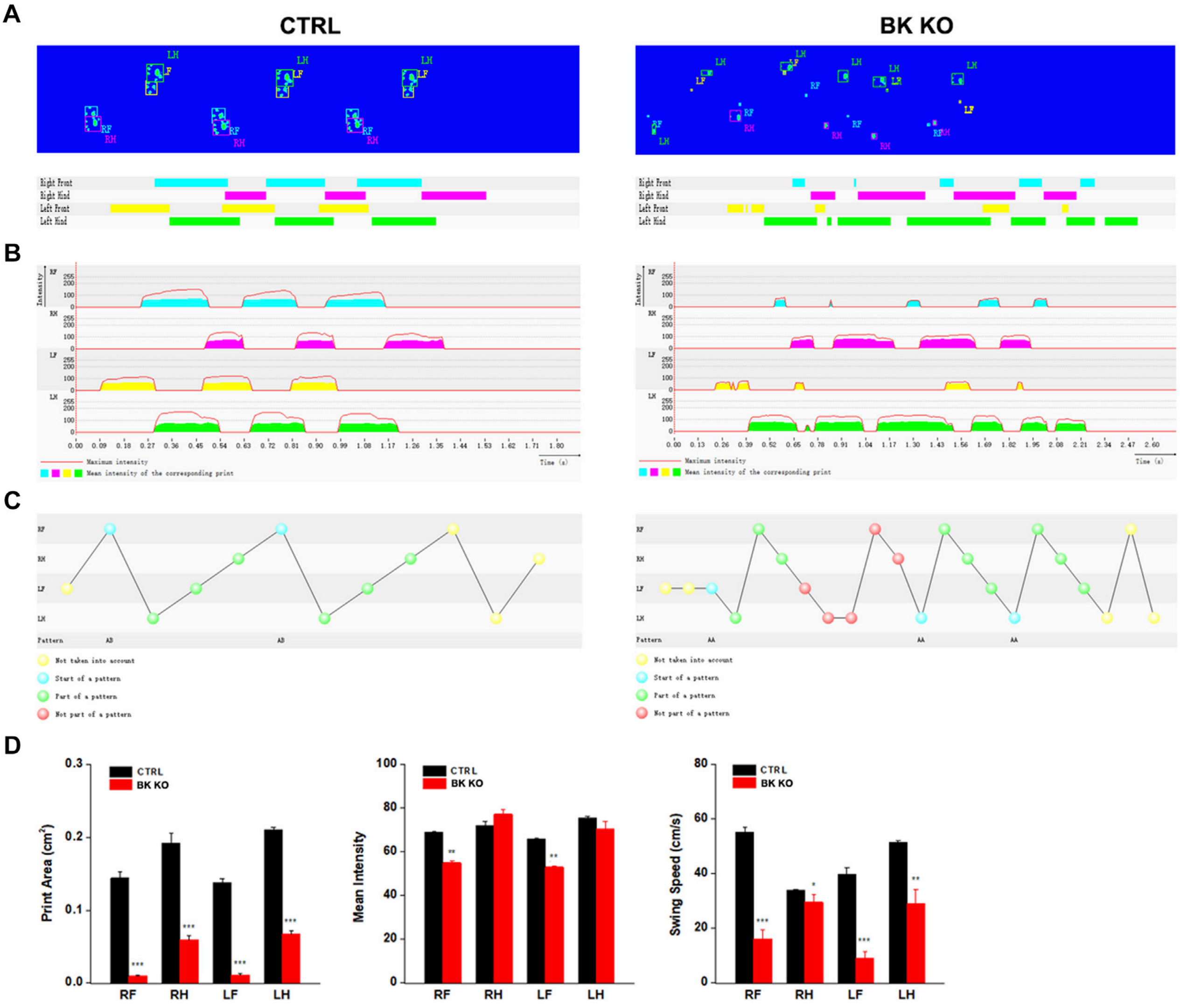

FIGURE 7 | Gait analysis was performed by DigiGait imaging system. **(A–C)** Schematic diagram of WT and BK KO mouse footprints. **(D)** Print area (cm^2), mean intensity and Swing speed (cm/s) of the right front (RF), the right hind (RH), the left front (LF), the left hind (LH) limb were chosen as the observation index. The Data are presented as means ± SEM. (Compared with control group, $^*p < 0.05$, $^{**}p < 0.01$, $^{***}p < 0.001$, $n = 5$).

LC3B, lysosome marker LAMP1 and microglia marker IBA-1 were co-labeled, indicating that the interaction and fusion of autophagosome and lysosome in hippocampal microglia was normal (**Figure 10A**), but in the hippocampus CA3 region of BK KO mice, LC3B, LAMP1 and IBA-1 were partially not co-labeled, indicating abnormal interaction and fusion of autophagosomes and lysosomes in microglia of BK KO mice (**Figure 10B**). During epilepsy, there may be abnormal interaction and fusion between autophagosomes and lysosomes in hippocampal microglia. TRPML1 (key calcium channel of autophagy) promotes the fusion of autophagosomes and lysosomes, and the lysosomal calcium release of TRPML1 is closely related to autophagy (Scotto Rosato et al., 2019; Zhang et al., 2019). BK channel and TRPML1-GCaMP3 were co-expressed in HEK293T. The opener NS1619 of BK channel could induce the calcium outflow of lysosomes. Paxilline (PAX), a specific inhibitor of BK channel, can significantly inhibit the lysosomal calcium outflow (**Figure 10C**). In general, the activation of BK channel could activate lysosomal TRPML1. It suggested that BK might regulate the autophagy pathway from TRPML1.

DISCUSSION

In this study, we identified three KCNMA1-LOF mutants (E155Q, R458T, E884K), of which E155Q was a *de novo* mutant. All three variants showed profound effects on BK channel function, and played its role through LOF mechanism (BK channel current decreased and I-V curve shifted to the positive voltage direction). Faster BK current activation directly increases neuronal firing rate by causing faster

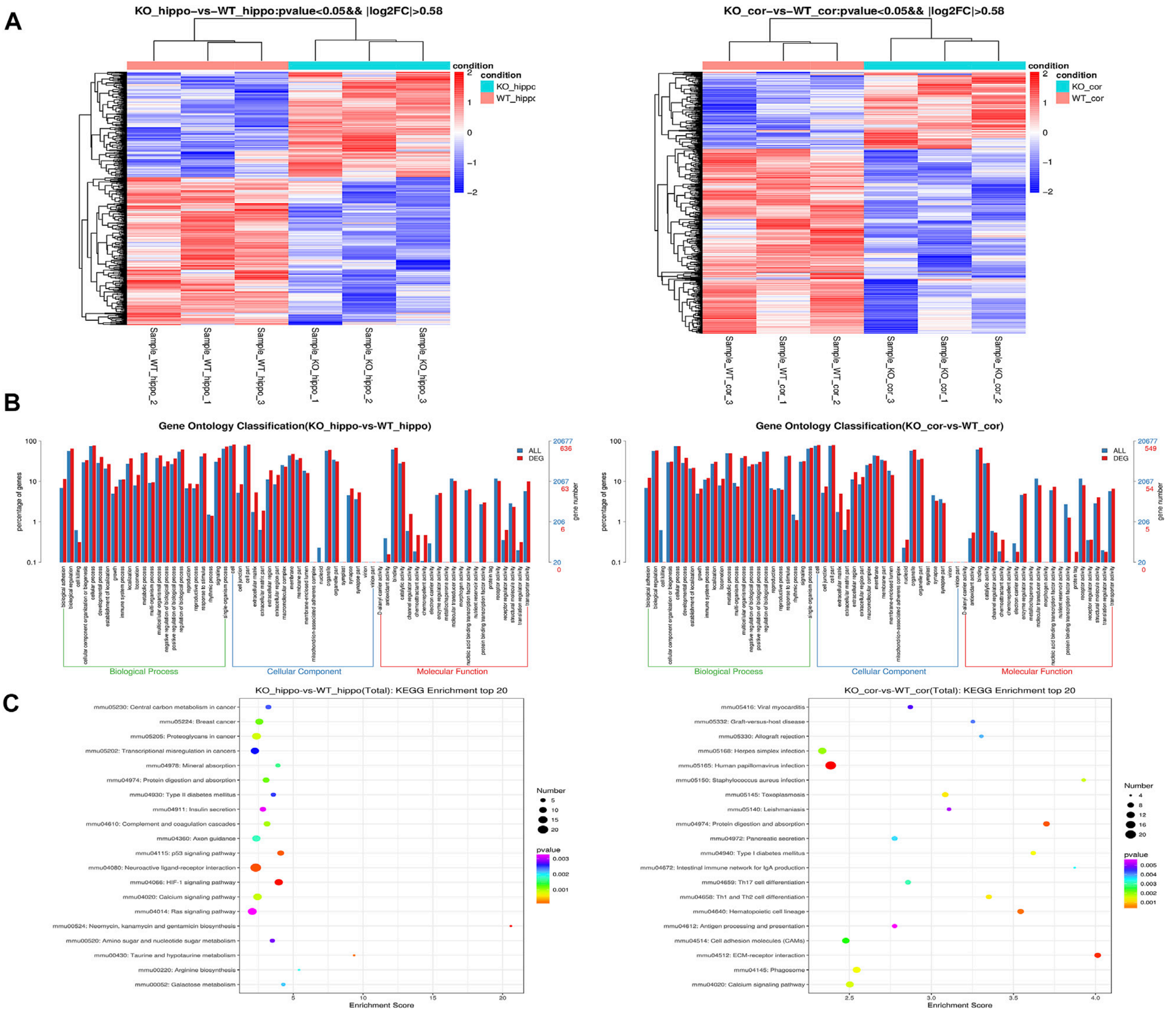

FIGURE 8 | Transcriptome profiling in the hippocampus and cortex tissues of mice. **(A)** Heatmap of the DEGs. **(B)** Enriched Biological Process pathway, cellular component and molecular function in GO analysis ($p < 0.05$). **(C)** KEGG enrichment analysis of DEGs. The intensity of the color depends on the *p* value. The size of plot depends on the gene count. ($n = 3$).

repolarization of action potentials (Jaffe et al., 2011; Contet et al., 2016), which might be the cause of BK-GOF mediated epilepsy. The causes of BK-LOF mediated epilepsy include the inhibition of repolarization of action potential, resulting the increase of neuronal excitability, and the role of neuroimmune inflammation. What's more, hβ4 had no effect on the I-V curve and current amplitude density of E155Q mutant, but activation time constant (τ) of E155Q+β4 channel was greater than that of E155Q mutant (**Supplementary Figure S1**).

Compared with wild-type littermates, *kcnma1* $^{-/-}$ mice lost weight, interestingly, so did the *kcnma1* $^{+/-}$ mice. Susan T Halm et al. speculated that the lack of *kcnma1* allele leads to insufficient grip in mice, which may limited the cubs' access to nutrition (Halm et al., 2017). It was worth noting that the fertility of adult BK KO mice decreased and failed without exception in the process of 15 mating (Transcriptomics results suggested that Adam18, Cabyr and other genes related to sperm function were abnormal, and Eqtn regulated the abnormality of sperm and egg plasma membrane fusion). In addition, the results of KEGG (**Figure 8C**) showed that insulin secretion was enriched, which provided possible evidence for the imbalance of body weight and fat in BK KO mice (Halm et al., 2017). Disturbance of insulin release may damage health and cause signals to convert energy for growth into fat storage. Of note, the malnutrition and developmental delay caused by the weak grip of BK KO mice are reminiscent of the developmental delay found in the patient with the KCNMA1-LOF (E155Q) variant.

Although the epileptic phenotypes of BK KO mice were similar with those of clinical patients, such as developmental

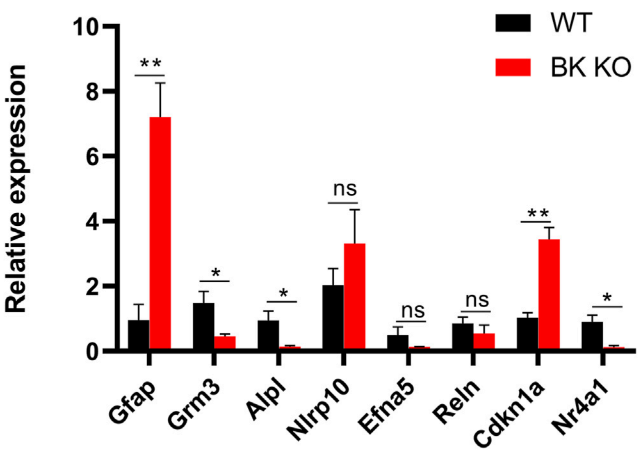

FIGURE 9 | Differential expression of mRNAs between the cortex and hippocampus of WT (Black) and BK KO (Red) mice validated by RT-PCR. Gfap and Grm3 associated with astrocyte activation, Alpl, and Nlrp10 associated with neuroinflammation, Efna5 and Reln associated with epilepsy, Cdkn1a and Nr4a1 associated with autophagy. Gfap, Grm3, Nlrp10, Alpl in cortex, and Efna5, Reln, Cdkn1a, Nr4a1 in hippocampus. Ns (no significant difference, $p > 0.05$), $*p < 0.05$, $**p < 0.01$.

delay and interictal epileptiform discharge (IED), the FP characteristics of BK KO mice were different from those of clinical patients. Specifically, the intensity of δ and θ energy rhythms in BK KO mice reduced, while rhythmic energy intensity of δ and θ increased in the patient carrying the E155Q mutation site. We guess that it is mainly caused by the difference in detection method and detection area. In clinical testing, non-invasive EEG recording is mainly used to detect the membrane potential of neurons in the cortex, and we use *in vivo* multichannel electrophysiological recording to detect the local field potential of the hippocampus in animals. In addition, abnormal background activity amplitude may also affect IED. Christine M. Muheim et al. pointed out that the delta slow wave power of BK KO mice was reduced in cortex (<4 Hz) (Muheim et al., 2019). In our experiment, in addition to the decrease of delta slow wave power, the power of θ wave (4–7 Hz) and γ wave (>30 Hz) also decreased. Of note, the power of α wave and β wave increased, which may be the cause of spontaneous epilepsy in BK KO mice. In the motor cortex, beta waves are mainly involved in grasping, muscle contraction and maintaining attention (Khanna and Carmena, 2015). The abnormal up regulation of β wave may lead to abnormal excitation of neurons, excessive increase of motor control ability, and then lead to motor dysfunction.

In addition, we found that BK KO mice have a dyskinetic phenotype through a series of behavioral experiments. And BK KO mice showed smaller time in the central area (**Supplementary Figure S2B**, $p < 0.001$, $n = 8$), frequency and aim-quadrant stay time (**Supplementary Figures S2D,E**, $p < 0.001$, $p < 0.05$, $n = 6$), and the percentage of spontaneous alternation (**Supplementary Figure S2F**, $p < 0.001$, $n = 8$). The frequency of seizures and the duration of the disease have a negative impact on cognitive impairment (Jokeit and Ebner, 1999; Allone et al., 2017). Although, motor impairment might have an impact on anxiety and cognitive impairment of BK KO mice, one study cleverly excluded interference of motor, proving that BK KO mice have the cognitive impairment phenotype (Sausbier et al., 2004). This strongly suggested that lacking *kcnma1* genes (BK KO) may cause anxiety and cognitive impairment in BK KO mice, which required further study.

We further explored the possible molecular mechanisms of BK-LOF-mediated epilepsy through transcriptomics in the hippocampus and cortex. Gene Ontology (GO) analysis showed that DEGs were related to protein labeling, protein binding transcription factor activity, development process and biological adhesion (**Figure 8B**). The kyoto encyclopedia of genes and genomes (KEGG) showed these DEGs were mainly enriched in insulin secretion, axon guidance, p53 signaling pathway, HIF-1 signaling pathway, calcium signaling pathway, cell adhesion molecules (CAMs), ECM-receptor interaction, and phagosome (**Figure 8C**). In the process of epilepsy, including the changes of gene expression, neuroinflammation, protein production and connection, these may be the targets of inhibiting epilepsy. The results of KEGG showed that Cdkn1a is closely related to the HIF-1 signaling pathway, and dysregulated HIF-1 signaling may play a role in the pathogenesis of epilepsy in hippocampus (Merelli et al., 2018). A large number of glial cells activate and proliferate, glutamate and the secretion of inflammatory factors increases, which reduces the convulsion threshold and increases the excitability of brain neurons, and accelerates spontaneous recurrent convulsions (Friedman and Dingledine, 2011; Huberfeld et al., 2015). Epilepsy like activity *in vitro* and prolonged seizures *in vivo* lead to increased p53 accumulation and transcriptional activity (Sakhi et al., 1994; Liu et al., 1999; Tan et al., 2002; Araki et al., 2004). Abnormal axon guidance may induce mossy fiber germination, and the “wrong” guidance of mossy fiber may be a necessary process of dentate nerve circuit homeostasis under the condition of epilepsy (Koyama and Ikegaya, 2018). Meanwhile, the mammalian target of rapamycin (mTOR) is inhibited by rapamycin to prevent mossy fiber sprouting and reduce seizures in rodent models of acquired epilepsy (Zeng et al., 2009). Cell adhesion molecules (CAMs) may form trans synaptic complexes that are essential to correctly identify synaptic partners and further for determine the establishment and dynamics of synapses (Gorlewicz and Kaczmarek, 2018). Dysfunction of transsynaptic adhesion is associated with epilepsy (Gorlewicz and Kaczmarek, 2018). This strongly suggested that the DEGs find in transcriptomics, particularly those related to astrocyte activation, neuroinflammation and autophagy, may be the molecular mechanism of BK-LOF mediated epilepsy.

In summary, we identified and functionally characterized three different LOF variants in the BK channel (E155Q, R458T, E884K), of which E155Q variant was a *de novo* mutant and affected one patient. All the above variants caused a positive shift of the I-V curve and played a role through the loss-of-function (LOF) mechanism. Moreover, the β4 subunit slowed down the activation of the E155Q mutant. BK KO mice had spontaneous epilepsy, motor

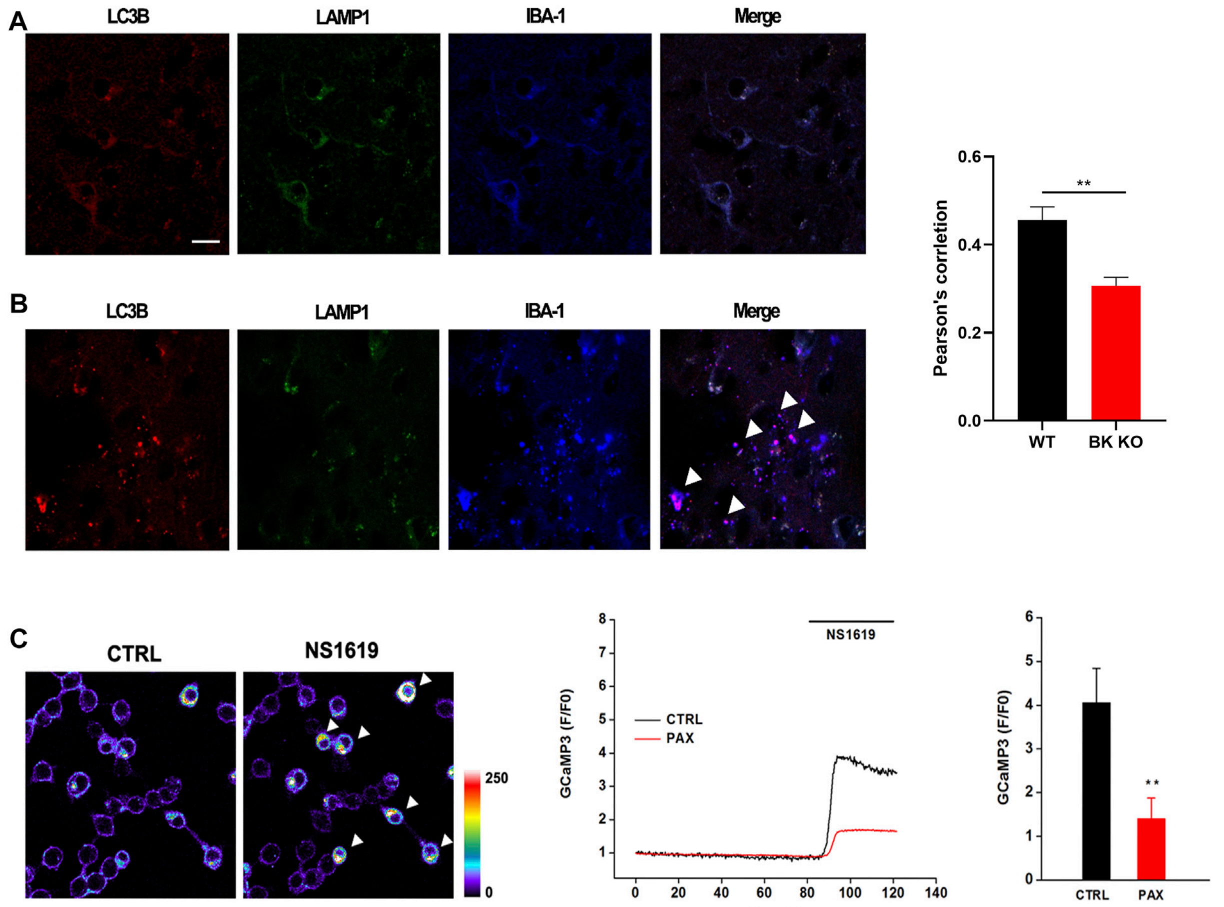

FIGURE 10 | Autophagy in BK KO mice was abnormal. Calcium imaging found that the activation of BK channel could activate lysosomal trpml1 (autophagy key calcium channel). **(A)** Co labeling of microglia, LC3B, IBA-1, and LAMP1 in control mice. **(B)** Co labeling of microglia, LC3B, IBA-1, and LAMP1 in BK KO mice. **(C)** NS1619 was applied to HEK293T transfected with BK channel and TRPML1-GCaMP3 in order to detect its regulation of lysosomal calcium outflow ($^{**}p < 0.01$, $n = 6$).

impairment, autophagic dysfunction, abnormal electroencephalogram (EEG) signals, as well as possible anxiety and cognitive impairment. In addition, BK might regulate the autophagy pathway from TRPML1. Dysregulation of gene expression, especially astrocyte activation, neuroinflammation and autophagy, might be the molecular mechanism of BK-LOF meditated epilepsy.

DATA AVAILABILITY STATEMENT

The data presented in the study are deposited in the GEO repository, accession number GSE191038.

ETHICS STATEMENT

The studies involving human participants were reviewed and approved by the Children's Hospital of Fudan University, Shanghai (National Children's Medical Center, Fudan University). Written informed consent to participate in this study was provided by the participants' legal guardian/next of kin. The animal study was reviewed and approved by the Ethics Committee of Shanghai University of traditional Chinese Medicine. Written informed consent was obtained from the individual(s), and minor(s)' legal guardian/next of kin, for the publication of any potentially identifiable images or data included in this article.

AUTHOR CONTRIBUTIONS

ZL, JT, YY, and YJ designed the research. YY and XJ performed the data analysis work. YY, DQ, LZ, YZ, and XC conducted experiments. YY and QZ wrote and revised the manuscript. YY, LZ, and XC drew the figures. JT was responsible for the statistical analyses. YY, DQ, and XJ are co-first author. All authors read and approved the final manuscript.

FUNDING

This work was supported by the grants from National Key Research and Development Program (2020YFA0803800), National Natural Science Foundation of China (Nos. 31771191, 82074162, 81903995, 81973385, and 81874325), Medical Guidance Projects (Traditional Chinese Medicine) of Shanghai Municipal Science and Technology Commission (No. 21Y11921700), Young Elite Scientists Sponsorship Program by CACM (No. CACM-2019-QNRC2-C10), Shanghai Municipal Commission of Health and Family Planning Fund (Nos. 20184Y0086 and 2018JQ003), Project for Capacity Promotion of Putuo District Clinical Special Disease (2019tszb02), Science and Technology Innovation Project of Putuo District Health System (Nos. ptkwws201902, ptkwws201908, and ptkwws202107).

SUPPLEMENTARY MATERIAL

The Supplementary Material for this article can be found online at: https://www.frontiersin.org/articles/10.3389/fphar.2021.775328/full#supplementary-material

REFERENCES

Allone, C., Lo Buono, V., Corallo, F., Pisani, L. R., Pollicino, P., Bramanti, P., et al. (2017). Neuroimaging and Cognitive Functions in Temporal Lobe Epilepsy: A Review of the Literature. *J. Neurol. Sci.* 381, 7–15. doi:10.1016/j.jns.2017.08.007

Araki, T., Shinoda, S., Schindler, C. K., Quan-Lan, J., Meller, R., Taki, W., et al. (2004). Expression, Interaction, and Proteolysis of Death-Associated Protein Kinase and P53 within Vulnerable and Resistant Hippocampal Subfields Following Seizures. *Hippocampus* 14, 326–336. doi:10.1002/hipo.10184

Bailey, C. S., Moldenhauer, H. J., Park, S. M., Keros, S., and Meredith, A. L. (2019). KCNMA1-linked Channelopathy. *J. Gen. Physiol.* 151, 1173–1189. doi:10.1085/jgp.201912457

Brayden, J. E., and Nelson, M. T. (1992). Regulation of Arterial Tone by Activation of Calcium-dependent Potassium Channels. *J. Sci.* 256, 532–535. doi:10.1126/science.1373909

Brenner, R., Chen, Q. H., Vilaythong, A., Toney, G. M., Noebels, J. L., and Aldrich, R. W. (2005). BK Channel Beta4 Subunit Reduces Dentate Gyrus Excitability and Protects against Temporal Lobe Seizures. *Nat. Neurosci.* 8, 1752–1759. doi:10.1038/nn1573

Contet, C., Goulding, S. P., Kuljis, D. A., and Barth, A. L. (2016). BK Channels in the Central Nervous System. *Int. Rev. Neurobiol.* 128, 281–342. doi:10.1016/bs.irn.2016.04.001

Du, W., Bautista, J. F., Yang, H., Diez-Sampedro, A., You, S. A., Wang, L., et al. (2005). Calcium-sensitive Potassium Channelopathy in Human Epilepsy and Paroxysmal Movement Disorder. *Nat. Genet.* 37, 733–738. doi:10.1038/ng1585

Du, X., Carvalho-de-Souza, J. L., Wei, C., Carrasquel-Ursulaez, W., Lorenzo, Y., Gonzalez, N., et al. (2020). Loss-of-function BK Channel Mutation Causes Impaired Mitochondria and Progressive Cerebellar Ataxia. *Proc. Natl. Acad. Sci. U S A.* 117, 6023–6034. doi:10.1073/pnas.1920008117

Fagerberg, L., Hallström, B. M., Oksvold, P., Kampf, C., Djureinovic, D., Odeberg, J., et al. (2014). Analysis of the Human Tissue-specific Expression by Genome-wide Integration of Transcriptomics and Antibody-Based Proteomics. *Mol. Cel Proteomics* 13, 397–406. doi:10.1074/mcp.M113.035600

Fathollahi, Y., Motamedi, F., Semnanian, S., and Zardoshti, M. (1997). Examination of Persistent Effects of Repeated Administration of Pentylenetetrazol on Rat Hippocampal CA1: Evidence from *In Vitro* Study on Hippocampal Slices. *Brain Res.* 758, 92–98. doi:10.1016/s0006-8993(97)00164-9

Feng, X., Hou, H., Zou, Y., and Guo, L. (2017). Defective Autophagy Is Associated with Neuronal Injury in a Mouse Model of Multiple Sclerosis. *Bosn J. Basic Med. Sci.* 17, 95–103. doi:10.17305/bjbms.2017.1696

Friedman, A., and Dingledine, R. (2011). Molecular Cascades that Mediate the Influence of Inflammation on Epilepsy. *Epilepsia* 52 (3), 33–39. doi:10.1111/j.1528-1167.2011.03034.x

Gorlewicz, A., and Kaczmarek, L. (2018). Pathophysiology of Trans-synaptic Adhesion Molecules: Implications for Epilepsy. *Front Cel Dev Biol* 6, 119. doi:10.3389/fcell.2018.00119

Halm, S. T., Bottomley, M. A., Almutairi, M. M., Di Fulvio, M., and Halm, D. R. (2017). Survival and Growth of C57BL/6J Mice Lacking the BK Channel, Kcnma1: Lower Adult Body Weight Occurs Together with Higher Body Fat. *Physiol. Rep.* 5, e13137. doi:10.14814/phy2.13137

Hamill, O. P., Marty, A., Neher, E., Sakmann, B., and Sigworth, F. J. (1981). Improved Patch-Clamp Techniques for High-Resolution Current Recording from Cells and Cell-free Membrane Patches. *Pflugers Arch.* 391, 85–100. doi:10.1007/BF00656997

Hampton, T. G., Stasko, M. R., Kale, A., Amende, I., and Costa, A. C. (2004). Gait Dynamics in Trisomic Mice: Quantitative Neurological Traits of Down Syndrome. *Physiol. Behav.* 82, 381–389. doi:10.1016/j.physbeh.2004.04.006

Huberfeld, G., Blauwblomme, T., and Miles, R. (2015). Hippocampus and Epilepsy: Findings from Human Tissues. *Rev. Neurol. (Paris)* 171, 236–251. doi:10.1016/j.neurol.2015.01.563

Jaffe, D. B., Wang, B., and Brenner, R. (2011). Shaping of Action Potentials by Type I and Type II Large-Conductance Ca^2+-Activated K+ Channels. *Neuroscience* 192, 205–218. doi:10.1016/j.neuroscience.2011.06.028

Jiang, X. W., Lu, H. Y., Xu, Z., Liu, T. Y., Wu, Q., Yang, Y., et al. (2018). In Silico Analyses for Key Genes and Molecular Genetic Mechanism in Epilepsy and Alzheimer's Disease. *CNS Neurol. Disord. Drug Targets* 17, 608–617. doi:10.2174/1871527317666180724150839

Jokeit, H., and Ebner, A. (1999). Long Term Effects of Refractory Temporal Lobe Epilepsy on Cognitive Abilities: a Cross Sectional Study. *J. Neurol. Neurosurg. Psychiatry* 67, 44–50. doi:10.1136/jnnp.67.1.44

Khanna, P., and Carmena, J. M. (2015). Neural Oscillations: Beta Band Activity across Motor Networks. *Curr. Opin. Neurobiol.* 32, 60–67. doi:10.1016/j.conb.2014.11.010

Koshimizu, H., Takao, K., Matozaki, T., Ohnishi, H., and Miyakawa, T. (2014). Comprehensive Behavioral Analysis of Cluster of Differentiation 47 Knockout Mice. *PloS one* 9, e89584. doi:10.1371/journal.pone.0089584

Koyama, R., and Ikegaya, Y. (2018). The Molecular and Cellular Mechanisms of Axon Guidance in Mossy Fiber Sprouting. *Front. Neurol.* 9, 382. doi:10.3389/fneur.2018.00382

Latorre, R., Castillo, K., Carrasquel-Ursulaez, W., Sepulveda, R. V., Gonzalez-Nilo, F., Gonzalez, C., et al. (2017). Molecular Determinants of BK Channel Functional Diversity and Functioning. *Physiol. Rev.* 97, 39–87. doi:10.1152/physrev.00001.2016

Liang, P., and Le, W. (2015). Role of Autophagy in the Pathogenesis of Multiple Sclerosis. *Neurosci. Bull.* 31, 435–444. doi:10.1007/s12264-015-1545-5

Lippiat, J. D., Standen, N. B., Harrow, I. D., Phillips, S. C., and Davies, N. W. (2003). Properties of BK(Ca) Channels Formed by Bicistronic Expression of hSloalpha and Beta1-4 Subunits in HEK293 Cells. *J. Membr. Biol.* 192, 141–148. doi:10.1007/s00232-002-1070-0

Liu, W., Rong, Y., Baudry, M., and Schreiber, S. S. (1999). Status Epilepticus Induces P53 Sequence-specific DNA Binding in Mature Rat Brain. *Brain Res. Mol. Brain Res.* 63, 248–253. doi:10.1016/s0169-328x(98)00285-x

Lorenz, S., Heils, A., Kasper, J. M., and Sander, T. (2007). Allelic Association of a Truncation Mutation of the KCNMB3 Gene with Idiopathic Generalized Epilepsy. *Am. J. Med. Genet. B Neuropsychiatr. Genet.* 144b, 10–13. doi:10.1002/ajmg.b.30369

Mao, X., Cai, T., Olyarchuk, J. G., and Wei, L. (2005). Automated Genome Annotation and Pathway Identification Using the KEGG Orthology (KO) as a Controlled Vocabulary. *Bioinformatics* 21, 3787–3793. doi:10.1093/bioinformatics/bti430

Merelli, A., Rodríguez, J. C. G., Folch, J., Regueiro, M. R., Camins, A., and Lazarowski, A. (2018). Understanding the Role of Hypoxia Inducible

Factor during Neurodegeneration for New Therapeutics Opportunities. *Curr. Neuropharmacol* 16, 1484–1498. doi:10.2174/1570159X16666180110130253

Moldenhauer, H. J., Matychak, K. K., and Meredith, A. L. (2020). Comparative Gain-Of-Function Effects of the KCNMA1-N999s Mutation on Human BK Channel Properties. *J. Neurophysiol.* 123, 560–570. doi:10.1152/jn.00626.2019

Muheim, C. M., Spinnler, A., Sartorius, T., Dürr, R., Huber, R., Kabagema, C., et al. (2019). Dynamic- and Frequency-specific Regulation of Sleep Oscillations by Cortical Potassium Channels. *Curr. Biol.* 29, 2983–e3. e3. doi:10.1016/j.cub.2019.07.056

Murrow, B. W., and Fuchs, P. A. (1990). Preferential Expression of Transient Potassium Current (IA) by 'short' Hair Cells of the Chick's Cochlea. *Proc. Biol. Sci.* 242, 189–195. doi:10.1098/rspb.1990.0123

Petersen, O. H., and Maruyama, Y. (1984). Calcium-activated Potassium Channels and Their Role in Secretion. *Nature* 307, 693–696. doi:10.1038/307693a0

Racine, R. J. (1972). Modification of Seizure Activity by Electrical Stimulation. II. Motor Seizure. *Electroencephalogr Clin. Neurophysiol.* 32, 281–294. doi:10.1016/0013-4694(72)90177-0

Robitaille, R., and Charlton, M. P. (1992). Presynaptic Calcium Signals and Transmitter Release Are Modulated by Calcium-Activated Potassium Channels. *J. Neurosci.* 12, 297–305. doi:10.1523/jneurosci.12-01-00297.1992

Sakhi, S., Bruce, A., Sun, N., Tocco, G., Baudry, M., and Schreiber, S. S. (1994). p53 Induction Is Associated with Neuronal Damage in the central Nervous System. *Proc. Natl. Acad. Sci. U S A.* 91, 7525–7529. doi:10.1073/pnas.91.16.7525

Sausbier, M., Hu, H., Arntz, C., Feil, S., Kamm, S., Adelsberger, H., et al. (2004). Cerebellar Ataxia and Purkinje Cell Dysfunction Caused by Ca2+-Activated K+ Channel Deficiency. *Proc. Natl. Acad. Sci. U S A.* 101, 9474–9478. doi:10.1073/pnas.0401702101

Scotto Rosato, A., Montefusco, S., Soldati, C., Di Paola, S., Capuozzo, A., Monfregola, J., et al. (2019). TRPML1 Links Lysosomal Calcium to Autophagosome Biogenesis through the Activation of the CaMKKβ/VPS34 Pathway. *Nat. Commun.* 10, 5630. doi:10.1038/s41467-019-13572-w

Tabarki, B., AlMajhad, N., AlHashem, A., Shaheen, R., and Alkuraya, F. S. (2016). Homozygous KCNMA1 Mutation as a Cause of Cerebellar Atrophy, Developmental Delay and Seizures. *Hum. Genet.* 135, 1295–1298. doi:10.1007/s00439-016-1726-y

Tan, Z., Sankar, R., Tu, W., Shin, D., Liu, H., Wasterlain, C. G., et al. (2002). Immunohistochemical Study of P53-Associated Proteins in Rat Brain Following Lithium-Pilocarpine Status Epilepticus. *Brain Res.* 929, 129–138. doi:10.1016/s0006-8993(01)03360-1

Wang, Y., Guo, Q., Hei, H., Tao, J., Zhou, Y., Dong, J., et al. (2019). BK Ablation Attenuates Osteoblast Bone Formation via Integrin Pathway. *Cell Death Dis* 10, 738. doi:10.1038/s41419-019-1972-8

Watanabe, Y., Tsujimura, A., Takao, K., Nishi, K., Ito, Y., Yasuhara, Y., et al. (2011). Relaxin-3-deficient Mice Showed Slight Alteration in Anxiety-Related Behavior. *Front. Behav. Neurosci.* 5, 50. doi:10.3389/fnbeh.2011.00050

Zeng, L. H., Rensing, N. R., and Wong, M. (2009). The Mammalian Target of Rapamycin Signaling Pathway Mediates Epileptogenesis in a Model of Temporal Lobe Epilepsy. *J. Neurosci.* 29, 6964–6972. doi:10.1523/JNEUROSCI.0066-09.2009

Zhang, X., Chen, W., Gao, Q., Yang, J., Yan, X., Zhao, H., et al. (2019). Rapamycin Directly Activates Lysosomal Mucolipin TRP Channels Independent of mTOR. *Plos Biol.* 17, e3000252. doi:10.1371/journal.pbio.3000252

Zheng, J., and Trudeau, M. (2015). *Handbook of Ion Channels || Genetic Methods for Studying Ion Channel Function in Physiology and Disease*, Handbook of Ion Channels, 167–188. doi:10.1201/b18027

Zhu, Y., Zhang, S., Feng, Y., Xiao, Q., Cheng, J., and Tao, J. (2018). The Yin and Yang of BK Channels in Epilepsy. *CNS Neurol. Disord. Drug Targets* 17, 272–279. doi:10.2174/1871527317666180213142403

Conflict of Interest: The authors declare that the research was conducted in the absence of any commercial or financial relationships that could be construed as a potential conflict of interest.

Publisher's Note: All claims expressed in this article are solely those of the authors and do not necessarily represent those of their affiliated organizations, or those of the publisher, the editors and the reviewers. Any product that may be evaluated in this article, or claim that may be made by its manufacturer, is not guaranteed or endorsed by the publisher.

Copyright © 2022 Yao, Qu, Jing, Jia, Zhong, Zhuo, Chen, Li, Tang, Zhu, Zhang, Ji, Li and Tao. This is an open-access article distributed under the terms of the Creative Commons Attribution License (CC BY). The use, distribution or reproduction in other forums is permitted, provided the original author(s) and the copyright owner(s) are credited and that the original publication in this journal is cited, in accordance with accepted academic practice. No use, distribution or reproduction is permitted which does not comply with these terms.

frontiers
in Pharmacology

REVIEW
published: 17 January 2022
doi: 10.3389/fphar.2021.775087

Post-Translational Modification of Cav1.2 and its Role in Neurodegenerative Diseases

Yun Li[1†], *Hong Yang*[1†], *Tianhan He*[1†], *Liang Zhang*[2*] *and Chao Liu*[1*]

[1]Jiangsu Province Key Laboratory of Anesthesiology, Jiangsu Province Key Laboratory of Anesthesia and Analgesia Application Technology, NMPA Key Laboratory for Research and Evaluation of Narcotic and Psychotropic Drugs, School of Anesthesiology, Xuzhou Medical University, Xuzhou, China, [2]Department of Neurology, Affiliated Hospital of Qingdao University, Qingdao, China

Cav1.2 plays an essential role in learning and memory, drug addiction, and neuronal development. Intracellular calcium homeostasis is disrupted in neurodegenerative diseases because of abnormal Cav1.2 channel activity and modification of downstream Ca^{2+} signaling pathways. Multiple post-translational modifications of Cav1.2 have been observed and seem to be closely related to the pathogenesis of neurodegenerative diseases. The specific molecular mechanisms by which Cav1.2 channel activity is regulated remain incompletely understood. Dihydropyridines (DHPs), which are commonly used for hypertension and myocardial ischemia, have been repurposed to treat PD and AD and show protective effects. However, further studies are needed to improve delivery strategies and drug selectivity. Better knowledge of channel modulation and more specific methods for altering Cav1.2 channel function may lead to better therapeutic strategies for neurodegenerative diseases.

Keywords: Cav1.2, PTM (post-translational modification), neurodegenerative disease, phosphorylation, ubiquitination

OPEN ACCESS

Edited by:
Jacques Joubert,
University of the Western Cape, South Africa

Reviewed by:
Brandon Peter Lucke-Wold,
University of Florida, United States
Yong Li,
Shanghai Jiao Tong University, China

Correspondence:
Liang Zhang
drzhangliang@126.com
Chao Liu
Chaoliu@xzhmu.edu.cn

†These authors have contributed equally to this work.

Specialty section:
This article was submitted to Pharmacology of Ion Channels and Channelopathies,
a section of the journal Frontiers in Pharmacology

Received: *13 September 2021*
Accepted: *08 December 2021*
Published: *17 January 2022*

Citation:
Li Y, Yang H, He T, Zhang L and Liu C (2022) Post-Translational Modification of Cav1.2 and its Role in Neurodegenerative Diseases. Front. Pharmacol. 12:775087. doi: 10.3389/fphar.2021.775087

INTRODUCTION

Cav1.2, encoded by the *CACNA1C* gene, is a high-voltage-activated (HVA), long-lasting (L-type), and dihydropyridine (DHP)-sensitive calcium channel. Cav1.2 mediates depolarization of the cell membrane potential, calcium (Ca^{2+}) influx, and activation of intracellular Ca^{2+} signaling cascades that alter gene expression, protein phosphorylation, and neurotransmitter release. Cellular excitability and signal transduction are affected by factors that modulate Cav1.2 activity. Cav1.2 channels are located in the cardiovascular system, the nervous system, and endocrine glands (Mikami et al., 1989), where they serve important physiopathological functions; for example, gain-of-function mutations in the *CACNA1C* gene cause Timothy Syndrome (Splawski et al., 2004; Moon et al., 2018). In neurons, two different L-type calcium channels (LTCCs) are expressed: Cav1.2 and Cav1.3 (Hell et al., 1993; Ertel et al., 2000). Cav1.2 is the major calcium channel isoform in neurons, constituting about 80% of neuronal LTCCs (Hell et al., 1993). Cav1.2 participates in learning and memory, drug addiction, and neuronal development (Striessnig et al., 2014). Large-scale genome-wide association studies have shown a strong association between susceptibility to psychiatric disorders and single nucleotide polymorphisms (SNPs) in the *CACNA1C* gene (Bhat et al., 2012). Yet, understanding of Cav1.2 function in the brain and its role in neurodegenerative disease remains limited.

The genetic regulation and channel modulation of Cav1.2 have been studied intensively. At the post-transcriptional level, alternative splicing of Cav1.2 increases protein diversity. Different splice

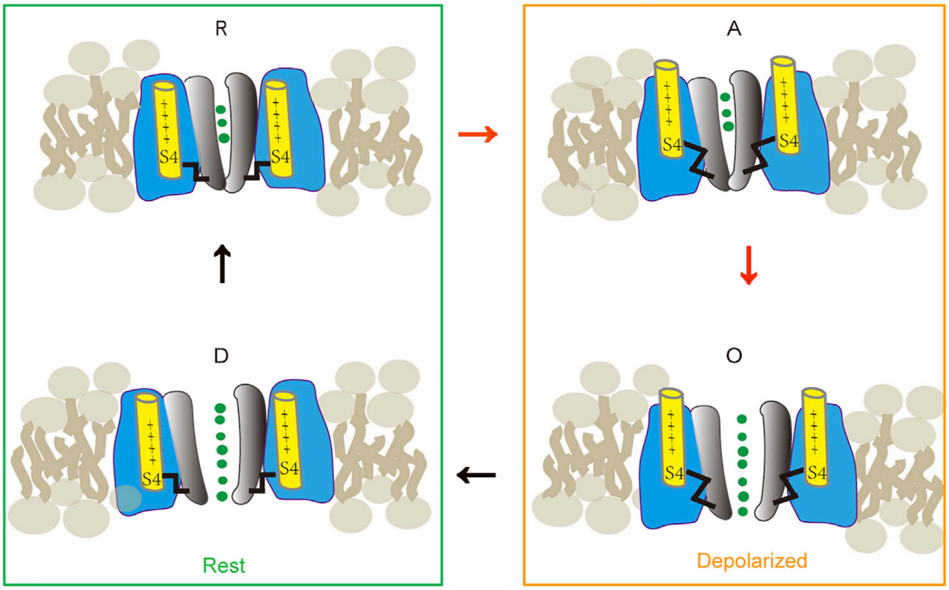

FIGURE 1 | Cav1.2 state transitions during activation [modified after (Beyl et al., 2009) (Hering et al., 2018)]. The channel gating is determined by two functionally distinct processes: a voltage-sensing mechanism and a conducting pore. These two processes defined 4 states: R, at rest, pore is closed and S4 segments in the "down" position lock the pore. A, when depolarized, voltage-sensing mechanism is activated and S4 segments move to the "up" position and release the pore; but the pore remains closed. O, during continuous depolarization, all four S4 segments are in the "up" position; the pore is open. D, when returned to the resting potential, the deactivated voltage-sensing segment moved toward a "down" position while the pore is still open. Subsequently, the pore will transit to its closed conformation and at a resting state.

variants have distinct channel properties, with tissue- and disease-specific variability (Wang et al., 2006). At the post-translational level, Cav1.2 is altered by a variety of modifications, which will be further discussed below.

Cav1.2 is an important drug target in the cardiovascular system. DHPs form a class of LTCC blockers and are the most widely prescribed drugs for hypertension and myocardial ischemia (Zamponi et al., 2015). In this review, we summarize the post-translational modifications of Cav1.2 and its role in neurodegenerative diseases, and further discuss the potential of Cav1.2 as a drug target for Alzheimer's disease (AD) and Parkinson's disease (PD).

STRUCTURE AND FUNCTION OF CAV1.2 IN THE CNS

Voltage-gated calcium channels play an important role in neuronal function (Goonasekera et al., 2012). Cav1.2 is a multi-protein complex. It generally consists of three subunits: a pore-forming subunit α1, a β subunit, and an α2δ subunit; in skeletal muscle, a γ subunit is also found (Goonasekera et al., 2012). The α1 subunit contains about 2000 amino acid residues, which forms four homologous domains (DI–DIV) connected by intracellular loops (Dai et al., 2009; Alves et al., 2019). Each domain consists of six transmembrane segments: S1 to S6 (Dai et al., 2009; Alves et al., 2019). Of these, S5 and S6 form the pore; and the S4 segment serves as a voltage sensor. The gating mechanism is shown in **Figure 1**. At rest, the S4 segments stay inward ("down") under the influence of the electrical field and lock the channel in its closed state. In this state, the S6 helices converge on the intracellular side, preventing ion penetration. When the membrane is depolarized, the S4 segments are released and move outward. The pore will be unlocked when all four S4 segments leave the "down" position. During continuous depolarization, the S6 gate disengages. When all the four S6 segments disengage and are in the "up" position, the pore opens. When returned to the resting potential, the deactivated voltage-sensing segment moved toward a "down" position while the pore is still open. Subsequently, the channel returns to its closed conformation at a rest state (Beyl et al., 2009; Hering et al., 2018).

The α1 subunit is the binding site of most regulators and drugs that act on the channel (Zamponi et al., 2015), whereas the main functions of the other subunits are transportation, anchoring, and regulation (Hofmann et al., 2014). Cav1.2 channels usually require intense depolarization to activate and have long-lasting activity (Hofmann et al., 2014). Ca^{2+} entering through Cav1.2 participates in a series of physiological processes as an important second messenger.

Cav1.2 is distributed universally in the brain. In humans, moderate-to-high mRNA level is detected in the cerebral cortex, the pituitary gland, the amygdala, the basal ganglia, and the cerebellum (Splawski et al., 2004). In mice, the olfactory region, the basal ganglia, the hippocampal formation, the amygdala, and the thalamus show moderate-to-high mRNA level of Cav1.2 (Hell et al., 1993; Splawski et al., 2004; Hetzenauer et al., 2006). At the protein level, the hippocampal formation, the thalamus, and the hypothalamus have moderate-to-strong signal intensity. At the subcellular level in neurons, Cav1.2 is in the soma and at the synapses (Alves et al., 2019).

Cav1.2 plays an important role in the regulation of synaptic plasticity. Researchers found that mice with an inactivated form of the *CACNA1C* gene in the hippocampus and neocortex display severely impaired hippocampus-dependent spatial memory (Moosmang et al., 2005). Cav1.2 is involved in the formation of long-lasting long-term potentiation (LTP) in the hippocampus (Moosmang et al., 2005; Moon et al., 2018; Nanou and Catterall, 2018). Long-lasting LTP needs activation of gene expression and protein synthesis (Malenka and Bear, 2004). The calcium entry from Cav1.2 activates Calmodulin-dependent protein kinase II (CamKII), which binds the C-terminus of Cav1.2; and downstream CamKIV, which phosphorylate CREB and activate downstream gene expression (Cohen et al., 2015). In another pathway, the calcium-regulated phosphatase calcineurin that binds to the C-terminal domain of Cav1.2 is also activated and dephosphorylates the transcription factor NFAT (nuclear factor of activated T-cells), allowing it to translocate into the nucleus and activate gene expression (Murphy et al., 2014). The above signaling cascade increases the synthesis of mRNA encoding synaptic proteins, causing long-lasting changes in synaptic function (Nanou and Catterall, 2018). Moreover, recent studies have found a β2-adrenergic receptor and Cav1.2 signaling complex that regulates synaptic plasticity. β2-adrenergic receptors affect calcium channel activity and long-term postsynaptic plasticity through their interactions with the C-terminus of Cav1.2 channels (Qian et al., 2017).

During aging, the viability of Cav1.2 channels increases, leading to high intracellular calcium (Navakkode et al., 2018) that may modulate the processing of amyloid precursor protein (APP) and promote AD pathogenesis (Anekonda and Quinn, 2011). The calcium hypothesis of AD holds that disturbing the intracellular Ca^{2+} balance affects intracellular signal transmission, leading to the formation of Aβ plaques and neurofibrillary tangles, which alter the plasticity of synapses and ultimately lead to the death of neurons (Khachaturian, 1989). Furthermore, Ca^{2+} imbalance promotes the phosphorylation of tau and leads to disordered autophagy in neurons (Anekonda and Quinn, 2011). Endoplasmic reticulum stress (ER stress) and subsequent tau hyperphosphorylation are increased in human chronic traumatic encephalopathy. Administration of docosahexaenoic acid, an endoplasmic reticulum stress inhibitor, lowers intracellular calcium concentration, which results in the decrease of tau hyperphosphorylation and improves cognitive performance (Begum et al., 2014; Lucke-Wold et al., 2016). Separately, salubrinal, a modulator of cellular stress, can reduce neuroinflammation in mice via decreasing ER stress and oxidative stress (Logsdon et al., 2016).

POST-TRANSLATIONAL MODULATION OF CAV1.2 AND ITS ROLE IN NEURODEGENERATIVE DISEASES

Post-translational modulation (PTM) is a process that converts synthesized proteins to mature proteins through covalent or enzymatic modifications. These modifications range from the enzymatic hydrolysis of peptide bonds to the covalent addition of specific chemical groups, lipids, carbohydrates, and even entire proteins and amino acid side chains. These chemical modifications after polypeptide chain biosynthesis expand the scope of the amino acid structure and properties, thereby diversifying the structure and function of proteins. PTM can occur at any point and regulates protein activity, localization, and interactions with other molecules (Knorre et al., 2009; Walker and Nestler, 2018).

Cav1.2 undergoes a series of PTMs before it becomes a mature and functional Ca^{2+} channel on the cell surface. These modifications influence the channel properties, trafficking, and location and hence significantly alter the channel function. Cav1.2 modification is dramatically changed in neurodegenerative disease and may be an important component of the pathology (summarized in **Figure 2**).

Phosphorylation

Phosphorylation of a molecule is the attachment of a phosphoryl group. Protein phosphorylation is the most abundant post-translational modification in eukaryotes. Phosphorylation can occur on serine, threonine, and tyrosine side chains (often called "residues") through phosphoester bond formation. Neural cells contain a plethora of protein kinases, protein phosphatases, and phosphorylated proteins, and many of these are essential for the regulation of neuronal morphology and for cell functions as diverse as membrane excitability, secretory processes, cytoskeletal organization, and cellular metabolism.

Phosphorylation of Cav1.2 channels can enhance Ca^{2+} influx four- to six-fold (Sculptoreanu et al., 1993; Kavalali et al., 1997). Cav1.2 channels can be phosphorylated by many protein kinases (PKA, PKC, PKG, and CAMKII) but, in most cases, the sites regulated by these kinases remain uncertain. The identified phosphorylation sites in Cav1.2 are summarized in **Table 1** (Perez-Reyes et al., 1992; De Jongh et al., 1996; Gerhardstein et al., 1999; Yang et al., 2005; Grueter et al., 2006; Gui et al., 2006; Yang et al., 2007; Blaich et al., 2010; Fuller et al., 2010; Huttlin et al., 2010; Bachnoff et al., 2011; Brandmayr et al., 2012; Pankonien et al., 2012; Lei et al., 2018; Li et al., 2020; Whitcomb et al., 2020). The central subunit of Cav1.2, α1C, is the major subunit involved in the PKA-mediated increase in channel activity. The α1C subunit is phosphorylated by PKA in intact hippocampal neurons, and a two-fold increase in Ca^{2+} influx has been observed in hippocampal neurons in old rats compared with adult rats, suggestive of increased PKA phosphorylation of Cav1.2 with aging. S1700 phosphorylation plays a greater modulatory role than S1928 phosphorylation in the heart, which is crucial for calcium homeostasis in cardiomyocytes and prevention of heart failure (Yang et al., 2016).

However, only S1928 has been shown to increase with normal aging in the hippocampus (Davare and Hell, 2003) and S1928 is important for the upregulation of channel activity by PKA. Protein phosphatase 2A (PP2A) constitutively bound to Cav1.2 is required for dephosphorylation of S1928 and subsequent down-regulation of Cav1.2 channel activity (Xu et al., 2010). Similar to PKA, PKC can also phosphorylate α1C at the same site (Weiss et al., 2012). The channel activity of Cav1.2 increases because of the convergence of the two kinases. PKC α and ε expression is decreased with aging in the prefrontal cortex

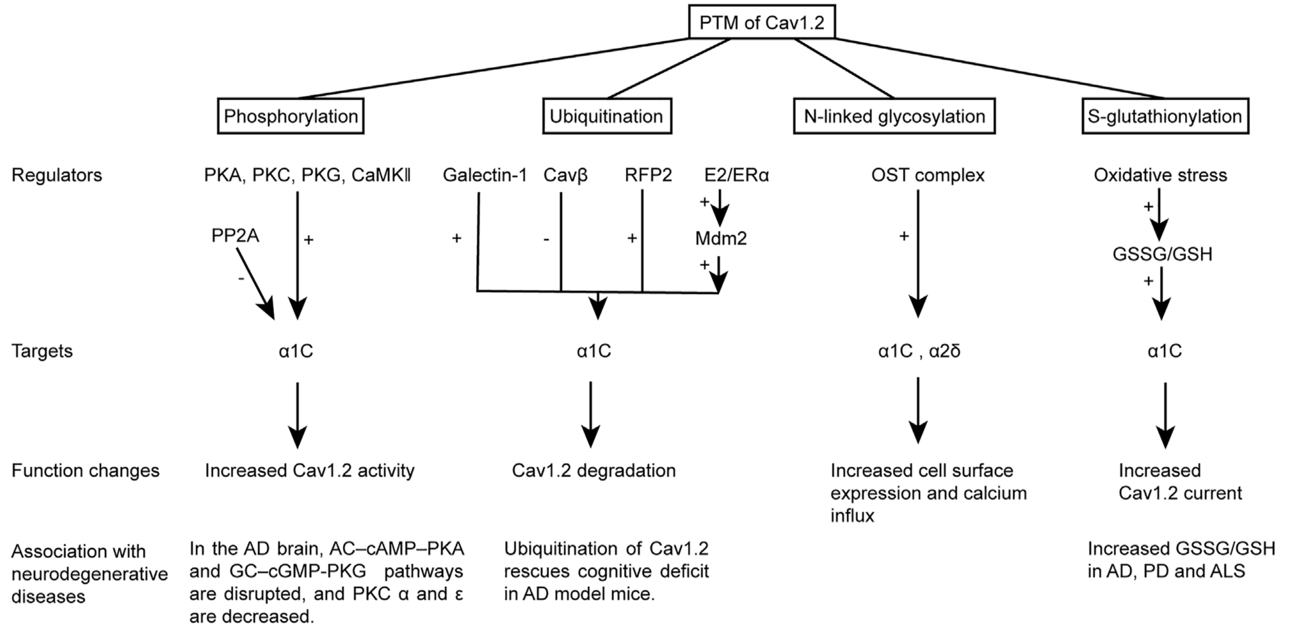

FIGURE 2 | Schematic representation of the PTM of Cav1.2 and its correlation with neurodegenerative diseases. The PTM changes the channel activity, degradation, and cell surface expression of Cav1.2. The PTM of Cav1.2 or the disruption of their regulating pathways was also observed in neurodegenerative diseases.

TABLE1 | Identified phosphorylation sites in Cav1.2 α1C and Cavβ2.

Species	Subunit	Kinases and phosphorylation sites			
		PKA	**PKC**	**CaMKII**	**PKG**
Human	α1	S1898 (Bachnoff et al., 2011)	—	—	—
Mouse	α1	S1897 (Whitcomb et al., 2020)	—	S1512 S1570 (Blaich et al., 2010)	—
		S107, 499, 838, 845, 1680, 1700, 1721, 1744, 1927, 2155 T501, 506 (Huttlin et al., 2010)			
	β2	S200, 202, 203, 211, 214, 510, 545, 522 T215, 549 (Huttlin et al., 2010)			
Rat	α1	—	—	T1604 (Li et al., 2020)	—
	β2	S478 S479 (Perez-Reyes et al., 1992; Bunemann et al., 1999)	—	T498 (Grueter et al., 2006)	—
Rabbit	α1	S1928 (De Jongh et al., 1996) S1700 T1704 (Fuller et al., 2010)	S1928 (Yang et al., 2005)	—	S1928 (Yang et al., 2007)
	β2	S296 (Pankonien et al., 2012) S459 S478 S479 (Gerhardstein et al., 1999)	—	—	S496 (Yang et al., 2007)
Guinea pig	α1	S1574 S1626 S1699 (Lei et al., 2018)	—	T1603 (Li et al., 2020)	—

The publications reporting phosphorylation of a specific amino acid are indicated by a reference in brackets. Notably, amino acids in all the references are not the canonical protein sequences and differ from each other. Please refer to the original publication for more detail.

and hippocampus (Perovic et al., 2013), and they are downregulated by Aβ in AD brains (Govoni et al., 1993; Lucke-Wold et al., 2015). PKC signal cascades along with altered calcium homeostasis contribute to the development of NFTs (neurofibrillary tangles) (Lucke-Wold et al., 2014).

The S1928 site is close to the C-terminus of α1C, present only in full-length α1C. With normal aging, there is a clear increase in S1928 phosphorylation in the hippocampus but the general levels of cyclic adenosine monophosphate (cAMP), PP2A, and protein phosphatase 1 (PP1) inhibitors remain unchanged (Davare and Hell, 2003). The dentate gyrus is the major region in the hippocampus where S1928 phosphorylation occurs; no significant changes are observed in other areas of the hippocampus (Núñez-Santana et al., 2014). S1928 phosphorylation by A-kinase-anchoring protein (AKAP)-anchored PKA plays an essential role in enhancing Cav1.2 channel activity and vasoconstriction under conditions of high glucose or in diabetes (Nystoriak et al., 2017). The level of cAMP is upregulated in cerebral vessels in AD hippocampus and is associated with vascular β-amyloid peptide (Aβ) (Martínez et al., 2001). It is well established that patients with type 2 diabetes have a higher incidence of cognitive decline and morbidity of AD than the general population (Surguchov, 2020), suggestive of a link with changes in Cav1.2 activity. In the AD brain, preclinical and neuropathological data suggest that both adenyl cyclase (AC)–cAMP–PKA and guanylate cyclase (GC)–cGMP–PKG signaling are disrupted. Overall PKA activity and nuclear PKA activity appear to be suppressed in AD (Sanders and Rajagopal, 2020), which may lead to abnormal changes in Cav1.2 phosphorylation state. Furthermore, the mechanism by which the β2-adrenergic receptor (β2AR) stimulates Cav1.2 channel activity depends on S1928 phosphorylation and constitutes a critical component of the molecular mechanism underlying stable and prolonged theta-tetanus-induced LTP (Qian et al., 2017). Multiple phosphorylation sites have been found in the C-terminal domain of the Cav1.2 β subunit *in vitro*. However, C-terminal knock-out mice survive with no apparent physiological deficits and, most importantly, show normal function of Cav1.2 in ventricular myocytes. Thus, the phosphorylation sites on the Cav1.2 β subunit may not have essential functional roles *in vivo*.

Ubiquitination

Ubiquitin (UB) is a highly conserved small protein that is found in all eukaryotic cells, from single-celled yeast to humans. Its main function is to mark proteins to be degraded by 26S proteasome (Lam et al., 2000; Bennett et al., 2005; Swatek and Komander, 2016). UB binds covalently to the lysine residue of the substrate protein and the ubiquitin-labeled protein is identified and rapidly degraded. Briefly, this process requires the sequential action of three enzymes (Swatek and Komander, 2016). The C-terminal glycine residue of ubiquitin is activated by E1. Next, activated ubiquitin is transferred to an active cysteine residue of E2. Finally, ubiquitin links its C-terminus to an ε-amino group of the substrate protein's lysine residues (Hershko and Ciechanover, 1998). In a nutshell, ubiquitination is a dynamic, multifaceted post-translational modification that is involved in nearly all physiological processes (Swatek and Komander, 2016). An abnormal UB signal is closely related to neurodegeneration.

Neurodegenerative diseases are characterized by the loss of neurons in the brain or spinal cord. Most samples from patients with neurodegenerative diseases are immunoreactive for anti-UB antibodies (Popovic et al., 2014) and abnormalities of the UB-dependent degradation systems and aggregation formation are associated with neurodegeneration (Hershko and Ciechanover, 1998; Lam et al., 2000; Bennett et al., 2005; Hara et al., 2006). In PD, α-synuclein in Lewy bodies (a diagnostic marker of PD) is modified by ubiquitin at lysines 77 and 78 (Popovic et al., 2014). Ubiquitination likely increases the aggregation and neurotoxicity of α-synuclein in cultured human dopaminergic cells (Popovic et al., 2014). In AD, a typical aggregate is ubiquitinated tau protein (Popovic et al., 2014). Thus, UB-dependent degradation systems, such as the UB-proteasome system and autophagy, likely play a role in the pathogenesis of these neurodegenerative diseases (Bennett et al., 2005; Popovic et al., 2014).

The ubiquitin–proteasome system (UPS) is closely linked to Cav1.2 degradation (Felix and Weiss, 2017). UB protein has seven lysine residues at positions 6, 11, 27, 29, 33, 48, and 63 (Ikeda and Dikic, 2008; Chen and Sun, 2009). Among these, K6/K29 take part in Cav1.2 degradation (Lai et al., 2019). E3 specifically recognizes the target proteins' lysine residue and tags it for degradation by the proteasome (Hershko and Ciechanover, 1998). Recent studies have shown that the Cavβ subunit may serve as a molecular switch that prevents the Cav1.2 α subunit from ubiquitination by the RFP2 ubiquitin ligase and subsequent transfer of Cav1.2 channels to the endoplasmic reticulum associated protein degradation (ERAD) complex; thus, the Cavβ subunit protects Cav1.2 channels from proteasomal degradation (Felix and Weiss, 2017). Separately, Galectin-1 acts as a negative Cav1.2 channel regulator by binding to the Cav1.2 I–II loop and exposing the lysine residues inside the loop to polyubiquitination and ERAD degradation, ultimately inhibiting channel function (Hu et al., 2018; Loh et al., 2020). Furthermore, in ovariectomized APP/PS1 mice (an AD animal model), systemic administration of E2 (17β-estradiol) or the estrogen receptor α (ERα) agonist propylpyrazoletriol (PPT) increased ubiquitination of Cav1.2 in the brain, reversed elevated levels of Cav1.2 protein, and improved cognitive functioning. The binding of the E3 ligase Mdm2 with Cav1.2 is promoted by activating ERα. In Mdm2-overexpressing neurons, the intensity of Cav1.2 decreased significantly. These results suggest that Mdm2-related ubiquitination is critical for ERα regulation of Cav1.2 protein levels and that a reduction in Cav1.2 protein levels may contribute to ERα-induced cognitive improvements (Lai et al., 2019).

N-Linked Glycosylation

N-linked glycosylation is a co-translational or post-translational modification of new peptide chains in which oligosaccharides are connected to the amide of asparagine residues. N-linked glycosylation can be divided into high mannose, compound, and heterozygous types. N-linked glycosylation consists of three main steps: synthesis, transfer, and modification. Synthesis and transfer of N-linked glycosylation are carried out in the endoplasmic reticulum, whereas modification occurs in both the endoplasmic reticulum and the Golgi matrix. This progress is necessary for membrane trafficking and protein expression on the cell surface. Recent studies showed that external glucose level alters N-glycosylation (Liu et al., 2014; Villacrés et al., 2015). There are four potential N-glycosylation sites in the rabbit Cav1.2: N124, N299, N1359, and N1410. The double mutant (N124, 299Q) showed a positive shift in the voltage-dependent gating curve; and the quadruple mutant (QM; N124, 299, 1,359, 1410Q) showed a positive shift in the voltage-dependent gating curve as well as a reduction of peak current. The weaker surface fluorescence intensity of QM suggested its lower surface expression than wild-type Cav1.2 (Park et al., 2015).

The α2δ subunit, an integral component of Cav1.2, is highly N-glycosylated by a 30-kDa oligosaccharide (Marais et al., 2001). Mutation of only 6/16 asparagine glycosylation sites was sufficient to decrease cell surface expression and protein stability of α2δ1 subunit, as well as α2δ1-mediated peak current density and voltage-dependent gating of the α1C subunit. Single mutation N663Q and double mutations N348Q/N468Q, N348Q/N812Q, and N468Q/N812Q decreased protein stability and abolished cell surface expression of α2δ1 as well as the α2δ1-induced up-regulation of Cav1.2 currents (Tétreault et al., 2016). However, it is still not clear whether N-glycosylation of Cav1.2 contributes to the mechanism of Ca^{2+} interruption in neurodegenerative diseases.

S-Glutathionylation

S-glutathionylation is a process in which glutathione forms a disulfide bond with cysteine residues of the target protein, and is a major redox-mediated thiol modulation. Oxidative stress facilitates S-glutathionylation. The ratio of reduced and oxidized glutathione (GSH/GSSG) is important for S-glutathionylation. Glutathionylation is a reversible redox modification: it directly changes the redox state of Cav1.2 and increases calcium influx (Tang et al., 2011). However, this process is considered an oxidant-mediated reaction with low specificity for target proteins. C543 in the cytoplasmic I-II loop is the major glutathiolation target in hCav1.2. C543S mutation alters post-translational folding and shifts the channel open probability, which may lead to the onset of disease pathology (Muralidharan et al., 2016). Inflammation and ROS are known to be critical pathological manifestations of neurodegenerative diseases. Moreover, imbalance of glutathione homeostasis and dysregulation in glutathione-dependent enzyme activities are implicated in the induction and progression of neurodegenerative diseases, including AD, PD, and ALS. Therefore, impaired S-glutathionylation of Cav1.2 may contribute to the pathology of neurodegenerative diseases.

CAV1.2 AS A POTENTIAL DRUG TARGET IN NEURODEGENERATIVE DISEASES

Cav1.2 is a classical drug target for cardiovascular disease. Members of the dihydropyridine family of calcium channel blockers (DHPs) have been used as first-line drugs for hypertension and myocardial ischemia for decades, including amlodipine, felodipine, and nifedipine (Zamponi et al., 2015). The sensitivity of LTCCs to DHPs varies in different tissues. Cav1.2 is more sensitive to DHPs than Cav1.3 and Cav1.4 (Xu and Lipscombe, 2001). The splice variants of Cav1.2 in arterial smooth muscle are more sensitive to DHPs than those in the myocardium (Liao et al., 2004; Cheng et al., 2009).

Because of the pathophysiological role of Cav1.2 in neurodegenerative disease, DHPs have been repurposed as a treatment for these diseases. DHPs have at least two advantages as drugs for CNS indications: safety and penetration of the blood–brain barrier (BBB). At therapeutic doses, no obvious side effects were observed for muscle function, hearing, CNS function, or insulin secretion, where LTCCs exert important functions (Levine et al., 2007). Several DHPs can cross the BBB in some species, including humans (Allen et al., 1983; Uchida et al., 1997). Intracerebral drug delivery methods have also improved recently (Patel et al., 2009; Lu et al., 2014).

Because of the known role of Cav1.2 in cognition and the imbalance in Ca^{2+} homeostasis found in AD, DHPs have been repurposed for AD treatment. In a survey of investigating the association between DHP or non-DHP calcium channel blocker and risk of developing AD or mortality, researchers found that the use of DHP did not reduce risk of AD but showed lower relative risk (Yasar et al., 2005). *In vitro*, nilvadipine, nitrendipine, and amlodipine reduced Aβ accumulation by affecting the production and clearance of Aβ. *In vivo*, nilvadipine and nitrendipine reduced Aβ deposition. In transgenic mouse models of AD (Tg APPsw (Tg2576) and Tg PS1/APPsw), chronic nilvadipine treatment resulted in lower Aβ levels and improved learning and spatial memory (Paris et al., 2011). These results suggest that some DHPs have significant benefits in the treatment of AD. Nilvadipine can also delay the degeneration of cognitive function in AD patients (Hanyu et al., 2007; Matsuda et al., 2008). Nitrendipine treatment reduced the risk of dementia by 55% in hypertensive patients compared with a control group (Forette et al., 2002). Since improvements in cognition are observed with non-DHP drugs like ACEI and thiazide (Bellew et al., 2004; Hanon and Forette, 2004; Fournier et al., 2009; Duron and Hanon, 2010), the protective effects of nivadipine and nitrendipine do not seem to be related to their antihypertensive effects. Although nilvadipine and nitrendipine have protective effects, their effectiveness depends on the severity of AD (Paris et al., 2011). After nilvadipine treatment, the very mild AD group showed less cognition decline whereas the moderate AD group showed greater cognition decline compared with their respective placebo-treated controls (Abdullah et al., 2020). This study suggests that AD severity affects the treatment results and nilvadipine may be restricted to patients with mild AD in the future.

The pathological mechanisms underlying PD are not yet clear. Symptomatic treatments are aimed at relieving deficits in motor symptoms and improving quality of life (Schulz et al., 2016; Obeso et al., 2017). Currently, pharmacotherapy includes dopamine mimetics (levodopa), synergists of levodopa (selegiline, carbidopa), dopamine receptor agonists (bromocriptine), dopamine-releasing drugs (amantadine), and anticholinergic drugs (trihexsyphenidyl). Neurosurgery and supportive treatments have been used clinically for many years (Oertel and Schulz, 2016; Schulz et al., 2016). However, none of these treatment methods can prevent or slow the progression of PD and the side effects of the treatments often limit the long-term benefits of symptomatic therapies. However, there are a few different drugs currently in preclinical trials. Because of LTCC-mediated Ca^{2+} load in SNc dopaminergic neurons, DHPs are considered for PD treatment. Studies have shown that isradipine has a significant neuroprotective effect on substantia nigral dopaminergic neurons in an MPTP-induced animal model of PD (Kupsch et al., 1995; Singh et al., 2016; Wang et al., 2017) and partially restores dopamine content in the striatum (Wang et al., 2017). Another DHP, nifedipine, was reported to improve apomorphine-induced rotation behavior in 6-OHDA-lesioned rats (Wang et al., 2012).

In humans, the ongoing phase III clinical study STEADY-PD is investigating the potential of the LTCC blocker isradipine for treatment of PD. Although the study showed that long-term treatment with immediate-release isradipine did not slow the clinical progression of early-stage PD, it did modestly decrease cumulative levodopa equivalent dose and

TABLE 2 | Summary of clinical trials and surveys on the effects of DHPs in neurodegenerative diseases

Drug	Stage	Duration	Dose	Number	Indication	Results	References
Nitrendipine	Survey	3.9 years	10–40 mg/d	148	AD	Treatment with nitrendipine reduced the risk of dementia by 55%	Forette et al. (2002)
DHP	Survey	2 years	—	1,092	AD	Relative risks were low with the DHP group	Yasar et al. (2005)
DHP	Survey	2 years	—	173	PD	Exposure to DHP reduced the risk of incidence, particularly in older patients, and mortality	Pasternak et al. (2012)
Isradipine	Clinical phase III	36 m	10 mg/d	336	PD	Treatment with isradipine did not slow the clinical progression of early-stage PD	Parkinson Study Group STEADY-PD III Investigators (2020)
Isradipine	Clinical phase III	36 m	10 mg/d	166	PD	Exposure to DHP reduced the risk of needing antiparkinsonian treatment	Venuto et al. (2021)
Isradipine	Clinical phase III	36 m	10 mg/d	162	PD	Treatment with isradipine slows progression of PD disability	https://clinicaltrials.gov/ct2/show/study/NCT02168842?term=isradipine&cond=Parkinson%27s+disease&draw=2&rank=2

the time needed for antiparkinsonian treatment (McFarthing and Simuni, 2019; Parkinson Study Group STEADY-PD III Investigators, 2020; Venuto et al., 2021). According to epidemiological studies (Becker et al., 2008; Ritz et al., 2010; Pasternak et al., 2012; Lee et al., 2014) and meta-analyses (Gudala et al., 2015; Lang et al., 2015; Mullapudi et al., 2016), patients treated with DHPs have a reduced risk of PD. Although DHPs have a history of safe use, the drug release time should be prolonged to avoid activation of the sympathetic nervous system, accompanied by reflex tachycardia and high cardiac oxygen consumption, flushing, hypotension, and headache (Carrara et al., 1994; Johnson et al., 2005). In some countries, extended-release formulations of isradipine are available and are already in phase II clinical trials in PD patients (Parkinson Study Group, 2013).

Other potential treatment strategies remain to be studied. Previous data show that the basal level of Cav1.2 in the hippocampus and cortex of ovariectomized APP/PS1 mice is significantly higher than that of wild-type mice. E2 or PPT could reverse this increased basal level of Cav1.2 by promoting the ubiquitination and degradation of Cav1.2 (Lai et al., 2019). Thus, ERα agonists (propylpyrazoletriol, dienestrol) may effectively alleviate the symptoms of AD. Hu et al. used a Tat-e9c peptide to compete for the Galectin-1 binding site on Cav1.2 and interfere with its ubiquitination and degradation (Hu et al., 2018), but whether Cavβ-derived peptides can be used to promote Cav1.2 degradation in the brain needs further study. The biggest concerns would be how to transport the peptide across the BBB and how to reduce the side effects in the cardiovascular system.

CONCLUSION

Cav1.2 plays important roles in the cardiovascular system, the CNS, and endocrine glands. In the brain, it mediates learning and memory, drug addiction, and neuronal development. Cav1.2 undergoes a variety of post-translational modifications, which are altered in neurodegenerative disease states. Recently identified modifications, such as S-nitrosylation, and their role in pathology require further study.

DHPs are widely prescribed for hypertension and myocardial ischemia and have been repurposed for use in neurodegenerative diseases including AD and PD. Several clinical trials show promising outcomes (summarized in **Table 2**). Although clinical studies have shown that DHPs have protective effects on neurodegenerative diseases, there are several issues with using DHPs to treat neurodegenerative diseases. First, achieving the requisite drug concentrations in the brain while avoiding fluctuations in blood pressure and cardiac function is a challenge. This may be addressed by the development of new drug-delivery strategies. Second, the relative lack of selectivity of DHPs is a big concern for their use in the CNS; unwanted effects may arise from antagonism of Cav1.3 channels. Furthermore, the universal expression of Cav1.2 may result in DHP side effects on normal brain functions. Further studies on channel modulation and more-specific methods of altering Cav1.2 channel function may lead to better therapeutic strategies for neurodegenerative diseases.

AUTHOR CONTRIBUTIONS

YL, HY, and TH drafted the manuscript. CL and LZ critically edited the manuscript. All authors approved the manuscript in its final form.

FUNDING

This work was supported by a general project (Grant number: 81974157) from the Natural Science Foundation of China, a Jiangsu Specially-Appointed Professorship (to CL) from the Jiangsu Education Department, a Jiangsu Province Innovative and Entrepreneurial Team Program (to HZ, AL, WW, CL and YS), and a starting grant of excellent talents (to CL) from Xuzhou Medical University.

REFERENCES

Abdullah, L., Crawford, F., Tsolaki, M., Börjesson-Hanson, A., Olde Rikkert, M., Pasquier, F., et al. (2020). The Influence of Baseline Alzheimer's Disease Severity on Cognitive Decline and CSF Biomarkers in the NILVAD Trial. *Front. Neurol.* 11, 149. doi:10.3389/fneur.2020.00149

Allen, G. S., Ahn, H. S., Preziosi, T. J., Battye, R., Boone, S. C., Boone, S. C., et al. (1983). Cerebral Arterial Spasm-Aa Controlled Trial of Nimodipine in Patients with Subarachnoid Hemorrhage. *N. Engl. J. Med.* 308 (11), 619–624. doi:10.1056/NEJM198303173081103

Alves, V. S., Alves-Silva, H. S., Orts, D. J. B., Ribeiro-Silva, L., Arcisio-Miranda, M., and Oliveira, F. A. (2019). Calcium Signaling in Neurons and Glial Cells: Role of Cav1 Channels. *Neuroscience* 421, 95–111. doi:10.1016/j.neuroscience.2019.09.041

Anekonda, T. S., and Quinn, J. F. (2011). Calcium Channel Blocking as a Therapeutic Strategy for Alzheimer's Disease: the Case for Isradipine. *Biochim. Biophys. Acta* 1812 (12), 1584–1590. doi:10.1016/j.bbadis.2011.08.013

Bachnoff, N., Cohen-Kutner, M., and Atlas, D. (2011). The Involvement of Ser1898 of the Human L-type Calcium Channel in Evoked Secretion. *Int. J. Endocrinol.* 2011, 746482. doi:10.1155/2011/746482

Becker, C., Jick, S. S., and Meier, C. R. (2008). Use of Antihypertensives and the Risk of Parkinson Disease. *Neurology* 70 (16 Pt 2), 1438–1444. doi:10.1212/01.wnl.0000303818.38960.44

Begum, G., Yan, H. Q., Li, L., Singh, A., Dixon, C. E., and Sun, D. (2014). Docosahexaenoic Acid Reduces ER Stress and Abnormal Protein Accumulation and Improves Neuronal Function Following Traumatic Brain Injury. *J. Neurosci.* 34 (10), 3743–3755. doi:10.1523/JNEUROSCI.2872-13.2014

Bellew, K. M., Pigeon, J. G., Stang, P. E., Fleischman, W., Gardner, R. M., and Baker, W. W. (2004). Hypertension and the Rate of Cognitive Decline in Patients with Dementia of the Alzheimer Type. *Alzheimer Dis. Assoc. Disord.* 18 (4), 208–213.

Bennett, E. J., Bence, N. F., Jayakumar, R., and Kopito, R. R. (2005). Global Impairment of the Ubiquitin-Proteasome System by Nuclear or Cytoplasmic Protein Aggregates Precedes Inclusion Body Formation. *Mol. Cell* 17 (3), 351–365. doi:10.1016/j.molcel.2004.12.021

Beyl, S., Kügler, P., Kudrnac, M., Hohaus, A., Hering, S., and Timin, E. (2009). Different Pathways for Activation and Deactivation in CaV1.2: a Minimal Gating Model. *J. Gen. Physiol.* 134 (3), 231–241. doi:10.1085/jgp.200910272

Bhat, S., Dao, D. T., Terrillion, C. E., Arad, M., Smith, R. J., Soldatov, N. M., et al. (2012). CACNA1C (Cav1.2) in the Pathophysiology of Psychiatric Disease. *Prog. Neurobiol.* 99 (1), 1–14. doi:10.1016/j.pneurobio.2012.06.001

Blaich, A., Welling, A., Fischer, S., Wegener, J. W., Köstner, K., Hofmann, F., et al. (2010). Facilitation of Murine Cardiac L-type Ca(v)1.2 Channel Is Modulated by Calmodulin Kinase II-dependent Phosphorylation of S1512 and S1570. *Proc. Natl. Acad. Sci. U S A.* 107 (22), 10285–10289. doi:10.1073/pnas.0914287107

Brandmayr, J., Poomvanicha, M., Domes, K., Ding, J., Blaich, A., Wegener, J. W., et al. (2012). Deletion of the C-Terminal Phosphorylation Sites in the Cardiac β-subunit Does Not Affect the Basic β-adrenergic Response of the Heart and the Ca(v)1.2 Channel. *J. Biol. Chem.* 287 (27), 22584–22592. doi:10.1074/jbc.M112.366484

Bunemann, M., Gerhardstein, B. L., Gao, T., and Hosey, M. M. (1999). Functional Regulation of L-Type Calcium Channels Via Protein Kinase A-Mediated Phosphorylation of the Beta(2) Subunit. *J. Biol. Chem.* 274 (48), 33851–33854. doi:10.1074/jbc.274.48.33851

Carrara, V., Porchet, H., and Dayer, P. (1994). Influence of Input Rates on (+/-)-isradipine Haemodynamics and Concentration-Effect Relationship in Healthy Volunteers. *Eur. J. Clin. Pharmacol.* 46 (1), 29–33. doi:10.1007/BF00195912

Chen, Z. J., and Sun, L. J. (2009). Nonproteolytic Functions of Ubiquitin in Cell Signaling. *Mol. Cell* 33 (3), 275–286. doi:10.1016/j.molcel.2009.01.014

Cheng, X., Pachuau, J., Blaskova, E., Asuncion-Chin, M., Liu, J., Dopico, A. M., et al. (2009). Alternative Splicing of Cav1.2 Channel Exons in Smooth Muscle Cells of Resistance-Size Arteries Generates Currents with Unique Electrophysiological Properties. *Am. J. Physiol. Heart Circ. Physiol.* 297 (2), H680–H688. doi:10.1152/ajpheart.00109.2009

Cohen, S. M., Li, B., Tsien, R. W., and Ma, H. (2015). Evolutionary and Functional Perspectives on Signaling from Neuronal Surface to Nucleus. *Biochem. Biophys. Res. Commun.* 460 (1), 88–99. doi:10.1016/j.bbrc.2015.02.146

Dai, S., Hall, D. D., and Hell, J. W. (2009). Supramolecular Assemblies and Localized Regulation of Voltage-Gated Ion Channels. *Physiol. Rev.* 89 (2), 411–452. doi:10.1152/physrev.00029.2007

Davare, M. A., and Hell, J. W. (2003). Increased Phosphorylation of the Neuronal L-type Ca(2+) Channel Ca(v)1.2 during Aging. *Proc. Natl. Acad. Sci. U S A.* 100 (26), 16018–16023. doi:10.1073/pnas.2236970100

De Jongh, K. S., Murphy, B. J., Colvin, A. A., Hell, J. W., Takahashi, M., and Catterall, W. A. (1996). Specific Phosphorylation of a Site in the Full-Length Form of the Alpha 1 Subunit of the Cardiac L-type Calcium Channel by Adenosine 3',5'-cyclic Monophosphate-dependent Protein Kinase. *Biochemistry* 35 (32), 10392–10402. doi:10.1021/bi953023c

Duron, E., and Hanon, O. (2010). Antihypertensive Treatments, Cognitive Decline, and Dementia. *J. Alzheimers Dis.* 20 (3), 903–914. doi:10.3233/JAD-2010-091552

Ertel, E. A., Campbell, K. P., Harpold, M. M., Hofmann, F., Mori, Y., Perez-Reyes, E., et al. (2000). Nomenclature of Voltage-Gated Calcium Channels. *Neuron* 25 (3), 533–535. doi:10.1016/s0896-6273(00)81057-0

Felix, R., and Weiss, N. (2017). Ubiquitination and Proteasome-Mediated Degradation of Voltage-Gated Ca2+ Channels and Potential Pathophysiological Implications. *Gen. Physiol. Biophys.* 36 (1), 1–5. doi:10.4149/gpb_2016037

Forette, F., Seux, M. L., Staessen, J. A., Thijs, L., Babarskiene, M. R., Babeanu, S., et al. (2002). The Prevention of Dementia with Antihypertensive Treatment: New Evidence from the Systolic Hypertension in Europe (Syst-Eur) Study. *Arch. Intern. Med.* 162 (18), 2046–2052. doi:10.1001/archinte.162.18.2046

Fournier, A., Oprisiu-Fournier, R., Serot, J. M., Godefroy, O., Achard, J. M., Faure, S., et al. (2009). Prevention of Dementia by Antihypertensive Drugs: How AT1-Receptor-Blockers and Dihydropyridines Better Prevent Dementia in Hypertensive Patients Than Thiazides and ACE-Inhibitors. *Expert Rev. Neurother* 9 (9), 1413–1431. doi:10.1586/ern.09.89

Fuller, M. D., Emrick, M. A., Sadilek, M., Scheuer, T., and Catterall, W. A. (2010). Molecular Mechanism of Calcium Channel Regulation in the Fight-Or-Flight Response. *Sci. Signal.* 3 (141), ra70. doi:10.1126/scisignal.2001152

Gerhardstein, B. L., Puri, T. S., Chien, A. J., and Hosey, M. M. (1999). Identification of the Sites Phosphorylated by Cyclic AMP-dependent Protein Kinase on the Beta 2 Subunit of L-type Voltage-dependent Calcium Channels. *Biochemistry* 38 (32), 10361–10370. doi:10.1021/bi990896o

Goonasekera, S. A., Hammer, K., Auger-Messier, M., Bodi, I., Chen, X., Zhang, H., et al. (2012). Decreased Cardiac L-type Ca^{2+} Channel Activity Induces Hypertrophy and Heart Failure in Mice. *J. Clin. Invest.* 122 (1), 280–290. doi:10.1172/JCI58227

Govoni, S., Bergamaschi, S., Racchi, M., Battaini, F., Binetti, G., Bianchetti, A., et al. (1993). Cytosol Protein Kinase C Downregulation in Fibroblasts from Alzheimer's Disease Patients. *Neurology* 43 (12), 2581–2586. doi:10.1212/wnl.43.12.2581

Grueter, C. E., Abiria, S. A., Dzhura, I., Wu, Y., Ham, A. J., Mohler, P. J., et al. (2006). L-type Ca2+ Channel Facilitation Mediated by Phosphorylation of the Beta Subunit by CaMKII. *Mol. Cell* 23 (5), 641–650. doi:10.1016/j.molcel.2006.07.006

Gudala, K., Kanukula, R., and Bansal, D. (2015). Reduced Risk of Parkinson's Disease in Users of Calcium Channel Blockers: A Meta-Analysis. *Int. J. Chronic Dis.* 2015, 697404. doi:10.1155/2015/697404

Gui, P., Wu, X., Ling, S., Stotz, S. C., Winkfein, R. J., Wilson, E., et al. (2006). Integrin Receptor Activation Triggers Converging Regulation of Cav1.2 Calcium Channels by C-Src and Protein Kinase A Pathways. *J. Biol. Chem.* 281 (20), 14015–14025. doi:10.1074/jbc.M600433200

Hanon, O., and Forette, F. (2004). Prevention of Dementia: Lessons from SYST-EUR and PROGRESS. *J. Neurol. Sci.* 226 (1-2), 71–74. doi:10.1016/j.jns.2004.09.015

Hanyu, H., Hirao, K., Shimizu, S., Sato, T., Kiuchi, A., and Iwamoto, T. (2007). Nilvadipine Prevents Cognitive Decline of Patients with Mild Cognitive Impairment. *Int. J. Geriatr. Psychiatry* 22 (12), 1264–1266. doi:10.1002/gps.1851

Hara, T., Nakamura, K., Matsui, M., Yamamoto, A., Nakahara, Y., Suzuki-Migishima, R., et al. (2006). Suppression of Basal Autophagy in Neural Cells Causes Neurodegenerative Disease in Mice. *Nature* 441 (7095), 885–889. doi:10.1038/nature04724

Hell, J. W., Westenbroek, R. E., Warner, C., Ahlijanian, M. K., Prystay, W., Gilbert, M. M., et al. (1993). Identification and Differential Subcellular Localization of the Neuronal Class C and Class D L-type Calcium Channel Alpha 1 Subunits. *J. Cell Biol* 123 (4), 949–962. doi:10.1083/jcb.123.4.949

Hering, S., Zangerl-Plessl, E. M., Beyl, S., Hohaus, A., Andranovits, S., and Timin, E. N. (2018). Calcium Channel Gating. *Pflugers Arch.* 470 (9), 1291–1309. doi:10.1007/s00424-018-2163-7

Hershko, A., and Ciechanover, A. (1998). The Ubiquitin System. *Annu. Rev. Biochem.* 67, 425–479. doi:10.1146/annurev.biochem.67.1.425

Hetzenauer, A., Sinnegger-Brauns, M. J., Striessnig, J., and Singewald, N. (2006). Brain Activation Pattern Induced by Stimulation of L-type Ca2+-Channels: Contribution of Ca(V)1.3 and Ca(V)1.2 Isoforms. *Neuroscience* 139 (3), 1005–1015. doi:10.1016/j.neuroscience.2006.01.059

Hofmann, F., Flockerzi, V., Kahl, S., and Wegener, J. W. (2014). L-type CaV1.2 Calcium Channels: from *In Vitro* Findings to *In Vivo* Function. *Physiol. Rev.* 94 (1), 303–326. doi:10.1152/physrev.00016.2013

Hu, Z., Li, G., Wang, J. W., Chong, S. Y., Yu, D., Wang, X., et al. (2018). Regulation of Blood Pressure by Targeting CaV1.2-Galectin-1 Protein Interaction. *Circulation* 138 (14), 1431–1445. doi:10.1161/CIRCULATIONAHA.117.031231

Huttlin, E. L., Jedrychowski, M. P., Elias, J. E., Goswami, T., Rad, R., Beausoleil, S. A., et al. (2010). A Tissue-specific Atlas of Mouse Protein Phosphorylation and Expression. *Cell* 143 (7), 1174–1189. doi:10.1016/j.cell.2010.12.001

Ikeda, F., and Dikic, I. (2008). Atypical Ubiquitin Chains: New Molecular Signals. 'Protein Modifications: Beyond the Usual Suspects' Review Series. *EMBO Rep.* 9 (6), 536–542. doi:10.1038/embor.2008.93

Johnson, B. A., Javors, M. A., Lam, Y. W., Wells, L. T., Tiouririne, M., Roache, J. D., et al. (2005). Kinetic and Cardiovascular Comparison of Immediate-Release Isradipine and Sustained-Release Isradipine Among Non-treatment-seeking, Cocaine-dependent Individuals. *Prog. Neuropsychopharmacol. Biol. Psychiatry* 29 (1), 15–20. doi:10.1016/j.pnpbp.2004.08.014

Kavalali, E. T., Hwang, K. S., and Plummer, M. R. (1997). cAMP-Dependent Enhancement of Dihydropyridine-Sensitive Calcium Channel Availability in Hippocampal Neurons. *J. Neurosci.* 17 (14), 5334–5348. doi:10.1523/jneurosci.17-14-05334.1997

Khachaturian, Z. S. (1989). Calcium, Membranes, Aging, and Alzheimer's Disease. Introduction and Overview. *Ann. N. Y Acad. Sci.* 568, 1–4. doi:10.1111/j.1749-6632.1989.tb12485.x

Knorre, D. G., Kudryashova, N. V., and Godovikova, T. S. (2009). Chemical and Functional Aspects of Posttranslational Modification of Proteins. *Acta Naturae* 1 (3), 29–51. doi:10.32607/actanaturae.10755

Kupsch, A., Gerlach, M., Pupeter, S. C., Sautter, J., Dirr, A., Arnold, G., et al. (1995). Pretreatment with Nimodipine Prevents MPTP-Induced Neurotoxicity at the Nigral, but Not at the Striatal Level in Mice. *Neuroreport* 6 (4), 621–625. doi:10.1097/00001756-199503000-00009

Lai, Y. J., Zhu, B. L., Sun, F., Luo, D., Ma, Y. L., Luo, B., et al. (2019). Estrogen Receptor α Promotes Cav1.2 Ubiquitination and Degradation in Neuronal Cells and in APP/PS1 Mice. *Aging Cell* 18 (4), e12961. doi:10.1111/acel.12961

Lam, Y. A., Pickart, C. M., Alban, A., Landon, M., Jamieson, C., Ramage, R., et al. (2000). Inhibition of the Ubiquitin-Proteasome System in Alzheimer's Disease. *Proc. Natl. Acad. Sci. U S A.* 97 (18), 9902–9906. doi:10.1073/pnas.170173897

Lang, Y., Gong, D., and Fan, Y. (2015). Calcium Channel Blocker Use and Risk of Parkinson's Disease: a Meta-Analysis. *Pharmacoepidemiol. Drug Saf.* 24 (6), 559–566. doi:10.1002/pds.3781

Lee, Y. C., Lin, C. H., Wu, R. M., Lin, J. W., Chang, C. H., and Lai, M. S. (2014). Antihypertensive Agents and Risk of Parkinson's Disease: a Nationwide Cohort Study. *PLoS One* 9 (6), e98961. doi:10.1371/journal.pone.0098961

Lei, M., Xu, J., Gao, Q., Minobe, E., Kameyama, M., and Hao, L. (2018). PKA Phosphorylation of Cav1.2 Channel Modulates the Interaction of Calmodulin with the C Terminal Tail of the Channel. *J. Pharmacol. Sci.* 137 (2), 187–194. doi:10.1016/j.jphs.2018.05.010

Levine, M., Boyer, E. W., Pozner, C. N., Geib, A. J., Thomsen, T., Mick, N., et al. (2007). Assessment of Hyperglycemia after Calcium Channel Blocker Overdoses Involving Diltiazem or Verapamil. *Crit. Care Med.* 35 (9), 2071–2075. doi:10.1097/01.ccm.0000278916.04569.23

Li, J., Wang, S., Zhang, J., Liu, Y., Zheng, X., Ding, F., et al. (2020). The CaMKII Phosphorylation Site Thr1604 in the CaV1.2 Channel Is Involved in Pathological Myocardial Hypertrophy in Rats. *Channels (Austin)* 14 (1), 151–162. doi:10.1080/19336950.2020.1750189

Liao, P., Yu, D., Lu, S., Tang, Z., Liang, M. C., Zeng, S., et al. (2004). Smooth Muscle-Selective Alternatively Spliced Exon Generates Functional Variation in Cav1.2 Calcium Channels. *J. Biol. Chem.* 279 (48), 50329–50335. doi:10.1074/jbc.M409436200

Liu, B., Spearman, M., Doering, J., Lattová, E., Perreault, H., and Butler, M. (2014). The Availability of Glucose to CHO Cells Affects the Intracellular Lipid-Linked Oligosaccharide Distribution, Site Occupancy and the N-Glycosylation Profile of a Monoclonal Antibody. *J. Biotechnol.* 170, 17–27. doi:10.1016/j.jbiotec.2013.11.007

Logsdon, A. F., Lucke-Wold, B. P., Nguyen, L., Matsumoto, R. R., Turner, R. C., Rosen, C. L., et al. (2016). Salubrinal Reduces Oxidative Stress, Neuroinflammation and Impulsive-like Behavior in a Rodent Model of Traumatic Brain Injury. *Brain Res.* 1643, 140–151. doi:10.1016/j.brainres.2016.04.063

Loh, K. W. Z., Liang, M. C., Soong, T. W., and Hu, Z. (2020). Regulation of Cardiovascular Calcium Channel Activity by post-translational Modifications or Interacting Proteins. *Pflugers Arch.* 472 (6), 653–667. doi:10.1007/s00424-020-02398-x

Lu, C. T., Zhao, Y. Z., Wong, H. L., Cai, J., Peng, L., and Tian, X. Q. (2014). Current Approaches to Enhance CNS Delivery of Drugs across the Brain Barriers. *Int. J. Nanomedicine* 9, 2241–2257. doi:10.2147/IJN.S61288

Lucke-Wold, B. P., Turner, R. C., Logsdon, A. F., Bailes, J. E., Huber, J. D., and Rosen, C. L. (2014). Linking Traumatic Brain Injury to Chronic Traumatic Encephalopathy: Identification of Potential Mechanisms Leading to Neurofibrillary Tangle Development. *J. Neurotrauma* 31 (13), 1129–1138. doi:10.1089/neu.2013.3303

Lucke-Wold, B. P., Turner, R. C., Logsdon, A. F., Nguyen, L., Bailes, J. E., Lee, J. M., et al. (2016). Endoplasmic Reticulum Stress Implicated in Chronic Traumatic Encephalopathy. *J. Neurosurg.* 124 (3), 687–702. doi:10.3171/2015.3.JNS141802

Lucke-Wold, B. P., Turner, R. C., Logsdon, A. F., Simpkins, J. W., Alkon, D. L., Smith, K. E., et al. (2015). Common Mechanisms of Alzheimer's Disease and Ischemic Stroke: the Role of Protein Kinase C in the Progression of Age-Related Neurodegeneration. *J. Alzheimers Dis.* 43 (3), 711–724. doi:10.3233/JAD-141422

Malenka, R. C., and Bear, M. F. (2004). LTP and LTD: an Embarrassment of Riches. *Neuron* 44 (1), 5–21. doi:10.1016/j.neuron.2004.09.012

Marais, E., Klugbauer, N., and Hofmann, F. (2001). Calcium Channel Alpha(2) delta Subunits-Structure and Gabapentin Binding. *Mol. Pharmacol.* 59 (5), 1243–1248. doi:10.1124/mol.59.5.1243

Martínez, M., Hernández, A. I., and Hernanz, A. (2001). Increased cAMP Immunostaining in Cerebral Vessels in Alzheimer's Disease. *Brain Res.* 922 (1), 148–152. doi:10.1016/s0006-8993(01)03009-8

Matsuda, H., Araki, N., Kuji, I., Ohkubo, T., Imabayashi, E., and Shimazu, K. (2008). Effect of Nilvadipine on Regional Cerebral Blood Flow in a Patient with Early Alzheimer Disease. *Clin. Nucl. Med.* 33 (1), 34–35. doi:10.1097/RLU.0b013e31815c4ff0

McFarthing, K., and Simuni, T. (2019). Clinical Trial Highlights: Phase III Study in Spotlight. *J. Parkinsons Dis.* 9 (1), 3–4. doi:10.3233/JPD-190002

Mikami, A., Imoto, K., Tanabe, T., Niidome, T., Mori, Y., Takeshima, H., et al. (1989). Primary Structure and Functional Expression of the Cardiac Dihydropyridine-Sensitive Calcium Channel. *Nature* 340 (6230), 230–233. doi:10.1038/340230a0

Moon, A. L., Haan, N., Wilkinson, L. S., Thomas, K. L., and Hall, J. (2018). CACNA1C: Association with Psychiatric Disorders, Behavior, and Neurogenesis. *Schizophr Bull.* 44 (5), 958–965. doi:10.1093/schbul/sby096

Moosmang, S., Haider, N., Klugbauer, N., Adelsberger, H., Langwieser, N., Müller, J., et al. (2005). Role of Hippocampal Cav1.2 Ca2+ Channels in NMDA Receptor-independent Synaptic Plasticity and Spatial Memory. *J. Neurosci.* 25 (43), 9883–9892. doi:10.1523/JNEUROSCI.1531-05.2005

Mullapudi, A., Gudala, K., Boya, C. S., and Bansal, D. (2016). Risk of Parkinson's Disease in the Users of Antihypertensive Agents: An Evidence from the Meta-Analysis of Observational Studies. *J. Neurodegener Dis.* 2016, 5780809. doi:10.1155/2016/5780809

Muralidharan, P., Cserne Szappanos, H., Ingley, E., and Hool, L. (2016). Evidence for Redox Sensing by a Human Cardiac Calcium Channel. *Sci. Rep.* 6, 19067. doi:10.1038/srep19067

Murphy, J. G., Sanderson, J. L., Gorski, J. A., Scott, J. D., Catterall, W. A., Sather, W. A., et al. (2014). AKAP-anchored PKA Maintains Neuronal L-type Calcium Channel Activity and NFAT Transcriptional Signaling. *Cell Rep* 7 (5), 1577–1588. doi:10.1016/j.celrep.2014.04.027

Nanou, E., and Catterall, W. A. (2018). Calcium Channels, Synaptic Plasticity, and Neuropsychiatric Disease. *Neuron* 98 (3), 466–481. doi:10.1016/j.neuron.2018.03.017

Navakkode, S., Liu, C., and Soong, T. W. (2018). Altered Function of Neuronal L-type Calcium Channels in Ageing and Neuroinflammation: Implications in Age-Related Synaptic Dysfunction and Cognitive Decline. *Ageing Res. Rev.* 42, 86–99. doi:10.1016/j.arr.2018.01.001

Núñez-Santana, F. L., Oh, M. M., Antion, M. D., Lee, A., Hell, J. W., and Disterhoft, J. F. (2014). Surface L-type Ca2+ Channel Expression Levels Are Increased in Aged hippocampus. *Aging Cell* 13 (1), 111–120. doi:10.1111/acel.12157

Nystoriak, M. A., Nieves-Cintrón, M., Patriarchi, T., Buonarati, O. R., Prada, M. P., Morotti, S., et al. (2017). Ser1928 Phosphorylation by PKA Stimulates the L-type Ca2+ Channel CaV1.2 and Vasoconstriction during Acute Hyperglycemia and Diabetes. *Sci. Signal.* 10 (463), eaaf9647. doi:10.1126/scisignal.aaf9647

Obeso, J. A., Stamelou, M., Goetz, C. G., Poewe, W., Lang, A. E., Weintraub, D., et al. (2017). Past, Present, and Future of Parkinson's Disease: A Special Essay on the 200th Anniversary of the Shaking Palsy. *Mov Disord.* 32 (9), 1264–1310. doi:10.1002/mds.27115

Oertel, W., and Schulz, J. B. (2016). Current and Experimental Treatments of Parkinson Disease: A Guide for Neuroscientists. *J. Neurochem.* 139 (Suppl. 1), 325–337. doi:10.1111/jnc.13750

Pankonien, I., Otto, A., Dascal, N., Morano, I., and Haase, H. (2012). Ahnak1 Interaction Is Affected by Phosphorylation of Ser-296 on Cavβ₂. *Biochem. Biophys. Res. Commun.* 421 (2), 184–189. doi:10.1016/j.bbrc.2012.03.132

Paris, D., Bachmeier, C., Patel, N., Quadros, A., Volmar, C.-H., Laporte, V., et al. (2011). Selective Antihypertensive Dihydropyridines Lower Aβ Accumulation by Targeting Both the Production and the Clearance of Aβ across the Blood-Brain Barrier. *Mol. Med.* 17 (3-4), 149–162. doi:10.2119/molmed.2010.00180

Park, H. J., Min, S. H., Won, Y. J., and Lee, J. H. (2015). Asn-Linked Glycosylation Contributes to Surface Expression and Voltage-dependent Gating of Cav1.2 Ca²⁺ Channel. *J. Microbiol. Biotechnol.* 25 (8), 1371–1379. doi:10.4014/jmb.1501.01066

Parkinson Study Group (2013). Phase II Safety, Tolerability, and Dose Selection Study of Isradipine as a Potential Disease-Modifying Intervention in Early Parkinson's Disease (STEADY-PD). *Mov Disord.* 28 (13), 1823–1831. doi:10.1002/mds.25639

Parkinson Study Group STEADY-PD III Investigators (2020). Isradipine versus Placebo in Early Parkinson Disease: A Randomized Trial. *Ann. Intern. Med.* 172 (9), 591–598. doi:10.7326/M19-2534

Pasternak, B., Svanström, H., Nielsen, N. M., Fugger, L., Melbye, M., and Hviid, A. (2012). Use of Calcium Channel Blockers and Parkinson's Disease. *Am. J. Epidemiol.* 175 (7), 627–635. doi:10.1093/aje/kwr362

Patel, M. M., Goyal, B. R., Bhadada, S. V., Bhatt, J. S., and Amin, A. F. (2009). Getting into the Brain: Approaches to Enhance Brain Drug Delivery. *CNS Drugs* 23 (1), 35–58. doi:10.2165/0023210-200923010-00003

Perez-Reyes, E., Castellano, A., Kim, H. S., Bertrand, P., Baggstrom, E., Lacerda, A. E., et al. (1992). Cloning and Expression of a Cardiac/brain Beta Subunit of the L-type Calcium Channel. *J. Biol. Chem.* 267 (3), 1792–1797. doi:10.1016/s0021-9258(18)46015-2

Perovic, M., Tesic, V., Mladenovic Djordjevic, A., Smiljanic, K., Loncarevic-Vasiljkovic, N., Ruzdijic, S., et al. (2013). BDNF Transcripts, proBDNF and proNGF, in the Cortex and hippocampus throughout the Life Span of the Rat. *Age (Dordr)* 35 (6), 2057–2070. doi:10.1007/s11357-012-9495-6

Popovic, D., Vucic, D., and Dikic, I. (2014). Ubiquitination in Disease Pathogenesis and Treatment. *Nat. Med.* 20 (11), 1242–1253. doi:10.1038/nm.3739

Qian, H., Patriarchi, T., Price, J. L., Matt, L., Lee, B., Nieves-Cintrón, M., et al. (2017). Phosphorylation of Ser1928 Mediates the Enhanced Activity of the L-type Ca2+ Channel Cav1.2 by the β2-adrenergic Receptor in Neurons. *Sci. Signal.* 10 (463). doi:10.1126/scisignal.aaf9659

Ritz, B., Rhodes, S. L., Qian, L., Schernhammer, E., Olsen, J. H., and Friis, S. (2010). L-Type Calcium Channel Blockers and Parkinson Disease in Denmark. *Ann. Neurol.* 67 (5), 600–606. doi:10.1002/ana.21937

Sanders, O., and Rajagopal, L. (2020). Phosphodiesterase Inhibitors for Alzheimer's Disease: A Systematic Review of Clinical Trials and Epidemiology with a Mechanistic Rationale. *J. Alzheimers Dis. Rep.* 4 (1), 185–215. doi:10.3233/ADR-200191

Schulz, J. B., Hausmann, L., and Hardy, J. (2016). 199 Years of Parkinson Disease - what Have We Learned and what Is the Path to the Future? *J. Neurochem.* 139 (Suppl. 1), 3–7. doi:10.1111/jnc.13733

Sculptoreanu, A., Rotman, E., Takahashi, M., Scheuer, T., and Catterall, W. A. (1993). Voltage-dependent Potentiation of the Activity of Cardiac L-type Calcium Channel Alpha 1 Subunits Due to Phosphorylation by cAMP-dependent Protein Kinase. *Proc. Natl. Acad. Sci. U S A.* 90 (21), 10135–10139. doi:10.1073/pnas.90.21.10135

Singh, A., Verma, P., Balaji, G., Samantaray, S., and Mohanakumar, K. P. (2016). Nimodipine, an L-type Calcium Channel Blocker Attenuates Mitochondrial Dysfunctions to Protect against 1-Methyl-4-Phenyl-1,2,3,6-Tetrahydropyridine-Induced Parkinsonism in Mice. *Neurochem. Int.* 99, 221–232. doi:10.1016/j.neuint.2016.07.003

Splawski, I., Timothy, K. W., Sharpe, L. M., Decher, N., Kumar, P., Bloise, R., et al. (2004). Ca(V)1.2 Calcium Channel Dysfunction Causes a Multisystem Disorder Including Arrhythmia and Autism. *Cell* 119 (1), 19–31. doi:10.1016/j.cell.2004.09.011

Striessnig, J., Pinggera, A., Kaur, G., Bock, G., and Tuluc, P. (2014). L-type Ca2+ Channels in Heart and Brain. *Wiley Interdiscip. Rev. Membr. Transp Signal.* 3 (2), 15–38. doi:10.1002/wmts.102

Surguchov, A. (2020). Caveolin: A New Link between Diabetes and AD. *Cell Mol Neurobiol* 40 (7), 1059–1066. doi:10.1007/s10571-020-00796-4

Swatek, K. N., and Komander, D. (2016). Ubiquitin Modifications. *Cell Res* 26 (4), 399–422. doi:10.1038/cr.2016.39

Tang, H., Viola, H. M., Filipovska, A., and Hool, L. C. (2011). Ca(v)1.2 Calcium Channel Is Glutathionylated during Oxidative Stress in guinea Pig and Ischemic Human Heart. *Free Radic. Biol. Med.* 51 (8), 1501–1511. doi:10.1016/j.freeradbiomed.2011.07.005

Tétreault, M. P., Bourdin, B., Briot, J., Segura, E., Lesage, S., Fiset, C., et al. (2016). Identification of Glycosylation Sites Essential for Surface Expression of the CaVα2δ1 Subunit and Modulation of the Cardiac CaV1.2 Channel Activity. *J. Biol. Chem.* 291 (9), 4826–4843. doi:10.1074/jbc.M115.692178

Uchida, S., Yamada, S., Nagai, K., Deguchi, Y., and Kimura, R. (1997). Brain Pharmacokinetics and *In Vivo* Receptor Binding of 1,4-dihydropyridine Calcium Channel Antagonists. *Life Sci.* 61 (21), 2083–2090. doi:10.1016/s0024-3205(97)00881-3

Venuto, C. S., Yang, L., Javidnia, M., Oakes, D., James Surmeier, D., and Simuni, T. (2021). Isradipine Plasma Pharmacokinetics and Exposure-Response in Early Parkinson's Disease. *Ann. Clin. Transl Neurol.* 8 (3), 603–612. doi:10.1002/acn3.51300

Villacrés, C., Tayi, V. S., Lattová, E., Perreault, H., and Butler, M. (2015). Low Glucose Depletes Glycan Precursors, Reduces Site Occupancy and Galactosylation of a Monoclonal Antibody in CHO Cell Culture. *Biotechnol. J.* 10 (7), 1051–1066. doi:10.1002/biot.201400662

Walker, D. M., and Nestler, E. J. (2018). Neuroepigenetics and Addiction. *Handb Clin. Neurol.* 148, 747–765. doi:10.1016/B978-0-444-64076-5.00048-X

Wang, D., Papp, A. C., Binkley, P. F., Johnson, J. A., and Sadée, W. (2006). Highly Variable mRNA Expression and Splicing of L-type Voltage-dependent Calcium Channel Alpha Subunit 1C in Human Heart Tissues. *Pharmacogenet Genomics* 16 (10), 735–745. doi:10.1097/01.fpc.0000230119.34205.8a

Wang, Q. M., Xu, Y. Y., Liu, S., and Ma, Z. G. (2017). Isradipine Attenuates MPTP-Induced Dopamine Neuron Degeneration by Inhibiting Up-Regulation of L-type Calcium Channels and Iron Accumulation in the Substantia Nigra of Mice. *Oncotarget* 8 (29), 47284–47295. doi:10.18632/oncotarget.17618

Wang, R., Ma, Z., Wang, J., and Xie, J. (2012). L-type Cav1.2 Calcium Channel Is Involved in 6-Hydroxydopamine-Induced Neurotoxicity in Rats. *Neurotox Res.* 21 (3), 266–270. doi:10.1007/s12640-011-9271-x

Weiss, S., Keren-Raifman, T., Oz, S., Ben Mocha, A., Haase, H., and Dascal, N. (2012). Modulation of Distinct Isoforms of L-type Calcium Channels by G(q)-coupled Receptors in Xenopus Oocytes: Antagonistic Effects of Gβγ and Protein Kinase C. *Channels (Austin)* 6 (6), 426–437. doi:10.4161/chan.22016

Whitcomb, V., Wauson, E., Christian, D., Clayton, S., Giles, J., and Tran, Q. K. (2020). Regulation of Beta Adrenoceptor-Mediated Myocardial Contraction and Calcium Dynamics by the G Protein-Coupled Estrogen Receptor 1. *Biochem. Pharmacol.* 171, 113727. doi:10.1016/j.bcp.2019.113727

Xu, H., Ginsburg, K. S., Hall, D. D., Zimmermann, M., Stein, I. S., Zhang, M., et al. (2010). Targeting of Protein Phosphatases PP2A and PP2B to the C-Terminus of the L-type Calcium Channel Ca v1.2. *Biochemistry* 49 (48), 10298–10307. doi:10.1021/bi101018c

Xu, W., and Lipscombe, D. (2001). Neuronal Ca(V)1.3alpha(1) L-type Channels Activate at Relatively Hyperpolarized Membrane Potentials and Are Incompletely Inhibited by Dihydropyridines. *J. Neurosci.* 21 (16), 5944–5951. doi:10.1523/jneurosci.21-16-05944.2001

Yang, L., Dai, D. F., Yuan, C., Westenbroek, R. E., Yu, H., West, N., et al. (2016). Loss of β-adrenergic-stimulated Phosphorylation of CaV1.2 Channels on Ser1700 Leads to Heart Failure. *Proc. Natl. Acad. Sci. U S A.* 113 (49), E7976–E7985. doi:10.1073/pnas.1617116113

Yang, L., Liu, G., Zakharov, S. I., Bellinger, A. M., Mongillo, M., and Marx, S. O. (2007). Protein Kinase G Phosphorylates Cav1.2 Alpha1c and Beta2 Subunits. *Circ. Res.* 101 (5), 465–474. doi:10.1161/CIRCRESAHA.107.156976

Yang, L., Liu, G., Zakharov, S. I., Morrow, J. P., Rybin, V. O., Steinberg, S. F., et al. (2005). Ser1928 Is a Common Site for Cav1.2 Phosphorylation by Protein Kinase C Isoforms. *J. Biol. Chem.* 280 (1), 207–214. doi:10.1074/jbc.M410509200

Yasar, S., Corrada, M., Brookmeyer, R., and Kawas, C. (2005). Calcium Channel Blockers and Risk of AD: the Baltimore Longitudinal Study of Aging. *Neurobiol. Aging* 26 (2), 157–163. doi:10.1016/j.neurobiolaging.2004.03.009

Zamponi, G. W., Striessnig, J., Koschak, A., and Dolphin, A. C. (2015). The Physiology, Pathology, and Pharmacology of Voltage-Gated Calcium Channels and Their Future Therapeutic Potential. *Pharmacol. Rev.* 67 (4), 821–870. doi:10.1124/pr.114.009654

Zhang, Y. Q., and Sarge, K. D. (2008). Sumoylation of Amyloid Precursor Protein Negatively Regulates Abeta Aggregate Levels. *Biochem. Biophys. Res. Commun.* 374 (4), 673–678. doi:10.1016/j.bbrc.2008.07.109

Conflict of Interest: The authors declare that the research was conducted in the absence of any commercial or financial relationships that could be construed as a potential conflict of interest.

Publisher's Note: All claims expressed in this article are solely those of the authors and do not necessarily represent those of their affiliated organizations, or those of the publisher, the editors, and the reviewers. Any product that may be evaluated in this article, or claim that may be made by its manufacturer, is not guaranteed or endorsed by the publisher.

Copyright © 2022 Li, Yang, He, Zhang and Liu. This is an open-access article distributed under the terms of the Creative Commons Attribution License (CC BY). The use, distribution or reproduction in other forums is permitted, provided the original author(s) and the copyright owner(s) are credited and that the original publication in this journal is cited, in accordance with accepted academic practice. No use, distribution or reproduction is permitted which does not comply with these terms.

Advantages of publishing in Frontiers

OPEN ACCESS
Articles are free to read
for greatest visibility
and readership

FAST PUBLICATION
Around 90 days
from submission
to decision

HIGH QUALITY PEER-REVIEW
Rigorous, collaborative,
and constructive
peer-review

TRANSPARENT PEER-REVIEW
Editors and reviewers
acknowledged by name
on published articles

Frontiers
Avenue du Tribunal-Fédéral 34
1005 Lausanne | Switzerland

Visit us: www.frontiersin.org
Contact us: frontiersin.org/about/contact

REPRODUCIBILITY OF RESEARCH
Support open data
and methods to enhance
research reproducibility

DIGITAL PUBLISHING
Articles designed
for optimal readership
across devices

FOLLOW US
@frontiersin

IMPACT METRICS
Advanced article metrics
track visibility across
digital media

EXTENSIVE PROMOTION
Marketing
and promotion
of impactful research

LOOP RESEARCH NETWORK
Our network
increases your
article's readership